THE CELLULAR BIOMINERALIZATION PATHWAYS OF MARINE ORGANISMS

EDITED BY: Andrew Stanley Mount, Alfred Portius Wheeler and Vera Bin San Chan

PUBLISHED IN: Frontiers in Marine Science

frontiers Research Topics

frontiers

ISSN 1664-8714
ISBN 978-2-88971-957-0
DOI 10.3389/978-2-88971-957-0

About Frontiers

Frontiers is more than just an open-access publisher of scholarly articles: it is a pioneering approach to the world of academia, radically improving the way scholarly research is managed. The grand vision of Frontiers is a world where all people have an equal opportunity to seek, share and generate knowledge. Frontiers provides immediate and permanent online open access to all its publications, but this alone is not enough to realize our grand goals.

Frontiers Journal Series

The Frontiers Journal Series is a multi-tier and interdisciplinary set of open-access, online journals, promising a paradigm shift from the current review, selection and dissemination processes in academic publishing. All Frontiers journals are driven by researchers for researchers; therefore, they constitute a service to the scholarly community. At the same time, the Frontiers Journal Series operates on a revolutionary invention, the tiered publishing system, initially addressing specific communities of scholars, and gradually climbing up to broader public understanding, thus serving the interests of the lay society, too.

Dedication to Quality

Each Frontiers article is a landmark of the highest quality, thanks to genuinely collaborative interactions between authors and review editors, who include some of the world's best academicians. Research must be certified by peers before entering a stream of knowledge that may eventually reach the public - and shape society; therefore, Frontiers only applies the most rigorous and unbiased reviews.
Frontiers revolutionizes research publishing by freely delivering the most outstanding research, evaluated with no bias from both the academic and social point of view. By applying the most advanced information technologies, Frontiers is catapulting scholarly publishing into a new generation.

What are Frontiers Research Topics?

Frontiers Research Topics are very popular trademarks of the Frontiers Journals Series: they are collections of at least ten articles, all centered on a particular subject. With their unique mix of varied contributions from Original Research to Review Articles, Frontiers Research Topics unify the most influential researchers, the latest key findings and historical advances in a hot research area! Find out more on how to host your own Frontiers Research Topic or contribute to one as an author by contacting the Frontiers Editorial Office: frontiersin.org/about/contact

THE CELLULAR BIOMINERALIZATION PATHWAYS OF MARINE ORGANISMS

Topic Editors:
Andrew Stanley Mount, Clemson University, United States
Alfred Portius Wheeler, Clemson University, United States
Vera Bin San Chan, Clemson University, United States

Citation: Mount, A. S., Wheeler, A. P., Chan, V. B. S., eds. (2021). The Cellular Biomineralization Pathways of Marine Organisms. Lausanne: Frontiers Media SA. doi: 10.3389/978-2-88971-957-0

Table of Contents

frontiers in Marine Science

ORIGINAL RESEARCH
published: 28 February 2018
doi: 10.3389/fmars.2018.00067

Reading the Fine Print: Ultra-Microstructures of Foraminiferal Calcification Revealed Using Focused Ion Beam Microscopy

Yukiko Nagai[1,2], *Katsuyuki Uematsu*[3], *Ryoji Wani*[4] *and Takashi Toyofuku*[2,5]*

[1] Graduate School of Environment and Information Sciences, Yokohama National University, Yokohama, Japan, [2] Department of Biodivesity, Japan Agency for Marine-Earth Science and Technology, Yokosuka, Japan, [3] Marine Works Japan LTD, Yokosuka, Japan, [4] Faculty of Environment and Information Sciences, Yokohama National University, Yokohama, Japan, [5] Tokyo University of Marine Science and Technology, Tokyo, Japan

The elemental composition of calcite is of critical value in paleoceanographic reconstructions, yet little is known about biological processes underlying elemental uptake by foraminifers during calcification. Especially crucial in the understanding of elemental composition and distribution is the involvement of organic templates separating different layers of calcite forming the wall of a foraminiferal chamber. In this study, we applied the focused ion beam (FIB) scanning electron microscopy (SEM) technique to the site of calcification (SOC) in a newly growing chamber of *Ammonia "beccarii"*, a benthic foraminifer, to reveal the ultra- and microstructure during calcification. This allowed cross-sections of both soft and hard tissues, allowing detailed observation of the SOC across a series of calcification stages. For the first time, we show that numerous voids of calcareous layers and internal organic structures are present within the SOC during the calcification process. The series of SEM observations suggest that organic layers are actively involved in calcite precipitation. We provide the first evidence that the SOC is isolated from surrounding seawater during calcification. Our findings improve the understanding of foraminiferal biomineralization and characterize key conditions under which element partitioning and isotope fractionation occur.

Keywords: foraminifera, biomineralization, ultrastructure, calcification, FIB, SEM, marine biology, micropaleontology

OPEN ACCESS

Edited by:
Andrew Stanley Mount, Clemson University, United States

Reviewed by:
Gary H. Dickinson, The College of New Jersey, United States
Dennis A. Bazylinski, University of Nevada, Las Vegas, United States

***Correspondence:**
Takashi Toyofuku
toyofuku@jamstec.go.jp

Specialty section:
This article was submitted to Marine Molecular Biology and Ecology, a section of the journal Frontiers in Marine Science

Received: *25 July 2017*
Accepted: *14 February 2018*
Published: *28 February 2018*

Citation:
Nagai Y, Uematsu K, Wani R and Toyofuku T (2018) Reading the Fine Print: Ultra-Microstructures of Foraminiferal Calcification Revealed Using Focused Ion Beam Microscopy. Front. Mar. Sci. 5:67. doi: 10.3389/fmars.2018.00067

INTRODUCTION

Foraminifera is a group of ameboid protists which form calcareous exoskeletons ("tests") that are commonly preserved in sediments and constitutes a widely used tool for paleoceanographic reconstructions. This is achieved by either using known ecological preferences of a particular group or by analyzing the test chemistry which reflects ambient environmental conditions during the foraminifer's lifespan. The incorporation of magnesium, for instance, is known to be primarily governed by temperature (Nürnberg et al., 1996; Elderfield and Ganssen, 2000; Anand et al., 2003) and therefore used to reconstruct oceanic thermal history (e.g., Lear et al., 2000).

Improved analytical techniques have enhanced our knowledge regarding spatial resolution and chemical characterization of foraminiferal tests. The use of spot analytical tools such as electron

probe micro analysis (EPMA), laser ablation inductively coupled plasma mass spectrometry (LA-ICP-MS), and secondary ionized mass spectrometry (SIMS) reveals large intra- and inter-specific variability in the elemental and isotopic composition of foraminiferal tests. These can be attributed to a combination of species-specific biological conditions and environmental factors such as temperature, salinity, and seawater chemistry (e.g., Eggins et al., 2003; Erez, 2003; Sadekov et al., 2005; Toyofuku and Kitazato, 2005; Kunioka et al., 2006; De Nooijer et al., 2014a). In addition, condensed bands of magnesium, barium and sulfur are found in close association with the organic template within chamber walls (e.g., Kunioka et al., 2006; Paris et al., 2014; Spero et al., 2015; Van Dijk et al., 2017). The origin of these bands and the physiological processes responsible for their elemental uptake and incorporation are only partly understood (Elderfield et al., 1996; Zeebe and Sanyal, 2002; Erez, 2003; Toyofuku et al., 2008, 2017; De Nooijer et al., 2014b). To improve the reliability of foraminifer-based proxies it is crucial to identify and understand complex components of their biomineralization.

A pioneering study by Angell (1967) observed the relationship between newly precipitated calcite and cell materials in the benthic foraminifer *Rosalina floridana* by combining optical microscopy (OM), transmission electron microscopy (TEM) and scanning electron microscopy (SEM). There were numerous foamy structures described to be present at the site of calcification (SOC), which were shown to form the base of the initial organic matrix, termed "*Anlage*." The *Anlage* is fibrous and composed of spherical structures. After its construction, microcrystals are deposited to form the layer of the chamber wall. Hemleben et al. (1986) also combined OM, TEM, and SEM to show the involvement of various foam-like structures during calcification in the planktonic foraminifer *Globorotalia truncatulinoides*. The *Anlage* was acting as an organic template for calcification in this species too. Later, the *Anlage* has also been referred to as Primary Organic Membrane (POM), and more recently the term Primary Organic Sheet (POS) has been proposed (Erez, 2003).

Spero (1988) showed TEM and SEM images of the calcification of the planktonic foraminifer *Orbulina universa*. Numerous vesiculate organic structures (submicron-1 μm in diameter) were present around the organic layers of both inner and outer surface of calcite wall, suggesting that this layer is actively involved in manipulating the chemistry of the fluid in the SOC. In addition, the primary organic sheet was found to be sandwiched by calcite layers, followed by outer and inner organic layers. It was also indicated that the primary organic sheet served as an organic calcification template on which the first layer of calcite was precipitated. The formation of pores, one important feature of foraminifera, was also shown. SEM micrographs of the constructing chamber showed that three organic layers (the outer organic layer, the inner organic layer, and the primary organic sheet) converged at the pore plates. In many subsequent studies (e.g., Spero, 1988; Bentov and Erez, 2006; De Nooijer et al., 2009a) it was assumed that the space between the primary organic sheet and the outer (as well as the inner) organic layer is completely filled by calcium carbonate during biomineralization.

A number of previous studies on biomineralization showed that the SOC (also termed the "deliminated space") in a variety of organisms are partly occupied by small volumes of fluid within calcite layers (Wilbur, 1964; Mann, 2001; Tambutté et al., 2011; Keul et al., 2017). These pockets of fluid, if present, likely reflect the manipulated solution from which calcium carbonate is precipitated. In foraminifera, it has recently been shown by ratiometric fluorescent probe with pyranine (De Nooijer et al., 2009a) and micro glass electrode (Glas et al., 2012) that this fluid has a considerably higher pH than the surrounding medium, a result of proton pumping during calcification (Toyofuku et al., 2017). The external-internal pH difference may be as large as 2 pH units, meaning the SOC is well separated from the outside environment. This has important implications for the incorporation of elements, since they have been proposed to result from seawater entering the SOC (Erez, 2003; Bentov and Erez, 2006).

Among various calcification models proposed for foraminifera, Nehrke et al. (2013) proposed that ions other than calcium and carbonate (e.g., Mg^{2+}, Sr^{2+}, $B(OH)_4^-$) enter the SOC via a combination of Transmembrane Transport (TMT) and Passive Transport (PT) which is compatible with the SOC being separated from surrounding seawater. This model could be extended if the microstructure of the SOC and the flux of ion inwards could be accurately established. Observations on the SOC are currently limited to SEM observations, only showing the surface of the outer organic layer or the calcite layer.

To reveal the detailed configuration of the SOC, we fixed calcifying specimens of the benthic foraminifer *Ammonia "beccarii"* and subsequently prepared cross-sections using focused ion beam (FIB) to observe the detailed microstructure. The exposed sites of calcification were analyzed to determine their appearance and development throughout the process of chamber formation. Here, we focus on the structures that constitute the SOC, which we define here as the combination of the organic structures, the precipitated calcium carbonate, and the spaces between them, that together form the foraminiferal chamber wall.

MATERIALS AND METHODS

Sample Collection and Laboratory Culture

Living foraminifera were collected from brackish salt marsh sediments of Hiragata bay, Natsushima-cho, Yokosuka, Japan (35°19′21″N, 139°38′5″E). Surface (the top 5 mm) sediments were collected and transported to the laboratory to serve as a stock from which foraminifera were isolated. Living specimens were recognized by their bright yellow coloration and pseudopodial activity. They were cleaned from excess sediment and debris under a stereomicroscope (SteREO Discovery V12, Zeiss Co. Ltd.) and then transferred to filtered (0.2 μm) natural seawater (salinity 35) in a Petri dish. The dishes were maintained as stock cultures at 20°C and a small amount of living microalgae (*Dunaliella tertiolecta*) were added to the Petri dishes twice a week. Within a few days after feeding, some individuals started chamber formation and were selected for observation.

Prior to chamber formation, foraminifera retract their psuedopodia and stay in a fixed location (**Figure 1A**). After that, the cytoplasm forms a shape corresponding to the new chamber

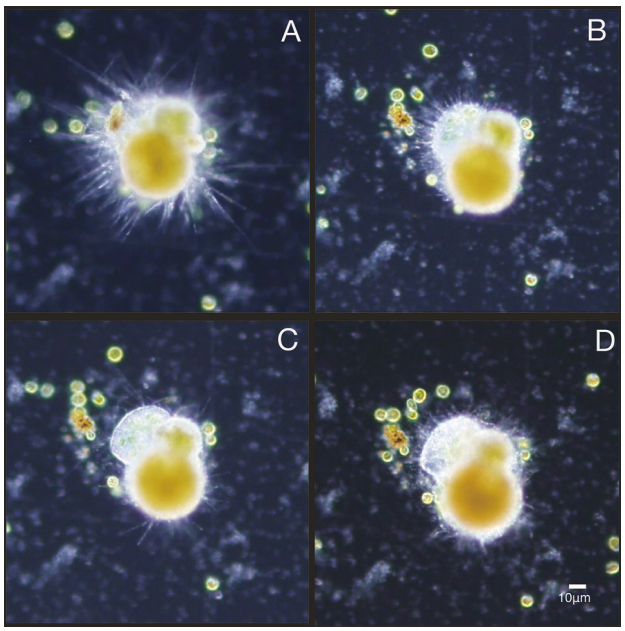

FIGURE 1 | Chamber formation of the studied species *Ammonia "beccarii"*. **(A)** Just before forming a new chamber, with many fine filamentous pseudopodia protruding from the existing test. **(B)** About 20 min after shell formation started. **(C)** About 2 h after shell formation started. **(D)** About 5 h from the start of shell formation when chamber thickening takes place.

to be formed (**Figure 1B**). Calcium carbonate precipitation can be identified by the bright rim of the formed cytoplasmic structure (**Figure 1C**) and then the chamber wall is thickened (**Figure 1D**). The formation of a new chamber takes 8–12 h in this species. By comparing with the sequence shown in **Figure 1**, our fixed specimens were estimated to have been fixed 2–4 h after the calcification process started. Five individuals with differing thickness of the new chamber wall were selected for FIB-SEM observation. These individuals were given sequential numbers #1-#5 from the thinnest to the thickest new chamber wall.

Microstructure Observation and EDS Analysis

All specimens were fixed simultaneously using a fixing solution (3% paraformaldehyde, 0.3% glutaraldehyde, 2% NaCl in PBS buffer, pH 7.8) and subsequently stored in 2.5% glutaraldehyde at 4°C to avoid any morphological changes in cell material by dehydration. They were then washed in filtered seawater, postfixed with 2% osmium tetra oxide filtered seawater for 2 h at 4°C. Then the specimens were rinsed with distilled water and conductive staining was performed by incubating in 0.2% aqueous tannic acid (pH 6.8) for 30 min. Following another wash using distilled water specimens were treated with 1% aqueous osmium tetra oxide for 1 h. Finally, they were dehydrated in a graded ethanol series and critical point dried (JCPD5; JEOL Ltd., Tokyo, Japan). All specimens were placed on glass plates for FIB cutting after drying to reduce handling damage. Specimens #1 and #3 were sputter coated with carbon, sectioned using a Hitachi MI4000L Focused Ion Beam SEM (FIB-SEM) system using gallium ion beam at the high voltage electron microscope (HVEM) laboratory, Nagoya university, Japan, with additional SEM observations carried out on a JSM6700F field emission scanning electron microscope (FE-SEM) in Japan Agency for Marine-Earth Science and Technology (JAMSTEC), Yokosuka, Japan. Specimens #2, #4, and #5 were osmium-coated and sectioned also using gallium ion beam with a FEI Helios G4 UX FIB-SEM (JAMSTEC). Elemental composition of all specimens was analyzed using a EDAX Octane Elite Super 70 energy dispersive spectrometer (EDS) equipped on the Helios G4 UX at JAMSTEC.

RESULTS

Scanning electron micrographs of cross sections of the newly forming chamber wall in the five specimens, representing different stages of calcification, are shown in **Figures 2**–**6**. For the ease of direct comparison, **Figure 7** shows the cross sections at the same scale. Specimen #1 had the thinnest SOC (**Figure 7A**). The width of the SOC increased with thickening of the crystal layers from Specimen #1 (**Figure 7A**; ∼0.5 μm) to Specimen #5 (**Figure 7E**; ∼1.5 μm). By having a series of five specimens in progressive calcification stages, the similarity of the structures in Specimen #1 and #5 can be confirmed, even if they appear quite different at the first glance. **Figure 8** shows the calcium (Ca) distribution from SEM-EDS measurement at the SOC in all specimens (**Figure 8**, **Figure S1**). Ca signals overlapped on the calcareous layers. The spot analyses showed there were carbon (C), oxygen (O) and Ca signals detected with silicon (Si), gallium (Ga), osmium (Os) on the wall layer (**Figure 8E**-3). The elements Ca, O, and C are consistent with chemical contents of calcium carbonate, Ga was the source of FIB used for specimen cutting, Os is from osmium coating of the specimens, and Si is interpreted to be from glass plates used to handle the specimens post-critical point drying.

The growth of SOC was documented sequentially from Specimen #1 to #5 (**Figures 2**–**7**). Calcareous layers were sparser in specimens #1 and #2 (**Figures 7A,B**) compared to specimens #3–#5 (**Figures 7C–E**). The calcareous layers were horizontally divided into the outer calcareous layer (OCL in **Figures 2C**, **6C**) and the inner calcareous layer (ICL in **Figures 2C**, **6C**) by the boundary (POS in **Figures 2C**, **6C**) on all specimens. The primary organic sheet is clearly visible in specimens #1–#3 (POS in **Figures 2C**, **4C**), but in specimens #4–#5 the primary organic sheet was not clearly visible and instead a series of small cavities were visible in the same position (POS in **Figures 5C**, **6C**). The outer calcareous layers were slightly thicker than the inner layers in specimens #4 and #5 (**Figures 5C**, **6C**). Focusing on the morphology of the materials in the calcareous layer, blocky, parabolic conical, and columnar shapes were observed in specimens #1 and #2 (C in **Figures 2D,E**, **3D,E**). All of these shapes were in contact with either the primary organic sheet, the inner/outer organic layers, or both. The horizontal space between these materials decreased in specimen #3 (**Figure 4C**). Then, calcareous layers further increased in abundance in specimens #4

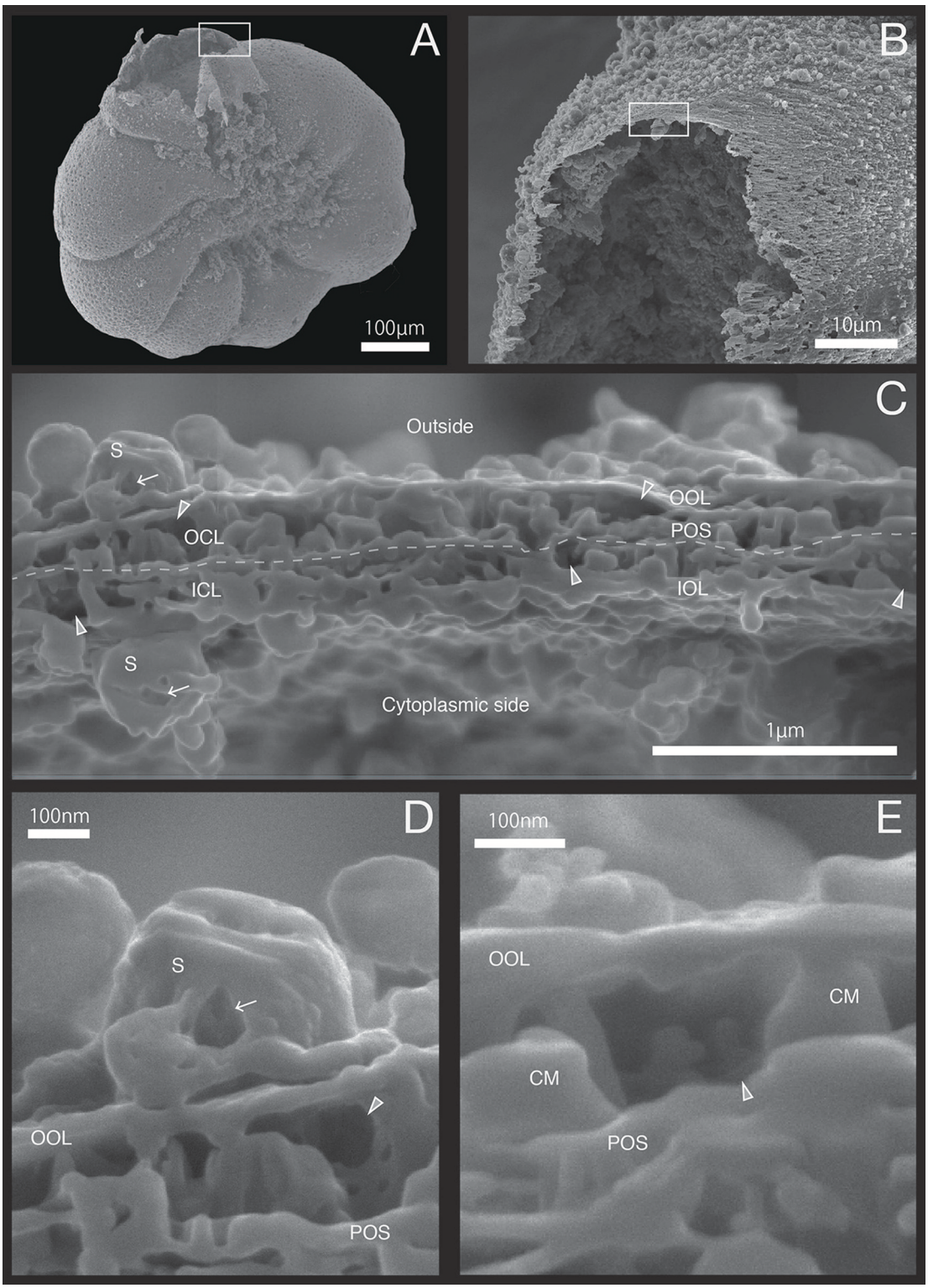

FIGURE 2 | SEM images showing the microstructure of the SOC in specimen #1 processed by FIB on the newly calcified chamber wall. **(A)** Overview. **(B)** The newly calcified chamber (white rectangle in **(A)**. The field of FIB processing is indicated by the white rectangle. **(C)** Composite SEM cross section of SOC of specimen #1. Upper side is the outside whereas the lower side is the cytoplasm side. The white dotted line in the calcareous layer indicates the boundary between outer side and cytoplasmic side of calcareous layer. **(D)** Magnified image of the empty inside of spherical structures on outer organic layer. **(E)** Higher magnification showing the void. OOL, outer organic layer; OCL, outer calcareous layer; POS, primary organic sheet; ICL, inner calcareous layer; IOL, inner organic layer; S, spherical structures; CM, calcareous materials; gray triangles, void; white arrows, cavities.

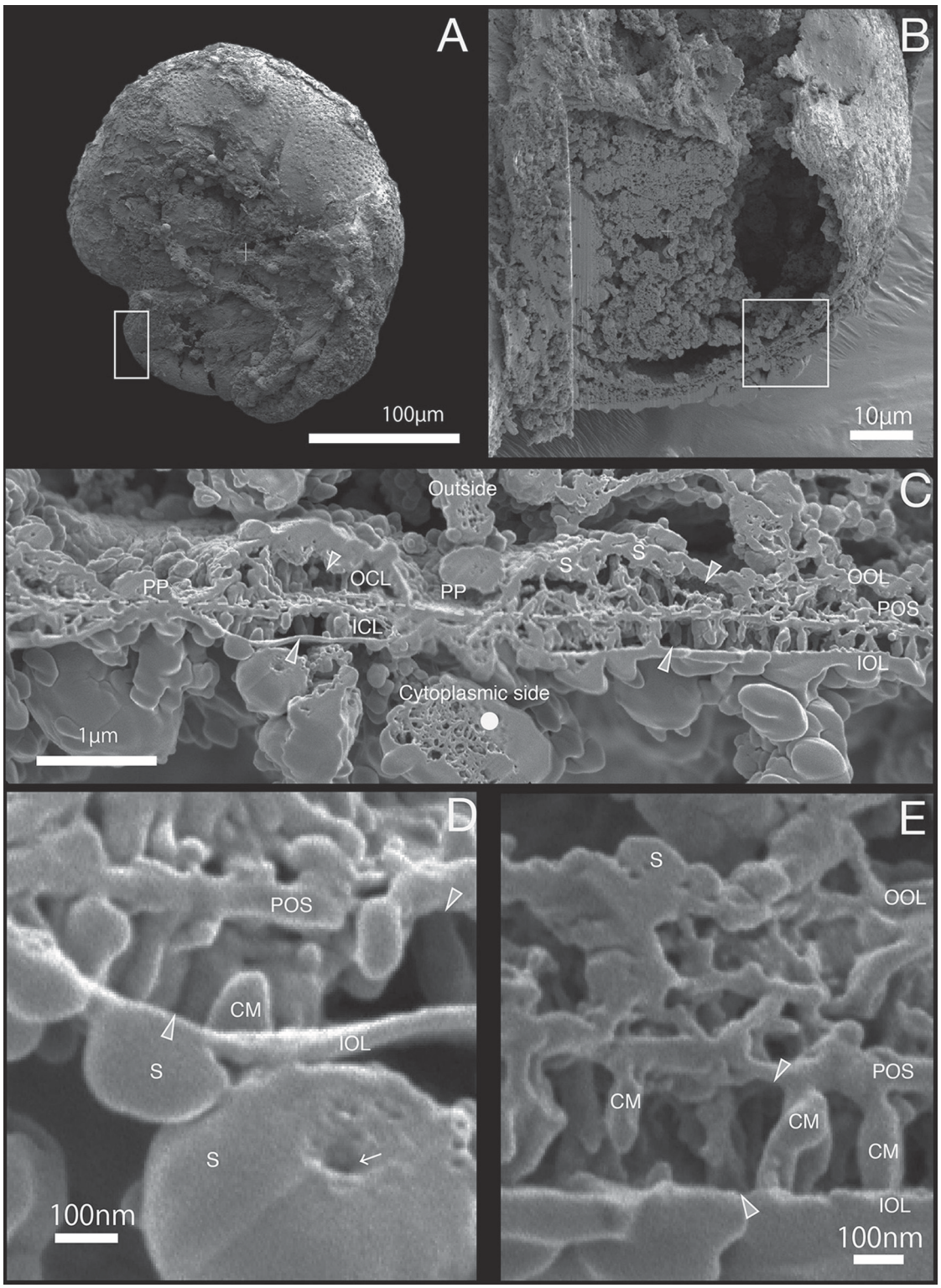

FIGURE 3 | SEM images of specimen #2. **(A)** Overview. The white rectangle indicates the obseved newly calcifing chamber. **(B)** The newly calcified chamber (white rectangle in **(A)**. The field of FIB processing is indicated by the white rectangle. **(C)** Composite SEM image of the FIB processed SOC. Upper side is the outside and whereas the lower side is the cytoplasmic side. The white dotted line in the calcareous layer indicates the boundary between outer side and cytoplasmic side of calcareous layer. **(D)** Magnified image of small calcareous materials. **(E)** Higher magnification showing the details of SOC. OOL, outer organic layer; OCL, outer calcareous layer; POS, primary organic sheet; ICL, inner calcareous layer; IOL, inner organic layer; S, spherical structures; CM, calcareous materials; PP, pore plate; gray triangles, void; white arrows, cavities; white dot, sponge like structure.

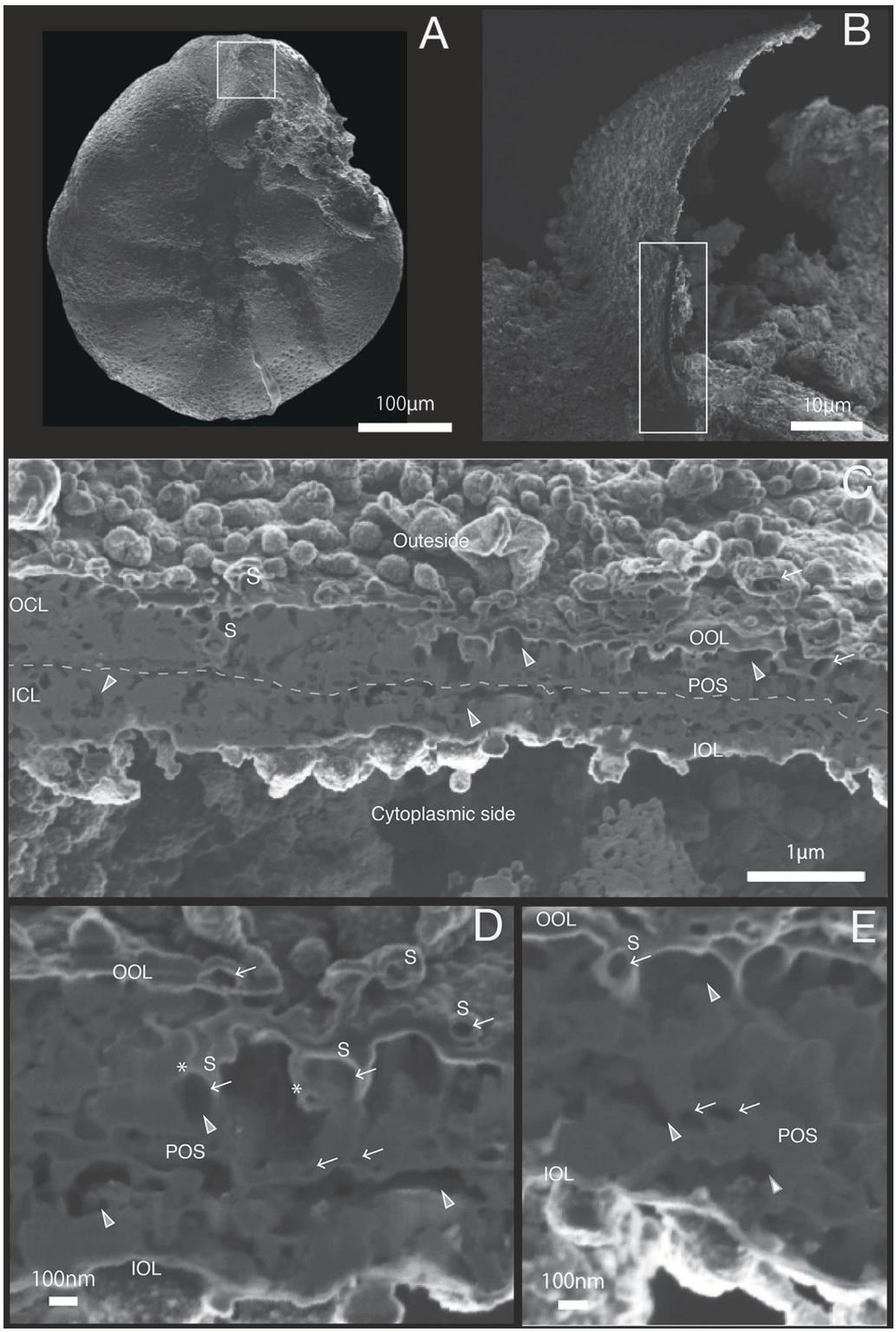

FIGURE 4 | SEM images of specimen #3. **(A)** Overview. **(B)** The newly calcified chamber (white rectangle in **(A)**. The field of FIB processing is indicated by the white rectangle. **(C)** Composite SEM image of the FIB processed SOC. Upper side is the outer side and whereas the lower side is the cytoplasmic side. White dotted line in the calcareous layer indicates the boundary between outer side and cytoplasmic side of calcareous layer. **(D)** Magnified image of porous structure of SOC. **(E)** Higher magnification showing the cavities within primary organic sheet and outer organic layer. OOL, outer organic layer; OCL, outer calcareous layer; POS, primary organic sheet; ICL, inner calcareous layer; IOL, inner organic layer; S, spherical structures; CM, calcareous materials; gray triangle, void; white arrow, cavity; asterisk, opening spherical structure from cavity into void.

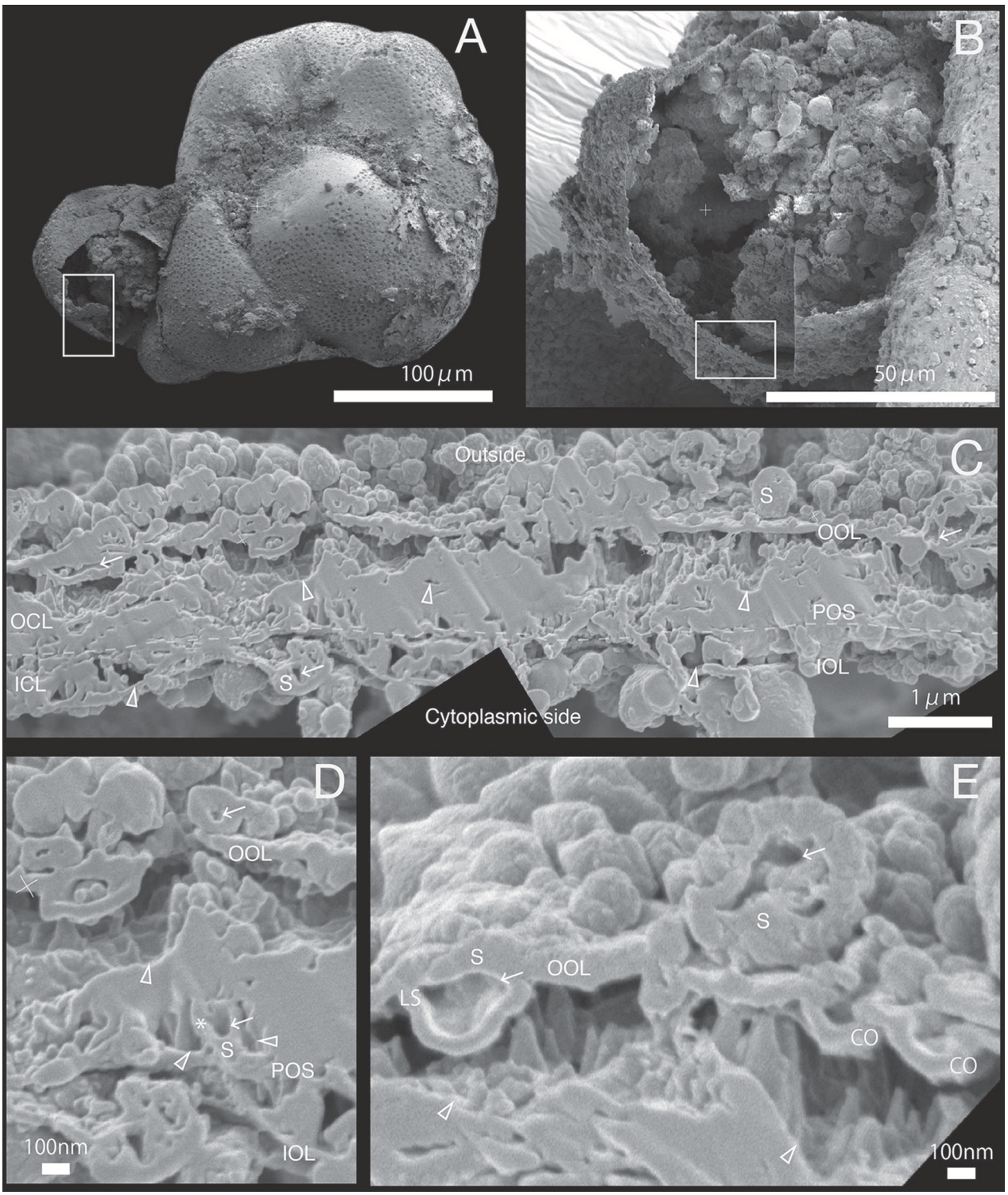

FIGURE 5 | SEM images of specimen #4. **(A)** Overview. **(B)** The newly calcified chamber (white rectangle in **(A)**. The field of FIB processing is indicated by the white rectangle.**(C)** Composite SEM image of the FIB processed SOC. The upper side is the outer side and whereas the lower side is the cytoplasmic side. White dotted line in the calcareous layer indicates the boundary between outer side and cytoplasmic side of calcareous layer. **(D)** Magnified image of spherical structure on primary organic sheet. **(E)** Higher magnification showing the outer organic layer is cave into void of outer calcareous layer (CO). A cavity (white arrow) can be identified on spherical structure of outer organic layer (LS). OOL, outer organic layer; OCL, outer calcareous layer; POS, primary organic sheet; ICL, inner calcareous layer; IOL, inner organic layer; S, spherical structures; CM, calcareous materials; PP, pore plate; gray triangles, void; white arrows, cavities in the organic structure; CO, concavity; asterisk, opening spherical structure from cavity into void; LS, spherical structure with larger cavity.

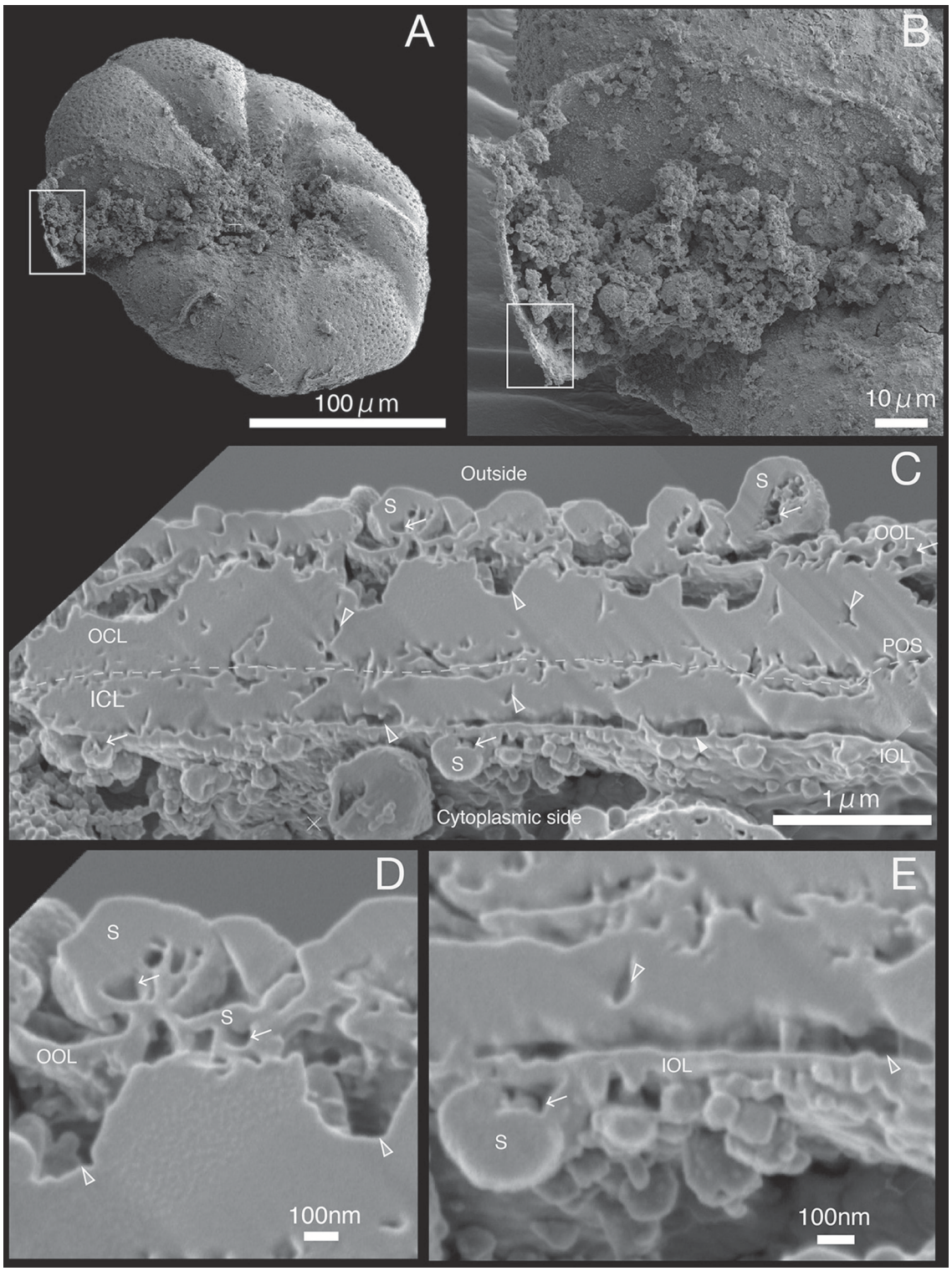

FIGURE 6 | SEM images of specimen #5. **(A)** Overview. **(B)** The newly calcified chamber (white rectangle in **(A)**. The field of FIB processing is indicated by the white rectangle. **(C)** Composite SEM image of the FIB processed SOC. The upper side is the outer side and whereas the lower side is the cytoplasmic side. White dotted line in the calcareous layer indicates the boundary between outer side and cytoplasmic side of calcareous layer. **(D)** Magnified image of the contact place between outer organic layer and outer calcareous layer. **(E)** Higher magnification showing the adjoining place between inner organic layers with inner calcareous layer. OOL, outer organic layer; OCL, outer calcareous layer; POS, primary organic sheet; ICL, inner calcareous layer; IOL, inner organic layer; S, spherical structures; CM, calcareous materials; gray triangles, void; white arrows, cavities in the organic structure.

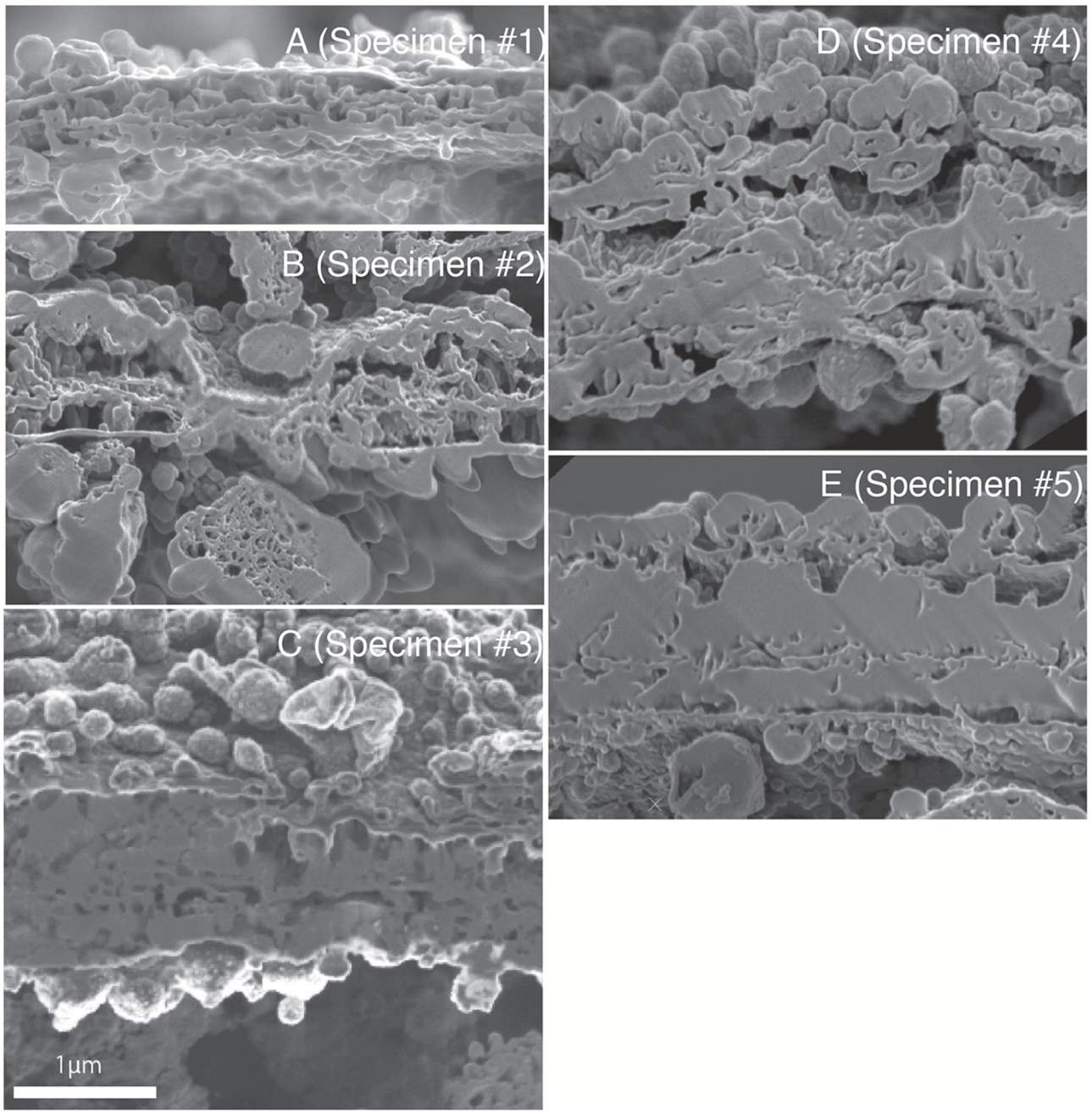

FIGURE 7 | The SEM image of the SOC on the same magnification of all observed specimens. (**A–E**) corresponding to Specimen #1 to #5, respectively.

and #5 (**Figures 5C**, **6C**). A sharp, serrated surface was seen on the calcareous layer of specimen #4 (**Figure 5E**).

Spatial voids existed between the calcareous layers, facing both outer and inner organic layers in all specimens (gray triangles in **Figures 2C**, **6C**). Some voids were also found around the primary organic sheet (gray triangles in **Figures 4D,E**, **5D**). Spherical structures were found in both outer and inner organic layers at all stages (S in **Figures 2**–**6**). Some cavities were found in the spherical structures and primary organic sheet (white arrows in **Figures 2**–**6**). These spherical structures varied in size between ∼100 nm and ∼1 μm. Occasionally, spherical structures with a diameter of ∼0.5–1 μm were seen with a spongy interior (white dot in **Figure 3C**). Convex structures were observed on calcareous sides of the organic layer and were positionally arranged toward the calcareous layer (asterisks in **Figure 4D**) and the primary organic sheet (asterisk in **Figure 5D**). As the calcareous layer developed, larger spherical structure were formed overhanging into the space of the calcareous layer side

from outer organic structure (LS in **Figure 5E**). Also, the convex shapes were found to intrude into the space toward calcareous layer (CO in **Figure 5E**). The spherical structures and cavities were more frequently found on the thicker specimens #3–#5 than the thinner specimens #1 and #2. Pore plates were also identified on specimen #2 (PP in **Figure 3C**). Outer and inner organic layers converged into each other at the position of the primary organic sheet.

DISCUSSION

The benthic foraminifer *Ammonia "beccarii"* and other *Ammonia* species are widely distributed and can be found in many coastal environments including tidal flats, harbors and brackish lakes. Due to its tolerance to a wide range of environmental parameters, it is a popular genus to employ in laboratory cultures and are used to calibrate elemental/isotopic geochemical signatures as functions of physical and chemical conditions. As a result, over 20 studies have analyzed geochemical signatures and calcification process in this genus (**Table 1**). This makes understanding the detailed micro-configuration of the SOC in this genus crucially important in the interpretation of the results from such studies. This was made possible in this study through application of the FIB-SEM technique which allows making sections through calcareous material at a fine scale.

Structures Within the Site of Calcification During Chamber Formation

The foraminiferal SOC has not been pictured before in cross-section and our results allow for the first time to characterize the distribution of calcareous materials between the primary organic sheet and the outer and inner organic layers during chamber formation (**Figures 2**–**8**). These materials are shown to grow over time by gradually filling the space between the primary organic sheet and outer and inner organic layers (**Figures 2C**, **6C**). Growth of the calcareous chamber wall is bidirectional from the primary organic sheet toward the outside as well as the cytoplasmic side, as was generally accepted. Meanwhile, some calcareous materials were found to attach only on the outer or inner organic layer (**Figure 3D**). At some locations, calcareous materials were bridged on either side of the primary organic sheet to the outer or inner organic layers (**Figures 2C**, **3C,D**), while the cavities between materials appeared to have been filled-in horizontally afterwards (Specimen #3–#5). We interpret that the calcification processes happens continuously and that thereby the chamber wall thickens over time. In some locations, no calcareous materials grew yet and voids remained, which would supply the source for construction of calcareous wall. Then these voids would be pushed away by the growing calcareous test and moved to the top of the growing surface. A schematic illustration is shown in **Figure 9**.

Although the composition of fluids within these voids has not been characterized yet, it would likely have a similar composition to the calcification fluid described for bivalves and corals (Wilbur, 1964; Erez, 2003; Tambutté et al., 2011; De Nooijer et al., 2014b; Keul et al., 2017; Toyofuku et al., 2017). Previous studies (e.g., Angell, 1979) showed that the distribution of organic structures within the foraminiferal chamber wall and assumed that small black dots adhering to the membrane were calcium carbonate microcrystals. In addition, such calcium carbonate crystals were assumed to have filled the vacant holes in ultrathin TEM sections in the later stages of calcification,

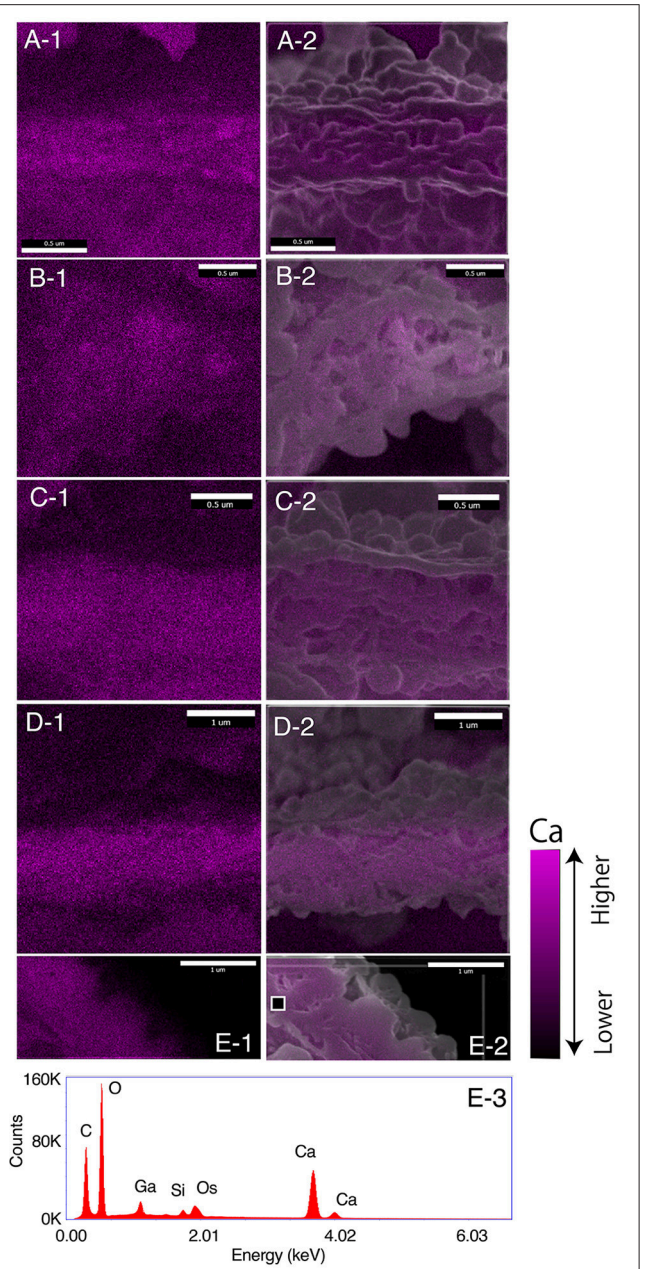

FIGURE 8 | EDS results on the SOC for specimens #1 to #5. **(A–E)** corresponding to specimen #1 to #5.−1, calcium distributions;−2, calcium image superimposed on the SEM image. The brightness of calcium distribution shows the intensity of calcium signal as legend of the bottom right. E-3, EDS spectrum of spot measurement on the black square on E-1 of specimen #5.

TABLE 1 | Evaluation of geochemical signatures and calcification process in *Ammonia* species.

Study	Species	Topic
Toyofuku et al., 2011	*Ammonia "beccarii"*	Temperature, Salinity on Mg/Ca, $\delta^{18}O$ from culture
Diz et al., 2012	*Ammonia tepida*	Salinity on Mg/Ca and Sr/Ca heterogeneity, $\delta^{18}O$, $\delta^{13}C$ from culture
De Nooijer et al., 2014a	*Ammonia tepida*	Mg and Sr heterogeneity in clones from culture
Dissard et al., 2010	*Ammonia tepida*	pCO_2 on Mg/Ca and Sr/Ca from culture
Dissard et al., 2010	*Ammonia tepida*	Salinity on Mg/Ca and Sr/Ca, from culture
Raitzsch et al., 2010	*Ammonia tepida*	$[Ca^{2+}]/\Omega_{Calcite}$ on Mg/Ca and Sr/Ca from culture
Dueñas-Bohórquez et al., 2011	*Ammonia tepida*	$[Ca^{2+}]$ and $[CO_3^{2-}]$ on Mg/Ca and Sr/Ca from culture
Mewes et al., 2014	*Ammonia aomoriensis*	$[Mg^{2+}]$ on Mg/Ca from culture
Mewes et al., 2015	*Ammonia aomoriensis*	$[Mg^{2+}]$ on Sr/Ca from culture
Keul et al., 2017	*Ammonia* sp.	$[CO_3^{2-}]$ on Sr/Ca from culture
Le Cadre and Debenay, 2006	*Ammonia beccarii*	$[Cu^{2+}]$ on Cu/Ca and distortion of morphology from culture
	Ammonia tepida	
Maréchal-Abram et al., 2004	*Ammonia beccarii*	$[Cd^{2+}]$ on Cd/Ca from culture.
Munsel et al., 2010	*Ammonia tepida*	$[Ni^{2+}]$, $[Cu^{2+}]$, $[Mn^{2+}]$ on Ni/Ca, Cu/Ca, Mn/Ca from culture
Havach et al., 2001	*Ammonia beccarii*	$[Ba^{2+}]$, $[Cd^{2+}]$ on Ba/Ca, Cd/Ca from culture
Keul et al., 2013a,b	*Ammonia* sp.	U/Casw on U/Ca from culture
De Nooijer et al., 2009b	*Ammonia tepida*	Seawater uptake and calcification via culture
Nehrke et al., 2013	*Ammonia aomoriensis*	$[^{44}Ca^{2+}]$ on $^{44}Ca/^{40}Ca$ and seawater uptake and calcification via culture
De Nooijer et al., 2008	*Ammonia beccarii*	pH imaging
De Nooijer et al., 2009a	*Ammonia beccarii*	pH imaging
Glas et al., 2012	*Ammonia* sp.	pH variability during calcification via culture
Toyofuku et al., 2008	*Ammonia beccarii*	Ca imaging during calcification via culture
Keul et al., 2013b	*Ammonia* sp.	$[CO_3^{2-}]$ on calcification via culture
Toyofuku et al., 2017	*Ammonia* sp.	pCO_2 on pH imaging during calcification via culture

so that the discontinuous shape of early calcareous tests (as we observe in specimens #1 and #2; **Figures 2**, **3**) may not have been fully preserved in former studies (e.g., Angell, 1979). In some previous TEM-studies (Angell, 1967), the sample preparation methods used likely resulted in artifacts in the prepared sections. As the resin used for embedding has a different hardness compared to the foraminiferal test, the cytoplasm (substituted with resin) was successfully thinly sliced while the calcite part of the test would be lost. It was therefore assumed that, any vacant spaces in the thin sections were completely filled with calcium carbonate crystals. In other studies (e.g., Spero, 1988) calcium carbonate were dissolved during sample preparation to enable ultrathin sectioning for the observation of the cytoplasm configuration during shell formation. With the calcareous materials absent, it was again assumed that the space between primary organic sheet and outer organic layer was completely filled by calcite crystals, which is different from what we observed here. On the other hand, the introduction of FIB technology made it possible to produce cross sections with both soft, delicate organic structures and hard, brittle calcium carbonate fully preserved, as exemplified by the present study. The results indicate that calcium carbonate grows not only from the primary organic sheet to the outer/inner organic layer but also *vice versa* unlike previously thought (Hemleben et al., 1977). Furthermore, this constitutes the first observation of numerous voids within both organic structures and calcareous layers. The primary organic sheet, outer and inner organic layers have been described previously and were also observed in this study. Previous studies suggested that the primary organic sheet was often discontinuous and does completely separate the outer from the inner lamellae in the bilamellar chamber wall (Spero, 1988).

Former studies have reported the existence of spherical structures thought to be vesicles around the outer and inner organic layers (Angell, 1967, 1979; Hemleben et al., 1986; Spero, 1988). Our observations confirm that there are many spherical structures associated with the outer and inner organic layers (S in **Figures 2C,D**, **3C–E**, **4C–E**, **5C,E**, **6C,D**). By using FIB-SEM to prepare the samples, we show that the inside of some spherical structures appeared to contain cavities (e.g., white allow in **Figure 2D**). In addition, cavities were also found as a seemingly integral part of the primary organic sheet (e.g., white arrows on POS in **Figures 4D,E**, **5D**). If such cavities were related to foraminiferal vesicles as previous studies have described, they are likely to be filled with fluids. In addition, spherical structures were formed from the outer organic layer in contact with surrounding water (CO in **Figures 5E**, **9**). It is likely that some of these spherical structures directly enclose a part of the surrounding seawater. In addition, a number of spherical structures with a diameter of $\sim$1 μm were characterized by a spongy inner structure (white dot in **Figure 3C**). These structures ($\sim$1 μm) correspond to mitochondria, since they are present at

high densities near organic layers during the calcification process (Spero, 1988). Furthermore, the voids and vesicles appeared to be connected to the outer and inner organic layers, indicating exocytosis (asterisks in **Figures 4D**, **5D**, **9**) and endocytosis (CO in **Figures 5E**, **9**).

One possible significance of these spherical structures is in increasing the total exchangeable area between the ambient seawater and the foraminiferal calcification fluid, since continuous calcium and carbon source supply is, naturally, required during calcification. Meanwhile, the chemistry of the fluid should be strongly governed by the organism thoughout the process. The numerous vesicles could reflect an increased density of transmembrane transporters to achieve a high flux of ions (i.e., Ca^{2+} and inorganic carbon) from seawater to the SOC. Tyszka (in prep.) considers that the outer and inner organic layers are not just organic sheets but are actively involved in calcification. Our results support the hypothesis that these organic structures are indeed involved in mineralization, perhaps by collecting ions necessary for calcification, transporting them to specific locations, or by releasing unnecessary substances from the SOC (**Figure 9**). The relative importance of vesicles in the outer and inner organic layers are interpreted to increase as calcification proceeds, since they were more numerous in specimens #3–#5 than specimens #1 and #2. Together, these observations show that the primary organic sheet is not just a template for calcium carbonate deposition, but instead is actively involved in biomineralization. For example, calcium ions, carbon sources, and acidic amino acids made of cytoplasm would be supplied to both sides of the primary organic sheet. The outer and inner organic layers and primary organic sheet would be active at these earlier phases of chamber formation. Banner and Williams (1973) reported that the primary organic sheet acts simply as a template upon where calcification occurs, which appears to be different from the results of the present study; further work is required in this area.

Regarding the calcareous layer, it is evident that calcium carbonate is present in both calcareous layers (outer and inner calcareous layers) in all individuals observed in this study (**Figure 8**). In specimens #3-#5, especially, it is presumed that the nature of the calcium carbonate are calcite crystals because they resemble ordinary test cross sections (Nakajima et al., 2016). In specimen #1 and #2, the form of the calcareous materials is not of a typical crystalline appearance but appeared rather irregular. This is different from the previously reported appearance of calcitic walls of this species (Nakajima et al., 2016). Elemental analysis results with SEM-EDS support that these structures are indeed calcium carbonate, but the crystallographical structure remain uncharacterized and is a subject of future studies. Submicron periodic lateral layers (∼200–450 nm) in a single lamellar structure has been reported previously and was considered to represent the smallest unit of crystal growth in foraminifera (Nakajima et al., 2016). These are comparable to crystals found in the planktonic *Globigerina* sp. and *Groborotalia* sp. (Cuif et al., 2011). In our cross-sections, the crystal units within the foraminiferal chamber wall do not appear to be formed by a spiral growth mode. This implies that partition coefficients for elements obtained from inorganic precipitation experiments (e.g., Rimstidt et al., 1998) are not directly comparable to those observed in foraminifera, since spiral crystal growth (e.g., Davis et al., 2000, 2004) has a different element incorporation rate than precipitation from an amorphous precursor (e.g., De Yoreo et al., 2015; Blue et al., 2017).

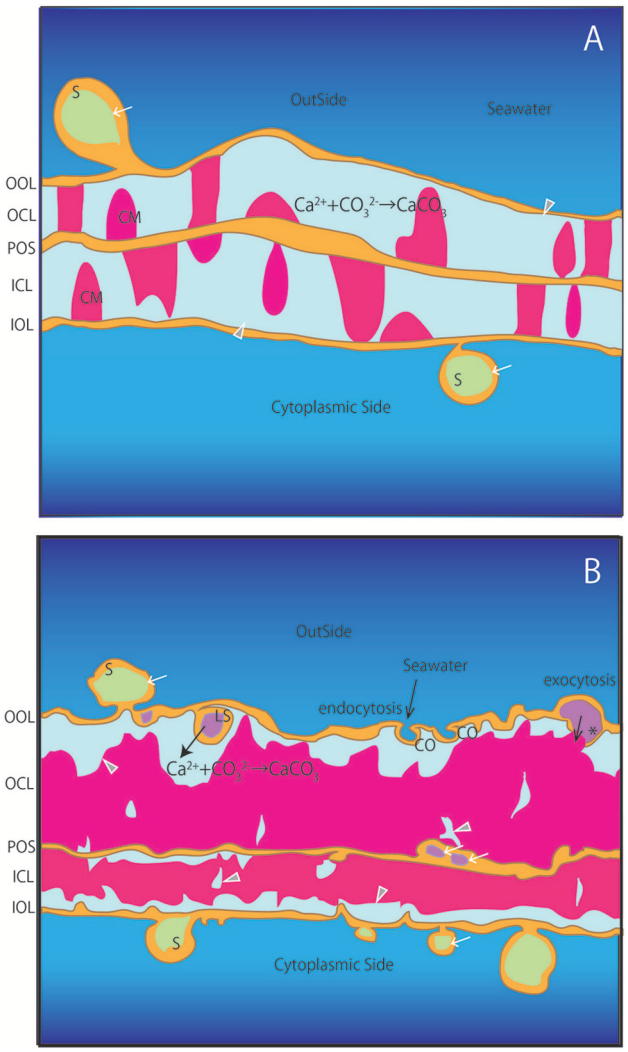

FIGURE 9 | Schematic illustration of the SOC. **(A)** Earlier stages corresponding to specimens #1 and #2. **(B)** Later stages corresponding to specimens #3-#5. OOL, outer organic layer; OCL, outer calcareous layer; POS, primary organic sheet; ICL, inner calcareous layer; IOL, inner organic layer; S, spherical structures; CM, calcareous materials; PP, pore plate; gray triangles, void; white arrows, cavities in the organic structure; CO, concavity; asterisk, opening spherical structure from cavity into void; LS, spherical structure with larger cavity inside projection to voids.

Contribution to Improvement of Suggested Foraminiferal Calcification Models

Our cross sections identified various structures within the foraminiferal SOC. Since there has been no study revealing the detailed ultrastructure of the SOC and the possible existence of

calcification fluid, these newly revealed findings are crucial in constraining calcification models in foraminifera (e.g., Nehrke et al., 2013). It has been reported that in *Ammonia* sp., calcification is achieved by active, outward proton transport (Toyofuku et al., 2017). Likely, these protons are exchanged for calcium which enters the SOC by transmembrane transport (TMT) (Nehrke et al., 2013; Toyofuku et al., 2017). The numerous spherical structures reported here are expected to play an important role in this ion exchange, for example by surface enlargement (S in **Figure 9**). These structures are likely be produced by seawater endocytosis and transported from the surface of the SOC inwards (CO and LS in **Figure 9**). Ion pumps can be active through the surface of these spheres, which will result in concentrated element composition in the vesicles within the organic layer that will be exocytosed into the voids where calcification takes place (asterisk in **Figure 9**). As the total amount of spherical structures and vesicles increases during calcification, it is proposed that these structures plays a key role in transporting substances for calcification. Presence of such transmembrane transporters and transport pathways will need to be further confirmed by immunostaining on the spherical structure and organic layers in the SOC.

It is assumed that the process of calcification is similar between the inner calcareous layer at the cytoplasmic side and the outer calcareous layer at the outer side, although the contribution of ions from seawater vs. the cell should differ. Particularly, as chamber formation progresses, the precipitated calcite layer seems to form a barrier that hampers the transport of ions from the surrounding seawater to the growing inner calcareous layer. Then, the importance of ion transportation from the cytoplasmic side would increase. It is possible that the ions transported from the inside are also seawater-derived, as the chamber that is being formed appears to are not fully filled with cytoplasm, but instead with seawater, which in turn, be circulated with ambient seawater through the aperture. It has been reported that the calcium signal of the cell body increases during later stages of chamber formation (Toyofuku et al., 2008), implying that the contribution of cell-derived calcium ions (Ca^{2+}) increases as chamber formation proceeds.

CONCLUSION

In this study, we observed the detailed structure of the SOC during chamber wall calcification in a foramnifer (*Ammonia "beccarii"*). By using the FIB-SEM technique we were able to observe the ultra- and microstructure of an intact SOC, complete with both calcified parts and the cytoplasm, which was not previously possible. For the first time, we show that numerous voids of calcareous layers and internal organic structures are present within the SOC during the calcification process and provide evidence to interpret their function which was previously totally unknown. Our results provide further support for the existence of calcification liquid within the enclosed SOC and suggest that organic layers are actively involved in calcite precipitation. By observing morphology of the SOC in great detail, we improved the understanding of foraminiferal biomineralization and key conditions under which element partitioning and isotope fractionation occur, which is widely significant as foraminifera is an important proxy in palaeoceanography.

AUTHOR CONTRIBUTIONS

Scientific conception and experimental design: YN and TT. Data acquisition and analysis: YN, TT, and KU. Data processing: YN. Data interpretation: YN, TT. Manuscript writing: YN, TT, KU, and RW.

ACKNOWLEDGMENTS

Our FIB work was partly supported by the Nagoya University microstructural characterization platform as a program of "Nanotechnology Platform" of the Ministry of Education, Culture, Sports, Science and Technology (MEXT), Japan. We thank S. Arai, T. Nakao, M. Nakano (Nagoya University), and S. Sadayama (FEI Japan) for FIB experiments. The authors thank Y. Iwadate, N. Kishigami, S. Kubo, S. Kawada (JAMSTEC), S. Kondo (JEOL), for their technical assistance and scientific advice on this study. Two reviewers are thanked for providing constructive and useful comments which improved the manuscript. We thank the editors and supporting staffs for their effort to publish this biomineralization special issue. We thank LJ De Nooijer (NIOZ), C. Chen (JAMSTEC) and B. Mamo (HKU) for constructive discussions and for improving the writing quality of the manuscript. We also acknowledge J. Bijma (AWI) for fruitful discussions. This work was supported by a grant from Faculty of Environment and Information Sciences, Yokohama National University (to YN) and a JSPS KAKENHI Grant Number 25247085 (to TT).

SUPPLEMENTARY MATERIAL

The Supplementary Material for this article can be found online at: https://www.frontiersin.org/articles/10.3389/fmars.2018.00067/full#supplementary-material

Figure S1 | EDS profiles on the site of calcification (SOC) for specimens #1 to #5. **(A–E)** corresponding to specimen #1 to #5 respectively. −1, white rectangles show the measurement area; −2, EDS profile of spot measurement on the white rectangles in from A-1 to E-1.

REFERENCES

Anand, P., Elderfield, H., and Conte, M. H. (2003). Calibration of Mg/Ca thermometry in planktonic foraminifera from a sediment trap time series. *Paleoceanography* 18:1050. doi: 10.1029/2002PA000846

Angell, R. W. (1967). The test structure and composition of the foraminifer *Rosalina floridana*. *J. Protozool.* 14, 299–307. doi: 10.1111/j.1550-7408.1967.tb02001.x

Angell, R. W. (1979). Calcification during chamber development *in Rosalina floridana*. *J. Foram. Res.* 9, 341–353. doi: 10.2113/gsjfr.9.4.341

Banner, F. T., and Williams, E. (1973). Test structure, organic skeleton and extrathalamous cytoplasm of *Ammonia* brüennich. *J. Foram. Res.* 3, 49–69. doi: 10.2113/gsjfr.3.2.49

Bentov, S., and Erez, J. (2006). Impact of biomineralization processes on the Mg content of foraminiferal shells: a biological perspective. *Geochem. Geophys. Geosyst.* 7:Q01P08. doi: 10.1029/2005GC001015

Blue, C. R., Giuffre, A., Mergelsberg, S., Han, N., De Yoreo, J. J., and Dove, P. M. (2017). Chemical and physical controls on the transformation of amorphous calcium carbonate into crystalline $CaCO_3$ polymorphs. *Geochim. Cosmochim. Acta* 196, 179–196. doi: 10.1016/j.gca.2016.09.004

Cuif, J.-P., Dauphin, Y., and Sorauf, J. E. (2011). *Biominerals and Fossils Through Time*. Cambridge, UK: Cambridge University Press.

Davis, K. J., Dove, P. M., and De Yoreo, J. J. (2000). The role of Mg^{2+} as an impurity in calcite growth. *Science* 290, 1134–1137. doi: 10.1126/science.290.5494.1134

Davis, K. J., Dove, P. M., Wasylenki, L. E., and De Yoreo, J. J. (2004). Morphological consequences of differential Mg^{2+} incorporation at structurally distinct steps on calcite. *Am. Mineral.* 89, 714–720. doi: 10.2138/am-2004-5-605

De Nooijer, L. J., Hathorne, E. C., Reichart, G.-J., Langer, G., and Bijma, J. (2014a). Variability in calcitic Mg/Ca and Sr/Ca ratios in clones of the benthic foraminifer *Ammonia tepida*. *Mar. Micropaleontol.* 107, 32–43. doi: 10.1016/j.marmicro.2014.02.002

De Nooijer, L. J., Langer, G., Nehrke, G., and Bijma, J. (2009b). Physiological controls on seawater uptake and calcification in the benthic foraminifer *Ammonia tepida*. *Biogeosciences* 6, 2669–2675. doi: 10.5194/bg-6-2669-2009

De Nooijer, L. J., Spero, H. J., Erez, J., Bijma, J., and Reichart, G.-J. (2014b). Biomineralization in perforate foraminifera. *Earth-Sci. Rev.* 135, 48–58. doi: 10.1016/j.earscirev.2014.03.013

De Nooijer, L. J., Toyofuku, T., and Kitazato, H. (2009a). Foraminifera promote calcification by elevating their intracellular pH. *Proc. Natl. Acad. Sci. U.S.A.* 106, 15374–15378. doi: 10.1073/pnas.0904306106

De Nooijer, L. J., Toyofuku, T., Oguri, K., Nomaki, H., and Kitazato, H. (2008). Intracellular pH distribution in foraminifera determined by the fluorescent probe HPTS. *Limnol. Oceanogr. Methods* 6, 610–618. doi: 10.4319/lom.2008.6.610

De Yoreo, J. J., Gilbert, P. U., Sommerdijk, N. A., Penn, R. L., Whitelam, S., Dove, P. M., et al. (2015). Crystallization by particle attachment in synthetic, biogenic, and geologic environments. *Science* 349:aaa6760. doi: 10.1126/science.aaa6760

Dissard, D., Nehrke, G., Reichart, G.-J., and Bijma, J. (2010). Impact of seawater *p*CO2 on calcification and Mg/Ca and Sr/Ca ratios in benthic foraminifera calcite: results from culturing experiments with *Ammonia tepida*. *Biogeosciences* 7, 81–93. doi: 10.5194/bg-7-81-2010

Diz, P., Barras, C., Geslin, E., Reichart, G.-J., Metzger, E., Jorissen, F., et al. (2012). Incorporation of Mg and Sr and oxygen and carbon stable isotope fractionation in cultured *Ammonia tepida*. *Mar. Micropaleontol.* 92, 16–28. doi: 10.1016/j.marmicro.2012.04.006

Dueñas-Bohórquez, A., Raitzsch, M., De Nooijer, L. J., and Reichart, G.-J. (2011). Independent impacts of calcium and carbonate ion concentration on Mg and Sr incorporation in cultured benthic foraminifera. *Mar. Micropaleontol.* 81, 122–130. doi: 10.1016/j.marmicro.2011.08.002

Eggins, S., De Deckker, P., and Marshall, J. (2003). Mg/Ca variation in planktonic foraminifera tests: implications for reconstructing palaeo-seawater temperature and habitat migration. *Earth Planet. Sci. Lett.* 212, 291–306. doi: 10.1016/S0012-821X(03)00283-8

Elderfield, H., and Ganssen, G. (2000). Past temperature and $\delta^{18}O$ of surface ocean waters inferred from foraminiferal Mg/Ca ratios. *Nature* 405, 442–445. doi: 10.1038/35013033

Elderfield, H., Bertram, C. J., and Erez, J. (1996). A biomineralization model for the incorporation of trace elements into foraminiferal calcium carbonate. *Earth Planet. Sci. Lett.* 142, 409–423. doi: 10.1016/0012-821X(96)00105-7

Erez, J. (2003). The source of ions for biomineralization in foraminifera and their implications for paleoceanographic proxies. *Rev. Mineral. Geochem.* 54, 115–149. doi: 10.2113/0540115

Glas, M. S., Langer, G., and Keul, N. (2012). Calcification acidifies the microenvironment of a benthic foraminifer (*Ammonia* sp.). *J. Exp. Mar. Biol. Ecol.* 424-425, 53–58. doi: 10.1016/j.jembe.2012.05.006

Havach, S. M., Chandler, G. T., Wilson-Finelli, A., and Shaw, T. J. (2001). Experimental determination of trace element partition coefficients in cultured benthic foraminifera. *Geochim. Cosmochim. Acta* 65, 1277–1283. doi: 10.1016/S0016-7037(00)00563-9

Hemleben, C., Be, A. W. H., Anderson, O. R., and Tuntivate, S. (1977). Test morphology, organic layers and chamber formation of the planktonic foraminifer *Globorotalia menardii* (d'Orbigny). *J. Foram. Res.* 7, 1–25. doi: 10.2113/gsjfr.7.1.1

Hemleben, C., Erson, O. R., Berthold, W., and Spindler, M. (1986). "Calcification and chamber formation in foraminifera - a brief overview," in *Biomineralization in Lower Plants and Animals: The Systematics Association*, eds R. Riding and L. BSC (Oxford: Clarendon Press), 237–249.

Keul, N., Langer, G., De Nooijer, L. J., and Bijma, J. (2013b). Effect of ocean acidification on the benthic foraminifera *Ammonia* sp. is caused by a decrease in carbonate ion concentration. *Biogeosciences* 10, 6185–6198. doi: 10.5194/bg-10-6185-2013

Keul, N., Langer, G., De Nooijer, L. J., Nehrke, G., Reichart, G.-J., and Bijma, J. (2013a). Incorporation of uranium in benthic foraminiferal calcite reflects seawater carbonate ion concentration. *Geochem. Geophys. Geosyst.* 14, 102–111. doi: 10.1029/2012GC004330

Keul, N., Langer, G., Thoms, S., De Nooijer, L. J., Reichart, G.-J., and Bijma, J. (2017). Exploring foraminiferal Sr/Ca as a new carbonate system proxy. *Geochim. Cosmochim. Acta* 202, 374–386. doi: 10.1016/j.gca.2016.11.022

Kunioka, D., Shirai, K., Takahata, N., Sano, Y., Toyofuku, T., and Ujiie, Y. (2006). Microdistribution of Mg/Ca, Sr/Ca, and Ba/Ca ratios in *Pulleniatina obliquiloculata* test by using a NanoSIMS: implication for the vital effect mechanism. *Geochem. Geophys. Geosyst.* 7:Q12P20. doi: 10.1029/2006GC001280

Le Cadre, V., and Debenay, J. P. (2006). Morphological and cytological responses of *Ammonia* (foraminifera) to copper contamination: implication for the use of foraminifera as bioindicators of pollution. *Environ. Pollut.* 143, 304–317. doi: 10.1016/j.envpol.2005.11.033

Lear, C. H., Elderfield, H., and Wilson, P. A. (2000). Cenozoic Deep-sea temperatures and global ice volumes from Mg/Ca in benthic foraminiferal calcite. *Science* 287, 269–272. doi: 10.1126/science.287.5451.269

Mann, S. (2001). *Biomineralization: Principles and Concepts in Bioinorganic Materials Chemistry*. New York, NY: Oxford University Press on Demand.

Maréchal-Abram, N., Debenay, J.-P., Kitazato, H., and Wada, H. (2004). Cadmium partition coefficients of cultured benthic foraminifera *Ammonia beccarii*. *Geochem. J.* 38, 271–283. doi: 10.2343/geochemj.38.271

Mewes, A., Langer, G., De Nooijer, L. J., Bijma, J., and Reichart, G. J. (2014). Effect of different seawater Mg concentrations on calcification in two benthic foraminifers. *Mar. Micropaleontol.* 113, 56–64. doi: 10.1016/j.marmicro.2014.09.003

Mewes, A., Langer, G., Reichart, G.-J., De Nooijer, L. J., Nehrke, G., and Bijma, J. (2015). The impact of Mg contents on Sr partitioning in benthic foraminifers. *Chem. Geol.* 412, 92–98. doi: 10.1016/j.chemgeo.2015.06.026

Munsel, D., Kramar, U., Dissard, D., Nehrke, G., Berner, Z., Bijma, J., et al. (2010). Heavy metal incorporation in foraminiferal calcite: results from multi-element enrichment culture experiments with *Ammonia tepida*. *Biogeosciences* 7, 2339–2350. doi: 10.5194/bg-7-2339-2010

Nakajima, K., Nagai, Y., Suzuki, M., Oaki, Y., Naito, K., Tanaka, Y., et al. (2016). Mesoscopic crystallographic textures on shells of a hyaline radial foraminifer *Ammonia beccarii*. *CrystEngComm* 18, 7135–7139. doi: 10.1039/C6CE01611A

Nehrke, G., Keul, N., Langer, G., De Nooijer, L. J., Bijma, J., and Meibom, A. (2013). A new model for biomineralization and trace-element signatures of Foraminifera tests. *Biogeosciences* 10, 6759–6767. doi: 10.5194/bg-10-6759-2013

Nürnberg, D., Bijma, J., and Hemleben, C. (1996). Assessing the reliability of magnesium in foraminiferal calcite as a proxy for water mass temperatures. *Geochim. Cosmochim. Acta* 60, 803–814. doi: 10.1016/0016-7037(95)00446-7

Paris, G., Fehrenbacher, J. S., Sessions, A. L., Spero, H. J., and Adkins, J. F. (2014). Experimental determination of carbonate-associated sulfate $\delta^{34}S$ in planktonic foraminifera shells. *Geochem. Geophys. Geosyst.* 15, 1452–1461. doi: 10.1002/2014GC005295

Raitzsch, M., Dueñas-Bohórquez, A., Reichart, G.-J., De Nooijer, L. J., and Bickert, T. (2010). Incorporation of Mg and Sr in calcite of cultured benthic foraminifera: impact of calcium concentration and associated calcite saturation state. *Biogeosciences* 7, 869–881. doi: 10.5194/bg-7-869-2010

Rimstidt, J. D., Balog, A., and Webb, J. (1998). Distribution of trace elements between carbonate minerals and aqueous solutions. *Geochim. Cosmochim. Acta* 62, 1851–1863. doi: 10.1016/S0016-7037(98)00125-2

Sadekov, A. Y., Eggins, S. M., and De Deckker, P. (2005). Characterization of Mg/Ca distributions in planktonic foraminifera species by electron microprobe mapping. *Geochem. Geophys. Geosyst.* 6:Q12P06. doi: 10.1029/2005GC000973

Spero, H. J. (1988). Ultrastructural examination of chamber morphogenesis and biomineralization in the planktonic foraminifer *Orbulina universa*. *Mar. Biol.* 99, 9–20. doi: 10.1007/BF00644972

Spero, H. J., Eggins, S. M., Russell, A. D., Vetter, L., Kilburn, M. R., and Honisch, B. (2015). Timing and mechanism for intratest Mg/Ca variability in a living planktic foraminifer. *Earth Planet. Sci. Lett.* 409, 32–42. doi: 10.1016/j.epsl.2014.10.030

Tambutté, S., Holcomb, M., Ferrier-Pagès, C., Reynaud, S., Tambutté, É., Zoccola, D., et al. (2011). Coral biomineralization: from the gene to the environment. *J. Exp. Mar. Biol. Ecol.* 408, 58–78. doi: 10.1016/j.jembe.2011.07.026

Toyofuku, T., and Kitazato, H. (2005). Micromapping of Mg/Ca values in cultured specimens of the high-magnesium benthic foraminifera. *Geochem. Geophys. Geosyst.* 6:Q11PQ05. doi: 10.1029/2005GC000961

Toyofuku, T., De Nooijer, L. J., Yamamoto, H., and Kitazato, H. (2008). Real-time visualization of calcium ion activity in shallow benthic foraminiferal cells using the fluorescent indicator Fluo-3 AM. *Geochem. Geophys. Geosyst.* 9:Q05005. doi: 10.1029/2007GC001772

Toyofuku, T., Matsuo, M. Y., De Nooijer, L. J., Nagai, Y., Kawada, S., Fujita, K., et al. (2017). Proton pumping accompanies calcification in foraminifera. *Nat. Commun.* 8:14145. doi: 10.1038/ncomms14145

Toyofuku, T., Suzuki, M., Suga, H., Sakai, S., Suzuki, A., Ishikawa, T., et al. (2011). Mg/Ca and $\delta^{18}O$ in the brackish shallow-water benthic foraminifer *Ammonia 'beccarii'*. *Mar. Micropaleontol.* 78, 113–120. doi: 10.1016/j.marmicro.2010.11.003

Van Dijk, I., De Nooijer, L. J., Boer, W., and Reichart, G. J. (2017). Sulfur in foraminiferal calcite as a potential proxy for seawater carbonate ion concentration. *Earth Planet. Sci. Lett.* 470, 64–72. doi: 10.1016/j.epsl.2017.04.031

Wilbur, K. M. (1964). "Shell formation and regeneration," in *Physiology of Mollusca*, eds K. M. Wilbur and C.W. Yong (New York, NY: Academic Press), 243–282.

Zeebe, R. E., and Sanyal, A. (2002). Comparison of two potential strategies of planktonic foraminifera for house building: Mg^{2+} or H^{+} removal? *Geochim. Cosmochim. Acta* 66, 1159–1169. doi: 10.1016/S0016-7037(01)00852-3

Conflict of Interest Statement: The authors declare that the research was conducted in the absence of any commercial or financial relationships that could be construed as a potential conflict of interest.

frontiers in Marine Science

ORIGINAL RESEARCH
published: 01 May 2018
doi: 10.3389/fmars.2018.00151

The Initiation and Early Stages of Postmolt Mineralization in the Blue Crab, *Callinectes sapidus*

Robert D. Roer and Richard M. Dillaman†*

Department of Biology and Marine Biology, University of North Carolina Wilmington, Wilmington, NC, United States

Crabs are encased in a rigid exoskeleton or cuticle that is hardened by both protein crosslinking and calcification. In order to grow, the exoskeleton must be periodically molted. The two outermost layers of the exoskeleton of crabs are deposited prior to the molt, but remain uncalcified until the animal sheds its old exoskeleton. The inhibition of premolt calcification and initiation of postmolt calcification are effected by biochemical changes in the organic matrix. In the 2 h after the molt, sugar moieties are enzymatically altered on cuticular glycoproteins by an N-acetylhexosaminidase secreted by the underlying epithelium. These alterations appear to unmask nucleation sites that allow calcification to commence. The initial deposition of mineral is in the form of amorphous calcium carbonate (ACC). As postmolt calcification continues and the principal layer (endocuticle) is deposited and mineralized, the ACC is largely converted to or overgrown by calcite. Prior to the onset of ACC deposition, silicon has been detected in those areas of the exoskeleton that are about to undergo mineralization. As calcification proceeds, silicon is no longer detected. It is hypothesized that silicon is involved in the stabilization of ACC by destabilizing the crystal lattice of calcite before it undergoes the transition to or is overgrown by crystalline calcite.

Keywords: *Callinectes*, molting, calcification, silicon, amorphous calcium carbonate, glycoproteins, N-acetylglycosaminidase

OPEN ACCESS

Edited by:
Alfred Portius Wheeler, Clemson University, United States

Reviewed by:
Gary H. Dickinson, The College of New Jersey, United States
Tara Essock-Burns, University of Hawaii, United States

****Correspondence:***
Robert D. Roer
roer@uncw.edu

†Deceased.

Specialty section:
This article was submitted to Marine Molecular Biology and Ecology, a section of the journal Frontiers in Marine Science

Received: *05 February 2018*
Accepted: *12 April 2018*
Published: *01 May 2018*

Citation:
Roer RD and Dillaman RM (2018) The Initiation and Early Stages of Postmolt Mineralization in the Blue Crab, Callinectes sapidus. Front. Mar. Sci. 5:151. doi: 10.3389/fmars.2018.00151

INTRODUCTION

In the words of Hans Lowenstam and Steve Weiner, "Crustaceans are the champions of mineral mobilization and deposition in the animal kingdom" (Lowenstam and Weiner, 1989). To illuminate and substantiate this claim, we will review work on the cellular and molecular control of biomineralization in decapod crustaceans and present some new preliminary data on the presence and role of silica in this process.

The utility of crustaceans as a model for studying biomineralization lies in the fact that they must molt their calcified exoskeletons periodically in order to grow (Roer and Dillaman, 1984, 1993; Luquet, 2012). The exoskeleton, as typified by the dorsal carapace of decapod crabs, consists of four layers, from the outermost: epicuticle, exocuticle, endocuticle, and membranous layer. The epicuticle contains a protein and lipid-rich organic matrix. The inner three cuticular layers all contain an organic matrix comprised of protein and chitin microfibrils arranged in sheets that parallel the body surface. The orientation of the sheets changes with successive layers, forming a helicoidal arrangement (Bouligand, 1972; Raabe et al., 2005). When fully formed, the outer three layers are impregnated with calcium carbonate in the form of calcite. A unique feature of the

exocuticle is the vertical partitioning of the layer into hexagonal prisms. The prisms are bounded by interprismatic septa which create a honeycomb-like arrangement within this layer (Roer and Dillaman, 1984). The role of the septa in the initial stages of calcification will be discussed below.

The membranous layer is underlain by a hypodermis. The outer cellular layer of the hypodermis is an epithelium that elaborates the exoskeletal layers after each molt and which extends microvilli through all the layers, terminating in the inner epicuticle. The microvilli become encased in cuticular material referred to as pore canals. We have also proposed that the interprismatic septa morphologically correspond to the lateral margins of the epithelial cells that persist following cuticular secretion (Roer and Dillaman, 1984).

The molt cycle is divided into four main stages: Intermolt (stage C_4) when the exoskeleton is fully elaborated, premolt (stages D_0, D_1, D_2, D_3, D_4), ecdysis (stage E), and postmolt (stages A_1, A_2, B_1, B_2, C_{1-3}) (Drach, 1939; Drach and Tchernigovtzeff, 1967). Premolt is initiated by apolysis, the enzyme-mediated separation of the epithelium from the overlying old cuticle. Late premolt (stage D_2) is the period during which resorption of mineral and organic material from the old exoskeleton peaks, along with the synthesis and elaboration of the organic matrix of the new epicuticle and exocuticle. While these "pre-exuvial" layers are fully formed prior to the molt, they remain uncalcified until after the molt to allow for expansion of the new, soft exoskeleton. Just prior to the molt (ecdysis), during stages D_3 and D_4, preformed sutures along the margin of the old carapace weaken and split open. The crab then emerges from the old exoskeleton (stage E), and enters postmolt (Roer and Dillaman, 1993).

Early postmolt (stages A_1 and A_2) are characterized by sclerotization of the pre-exuvially deposited epi- and exocuticle, and within 3 h after the molt, the initiation of calcification of these layers (Shafer et al., 1995). Mineralization begins along the epicuticle, the inner and outer edges of the exocuticle, and at the distal and proximal margins of the interprismatic septa. Calcification of the septa continues until the mineralization fronts meet between 5 and 8 h after ecdysis. At this point the pattern of mineralization resembles corrugated cardboard, lending early stability and strength to the exoskeleton (Dillaman et al., 2005).

The mineral that is first deposited along the septa and exocuticular margins is amorphous calcium carbonate (ACC). This is evident by the high solubility of the initial mineral (Dillaman et al., 2005). This labile mineral persists along the outer and inner exocuticular margins and interprismatic septa through 12 h postecdysis. By 48 h postmolt, as mineralization continues, the ACC is no longer observed and was presumed to be transformed to calcite (Dillaman et al., 2005).

During the late postmolt stages B and C_{1-3}, mineralization of the exocuticle within the prisms continues along with the concurrent deposition and calcification of the endocuticle. Termination of exoskeletal deposition and mineralization are marked by the secretion of the non-calcified membranous layer, signaling the transition to intermolt (stage C_4) (Roer and Dillaman, 1993; Dillaman et al., 2005).

Premolt resorption of calcium from the old exoskeleton is mediated by Ca-ATPase and Na/Ca exchangers localized along the basolateral membranes of the epithelial cells (Roer, 1980; Greenaway et al., 1995). Postmolt translocation of calcium from the hemolymph into the new cuticle is also accomplished by the same transporters, but now they are localized to the apical cell membranes and the microvilli that extend into the cuticle via the pore canals (Roer, 1980; Greenaway et al., 1995; Roer and Towle, 2005). Bicarbonate transport into the mineralizing exoskeleton involves carbonic anhydrase and a HCO_3-ATPase (Roer and Dillaman, 1993).

The sequence of events during the molt cycle described above clearly demonstrates why decapod crustaceans are such a valuable model for studying the mechanisms and control of mineralization. It also poses questions that have been the subject of intense study in our research group over the past few decades. The first of these is how the pre-exuvial layers are prevented from calcifying prior to the molt and then promoted to initiate mineralization within 2 h after ecdysis.

The control of mineralization in the pre- and postmolt cuticle resides in the biochemistry of the organic matrix. Samples of cuticle, devoid of epithelium, from pre-exuvial epi- and exocuticle are incapable of forming calcite crystals *in vitro*. However, decalcified early postmolt epi- and exocuticle samples nucleate crystal formation under identical conditions (Roer et al., 1988). This change in the ability of the matrix to support calcification temporally and spatially corresponds to changes in the profiles of glycoproteins within the cuticle. Marlowe et al. (1994) demonstrated the changes in the sugar moieties within the cuticle histologically, using labeled lectins. Shafer et al. (1994, 1995) characterized the change in sugar moieties on individual glycoproteins and demonstrated that these changes coincided with the alteration of the cuticle's ability to nucleate mineral deposition.

A causal relationship was first established by Coblentz et al. (1998) using a pH-drift *in vitro* mineralization assay. Protein extracts from pre-exuvial exocuticle had no effect on calcite precipitation, but acetic acid extracts of cuticle 1.5 or more hours postecdysis were found to bind to nascent calcite crystals and inhibit nucleation. These data suggest that two proteins in postecdysial cuticle, when fixed to the chitin protein fibrils act as nucleation sites, but these proteins are shielded prior to the postmolt transition in the cuticle.

The hypothesis that the shielding of the nucleating glycoproteins involved one or more sugar moieties was suggested by the discovery of a glycosidase extracted from postecdysial cuticle with both N-acetylglucosaminidase and N-acetylgalactosaminidase activity (Roer et al., 2001). A partial sequence of this putative cuticular N-acetylhexosaminidase was determined (Roer and Towle, 2004). The potential role for this enzyme in mediating the onset of nucleation was supported by experiments in which pre-exuvial cuticle was treated with an exogenous N-acetylhexosaminidase (Pierce et al., 2001). The untreated pre-exuvial cuticle was incapable of nucleating calcite *in vitro*. However, after treatment with the N-acetylhexosaminidase, the pre-exuvial cuticle nucleated calcite deposition as well as postmolt cuticle samples did.

Faircloth and Shafer (2007) were able to identify cuticular proteins that are likely to be involved in biomineralization by comparing transcripts that were found in calcifying dorsal carapace tissue of the blue crab to transcripts that were only found in the tissue underlying the arthrodial membrane of the joints which doesn't mineralize. Four transcripts found only in arthrodial membrane tissue (CsAMP's) all contained the Rebers-Riddiford motif (RR-1) that is a chitin-binding sequence. One of these, CsAMP9.3 was concluded to code for a structural element of the exocuticle, since it was only detected in premolt tissue (the stage when exocuticular synthesis occurs). Of the four transcripts isolated from calcifying tissue, two (CsCP6.1 and CsCP19.0) are only expressed during postmolt, suggesting that they may be involved with the calcification of the endocuticle, while a third (CsCP15.0) is expressed in both pre- and postmolt. The fourth (CsCP14.1) also possessed the RR-1 motif and was only expressed during pre-molt. It was hypothesized that CsCP14.1 binds to chitin-protein fibrils during premolt and prevents pre-exuvial nucleation of $CaCO_3$, and that CsCP6.1 is expressed during postmolt to initiate mineralization.

Tweedie et al. (2004) isolated a glycoprotein from blue crab exocuticle and created an antibody to it. They employed immunohistochemistry to localize the glycoprotein *in situ*. The glycoprotein was widely distributed in the exocuticle immediately after the molt, but at the time that calcification began (∼1.5 h postecdysis), the glycoprotein disappeared from the interprismatic septa. Thus, its disappearance corresponded temporally and spatially to the nucleation of $CaCO_3$. It was hypothesized that this glycoprotein was involved in preventing pre-exuvial mineralization of the exocuticle.

Kuballa and Elizur (2008) characterized two cuticular proteins from the crab *Portunus pelagicus*, a C-type lectin receptor that was up-regulated in premolt and a mannose-binding protein that was only expressed postmolt. They hypothesized that the former was involved in inhibiting pre-exuvial calcification and the latter in promoting postmolt mineralization. A more detailed discussion of proteins that are potentially involved with the initiation and control of mineralization in decapod crustaceans can be found in Roer et al. (2015).

Another question raised by our previous work regards the presence of ACC during the early stages of postmolt calcification. Over the past few decades, it has been shown that numerous mineralized structures across a wide array of taxa display a transient, amorphous phase prior to the appearance of the crystalline phase (Addadi et al., 2012). The problem is that amorphous phases are very unstable and, at least in the case of $CaCO_3$, generally undergoes nearly instantaneous transition to crystalline calcite or aragonite. How ACC is stabilized for rather prolonged periods during early premolt in the blue crab has not been explained. There is, however, evidence in the cystoliths from an angiosperm (*Morus alba*) and synthetic ACC, that the amorphous phase is stabilized by the presence of silicate (Gal et al., 2010). The possible mechanism for ACC stabilization proposed by Gal et al. (2010) is "geometric frustration" of the calcite crystal lattice. The calcite lattice is characterized by a planar arrangement of carbonate ions. It is hypothesized that the relatively large tetrahedral silicate ion, with four negative charges, would both interrupt the lattice and the charge equilibrium at the crystal surface.

It has also been reported that silicon is either involved in the process of calcification (coccolithophorids, Durak et al., 2016) or is detected at the initial sites of calcification in bone (Carlisle, 1970; Landis et al., 1986), brachiopod shell (Williams et al., 2001), cyanobacteria and isopod crustacean exoskeletons (Matsko et al., 2011). In the latter study, silicon was localized in the region of the mineralizing cuticle where calcite would subsequently be found.

To determine if silicon is present during the initial stages of mineralization in the blue crab and if it might play a role in stabilizing ACC in early premolt, we undertook the present study. We employed scanning electron microscopy with energy-dispersive analysis of X-rays (EDAX) to compare the distribution and the relative amounts of Ca and Si in relation to the patterns of initial mineralization. We employed both the dorsal carapace, which mineralizes, and (as a control) the arthrodial membrane of the joints, which never calcifies. Both tissues were sampled from animals in both premolt and early postmolt. If Si plays a role in calcification, we would expect to find it associated with the sites of the initial stages of mineralization (i.e., early postmolt) in the carapace, but absent or less prevalent in the non-mineralizing arthrodial membrane.

MATERIALS AND METHODS

Samples of the dorsal carapace (from above the cardiac region) and arthrodial membrane (from between the merus and carpus of the chelipeds) were dissected from 18 blue crabs (*Callinectes sapidus*; Rathbun, 1896), six from each of the following molt stages: D_3, A_1, and A_2. Molt stages were determined according the criteria of Drach (1939) and Drach and Tchernigovtzeff (1967). Crabs were obtained at Endurance Seafood, a commercial crab shedding operation in Colington, NC, and locally in Wilmington, NC. Samples were fixed and stored in 95% ethanol.

Samples across all molt stages were prepared for scanning electron microscopy (SEM) analysis. For late premolt (stage D_3), the old and new cuticle separate on dissection and only the new, pre-exuvial cuticle was used. Samples were trimmed with a razor blade, and dehydrated using two, 20-min-long changes of 100% ethanol, followed by two 20-min-long changes of 1:1 propanol:ethanol and two 20-min-long changes of 100% propanol. After dehydration these samples were left to air dry overnight. All samples were then mounted on aluminum stubs (Ted Pella Prod. No. 16111) with a carbon adhesive (Ted Pella Prod. No. 16084-1) and coated with 10-nm of platinum/palladium (Pt/Pd) alloy in a Cressington 208HR sputter coater.

All imaging was performed on a Phillips XL30-S FEG system running the software program Microscope Control version 6.0. Secondary electron micrographs were collected using a working distance of 7.5 mm, beam strength of 5 Kev, and spot size 3. Energy dispersive X-ray analysis (EDAX) (beam strength 25 Kev,

spot size 4, working distance of 7.5 mm) was used to analyze the chemical composition of the embedded tissue samples. X-ray emission spectra were obtained using the program EDX Control version 3.3 with a dead time of approximately 20% and counts per second above 1500 for a total of 200 live seconds; the spatial distribution of the identified significant peaks was mapped using program EDX Map version 3.3. Semi-quantitative compositional analysis to determine relative proportions by weight percent of each element in the sample was obtained through the "Quantify" function in EDX Control including all identified significant peaks. Compensation for sample-to-sample variations due to differences in surface features or orientation were accomplished by using the ratios of Ca and Si to each other and to Pt, which was applied at the same thickness to all samples and therefore could be used as a reference.

RESULTS

SEM examination of samples from the dorsal carapace just before ecdysis (stage D_3), those just after the molt (stage A_1), and those taken 6 h postmolt (stage A_2) showed no differences in cuticular thickness, nor any gross morphological differences. The fiber and lamellar structure of the exocuticle became more apparent after the molt, as did the vertical structural elements of the epicuticle. The structure of the arthrodial membrane cuticle showed similar morphological characteristics and differed most markedly from that of the dorsal carapace in that the former was approximately two-thirds the thickness of the latter (**Figure 1**).

Elemental mapping of Ca and Si across the D_3 dorsal carapace samples showed a sparse and homogeneous distribution of both elements across the entire expanse of the epi- and exocuticle. This was the same pattern observed in all premolt and postmolt arthrodial membrane cuticle samples. In the dorsal carapace samples at stage A_1, the Si distribution was still rather homogeneous, but observably denser than during premolt. The Ca signal was also far more intense, but also was no longer homogeneously distributed. Instead, there was a more intense Ca signal on the outer surface of the cuticle and throughout the exocuticle. Less Ca was seen within the epicuticle, than in the exocuticle (**Figure 1**).

Stage A_2 dorsal carapace samples showed a decrease in both the density and homogeneity of the Si signal relative to stage A_1. The Ca signal showed a very high intensity at the outer and inner margins of the exocuticle, corresponding to areas of initial mineralization at this stage. The Ca+Si composite (**Figure 1**, rightmost column) showed that the Si distribution appeared to be more highly localized to those areas that had not yet begun to calcify—the epicuticle and mid-region of the exocuticle.

The quantitative data support the observations based on the EDAX elemental maps (**Figure 2**). Whether viewed as a straight atomic % or relative to the reference atomic % of Pt, the arthrodial membrane cuticle showed immeasurably low levels of Si, and very low levels of Ca throughout early postmolt (**Figures 2A,B**). In premolt, pre-exuvial carapace cuticle, there were very low levels of both Ca and Si (**Figures 2A,B**), and the levels of each element were very close to the same, as shown in their atomic % ratios (**Figures 2C,D**).

In postmolt carapace samples, it appeared that as the atomic % of Ca increased, there was a concomitant decrease in the atomic % of Si. There was considerable variation between samples in early premolt (stage A_1). The sample from crab #6 (A1 C-6 in **Figures 2A,B**) had levels that were intermediate to those from premolt (sample D3 C-3) and a different early postmolt sample from crab #1 (A1 C-1). The latter showed levels of Ca and Si very similar to the representative stage A_2 sample (A2 C-3) (**Figures 2A,B**). The Ca/Si ratio increased (and Si/Ca decreased) as mineralization commenced during postmolt (**Figures 2C,D**).

DISCUSSION

Interest in the involvement of Si in biomineralization in Crustacea is not new. Reports of silicified mandibles have been reported in copepods (Beklemishev, 1954; Miller et al., 1990; Michels et al., 2012; Michels and Gorb, 2015) and amphipods (Mekhanikova et al., 2012). More recently we described silicified teeth in the gastric mill of the blue crab (Vatcher et al., 2015; Nesbit and Roer, 2016). However, an association of Si with calcification in crustaceans has only been suggested by one study on the isopod *Ligia italica* (Matsko et al., 2011). Matsko and colleagues detected the presence of Si in the developing, unmineralized matrix of the exocuticle at the margins of the chitin-protein fibrils. These corresponded precisely to the sites where calcite would be later located in the mature cuticle. The authors hypothesized that Si may form a bridge between the chitin-protein fibrils and the calcium minerals, acting as a nucleation site.

The present study also found Si to be present prior to the onset of mineralization, but its distribution was more homogeneous that that observed by Matsko et al. (2011). Si, presumably in the form of silica, was found diffusely throughout the dorsal carapace exocuticle during late premolt. Ca was also present at similarly low and diffuse levels in this tissue prior to ecdysis. After the molt, Ca concentration increased markedly through stage A_1, as evidenced by the two examples presented in **Figure 2**. Just after the molt, Si appeared to increase (A1 C-6 in **Figure 2A**). While this could possibly be due to a decrease in other elements, thereby increasing the % atomic composition of Si, the increase in the ratio of Si to Pt (**Figure 2B**) argues for an actual increase in Si content.

As stage A_1 progresses to stage A_2, there was a sharp increase in Ca concentration. This corresponds both spatially and temporally to the initial deposition of $CaCO_3$ along the inner and outer exocuticular margins (Dillaman et al., 2005). Concomitant with the increase in Ca was a decrease in the Si signal (**Figure 2A**). Again, this could have been due to the increase in Ca atomic % which would make Si have a relatively lower atomic %. However, the Si to Pt ratio also decreases markedly suggesting that there is an actual decrease in the amount of Si in the exoskeleton (**Figure 2B**).

We hypothesize that Si plays some role in calcification since Si is only present to a detectable level in the mineralizing tissue and

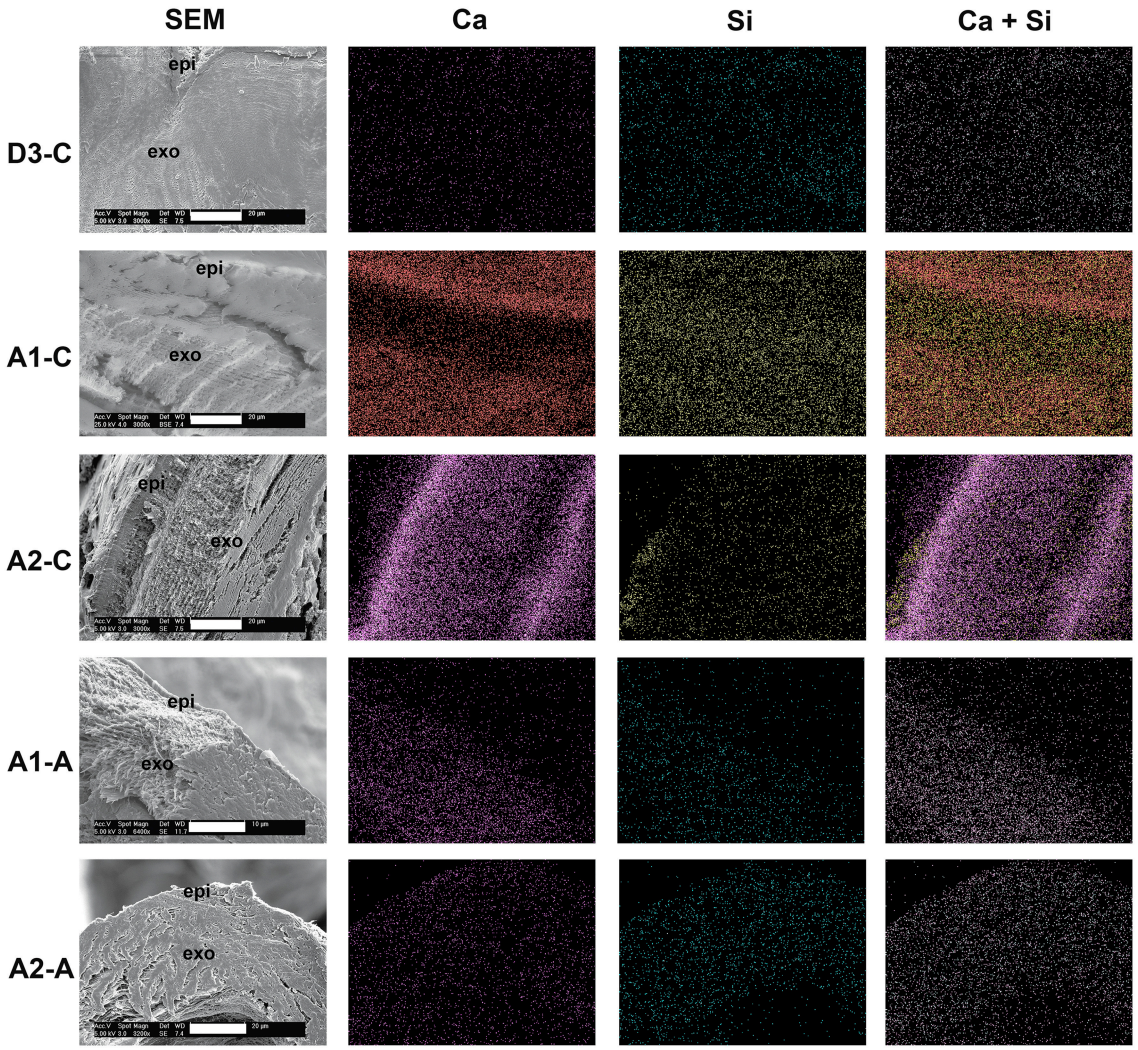

FIGURE 1 | SEM images and corresponding EDAX maps of the elemental distributions of Ca, Si and a composite of the Ca and Si (Ca+Si) within the carapace [C] and arthrodial membrane [A]. The labels on the left specify the molt stage followed by the tissue type. Thus D3-C refers to stage D3 carapace while A1-A is stage A1 arthrodial membrane. Orientation is indicated in the SEM images by the location of the epicuticle [epi] and exocuticle [exo]. Maps revealed that silicon levels were approximately equal to those of calcium in carapace prior to the onset of mineralization (stage D3). The proportional contribution of the Si signal decreased as that of calcium increased as mineralization began (stages A1 and A2). Silicon and calcium were present in low amounts in non-mineralizing arthrodial membrane at both stage A1 and A2. Scale bars (white) on each SEM image are 20 μm, except for A1-A which is 10 μm.

is absent at all stages observed in the non-calcifying arthrodial membrane cuticle. The function of Si in the earliest stages of $CaCO_3$ deposition has not been determined. Studies on other systems have suggested some possible roles.

Durak et al. (2016) found that some species of coccolithophores (*Coccolithus braarudii*, *Calcidiscus leptoporus*, *Scyphosphaera apsteinii*) possess a Na^+-coupled high-affinity Si transporter (SIT) or SIT-like transporter similar to that found in silicifying diatoms. SITs are competitively inhibited by germanium. They discovered that incubating these species of coccolithophores in the presence of Ge inhibited calcification and caused malformed coccoliths to be produced.

Silica has been implicated in the early stages of the mineralization of a variety of calcified tissues, potentially involved in either the synthesis of organic matrix components or in the nucleation of the calcium minerals. Silicates were observed in the pre-mineralized osteoid in bones of chicks, mice and rats (Carlisle, 1970; Landis et al., 1986). There is evidence that Si may be a necessary factor in the synthesis of collagen and can promote osteoblast proliferation and activity. The larval shell of the brachiopod, *Discinisca*, is mineralized by the formation of siliceous tablets. However, when the larva settles, the mantle epithelium begins to deposit apatite. Williams et al. (2001) hypothesized that the silica catalyzed the precipitation of apatite.

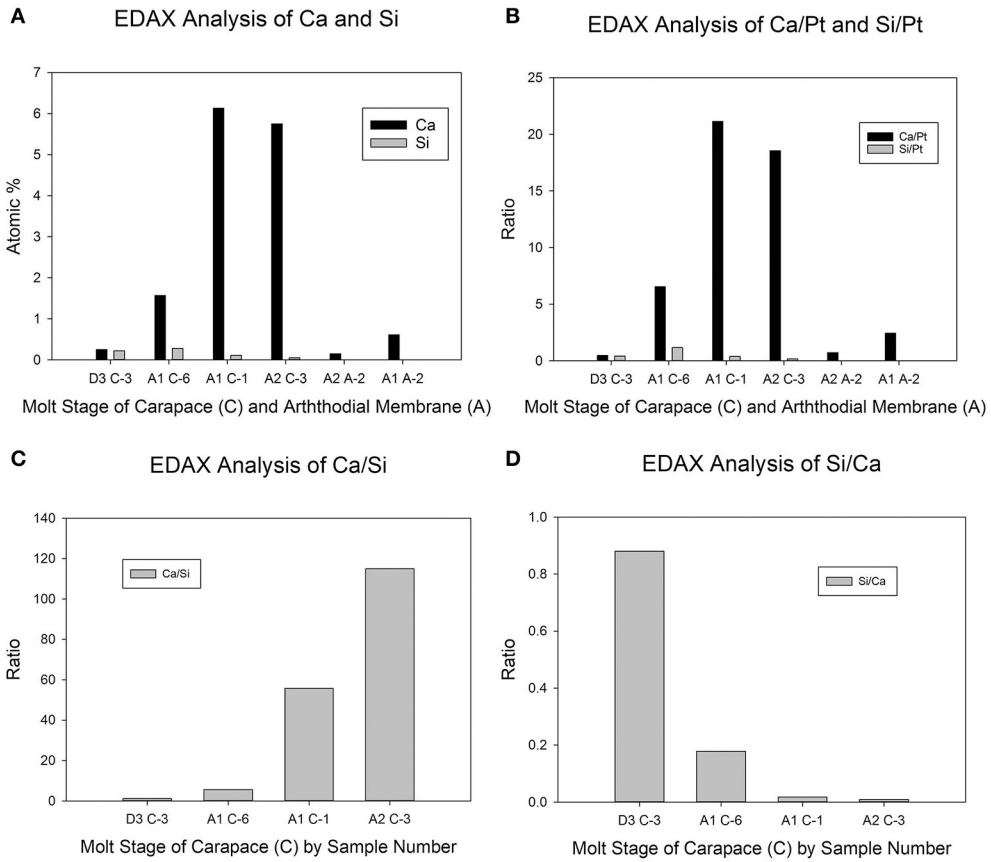

FIGURE 2 | Semiquantitative elemental analysis of EDAX maps. The x-axis legends represent the molt stage (D3, A1, or A2) followed by the tissue type (C = carapace; A = arthrodial membrane) followed by the sample number (1–6 for a given tissue type and molt stage). **(A)** Atomic percent of Ca and Si. **(B)** The same data as in 2A, but represented as the ratio of the Ca or Si atomic percent with that of Pt. **(C)** The data for the carapace samples in 2A represented as the Ca:Si ratio. **(D)** The same data as in 2C, but represented as the Si:Ca ratio. Neither of the semiquantitative analyses in panels **(A,B)** showed significant levels of Si in arthrodial membrane, hence these samples were excluded from the ratios **(C,D)**.

Matsko et al. (2011) also proposed that Si binds to N-acetyl-glucosamine (the monomer of chitin) to attract bicarbonate ions and serve as nucleation sites for calcium carbonate precipitation.

Gal et al. (2010) have produced definitive data on the ability of Si to stabilize ACC. They compared the temperature stability of ACC in the cystoliths in the leaves of two angiosperms, *Ficus microcarpa* and *M. alba*. In both species, the cystoliths retain ACC throughout the life of the leaf *in vivo*. Elemental mapping showed no evidence of Si associated with the ACC phase in *F. microcarpa*, but a small Si peak in the cystolith ACC of *M. alba*. The isolated cystolith ACC will crystalize to calcite *in vitro* upon heating as the hydrated ACC loses its bound water. The authors demonstrated that the ACC from *F. microcarpa* crystallized at a significantly lower temperature than that from *M. alba*, suggesting that the presence of Si stabilized the ACC. The authors confirmed this hypothesis by creating synthetic ACC with varying Si content. The greater the Si content, the higher the transition temperature at which ACC crystalized to calcite.

The temporal and spatial distribution of Si and Ca in the postmolt dorsal carapace cuticle of the blue crab are consistent with this hypothesis of ACC stabilization. The concentration and distribution of Si were highest at the time and region of initial calcification in the new exocuticle. The initial phase of the mineral deposition in these regions is ACC (Dillaman et al., 2005). The level of Si decreased at the time (stage A_2) when ACC transforms to calcite. The crustacean exoskeleton presents an excellent model in which to further investigate this hypothetical framework as well as other aspects of biomineralization.

ETHICS STATEMENT

The study was exempt from the above requirements in that it only utilized invertebrate organisms.

AUTHOR CONTRIBUTIONS

Both authors made substantial, direct and intellectual contributions to the work. The manuscript was written by RR after the death of RD.

ACKNOWLEDGMENTS

This paper is dedicated to the memory of RD, a friend, colleague, and collaborator for over 40 years. Dick was a gentleman and scholar, dedicated to the study of biomineralization in a wide range of taxa. He touched the lives of innumerable students and colleagues as a consummate teacher, mentor, and microscopist. This work, and that reviewed, was supported by a number of grants from the NSF and NC Sea Grant. Most recent support was by NCSG 2014-1751.

REFERENCES

Addadi, L., Vidavsky, N., and Weiner, S. (2012). Transient precursor amorphous phases in biomineralization. In the footsteps of Heinz A. *Lowenstam. Z. Kristallogr.* 227, 711–717. doi: 10.1524/zkri.2012.1524

Beklemishev, K. V. (1954). The discovery of siliceous formations in the epidermis of lower crustaceans. *Dokl. Akad. Nauk. SSSR* 3, 543–545.

Bouligand, Y. (1972). Twisted fibrous arrangements in biological materials and cholesteric mesophases. *Tissue Cell* 4, 189–190, 192–217. doi: 10.1016/S0040-8166(72)80042-9

Carlisle, E. M. (1970). Silicon: a possible factor in bone calcification. *Science* 167, 279–280. doi: 10.1126/science.167.3916.279

Coblentz, F. E., Shafer, T. H., and Roer, R. D. (1998). Cuticular proteins from the blue crab alter *in vitro* calcium carbonate mineralization. *Comp. Biochem. Physiol.* 121B, 349–360. doi: 10.1016/S0305-0491(98)10117-7

Dillaman, R., Hequembourg, S., and Gay, M. (2005). Early pattern of calcification in the dorsal carapace of the blue crab, *Callinectes sapidus*. *J. Morphol.* 263, 356–374. doi: 10.1002/jmor.10311

Drach, P. (1939). Mue et cycle d'intermue chez les crustacés décapodes. *Ann. Inst. Oceanogr.* 19, 103–391.

Drach, P., and Tchernigovtzeff, C. (1967). Sur la méthode de détermination des stades d'intermue et son application générale aux crustaces. *Vie Milieu* 18, 595–610.

Durak, G. M., Taylor, A. R., Walker, C. E., Probert, I., de Vargas, C., Audic, S., et al. (2016). A role for diatom-like silicon transporters in calcifying coccolithophores. *Nat. Commun.* 7:10543. doi: 10.1038/ncomms10543

Faircloth, L. M., and Shafer, T. H. (2007). Differential expression of eight transcripts and their roles in the cuticle of the blue crab, *Callinectes sapidus*. *Comp. Biochem. Physiol.* 146B, 370–383. doi: 10.1016/j.cbpb.2006.11.008

Gal, A., Weiner, S., and Addadi, L. (2010). The stabilizing effect of silicate on biogenic and synthetic amorphous calcium carbonate. *J. Am. Chem. Soc.* 132, 13206–13211. doi: 10.1021/ja106883c

Greenaway, P., Dillaman, R. M., and Roer, R. D. (1995). Quercitin-dependent ATPase activity in the hypodermal tissue of *Callinectes sapidus* during the moult cycle. *Comp. Biochem. Physiol.* 111A, 303–312. doi: 10.1016/0300-9629(94)00205-8

Kuballa, A. V., and Elizur, A. (2008). Differential expression profiling of components associated with exoskeletal hardening in crustaceans. *BMC Genomics* 9:575. doi: 10.1186/1471-2164-9-575

Landis, W. J., Lee, D. D., Brenna, J. T., Chandra, S., and Morrison, G. H. (1986). Detection and localization of silicon and associated elements in vertebrate bone tissue by imaging ion microscopy. *Calcif. Tissue Res.* 38, 52–59. doi: 10.1007/BF02556595

Lowenstam, H. A., and Weiner, S. (1989). *On Biomineralization*. New York, NY: Oxford University Press.

Luquet, G. (2012). Biomineralizations: insights and prospects from crustaceans. *Zookeys* 176, 103–121. doi: 10.3897/zookeys.176.2318

Marlowe, R. L., Dillaman, R. M., and Roer, R. D. (1994). Lectin binding by crustacean cuticle: the cuticle of *Callinectes sapidus* throughout the molt cycle, and the intermolt cuticle of *Procambarus clarkii* and *Ocypode quadrata*. *J. Crust. Biol.* 14, 231–246. doi: 10.2307/1548904

Matsko, N. B., Znidaršic, N., Letofsky-Papst, I., Dittrich, M., Grogger, W., Strus, J., et al. (2011). Silicon: the key element in early stages of biocalcification. *J. Struct. Biol.* 174, 180–186. doi: 10.1016/j.jsb.2010.09.025

Mekhanikova, I. V., Andreev, D. S., Belozerova, O. Y., Mikhlin, Y. L., Lipko, S. V., Klimenkov, I. V., et al. (2012). Specific features of mandible structure and elemental composition in the polyphagous amphipod *Acanthogammarus grewingkii* endemic to Lake Baikal. *PLoS ONE* 7:e43073. doi: 10.1371/journal.pone.0043073

Michels, J., and Gorb, S. N. (2015). Mandibular gnathobases of marine planktonic copepods – feeding tools with complex micro- and nanoscale composite architectures. *Beilstein J. Nanotechnol.* 6, 674–685. doi: 10.3762/bjnano.6.68

Michels, J., Vogt, J., and Gorb, S. N. (2012). Tools for crushing diatoms - opal teeth in copepods feature a rubber-like bearing composed of resilin. *Sci. Rep.* 2:465. doi: 10.1038/srep00465

Miller, C. B., Nelson, D. M., Weiss, C., and Soeldner, A. H. (1990). Morphogenesis of opal teeth in calanoid copepods. *Mar. Biol.* 106, 91–101. doi: 10.1007/BF02114678

Nesbit, K. T., and Roer, R. D. (2016). Silicification of the medial tooth in the blue crab *Callinectes sapidus*. *J. Morphol.* 277, 1648–1660. doi: 10.1002/jmor.20614

Pierce, D. C., Butler, K. D., and Roer, R. D. (2001). Effects of exogenous N-acetylhexosamindase on the structure and mineralization of the postecdysial exoskeleton of the blue crab, *Callinectes sapidus*. *Comp. Biochem. Physiol.* 128B, 691–700. doi: 10.1016/S1096-4959(00)00362-6

Raabe, D., Romano, P., Sachs, C., Al-Sawalmih, A., Brokmeier, H.-G., Yi, S.-B., et al. (2005). Discovery of a honeycomb structure in the twisted plywood patterns of fibrous biological nanocomposite tissue. *J. Crystal Growth* 283, 1–7. doi: 10.1016/j.jcrysgro.2005.05.077

Rathbun, M. J. (1896). The genus *Callinectes*. *Proc. U.S. Nat. Mus.* 18, 349–375. doi: 10.5479/si.00963801.18-1070.349

Roer, R. D. (1980). Mechanisms of resorption and deposition of calcium in the carapace of the crab *Carcinus maenas*. *J. Exp. Biol.* 88, 205–218.

Roer, R. D., Abehsera, S., and Sagi, A. (2015). Exoskeletons across the Pancrustacea: a comparison of cuticular morphology, physiology, biochemistry and genetics between Decapoda and Hexapoda. *Integr. Comp. Biol.* 5, 771–791. doi: 10.1093/icb/icv080

Roer, R. D., Burgess, S. K., Miller, C. G., and Dail, M. B. (1988). "Control of calcium carbonate nucleation in pre- and postecdysial crab cuticle," in *Chemical Aspects of Regulation of Mineralization*, eds C. S. Sikes and A. P. Wheeler (Mobile, AL: Univ. of South Alabama Publication Service), 21–24.

Roer, R. D., and Dillaman, R. M. (1984). The structure and calcification of the crustacean cuticle. *Am. Zool.* 24, 893–909. doi: 10.1093/icb/24.4.893

Roer, R. D., and Dillaman, R. M. (1993). "Molt-related change in integumental structure and function," in *The Crustacean Integument - Morphology and Biochemistry*, eds M. Horst and J. A. Freeman (Boca Raton, FL: CRC Press), 1–37.

Roer, R. D., Halbrook, K. E., and Shafer, T. H. (2001). Glycosidase activity in the postecdysial cuticle of the blue crab, *Callinectes sapidus*. *Comp. Biochem. Physiol.* 128B, 683–690. doi: 10.1016/S1096-4959(00)00363-8

Roer, R., and Towle, D. (2004). Partial nucleotide sequence of a putative cuticular hexosaminidase from the blue crab, *Callinectes sapidus*. *MDIBL Bull.* 43, 40–42.

Roer, R., and Towle, D. (2005). Partial nucleotide sequence and expression of plasma membrane Ca-ATPase in the hypodermis of the blue crab, *Callinectes sapidus*. *MDIBL Bull.* 44, 40–43.

Shafer, T. H., Roer, R. D., Midgette-Luther, C., and Brookins, T. A. (1995). Postecdysial cuticle alteration in the blue crab, *Callinectes sapidus*: synchronous changes in glycoproteins and mineral nucleation. *J. Exp. Zool.* 271, 171–182. doi: 10.1002/jez.1402710303

Shafer, T. H., Roer, R. D., Miller, C. G., and Dillaman, R. M. (1994). Postecdysial changes in the protein and glycoprotein composition of the cuticle of the blue crab *Callinectes sapidus*. *J. Crust. Biol.* 14, 210–219. doi: 10.2307/1548901

Tweedie, E. P., Coblentz, F. E., and Shafer, T. H. (2004). Purification of a soluble glycoprotein from the uncalcified ecdysial cuticle of the blue crab *Callinectes sapidus* and its possible role in initial mineralization. *J. Exp. Biol.* 207, 2589–2598. doi: 10.1242/jeb.01070

Vatcher, H. E., Roer, R. D., and Dillaman, R. M. (2015). Structure and molt cycle dynamics of the dorsal ossicle complex in the gastric mill of the blue crab, *Callinectes sapidus*. *J. Morphol.* 276, 1358–1367. doi: 10.1002/jmor.20423

Williams, A., Lüter, C., and Cusack, M. (2001). The nature of siliceous mosaics forming the first shell of the brachiopod *Discinisca*. *J. Struct. Biol.* 134, 25–34. doi: 10.1006/jsbi.2001.4366

Conflict of Interest Statement: The authors declare that the research was conducted in the absence of any commercial or financial relationships that could be construed as a potential conflict of interest.

frontiers in Marine Science

ORIGINAL RESEARCH
published: 12 June 2018
doi: 10.3389/fmars.2018.00203

Production of Calcium-Binding Proteins in *Crassostrea virginica* in Response to Increased Environmental CO_2 Concentration

Mackenzie Richards[1,2], *Wei Xu*[1,2*], *Amy Mallozzi*[3], *Reagan M. Errera*[2] *and John Supan*[1,2,4]

[1] *The Agricultural Center, Louisiana State University, Baton Rouge, LA, United States,* [2] *School of Renewable Natural Resources, Louisiana State University, Baton Rouge, LA, United States,* [3] *College of the Coast and Environment, Louisiana State University, Baton Rouge, LA, United States,* [4] *Louisiana Sea Grant Oyster Research Laboratory, Grand Isle, LA, United States*

Biomineralization is a complexed process by organisms producing protective and supportive structures. Employed by mollusks, biomineralization enables creation of external shells for protection against environmental stressors. The shell deposition mechanism is initiated in the early stages of development and is dependent upon the concentration and availability of calcium carbonate ions. Changes in concentrations of the critical ions required for shell formation can result in malformation of shells. As pCO_2 concentrations in the atmosphere continue to increase, the oceans are becoming more acidified. This process, known as ocean acidification (OA), has demonstrated adverse effects on shell formation in calcifying organisms across taxa. Although OA is known to inhibit the shell deposition in mollusks, the impact of OA on the gene regulation of calcium deposition remains unknown. Here we show the responses of four calcium-binding protein genes, caltractin (*cetn*), calmodulin (*calm*), calreticulin (*calr*), and calnexin (*canx*), to CO_2-derived OA using a *Crassostrea virginica* mantle cell (*Cv*MC) culture model and a larval *C. virginica* model. These four genes were cloned from *C. virginica* and the three-dimensional structures of the proteins encoded by these four genes were fully characterized using homolog modeling methods. Although an acidified environment by increased atmospheric pCO_2 (1,000 ppm) did not result in significant effects on *Cv*MC proliferation and apoptosis, lower environmental pH induced upregulations of all four calcium-binding protein genes in *Cv*MCs. Similarly, increased pCO_2 did not affect the growth of larval *C. virginica* in the early stages of development. However, elevated pCO_2 concentrations enhanced the expression of these calcium-binding protein genes at the protein level. The four calcium-binding protein genes demonstrated responsive expression profiles to an acidified environment at both cellular and individual levels. Further investigation of these genes may provide insight into the molecular regulation of mollusk biomineralization under OA stress.

Keywords: biomineralization, *Crassostrea virginica*, ocean acidification, calcium-binding proteins, mantle cell culture

OPEN ACCESS

Edited by:
Andrew Stanley Mount, Clemson University, United States

Reviewed by:
Gary H. Dickinson, The College of New Jersey, United States
Marta Gomez-Chiarri, University of Rhode Island, United States

***Correspondence:**
Wei Xu
wxu@agcenter.lsu.edu

Specialty section:
This article was submitted to Marine Molecular Biology and Ecology, a section of the journal Frontiers in Marine Science

Received: *23 December 2017*
Accepted: *25 May 2018*
Published: *12 June 2018*

Citation:
Richards M, Xu W, Mallozzi A, Errera RM and Supan J (2018) Production of Calcium-Binding Proteins in Crassostrea virginica in Response to Increased Environmental CO_2 Concentration. Front. Mar. Sci. 5:203. doi: 10.3389/fmars.2018.00203

INTRODUCTION

Mollusca have developed hard external structures (shells) to protect their soft tissues against pathogens, predation, and other environmental stressors (Marin et al., 2012; Arivalagan et al., 2017). These protective structures are commonly formed by a biologically controlled process called biomineralization. Mollusk shells contain approximately 95% calcium carbonate ($CaCO_3$) and 5% organic matter (Lowenstam and Weiner, 1989). The major forms of environmental $CaCO_3$ are aragonites, calcites, or vaterites. Although $CaCO_3$ is also the main component, the shells formed by molluscan species are thousands fold tougher than any of these environmental $CaCO_3$ polymorphs (Currey, 1977), which suggests a unique biomineralized structure within shells (Harper, 2000). The hypothesis of the synthesis of this unique structure suggests that shell fabrication is regulated by specialized cells in the host where activities are controlled by a cascade of genes (Mann, 1983).

Biomineralization occurs primarily in the extrapallial cavity, which contains extrapallial fluid with a substantially higher concentration of calcium and carbonate ions compared to the surrounding environment. Numerous calcium-binding proteins, passive calcium transporters, and active calcium pumps are involved in calcium transport and ion regulation to maintain a high $CaCO_3$ saturation state within the extrapallial fluid (Ip et al., 2006). Therefore, the concentrations and availability of environmental calcium and carbonate ions are critical to the shell formation mechanism.

The availability of calcium and carbonate ions in the ocean can be manipulated by a number of environmental factors. Atmospheric CO_2 levels are continuing to increase due to anthropogenic activities. The oceans are currently the sink for ∼30% of anthropogenic carbon dioxide (Sabine et al., 2004). The relationship between atmospheric CO_2 concentration and carbonate ion concentration in water is represented with the following chemical equation (Orr et al., 2005; Zeebe, 2012):

$$CO_2(\text{atmospheric}) \leftrightarrow CO_2(\text{aqueous}) + H_2O \leftrightarrow H_2CO_3 \leftrightarrow H^+ + HCO_3^- \leftrightarrow 2H^+ + CO_3^{2-}$$
$$+$$
$$CO_3^{2-} \rightarrow 2HCO_3^-$$

As a result of increased atmospheric CO_2, the balance of inorganic carbon is shifting toward generating more bicarbonate, carbonate, and H^+, a process known as ocean acidification (OA). Meanwhile, increased H_2CO_3 compete with calcifiers on carbonate to generate more bicarbonate, which leads insufficient $CaCO_3$ deposition during biomineralization. As a result, the homeostasis of carbonate and calcium ions in the extrapallial fluid of mollusks is disrupted, which ultimately inhibits the biomineralization process.

It is well known that the early-life history stages of bivalves, including gametes, embryos and larvae are vulnerable to environmental stressors. Although studies have revealed the potential impact of ocean acidification on larval stages of oysters (Parker et al., 2010; Gazeau et al., 2011; Waldbusser et al., 2013), efforts in understanding the mechanism of this impact are limited. Several critical developmental phases, along with significant morphological changes, are involved in the oyster life cycle following gamete fertilization. The first vital development event is initiated 24 h post fertilization in larva when the shell begins to form. In this stage, bivalve larvae are particularly sensitive to decreases in environmental pH (Waldbusser et al., 2013). Within the ocean, pH, dissolved inorganic carbon (DIC), and mineral solubility are regulated by the balance of pCO_2 and carbonate ions (Waldbusser et al., 2014). Bivalve larvae utilize dissolved calcium and carbonate ions to deposit their shells through calcification processes. Fluctuation of dissolved CO_2 results in equilibrium disruption of pH, mineral solubility and DIC, which disrupts the mechanisms of larval bivalve shell calcification.

Numerous genes that are potentially involved in biomineralization have been identified from various mollusk species with the completion of genome sequencing and the development of high-throughput sequencing. Zhang et al. predicted over 250 shell formation related genes from the genome of *Crassostrea gigas* by looking for the classic calcium-binding domain, E-F hand structures (Friedberg, 1988) in translated amino acid sequences (Zhang et al., 2012). Another study using a *Pinctada fucata* microarray containing over 58,000 transcript represented probes suggested that 31 gene regulation pathways were likely to be involved in shell formation during larval development. One identified pathway was directly related to calcium signaling in the database of Kyoto Encyclopedia of Genes and Genomes (KEGG, ko04020) (Liu et al., 2015). The most recent genomic study obtained a group of shell formation related genes from 14 released molluscan genomes (Takeuchi, 2017). In addition to genes identified by high-throughput techniques, many biomineralization-related individual genes were also recognized as calcium-binding protein encoding genes (Weiss et al., 2000; Hattan et al., 2001; Huang et al., 2007; Yan et al., 2007; Takagi and Miyashita, 2010; Su et al., 2013). Unfortunately, most of the calcium-binding protein encoding genes have not been sequenced or identified in the model species of the current study, *C. virginica*. Therefore, the first goal of this study is to clone and fully characterize the structures of the full length of some calcium-binding protein genes from *C. virginica*.

Four calcium binding proteins were investigated in the current study. Calmodulin (CALM) is a well-studied calcium-binding protein in mollusk biomineralization. Several calmodulins and the homologs have been identified and cloned from various mollusk species, including *Pinctada fucata* (Li et al., 2004; Yan et al., 2007), *Hyriopsis schlegelii* (Peng et al., 2017), and *C. gigas* (Li et al., 2016). Through studying bivalve organs and tissues in mollusks, it was determined that mantle tissue produced the highest number of calmodulins in *P. fucata* (Li et al., 2005). The recombinant calmodulin *in vitro* was established as a protein

that modifies calcite formation and nucleate aragonite during biomineralization (Yan et al., 2007). Less frequently studied in mollusk biomineralization, caltractin (CETN), also known as centrin, was recognized as a calmodulin-related protein (Nishi et al., 2013). Identified from various species ranging from yeast to human, caltractins were believed to participate in numerous calcium-related cell activities (Nishi et al., 2013). Calreticulin (CALR) and calnexin (CANX) were additionally studied in mollusk species as biomineralization-related genes. Originally discovered in the cell endoplasmic reticulum, CALR has also been located in the cell surface (Arosa et al., 1999), bloodstream (Sueyoshi et al., 1991), and extracellular matrix (Somogyi et al., 2003) in many cell types and species (Coppolino and Dedhar, 1998). These are consistent to another finding which suggests that the biomineralization proteins can be provided through other resources, such as hemolymph (Mount et al., 2004). Similarly, CANX, a close relative to calreticulin, demonstrated strong calcium binding abilities in various signaling pathways in cells (Corbett and Michalak, 2000; Michalak et al., 2002).

Atmospheric CO_2 is expected to reach 1,000 ppm by the year 2100, which is more than double the amount of current CO_2 in the air (400 ppm), according to the Intergovernmental Panel on Climate Change (IPCC, 2007). Therefore, it is critical to identify the potential impacts of increased atmospheric CO_2 on the biomineralization process of calcifying mollusks, many of which are important both economically and ecologically in coastal areas. The second goal of this study is to investigate the effect of elevated pCO_2 on the regulation of these proteins in biomineralization. Expression levels of four calcium-binding protein encoding genes, caltractin (*calt*), calmodulin (*calm*), calreticulin (*calr*), and calnexin (*canx*) were investigated during the development of larval *C. virginica* at two atmospheric pCO_2 concentrations. Cells cultured from the mantle of *C. virginica* were established and utilized to study the regulation of these four calcium-binding proteins in response to elevated pCO_2 since over 80% biomineralization-related genes in *C. gigas* are mantle tissue specific (Zhang et al., 2012). Our results indicate that CO_2-derived OA alters the larval mollusk shell formation through the regulation of calcium-binding proteins. These calcium-binding proteins can potentially be used as indicators of successful development and stress levels in larval mollusks, and as selective breeding markers for the improvement of OA resistant lines in mollusk aquaculture.

MATERIALS AND METHODS

Cloning and Bioinformatics Analyses of Calcium-Binding Protein Genes From *C. virginica*

All the oysters used in this study were maintained at the Michael C. Voisen Louisiana Sea Grant Oyster Research Laboratory. The original oyster individuals were collected from the Barataria Bay near Grand Isle, Louisiana. The current individuals were generated from those original individuals through several passages. The water condition in the Oyster Research Laboratory was created to mimic the natural environment near the coast of Grand Isle (pH8.5; salinity 15 ppt).

Four calcium-binding protein encoding genes, caltractin (*cetn*), calmodulin (*calm*), calreticulin (*calr*), and calnexin (*canx*), were cloned. Briefly, a pair of cloning primers were designed based on expressed sequence tag (EST) in the GenBank database from *Crassostrea* spp. (**Table 1**). The *C. virginica* individuals used for gene cloning were obtained from Grand Isle, Louisiana. The total RNA was isolated from homogenized *C. virginica* mantle tissues using TRIzol® Reagent (Life Technologies, Carlsbad, CA) followed by DNA removal with TURBO DNA-free™ Kit (Thermo-Fisher Scientific, Plaquemine, LA). The total RNA was then used for cDNA synthesis with SuperScript IV Reverse Transcriptase (Thermo-Fisher Scientific) following the manufacturer's instructions. Fragments of the four calcium-binding protein genes were amplified using the gene cloning primers and GoTaq® DNA Polymerase (Promega Biotechnology Co., Madison, WI) using regular PCR cycles (94°C 5 min followed by 32 cycles of 94°C 30 s-55°C 30 s-72°C 30 s, and a final extension step at 72°C for 7 min). The PCR product was then purified from a 7% polyacrylamide-TBE gel using a DNA dialysis collection method following the standard protocol (Sambrook and Russell, 2006b). The purified PCR products were cloned to the pGEM®-T Easy Vector Systems (Promega Biotechnology Co.) and transformed into DH5α competent *Escherichia coli* following a standard protocol (Sambrook and Russell, 2006a). The bacterial suspension was spread on LB plate containing 100 ng/ml ampicillin overnight at 37°C. Colonies were randomly picked, verified, and submitted for sequencing at the Gene Lab of the Louisiana State University, School of Veterinary Medicine (Baton Rouge, LA). For plasmids isolated from each bacterial inoculate, the inserts of the plasmids were sequenced from two directions with T7 and SP6 primers, respectively. The two reads of each insert were aligned using BLASTn. The aligned sequences were trimmed with VecScreen to remove the sequence of pGEM-T Easy vector.

With the obtained fragment of *calr* and *canx*, new primers were designed using the primer design software provided by the IDT DNA website. These specific primers were used for both full-length gene cloning and qPCR. Cloning of full length sequences of the four genes was performed using the Rapid Amplification of cDNA Ends (RACE) system from Invitrogen (Life Technologies). PCR products for 3′ or 5′ end gene fragments were loaded and run on a 0.8% agarose TAE gel and purified using Zymoclean Gel DNA Recovery Kit (Zymo Research, Irvine, CA) following the manufacturer's directions. The purified PCR products were submitted for sequencing at the Gene Lab using the gene specific primers for each gene.

The obtained 3′ and 5′ end sequences of each gene along with the originally cloned fragment in step 2 were assembled using BLASTn for two sequences. The protein sequence of each gene was predicted by the mRNA translation tool in Expert Protein Analysis System (ExPaSy) (Artimo et al., 2012). The open reading frame (ORF) of each gene was identified based on the length of predicted ORF and the length of the

TABLE 1 | PCR primers used in the study.

Target gene	Primer ID	Roles	Sequence
ef1α[*]	Cv01 (F) Cv02 (R)	qPCR qPCR	5′-ATC AAC TTC CAC TGG CCA TC-3′ 5′-TTT TCC CAT CTC AGC TGC TT-3′
cetn	Cv29 (F)	Cloning/qPCR	5′-GAA GCA AGG CAA TCT CCA AAG-3′
	Cv30 (R)	Cloning/qPCR	5′-CCG TCC GAA TTA GCA TCA CA-3′
calm	Cv31 (F)	Cloning/qPCR	5′-ACA GAT GAA GAG GTA GAT GAA ATG A-3′
	Cv32 (R)	Cloning/qPCR	5′-GCT ATA CAA GCA GTT GCC ATT C-3′
calr	Cv33 (F)	Cloning (Fragment)	5′-ATT GAC TGT GGG GGT GGA TA-3′
	Cv34 (R)	Cloning (Fragment)	5′-ACC TTC TTG GTG CCT GGT C-3′
	Cv51 (F)	qPCR/3′RACE	5′-CCC AAA GAT CTC GAC CAG AAA-3′
	Cv52 (R)	qPCR/5′RACE	5′-GGT GCC TGG TCC ACA AAT A-3′
canx	Cv35 (F)	Cloning (Fragment)	5′-CCT CAA GTC CAA AGC AAA GC-3′
	Cv36 (R)	Cloning (Fragment)	5′-AGG CTC CTC CAC AGT CGA TA-3′
	Cv57 (F)	qPCR/3′RACE	5′-CCA GAC AAA TGT GGA TTG GAT AAC-3′
	Cv58 (R)	qPCR/5′RACE	5′-CTT CCA GCA GTG ATC CTT CAT-3′

**Elongation factor 1α gene.*

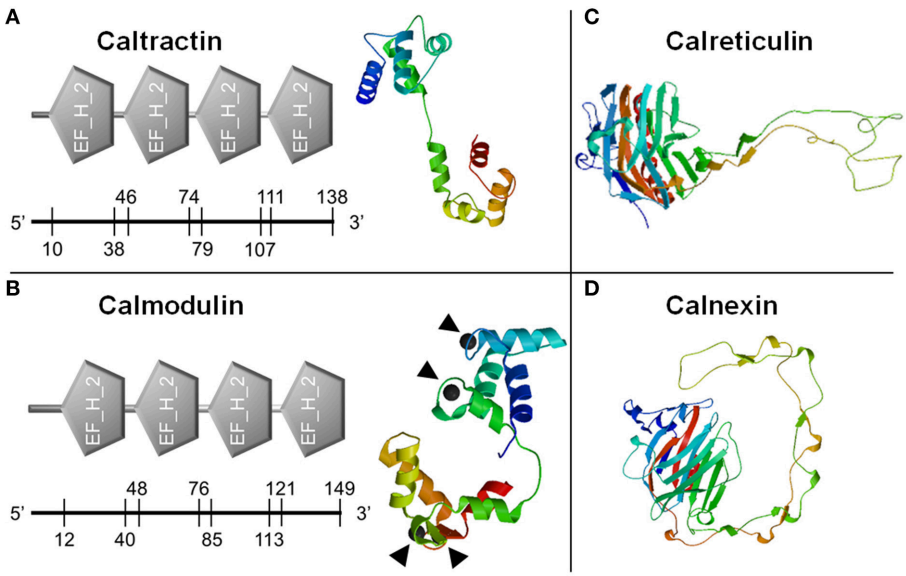

FIGURE 1 | Prediction of calcium-binding domains and three dimensional structures of calcium binding proteins. Classic calcium-binding domains, E-F hands (EF_H_2), were identified from caltractin **(A, left)** and calmodulin **(B, left)**. Four calcium-binding locations in calmodulin were also predicted (▲). The three dimensional structures of caltractin **(A, right)**, calmodulin **(B, right)**, calreticulin **(C)**, and calnexin **(D)** were simulated. The numbers on the axis under each domain were starting and ending amino acid sites in each protein.

ORFs in homologous sequences in GenBank database. The translated protein sequence for each gene was first submitted to GenBank for homologous sequence searching using BLASTp. Then motifs and signature sequences of each protein were predicted using the simple modular architecture research tool (SMART) (Schultz et al., 1998; Letunic et al., 2015). Finally, the three-dimensional structure of each protein was predicted based on protein structure homology-modeling system (SWISS-MODEL, **Figure 1**) (Arnold et al., 2006; Kiefer et al., 2009; Biasini et al., 2014). To select the best structure from multiple predictions for each protein, we used GMQE (Global Model Quality Estimation) and the QMEAN as parameters. The 3D structure with the highest GMQE and QMEAN scores was chosen for each protein.

C. virginica Mantle Cell (*Cv*-MC) Culture

Adult eastern oysters were obtained from the Michael C. Voisen Louisiana Sea Grant Oyster Research Laboratory, where they were maintained in off bottom culture cages. Oysters were then transferred to the indoor facility with recirculating systems containing artificial seawater and acclimated to 25ppt salinity at 22°C. Prior to cell culture, selected oysters were

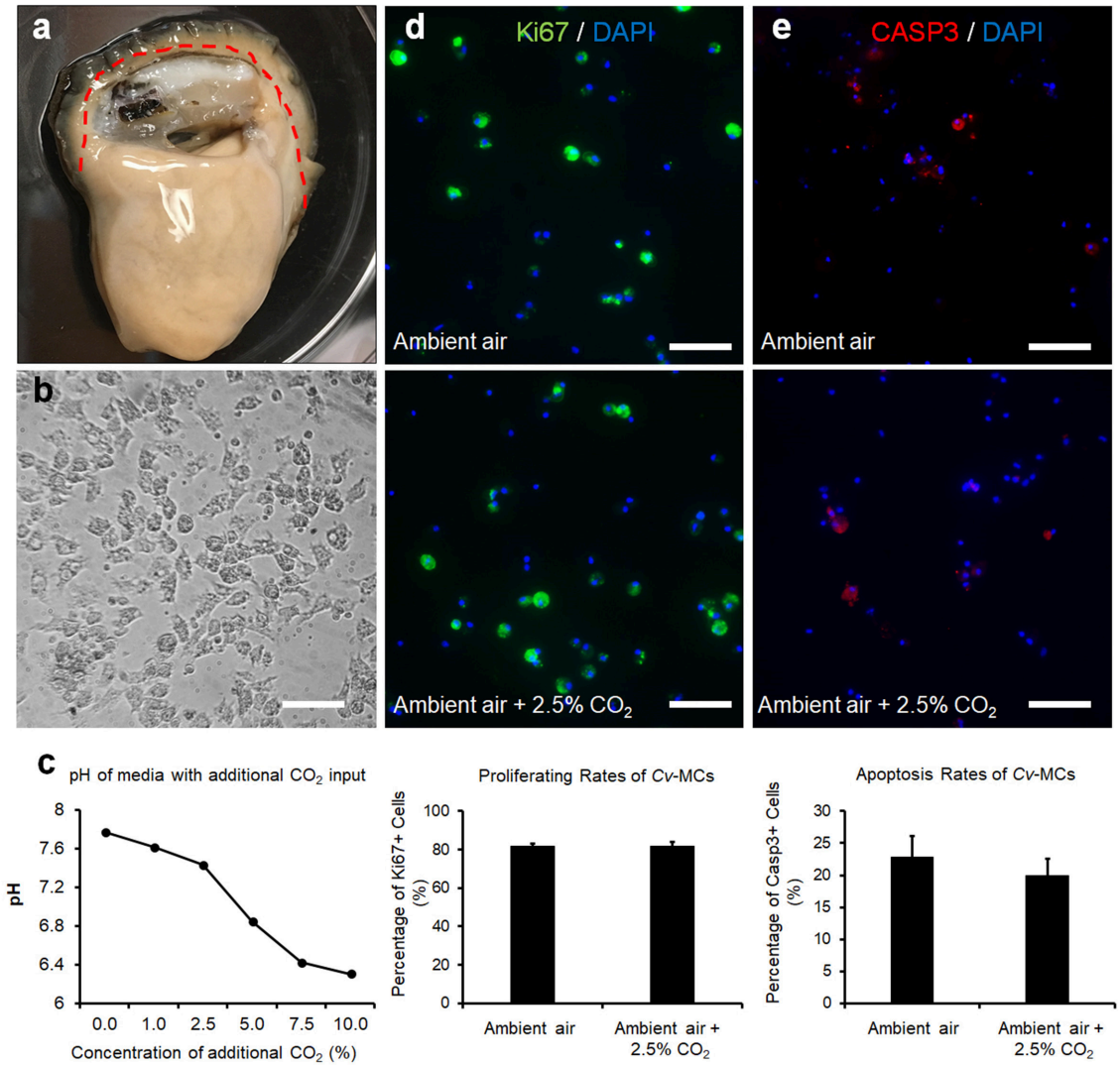

FIGURE 2 | *Cv*MC proliferation and apoptosis assays. The location of mantle tissue used for cell culture was indicated by dashed line **(a)**. *Cv*MCs after 48-h culture was shown **(b)**. Changes of medium pH in response to increased atmospheric CO_2 ($n = 4$), **(c)**. Results of IFs with Ki-67 **(d)** and caspase 3 **(e)** were also quantified with the cells treated by ambient air and increased CO_2 concentration (2.5%). $n = 8$. Scale bar: 50 μm. Error bar: standard error of mean.

kept in sterilized Ca^{2+} and Mg^{2+} free artificial seawater solution (CMFSS, including 436 mM NaCl, 10.7 mM KCl, 21.2 mM Na2HPO4, 16.7 mM Glucose, and 12.0 mM HEPES) supplemented with 100 units/mL of penicillin and 100 μg/mL of streptomycin (CMFF-Pen/Strep) overnight at 4°C. The sterilized oysters were dissected and the connective tissues along the edge of the mantle were collected (**Figure 2a**). The collected *C. virginica* mantle tissues were thoroughly washed with CMFF-Pen/Strep and digested with 0.2% collagenase I (Thermo-Fisher Scientific) in CMFF-Pen/Strep solution overnight at room temperature. The digested tissue suspension was mixed with oyster cell culture medium (OCCM, Leibovitz-L15 basal medium with additional 345.6 mM NaCl, 7.2 mM KCl, 5.4 mM $CaCl_2$, 4.0 mM $MgSO_4 \bullet 7H_2O$, 19.2 mM $MgCl_2 \bullet 6H_2O$, and 4.0 mM L-Glutamine) supplemented with 10% (v/v) chicken serum (Life Technologies, Carlsbad, CA), 100 units/mL of penicillin and 100 μg/mL of streptomycin (OCCM-Pen/Strep). The mixture was then filtered with a 100 μm cell strainer (VWR International, Radnor, PA) to remove the non-digested tissue. The flow-through solution was centrifuged at 500 × g for 5 min to collect cells and the supernatant was discarded. Fresh OCCM-Pen/Strep medium was added to the cell pellet to re-suspend the cells. The fully suspended *C.virginica* mantle cells (*Cv*MCs) in medium were then seeded in a 24-well cell culture plate pre-coated with 0.01% Poly-L-lysine in CMFSS solution. All seeded plates were incubated at 27°C for 24–48 h to allow the adhesion of cells to the bottom of the plate. Cells were observed under a microscope to ensure attachment and to confirm the cell confluence at ∼80% (**Figure 2b**).

Stimulation of *Cv*MCs With Increased pCO_2

*Cv*MCs from each *C. virginica* individual were cultured in two 24-well plates until reaching 80% confluences. Medium in each well was replaced with fresh medium prior to the treatment. All the cell cultures were kept in a CO_2 cell culture incubator. The concentration of CO_2 in the input air can be regulated by the incubator. The increased CO_2 concentration in the input air mimics the increased atmospheric CO_2 level in nature. One plate of *Cv*MCs were treated with ambient air (Control) and the cells in the other plate were treated with additional 1, 1.5, or 2.5% CO_2 input. All cells were kept at 27°C for 24 h prior to harvesting. Half of the wells were harvested using TRIzol® Reagent for RNA isolation while the other half were fixed in 4% paraformaldehyde (PFA) for immunofluorescent staining. The cell culture medium was collected from each cell culture and the pH of each medium sample was measured immediately using a bench top pH meter (VWR International). Cells from eight *C. virginica* individuals were used as eight biological replicates for this study.

Stimulation of Larval *C. virginica* With Increased pCO_2

The production of *C. virginica* larvae was performed at the Michael C. Voisen Louisiana Sea Grant Oyster Research Laboratory following a previously established protocol. Briefly, individual sexually matured *C. virginica* were maintained at 22°C, until spawning was thermally induced through exposure of estuarine water from Grand Isle, Louisiana raised to 34°C. Once spawning concluded, isolated eggs and sperm were pooled and thoroughly mixed to initiate fertilization. Successfully fertilized eggs, determined by light microscopy, were used for the experiment 2 h post fertilization. Following fertilization, triplicate larval cultures were established for each treatment at a density of 100 eggs/ml. After 48 h, the larvae were restocked at 50 larvae/ml to meet the culture standards and were established in new pre-conditioned estuarine water.

Acidification treatments included a current pCO_2 of 400 ppm and a future by year 2100 pCO_2 of 1,000 ppm based on IPCC (IPCC, 2007). Compressed zero air tanks with added CO_2 where prepared gravimetrically and certified to the specified CO_2 concentrations within a 2% analytical tolerance (AirGas, Baton Rouge, LA). Air was bubbled into the estuarine water through an air stone. The estuarine water was bubbled with the proper pCO_2 for at least a 3-day period to ensure proper dissolution of CO_2 (pre-conditioned water). Bubbling of the treatment CO_2 was continued in the pre-conditioned water and culturing vessel after *C. virginica* were introduced. Bubbling rates were adjusted to ensure consistent turbulence between biological replication.

Larval samples from each treatment group were collected at 0, 24, and 48 h post fertilization. The larvae provided with a daily algal mixture of *Tisochrysis lutea*, *Cisochrysis galbana*, *Chaetoceros calcitrans*, *Chaetoceros muelleri*, and *Pavlova luthen*, at concentrations of 40,000 cells mL^{-1}. Temperature, pH, and salinity were measured daily (Orion 370 PerpHecT benchtop pH/ORP/ISE/T meter, Thermo Fisher Scientific, Waltham, MA). Total alkalinity was measured from water that had been treated with supersaturated 0.02% mercuric chloride and frozen prior to analysis. Briefly, total alkalinity samples were titrated with 0.097N hydrochloric acid (HCl) to achieve a pH of 3.5 using a Schott Titroline easy titrator (General Laboratory Supply, Pasadena, TX) (Dickson et al., 2007). Samples were then left to de-gas for 3 min and titrated step-wise at 20 s intervals in 0.05 ml increments until pH 3.0 to create a Gran Line, using the SeaCarb (http://CRAN.Rproject.org/package=seacarb) program in R Studio (Boston, MA). Larval samples were harvested and maintained in 4% PFA for microscopy and immunofluorescence (IF). The shell length of each larva was measured as the maximum distance between two points on the edge of the shell.

Quantitative PCR (qPCR)

Total RNAs from *Cv*MC were isolated and used for cDNA synthesis as described above. qPCRs with synthesized cDNAs were performed using Sybr Green method in a 7900HT Real-Time PCR System (Applied Biosystems, Grand Island, NY). The qPCR reaction was run at 50°C for 2 min, 94°C for 2 min, followed by 40 cycles at 94°C for 30 s, 55°C for 30 s and 72°C for 30 s. The cycle threshold (Ct) values generated from the system for all samples were used for relative expression analysis using $2^{-\Delta\Delta Ct}$ method (Rao et al., 2013).

Immunofluorescence With *Cv*MCs and Larval *C. virginica*

Immunofluorescence (IF) was used to visualize and quantify the proliferation and apoptosis of mantle cells in both the control and treatment. Cells or larval *C. virginica* fixed in 4% PFA were washed with phosphate-buffered saline (PBS). Samples were then blocked for 2 h at room temperature with 10% lamb serum in PBS in each well. After 3 washes with PBS, a primary antibody diluted in PBS was applied to cover the samples in each well and incubated at 4°C overnight. Following removal of primary antibody and three washes with PBS, the secondary antibody conjugated with either Alexa flour 594 (red) or Alexa flour 488 (green) dye, was diluted and allocated into the wells. The plates were incubated in a dark area for 2 h. After secondary antibody incubation and three washes in PBS, a 10-min counterstaining with a nuclear dye, 4′,6-diamidino-2-phenylindole (DAPI, blue, Biotium Inc., Fremont, CA) was performed on each sample with 0.1 μg/ml DAPI in PBS. Primary antibodies used in this study include mouse-anti-human Ki-67 (Novus Biologicals, Littleton, CO), rabbit-anti-human caspase 3 (Casp3, Boster Biological Technology, Pleasanton, CA), and three mouse originated calcium-binding protein antibodies (all from the Developmental Studies Hybridoma Bank at the University of Iowa, Iowa City, IA). The use of Ki-67 and Casp3 antibodies was to test cell proliferation and apoptosis, respectively. The ideal pCO_2 concentrations created in our study were expected to induce the differential gene expression without significantly changing cell proliferation and apoptosis. Therefore, the IF with these two antibodies was to avoid overdosing the cells with excessive CO_2 input.

The secondary antibodies were all from Life Technologies. Dilutions for primary antibodies varied based on the optimized results: 1:500 for Ki-67 antibody, 1:200 for caspase 3 antibody,

and 1:100 for all three calcium-binding protein antibodies. All dilutions for secondary antibodies were 1:500. To test autofluorescence of the background, we tested the secondary antibodies on each sample with the absence of primary antibodies (Supplementary Figure 5). Four calcium-binding primary antibodies (CALR, CALM, CETN, and CANX) were tested before the application in this study. Only the antibodies for CALR, CALM, and CANX were confirmed to be reliable in *C. virginica* tissues and cells. The samples were observed under the Nikon Eclipse T*i* fluorescent microscope (Nikon USA) immediately after IF staining. Pictures were taken for each observation under various colored filters. The green and blue channels or red and blue channels of each observation field were merged using ImageJ (Schneider et al., 2012). To eliminate the effects of autofluorescence during quantification, we adjusted the exposure time of the image to minimize the signal from the negative control of each antibody. Same exposure time was used on all photos of each antibody.

Statistical Analyses

For IF of Ki-67 and caspase 3, the total number of cells (only blue signals) and Ki-67 positive cells (cells with both blue and green signals or with both blue and red signals) were counted using ImageJ and the proliferating/apoptosis rate of each cell culture was calculated as:

$$\textit{Percentage of positive cells}\ (\%) = \frac{\textit{number of Ki}-67\ \textit{positive}\ (\textit{or caspase 3 positive})}{\textit{total number of cells}} \times 100.$$

For the IF of calcium-binding proteins in *Cv*MCs, the total calcium-binding protein signal intensity of each photo was measured using ImageJ and the total number of cells was obtained by counting the number of nuclei as described above (DAPI signals). The mean calcium-binding protein level of the cells in each photo was calculated as:

$$\textit{Average expression level} = \frac{\textit{signal intensity of calcium binding protein}}{\textit{total cell number}}.$$

The average calcium-binding production in cells with each treatment was normalized using average calcium-binding protein production in control cells. Similarly, IF signal intensities of calcium binding proteins in larval *C.virginica* were also digitalized using ImageJ. The intensity values were all normalized against control samples to generate relative calcium-binding protein productions. Comparisons of cell proliferation, cell apoptosis, and calcium-binding protein productions in cells and larvae were made between control and treated groups using *t*-tests.

RESULTS

Calcium Binding Protein Sequence Analyses

Full sequences of the four calcium-binding protein genes were obtained through cloning and fragment assembly. All four gene sequences have been submitted to NCBI GenBank database with accession numbers (MG029428-MG029431) with detailed information of the sequences in **Table 2**. The homologous sequences of the four calcium-binding protein genes were identified by GenBank database searching using BLASTx. Their homologs are listed in **Table 2**. The translated protein sequences of calcium-binding proteins were screened in ScanProsite for signature domain analyses (de Castro et al., 2006). The proteins CETN (**Figure 1A**) and CALM (**Figure 1B**) both include four E-F hand motifs, which primarily consist of α-helixes. Four calcium binding sites from CALM were located by SWISS MODEL (**Figure 1B**) while no obvious calcium-binding sites were predicted in CETN (**Figure 1A**). Protein CALR and CANX also demonstrated similarities in 3D structures (**Figures 1C,D**). Each one of them had a long low complexity fragment in protein sequence. In high complexity areas, β-sheets are the major secondary structures in both CALR and CANX (**Figures 1C,D**). No clear calcium-binding sites were identified from CALR or CANX. The detailed amino acid sequence in each α-helix or β-sheet from each sequence was highlighted in the sequence (Supplementary Figures 1–4).

C. virginica Mantle Cells (*Cv*MCs) in Response to Increased pCO_2 Stimulation

A decline in the pHs of cell culture medium was observed with increasing input of CO_2 in the cell culture incubator (**Figure 2c**). The pH levels of media decreased from 7.78 to 7.44 when the atmospheric CO_2 level was increased from ambient concentration to 2.5%. A more dramatic decrease of pH values was observed when atmospheric CO_2 was over 2.5%. The pH levels of media at 5 and 7.5% CO_2 input dropped to 6.85 and 6.43, respectively, and was dropped further to 6.31 when the concentration of CO_2 reached 10% (**Figure 2c**). The *Cv*MCs cultured in 5% CO_2 and above demonstrated minimum numbers of cells attached on the bottom of the plate during culture. The proliferation of *Cv*MC cultures was estimated by IF with Ki-67 antibody. Under control conditions, the average proliferating rate of *Cv*MCs was 82 ± 1.6%. With a 2.5% CO_2 input, the *Cv*MCs showed an 82 ± 2.0% proliferating rate, which was not significantly different than cells in control conditions ($p = 0.92$, **Figure 2d**). Cell apoptosis was also estimated using caspase 3 (Casp3) as a marker. There were 23 ± 3.3% Casp3 positive *Cv*MCs in control conditions while 20 ± 2.6% *Cv*MCs were Casp3 positive in 2.5% CO_2 conditions ($p = 0.50$, **Figure 2e**). Although there was nearly 3% difference in cell apoptosis between control and 2.5% CO_2 treated cells, the difference was not statistically different ($p = 0.50$). This suggested that stresses from CO_2 under 2.5% in the atmosphere did not cause lethal effect on *Cv*MCs.

Expression of Calcium-Binding Proteins in *Cv*MCs in Elevated Atmospheric CO_2

Expressions of the four calcium-binding protein encoding genes at the mRNA level were all significantly upregulated based on qPCR analysis (**Figure 3a**). Expressions of *calm* in *Cv*MCs at mRNA level were upregulated by 1.9 ($p = 0.031$) and 1.8 ($p = 0.049$) fold under 1 and 2.5% CO_2 conditions, respectively,

TABLE 2 | Sequencing information of *C. virginica* calcium-binding protein genes and their homologs.

Gene name	Accession #	Full length (bp)	ORF (bp)	Protein (aa)	5′ UTR (bp)	3′ UTR (bp)	Homologs (accession #)	Identities (%)	*E*-value
Cv-calr	MG029428	1,779	1,314	438	16	449	*C. gigas calr* (XP_022318558)	99	0.0
Cv-canx	MG029429	3,156	1,380	460	95	1,681	*C. gigas canx* (EKC32723)	82	0.0
Cv-cetn	MG029430	1,023	417	139	148	458	*C. gigas cetn* (XP_011447406)	92	2×10^{-76}
Cv-calm	MG029431	1,069	450	150	115	504	*Polistes Canadensis calm* (XP_014613282)	99	3×10^{-99}

ORF, open reading frame; UTR, untranslated region; E-values indicate the probabilities of mismatching.

compared to control condition with an ambient CO_2 level. Upregulation of *calt* expression was also observed at the mRNA level. The amount of mRNAs in cells cultivated at 1 and 2.5% CO_2 treatment was upregulated by 4.7 ($p = 0.042$) and 3.4 ($p = 0.041$) fold, respectively compared to control cells. (**Figure 3a**). The *calr* expression displayed upregulation at both the mRNA and protein levels in cells stimulated with elevated pCO_2. Although mRNAs of *calr* were only upregulated by 2.1 fold ($p = 0.031$) with 1% CO_2 stimulation, a 9.7 ($p = 0.006$) fold increase of mRNA level was seen in *Cv*MCs at 2.5% CO_2 conditions (**Figure 3a**). The elevation of *canx* was found at the mRNA level in CO_2 treated *Cv*MCs as well. However, only the 2.6-fold increase in 1% CO_2 induced cells was statistically significant ($p = 0.018$, **Figure 3a**), while the expression levels of *canx* in cells treated with 2.5% CO_2 was not statistically different than in control cells ($p = 0.283$).

Similarly, higher *calm* expression at the protein level was also detected in *Cv*MCs cultivated in 2.5% atmospheric CO_2 compared to cells cultured in ambient CO_2 conditions (41% more in 2.5% CO_2 treated cells than in control cells, $p = 0.040$, **Figure 3b**). Accordingly, a 64% ($p = 0.034$) elevation in CALR protein was induced by 2.5% CO_2 (**Figure 3c**). Statistical analyses also did not show any significant difference of CANX protein production in *Cv*MCs responding to 2.5% CO_2 stimulation compared to control condition (**Figure 3d**, $p = 0.273$).

Production of Calcium-Binding Proteins in Larval *C. virginica* Under Increased pCO_2

In the larval *C. virginica* development assay, elevated pCO_2 treatment (1,000 ppm) in water decreased the water pH by 0.15 [$F_{(1,28)} = 23.49$, $p < 0.0001$] compared to the current pCO_2 conditions. No significant changes in total alkalinity, temperature, and salinity were observed in elevated pCO_2. Additionally, there was also no significant difference in the mortality and shell length of larval *C. virginica* between the two different pCO_2 treatments. Maximum shell length was 69.9 ± 0.75 μm at 400 ppm pCO_2 vs. 69.8 ± 0.60 μm at 1,000 ppm pCO_2, $F_{(1,28)} = 0.02$, $p = 0.89$. However, differential expression of *calm*, *calr*, and *canx* at the protein level was identified between larvae in different pCO_2 treatments. Productions of CALM, CALR, and CANX in larvae cultivated at 1,000 pCO_2 concentrations were elevated by 38% ($p = 0.024$, **Figure 4a**), 52% ($p = 0.033$, **Figure 4b**), and 26% ($p = 0.025$, **Figure 4c**), respectively. According to the statistical analysis (**Figure 4d**).

DISCUSSION

Populations of *C. virginica* endemic to Louisiana's Gulf coast flourish in unique estuarine habitats, differing from ecosystems along the Atlantic coast, that receive extremely high volumes of freshwater discharge, variable by season, from the Mississippi and Atchafalaya River systems (Guo et al., 2012). In addition to high water discharge, massive river basins input large nutrient loads and sediment into Louisiana estuaries exported from land-based runoff, contributing to alterations in carbonate chemistry and pH levels within the ecosystem (Doney et al., 2009). Oysters living in this environment may have adapted to the stressful conditions through alteration in genomics and epigenetic regulation. Responses of oysters to experimental conditions will be also determined by a variety of factors, including the evolutionary history of the source population and epigenetic changes due to previous environmental conditions. The oysters used in this study were maintained long term at the LA State Oyster Hatchery in controlled conditions similar to the average observed at the site for the source population. This minimized the alteration in genomic responses and epigenetic regulation to the long-term stresses.

The goal of our study was to understand the responses of the calcium-binding protein genes to OA during shell development in bivalves. Two different models were implemented to test our hypothesis stating that the regulation of calcium-binding protein genes involved in biomineralization are influenced by OA. The results obtained from the larval development assay clearly demonstrated the different protein productions CALM, CALR, and CANX. However, due to the difference between individuals of larval oysters, no strong conclusions were drawn based on the profile changes of mRNA levels of the calcium-binding protein genes exposed to OA stress. However, the results obtained from larval experiment were validated by the mantle cell culture assay, which suggested that the *in vitro* cell culture assay can be a sufficient tool for *in vivo* oyster studies.

Efforts were previously made to isolate and culture cells from various tissues of mollusk species, however, there was limited success in the past two decades. Only one cell line has been established from *Biomphalaria glabrata*, a freshwater snail (Hansen, 1976). Mantle tissue in mollusks is the key tissue involved in shell formation and was primarily used for studies of the biominearlization process. Previously, establishment of

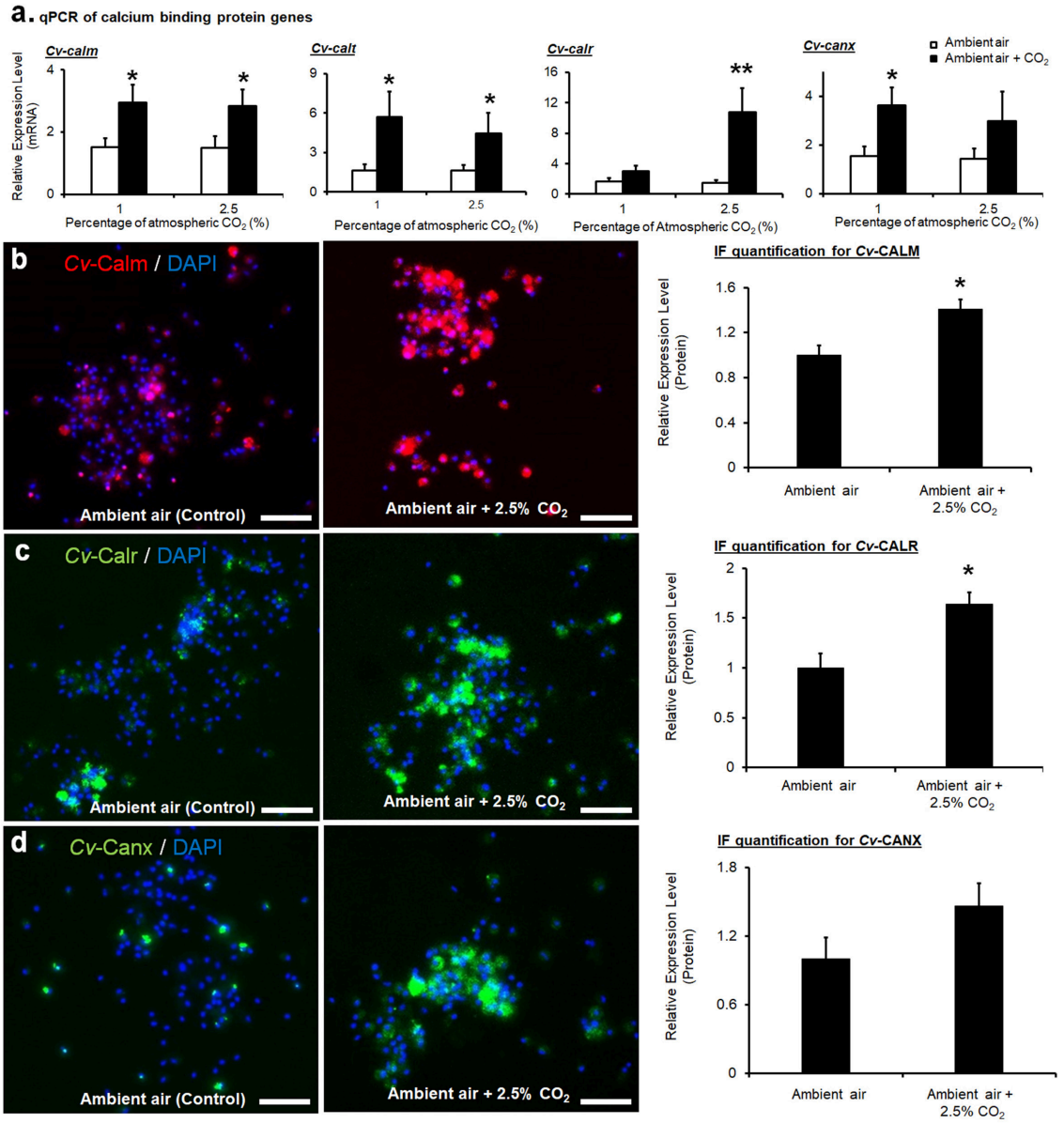

FIGURE 3 | Expressions of calcium-binding proteins in *Cv*MCs. The relative amount of mRNA of *cetn*, *calm*, *calr*, and *canx*, was quantified and compared between ambient air and increased CO_2 treatments ($n = 16$–24), **(a)**. Protein levels of CALM **(b)**, CALR **(c)**, and CANX **(d)** with control and 2.5% increase of CO_2 treatments were estimated using IF, and the results were quantified using ImageJ ($n = 8$). All treatments were applied on cells for 24 h. *$0.01 < p < 0.05$; **$p < 0.01$. Scale bar: 50 μm. Error bar: standard error of mean.

mantle cell primary cultures has been accomplished in *Mytilus galloprovincialis* (Cornet, 2006), *P. fucata* (Awaji and Suzuki, 1998), *Haliotis tuberculate* (Poncet et al., 2000; Sud et al., 2001), and *Dreissena polymorpha* (Quinn et al., 2009). Despite difficulties in maintaining the cells in sterile conditions, mantle cells with high proliferative capacity and viability can be used as a reliable tool for biomineralization studies in bivalves. The *Cv*MCs cultured in the current study showed high proliferating rates in both ambient and increased environmental CO_2 conditions. Cell apoptosis was not induced by increased atmospheric CO_2 environments. Compared to the high mortality rate of larval *C. virgnica* cultured during the experiment, the cell culture assay provided a more efficient and convenient method to study the impact of environmental stressors on mollusk biomineralization.

In our larval developmental study, no significant difference was identified in mortality, growth, or morphology of the larvae grown in ambient and elevated pCO_2 conditions. However, the substantial alteration of calcium-binding protein expression suggested that the process of biomineralization was affected

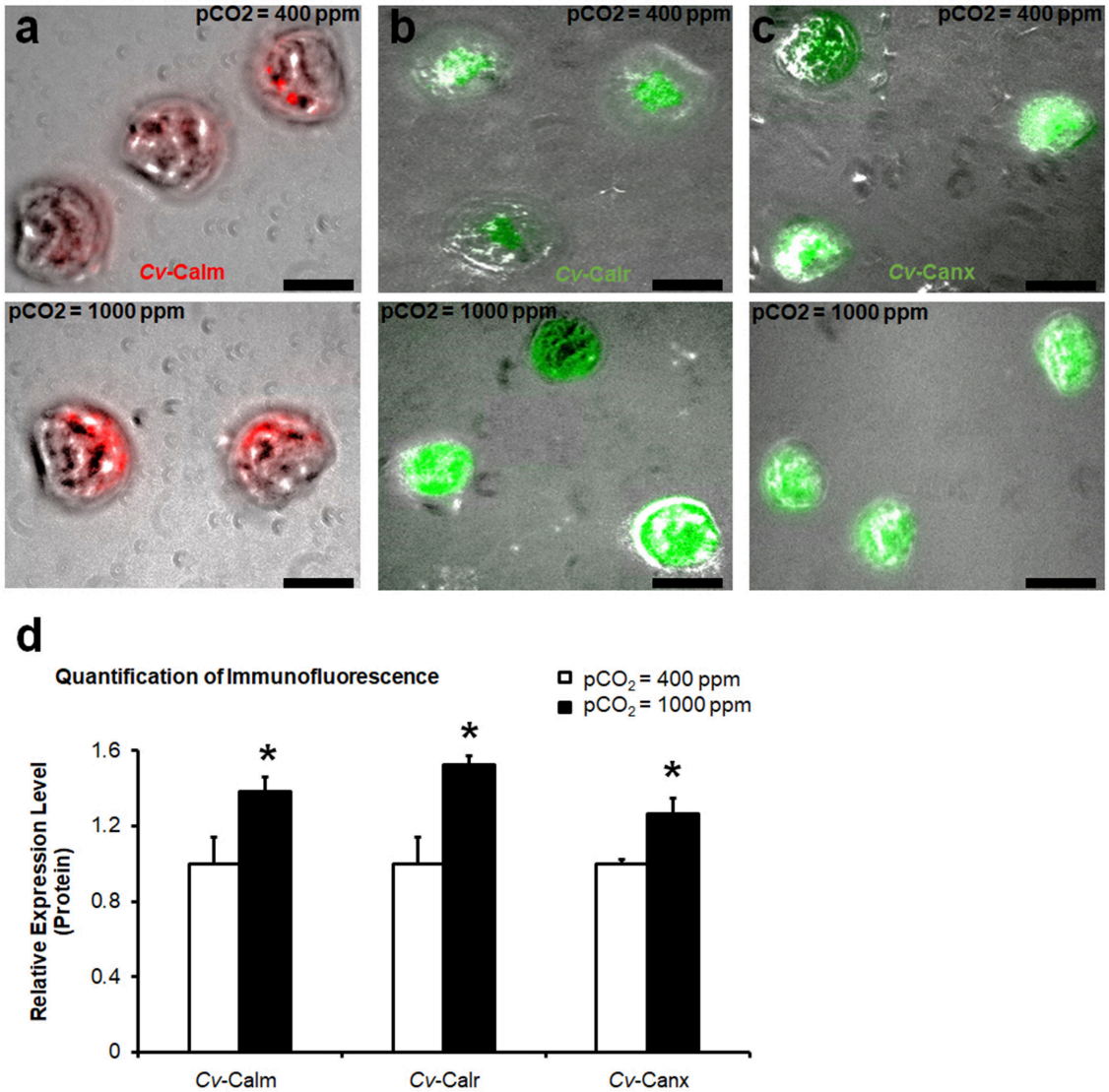

FIGURE 4 | Production of calcium-binding proteins in larval *C. virginica*. The relative amount of protein levels of CALM **(a)**, CALR **(b)**, and CANX **(c)** in larvae with control (400 ppm *p*CO2) and increased pCO_2 (1,000 ppm pCO_2) treatments were estimated using IF and the results were quantified using ImageJ ($n = 8$), **(d)**. Samples were collected at 48-h post treatment. *$0.01 < p < 0.05$. Scale bar: 50 μm.

by increased acidification. Increased production of calcium-binding proteins and transportation of calcium ions to overcome the adverse effects of elevated pCO_2 results in higher energy demands in calcifying mollusks (Melzner et al., 2011; Thomsen et al., 2013). In addition, the shell composition as well as metabolic rates of larvae may be dramatically modified in stressful conditions. Further identifying these alterations to biomineralization in response to environmental stressors will generate a clearer understanding of the impact of OA on mollusk larval development.

The responsive expression profiles of the selected calcium-binding proteins supported our hypothesis that OA manipulates the regulation of biomineralization related genes, which are involved in calcium deposition during mollusk larval development. The four targeted calcium-binding proteins in the current study were selected according to previous reports, all of which demonstrated critical involvement of these proteins in shell formation. Based on the findings from the current study, CETN and CALM both have multiple calcium-binding domains, E-F hands, in their 3-D structures, suggesting strong association with calcium transportation. Identification of the E-F hands and 3-D structures of *C. virginica* CETN in this study indicated that this protein may play a similar role in biomineralization as by calmodulin. Unlike CALM and CETN, no E-F hand signature domains for calcium-binding in the 3-D structures were located in CALR and CANX. However, previous studies

detected a domain near the C-terminal of CALR and CANX, which demonstrated high affinity to calcium ions (Corbett and Michalak, 2000). These two calcium-binding proteins were able to maintain a high calcium concentration in the endoplasmic reticulum through modulating Ca^{2+} ATPase activity (Camacho et al., 2013). Maintenance of high calcium concentration is essential to calcium capture and deposition, and necessary for shell calcification in mollusks. Therefore, CALR and CANX, in addition to CETN and CALM, are hypothesized to be heavily involved in mollusk biomineralization.

In this study, the relative expression of four newly sequenced shell formation-related genes and the three linked calcium-binding proteins were evaluated after 24 h of incubation in elevated CO_2 concentrations. Similarly, a previous study found gene expression upregulated in *cetn*, *calm* and various other proteins associated with calcification in *C. hongkongensis* larvae exposed to stressful CO_2 conditions (Dineshram et al., 2015). Upregulation in expression of biomineralization-related genes and calcium-binding proteins suggested that the biomineralization mechanisms were still active in mantle cells exposed to elevated CO_2 conditions. However, in comparison to normal expression of the target genes in controlled conditions, upregulation in cells cultivated in increased CO_2 indicated that there were still impacts to the shell deposition mechanisms. Cells within the mantle tissue of adult *C. virginica* may have induced expression to combat or compensate for environmental stress. It appears that the results from primary cell culture are complimentary to the larval experiments, both of which were utilized to study the impacts of acidification on the molecular regulation of the biomineralization process. In addition, the cell culture study provides an adequate model for observing the genomic, and possible physiological responses of *C. virginica*.

AUTHOR CONTRIBUTIONS

MR, WX, AM, and RE designed the experiment; MR, WX, AM, and JS performed the experiment; MR and WX performed the data analyses; MR, WX, and RE prepared the manuscript.

ACKNOWLEDGMENTS

We would like to thank Drs. Jerome La Peyre and Sandra Casas Liste from LSU School of Animal Sciences for providing healthy oysters for cell culture in this study. This study was supported by the internal grant of LSU Agricultural Center.

SUPPLEMENTARY MATERIAL

The Supplementary Material for this article can be found online at: https://www.frontiersin.org/articles/10.3389/fmars.2018.00203/full#supplementary-material

REFERENCES

Arivalagan, J., Yarra, T., Marie, B., Sleight, V. A., Duvernois-Berthet, E., Clark, M. S., et al. (2017). Insights from the shell proteome: biomineralization to adaptation. *Mol. Biol. Evol.* 34, 66–77. doi: 10.1093/molbev/msw219

Arnold, K., Bordoli, L., Kopp, J., and Schwede, T. (2006). The SWISS-MODEL workspace: a web-based environment for protein structure homology modelling. *Bioinformatics* 22, 195–201. doi: 10.1093/bioinformatics/bti770

Arosa, F. A., de Jesus, O., Porto, G., Carmo, A. M., and de Sousa, M. (1999). Calreticulin is expressed on the cell surface of activated human peripheral blood T lymphocytes in association with major histocompatibility complex class I molecules. *J. Biol. Chem.* 274, 16917–16922. doi: 10.1074/jbc.274.24.16917

Artimo, P., Jonnalagedda, M., Arnold, K., Baratin, D., Csardi, G., de Castro, E., et al. (2012). ExPASy: SIB bioinformatics resource portal. *Nucleic Acids Res.* 40, W597–W603. doi: 10.1093/nar/gks400

Awaji, M., and Suzuki, T. (1998). Monolayer formation and DNA synthesis of the outer epithelial cells from pearl oyster mantle in coculture with amebocytes. *In Vitro Cell. Dev. Biol. Anim.* 34, 486–491. doi: 10.1007/s11626-998-0083-0

Biasini, M., Bienert, S., Waterhouse, A., Arnold, K., Studer, G., Schmidt, T., et al. (2014). SWISS-MODEL: modelling protein tertiary and quaternary structure using evolutionary information. *Nucleic Acids Res.* 42, W252–W258. doi: 10.1093/nar/gku340

Camacho, P., John, L., Li, Y., Paredes, R. M., and Roderick, H. L. (2013). *Calnexin and Calreticulin, ER Associated Modulators of Calcium Transport in the ER, in: 2000-2013.* Austin, TX: Landes Bioscience.

Coppolino, M. G., and Dedhar, S. (1998). Calreticulin. *Int. J. Biochem. Cell Biol.* 30, 553–558. doi: 10.1016/S1357-2725(97)00153-2

Corbett, E. F., and Michalak, M. (2000). Calcium, a signaling molecule in the endoplasmic reticulum? *Trends Biochem. Sci.* 25, 307–311. doi: 10.1016/S0968-0004(00)01588-7

Cornet, M. (2006). Primary mantle tissue culture from the bivalve mollusc *Mytilus galloprovincialis*: investigations on the growth promoting activity of the serum used for medium supplementation. *J. Biotechnol.* 123, 78–84. doi: 10.1016/j.jbiotec.2005.10.016

Currey, J. D. (1977). Mechanical properties of mother of pearl in tension. *Proc. R. Soc. Lond. B* 196, 443–463. doi: 10.1098/rspb.1977.0050

de Castro, E., Sigrist, C. J., Gattiker, A., Bulliard, V., Langendijk-Genevaux, P. S., Gasteiger, E., et al. (2006). ScanProsite: detection of PROSITE signature matches and ProRule-associated functional and structural residues in proteins. *Nucleic Acids Res.* 34, W362–W365. doi: 10.1093/nar/gkl124

Dickson, A. G., Sabine, C. L., and Christian, J. R. (2007). "Guide to best practices for ocean CO_2 measurements," in *PICES Special Publication* 3 (Sidney, BC: North Pacific Marine Science Organization), 73–87.

Dineshram, R., Quan, Q., Sharma, R., Chandramouli, K., Yalamanchili, H. K., Chu, I., et al. (2015). Comparative and quantitative proteomics reveal the adaptive strategies of oyster larvae to ocean acidification. *Proteomics* 15, 4120–4134. doi: 10.1002/pmic.201500198

Doney, S. C., Fabry, V. J., Feely, R. A., and Kleypas, J. A. (2009). Ocean acidification: the other CO_2 problem. *Ann. Rev. Mar. Sci.* 1, 169–192. doi: 10.1146/annurev.marine.010908.163834

Friedberg, F. (1988). Calcium binding protein families: the 'E-F Hand' family. *Biochem. Edu.* 16, 35–36. doi: 10.1016/0307-4412(88)90017-9

Gazeau, F., Gattuso, J. P., Greaves, M., Elderfield, H., Peene, J., Heip, C. H., et al. (2011). Effect of carbonate chemistry alteration on the early embryonic development of the Pacific oyster (*Crassostrea gigas*). *PLoS ONE* 6:e23010. doi: 10.1371/journal.pone.0023010

Guo, X., Cai, W., Huang, W., Wang, Y., Chen, F., Murrell, M. C., et al. (2012). Carbon dynamics and community production in the Mississippi River plume. *Limnol. Oceanogr.* 57, 1–17. doi: 10.4319/lo.2012.57.1.0001

Hansen, E. L. (1976). "A cell line from embryos of *Biomphalaria glabrata* (Pulmonata): Establishment and characteristics," in *Invertebrate Tissue Culture: Research Applications*, ed K. Maramorosch (New York, NY: Academic Press), 75–97.

Harper, E. M. (2000). Are calcitic layers an effective adaptation against shell dissolution in the Bivalvia? *J. Zool.* 251, 179–186. doi: 10.1111/j.1469-7998.2000.tb00602.x

Hattan, S. J., Laue, T. M., and Chasteen, N. D. (2001). Purification and characterization of a novel calcium-binding protein from the extrapallial fluid of the mollusc, *Mytilus edulis*. *J. Biol. Chem.* 276, 4461–4468. doi: 10.1074/jbc.M006803200

Huang, J., Zhang, C., Ma, Z., Xie, L., and Zhang, R. (2007). A novel extracellular EF-hand protein involved in the shell formation of pearl oyster. *Biochim. Biophys. Acta* 1770, 1037–1044. doi: 10.1016/j.bbagen.2007.03.006

Ip, Y. K., Loong, A. M., Hiong, K. C., Wong, W. P., Chew, S. F., Reddy, K., et al. (2006). Light induces an increase in the pH of and a decrease in the ammonia concentration in the extrapallial fluid of the giant clam *Tridacna squamosa*. *Physiol. Biochem. Zool.* 79, 656–664. doi: 10.1086/501061

IPCC (2007). *Climate Change 2007: Synthesis Report. Contribution of Working Groups, I., II and III to the Fourth Assessment Report of the Intergovernmental Panel on Climate Change*. eds R. K. Pachauri and A. Reisinger (Geneva: Intergovernmental Panel on Climate Change).

Kiefer, F., Arnold, K., Künzli, M., Bordoli, L., and Schwede, T. (2009). The SWISS-MODEL Repository and associated resources. *Nucleic Acids Res.* 37, D387–D392. doi: 10.1093/nar/gkn750

Letunic, I., Doerks, T., and Bork, P. (2015). SMART: recent updates, new developments and status in 2015. *Nucleic Acids Res.* 43, D257–D260. doi: 10.1093/nar/gku949

Li, S., Xie, L., Ma, Z., and Zhang, R. (2005). cDNA cloning and characterization of a novel calmodulin-like protein from pearl oyster *Pinctada fucata*. *FEBS J.* 272, 4899–4910. doi: 10.1111/j.1742-4658.2005.04899.x

Li, S., Xie, L., Zhang, C., Zhang, Y., Gu, M., and Zhang, R. (2004). Cloning and expression of a pivotal calcium metabolism regulator: calmodulin involved in shell formation from pearl oyster (Pinctada fucata). *Comp. Biochem. Physiol. B. Biochem. Mol. Biol.* 138, 235–243. doi: 10.1016/j.cbpc.2004.03.012

Li, X. X., Yu, W. C., Cai, Z. Q., He, C., Wei, N., Wang, X. T., et al. (2016). Molecular cloning and characterization of full-length cDNA of calmodulin gene from Pacific Oyster *Crassostrea gigas*. *Biomed Res. Int.* 2016:5986519. doi: 10.1155/2016/5986519

Liu, J., Yang, D., Liu, S., Li, S., Xu, G., Zheng, G., et al. (2015). Microarray: a global analysis of biomineralization-related gene expression profiles during larval development in the pearl oyster, *Pinctada fucata*. *BMC Genomics* 16:325. doi: 10.1186/s12864-015-1524-2

Lowenstam, H. A., and Weiner, S. (1989). *On Biomineralization*. London: Oxford University Press.

Mann, S. (1983). Mineralization in biological systems. *Struct. Bond.* 54, 125–174. doi: 10.1007/BFb0111320

Marin, F., Le Roy, N., and Marie, B. (2012). The formation and mineralization of mollusk shell. *Front. Biosci. (Schol. Ed).* 4, 1099–1125. doi: 10.2741/s321

Melzner, F., Stange, P., Trübenbach, K., Thomsen, J., Casties, I., Panknin, U., et al. (2011). Food supply and seawater pCO2 impact calcification and internal shell dissolution in the blue mussel *Mytilus edulis*. *PLoS ONE* 6:e24223. doi: 10.1371/journal.pone.0024223

Michalak, M., Robert Parker, J. M., and Opas, M. (2002). Ca2+ signaling and calcium binding chaperones of the endoplasmic reticulum. *Cell Calcium* 32, 269–278. doi: 10.1016/S0143416002001884

Mount, A. S., Wheeler, A. P., Paradkar, R. P., and Snider, D. (2004). Hemocyte-mediated shell mineralization in the eastern oyster. *Science* 304, 297–300. doi: 10.1126/science.1090506

Nishi, R., Sakai, W., Tone, D., Hanaoka, F., and Sugasawa, K. (2013). Structure-function analysis of the EF-hand protein centrin-2 for its intracellular localization and nucleotide excision repair. *Nucleic Acids Res.* 41, 6917–6929. doi: 10.1093/nar/gkt434

Orr, J. C., Fabry, V. J., Aumont, O., Bopp, L., Doney, S. C., Feely, R. A., et al. (2005). Anthropogenic ocean acidification over the twenty-first century and its impact on calcifying organisms. *Nature* 437, 681–686. doi: 10.1038/nature04095

Parker, L. M., Ross, P. M., and O'connor, W. A. (2010). Comparing the effect of elevated pCO_2 and temperature on the fertilization and early development of two species of oysters. *Mar. Biol.* 157, 2435–2452.

Peng, K., Liu, F., Wang, J., and Hong, Y. (2017). Calmodulin highly expressed during the formation of pearl sac in freshwater pearl mussel (*Hyriopsis schlegelii*). *Thalassas*. doi: 10.1007/s41208-017-0054-x

Poncet, J., Serpentini, A., Thiébot, B., Villers, C., Bocquet, J., Boucaud-Camou, E., et al. (2000). *In vitro* synthesis of proteoglycans and collagen in primary cultures of mantle cells from the Nacreous Mollusk, *Haliotis tuberculata*: a new model for study of molluscan extracellular matrix. *Mar. Biotechnol.* 2, 387–398. doi: 10.1007/PL00021685

Quinn, B., Costello, M. J., Dorange, G., Wilson, J. G., and Mothersill, C. (2009). Development of an *in vitro* culture method for cells and tissues from the zebra mussel (*Dreissena polymorpha*). *Cytotechnology* 59, 121–134. doi: 10.1007/s10616-009-9202-3

Rao, X., Huang, X., Zhou, Z., and Lin, X. (2013). An improvement of the 2^(−*deltadeltaCT*) method for quantitative real-time polymerase chain reaction data analysis. *Biostat. Bioinforma. Biomath.* 3, 71–85.

Sabine, C. L., Feely, R. A., Gruber, N., Key, R. M., Lee, K., Bullister, J. L., et al. (2004). The oceanic sink for anthropogenic CO_2. *Science* 305, 367–371. doi: 10.1126/science.1097403

Sambrook, J., and Russell, D. W. (2006a). Preparation and transformation of competent, *E. coli* using Calcium Chloride. *CSH Protoc.* 2006:320. doi: 10.1101/pdb.prot3932

Sambrook, J., and Russell, D. W. (2006b). Recovery of DNA from agarose and polyacrylamide gels: electroelution into dialysis bags. *CSH Protoc.* 2006:207. doi: 10.1101/pdb.prot4023

Schneider, C. A., Rasband, W. S., and Eliceiri, K. W. (2012). NIH Image to ImageJ: 25 years of image analysis. *Nat. Methods* 9, 671–675. doi: 10.1038/nmeth.2089

Schultz, J., Milpetz, F., Bork, P., and Ponting, C. P. (1998). SMART, a simple modular architecture research tool: identification of signaling domains. *Proc. Natl. Acad. Sci. U.S.A.* 95, 5857–5864. doi: 10.1073/pnas.95.11.5857

Somogyi, E., Petersson, U., Hultenby, K., and Wendel, M. (2003). Calreticulin–an endoplasmic reticulum protein with calcium-binding activity is also found in the extracellular matrix. *Matrix Biol.* 22, 179–191. doi: 10.1016/S0945-053X(02)00117-8

Su, J., Liang, X., Zhou, Q., Zhang, G., Wang, H., Xie, L., et al. (2013). Structural characterization of amorphous calcium carbonate-binding protein: an insight into the mechanism of amorphous calcium carbonate formation. *Biochem. J.* 453, 179–186. doi: 10.1042/BJ20130285

Sud, D., Doumenc, D., Lopez, E., and Milet, C. (2001). Role of water-soluble matrix fraction, extracted from the nacre of *Pinctada maxima*, in the regulation of cell activity in abalone mantle cell culture (*Haliotis tuberculata*). *Tissue Cell* 33, 154–160. doi: 10.1054/tice.2000.0166

Sueyoshi, T., McMullen, B. A., Marnell, L. L., Du Clos, T. W., and Kisiel, W. (1991). A new procedure for the separation of protein Z, prothrombin fragment 1.2 and calreticulin from human plasma. *Thromb. Res.* 63, 569–575. doi: 10.1016/0049-3848(91)90184-X

Takagi, R., and Miyashita, T. (2010). Prismin: a new matrix protein family in the Japanese pearl oyster (*Pinctada fucata*) involved in prismatic layer formation. *Zool. Sci.* 27, 416–426. doi: 10.2108/zsj.27.416

Takeuchi, T. (2017). Molluscan genomics: implications for biology and aquaculture. *Curr. Mol. Biol. Rep.* 3, 297–305. doi: 10.1007/s40610-017-0077-3

Thomsen, J., Casties, I., Pansch, C., Körtzinger, A., and Melzner, F. (2013). Food availability outweighs ocean acidification effects in juvenile *Mytilus edulis*: laboratory and field experiments. *Glob. Chang. Biol.* 19, 1017–1027. doi: 10.1111/gcb.12109

Waldbusser, G. G., Brunner, E. L., Haley, B. A., Hales, B., Langdon, C. J., and Prahl, F. G. (2013). A developmental and energetic basis linking larval oyster shell formation to acidification sensitivity. *Geophys. Res. Lett.* 40, 2171–2176. doi: 10.1002/grl.50449

Waldbusser, G. G., Hales, B., Langdon, C. J., Haley, B. A., Schrader, P., Brunner, E. L., et al. (2014). Saturation-state sensitivity of marine bivalve larvae to ocean acidification. *Nat. Clim. Change* 5, 273–280. doi: 10.1038/nclimate2479

Weiss, I. M., Kaufmann, S., Mann, K., and Fritz, M. (2000). Purification and characterization of perlucin and perlustrin, two new proteins from the shell

of the mollusc *Haliotis laevigata*. *Biochem. Biophys. Res. Commun.* 267, 17–21. doi: 10.1006/bbrc.1999.1907

Yan, Z., Fang, Z., Ma, Z., Deng, J., Li, S., Xie, L., et al. (2007). Biomineralization: functions of calmodulin-like protein in the shell formation of pearl oyster. *Biochim. Biophys. Acta* 1770, 1338–1344. doi: 10.1016/j.bbagen.2007.06.018

Zeebe, R. E. (2012). History of seawater carbonate chemistry, atmospheric CO_2, and ocean acidification. *Annu. Rev. Earth Planet. Sci.* 40, 141–165. doi: 10.1146/annurev-earth-042711-105521

Zhang, G., Fang, X., Guo, X., Li, L., Luo, R., Xu, F., et al. (2012). The oyster genome reveals stress adaptation and complexity of shell formation. *Nature* 490, 49–54. doi: 10.1038/nature11413

Conflict of Interest Statement: The authors declare that the research was conducted in the absence of any commercial or financial relationships that could be construed as a potential conflict of interest.

frontiers in Marine Science

ORIGINAL RESEARCH
published: 28 August 2018
doi: 10.3389/fmars.2018.00309

The Role of the Vascular Endothelial Growth Factor (VEGF) Signaling in Biomineralization of the Oyster *Crassostrea gigas*

Anna V. Ivanina[1], Ballav Borah[2], Tadas Rimkevicius[1], Jason Macrander[1], Helen Piontkivska[3], Inna M. Sokolova[4,5] and Elia Beniash[2]**

[1] Department of Biological Sciences, The University of North Carolina at Charlotte, Charlotte, NC, United States, [2] Department of Oral Biology, School of Dental Medicine, University of Pittsburgh, Pittsburgh, PA, United States, [3] Department of Biological Sciences, Kent State University, Kent, OH, United States, [4] Department of Marine Biology, Institute of Biosciences, University of Rostock, Rostock, Germany, [5] Department of Maritime Systems, Interdisciplinary Faculty, University of Rostock, Rostock, Germany

OPEN ACCESS

Edited by:
Vera Bin San Chan, Clemson University, United States

Reviewed by:
Daniele Tibullo, Università degli Studi di Catania, Italy
Tara Essock-Burns, University of Hawaii, United States

***Correspondence:**
Inna M. Sokolova
inna.sokolova@uni-rostock.de
Elia Beniash
ebeniash@pitt.edu

Specialty section:
This article was submitted to Marine Molecular Biology and Ecology, a section of the journal Frontiers in Marine Science

Received: *13 March 2018*
Accepted: *10 August 2018*
Published: *28 August 2018*

Citation:
Ivanina AV, Borah B, Rimkevicius T, Macrander J, Piontkivska H, Sokolova IM and Beniash E (2018) The Role of the Vascular Endothelial Growth Factor (VEGF) Signaling in Biomineralization of the Oyster Crassostrea gigas. Front. Mar. Sci. 5:309. doi: 10.3389/fmars.2018.00309

Vascular endothelial growth factor (VEGF) and vascular endothelial growth factor receptor (VEGFR) play a role in early development, organogenesis, and regeneration, as well as biomineralization of invertebrates. The involvement of VEGF and VEGFR in biomineralization was demonstrated in sea urchin larvae but its role in the biomineralization of other invertebrate groups such as mollusks is not known. We assessed the potential role of VEGF signaling on biomineralization of a model marine bivalve, the Pacific oyster *Crassostrea gigas*, by analyzing the effects of a VEGFR inhibitor (50 nM axitinib) on shell growth, shell hardness, and expression profiles of biomineralization-related genes. Bioinformatics analysis identified a wide range of biomineralization-related genes potentially activated by VEGF including carbonic anhydrases (CAs), sodium/proton and sodium/calcium exchangers, calmodulins, and genes involved in chitin metabolism. Exposure to a VEGFR inhibitor axitinib led to upregulation of CAs (CA7 and CA12), sodium/proton exchanger 10, sodium/calcium exchanger 1 and 3, as well as calmodulin mRNA in hemocytes (HCs). In the mantle tissue, axitinib exposure led to a compensatory upregulation of VEGFR mRNA but did not affect the expression of other studied biomineralization genes. Expression of VEGF, VEGFR mRNA, or that of the downstream biomineralization-related genes in a non-biomineralizing tissue (the gill) was not affected by axitinib. The shell mass was higher in the axitinib treatment group. Inhibition of VEGFR led to significant increase in shell microhardness, and to a small but statistically significant decrease in crystallinity. Our results therefore indicate that, although VEGF signaling might not play a crucial role in shell biomineralization of *C. gigas* as it does in mammals and echinoderms, it is involved in regulation of shell formation in bivalves and that effects of VEGF on biomineralization are likely mediated by HCs.

Keywords: biomineralization, mollusk, VEGF, gene expression regulation, hardness, crystallinity, respiration

INTRODUCTION

Mollusk shells are composite organomineral structures made of calcium carbonate mineral (primarily calcite and aragonite), and a minor but structurally important organic fraction. Shell formation is a complex biologically regulated process (Zhang et al., 2012) which often occurs under the physicochemical conditions of low or under-saturation with respect to $CaCO_3$ precipitation (Beniash et al., 2010; Dickinson et al., 2013; Ivanina et al., 2013b). Two major tissue types – the mantle and the blood cells [hemocytes (HCs)] – have been identified as the major players in molluscan biomineralization. Epithelial cells of the mantle edge (ME) are traditionally associated with the shell formation as they produce the extracellular matrix (ECM) proteins directing $CaCO_3$ deposition and controlling the structure, orientation and size of $CaCO_3$ crystals (Falini et al., 1996; Nudelman et al., 2006). Transcriptomic studies of the cells of the ME revealed high expression levels of genes encoding ECM proteins thereby supporting earlier reports of the role of the ME in the regulation of shell biomineralization (Marie et al., 2012; Ivanina et al., 2017). Recent studies also implicate mollusk HCs in the biomineralization process. HCs are multifunctional cells involved in the immune defense, wound repair and biomineralization (Roch, 1999; Sokolova, 2009). Different HC populations are specialized on either immune defense or biomineralization (O'Neill et al., 2013; Li et al., 2016a; Ivanina et al., 2017). Biomineralizing HCs accumulate calcium carbonate mineral particles and can move by diapedesis from the blood stream to the extrapallial space (between the mollusk mantle and the shell) depositing $CaCO_3$ onto the shell surface (Mount et al., 2004; Li et al., 2016b). The transcriptomic profiles of the putative biomineralization HCs indicate that they play a role in the mineral transport, and potentially contribute to the shell matrix formation (Ivanina et al., 2017). To date, the molecular mechanisms controlling molluscan biomineralization and regulating the interplay between different biomineralizing cells are not well understood. Knowledge of such mechanisms is essential for understanding the impacts of environmental change on the shell, the main protective structure of mollusks, and thus on the survival and performance of mollusks, many of whom are key aquaculture species and ecosystem engineers (Beniash et al., 2010; Dickinson et al., 2012; Ivanina et al., 2013a).

Vascular endothelial growth factor (VEGF) stimulates angiogenesis and osteogenesis in mammals (Street et al., 2002). Angiogenesis and osteogenesis are closely associated (Schipani et al., 2009), and bone mineralization initiates around blood vessels and potentially involves blood cells (Akiva et al., 2015; Kerschnitzki et al., 2016). In mammals, VEGF induces differentiation of osteoblasts and mineralizing chondrocytes and plays a critical role in bone formation, healing and regeneration (d'Aquino et al., 2007; Wang et al., 2007; Liu et al., 2012; Chan et al., 2015; Hu and Olsen, 2016). Recently, VEGF was found to play a critical role in the regulation of mineralization in echinoderms (sea urchin larvae) where it controls skeleton morphogenesis (Duloquin et al., 2007; Sun and Ettensohn, 2014). VEGF signaling is essential for regulation of morphogenetic patterning of the primary mesenchyme cells (a major biomineralizing cell type of echinoderms) and for activation of the skeletogenic gene regulatory network (Duloquin et al., 2007; Adomako-Ankomah and Ettensohn, 2013, 2014; Sun and Ettensohn, 2014), so that inhibition of VEGF signaling causes significant defects in skeletogenesis (Adomako-Ankomah and Ettensohn, 2013). Furthermore, addition of VEGF to isolated sea urchin micromeres *in vitro* induces formation of calcitic spicules (Knapp et al., 2012). These data indicate that VEGF is an evolutionary conserved and potent regulator of skeletal morphogenesis. Based on these findings, we hypothesized that VEGF may be involved in the control of mollusk shell formation by regulating the biomineralizing functions of the circulatory HCs and/or those of the biomineralizing mantle cells. To test these hypotheses, we used a specific VEGF receptor (VEGFR) inhibitor axitinib to disrupt VEGF signaling in juvenile and adult *C. gigas*, and tested the effects of this disruption on transcriptomic profile of key biomineralization genes in the HCs and the mantle as well as on the mechanical and mineralogical properties of the shells.

MATERIALS AND METHODS

Animal Care and Experimental Exposures

Juvenile (5–10 mm shell length) and adult *Crassostrea gigas* (6–7 cm shell length) were obtained from Ocean Alaska Hatchery (Alaska, United States) and Fanny Bay (British Columbia, Canada), respectively. Prior to the experiments, the oysters were acclimated for a week at 20°C and salinity 30 practical salinity units (PSU) in re-circulating water tanks with artificial sea water (ASW; Instant Ocean®, Kent Marine) prior to experiments.

A stock solution of axitinib (ApexBio Technology, Houston, TX, United States) was prepared in DMSO and stored at −20°C. Axitinib is a potent and highly selective inhibitor of VEGFR tyrosine kinase 1, 2, and 3 that binds to the intracellular ATP site domain of the VEGFR thereby inhibiting signal transduction by VEGF at low nanomolar concentrations of axitinib (Gross-Goupil et al., 2013). Oysters were cultured in ASW containing 50 nM axitinib (VEGF-inhibited) or the equivalent concentration of DMSO (control). The working concentration of axitinib was chosen based on the previous published research (Adomako-Ankomah and Ettensohn, 2013; Sun and Ettensohn, 2014) and tested for non-specific toxicity by measuring respiration of juvenile oysters in the presence of different concentrations of axitinib. These pilot studies showed that 50 nM axitinib did not inhibit oyster respiration indicating the lack of non-specific toxicity.

Oysters were divided into eight batches and randomly assigned to either axitinib or control (DMSO) treatment. For each treatment, four replicate tanks for juveniles or two tanks for adults were set up, each tank containing 5 L of ASW with ∼50 juveniles or 5 adult oysters per tank. Water temperature was maintained at 21 ± 1°C and salinity at 30 ± 0.5 PSU in all tanks. Water was changed daily, and axitinib or DMSO was added after each water change. Juvenile oysters were exposed for 14 weeks, and adults for 2 weeks.

Oysters were fed *ad libitum* every day with a commercial algal blend (2 ml tank^{-1}) containing *Nannochloropsis oculata*, *Phaeodactylum tricornutum*, and *Chlorell*a spp. (DT's Live Marine Phytoplankton, Sycamore, IL, United States). Algae were added to the tanks immediately following the water change. No mortality was detected throughout the experiments.

Whole-Organism O_2 Consumption Rates

The O_2 consumption rates (MO_2) were measured in juvenile oysters every week for 14 weeks by closed-chamber respirometry. MO_2 was measured in 3 ml water-jacketed chambers using Clarke-type oxygen electrodes (OX1LP-3 ml, Qubit Systems, Kingston, ON, Canada) in ASW at 20°C and salinity 30. For each measurement, two similar-sized juveniles were placed into the chamber and allowed to recover for 30 min from the handling stress. The chambers were then closed, and O_2 consumption was monitored for 20–30 min. After the MO_2 determinations, all juvenile oysters were collected and stored in 70% ethanol for body and shell mass measurements.

Body and Shell Mass Measurements

Juveniles of *C. gigas* from control and axitinib-treated groups were collected at time 0 (prior to exposures) and after 14 weeks of exposure. Total wet body mass of specimens was determined using a microbalance XP 56 (Metler-Toledo, Toledo, OH, United States) with a precision of 0.01 mg or better, and dry tissue mass was calculated from the total dry mass by subtracting the mass of the shell. To obtain the shell mass, juveniles were crushed and incubated in NaOCl overnight to digest the tissues; the remaining shell pieces were then washed in ultrapure water followed by 70% ethanol, freeze dried, and their mass determined using a microbalance.

Phylogenetic Analysis of Putative VEGF and VEGFR Homologs From the Oyster (*Crassostrea gigas*) Genome

To ascertain whether sequences annotated as predicted VEGF-A (XP_011449745.1), VEGF-D (EKC18709.1), and VEGFR1 (EKC41995) loci in the *C. gigas* genome belong to the VEGF and VEGFR gene families in invertebrates, we conducted phylogenetic analysis. Protein sequences were identified using BLASTp at the NCBI, using *C. gigas* sequences EKC18709 and EKC41995 as queries. Described Pvf1/VEGF (McDonald et al., 2003) and PDGF/VEGF-receptor-related (Pvr) (Parsons and Foley, 2013) homologs from two *Drosophila* species and representative molluscan genomes were collected. Representative VEGF-A, -B, -C, and -D, and VEGFR1 and VEGFR2 (Holmes and Zachary, 2005) family members from four mammalian genomes (human, chimpanzee, mouse, and rat), collected from Ensembl[1], were also included in the analysis. Amino acid sequences were aligned using MUSCLE (Edgar, 2004) as implemented in MEGA7 (Kumar et al., 2016). The resultant multiple sequence alignments of VEGF and VEGFR homologs, respectively, were used to reconstruct the maximum-likelihood trees based on the JTT (Jones et al., 1992) substitution model using MEGA7 (Kumar et al., 2016). Gamma distribution was used to account for the rate of heterogeneity across sites, estimated as ∼7.4 and ∼4 for VEGF and VEGFR datasets, respectively. To maximize the number of shared sites used in the analysis, we used a partial deletion option with a cut-off of 90% coverage to eliminate positions with multiple gaps. In other words, only positions that had less than 10% of gaps across all sequences were included in the tree reconstruction, resulting in 166 and 1027 shared positions used in VEGF and VEGFR tree reconstructions. About 100 bootstrap replications were used to evaluate the reliability of internal branches. Pvf2 and Pvf3 sequences from *Drosophila melanogaster* and *D. simulans* were also included in the VEGF phylogenetic tree (Holmes and Zachary, 2005; Tarsitano et al., 2006). Pvf-1 sequences, representing Pvr genes from nematodes *Caenorhabditis elegans* (Tarsitano et al., 2006) and *C. briggsae* were used to root the VEGF tree. The VEGFR tree was rooted with human and chimpanzee sequences of PTK7 (tyrosine kinase receptor with seven Ig-like domains), a distant homolog of VEGF (Seipel et al., 2004).

Prediction of Putative VEGF-Regulated Gene Networks

To identify the potential biomineralization genes regulated by the VEGF-dependent signaling cascade, we used a custom bioinformatic pipeline to identify genes that were adjacent to or contained STAT3, AP-1, and CREB binding sites in their promoter regions using annotated genome of the oyster (*Crassostrea gigas*) (version 9). These transcription factors are key signal transducers activated by the VEGF-VEGFR signaling (Abdollahi et al., 2007; Cao, 2010; Gao et al., 2017). Briefly, the genome was screened for the consensus binding sites for STAT 3 (5′-TTCC C/G T/G AA-3′), AP-1 (5′-TGA G/C TCA-3′), and CREB (5′-TGACGTCA-3′). About 70 base-pair regions containing each potential binding site were obtained from the genome and used in a subsequent BLASTn search to identify its position within the *C. gigas* genome scaffolds. Position information was then used in combination with a custom Python script (**Supplementary Table 1**) to isolate 1000 bases upstream within each genome scaffold. For each potential binding site, an approximately 2-kb downstream region of the genome was used to search for annotated genes from the *C. gigas* genome project, using predicted proteins as query sequences in a BLASTx search. Predicted proteins with e-values less than $1e^{-10}$ and an identity score greater than 95% were assessed for their possible function through gene ontology (GO) analysis. GO terms were clustered in the program REVIGO with the whole UniProt database used to reference the size of each term and semantic similarities were determined using SimRel medium (0.7) similarity. Among 12,436 genes that have binding sites for STAT3 (1528 genes), AP-1 (7976 genes), and CREB (3932 genes) in the promoter, we identified five isoforms of carbonic anhydrase (CA2, CA3, CA7, CA12, and CA13), two isoforms of sodium-calcium exchangers (NaHE1 and NaHE3), two isoforms of sodium-calcium exchangers (NaCaE1 and NaCaE3), a sarcoplasmic Ca binding protein, two isoforms of calmodulin (1 and 12) as

[1] ensembl.org

well as four isoforms of CSs (CSC, CS1, CS6, and CS8), which were further used for transcription analyses (**Supplementary Table 2**).

Expression of Transcripts of Biomineralization Genes

The mRNA expression of selected biomineralization-related genes (**Table 1**) was determined in the ME, central mantle (CM), gills, and HCs of adult *C. gigas* exposed to axitinib or DMSO for 2 weeks. Total RNA was extracted from 50 to 100 mg of the mantle or gill tissues using TRI Reagent (Sigma-Aldrich, St. Louis, MO, United States) according to the manufacturer's protocol. RNA from HCs was isolated using mini ZR RNA MiniPrep^{TM} kit (Zymo Research, Irvine, CA, United States) according to the manufacturer's instructions. RNA concentration was determined using NanoDrop 2000 spectrophotometer (Thermo Scientific, Pittsburg, CA, United States). Single-stranded cDNA was obtained from 0.2 μg of the total RNA using 50 U μl^{-1} SMARTScribe^{TM} reverse Transcriptase (Clontech, Mountain View, CA, United States) and 20 $\mu mol\ l^{-1}$ of oligo$(dT)_{18}$ primers. Transcript expression of the target genes was determined by qRT-PCR using a 7500 Fast Real-Time PCR System (Applied BioSystems/Life Technologies, Carlsbad, CA, United States) and SYBR® Green PCR kit (Life Technologies, Bedford, MA, United States) according to the manufacturer's

TABLE 1 | Primers used to amplify the target VEGF regulated biomineralization genes of *C. gigas*.

Target	Accession number	Primer sequence	T_m (°C)
VEGF	XM_011451443.2	FW 5′-CCGGTGCATGTGTACCAATA-3′	55
		Rev 5′-TGATTTCCTCGTCAGTCATTCC-3′	
VEGFR	XM_011457891.1	FW 5′-CGGTCTATGGCTCTGCATAAA-3′	55
		Rev 5′-CAAATGCACCTTGACCCAATAC-3′	
CAII	XM_011449596.1	FW 5′-CATCAACCAGCAGTCAGAAGTA-3′	55
		Rev 5′-TGTTCCGATCCCTTGTCATTAG-3′	
CAIII	XM_011413668.2	FW 5′-CTACCCTACAACAGGGAGTTCTA-3′	55
		Rev 5′-CTGGTCTGAAATTGCCGTATCT-3′	
CAVII	XM_011441430.2	FW 5′-GCGGGAATGTAAGGGAGAAA-3′	55
		Rev 5′-GCATTGCTCTCCATGGTTATTG-3′	
CAXII	EKC34762.1	FW 5′-AAATGGTCAACAACTACCGA-3′	55
		Rev 5′-ATTGCCAGGGAAATTCCAA-3′	
CAXIII	EKC34781.1	FW 5′-ATACTACGAGAAAACCCGAC-3′	55
		Rev 5′-AGTTCCAACTGTAAGGAAGG-3′	
NHX9	XM_011426556.2	FW 5′-TGGTGAAGCTGACTGGTATTG-3′	55
		Rev 5′-CAATGGTTGCCGTCACAAAG-3′	
NHE10	EKC18191.1	FW 5′-AGAGATCTAGGTGCCTCTAA-3′	58
		Rev 5′-GCCAGTTTAACAAAGACGTT-3′	
NaCaE1	EKC29014.1	FW 5′-CTTCTTTGGAGTTTCATGGC-3′	55
		Rev 5′-TTGTAACCAGTCTCACTAGC-3′	
NaCaE3	EKC29016.1	FW 5′-ATGGTGGACCTCTACAACTA-3′	55
		Rev 5′-AAAAATTCGTAACCCCGTTG-3′	
Calmodulin-like protein 1	EKC29572.1	FW 5′-ACATATTCCCCCTGATGAAG-3′	58
		Rev 5′-GCTCGTTAATGTTGCCATAG-3′	
Calmodulin 12	EKC42677.1	FW 5′-TAAGGACGGAAGTGGAAAAA-3′	58
		Rev 5′-GCCTTGATCATTTCGTCTAC-3′	
Sarcoplasmic calcium-binding protein	EKC29123.1	FW 5′-AGATGTGGTACAAGTCTCTG-3′	55
		Rev 5′-ACCATTTCTTCATGTCGTTTT-3′	
Chitin synthase C	EKC28568.1	FW 5′-AAGTTGAACATGAGACGACA-3′	55
		Rev 5′-TTCCATTTTCGCAAAACACA-3′	
Chitin synthase 1	EKC40984.1	FW 5′-CTTTAAAGACGACAACCGTG-3′	55
		Rev 5′-GACATCTGGCCATATCTGTT-3′	
Chitin synthase 6	EKC34858.1	FW 5′-AGGTTGGAAATAGTGACTCAG-3′	55
		Rev 5′-TGGACCTTAAAAGGGTTCTC-3′	
Chitin synthase 8	EKC20511.1	FW 5′-CCGAATACAGATGGTTGTTG-3′	55
		Rev 5′-GCAAGACAAACAACTTTTGC-3′	
β-actin	X75894	FW 5′-TTGGACTTCGAGCAGGAGATGGC-3′	55
		Rev 5′-ACATGGCCTCTGGGCACCTGA-3′	

NCBI accession numbers of the sequences used for primer design and annealing temperatures (T_m) are given for each primer pair.

instructions. The qRT-PCR reaction mixture consisted of 7.5 μl of 2X SYBR® Green master mix, 0.3 μmol l^{-1} of each forward and reverse gene-specific primers (**Table 1**), and 1.5 μl of 10X diluted cDNA template and water to adjust to 15 μl. The reaction mixture was subjected to the following cycling: 10 min at 95°C to denature DNA and activate Taq polymerase, and 40 cycles each of 15 s at 94°C, 30 s at 60°C, and 30 s at 72°C. Serial dilutions of a single cDNA sample (from the ME) were amplified during each run to determine amplification efficiency and to test for potential run-to-run amplification variability (Pfaffl, 2001). The target gene mRNA expression was standardized relative to β-actin mRNA and the internal cDNA standard (Pfaffl, 2001).

FTIR Spectroscopy of Juvenile Shells

Juveniles of *C. gigas* from control and axitinib-treated groups were collected at time 0 (prior to exposures), 2 days, 6 weeks, and 14 weeks of exposure and fixed in 70% ethanol. Juveniles were placed overnight in 4% NaOCl solution to remove organic material, washed two times 30 min each with deionized water followed by a wash in 70% ethanol. Isolated shells were lyophilized for 24 h, and five specimens per group were ground and pressed in KBr pellets. Pellets were analyzed using a FTIR spectrometer (Bruker Vertex 70, Bruker, Billerica, MA, United States) in a transmittance mode with the resolution of 4 cm^{-1} and 128 scans per sample. Absorbance spectra were processed using Spectrum 5.1 software (Perkin Elmer, Shelton, CN, United States). The 600–1000 cm^{-1} regions of the spectra were isolated, baseline corrected and normalized, and the positions and heights of absorption peaks of ν4 and ν2 vibrational bands were measured. The ν4/ν2 band intensity ratio is inversely proportional to calcite crystal and is commonly used as a proxy for the crystallinity of the mineral phase (Beniash et al., 1997; Gueta et al., 2007).

Microhardness Tests on the Shells of Juvenile Oysters

The lyophilized right valves of the juvenile oysters were mounted and polymerized in Epofix epoxy resin (EMS, Hatfield, PA, United States) at room temperature. Five individuals from the axitinib-treated and control groups collected at time 0, 2 days, 6 weeks, and 14 weeks of exposure were used for analyses. To expose shells, the blocks were manually polished with 320 grit paper in the plane normal to the surface and transecting the shell from acute apical tip to its most distal edge until the midline of the shell was exposed. The samples were further polished with 400, 600, and 800 grit paper using Buehler Minimet 1000 polisher, followed by fine polishing with Metadi diamond suspensions down to 0.25 μm. All polishing was carried out in $CaCO_3$-saturated water. The microhardness tests were performed using Identamet (Buehler, Lake Bluff, IL, United States) microindenter at 0.25 N load and 5 s dwelling time with Vickers tip. Five indentations were conducted per each sample. To avoid edge effects, each indentation was positioned at least two indentation diagonals away from the neighboring indentations and the edges of the shell. Microhardness values were averaged for five indentations from each shell, and the average value used as a biological replicate.

Statistical Analyses

Two-way ANOVA was used to test the effects of the tissues and presence/absence of VEGF inhibitor on the studied traits (**Table 2**). For shell traits, one-way ANOVA and/or Student's *t*-test were used. Prior to analyses, data were tested for normality and homogeneity of variance by Kolmogorov-Smirnoff and Levine's tests, respectively, and normalized as needed using Box-Cox common transforming method. Fisher's Least Significant Differences (LSD) tests were used for planned *posthoc* comparisons of the differences between the pairs of means of interest. All statistical analyses were performed with JMP Pro 12 (Cary, NC, United States) or OriginPro 2015 software package (Northampton, MA, United States). Differences were considered significant if the probability of Type I error was less than 0.05. The data are presented as means ± standard errors of means (SEM) unless indicated otherwise.

RESULTS

Effects of Axitinib on Shell and Body Mass and Metabolism of Oyster Juveniles

Dry mass of the soft tissues of juveniles prior to experiment was 0.32 ± 0.05 mg (N = 10); after 14 weeks of exposure it increased to 0.42 ± 0.06 mg (N = 15) and 0.47 ± 0.11 mg (N = 15) in the control and axitinib-exposed group, respectively ($p > 0.05$ for the differences between the groups). There was no significant difference in shell mass between 0 and 14 weeks time-points in the control group (5.31 ± 0.32 mg, N = 10 and 5.27 ± 0.25 mg, N = 15), respectively. A difference approaching significance in the shell mass was found between the time 0 and 14 weeks of exposure to axitinib-group (p = 0.074), with masses of 5.31 ± 0.32 mg (N = 10) and 6.28 ± 0.39 mg (N = 15), respectively. Importantly, significant difference in the shell mass was found after 14 weeks of exposure between the axitinib-treated and control juveniles (p = 0.048). These data indicate that inhibition of VEGF signaling pathway lead to a small but significant increase in the shell mass while the soft tissue mass was not affected.

The duration of experimental exposure had no significant effect on the respiration of control or axitinib-exposed juvenile oysters ($F_{165,13}$ = 1.56, p = 0.149); therefore, data for different time points within each experimental group were pooled for subsequent analyses. Exposure to axitinib had no effect on O_2 consumption rates of juveniles (24.17 ± 2.8 μmol O_2 $animal^{-1}$ h^{-1} and 28.47 ± 3.09 μmol O_2 $animal^{-1}$ h^{-1} for control and axitinib-exposed group, respectively, N = 82–84, p = 0.307).

TABLE 2 | ANOVA: Effects of the axitinib on the expression of biomineralization mRNAs in *Crassostrea gigas*.

Genes	Factor effect		
	Tissue	**Inhibitor**	**Tissue × Inhibitor**
VEGF	$\mathbf{F_{1,35} = 8.9448\ p = 0.0003}$	$F_{3,35} = 1.8166\ p = 0.1885$	$F_{3,35} = 0.1413\ p = 0.9344$
VEGF receptor*	$\mathbf{F_{1,35} = 17.2279\ p = 0.0008}$	$F_{3,35} = 0.1379\ p = 0.7200$	$F_{3,35} = 2.4541\ p = 0.1379$
CAII*	$F_{3,24} = 2.1602\ p = 0.1707$	$\mathbf{F_{1,24} = 6.3606\ p = 0.0357}$	$F_{3,24} = 0.1236\ p = 0.9435$
CAIII*	$F_{3,24} = 3.1807\ p = 0.0847$	$F_{1,24} = 0.4613\ p = 0.5162$	$F_{3,24} = 0.3988\ p = 0.7577$
CAVII*	$F_{3,24} = 1.1568\ p = 0.3842$	$F_{1,24} = 2.1295\ p = 0.1826$	$F_{3,24} = 0.7326\ p = 0.05611$
CAXII*	$F_{3,24} = 1.2385\ p = 0.3579$	$F_{1,24} = 0.2265\ p = 0.6468$	$F_{3,24} = 0.6416\ p = 0.6094$
CAXIII	$F_{3,24} = 0.1349\ p = 0.9379$	$F_{1,24} = 0.2521\ p = 0.6220$	$F_{3,24} = 0.5214\ p = 0.96733$
NHX9*	$\mathbf{F_{3,32} = 21.5863\ p = 0.0003}$	$F_{1,32} = 0.0481\ p = 0.8319$	$F_{3,32} = 2.3698\ p = 0.1465$
NHX10*	$F_{3,32} = 3.7221\ p = 0.0609$	$F_{1,32} = 1.691\ p = 0.2297$	$F_{3,32} = 2.2883\ p = 0.1553$
NaCaE1*	$F_{3,32} = 1.6629\ p = 0.2511$	$F_{1,32} = 1.1714\ p = 0.3107$	$F_{3,32} = 0.2887\ p = 0.8325$
NaCaE3*	$F_{3,32} = 2.4989\ p = 0.1336$	$F_{1,32} = 2.7951\ p = 0.1331$	$F_{3,32} = 0.0677\ p = 0.9755$
Sarc Ca-binding*	$F_{3,35} = 0.1235\ p = 0.9436$	$F_{1,35} = 0.0026\ p = 0.9607$	$F_{3,35} = 0.2248\ p = 0.8765$
Calmodulin 1	$\mathbf{F_{3,35} = 22.5625\ p < 0.0001}$	$F_{1,35} = 0.1953\ p = 0.6620$	$F_{3,35} = 1.4397\ p = 0.2523$
Calmodulin 12*	$F_{3,35} = 3.1445\ p = 0.0867$	$F_{1,35} = 0.7283\ p = 0.4182$	$F_{3,35} = 0.1793\ p = 0.9075$
Chitin synthase C*	$F_{3,35} = 3.3730\ p = 0.0751$	$\mathbf{F_{1,35} = 7.2938\ p = 0.0270}$	$F_{3,35} = 2.3564\ p = 0.1479$
Chitin synthase 1*	$F_{3,35} = 2.2835\ p = 0.1559$	$F_{1,35} = 0.0206\ p = 0.8894$	$F_{3,35} = 2.8012\ p = 0.1085$
Chitin synthase 6*	$F_{3,35} = 0.2413\ p = 0.8652$	$F_{1,35} = 1.9504\ p = 0.2001$	$F_{3,35} = 0.2163\ p = 0.8824$
Chitin synthase 8*	$F_{3,35} = 3.1039\ p = 0.0889$	$F_{1,35} = 0.0214\ p = 0.8874$	$F_{3,35} = 0.5138\ p = 0.6841$

*F ratios (with the degrees of freedom for the factor effect and the error shown as a subscript) are given. Significant effects ($p < 0.05$) are highlighted in bold. * Data were normalized using Box-Cox common transformation method.*

Mineralogical and Mechanical Properties of the Shells of Oyster Juveniles

The FTIR spectroscopic analysis showed a significantly higher ν_4/ν_2 intensity ratio in the shells of juveniles from the axitinib-treated group compared with those from the control group (3.24 ± 0.28 and 2.91 ± 0.06, respectively, $p = 0.046$) after 14 weeks exposure. This indicates that the mineral of the shells in the axitinib-treated group is less crystalline than in the controls (Beniash et al., 1997; Gueta et al., 2007).

The Vickers microhardness of shells of juveniles in the axitinib-treated group was higher than in the control (ANOVA for the effect of treatment: $F_{1,26} = 23.48$, $p < 0.001$) and increased with the exposure duration (i.e., the age of oysters) in both groups (ANOVA for the effect of exposure time: $F_{2,26} = 8.08$, $p = 0.002$). After 14 weeks of exposure, the Vickers microhardness was ∼20% higher (202.74 ± 21.72) in the axitinib-treated group compared to the controls (166.75 ± 24.17) ($p = 0.04$).

Phylogenetic Analysis of VEGF and VEGFR Homologs

Phylogenetic analysis confirmed presence of VEGF and VEGFR homologs in the oyster genome. As **Figure 1A** shows, both *C. gigas* sequences annotated as VEGF (XP_011449745.1, annotated as VEGF-A, and EKC18709.1, annotated as VEGF-D) cluster with other molluscan VEGF-like sequences, including XP_022327278.1 sequence from *C. virginica* annotated as VEGF C-like. Oyster VEGF-like sequences form a cluster with a pair of sequences, one of which is annotated as a platelet-derived growth factor subunit B (PDGF-B) from Yesso scallop grouped with a recently described PDGF/VEGF homolog from the pearl oyster *Pinctada fucata* (Huang et al., 2017), although the internal branch lacks significant bootstrap support. Jointly, these bivalve sequences, together with representatives of gastropods, form a clade with Pvf1 sequences from *Drosophila* genomes. Mammalian representatives of VEGF gene family form a separate clade from the invertebrate Pvf1-like group, subdivided into VEGF-A and -B, and VEGF-C and -D clusters, supported by the bootstrap values of 89, 94, and 100%, respectively. Pvf2 and Pvf3 sequences from *Drosophila* cluster together outside of this mammalian clade, with the bootstrap support of 85%, thus, offering (albeit weak) support for the hypothesis that oyster VEGF-like sequences are more closely related to Pvf1 genes. The lack of strong bootstrap support for internal branches representing deeper divergences within this gene superfamily likely reflects ancient divergence times between taxa, for example, the estimated divergence time between oysters and *Drosophila* is ∼753 MYA, per TimeTree.org (Hedges et al., 2015) as well as a relatively small number of shared sites available in this alignment (166 amino acid sites were used in tree reconstruction, out of total 328 amino acids in *C. gigas* protein).

Likewise, predicted VEGFR sequence from *C. gigas* is clustered with the VEGFR-like sequence from *C. virginica*, joined by a VEGFR sequence from Yesso scallop (**Figure 1B**). These bivalve sequences form a clade with representatives of gastropods, supported by a 82% bootstrap, and together they form a molluscan clade with cephalopod representatives (99% support). Representative mammalian VEGFR1 (FLT1) and VEGFR2 (KDR) sequences form a separate sister clade, split into two clusters, supported by 100% bootstrap values, with *Drosophila* representatives clustered outside of this grouping, with 61%

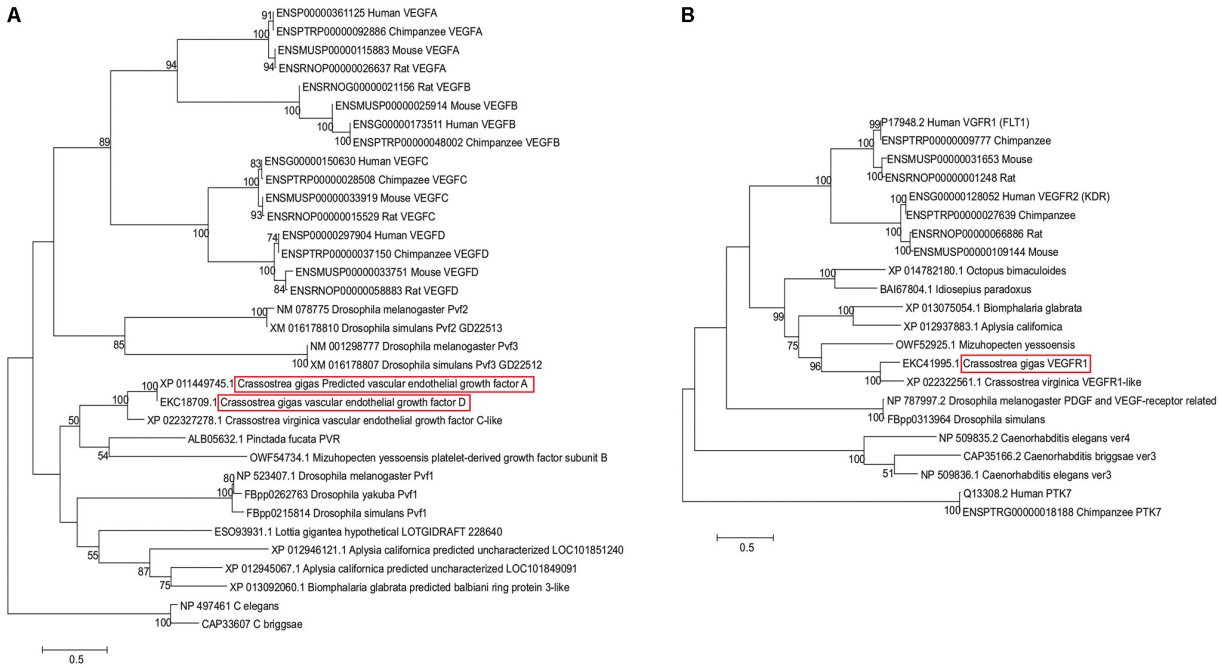

FIGURE 1 | Maximum-likelihood-based phylogenetic trees of VEGF **(A)** and VEGFR **(B)** sequences reconstructed using JTT+gamma substitution model. Each sequence is designated by its GenBank or Ensembl accession number and species name. Sequences from *C. gigas* are highlighted with red boxes. Numbers above branches represent percent bootstrap support.

support for the joint cluster. This indicates that oyster VEGFR-like sequences are likely related to mammalian VEGFR1 and -R2 sequences. Interestingly, according to the multiple sequence alignment, the binding region of axitinib at human VEGFR2 protein [residues 801–826 (McTigue et al., 2012)] appears to share multiple sites with amino acid residues that have the same physicochemical properties not only with mammalian VEGFR1 sequences, but also with invertebrate sequences (**Figure 2**). Such conservation at the level of physicochemical amino acid properties suggests that similar to interactions with the mammalian VEGFR2 proteins, axitinib likely has an inhibitory effect on oyster VEGF receptors.

Functional Annotation of VEGF-Regulated Genes

Our bioinformatic pipeline recovered 79859 predicted total sites for the studied transcription factors, including 6040 sites for STAT3, 42967 sites for AP1, and 30852 sites for CREB. Of these, there were 12436 genes found adjacent to the transcription factors, specifically with 1528 adjacent to STAT3; 7976 to AP1 and 3932 to CREB. Of these, 996, 5152, and 2522 genes contained GO information for STAT3, AP1, and CREB, respectively (**Supplementary Table 1**). In total 526, 1663, and 897 GO groups were used in the program REVIGO for STAT3, AP1, and CREB, respectively.

Across all three transcription factors, we found similar REVIGO profiles associated with different GO groups in the Biological Process and Molecular Function domains. Some of the most abundant GO groups for the Biological Process domain were relatively large and encompassing GO groups, including metabolism [GO:0008152], regulation of DNA-templated transcription [GO: 0006355], carbohydrate metabolism [GO:0005975], intracellular signal transduction [GO:0035556], and transmembrane transport [GO:0055085]. Some of the smaller GO categories found in high abundance associated with the transcription factors included chitin metabolism [GO:0006030], hemophilic cell adhesion via plasma membrane adhesion molecules [GO:0007156], and integrin-mediated signaling pathway [GO:0007229] (**Supplementary Figure 1**).

In the Molecular Function domain, the most abundant GO groups corresponded to large encompassing groups, such as ATP binding [GO:0005524] and zinc ion binding [GO:0008270]. There were also abundant groups associated with intermediate GO encompassing groups, such as calcium ion binding [GO:0005509] and G-protein coupled receptor activity [GO:0004930]. Finally, among the lower abundant GO groups, there was proportionately larger representation of chitin binding [GO:0008061] and scavenger receptor activity [GO:0005044] compared to other GO categories occurring in similar frequencies (**Supplementary Figure 1**). Among these, one of the G-protein coupled receptors was linked back to a kisspeptin protein (K1PWK8_CRAGI) which has putative regulatory role in the mantle function (Cardoso et al., 2016). Additionally, there were numerous proteins associated with calcium ion binding, chitin binding, and other GO groups relevant to mantle function and formation selected for further investigation of the transcript levels (as described below).

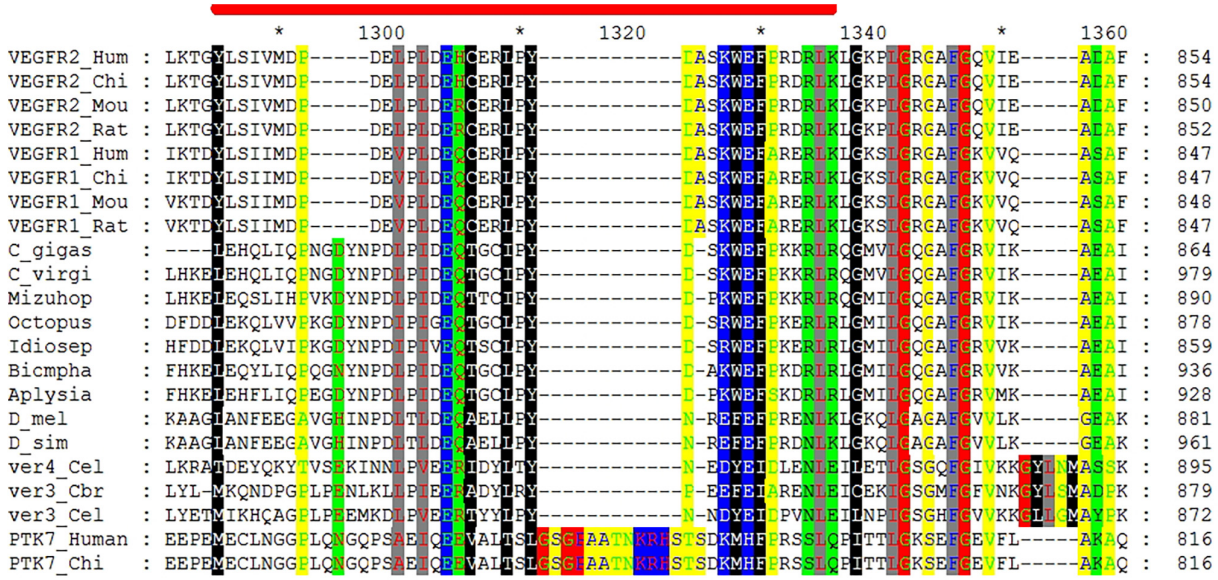

FIGURE 2 | Section of the multiple sequence alignment of VEGFR proteins sequences that shows conservation of physicochemical properties of residues involved in interactions with axitinib. The coordinates on right refer to the absolute amino acid position number for each sequence, while coordinates above the alignment refer to the position in the alignment. Red stripe marks the span between Y801 and K826 residues of human VEGFR2 involved in axitinib binding according to McTigue et al. (2012). The species name abbreviations, top to bottom, are Hum (human), Chi (chimpanzee), Mou (mouse), Rat (rat), *C. gigas*, *C. virgi* (*C. virginica*), Mizuhop (*Mizuhopecten yessoensis*), Octopus (*Octopus bimaculoides*), Idiosep (*Idiosepius paradoxus*), Biompha (*Biomphalaria glabrata*), Aplysia (*Aplysia californica*), D_mel (*Drosophila melanogaster*), D_sim (*Drosophila simulans*), Cel (*Caenorhabditis elegans*), and Cbr (*Caenorhabditis briggsae*). The following sequences (GenBank, FlyBase, or Ensembl accession numbers) were used in the alignment (top to bottom): ENSG00000128052, ENSPTRP00000027639, ENSMUSP00000109144, ENSRNOP00000066886, P17948.2, ENSPTRP00000009777, ENSMUSP00000031653, ENSRNOP00000001248, EKC41995.1, XP_022322561.1, OWF52925.1, XP_014782180.1, BAI67804.1, XP_013075054.1, XP_012937883.1, NP_787997.2, FBpp0313964, NP_509835.2, CAP35166.2, NP_509836.1, Q13308.2, and ENSPTRG00000018188. Conserved sites containing amino acid residues with identical physicochemical properties show polar (black lettering, green background), hydrophobic (white lettering, black background), positively charged (pink lettering, blue background), amphoteric (red lettering, green background), small (green lettering, yellow background), aliphatic (red lettering, gray background), negatively charged (green lettering, blue background), and charged (white lettering, blue background) residues.

mRNA Expression of the VEGF-Regulated Genes

VEGF and VEGF Receptor (VEGFR)

Under the control conditions, VEGF mRNA expression varied among the tissues of adult oysters, with significantly lower expression levels in HCs than in the ME or the gills, and intermediate values in the CM (**Figure 3A**). The exposure to axitinib led to a modest increase in the VEGF expression in HCs, which eliminated the tissue-specific differences in VEGF mRNA levels (**Figure 3A**). Expression of VEGFR in the control group was significantly higher in gills than in the tissues involved in biomineralization (**Figure 3B**). Exposure to axitinib led to an increase of VEGFR mRNA expression in the mantle and a decrease in the gills (**Figure 3B**).

Genes Involved in Acid-Base and Ion Regulation

Out of five studied CA isoforms (CA2, CA3, CA7, CA12, and CA134), only CA2 was differentially expressed in the studied tissues with higher mRNA level in the gills compared with the mantle or HCs (**Figures 3C–G**). Exposure to VEGFR inhibitor significantly affected expression profile of CA2 but not that of other studied CA isoforms in oyster tissues (**Figures 3C–G** and **Table 2**). Notably, exposure to axitinib led to a strong increase in mRNA expression of CA2, CA7, and CA12 in HCs (by ∼9, 12- and 5-fold, respectively); however, this increase was not statistically significant due to a large variation and relatively small sample size (N = 3–5).

Under the control conditions, expression of NaHE9 transporter was higher in the gills than in the other studied tissues (**Figure 4A** and **Table 2**), while mRNA expression of NaHE10 was significantly lower in the gills than in the ME cells (**Figure 4B**). Expression of NaCaE1 was significantly elevated in HCs (**Figure 4C**), where expression of NaCaE3 was similar in all studied tissues (**Figure 4D**). Exposure to axitinib led to a notable albeit statistically non-significant increase of NaHE10, NaCaE1 and NaCaE3 mRNA expression in HCs (by ∼4.5, 2- and 4-fold, respectively), whereas NaHE9 expression remained low (**Figure 4**). Axitinib exposure also significantly stimulated NaHE10 mRNA expression in the gills by 85% (**Figure 4B**).

Genes Involved in Ca^{2+} Binding

Among the three studied Ca^{2+}-binding genes [calmodulin 1 (CAM1), calmodulin 12 (CAM12) and sarcoplasmic calcium-binding protein (SCP)], mRNA expression or CAM1 and CAM12 were lower in HCs than in other tissues of the control oysters

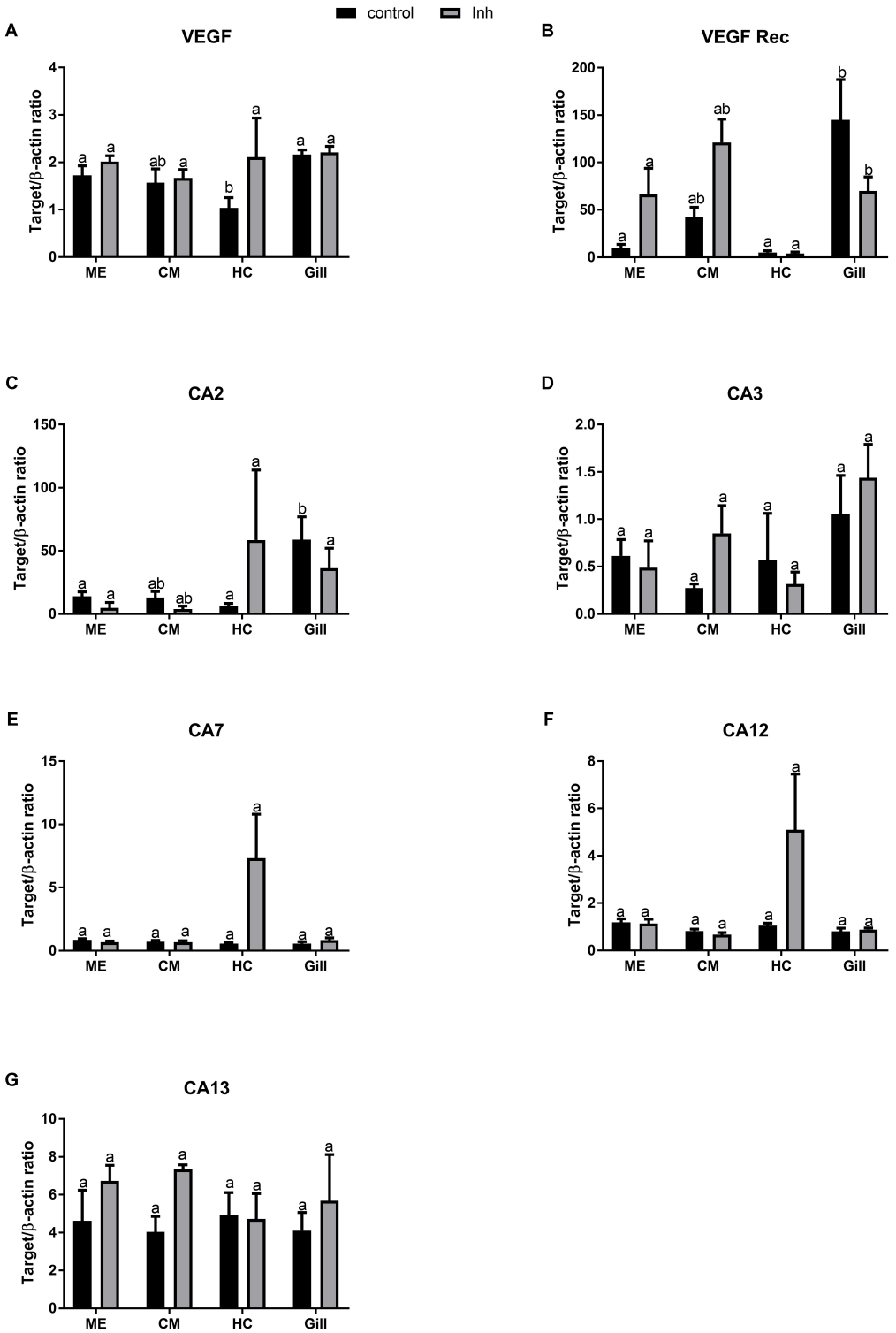

FIGURE 3 | Levels of mRNA expression of VEGF, VEGF receptor, and different isoforms of carbonic anhydrase in tissues of adult *C. gigas* in response to a 2-week axitinib exposure. Genes: **(A)** VEGF – vascular endothelial growth factor, **(B)** VEGF Rec – vascular endothelial growth factor receptor; **(C–G)** CA2, CA3, CA7, CA12, and CA13 – carbonic anhydrases 2, 3, 7, 12, and 13, respectively. Control – control oysters and Inh – axitinib-exposed oysters. Expression levels in the mantle edge (ME), central mantle (CM), hemocytes (HC), and the gills (Gill) are shown. Different letters indicate significant differences between different tissues under the same treatment conditions (i.e., control or axitinib exposure); columns that do not share a letter are significantly different ($p < 0.05$). $N = 3–5$.

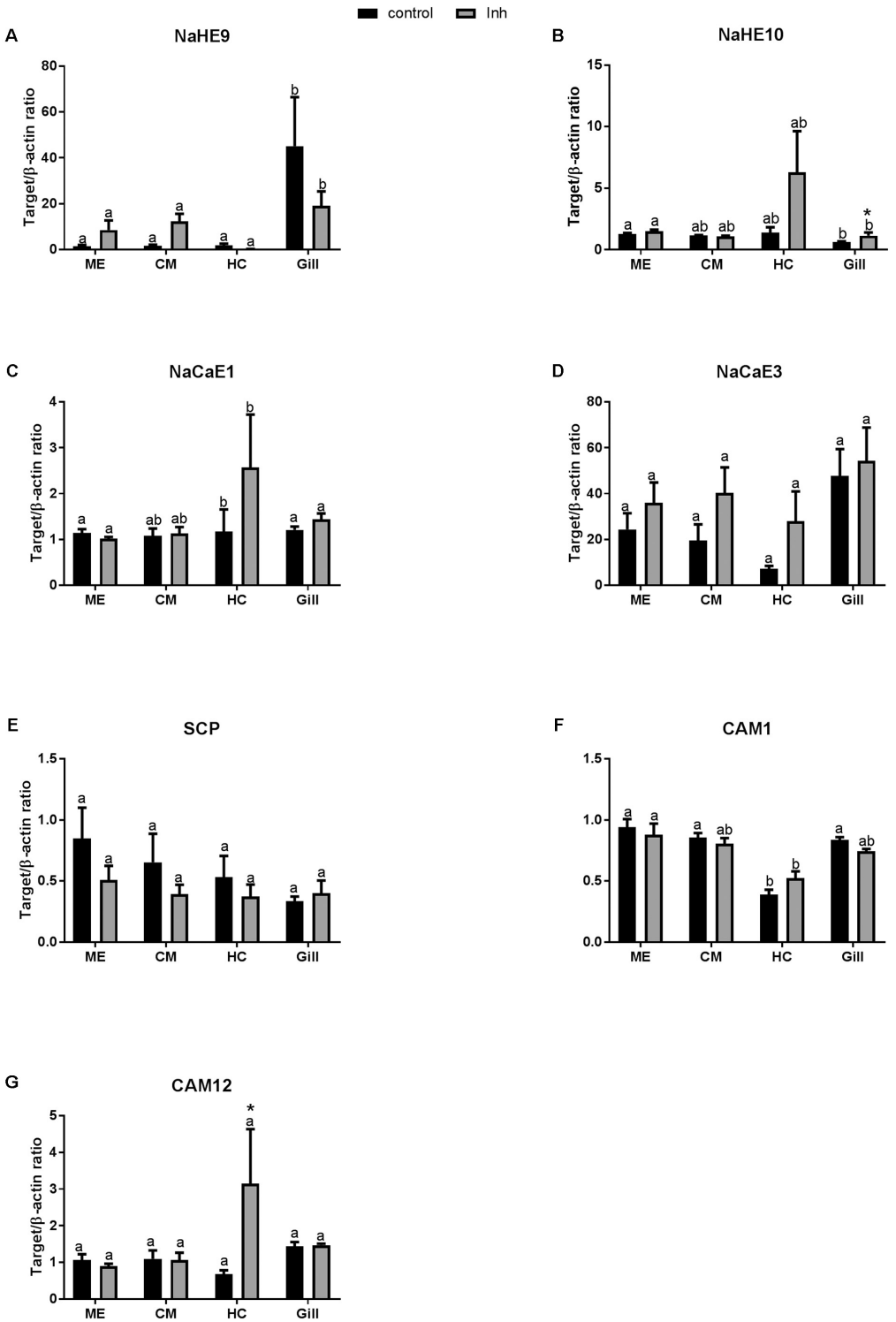

FIGURE 4 | Levels of mRNA expression of ion transporters and Ca binding proteins in tissues of adult *C. gigas* in response to a 2-week axitinib exposure. Genes: **(A,B)** NaHE9 and NaHE10 – Na^+/H^+ exchangers 9 and 10, respectively; **(C,D)** NaCaE1 and NaCaE3 – Na^+/Ca^{2+} exchangers 1 and 3, respectively; **(E)** SCP – sarcoplasmic calcium-binding protein; **(F,G)** CAM 1 and CAM 12 – calmodulin 1 and 12, respectively. Control – control oysters and Inh – axitinib-exposed oysters. Expression levels in the mantle edge (ME), central mantle (CM), hemocytes (HC), and the gills (Gill) are shown. Different letters indicate significant differences between different tissues under the same treatment conditions (i.e., control or axitinib exposure); columns that do not share a letter are significantly different ($p < 0.05$). Asterisks indicate significant differences between the control and axitinib-exposed oysters in the same tissue. $N = 3–5$.

(**Figures 4E–G** and **Table 2**). Expression levels of CAM1 and SCP mRNA were not significantly affected by axitinib exposure (**Figures 4E,F**). In contrast, mRNA expression of CAM12 was significantly higher in HC of animals exposed to the VEGFR inhibitor compared with the respective controls (**Figure 4G**).

Chitin Synthases (CSs)

In control oysters, mRNA expression of chitin synthase C (CSC) and chitin synthase 6 (CS6) were similar in all studied tissues (**Figures 5A,C**). Expression of CS1 mRNA was lower in the gills than in the other tissues, although the differences were only significant between the gills and the CM cells (**Figure 5B**). Expression of CS8 mRNA was the lowest in HCs compared with other tissues (**Figure 5D**). Axitinib treatment led to a statistically significant increase in CSC expression in the gills (**Figure 5A** and **Table 2**). The expression of CS1 was higher in CM than in other tissues, and this difference was significant between CM and gills (**Figure 3B**). The exposure to the VEGFR inhibitor led to a decrease in CS1 expression in CM, yet significant differences remained between CM and gills (**Figure 5B**). Notably, axitinib exposure led to a strong upregulation of CS6 and CS8 mRNA expression in HCs (by ∼15 and 45-fold, respectively) albeit these differences were not statistically significant (**Figures 5C,D**).

DISCUSSION

Disruption of VEGF signaling did not result in the detrimental effects on biomineralization in juvenile *C. gigas*. The shell mass after 14 weeks of axitinib exposure was significantly higher than in the controls, suggesting that VEGF signaling might act as a suppressor of shell growth. Notably, calcite crystallinity slightly but significantly decreased, while there was a significant 20% increase in the microhardness of the shells from the specimens exposed to axitinib, suggesting a complex effects of this inhibitor on shell formation. However, the body growth (assessed by the soft body mass) and metabolic rates were similar in the control and axitinib-exposed juveniles indicating that the disruption of VEGF signaling does not lead to major negative systemic effects in oysters. This contrasts findings in sea urchin larvae where axitinib exposure disrupts the skeletogenic gene regulatory network, resulting in a dramatic disruption of skeletogenesis (Adomako-Ankomah and Ettensohn, 2013, 2014; Sun and Ettensohn, 2014) and the fact that VEGF activates

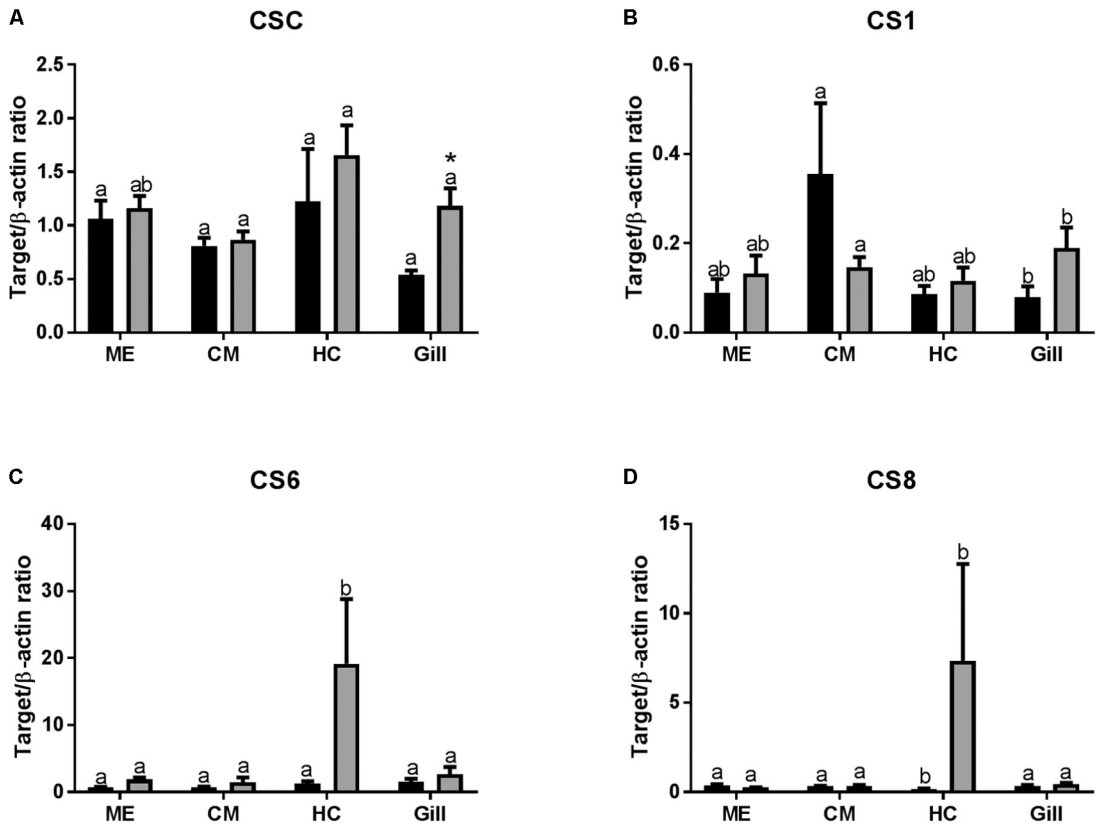

FIGURE 5 | Levels of mRNA expression of chitin synthases in tissues of adult *C. gigas* in response to a 2-week axitinib exposure. Genes: **(A–D)** CSC, CS1, CS6, and CS8 – chitin synthases C, 1, 6, and 8, respectively. Control – control oysters and Inh – axitinib-exposed oysters. Expression levels in the mantle edge (ME), central mantle (CM), hemocytes (HC), and the gills (Gill) are shown Different letters indicate significant differences between different tissues under the same treatment conditions (i.e., control or axitinib exposure); columns that do not share a letter are significantly different ($p < 0.05$). Asterisks indicate significant differences between the control and axitinib-exposed oysters in the same tissue. $N = 3–5$.

spiculogenesis in the *in vitro* sea urchin PMC culture (Knapp et al., 2012). Lack of the major disruption of shell formation in *C. gigas* juveniles during prolonged (14 weeks) exposure to axitinib may indicate that VEGF signaling plays a less prominent and potentially different role in biomineralization in bivalves than in echinoderms and vertebrates (d'Aquino et al., 2007; Wang et al., 2007; Liu et al., 2012; Adomako-Ankomah and Ettensohn, 2013, 2014; Sun and Ettensohn, 2014; Chan et al., 2015; Hu and Olsen, 2016). Alternatively, this may indicate lower sensitivity of the bivalve VEGFR to axitinib. Although the axitinib-binding properties of the bivalve VEGFR have not been studied, the latter explanation appears less probable, given similarity of the putative axitinib-binding sites of oyster and mammalian VEGFR (**Figure 2**) and consistent responses of the shell mass and mechanical properties as well as the transcription profiles of VEGF-responsive genes to axitinib exposure in oysters.

It is worth noting that mineral crystallinity of the shells of juvenile *C. gigas* under control conditions was higher than the reported crystallinity values for the shells of the juveniles of a closely related eastern oyster *Crassostrea virginica* (Beniash et al., 2010), with ν4/ν2 ratios 2.9 vs. 3.9, respectively. The microhardness of the shell was lower in the juveniles of *C. gigas* than in the juveniles of *C. virginica*, 170 VH vs. 250 VH (Beniash et al., 2010). The reasons for these differences in shell properties between two morphologically and ecologically similar species are presently unknown, but emphasize the notion that shell formation in bivalves is under the tight and potentially species-specific biological control (Addadi et al., 2006; Checa et al., 2009; Marin et al., 2012).

Our bioinformatic analyses identified three closely related isoforms of VEGF (VEGF-A, -C, and -D) and two isoforms of VEGF receptor (similar to the vertebrate VEGFR1) in the genome of *C. gigas*. Transcriptomic profiles of biomineralization-related genes showed modest change in response to a 2-week exposure to a potent VEGFR inhibitor, axitinib, in adult *C. gigas*. Expression patterns of the studied CAs, ion transporters, Ca^{2+} binding proteins and shell matrix producing enzymes (CSs) did not strongly respond to VEGF inhibition in a major biomineralizing tissue, the mantle. This was similar to the general lack of a transcriptomic response of these genes in a non-biomineralizing tissue (the gills), except for the slight but significant upregulation of mRNA level of Na^+/H^+ exchanger 10 and CSC in the gills of axitinib-exposed oysters. Interestingly, HCs showed the strongest transcriptomic response to VEGFR inhibition of all the studied tissues, with upregulation of multiple genes by 2- to 45-fold in axitinib treatments. Albeit many of these increases were statistically not significant due to the large individual variation and a limited sample size, the consistent trend shows an increase in VEGF expression in HCs of axitinib-treated oysters, as well as a strong upregulation of mRNA for CAs (CA2, CA7, and CA12), Na^+-dependent ion transporters (NaHE10, NaCaE1), calmodulin 12, and CSs (CS6 and CS8). This indicates that HCs are more sensitive to the disruption of VEGF signaling and may potentially compensate for it by increased production of VEGF. Furthermore, this indicates that transcriptional regulation of the same genes differs in different tissues of oysters potentially reflecting tissue-specific differences in the densities and/or properties of VEGFR and/or epigenetic changes in the gene promoters that alter sensitivity to VEGF-derived signals. It is intriguing to speculate that the relatively high sensitivity of oyster HCs to VEGF-related signals may be related to the mesodermal origin of these cells (Smith et al., 2016) similar to the primary mesenchyme cells of echinoderms, as well as the mineralizing odontoblasts and chondrocytes of vertebrates, and opposed to the less VEGF-sensitive ectoderm-originated tissues such as the mantle and the gills. This hypothesis as well as the mechanisms underlying the differential sensitivity of tissue types and biomineralization processes to VEGF signaling in different invertebrates require further investigation.

As a corollary, our present study shows that although VEGF might play a role in some aspects of shell formation in mollusks, it is not a key regulator of the mineralization processes as in vertebrates and echinoderms (Mayer et al., 2005; Duloquin et al., 2007; Knapp et al., 2012; Liu et al., 2012) hinting toward a possibility that the involvement of VEGF in biomineralization may have developed in deuterostomata. Future studies are needed to determine the physiological roles of VEGF-VEGFR signaling in oysters and other mollusks such as involvement in the regulation of energy and carbohydrate metabolism, DNA transcription and G-protein coupled receptor signaling identified as the candidate processes for VEGF regulation in our bioinformatic pipeline.

AUTHOR CONTRIBUTIONS

EB and IS conceived the study, developed the research design, analyzed the data, and wrote the manuscript. AI participated in the development of the experimental design, conducted the axitinib exposure experiments, performed the gene expression and respiration studies, and participated in the manuscript writing. BB conducted the microhardness tests and FTIR spectroscopy of the shells and performed the mass measurements. TR assisted AI and BB in conducting the experiments, sample preparation, and data collection. HP conducted the phylogenetic analysis and participated in the manuscript preparation. JM conducted the bioinformatic analysis of gene networks and participated in the manuscript preparation.

FUNDING

This work was supported by the United States National Science Foundation (awards IOS-1557870 and IOS-1557551 to IS and EB). JM was supported by the United States National Science Foundation award OCE-1536530. TR is a participant in the REU program supported by NSF awards IOS-1557870 and IOS-1557551.

SUPPLEMENTARY MATERIAL

The Supplementary Material for this article can be found online at: https://www.frontiersin.org/articles/10.3389/fmars.2018.00309/full#supplementary-material

REFERENCES

Abdollahi, A., Schwager, C., Kleeff, J., Esposito, I., Domhan, S., Peschke, P., et al. (2007). Transcriptional network governing the angiogenic switch in human pancreatic cancer. *Proc. Natl. Acad. Sci. U.S.A.* 104, 12890–12895. doi: 10.1073/pnas.0705505104

Addadi, L., Joester, D., Nudelman, F., and Weiner, S. (2006). Mollusk shell formation: a source of new concepts for understanding biomineralization processes. *Chem. Eur. J.* 12, 981–987. doi: 10.1002/chem.200500980

Adomako-Ankomah, A., and Ettensohn, C. A. (2013). Growth factor-mediated mesodermal cell guidance and skeletogenesis during sea urchin gastrulation. *Development* 140, 4214–4225. doi: 10.1242/dev.100479

Adomako-Ankomah, A., and Ettensohn, C. A. (2014). Growth factors and early mesoderm morphogenesis: insights from the sea urchin embryo. *Genesis* 52, 158–172. doi: 10.1002/dvg.22746

Akiva, A., Malkinson, G., Masic, A., Kerschnitzki, M., Bennet, M., Fratzl, P., et al. (2015). On the pathway of mineral deposition in larval zebrafish caudal fin bone. *Bone* 75, 192–200. doi: 10.1016/j.bone.2015.02.020

Beniash, E., Aizenberg, J., Addadi, L., and Weiner, S. (1997). Amorphous calcium carbonate transforms into calcite during sea urchin larval spicule growth. *Proc. R. Soc. Lond. B* 264, 461–465. doi: 10.1098/rspb.1997.0066

Beniash, E., Ivanina, A., Lieb, N. S., Kurochkin, I., and Sokolova, I. M. (2010). Elevated levels of carbon dioxide affect metabolism and shell formation in oysters *Crassostrea virginica*. *Mar. Ecol. Prog. Ser.* 419, 95–108. doi: 10.3354/meps08841

Cao, Y. (2010). Wake-up call for endothelial cells. *Blood* 115, 2336–2337. doi: 10.1182/blood-2009-12-256933

Cardoso, J. C. R., Félix, R. C., Bjärnmark, N., and Power, D. M. (2016). Allatostatin-type A, kisspeptin and galanin GPCRs and putative ligands as candidate regulatory factors of mantle function. *Mar. Genomics* 27, 25–35. doi: 10.1016/j.margen.2015.12.003

Chan, C. K., Seo, E. Y., Chen, J. Y., Lo, D., Mcardle, A., Sinha, R., et al. (2015). Identification and specification of the mouse skeletal stem cell. *Cell* 160, 285–298. doi: 10.1016/j.cell.2014.12.002

Checa, A. G., Esteban-Delgado, F. J., Ramírez-Rico, J., and Rodríguez-Navarro, A. B. (2009). Crystallographic reorganization of the calcitic prismatic layer of oysters. *J. Struct. Biol.* 167, 261–270. doi: 10.1016/j.jsb.2009.06.009

d'Aquino, R., Graziano, A., Sampaolesi, M., Laino, G., Pirozzi, G., De Rosa, A., et al. (2007). Human postnatal dental pulp cells co-differentiate into osteoblasts and endotheliocytes: a pivotal synergy leading to adult bone tissue formation. *Cell Death Differ.* 14, 1162–1171. doi: 10.1038/sj.cdd.4402121

Dickinson, G. H., Ivanina, A. V., Matoo, O. B., Pörtner, H. O., Lannig, G., Bock, C., et al. (2012). Interactive effects of salinity and elevated CO2 levels on juvenile eastern oysters, *Crassostrea virginica*. *J. Exp. Biol.* 215, 29–43. doi: 10.1242/jeb.061481

Dickinson, G. H., Matoo, O. B., Tourek, R. T., Sokolova, I. M., and Beniash, E. (2013). Environmental salinity modulates the effects of elevated CO2 levels on juvenile hard shell clams, *Mercenaria mercenaria*. *J. Exp. Biol.* 216, 2607–2618. doi: 10.1242/jeb.082909

Duloquin, L., Lhomond, G., and Gache, C. (2007). Localized VEGF signaling from ectoderm to mesenchyme cells controls morphogenesis of the sea urchin embryo skeleton. *Development* 134, 2293–2302. doi: 10.1242/dev.005108

Edgar, R. C. (2004). MUSCLE: multiple sequence alignment with high accuracy and high throughput. *Nucleic Acids Res.* 32, 1792–1797. doi: 10.1093/nar/gkh340

Falini, G., Albeck, S., Weiner, S., and Addadi, L. (1996). Control of aragonite or calcite polymorphism by mollusk shell macromolecules. *Science* 271, 67–69. doi: 10.1126/science.271.5245.67

Gao, P., Niu, N., Wei, T., Tozawa, H., Chen, X., Zhang, C., et al. (2017). The roles of signal transducer and activator of transcription factor 3 in tumor angiogenesis. *Oncotarget* 8, 69139–69161. doi: 10.18632/oncotarget.19932

Gross-Goupil, M., François, L., Quivy, A., and Ravaud, A. (2013). Axitinib: a review of its safety and efficacy in the treatment of adults with advanced renal cell Carcinoma. *Clin. Med. Insights Oncol.* 7, 269–277. doi: 10.4137/CMO.S10594

Gueta, R., Natan, A., Addadi, L., Weiner, S., Refson, K., and Kronik, L. (2007). Local atomic order and infrared spectra of biogenic calcite. *Angew. Chem. Int. Ed. Engl.* 46, 291–294. doi: 10.1002/anie.200603327

Hedges, S. B., Marin, J., Suleski, M., Paymer, M., and Kumar, S. (2015). Tree of life reveals clock-like speciation and diversification. *Mol. Biol. Evol.* 32, 835–845. doi: 10.1093/molbev/msv037

Holmes, D. I., and Zachary, I. (2005). The vascular endothelial growth factor (VEGF) family: angiogenic factors in health and disease. *Genome Biol.* 6:209. doi: 10.1186/gb-2005-6-2-209

Hu, K., and Olsen, B. R. (2016). Osteoblast-derived VEGF regulates osteoblast differentiation and bone formation during bone repair. *J. Clin. Investig.* 126, 509–526. doi: 10.1172/JCI82585

Huang, X. D., Zhang, H., and He, M. X. (2017). A PDGF/VEGF homologue provides new insights into the nucleus grafting operation and immune response in the pearl oyster *Pinctada fucata*. *Gene* 637, 1–8. doi: 10.1016/j.gene.2017.09.019

Ivanina, A. V., Beniash, E., Etzkorn, M., Meyers, T. B., Ringwood, A. H., and Sokolova, I. M. (2013a). Short-term acute hypercapnia affects cellular responses to trace metals in the hard clams *Mercenaria mercenaria*. *Aquat. Toxicol.* 14, 123–133. doi: 10.1016/j.aquatox.2013.05.019

Ivanina, A. V., Dickinson, G. H., Matoo, O. B., Bagwe, R., Dickinson, A., Beniash, E., et al. (2013b). Interactive effects of elevated temperature and CO2 levels on energy metabolism and biomineralization of marine bivalves *Crassostrea virginica* and *Mercenaria mercenaria*. *Comp. Biochem. Physiol. A Mol. Integr. Physiol.* 166, 101–111. doi: 10.1016/j.cbpa.2013.05.016

Ivanina, A. V., Falfushynska, H. I., Beniash, E., Piontkivska, H., and Sokolova, I. M. (2017). Biomineralization-related specialization of hemocytes and mantle tissues of the Pacific oyster *Crassostrea gigas*. *J. Exp. Biol.* 220, 3209–3221. doi: 10.1242/jeb.160861

Jones, D. T., Taylor, W. R., and Thornton, J. M. (1992). The rapid generation of mutation data matrices from protein sequences. *Bioinformatics* 8, 275–282. doi: 10.1093/bioinformatics/8.3.275

Kerschnitzki, M., Akiva, A., Ben Shoham, A., Koifman, N., Shimoni, E., Rechav, K., et al. (2016). Transport of membrane-bound mineral particles in blood vessels during chicken embryonic bone development. *Bone* 83, 65–72. doi: 10.1016/j.bone.2015.10.009

Knapp, R. T., Wu, C. H., Mobilia, K. C., and Joester, D. (2012). Recombinant sea urchin vascular endothelial growth factor directs single-crystal growth and branching in vitro. *J. Am. Chem. Soc.* 134, 17908–17911. doi: 10.1021/ja309024b

Kumar, S., Stecher, G., and Tamura, K. (2016). MEGA7: molecular evolutionary genetics analysis version 7.0 for bigger datasets. *Mol. Biol. Evol.* 33, 1870–1874. doi: 10.1093/molbev/msw054

Li, S., Liu, C., Huang, J., Liu, Y., Zhang, S., Zheng, G., et al. (2016a). Transcriptome and biomineralization responses of the pearl oyster *Pinctada fucata* to elevated CO2 and temperature. *Sci. Rep.* 6:18943. doi: 10.1038/srep18943

Li, S. G., Liu, Y. J., Liu, C., Huang, J. L., Zheng, G. L., Xie, L. P., et al. (2016b). Hemocytes participate in calcium carbonate crystal formation, transportation and shell regeneration in the pearl oyster *Pinctada fucata*. *Fish Shellfish Immunol.* 51, 263–270. doi: 10.1016/j.fsi.2016.02.027

Liu, Y., Berendsen, A. D., Jia, S., Lotinun, S., Baron, R., Ferrara, N., et al. (2012). Intracellular VEGF regulates the balance between osteoblast and adipocyte differentiation. *J. Clin. Invest.* 122, 3101–3113. doi: 10.1172/JCI61209

Marie, B., Joubert, C., Tayale, A., Zanella-Cleon, I., Belliard, C., Piquemal, D., et al. (2012). Different secretory repertoires control the biomineralization processes of prism and nacre deposition of the pearl oyster shell. *Proc. Natl. Acad. Sci. U.S.A.* 109, 20986–20991. doi: 10.1073/pnas.1210552109

Marin, F., Le Roy, N., and Marie, B. (2012). The formation and mineralization of mollusk shell. *Front. Biosci.* 4:1099–10125. doi: 10.2741/s321

Mayer, H., Bertram, H., Lindenmaier, W., Korff, T., Weber, H., and Weich, H. (2005). Vascular endothelial growth factor (VEGF-A) expression in human mesenchymal stem cells: autocrine and paracrine role on osteoblastic and endothelial differentiation. *J. Cell. Biochem.* 95, 827–839. doi: 10.1002/jcb.20462

McDonald, J. A., Pinheiro, E. M., and Montell, D. J. (2003). PVF1, a PDGF/VEGF homolog, is sufficient to guide border cells and interacts genetically with Taiman. *Development* 130, 3469–3478. doi: 10.1242/dev.00574

McTigue, M., Murray, B. W., Chen, J. H., Deng, Y. L., Solowiej, J., and Kania, R. S. (2012). Molecular conformations, interactions, and properties associated with drug efficiency and clinical performance among VEGFR TK inhibitors. *Proc. Natl. Acad. Sci. U.S.A.* 109, 18281–18289. doi: 10.1073/pnas.1207759109

Mount, A. S., Wheeler, A. P., Paradkar, R. P., and Snider, D. (2004). Hemocyte-mediated shell mineralization in the eastern oyster. *Science* 304, 297–300. doi: 10.1126/science.1090506

Nudelman, F., Gotliv, B. A., Addadi, L., and Weiner, S. (2006). Mollusk shell formation: mapping the distribution of organic matrix components underlying a single aragonitic tablet in nacre. *J. Struct. Biol.* 153, 176–187. doi: 10.1016/j.jsb.2005.09.009

O'Neill, M., Gaume, B., Denis, F., and Auzoux-Bordenave, S. (2013). Expression of biomineralisation genes in tissues and cultured cells of the abalone Haliotistuberculata. *Cytotechnology* 65, 737–747. doi: 10.1007/s10616-013-9576-0

Parsons, B., and Foley, E. (2013). The drosophila platelet-derived growth factor and vascular endothelial growth factor-receptor related (Pvr) protein ligands Pvf2 and Pvf3 control hemocyte viability and invasive migration. *J. Biol. Chem.* 288, 20173–20183. doi: 10.1074/jbc.M113.483818

Pfaffl, M. W. (2001). A new mathematical model for relative quantification in real-time RT-PCR. *Nucleic Acids Res.* 29, 2002–2007. doi: 10.1093/nar/29.9.e45

Roch, P. (1999). Defense mechanisms and disease prevention in farmed marine invertebrates. *Aquaculture* 172, 125–145. doi: 10.1016/S0044-8486(98)00439-6

Schipani, E., Maes, C., Carmeliet, G., and Semenza, G. L. (2009). Regulation of osteogenesis-angiogenesis Coupling by HIFs and VEGF. *J. Bone Min. Res.* 24, 1347–1353. doi: 10.1359/jbmr.090602

Seipel, K., Eberhardt, M., Muller, P., Pescia, E., Yanze, N., and Schmid, V. (2004). Homologs of vascular endothelial growth factor and receptor, VEGF and VEGFR, in the jellyfish *Podocoryne carnea*. *Dev. Dyn.* 231, 303–312. doi: 10.1002/dvdy.20139

Smith, V. J., Accorsi, A., and Malagoli, D. (2016). "Chapter 1 - hematopoiesis and hemocytes in pancrustacean and molluscan models," in *The Evolution of the Immune System*, ed. D. Malagoli (Cambridge, MA: Academic Press), 1–28.

Sokolova, I. M. (2009). Apoptosis in molluscan immune defense. *Invertebrate Surviv. J.* 6, 49–58.

Street, J., Bao, M., Bunting, S., Peale, F. V., Ferrara, N., Steinmetz, H., et al. (2002). Vascular endothelial growth factor stimulates bone repair by promoting angiogenesis and bone turnover. *Proc. Nat. Acad. Sci. U.S.A.* 99, 9656–9661. doi: 10.1073/pnas.152324099

Sun, Z., and Ettensohn, C. A. (2014). Signal-dependent regulation of the sea urchin skeletogenic gene regulatory network. *Gene Expr. Patterns* 16, 93–103. doi: 10.1016/j.gep.2014.10.002

Tarsitano, M., De Falco, S., Colonna, V., Mcghee, J. D., and Persico, M. G. (2006). The C. elegans pvf-1 gene encodes a PDGF/VEGF-like factor able to bind mammalian VEGF receptors and to induce angiogenesis. *FASEB J.* 20, 227–233. doi: 10.1096/fj.05-4147com

Wang, Y., Wan, C., Deng, L. F., Liu, X. M., Cao, X. M., Gilbert, S. R., et al. (2007). The hypoxia-inducible factor a pathway couples angiogenesis to osteogenesis during skeletal development. *J. Clin. Investig.* 117, 1616–1626. doi: 10.1172/JCI31581

Zhang, G. F., Fang, X. D., Guo, X. M., Li, L., Luo, R. B., Xu, F., et al. (2012). The oyster genome reveals stress adaptation and complexity of shell formation. *Nature* 490, 49–54. doi: 10.1038/nature11413

Conflict of Interest Statement: The authors declare that the research was conducted in the absence of any commercial or financial relationships that could be construed as a potential conflict of interest.

frontiers in Marine Science

ORIGINAL RESEARCH
published: 30 August 2018
doi: 10.3389/fmars.2018.00306

An Extracellular Polysaccharide-Rich Organic Layer Contributes to Organization of the Coccosphere in Coccolithophores

*Charlotte E. Walker[1,2], Sarah Heath[1], Deborah L. Salmon[3], Nicholas Smirnoff[3], Gerald Langer[1], Alison R. Taylor[4], Colin Brownlee[1,2] and Glen L. Wheeler[1]**

[1] Marine Biological Association, Plymouth, United Kingdom, [2] School of Ocean and Earth Science, University of Southampton, Southampton, United Kingdom, [3] Biosciences, College of Life and Environmental Sciences, University of Exeter, Exeter, United Kingdom, [4] Department of Biology and Marine Biology, University of North Carolina Wilmington, Wilmington, NC, United States

Coccolithophores are globally abundant marine microalgae characterized by their ability to form calcite platelets (coccoliths). The coccoliths are produced internally in a Golgi-derived vesicle. Mature coccoliths are extruded from the cell to form a protective covering on the cell surface, known as the coccosphere. Current evidence indicates that calcite precipitation in the coccolith vesicle (CV) is modulated by coccolith-associated polysaccharides (CAPs). Whilst previous research into CAPs has focussed on their roles in calcite precipitation within the CV, little is known of their extracellular roles. Using fluorescent lectins, we visualize the extracellular polysaccharide-rich organic layer associated with external coccoliths and demonstrate that it differs between species in structure and composition. Biochemical analysis of polysaccharide extracted from coccoliths indicated substantial differences between species in monosaccharide composition and uronic acid content. In *Coccolithus braarudii* our studies indicate that polysaccharide-rich material is extruded with the coccoliths, where it plays a role in the adhesion of the coccoliths to the cell surface and contributes to the overall organization of the coccosphere. Together, these results highlight the important extracellular roles of CAPs and their contribution to the dynamic nature of the coccosphere.

Keywords: coccolithophore, calcification, *Coccolithus braarudii*, polysaccharide, lectin

OPEN ACCESS

Edited by:
Alfred Portius Wheeler, Clemson University, United States

Reviewed by:
Yoshihiro Shiraiwa, University of Tsukuba, Japan
Karina Krarup Sand, University of Copenhagen, Denmark

****Correspondence:***
Glen L. Wheeler
glw@mba.ac.uk

Specialty section:
This article was submitted to Marine Molecular Biology and Ecology, a section of the journal Frontiers in Marine Science

Received: *24 May 2018*
Accepted: *10 August 2018*
Published: *30 August 2018*

Citation:
Walker CE, Heath S, Salmon DL, Smirnoff N, Langer G, Taylor AR, Brownlee C and Wheeler GL (2018) An Extracellular Polysaccharide-Rich Organic Layer Contributes to Organization of the Coccosphere in Coccolithophores. Front. Mar. Sci. 5:306. doi: 10.3389/fmars.2018.00306

INTRODUCTION

Coccolithophores are photosynthetic unicellular marine algae that are characterized by their ability to form intricate calcite platelets known as coccoliths (Taylor et al., 2017). Coccoliths are produce internally in a Golgi-derived coccolith vesicle (CV). Coccolithophores transport Ca^{2+} and HCO_3^- from the environment into the CV where the precipitation of calcite occurs (Brownlee and Taylor, 2004). Mature coccoliths are extruded and organized into an extracellular layer (the coccosphere) covering the cell surface (Young and Henriksen, 2003; Brownlee and Taylor, 2004). Coccolithophores are globally abundant, with some species forming vast blooms that can be visible from space (Westbroek et al., 1993), making them important global producers and significant contributors to the ocean carbon cycle (Rost and Riebesell, 2004). The important

role coccolithophores play in biogeochemical cycling has driven much research investigating the underlying cellular mechanisms of calcification and the roles of the extracellular covering of coccoliths.

Coccolith-associated polysaccharides (CAPs) are thought to play an important role in the nucleation and shaping of the calcite crystals (Borman et al., 1982; Marsh, 2003). There is considerable variability in the morphology of coccoliths and the nature of the coccosphere between species. For example, the heavily-calcified placolith-bearing species such as *Coccolithus braarudii* or *Calcidiscus leptoporus*, which contribute significantly to calcite production in the Atlantic Ocean, exhibit a single layer of interlocking coccoliths (Young et al., 2003; Daniels et al., 2014). The cosmopolitan bloom forming species *Emiliania huxleyi* also produces placoliths, but these can be arranged into either single or multiple layers within its coccosphere (Paasche, 2001). *Scyphosphaera apsteinii* is broadly distributed in tropical and sub-tropical waters and produces a dimorphic coccosphere, comprising of flat muroliths and barrel-shaped lopadoliths (Drescher et al., 2012). These form a single layer on the cell surface, but are not interlocking (Young et al., 2003). The proportion of muroliths and lopadoliths in the coccosphere of *S. apsteinii* can vary due to environmental conditions, with a greater proportion of lopadoliths observed in cells grown at low light intensities (Drescher et al., 2012). The coccosphere of all species likely forms a protective covering around the cell (Monteiro et al., 2016), which must be both flexible (to enable cell growth and division) but also tightly organized to ensure full covering of the cell surface and to prevent excess shedding of coccoliths.

The mechanisms supporting the arrangement of coccoliths on the cell surface and their tethering to the plasma membrane have not been closely investigated. There are several reports describing an organic layer surrounding the cell, which is integrated with the coccoliths and comprised of several distinct components (van der Wal et al., 1983a,b; Marsh, 1994; Taylor et al., 2007). In the majority of coccolithophores, a layer of organic scales composed of cellulose or similar polysaccharide can be observed underneath the coccosphere (Drescher et al., 2012; Taylor et al., 2017), that are secured to the plasma membrane via distinct fibrillar material. A few coccolithophore species, most notably *E. huxleyi*, lack this layer of organic scales (van der Wal et al., 1983b). The organic scales are produced intracellularly and are secreted to the surface (Outka and Williams, 1971). Whilst these scales cover the majority of the cell surface, they are not found directly beneath the central region of the coccolith baseplate. Instead, the fibrillar material can be observed in direct contact with the mineralized coccolith in these regions, which is thought to play a role in tethering the coccolith to the plasma membrane (Drescher et al., 2012; Taylor et al., 2017). The organic scales may be bound by amorphous polysaccharide (Pienaar, 1994). TEM imaging in combination with ruthenium red staining to reveal polysaccharides identified a layer of amorphous polysaccharide coating the coccoliths of *S. apsteinii*, as well as heavy staining of organic scales and fibrillar material (Drescher et al., 2012). However, the nature of these polysaccharides and their roles in different coccolithophores with distinct coccolith morphologies are not known.

While there has been considerable interest in the role of polysaccharides in modulating calcite precipitation (Westbroek et al., 1973; De Jong et al., 1976), little is known about the extracellular CAPs in coccolithophores. CAPs are predominantly classified as water-soluble acidic polysaccharides primarily composed of neutral monosaccharides, acidic sulfate esters and uronic acid residues (De Jong et al., 1976). The uronic acid residues are pivotal in modulating calcification because their negatively charged carboxyl groups are known to bind to Ca^{2+} cations and are thought to impede calcite precipitation at key points in coccolith production. Studies both *in vivo* and *in vitro* have demonstrated that CAPs regulate the precipitation of calcite in various species of coccolithophore (Borman et al., 1982, 1987; Henriksen and Stipp, 2009; Kayano et al., 2011; Gal et al., 2016).

Localization studies have shown polysaccharide situated internally in the CV in *E. huxleyi* (van der Wal et al., 1983b) and *Chrysotila carterae* (formerly *Pleurochrysis carterae*) (van der Wal et al., 1983a; Marsh, 1994). It is also clear that extracellular coccoliths are coated with an organic layer that may have an important influence on the dissolution of coccoliths (Young et al., 1999; Engel et al., 2004; Hirokawa et al., 2005). It is likely that polysaccharides contribute significantly to this organic layer (Hirokawa et al., 2005), but their origin and potential roles in relation to the extruded coccolith have not been extensively investigated.

The CAPs that have been isolated so far from coccolithophores show diversity between species in both their biochemical composition and in the number of isoforms present. For example, a single CAP was isolated from *E. huxleyi* (Borman et al., 1987) whereas three distinct forms were identified in *C. carterae* (Marsh, 2003). It has been proposed that the additional polysaccharides in *C. carterae* may function as a component of a Ca^{2+} delivery system, possibly replacing the function of the reticular body, a membrane-rich organelle that is not found in *Chrysotila* species (Marsh and Dickinson, 1997), but is a predominant feature in other species such as *E. huxleyi* and *C. braarudii* (Taylor et al., 2007, 2017). Moreover, the chemical composition of CAPs differs between species and strains (Borman et al., 1987; Lee et al., 2016). Significant differences in the uronic acid content of CAPs have been proposed to influence the shaping of the calcite crystals (Marsh and Dickinson, 1997) or to reflect adaptations to differing calcite saturation states of the CV (Lee et al., 2016).

A degree of ambiguity surrounds the nature and roles of CAPs due to the aforementioned diversity between species and because many investigations use different polysaccharide extraction procedures (**Supplementary Table 1**). Although CAPs are often referred to collectively, the varied extraction techniques used will not always differentiate between polysaccharides from the CV and those found extracellularly. Note that intracoccolith extractions have previously been referred to as intracrystalline (Westbroek et al., 1973; Lee et al., 2016), but as the localization of polysaccharides internally in calcite crystals is subject to debate we shall refer to these fractions as intracoccolith in this discussion. Previous investigations

into CAPs have predominately focussed on the water-soluble components, although stable water-insoluble polysaccharides are also associated with the coccoliths (van der Wal et al., 1983b). The nature of the polysaccharides in the organic layer surrounding the cell has not been explored in detail. This layer appears to play an important role in the organization of the coccosphere, but whether these polysaccharides are related to those characterized in previous analyses of CAPs is not clear.

We have recently demonstrated that polysaccharides can be visualized around the coccolithophore *C. braarudii* using fluorescent dyes conjugated to lectins (Walker et al., 2018). In the present study, we use fluorescence microscopy to examine the extracellular polysaccharides associated with coccoliths in five coccolithophore species. We show that there are significant differences in the nature of the insoluble polysaccharides associated with coccoliths between species. Biochemical analyses suggest that these polysaccharides also differ in monosaccharide and uronic acid content. We show that the extracellular polysaccharides of *C. braarudii* are likely produced internally with the coccolith and play a subsequent role in the adhesion and organization of the coccosphere.

MATERIALS AND METHODS

General Culture Conditions

Coccolithus braarudii (PLY182g) (formerly *Coccolithus pelagicus* ssp. *braarudii*), *C. leptoporus* (RCC1130), *C. carterae* (PLY406), and *E. huxleyi* (CCMP1516) were grown in filtered seawater (FSW) with added f/2 nutrients (Guillard and Ryther, 1962). *S. apsteinii* (RCC 1456) was grown in FSW with added f/2 nutrients and 10% K medium. Cells were grown in batch cultures, incubated at 15°C and illuminated with 65–75 μmol photons m^{-2} s^{-1} in a 16:8 light:dark cycle.

Decalcification of Coccolithophores

Coccolithophores were allowed to settle and excess f/2 media removed. To decalcify, the cells were washed in Harrison's broad spectrum artificial seawater (ASW) (Harrison et al., 1980) without $CaCl_2$ and pH adjusted to 7.0 with HCl. Cells were washed twice to remove any residual Ca^{2+} and adjust the pH, with time allowed for cells to settle between washes. Cells were incubated in the ASW for approximately 30 min to decalcify, allowed to settle and finally re-suspended in FSW f/2 media prior to staining.

Staining and Confocal Microscopy

Extracellular polysaccharides were stained using the fluorescent lectins Concanavalin A (ConA) (100 μg/ml) and wheat germ agglutinin (WGA) (100 μg/ml) conjugated to either fluorescein isothiocyanate (FITC) or Texas Red (all lectins: Invitrogen, United Kingdom). Cells were imaged using a Zeiss LSM 510 laser scanning confocal microscope, with excitation at 488 nm and emission at 500–530 nm (FITC) and 650–715 nm (chlorophyll). Where stated, certain samples were also visualized using a Nikon Ti epifluorescent microscope with a Photometrics Evolve EM-CCD camera (excitation 475–495 nm, emission 505–535 nm).

Electron Microscopy

Samples for SEM were filtered onto a 13 mm 0.4 μm Isopore filter (Millipore EMD) and rinsed with 5 ml of 1 mM HEPES buffered (pH 8.2) MilliQ water to remove any salt. Filters were air dried, mounted onto aluminum stubs and sputter coated with 10 nm Pt/Pd (Cressington, United States). Samples were examined using a Phillips XL30S FEG SEM (FEI-Phillips, United States) and imaged in high-resolution secondary electron mode with beam acceleration of 5 kV.

Coccolith Preparation

Late exponential phase cultures were harvested by centrifugation at 4800 *g*, 4°C for 5 min. Cells were resuspended in 10 ml of f/2 FSW and subjected to probe sonication (Soncs Vibra Cell VCX750) at 30% amplification for two 10 s pulses. Cells were mixed by inverting the tube between pulses. The cell debris and coccoliths were pelleted by centrifugation (4800 *g*, 4°C for 5 min) and the supernatant removed. The pellet was resuspended in 50% Percoll® (Sigma-Aldrich, United Kingdom) to separate the cell debris and coccoliths by density centrifugation. The mixture was centrifuged at 4800 *g*, at 4°C for 20 min. The density centrifugation step was repeated twice to ensure a clean coccolith preparation. The Percoll® was then removed from the coccoliths by washing three times in NH_4HCO_3 0.5 M. The coccolith preparation was then subjected to polysaccharide extraction.

A sample of the coccolith preparation was cleaned by incubating in 10% NaClO at room temperature overnight to remove all organic material. The coccoliths were pelleted and the supernatant removed. The cleaned calcite was then stained using FITC-ConA to test if the lectin bound non-specifically to the coccoliths.

Polysaccharide Extraction and GC–MS Analysis

The composition of polysaccharides extracted from coccolith preparations for *C. braarudii, S. apsteinii, C. carterae,* and *E. huxleyi* was determined using GC–MS. Calcite and other soluble material was removed by resuspending the coccolith pellets in 0.1 M EDTA (pH 8.0). The mixture was then centrifuged at 16000 *g* for 5 min and the supernatant removed. This step was repeated twice. Insoluble polysaccharides in this pellet were further cleaned by washing in 80% ethanol three times (centrifugation at 16000 *g* for 5 min).

Polysaccharides were hydrolyzed by heating to 105°C for 2 h in the presence of 2 M trifluoroacetic acid (200 μl). 50 μl of hydrolyzed sample was centrifuged at 16000 *g* for 10 min to remove any solid material. 40 μl of supernatant was transferred to glass MS vials and 10 μl of internal standard added (*myo*-inositol, final concentration 2 μM). Samples were air dried and 20 μl of 20 mg ml^{-1} methoxyamine hydrochloride dissolved in pyridine was added to each sample before incubation at 37°C for 2 h. 35 μl of *N*-methyl-*N*-trimethylsilyltrifluoroacetamide (MSTFA)

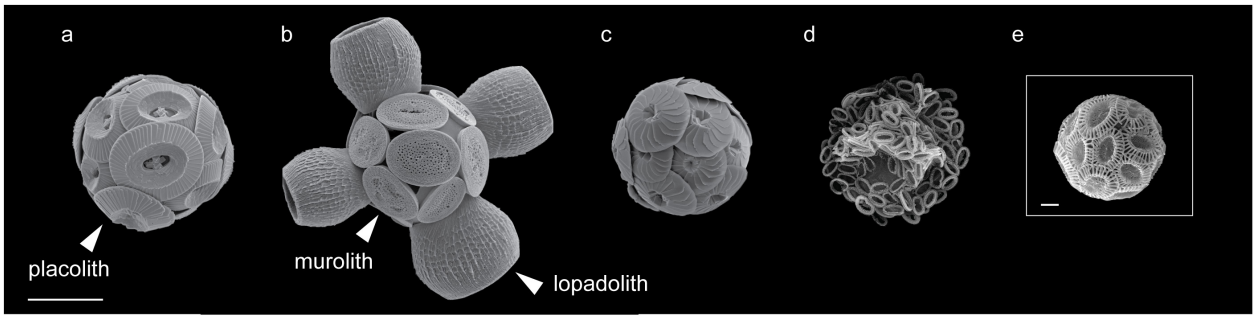

FIGURE 1 | Scanning electron microscopy images of coccolithophore species included in this study. **(a)** *Coccolithus braarudii*, **(b)** *Scyphosphaera apsteinii*, **(c)** *Calcidiscus leptoporus*, **(d)** *Chrysotila carterae,* and **(e)** *Emiliania huxleyi*. All species included are placolith bearing with the exception of *S. apsteinii* **(b)** which bears disk-shaped muroliths and barrel-shaped lopadoliths, representative examples of each coccolith type are labeled (arrowhead). Scale bars represent 10 μm **(a–d)** and 1 μm **(e)**.

was then added and the samples returned to 37°C for a further 30 min. Derivatising agents were purchased from Sigma-Aldrich, United Kingdom.

Blanks (TFA) and sugar standards were treated in the same way, along with a derivatization agent only blank. A standard mix was prepared containing D-glucose, D-galactose, D-mannose, D-xylose, D-arabinose, L-fucose, L-rhamnose, D-galacturonic acid, D-glucuronic acid, and *myo*-inositol.

Derivatised samples were analyzed using an Agilent 7200 series accurate mass Q-TOF GC–MS together with a 7890A GC system (Agilent Technologies, Santa Clara, CA, United States), equipped with an electron ionization ion source. 5 μl of each sample was injected into a non-deactivated, baffled glass liner with a 12:1 split ratio (14.448 ml min^{-1} split flow) and the inlet temperature was maintained at 250°C. A 3 ml min^{-1} septum purge flow was applied. A Zebron semi-volatiles (Phenomenex, Torrance, CA, United States) column (30 m × 250 μm × 0.25 μm) coupled with a 10 m guard column, was maintained at a constant helium flow of 1.2 ml min^{-1}. The temperature gradient of the GC was ramped up at a rate of 15°C min^{-1}, from 70 to 310°C over 16 min, and then held at 310°C for a further 6 min. The total run time of 22 min, was followed by a 7 min backflush at 310°C to clean the column at the end of every run. The MS emission current and emission voltage were held at 35 μA and 70 eV respectively, and the MS was automatically calibrated after every run. The mass range was set from 50 to 600 amu, with an acquisition rate of 5 spectra s^{-1}, and a solvent delay of 3.5 min. Extraction solvent blanks were run at the beginning and end of the run.

Data were analyzed using Agilent technologies MassHunter qualitative and quantitative software. Peak areas were normalized for the internal standard and then peak areas for each monosaccharide residue was then individually normalized to the internal its standard for each sample. Normalized peak areas were then divided by that of the corresponding compound standard (to negate differences in ionization). Data are expressed as the percentage for each compound of the total peak areas of positively identified monosaccharide residues for each species.

RESULTS

Localization of Extracellular Polysaccharides Using the Fluorescent Lectin FITC-ConA

We examined the nature of the extracellular polysaccharides found in five diverse coccolithophore species. *C. braarudii, S. apsteinii, C. leptoporus, C. carterae,* and *E. huxleyi* were chosen as they represent a range of cell sizes, coccolith morphologies (**Figure 1**), biogeographical distributions and distinct phylogenic clades (Liu et al., 2010). To examine the distribution of extracellular polysaccharides, we stained both calcified and decalcified cells with fluorescent conjugates of the lectin Concanavalin A (ConA), which binds primarily to D-mannose and D-glucose residues, and imaged them using confocal microscopy.

Decalcified cells of all five species displayed FITC-ConA staining in a layer surrounding the cells (**Figure 2**). This indicates that cells from each species are coated in a polysaccharide-rich organic layer containing D-glucose and/or D-mannose residues. Some structural diversity was observed in the polysaccharide layers between species. *C. braarudii* exhibited a granular polysaccharide layer with distinct regularly spaced areas in which staining was absent (**Figure 2A**), as observed previously (Walker et al., 2018). These regular ellipsoidal regions likely correspond to the position of the coccoliths. Interestingly, this distinctive structural organization was not observed in the closely related species *C. leptoporus*. Although some irregularities were observed in the staining of the polysaccharide layer in *C. leptoporus*, these clearly differ from the regularly spaced oval-shaped areas found in *C. braarudii* (**Figure 2B**). In the other three species, the FITC-ConA staining revealed a relatively smooth consistently-stained polysaccharide layer on the cell surface (**Figures 2C–E**).

To investigate the interaction of this polysaccharide layer with the coccosphere, we also imaged FITC-ConA staining in calcified cells. All five species exhibited positive staining (**Figure 3** and **Table 1**). Images of fully calcified *C. braarudii* cells revealed additional staining patterns with similar dimensions

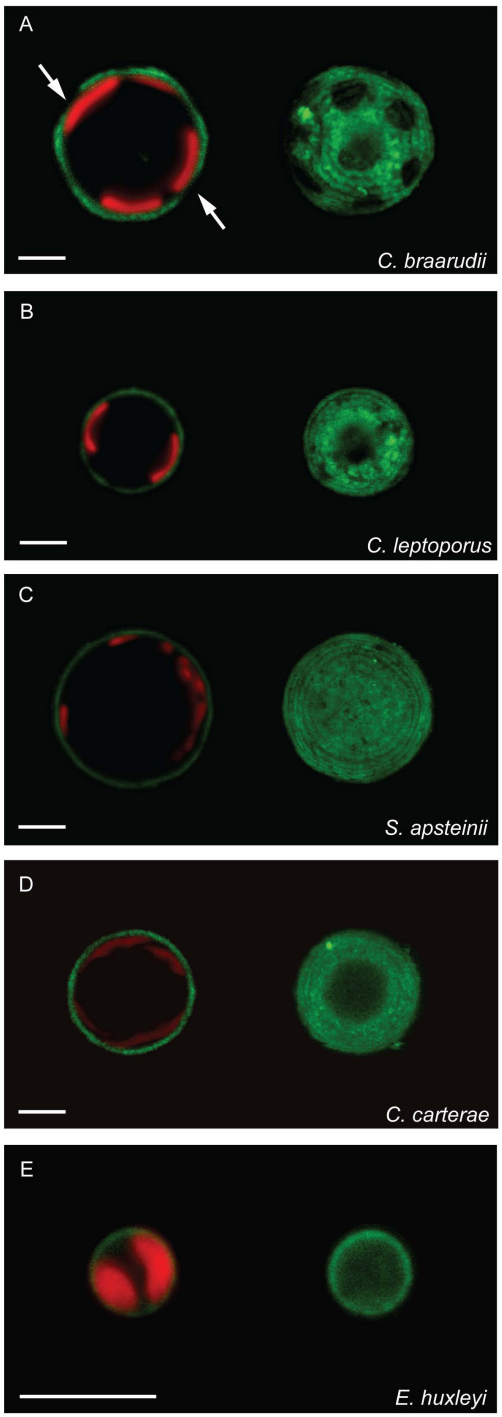

FIGURE 2 | A polysaccharide layer on the cell surface of decalcified coccolithophores. Confocal microscopy imaging of decalcified coccolithophores stained with the fluorescent lectin FITC-ConA (green). Chlorophyll autofluorescence is also shown (red). The staining revealed a layer of polysaccharide on the cell surface of all five species. An individual confocal image (left) and a 3D reconstruction from a Z-stack (right) are shown for each species. **(A)** *C. braarudii* exhibits regular ellipsoidal intervals in the FITC-ConA staining. **(B)** *C. leptoporus* shows some irregularities in the FITC-ConA staining, **(C–E)** all other species have a smooth consistent layer. Scale bars represent 5 μm.

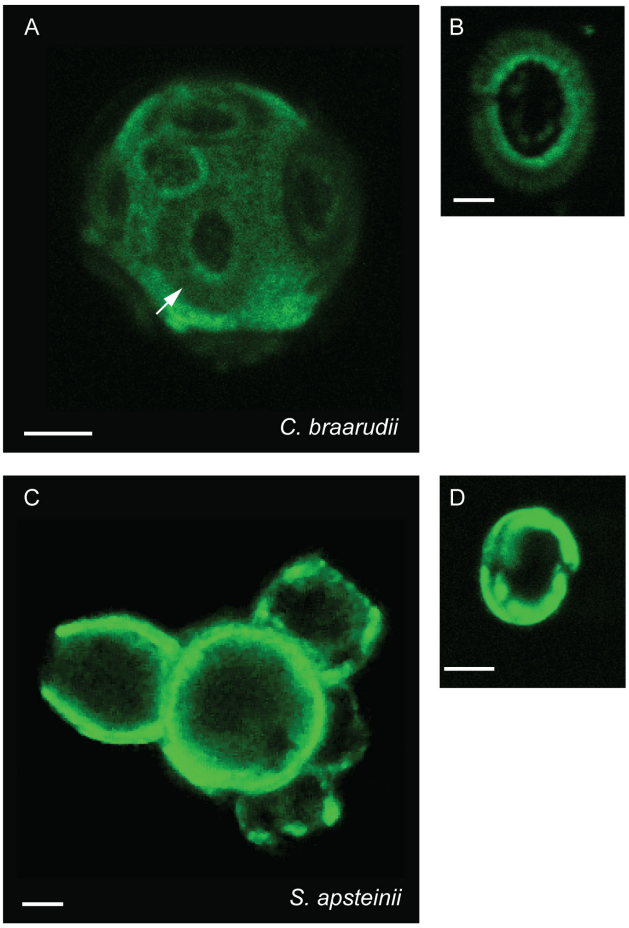

FIGURE 3 | Polysaccharides associated with coccosphere. Confocal microscopy imaging of calcified coccolithophores stained with the lectin FITC-ConA. **(A)** z-stack projection of a calcified *C. braarudii* cell. Distinct coccolith shaped details are apparent (arrowed). **(B)** Discarded coccolith from *C. braarudii*. **(C)** z-Stack projection of a calcified *S. apsteinii* cell showing polysaccharide associated with the coccoliths (arrowed). **(D)** Discarded murolith from *S. apsteinii.* Scale bars represent 5 μm **(A,C)** and 2 μm **(B,D)**.

to coccoliths (**Figure 3A**). To confirm whether this was due in part to a polysaccharide coating on the coccoliths, we imaged discarded *C. braarudii* coccoliths. These were positively stained by FITC-ConA, indicating a coating of polysaccharide (**Figures 1a**, **3B** SEM for comparison). Treatment of discarded coccoliths with sodium hypochlorite to remove organic material prevented fluorescent staining with FITC-ConA, indicating that the lectin staining of the coccolith related to exogenous organic material (**Supplementary Figure 1**). Staining of cells with an alternative fluorophore (Texas Red-ConA) ensured that the fluorescence observed with FITC-ConA was not due to cellular autofluorescence or non-specific binding of FITC. We observed identical staining patterns in cells treated with FITC-ConA and Texas Red-ConA (**Supplementary Figure 2**).

Calcified cells exhibited FITC-ConA staining around the cell body and lopadoliths (**Figure 3C**). The large size

TABLE 1 | Results of polysaccharide lectin staining in coccolithophores.

Species	ConA		WGA	
	Calcified	Decalcified	Calcified	Decalcified
Coccolithus braarudii	✓	✓	×	×
Scyphosphaera apsteinii	✓	✓	✓	✓
Calcidiscus leptoporus	✓	✓	×	×
Chrysotila carterae	✓	✓	×	×
Emiliania huxleyi	✓	✓	×	×

of the lopadoliths in *S. apsteinii* cells enabled very clear imaging of the polysaccharide coating on the coccoliths. Staining of muroliths within the coccosphere was not clear, although imaging of discarded muroliths revealed distinct ConA staining (**Figure 3D**). Our combined observations indicate that extracellular polysaccharides both surround the coccoliths and form an organic layer around the cell in multiple species. It is important to note that the polysaccharides observed in each location are not necessarily identical and could exhibit some degree of biochemical variability. Indeed, the lectins may bind to multiple components within the organic layer surrounding the cell, including amorphous polysaccharide, organic scales and fibrillar material, as all of these components are composed of polysaccharide (Drescher et al., 2012).

Localization of Extracellular Polysaccharides Using Wheat Germ Agglutinin

To further examine the nature of the polysaccharides surrounding the cell and the coccoliths, we stained each species with an additional lectin, WGA, which binds predominately to *N*-acetyl-D-glucosamine and sialic acid residues. Interestingly, FITC-WGA staining was negative in all species except *S. apsteinii* (**Table 1**). Calcified *S. apsteinii* cells stained with WGA revealed a polysaccharide coating on lopadoliths and muroliths, as well as a polysaccharide layer surrounding the cell body (**Figures 4A,B**). In decalcified cells, we observed that extracellular polysaccharide could be observed that retained the shape of lopadoliths (**Figures 4C,D**). It is likely that these polysaccharides were associated with the coccoliths prior to decalcification, either externally and/or within the coccolith (intracoccolith polysaccharide). The observed staining pattern suggests that *S. apsteinii* produces a polysaccharide that also contains *N*-acetyl-D-glucosamine and/or sialic acid residues and therefore differs in composition from those of the other four species.

To identify if the two lectins applied to *S. apsteinii* localized to different regions of the extracellular polysaccharide, we utilized FITC-ConA and Texas Red-WGA simultaneously on the same sample of decalcified cells. We found that both lectins positively stain the cell body (**Figure 5**). In addition, Texas Red-WGA stained polysaccharide left after dissolution of the lopadolith. As the residual polysaccharide was not stained by FITC-ConA, the WGA-positive residues may be found in intracoccolith polysaccharides revealed after decalcification.

Polysaccharide Extraction and Composition

To examine whether the extracellular polysaccharides identified by lectin staining exhibited significant variability in their biochemical composition, we analyzed polysaccharides from each species by gas chromatography mass spectrometry (GC–MS). We reasoned that it would not be possible to easily separate extracellular polysaccharide from intracellular polysaccharides in whole cell fractions. As we had previously determined that discarded coccoliths are coated in ConA-binding polysaccharide (**Figures 3C,D**), we isolated coccolith fractions from each species using density centrifugation through Percoll gradients. FITC-ConA staining after density centrifugation confirmed that coccoliths isolated in this manner retain their polysaccharide coating (**Supplementary Figure 3**). This fraction therefore contains polysaccharides that coat the coccolith, but may also contain polysaccharide components associated with the organic layer around the cell. As the extracellular polysaccharides surrounding coccolithophores are likely to be poorly water-soluble, insoluble polysaccharides were extracted from the coccoliths using 0.1 M EDTA to dissolve calcite and were then washed with 80% ethanol to remove any remaining soluble components.

GC–MS analysis of the monosaccharide residues released by acid hydrolysis of the extracellular polysaccharide fractions recovered from coccoliths revealed distinct differences between species (**Figure 6**). The results are expressed as the percentage of the monosaccharide and uronic acid residues that could be positively identified. It is possible that rare or unusual sugars could also contribute to the total polysaccharide in these extracts that have been not included in our analysis. We also did not attempt to differentiate between isomers and so it is likely that the galactose peak contains D-galactose and L-galactose, as L-galactose residues are common in many algal polysaccharides (Percival, 1970; Fichtinger-Schepman et al., 1979). L-Mannose has also been previously identified in coccolithophore polysaccharides (Fichtinger-Schepman et al., 1979). The GC–MS analysis also did not allow us to determine whether the polysaccharides were sulfated.

The polysaccharide fractions isolated from *C. carterae* were notably lower in xylose (2.6 ± 0.1% SE of total polysaccharide) and rhamnose (1.5 ± 0.1% SE) than the other species (**Figure 6**). Polysaccharides from *S. apsteinii* had higher proportions of xylose (21.7 ± 1.6% SE) but lower proportions of galactose (9.1 ± 2.4% SE). However, the most striking differences were found in the uronic acid content, both glucuronic acid and galacturonic acid. Polysaccharides from *E. huxleyi* and *C. carterae* were relatively high in uronic acids, containing 14.8 ± 2.3% SE and 7.0 ± 2.6% SE respectively. In contrast the uronic acid content of the polysaccharides isolated from *C. braarudii* and *S. apsteinii* were much lower, representing 2.6 ± 1.2 and 0.9 ± 0.4%, respectively of the identified monosaccharide residues.

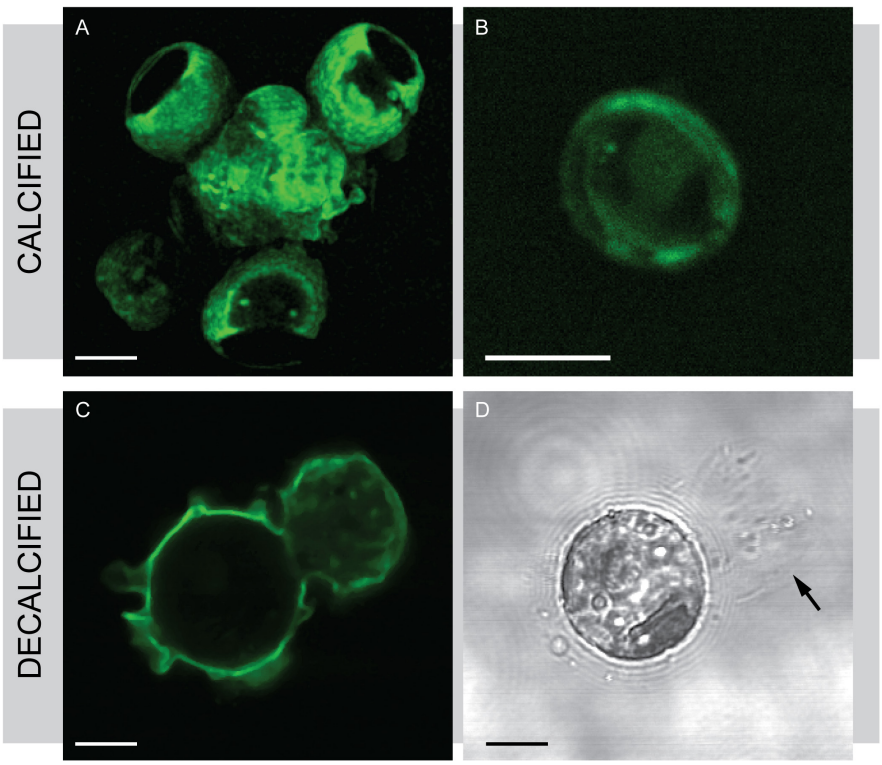

FIGURE 4 | Wheat germ agglutinin (WGA) staining in *S. apsteinii.* Confocal microscopy imaging of FITC-WGA staining in *S. apsteinii*. **(A)** FITC-WGA positively stains lopadoliths, muroliths and an extracellular layer surrounding a fully calcified cell. **(B)** A discarded murolith. **(C)** FITC-WGA staining of a decalcified cell reveals a polysaccharide residue that closely resembles the shape of a lopadolith. **(D)** Transmitted light image corresponding to **(C)**. Residual polysaccharide from a dissolved lopadolith can be seen (arrowed). Scale bars represent 5 μm.

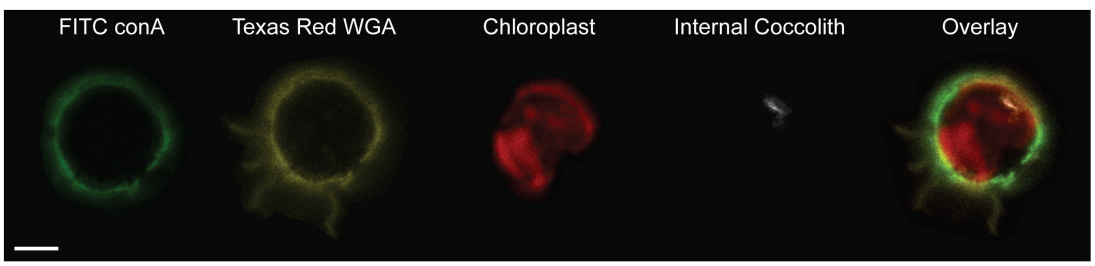

FIGURE 5 | Differential localization of ConA and WGA lectin stains in *S. apsteinii.* Confocal sections of a decalcified *S. apsteinii* cell stained simultaneously with FITC-ConA and Texas Red-WGA. Both lectins localize around the cell body but Texas Red-WGA staining is additionally found on the residual polysaccharides from the dissolved lopadoliths (yellow). Chlorophyll autfluorescence (red) and reflectance of the internal coccolith (white) is also shown. Scale bar represents 5 μm.

Production and Role of Extracellular Polysaccharides in *C. braarudii*

The distinctive morphology of the extracellular polysaccharide observed in decalcified *C. braarudii* cells (**Figure 2A**) led us to examine this in greater detail. As the oval-shaped regions are preserved even after decalcification, it suggests that the polysaccharide-rich organic layer in *C. braarudii* possesses structural properties that may contribute to the organization of the coccosphere. We have previously shown that the non-stained regions in the organic layer are reduced in number or absent when coccolith production is disrupted by treatment with germanium (Ge) (Walker et al., 2018), suggesting that they represent apertures in the polysaccharide layer corresponding to the position of the coccoliths. To test this hypothesis we partially decalcified *C. braarudii* cells so that we could image the position of the coccoliths in the polysaccharide layer. The non-stained regions correspond exactly to the position of the central-area of the coccoliths (i.e., the inner section excluding the shields) (**Figures 7A–C**). It is therefore likely that the positioning of the coccoliths in the polysaccharide-rich organic layer causes the formation of the ellipsoidal apertures in this layer.

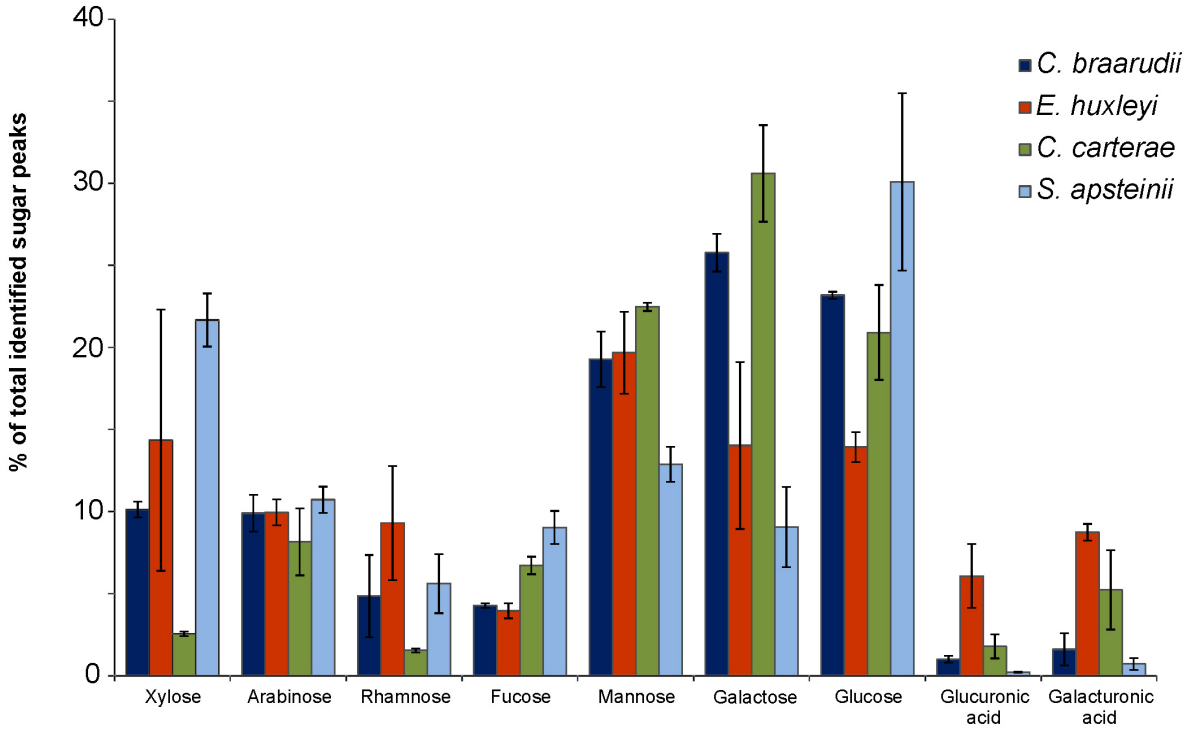

FIGURE 6 | Biochemical composition of coccolith-associated polysaccharides (CAPs). Monosaccharides and uronic acids released by acid hydrolysis of 0.1 M EDTA insoluble polysaccharides extracted from purified coccolith fractions from four coccolithophore species (*C. braarudii, E. huxleyi, C. carterae, S. apsteinii*). Data are presented as the proportion of total identified residues following GC–MS analysis of trimethylsilyl derivatives. $n = 3$. Error bars represent standard errors.

Further imaging of decalcified cells demonstrated that a small proportion of cells have lost the polysaccharide-rich organic layer, presumably due to the experimental manipulations associated with decalcification (**Supplementary Figure 4**). Several cells were observed where the polysaccharide layer was partially detached ($n = 3$), allowing us to confirm that this layer possesses considerable structural integrity even when dissociated from the cell (**Supplementary Figure 4**).

The occurrence of decalcified cells lacking a polysaccharide layer allowed us to examine how this layer was formed during coccolith secretion. When these cells were allowed to re-calcify, we found that the newly produced coccoliths exhibited a localized region of FITC-ConA stained polysaccharide on the underside of the coccolith (**Figures 7D–F**). The data suggests that the insoluble polysaccharide is produced internally and extruded with the coccolith, an observation that correlates with previous polysaccharide studies (van der Wal et al., 1983a,b; Marsh, 1994). The organic layer therefore appears to be formed by the aggregation of polysaccharide-rich material secreted with each coccolith, rather than pre-formed as a complete layer. The close association of the polysaccharide with the underside of the coccolith may indicate that these polysaccharides are involved in adhering the coccoliths to the cell surface, aiding the formation and structure of the complete coccosphere.

Like most phytoplankton cells, the surface area of a coccolithophore cell increases substantially as its volume increases throughout the cell cycle. The cell must therefore continuously produce new coccoliths to ensure that its surface area remains fully covered. This suggests that each new coccolith must be secreted through the existing polysaccharide layer, which must therefore retain a substantial flexibility in order to incorporate this coccolith in to the coccosphere. To determine whether coccoliths were secreted through the organic layer, we imaged coccolith secretion in decalcified cells in which this layer remained intact. The newly-secreted coccoliths were observed external to the organic layer, indicating that they can pass through the layer (**Supplementary Figure 5**). In addition, coccoliths produced in these cells were coated with polysaccharide on both the underside and the topside of the coccolith. We hypothesize that the coccolith is further coated with polysaccharide as it moves through the existing polysaccharide layer on the cell surface.

DISCUSSION

Previous studies have largely focussed on the ability of CAPs to modulate the precipitation of calcite within the CV, with little research conducted on extracellular role of these polysaccharides. Here we show that polysaccharide material is extruded with the coccolith, which coats the coccolith and contributes to an organic layer associated with the coccosphere. The term CAP has been used to describe polysaccharides found in four distinct cellular locations

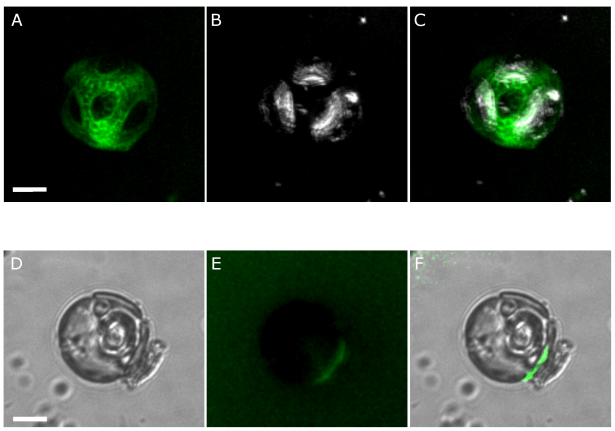

FIGURE 7 | Detailed characterization of the extracellular polysaccharide layer in *C. braarudii*. **(A)** A partially-decalcified *C. braarudii* cell stained with the lectin FITC-ConA (green). A 3D projection generated from a Z-stack is shown. **(B)** The same cell showing the position of three remaining coccoliths (white). **(C)** Merged image indicating that the ellipsoidal intervals in the FITC-ConA staining correspond to the position of the three remaining coccoliths on the cell surface. An additional coccolith corresponding to the central ellipsoid region has become detached. **(D)** Differential interference contrast microscopy image of a recalcifying decalcified *C. braarudii* cell. The position of an internal coccolith and a newly-secreted external coccolith can be seen. **(E)** Epifluorescence image of the same cell stained with FITC-ConA showing a region of polysaccharide at the cell surface corresponding to the position of the coccolith. Note that this cell has lost its external polysaccharide layer. **(F)** Merged image. Scale bars represent 5 μm.

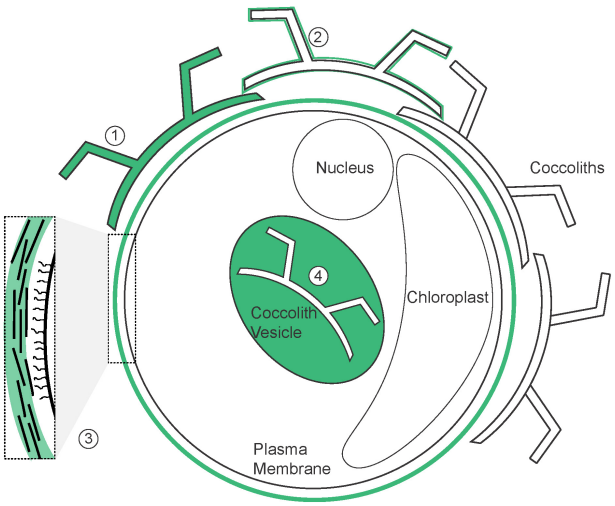

FIGURE 8 | Potential localization of CAPs. Schematic illustration of a coccolithophore cell (based on *C. braarudii*) demonstrating the localization of CAPs identified both in previous research and in this study (highlighted in green). (1) Intracoccolith; (2) coccolith surface; (3) organic layer; (4) coccolith vesicle. Inset shows details of the components of the organic layer; including amorphous polysaccharide (green), organic scales and fibrillar material.

(**Figure 8** and **Supplementary Table 1**). These are intracoccolith polysaccharides, polysaccharides within the CV actively involved in the modulation of calcite precipitation, polysaccharides coating the surface of coccoliths and polysaccharides covering the cell body. Whilst it is likely that there is a degree of overlap in the nature of these polysaccharides (for example, polysaccharides involved in calcite precipitation and those found within the coccolith are likely to be identical), there may be important differences between them and we suggest that it is important to define the localization of the polysaccharide when using the term CAPs.

There is some evidence from *C. carterae* of differentiation of CAPs, even within the CV. Two CAPs (PS1 and PS2) are involved in nucleation of calcite crystal and formation of the protococcolith ring, with the highly acidic PS2 in particular acting as a high capacity Ca^{2+} buffer to modulate nucleation (Marsh, 2003). Further growth of the coccolith requires the presence of a third polysaccharide, the galacturonomannan PS3 (Marsh et al., 2002). PS2 and PS3 contribute directly to calcite nucleation and mutants that do not produce either polysaccharide exhibit significant defects in coccolith formation (Marsh and Dickinson, 1997; Marsh, 2003). The mature coccolith acquires a coating of polysaccharide comprising of PS1 and PS2 prior to secretion, indicating that polysaccharides that contribute to calcite precipitation in *C. carterae* also contribute to the coating on external coccoliths (Marsh, 2003). Thus, the extracellular polysaccharides that we have visualized using fluorescent lectins may also be involved in calcite precipitation. The direct association of fluorescently-labeled polysaccharide with newly secreted coccoliths in *C. braarudii* supports the presence of this polysaccharide in the CV.

Our analyses of the biochemical composition of the polysaccharides extracted from coccoliths indicated that they exhibit some similarities to intracoccolith polysaccharides. Lee et al. (2016) demonstrated that EDTA-soluble intracoccolith polysaccharides derived from *E. huxleyi* had a much higher uronic acid content (up to 60%) than those derived from *C. braarudii* (27%). We found a similar trend in the EDTA-insoluble polysaccharide isolated from coccoliths, although the uronic acids represented a lower proportion of the monosaccharides released by acid hydrolysis. This indicates that there is some overlap in the biochemical nature of these polysaccharides, but more detailed examination will be required to determine whether the polysaccharides present in each fraction are structurally similar.

Our research highlights extracellular roles for CAPs that are additional to their roles in modulation of calcite precipitation. The layer of insoluble polysaccharide found on the exterior of the coccolith likely offers a degree of protection from the environment. A previous study suggests that the organic covering prevents dissolution of the calcite in unfavorable conditions (Henriksen et al., 2004). Recent studies have shown that polysaccharides extracted from coccolith-containing ancient sediments (c. 70 Ma) were still functional in protecting coccoliths from dissolution (Sand et al., 2014). The predicted decrease in the calcite saturation state of future oceans will increase the potential for dissolution of calcite structures (Tyrrell et al., 2008), necessitating the requirement for a better understanding of the protective properties of this organic coating.

In addition to protecting coccoliths from dissolution, extracellular polysaccharide appears to play an important role in the formation and organization of the coccosphere. The lectin staining observed around the cell may reflect binding to multiple polysaccharide-rich components within this layer, such as amorphous polysaccharide, organic scales and fibrillar material. In *C. braarudii,* the polysaccharide material secreted with the coccolith acts to adhere the newly-produced coccolith to the cell surface. Presumably, the continued secretion of multiple coccoliths results in the formation of a complete organic layer around the cell that both ensures the adhesion of the coccoliths to the cell and allows them to be held in position relative to each other. The role of this extracellular organic layer in organizing the coccosphere is clearly visualized in *C. braarudii,* where the polysaccharide material has a defined structure not seen in other species. Apertures in this layer correspond with the position of the coccoliths, allowing the interlocking coccoliths to be held in a single layer around the cell (Walker et al., 2018). Observations from TEM studies indicate that the organic scales are absent from the central regions underlying coccoliths (Taylor et al., 2007). This distribution suggests that organic scales form a major component of the organic layer visualized by FITC-ConA staining. The presence of organic scales in this layer is likely to contribute to its structural rigidity, but still allow sufficient flexibility for coccoliths to be secreted through the layer. *C. braarudii* cells always maintain a complete coccosphere as their cell volume increases, comprising of 8–20 coccoliths in healthy cultures (Gibbs et al., 2013; Durak et al., 2016). The rigidity observed in the organic layer may therefore relate to the need for precise organization of the highly ordered interlocking coccoliths. However, the polysaccharide-rich organic layer around *C. leptoporus* did not exhibit a similar arrangement to *C. braarudii*, which is surprising given the similar nature of the coccospheres in these species ($\sim$15 coccolith cell^{-1}) (Langer et al., 2006; Liu et al., 2010).

The distribution of organic scales in *S. apsteinii* cells is similar to *C. braarudii* in that they are also absent from the areas underlying the coccoliths (Drescher et al., 2012). However, in decalcified *S. apsteinii* cells the polysaccharide material stained by lectins has a smooth appearance, without apertures corresponding to the position of the coccoliths. It may be that the non-interlocking nature of the coccoliths in *S. apsteinii* (both lopadoliths and muroliths) results in a much more fluid arrangement of the coccosphere and so any patterns in the distribution of the organic layer are lost following decalcification. The differential staining of lopadoliths in *S. apsteinii* is also an interesting area for further research as this was the only species included in the study with a dimorphic coccosphere (two coccolith types). The presence of WGA-binding residues within the lopadoliths may relate to unique properties of these CAPs that are associated with the formation or structural maintenance of these much larger coccoliths.

The absence of defined features in the polysaccharide-rich organic layers around *E. huxleyi* and *C. carterae* cells may reflect the less ordered nature of their coccospheres and a greater turnover of coccoliths within these coccospheres. For example, *E. huxleyi* produces between 23 and 36 coccoliths per cell in optimal growing conditions and as many as 20 of these are discarded (Paasche, 1998, 1999, 2001). Organic scales are also absent from *E. huxleyi*, which will likely alter the structural properties of its organic layer considerably. As the arrangement of the coccospheres in these species is less rigid, the organic layer may act primarily to adhere the coccoliths to the cell, rather than hold them in a specific position. The ability of the coccoliths to move flexibly within a layer of polysaccharide is important for the ability of *E. huxleyi* coccospheres to resist a mechanical load, suggesting that the polysaccharide layer contributes directly to the protective role of coccosphere (Jaya et al., 2016).

The diversity in the composition and functional roles of CAPs between species is important when the energetic cost of polysaccharide production is considered. Recent estimates suggest that the single intracoccolith CAPs produced by *E. huxleyi* and *C. braarudii* require 7 and 0.2% of total cellular fixed organic carbon respectively (Monteiro et al., 2016). In contrast, production of multiple CV-associated CAPs in *C. carterae* was calculated to cost of 50% of the total fixed organic carbon, a significantly higher cost of production (Brownlee and Taylor, 2004). The large range of these values reflects different assumptions over the role of CAPs. The former estimates are based primarily on the amounts of intracoccolith CAPs recovered from purified coccoliths, whereas the latter calculation assumes CAPs are involved in the stoichiometric delivery of Ca^{2+} to the CV. Our results clearly indicate that the extracellular polysaccharide components constitute a major additional sink for fixed carbon associated with coccolith production that has so far not been included in these estimates.

In this study we have expanded on the current understanding of CAPs and their role within coccolithophore calcification. CAPs are a group of polysaccharides involved in coccolith precipitation, coccolith adhesion, organization, and protection of the coccosphere. We have visualized extracellular polysaccharide material coating the coccoliths and contributing to the formation of an organic layer around the cell. These differing roles suggest that CAPs likely exhibit significant diversity in function and composition that remains to be fully understood. However, it is imperative that their abundance and role should be taken in to account in considerations of energy budgeting and response of coccolithophores to future ocean conditions.

AUTHOR CONTRIBUTIONS

CW performed all experimental analyses. SH provided additional imaging of extracellular polysaccharides. AT supported SEM analysis. DS and NS contributed to GC–MS analysis of coccolith polysaccharides. GW, CB, and CW designed the study. CW, CB, AT, GL, and GW wrote the manuscript.

FUNDING

The authors acknowledge funding from NERC SPITFIRE DTP studentship to CW. GW and CB acknowledge support

from NERC (NE/N011708/1) and the European Research Council (ERC-ADG 670390). CW was additionally supported by the Gillings Graduate Exchange Programme (University of Southampton/University of North Carolina Wilmington). AT acknowledges NSF support (NSFGEO-NERC-1638838).

SUPPLEMENTARY MATERIAL

The Supplementary Material for this article can be found online at: https://www.frontiersin.org/articles/10.3389/fmars.2018.00306/full#supplementary-material

REFERENCES

Borman, A. H., De Jong, E. W., Huizinga, M., Kok, D. J., Westbroek, P., and Bosch, L. (1982). The role in $CaCO_3$ crystallization of an Acid Ca^{2+}-Binding polysaccharide associated with coccoliths of *Emiliania huxleyi*. *Eur. J. Biochem.* 129, 179–183. doi: 10.1111/j.1432-1033.1982.tb07037.x

Borman, A. H., De Jong, E. W., Thierry, R., Westbroek, P., and Bosch, L. (1987). Coccolith-associated polysaccharides from cells of *Emiliania huxleyi* (Haptophyceae). *J. Phycol.* 23, 118–125. doi: 10.1111/j.1529-8817.1987.tb04433.x

Brownlee, C., and Taylor, A. (2004). "Calcification in coccolithophores: a cellular perspective," in *Coccolithophores: From Molecular Processes to Global Impact*, eds H. Thierstein and J. Young (New York, NY:: Springer), 31–49.

Daniels, C. J., Sheward, R. M., and Poulton, A. J. (2014). Biogeochemical implications of comparative growth rates of *Emiliania huxleyi* and *Coccolithus* species. *Biogeosciences* 11, 6915–6925. doi: 10.5194/bg-11-6915-2014

De Jong, E. W., Bosch, L., and Westbroek, P. (1976). Isolation and characterization of a Ca^{2+} binding polysaccharide associated with Coccoliths of *Emiliania huxleyi* (Lohmann) Kamptner. *Eur. J. Biochem.* 70, 611–621. doi: 10.1111/j.1432-1033.1976.tb11052.x

Drescher, B., Dillaman, R. M., and Taylor, A. R. (2012). Coccolithogenesis in *Scyphosphaera apsteinii* (Prymnesiophyceae). *J. Phycol.* 48, 1343–1361. doi: 10.1111/j.1529-8817.2012.01227.x

Durak, G. M., Taylor, A. R., Walker, C. E., Probert, I., De Vargas, C., Audic, S., et al. (2016). A role for diatom-like silicon transporters in calcifying coccolithophores. *Nat. Commun.* 7:10543. doi: 10.1038/ncomms10543

Engel, A., Delille, B., Jacquet, S., Riebesell, U., Rochelle-Newall, E., Terbruggen, A., et al. (2004). Transparent exopolymer particles and dissolved organic carbon production by *Emiliania huxleyi* exposed to different CO_2 concentrations: a mesocosm experiment. *Aquat. Microb. Ecol.* 34, 93–104. doi: 10.3354/ame034093

Fichtinger-Schepman, A. M. J., Kamerling, J. P., Vliegenthart, J. F. G., Dejong, E. W., Bosch, L., and Westbroek, P. (1979). Composition of a methylated, acidic polysaccharide associated with coccoliths of *Emiliania-huxleyi* (Lohmann) Kamptner. *Carbohydr. Res.* 69, 181–189. doi: 10.1016/S0008-6215(00)85763-8

Gal, A., Wirth, R., Kopka, J., Fratzl, P., Faivre, D., and Scheffel, A. (2016). Macromolecular recognition directs calcium ions to coccolith mineralization sites. *Science* 353, 590–593. doi: 10.1126/science.aaf7889

Gibbs, S. J., Poulton, A. J., Brown, P. R., Daniels, C. J., Hopkins, J., Young, J. R., et al. (2013). Species-specific growth response of coccolithophores to palaeocene–eocene environmental change. *Nat. Geosci.* 6, 218–222. doi: 10.1038/ngeo1719

Guillard, R. R. L., and Ryther, J. H. (1962). Studies of marine planktonic diatoms. *Can. J. Microbiol.* 8, 229–239. doi: 10.1139/m62-029

Harrison, P. J., Waters, R. E., and Taylor, F. (1980). A broad spectrum artificial sea water medium for coastal and open ocean phytoplankton. *J. Phycol.* 16, 28–35. doi: 10.1111/j.1529-8817.1980.tb00724.x

Henriksen, K., and Stipp, S. L. S. (2009). Controlling biomineralization: the effect of solution composition on coccolith polysaccharide functionality. *Cryst. Growth Des.* 9, 2088–2097. doi: 10.1021/cg8004272

Henriksen, K., Young, J., Bown, P., and Stipp, S. (2004). Coccolith biomineralisation studied with atomic force microscopy. *Palaeontology* 47, 725–743.

Hirokawa, Y., Fujiwara, S., and Tsuzuki, M. (2005). Three types of acidic polysaccharides associated with coccolith of *Pleurochrysis haptonemofera*: comparison with *Pleurochrysis carterae* and analysis using fluorescein-isothiocyanate-labeled lectins. *Mar. Biotechnol.* 7, 634–644. doi: 10.1007/s10126-004-5148-9

Jaya, B. N., Hoffmann, R., Kirchlechner, C., Dehm, G., Scheu, C., and Langer, G. (2016). Coccospheres confer mechanical protection: new evidence for an old hypothesis. *Acta Biomater.* 42, 258–264. doi: 10.1016/j.actbio.2016.07.036

Kayano, K., Saruwatari, K., Kogure, T., and Shiraiwa, Y. (2011). Effect of coccolith polysaccharides isolated from the coccolithophorid, *Emiliania huxleyi*, on calcite crystal formation in in vitro $CaCO_3$ crystallization. *Mar. Biotechnol.* 13, 83–92. doi: 10.1007/s10126-010-9272-4

Langer, G., Geisen, M., Baumann, K.-H., Kläs, J., Riebesell, U., Thoms, S., et al. (2006). Species-specific responses of calcifying algae to changing seawater carbonate chemistry. *Geochem. Geophys. Geosyst.* 7:Q09006. doi: 10.1029/2005GC001227

Lee, R. B. Y., Mavridou, D. A. I., Papadakos, G., Mcclelland, H. L. O., and Rickaby, R. E. M. (2016). The uronic acid content of coccolith-associated polysaccharides provides insight into coccolithogenesis and past climate. *Nat. Commun* 7:13144. doi: 10.1038/ncomms13144

Liu, H., Aris-Brosou, S., Probert, I., and De Vargas, C. (2010). A time line of the environmental genetics of the haptophytes. *Mol. Biol. Evol.* 27, 161–176. doi: 10.1093/molbev/msp222

Marsh, M. (1994). Polyanion-mediated mineralization — assembly and reorganization of acidic polysaccharides in the Golgi system of a coccolithophorid alga during mineral deposition. *Protoplasma* 177, 108–122. doi: 10.1007/BF01378985

Marsh, M. E. (2003). Regulation of $CaCO_3$ formation in coccolithophores. *Comp. Biochem. Physiol. B Biochem. Mol. Biol.* 136, 743–754. doi: 10.1016/S1096-4959(03)00180-5

Marsh, M. E., and Dickinson, D. P. (1997). Polyanion-mediated mineralization — mineralization in coccolithophore (*Pleurochrysis carterae*) variants which do not express PS2, the most abundant and acidic mineral-associated polyanion in wild-type cells. *Protoplasma* 199, 9–17. doi: 10.1007/BF02539801

Marsh, M. E., Ridall, A. L., Azadi, P., and Duke, P. J. (2002). Galacturonomannan and Golgi-derived membrane linked to growth and shaping of biogenic calcite. *J. Struct. Biol.* 139, 39–45. doi: 10.1016/S1047-8477(02)00503-8

Monteiro, F. M., Bach, L. T., Brownlee, C., Bown, P., Rickaby, R. E. M., Poulton, A. J., et al. (2016). Why marine phytoplankton calcify. *Sci. Adv.* 2:e1501822. doi: 10.1126/sciadv.1501822

Outka, D. E., and Williams, D. C. (1971). Sequential coccolith morphogenesis in *Hymenomonas-carterae*. *J. Protozool.* 18, 285–297. doi: 10.1111/j.1550-7408.1971.tb03319.x

Paasche, E. (1998). Roles of nitrogen and phosphorus in coccolith formation in *Emiliania huxleyi* (Prymnesiophyceae). *Eur. J. Phycol.* 33, 33–42. doi: 10.1080/09670269810001736513

Paasche, E. (1999). Reduced coccolith calcite production under light-limited growth: a comparative study of three clones of *Emiliania huxleyi* (Prymnesiophyceae). *Phycologia* 38, 508–516. doi: 10.2216/i0031-8884-38-6-508.1

Paasche, E. (2001). A review of the coccolithophorid *Emiliania huxleyi* (Prymnesiophyceae), with particular reference to growth, coccolith formation, and calcification-photosynthesis interactions. *Phycologia* 40, 503–529. doi: 10.2216/i0031-8884-40-6-503.1

Percival, E. (1970). "Algal polysaccharides," in *The Carbohydrates. Chemistry and Biochemistry*, ed. W. Pigman (New York, NY: Academic Press), 537–569.

Pienaar, R. N. (1994). "Ultrastructure and calcification of coccolithophores," in *Coccolithophores*, eds A. Winter and W. G. Siesser (Cambridge: Cambridge University Press), 13–38.

Rost, B., and Riebesell, U. (2004). "Coccolithophores and the biological pump: responses to environmental changes," in *Coccolithophores: From Molecular Process to Global Impact*, eds H. Thierstein and J. Young (Heidelberg: Springer), 99–126.

Sand, K., Pedersen, C., Sjoberg, S., Nielsen, J., Makovicky, E., and Stipp, S. (2014). Biomineralization: long-term effectiveness of polysaccharides on the growth and dissolution of calcite. *Cryst. Growth Des.* 14, 5486–5494. doi: 10.1021/cg5006743

Taylor, A. R., Brownlee, C., and Wheeler, G. (2017). Coccolithophore cell biology: chalking up progress. *Ann. Rev. Mar. Sci.* 9, 283–310. doi: 10.1146/annurev-marine-122414-034032

Taylor, A. R., Russell, M. A., Harper, G. M., Collins, T. F. T., and Brownlee, C. (2007). Dynamics of formation and secretion of heterococcoliths by *Coccolithus pelagicuss* sp.*braarudii*. *Eur. J. Phycol.* 42, 125–136. doi: 10.1080/09670260601159346

Tyrrell, T., Schneider, B., Charalampopoulou, A., and Riebesell, U. (2008). Coccolithophores and calcite saturation state in the Baltic and Black Seas. *Biogeosciences* 5, 485–494. doi: 10.5194/bg-5-485-2008

van der Wal, P., De jong, E. W., Westbroek, P., Debruijn, W. C., and Mulderstapel, A. A. (1983a). Polysaccharide localization, coccolith formation, and golgi dynamics in the coccolithophorid *Hymenomonas carterae*. *J. Ultrastr. Res.* 85, 139–158.

van der Wal, P., De Jong, E. W., Westbroek, P., De Bruijn, W., and Mulder-Stapel, A. (1983b). Ultrastructural polysaccharide localization in calcifying and naked cells of the coccolithophorid *Emiliania huxleyi*. *Protoplasma* 118, 157–168. doi: 10.1007/BF01293073

Walker, C. E., Taylor, A. R., Langer, G., Heath, S., Probert, I., Tyrrell, T., et al. (2018). The requirement for calcification differs between ecologically important coccolithophore species. *New Phytol.* doi: 10.1111/nph.15272

Westbroek, P., Brown, C. W., Bleijswijk, J. V., Brownlee, C., Brummer, G. J., Conte, M., et al. (1993). A model system approach to biological climate forcing. The example of *Emiliania huxleyi*. *Glob. Planet. Chang.* 8, 27–46. doi: 10.1016/0921-8181(93)90061-R

Westbroek, P., De Jong, E., Dam, W., and Bosch, L. (1973). Soluble intracrystalline polysaccharides from coccoliths of *Coccolithus huxleyi* (Lohmann) kamptner (I). *Calcif. Tissue Int.* 12, 227–238. doi: 10.1007/BF02013737

Young, J., Geisen, M., Cros, L., Kleijne, A., Sprengel, C., Probert, I., et al. (2003). A guide to extant coccolithophore taxonomy. *Int. Nannoplankton Assoc.* 1:125.

Young, J. R., Davis, S. A., Bown, P. R., and Mann, S. (1999). Coccolith ultrastructure and biomineralisation. *J. Struct. Biol.* 126, 195–215. doi: 10.1006/jsbi.1999.4132

Young, J. R., and Henriksen, K. (2003). Biomineralization within vesicles: the calcite of coccoliths. *Rev. Mineral. Geochem.* 54, 189–215. doi: 10.2113/0540189

Conflict of Interest Statement: The authors declare that the research was conducted in the absence of any commercial or financial relationships that could be construed as a potential conflict of interest.

frontiers in Marine Science

METHODS
published: 18 September 2018
doi: 10.3389/fmars.2018.00326

Calcein Staining as a Tool to Investigate Coccolithophore Calcification

*Emily Fox, Erin Meyer, Natalie Panasiak and Alison R. Taylor**

Department of Biology and Marine Biology, University of North Carolina, Wilmington, Wilmington, NC, United States

Despite the oceanographic and geological significance of coccolithophores, the cellular mechanisms that underlie the intracellular production and subsequent secretion of their $CaCO_3$ coccoliths remain poorly understood. Tools for labeling coccoliths and coccospheres in order to track their production would be of great value. We therefore evaluated the use of calcein, a derivative of fluorescein, as a method to fluorescently label coccoliths. The calcein method readily labeled pre-existing coccospheres in a range of coccolithophore species, including diploid and haploid life history phases, without compromising the coccolith structure. Calcite staining was verified though epifluorescence and confocal microscopy, and both stained and unstained cells and coccoliths were readily distinguished using flow cytometry. The fluorescence of stained coccoliths was retained for >3 days allowing us to confirm their polar secretion by distinguishing pre-existing coccoliths from the accumulation and distribution of non-fluorescent coccoliths produced after calcein exposure. The calcein treatment had no significant effect on photosynthetic physiology, external calcite morphology, or growth rates of the cells over an 8-day period. The calcein staining method therefore represents a simple non-invasive, non-toxic optical technique to 'tag' calcium carbonate coccoliths and track their production in response to environmental manipulations or pharmacological treatments. Moreover, calcein staining of the coccosphere allowed for heterogenous patterns of calcification, growth, and cell division to be detected in a population of cells. This is the first description of the use of calcein to stain the biomineral structures of calcifying phytoplankton and this approach has the potential to be applied to detailed cytological investigations as well as high-throughput analysis of cultured cells or field populations.

Keywords: coccolithophore, coccolith, calcein, calcification, haptophyte, secretion, flow cytometry, bet hedging

OPEN ACCESS

Edited by:
Alfred Portius Wheeler,
Clemson University, United States

Reviewed by:
Gary H. Dickinson,
The College of New Jersey, United States
Christine Ferrier-Pagès,
Scientific Centre of Monaco, Monaco

***Correspondence:**
Alison R. Taylor
taylora@uncw.edu

Specialty section:
This article was submitted to Marine Molecular Biology and Ecology, a section of the journal Frontiers in Marine Science

Received: *20 April 2018*
Accepted: *24 August 2018*
Published: *18 September 2018*

Citation:
Fox E, Meyer E, Panasiak N and Taylor AR (2018) Calcein Staining as a Tool to Investigate Coccolithophore Calcification. Front. Mar. Sci. 5:326. doi: 10.3389/fmars.2018.00326

INTRODUCTION

Biomineralization in Marine Systems

Coccolithophores are a group of calcifying unicellular marine phytoplankton recognized for production of extracellular calcium carbonate ($CaCO_3$) plates known as coccoliths. Coccolithophores are the most abundant marine calcifying organism in the world's oceans (Taylor A.R. et al., 2017) and dominate annual global pelagic calcification, estimated at around 1.6 ± 0.3 Pg y^{-1} (Balch et al., 2007). They therefore play a significant role in biogeochemical

cycles by removing CO_2 from the atmosphere via photosynthesis, while also contributing to the carbonate counter pump through the use of bicarbonate (HCO_3^-) to produce coccoliths. Coccolithophore calcification plays a critical role in carbon export dynamics (Balch, 2018) as the calcite structures facilitate formation of organic aggregates in marine snow, and ultimately coccolith sedimentation results in calcareous deposits on the ocean floor which gave rise to major chalk formations over geological time-scales (De Vargas et al., 2007). In spite of their global importance, the cellular mechanism by which coccolithophores produce their $CaCO_3$ coccoliths, the regulation of this process, and the coordination of coccolith production with cellular metabolism remain poorly understood. Nevertheless, it is well established that diploid heterococcolith bearing species produce coccoliths formed by complex radial crystal units within the cell before secreting them onto the cell surface where they are integrated into the covering of the cell termed the coccosphere. Coccolithophores exhibit a haplo-diplontic life cycle with motile haploid cells producing calcified scales comprising numerous simple calcite rhombohedra suggesting a distinct calcification mechanism (see Taylor A.R. et al., 2017 and references therein).

The study of coccolithophore calcification has been facilitated by a variety of experimental techniques. For example, flow cytometry has been used for over 20 years to investigate natural populations of coccolithophores (Brussaard et al., 2001; Jacquet et al., 2002; Wilson et al., 2002) and in laboratory studies of single coccolithophore strains (Green et al., 1996). The distinctive side scatter (SSC) signature of the outer coccoliths, a measure of cell surface granularity or roughness, enables coccolithophore populations to be identified, although in mixed populations non-coccolith cell wall structures or granular morphologies may confound interpretation. Polarized light flow cytometry and circularly polarized light microscopy have also been successfully applied to selectively detect coccolithophores and to estimate PIC and individual coccolith mass in selected species (Beaufort, 2005; von Dassow et al., 2012; Fuertes et al., 2014). However, implementation of these methods requires specialized optics. An additional challenge is how to track coccolith production at the single cell level. Thus, we tested a simple non-invasive optical technique to 'tag' the external calcium carbonate produced by live coccolithophore cells with the fluorescent calcium binding dye calcein.

Calcein is a fluorescein-based metallofluorescent indicator (**Figure 1**) that has been used in complexometric determination of Ca^{2+} in solution due to its reversible fluorescence in the bound/unbound form (Markuszewski, 1976). When excited with blue light (of ~488 nm) the calcein-Ca^{2+} complex emits a green fluorescence (~520 nm) with a pH optimum between pH 8–9 (Markuszewski, 1976). Calcein also binds to Ca^{2+} in biominerals, and has been used extensively to label calcified skeletal structures of marine metazoans such as fishes, molluscs, cnidarians, echinoderms, and crustaceans (see **Table 1** for review of literature). However, few studies have utilized calcein to study calcification in protists. One notable exception are the foraminifera, in which calcein serves as a valuable non-toxic probe used to discriminate pre-existing and newly formed calcite chambers, understand various processes associated with shell production, examine ontogenetic variations, facilitate validation of biomineral proxies, and detect meifaunal calcifiers *in situ* (Bernhard et al., 2004, 2015; Bentov et al., 2009; Dissard et al., 2009; Kurtarkar et al., 2015).

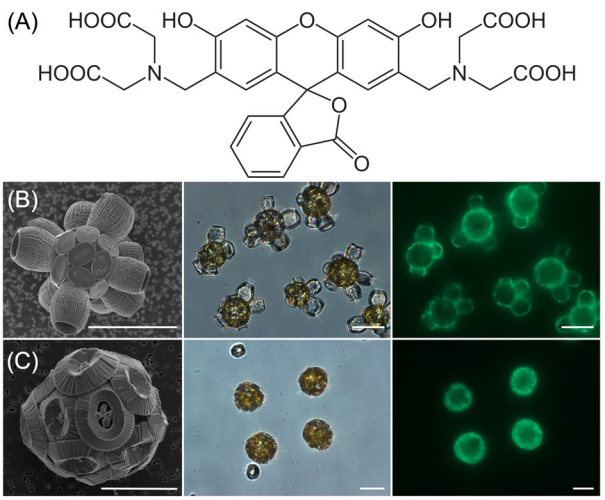

FIGURE 1 | Calcein staining of calcium carbonate coccoliths using epifluorescence. **(A)** The structure of calcein (Bis[*N*,*N*-bis(carboxymethyl)aminomethyl]fluorescein) with four carboxyl groups that coordinate and bind with Ca^{2+} ions, thereby altering fluorescence properties. **(B)** *Scyphosphaera apsteinii*, from left to right; SEM, DIC micrograph and corresponding calcein epifluorescence (FITC filterset) image of cells 24 h after calcein staining and washing protocol. **(C)** *Coccolithus braarudii,* from left to right; SEM, DIC micrograph, and corresponding calcein epifluorescence image of cells 24 h after calcein staining and washing protocol. Scale bars represent 10 μm.

Our goal was to evaluate the effectiveness of calcein staining to fluorescently label coccolithophore calcite and validate its application to calcification studies. The study focused on five species of coccolithophore representing three of the four major coccolithophore groups (Isochrysidales, Coccolithales, and Zygodiscales). In order to validate the calcein method for coccolithophore research we devised several objectives; (1) Develop a calcein staining protocol and verify in five species of coccolithophore, (2) Confirm the calcein staining protocol did not significantly affect coccolith structure, (3) Verify that calcein staining has no short or long-term deleterious effects on live coccolithophore cells, (4) Test the stability of calcein staining over multiple days, (5) Use calcein staining to track coccolith production/calcification, and (6) Evaluate the potential for use in flow cytometry.

MATERIALS AND METHODS

Phytoplankton Culture

Diploid heterococcolithophore strains of *Scyphosphaera apsteinii* (RCC 1456), *Calcidiscus leptoporus* (RCC 1130), *Gephyrocapsa oceanica* (RCC 1303) and haploid holococcolithophore strains of *Coccolithus braarudii* (RCC 3777) and *Syracosphaera pulchra* (RCC 1461) were obtained from the Roscoff Culture Collection,

TABLE 1 | Survey of the use of calcein to investigate biomineral structures in marine organisms.

Phylum	Class	Species	Biomineral structure	Calcein concentration	Immersion incubation	Citation
Foraminifera	Globothalamea	*Ammonia tepida*	Foraminiferal chambers	5 mg L^{-1} [8.0×10^{-6} M]	1 month	Dissard et al., 2009
Foraminifera	Globothalamea	*Ammonia tepida*	Foraminiferal tests, Sediment	10 mg L^{-1} [1.6×10^{-5} M]	7 days	Diz et al., 2012
Foraminifera	Globothalamea	*Amphistegina lobifera*	Seawater vacuoles	12.5 mg L^{-1} [2.0×10^{-5} M]	Various periods, 1 h	Bentov et al., 2009
Foraminifera	Globothalamea	*Rosalina* sp.	Foraminiferal tests, foraminiferal chambers	5–20 mg L^{-1} [$0.8\text{-}3.2 \times 10^{-5}$ M]	16 weeks	Kurtarkar et al., 2015
Foraminifera	Globothalamea Tubothalamea Foraminifera incertae sedis	15 species	Foraminiferal Tests	10 mg L^{-1} [1.6×10^{-5} M]	2–3 weeks	Bernhard et al., 2004
Cnidaria	Anthozoa	*Anemonia viridis Stylophora pistillata*	Skeleton, microcolonies, $CaCO_3$ precipitation	2,000 mg L^{-1} [2.0×10^{-5} M; 3.2×10^{-3} M]	20 min, 2, 4, 6, and 24 h	Tambutte et al., 2012
Cnidaria	Anthozoa	*Corallium rubrum*	Axial calcareous skeleton	10 mg L^{-1} [1.6×10^{-5} M]	24 h	Marschal et al., 2004
Cnidaria	Anthozoa	*Eunicea fusca*	Individual sclerites	50 mg L^{-1} [8.0×10^{-5} M]	5 h	Gómez et al., 2014
Cnidaria	Scyphozoa	*Aurelia aurita*	Statoliths	[5×10^{-5} M; 1×10^{-4} M]	3 days, 6 days	Sotje et al., 2017
Arthropoda	Maxillopoda	*Pollicipes pollicipes*	Capitular plates	200 mg L^{-1} [3.2×10^{-4} M]	20–22 h	Jacinto et al., 2015
Mollusca	Bivalvia	*Anadara broughtonii*	Ark shell	200–300 mg L^{-1} [$3.2\text{–}4.8 \times 10^{-4}$ M]	24 h	Zhou et al., 2016
Mollusca	Bivalvia	*Perna canaliculus* (Larval)	Larval shells	50–200 mg L^{-1} [$0.8\text{–}3.2 \times 10^{-4}$ M]	24 h	Fitzpatrick et al., 2013
Mollusca	Bivalvia	*Perna perna*	Bivalve shells	150–500 mg L^{-1} [$2.4\text{–}8.0 \times 10^{-4}$ M]	4 h	Kaehler and McQuaid (1999)
Brachiopoda	Rhynchonellata	*Calloria inconspicua*	Shell, loop, muscle scars, individual calcite crystals	500 mg L^{-1} [8.0×10^{-4} M]	3–72 h, mostly 24 h; 10 mL/kg body weight injection; added to diet	Rowley and MacKinnon, 1995
Echinodermata	Echinoidea	*Strongylocentrotus franciscanus*	Jaw, test ossicles	125 mg L^{-1} [2.0×10^{-4} M]	24 h	Rogers-Bennett et al., 2003
Echinodermata	Ophiuroidea	*Ophionereis annulata, O. esmarki*	Ossicles	1.25 mg L^{-1} [2.0×10^{-6} M]	24 h	Medeiros-Bergen and Ebert, 1995
Echinodermata		*Paracentrotus lividus*	Larval spicule formation	20 μM	From fertilization to prism or pluteus stage	Vidavsky et al., 2016
Chordata	Ascidiacea	*Pyura pachydermatina*	Body spicules, tunic spicules	500 ppm [8.0×10^{-2} M]	1–4 days	Lambert and Lambert, 1996
Chordata	Actinopterygii	*Hypomesus transpacificus*	Pectoral fins, pelvic fins, caudal fins, jaw, operculum, scales	2.5–5.0 g L^{-1} [$4.0\text{–}8.0 \times 10^{-3}$M]	1–7 min	Castillo et al., 2014
Chordata	Actinopterygii	*Salmo salar* (Larval)	Caudal fin, fin rays, bony structures	125–250 mg L^{-1} [$2.0\text{–}4.0 \times 10^{-4}$ M]	48 h	Mohler, 1997

(Continued)

TABLE 1 | Continued

Phylum	Class	Species	Biomineral structure	Calcein concentration	Immersion incubation	Citation
Chordata	Actinopterygii	*Sander vitreus* (Juvenile)	Fin rays, operculum, ventral jaw surface, dorsal head surface, body scales, otoliths	5 g L^{-1} [8.0 × 10^{-3} M]	4 min	Logsdon and Pittman, 2012
Chordata	Actinopterygii	*Scaphirhynchus platorynchus*	Ventral head portion, pectoral fin girdle, gut region, anal region	0.5% [8.0 × 10^{-3} M]	3.5 min	Honeyfield et al., 2011
Chordata	Actinopterygii	*Spinibarbus sinensis*	Otoliths, cycloid scales, barbs, fin rays, fin spines	50–250 mg L^{-1} [0.8–4.0 × 10^{-4} M]	24 h	Lü et al., 2017
Chordata	Actinopterygii	*Danio rerio* (7 dpf embryo)	Vertebrate column	1.0% [1.6 × 10^{-3} M]	10 min	Chen et al., 2017

France. Heterococcolithophore strains of *Emiliania huxleyi* B92/11 and *Coccolithus braarudii* 182G were obtained from the Plymouth Algal Culture Collection, United Kingdom. All strains were maintained in semi-continuous unialgal batches of 40 mL in disposable polystyrene flasks containing autoclaved and filter-sterilized seawater supplemented with either LH nutrients and silicon (for *S. apsteinii, C. leptoporus, G. oceanica*) or F/2 nutrients (for *E. huxleyi* and *C. braarudii*). Cultures were grown at 16°C in a 14:10 light dark cycle with a light intensity of ∼100 μmol m^{-2} s^{-1} with sub-culturing at mid-late exponential growth phase. For calcein staining, cells were harvested from cultures that were early to mid-exponential phase, as determined by cell counting using either a Sedgwick Rafter chamber or hemocytometer. Under the growth conditions specified above, this was typically 6–8 days for *E. huxleyi* and *G. oceanica*, 8–14 days for *C. leptoporus* and *C. braarudii*, and 10–16 days for *S. apsteinii*.

Calcein Staining

We reviewed pertinent literature in which calcein has been used to mark $CaCO_3$ biominerals (**Table 1**) to determine a suitable staining protocol for single cells. The best staining results were achieved by making a fresh 20 mM stock of calcein (Bis[*N*,*N*-bis(carboxymethyl)aminomethyl]fluorescein, C0875, Sigma-Aldrich, **Figure 1A**) in dry dimethyl sulfoxide (DMSO) immediately prior to each experiment and storing on ice in the dark until needed. For staining, 5 mL aliquots of cells were transferred to a 7 mL polystyrene bijou bottle and allowed to settle, before drawing off the culture media and replacing with 5 mL of F/2 seawater that was buffered with 2 mM HEPEs and adjusted to pH 8.2 with NaOH. Calcein staining was started by adding 50 μL of the 20 mM calcein stock to the 5 mL aliquot of cells in buffered F/2 seawater followed by gentle mixing. This resulted in a final concentration of 0.2 mM calcein with 0.01% DMSO. Use of buffered F/2 was important because addition of 0.2 mM calcein to unbuffered culture media caused a decrease of ∼0.75 pH unit that could affect homeostasis, recalcification, and structure of coccoliths (Taylor et al., 2011). Addition of 0.2 mM calcein to buffered F/2 resulted in drop of <0.2 pH unit. Bijou bottles were replaced in the incubator under normal growth conditions and gently inverted a few times every 15 min to insure cells were resuspended and well mixed during the 2 h calcein staining period. After 2 h incubation, cells were washed at least three times by gentle centrifugation (1,000–3,000 rpm for 1 min), removal of supernatant, and addition of fresh F/2 or LH media depending on the species.

Growth Rate and Physiology

Growth rates were determined after calcein treatment by daily cell counting using a Sedgwick Rafter chamber for the larger species and a hemocytometer for the smaller species. For each replicate culture ($N = 4$), a 1.5 mL aliquot of cells was treated with calcein as described above, or DMSO alone (control). After incubation and washing, the aliquots of cells were placed into 40 mL of fresh media in a culture flask and cell numbers determined at the same time each day over several days (up to 10 days for the slower growing species). A minimum of five grids and 300 cells were

counted for each independent culture replicate. Cell numbers (N) over the days (t) in exponential growth (maximum growth) were used to determine growth rate (r) using the equation:

$$r = \frac{\ln(Nt_2 - Nt_1)}{(t_2 - t_1)}$$

With doublings d^{-1} calculated:

$$k = \frac{r}{0.6931}$$

Photophysiology measurements were also determined after a 2 h calcein treatment (as above) and compared with control cells that had only been treated with DMSO. The quantum yield of photosystem II for dark adapted cells (F_v/F_m) was determined using an Aqua Pen AP-100 (PSI, Drasov, Czechia). An aliquot of cells from each treatment replicate ($N = 4$) was dark adapted at 16°C for 10 min before placing in a spectrophotometry cuvette for F_v/F_m measurements. An average of three measurements (with a 20 s delay between each) was taken for every replicate.

SEM Analysis of Coccolith Structure

For SEM observations, 1.5 mL aliquots of cells were filtered onto 13 mm 0.4 μm isopore filters (Merck Millipore Ltd.) and rinsed with 5 mL of Nanopure water buffered with 1 mM HEPES to pH 8.0 to remove salts without affecting the coccolith calcite. Filters were air-dried, mounted onto an aluminum SEM stub with carbon adhesive tabs before sputter coating with 10 nm Pt/Pd. Samples were imaged using a Phillips XL-FEG SEM in high resolution secondary electron mode with a primary beam acceleration of 5 KeV and spot size 3.

Confocal Imaging

Following staining and washing, the cells were transferred to 35 mm glass coverslip petri dishes and visualized using a Leica SP8 confocal microscope supported by LASX (Leica) application suite for acquisition and analysis. A 488 nm laser was used to excite both calcein and chlorophyll, the emissions of which were collected at 500–520 nm and 650–750 nm, respectively. To minimize photodamage of the chloroplasts and avoid any photobleaching of the calcein stained coccoliths, laser strength was set to ≤3% and photomultiplier voltages were set to 680 and 550 V for calcein and chlorophyll channels, respectively. A pinhole of 1.5 Airy units was used with a high numerical aperture ×40 or ×63 oil immersion lens resulting in a confocal optical thickness of 1.04 and 0.90 μm, respectively. Lower (at the coverslip) and mid optical sections were acquired though each group of cells that were subsequently scored for calcein staining. A look-up table ('glow under-over') was applied in order to determine pixel saturation, and cells were scored as intensely stained when >20% of their calcein signal reached pixel saturation.

Flow Cytometry

A BD FACS Celesta flow cytometer (FC) was used to analyze samples of stained and unstained coccolithophores. A 488 nm excitation laser with a 530 ± 30 nm FITC emission filter (labeled BB515 channel) was used to detect calcein fluorescence and a 695 ± 40 nm PerCP-Cy5.5 filter to detect chlorophyll autofluorescence. An unstained mixed sample of *S. apsteinii* (the largest coccolithophore at ∼25 μm diameter) and *E. huxleyi* (the smallest at ∼4 μm diameter) was run to ensure that the full size range of the species investigated could be detected and adequately discriminated. Mixing of coccolithophore samples by inversion of the sample tube immediately prior to mounting on the cytometer was especially important for the larger heavier species because they can sediment rapidly. Detector settings for SSC, forward scatter (FSC), FITC, and Chl were subsequently set for each species to ensure adequate signal collection over five decades on a logarithmic scale when comparing stained and unstained samples. Each species was calcein labeled for 2 h according to the procedure described above, washed three times by gentle centrifugation and resuspended in fresh culture media before FC analysis. Optimal flow and detector settings were established for stained *E. huxleyi* and *C. braarudii* before running the unstained samples with the same cytometer parameters. Mixtures of stained and unstained cells were also analyzed. No specific gating was applied, but in some cases a low threshold was applied to the FSC to eliminate spurious events due to debris or bacteria. Either 5,000, 10,000, or 20,000 cells were counted for any given experiment. All flow cytometer trials were run on duplicate cultures in two independent experiments yielding reproducible results. FlowJo (Ashland, OR, United States) or Flowing Software version 2.5.1 (Perttu Terho, Turku Centre for Biotechnology) was used for data visualization and construction of dot plots.

RESULTS

Calcein Labeling and Confocal Imaging of Coccolithophores

Calcein staining trials using epi-fluorescence demonstrated the intense staining of coccolith calcite (**Figures 1B,C**) that persisted for 24 h. Examination of stained, washed cells with confocal imaging allowed for increased sensitivity and higher spatial resolution of the fluorescence signal, especially for tracking production of new coccoliths. For each species, 100% of cells were stained using the buffered calcein protocol (**Figure 2**). Stain intensity was generally strong but varied among the population, with a proportion of cells in any given field exhibiting a saturated signal (**Supplementary Figure S1**). Discarded coccoliths or empty coccospheres were also strongly labeled (not shown). Staining of coccoliths was heterogenous as some morphological features of the coccoliths exhibited more intense calcein fluorescence signal (**Figure 3**). Detailed morphological features of the coccoliths were therefore visible in the calcein channel, suggesting preferential staining of specific crystal edges of the coccoliths (**Figure 3**) or where access to Ca^{2+} ions within the biomineral structure was greater. For example, the edges of radial crystals were labeled brightly in *C. leptoporus* and *C. braarudii*. Holococcoliths from haploid phases were also readily labeled by incubation with calcein (**Figure 4**).

In order to validate the calcein labeling method as an approach to study coccolithophore calcification, we first conducted SEM

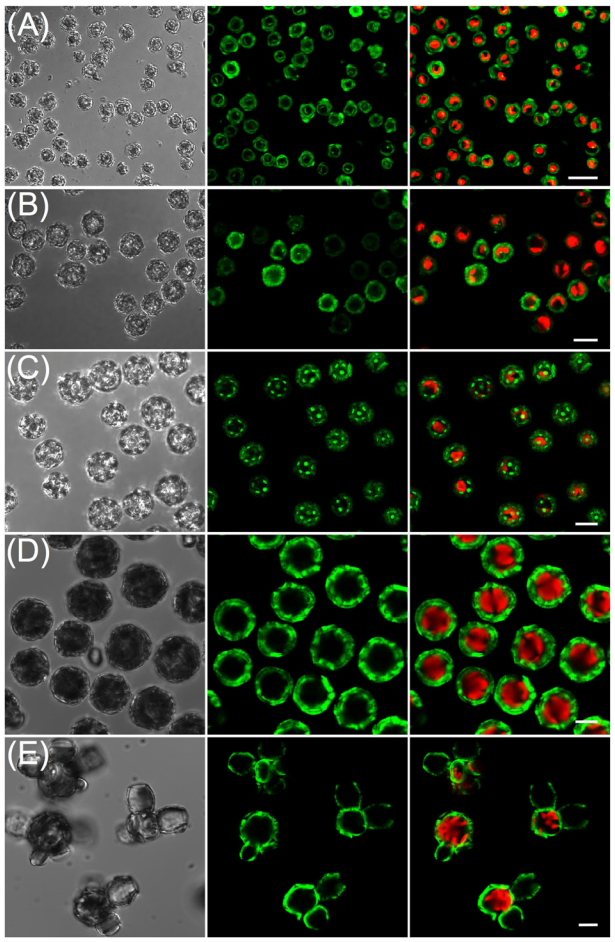

FIGURE 2 | Confocal microscopy of coccolithophore species stained with calcein. Five species of heterococcolithophore cultures were stained for 2 h with 0.2 mM calcein in buffered FSW and then washed before confocal imaging. **(A)** *Emiliania huxleyi*; **(B)** *Gephyrocapsa oceanica*; **(C)** *Calcidiscus leptoporus*; **(D)** *Coccolithus braarudii*; **(E)** *Scyphosphaera apsteinii.* Left panels show cells viewed in differential-phase contrast (DIC), middle panels show the calcein channel, and the right hand panel is the chlorophyll autofluorescence (shown in red) with overlay of calcein fluorescence (shown in green). Scale bars represent 10 μm.

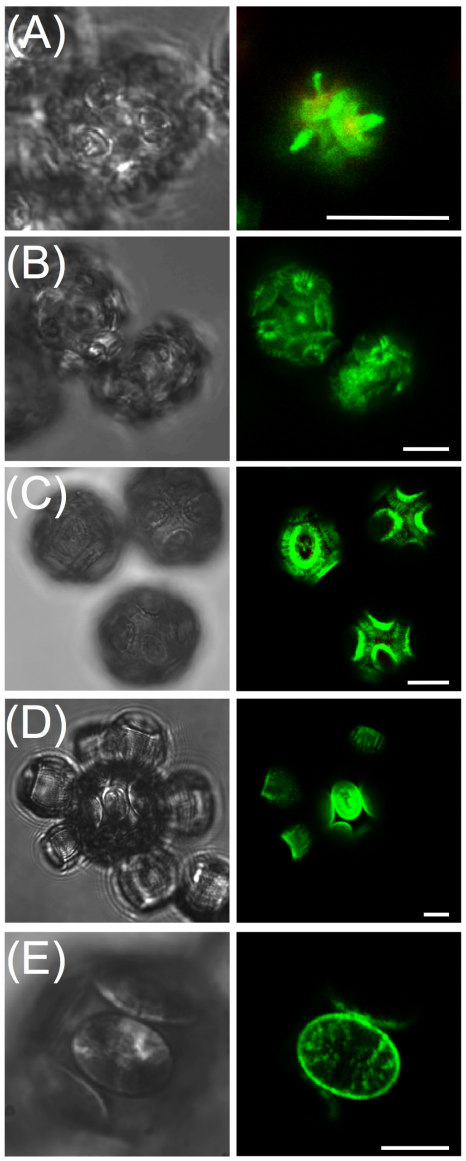

FIGURE 3 | Calcein labeled coccoliths. Confocal sections illustrating the heterogeneous calcein labeling of heterococcoliths. **(A)** *Gephyrocapsa oceanica*; **(B)** *Calcidiscus leptoporus*; **(C)** *Coccolithus braarudii*; **(D)** *Scyphosphaera apsteinii.* **(E)** Detail of a murolith of *S. apsteinii*. Scale bars represent 5 μm.

analysis to examine whether the 2 h calcein treatment affected coccolith structure. No defects were found when the external culture medium was HEPES buffered and adjusted to pH 8.2 prior to addition of the calcein (**Figure 5A**), even though this resulted in a ∼0.2 pH unit drop in the extracellular medium. We also examined whether cells exposed to the dye maintained normal photosynthetic physiology (F_v/F_m) immediately post-labeling and subsequently maintained normal growth rates over an 8-day period (**Figures 5B,C**). No significant differences were observed in quantum yield of photosynthesis following a 2 h calcein staining period ($N = 4$ independent replicates, $p \geqq 0.1$ Student's *t*-test). Similarly, for each species examined, no significant effect on exponential phase growth rate was observed, and dividing cells were frequently observed in cultures that were monitored over several hours (e.g., **Figure 5D**, $N = 3$ independent replicates, $p \geqq 0.4$, Student's *t*-test). Together these data demonstrate a 2 h calcein treatment had no immediate or longer-term detrimental effect on cell division, metabolism, or homeostasis, which is consistent with lack of toxicity that is widely reported in the calcein literature.

Having established the efficacy of the labeling protocol, we tested whether new coccolith production could be tracked by calcein labeling, washing, and tracking coccolith fluorescence over 3 days. Production of new (unlabeled) heterococcoliths was demonstrated for each species (**Figure 6**) which typically exhibited a non-random distribution (e.g., **Figures 6C,D**), with

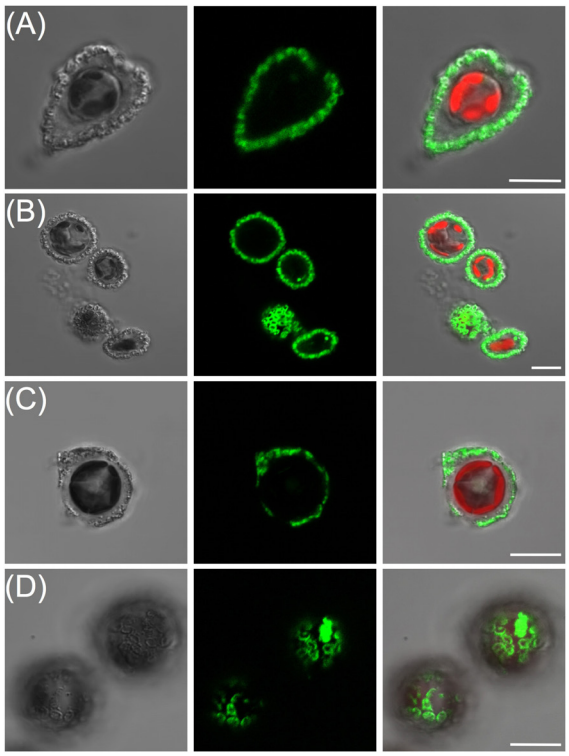

FIGURE 4 | Calcein readily labels holococcolith bearing strains. From left to right panels are DIC, calcein, and overlay of DIC, calcein and chlorophyll. **(A)** *Syracosphaera pulchra* showing brightly labeled holococcoliths associated with the organic layer surrounding the cell. **(B)** Lower confocal section through haploid *S. pulchra* cells showing intense rings of fluorescence corresponding to holococcoliths imaged at the coverslip surface. **(C)** *Coccolithus braarudii* haploid holococcolith stage showing stained holococcoliths and **(D)** lower confocal section closest to the cover-slip showing ring-like pattern of calcein stained holococcoliths. Scale bars represent 10 μm.

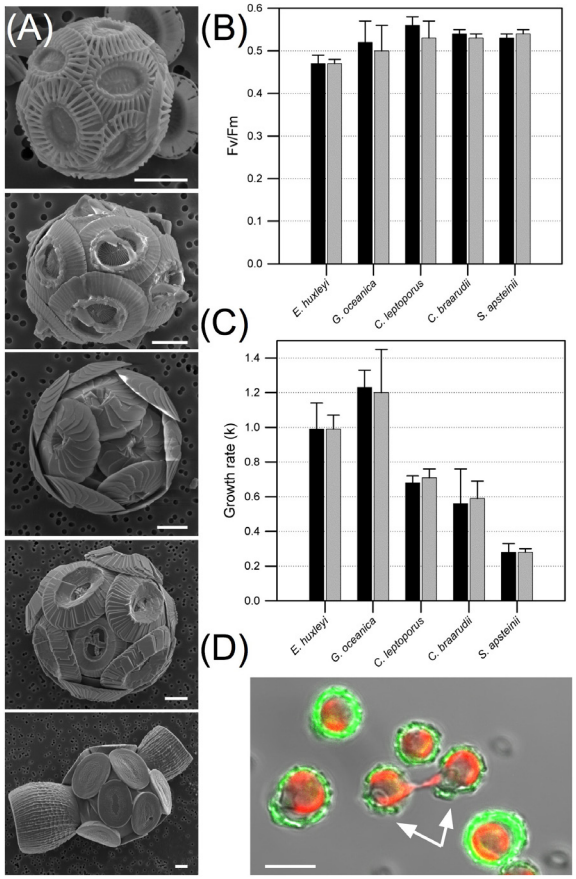

FIGURE 5 | Growth, physiology and coccolith structure are unaffected by calcein treatment. **(A)** Scanning electron micrographs showing representative coccolithophore cells treated for 2 h with calcein in buffered seawater media. Species from top; *Emiliania huxleyi*, *Gephyrocapsa oceanica*, *Coccolithus braarudii, Calcidiscus leptoporus,* and *Scyphosphaera apsteinii*. Scale bars represent 2 μm. **(B)** Quantum yield of photosystem II (F_v/F_m) of dark adapted cells processed for 2 h in the presence (gray bars) and absence (DMSO only, black bars) of calcein ($N = 4$ independent replicates for each species ± SD, no significant differences with *t*-test, $p \geqq 0.1$). **(C)** Growth rates (k) of coccolithophores determined over 8 days post-calcein staining (gray bars) compared to 2 h treatment with DMSO solvent alone (black bars; $N = 3$ independent replicates for each species ± SD, no significant differences with *t*-test, $p \geqq 0.4$). **(D)** Dividing *E. huxleyi* cells (indicated with white arrows) 8 h after calcein labeling. Scale bar represents 5 μm.

new coccoliths integrated into the coccosphere in the same region. Calcein labeling also proved a useful tool to detect metabolically quiescent cells in a population of coccolithophores (**Figure 7**). In the case of cells harvested from an early exponential phase *E. huxleyi* culture, the majority of cells examined after 10 h incubation in the light had produced multiple new unstained coccoliths (**Figure 7A**). However, in populations from a late exponential to stationary phase culture, a subset of cells continued to calcify and divide by 12 h post-staining while the rest of the population remained quiescent, as evidenced by cells with intact and completely stained coccospheres (i.e., no new coccoliths produced and no cell division). The same batch of cells sampled 40 h post staining showed the majority of cells had resumed calcification with a few retaining mostly stained coccoliths showing they were yet to fully resume calcification and cell division.

Calcein Analysis Using Flow Cytometry

The potential application of the calcein method to high throughput modes of detection was examined with flow cytometry. First, a mixed population of unstained *S. apsteinii* and *E. huxleyi* were analyzed in the flow cytometer to establish suitable detector settings and ensure that the full size range of species were amenable to detection and quantification (**Supplementary Figure S2**). FSC (proxy for particle size) and SSC (granularity/roughness) signals were lower for *E. huxleyi* than *S. apsteinii,* as expected based on their very different size and coccolith morphology (**Figure 5A**). Next, stained and unstained samples of *E. huxleyi* (**Figure 8**) and the much larger *C. braarudii* (**Figure 9**) were analyzed. For each species, unstained and stained cells and detached coccoliths were clearly discriminated in the BB515 channel (calcein green fluorescence) but were no different in the PerCp-Cy5 (chlorophyll) channel. A background

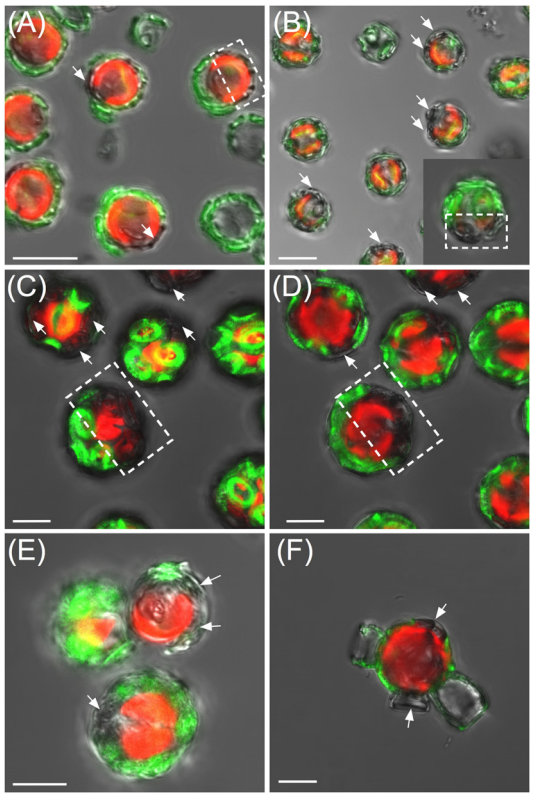

FIGURE 6 | Tracking of heterococcolith production using calcein. **(A)** *Emiliania huxleyi* 10 h post-staining showing cells that have secreted several new coccoliths, examples highlighted with arrows. In some cells, a clear polarity was observed in the position of the newly synthesized coccoliths (unstained, highlighted by dotted box). **(B)** *Gephyrocapsa oceanica* 10 h post-staining. **(C)** *Coccolithus braarudii* 24 h post-staining. **(D)** Mid-section of the same *Coccolithus braarudii* cells in **(C)**. **(E)** *Calcidiscus leptoporus* 18 h post-staining. **(F)** *Scyphosphaera apsteinii* 24 h post-staining. Fluorescence was retained for individual coccoliths for at least 72 h, although overall fluorescence per cell diminished as new coccoliths were produced and cells divided. Scale bars represent 5 μm.

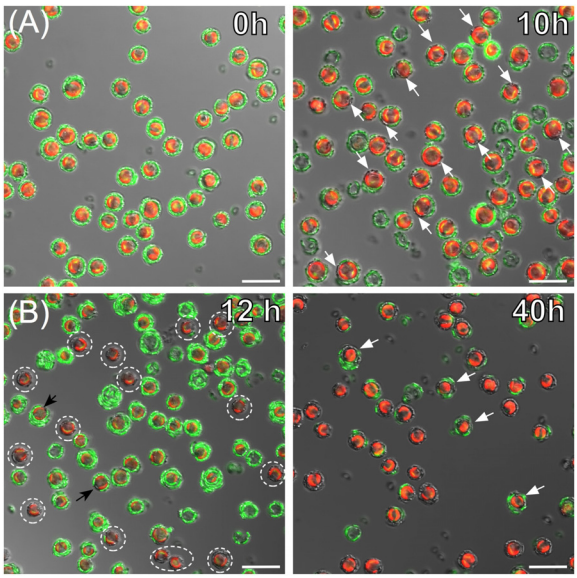

FIGURE 7 | Visualizing growth dynamics and calcification in exponential and stationary cultures of *Emiliania huxleyi.* **(A)** DIC, calcein (green), and chlorophyll (red) confocal overlay images of cells from an early exponential phase culture immediately after calcein staining (0 h left panel) and 10 h post-staining (right panel). By 10 h, the majority of cells have secreted new unstained coccoliths (examples indicated with white arrows). **(B)** Cells from a stationary phase culture after 12 h post-calcein staining in fresh nutrient replete media (left), and after 40 h in nutrient replete media (right). At 12 h a sub-set of cells (dotted circles) have calcified and are actively dividing among a population of cells that appear metabolically inactive as evidenced by intact, stained coccospheres. After 40 h in nutrient replete conditions all cells have resumed calcification and cell division which is supported by coccospheres with none or just 1–2 fluorescent coccoliths. A few cells (white arrows) still have the majority of their coccoliths labeled with calcein, suggesting a recent resumption of calcification compared to the majority of cells.

green fluorescence signal was detected for unstained cells in the calcein channel, which likely reflects a degree of cross-talk with plastid autofluorescence. This could be eliminated with a bespoke emission filter and/or application of compensation protocols.

To further support the efficacy of calcein staining at the population level, we tracked a population of early exponential *E. huxleyi* cells post-calcein staining with flow cytometry (**Figure 10**). As predicted from analysis with confocal imaging, a shift in the calcein signal of the population toward an 'unstained' signature was detected within a few hours after staining (**Supplementary Figure S3**).

DISCUSSION

Staining Method and Confocal Analysis

We examined the utility of calcein as a non-toxic marker for coccolithophore calcification and established that this fluorescent probe is suitable for labeling of both hetero- and holococcoliths across a range of species. Staining in buffered media between pH 7.7–8.0 had no effect on coccolith structure. Calcein treatment also had no effect on coccolithophore viability, which is consistent with multiple studies on fishes, corals, bivalves, gastropods, and foraminifera (e.g., Moran, 2000; Frenkel et al., 2002; Fitzpatrick et al., 2013; Holcomb et al., 2013; Kurtarkar et al., 2015). Although calcein has been reported to be stable in buffered seawater and can be reused (Rowley and MacKinnon, 1995), we found the most consistent coccolith calcite staining was achieved when using freshly made stock solutions and dilutions. Once stained, calcein labeled coccoliths could be detected in the coccosphere surrounding the cell for at least 3 days and likely over longer periods, although this was not examined because of the relatively fast growth and cell division rates of these algae. It is possible that some photobleaching of the calcein bound to coccolith calcite could occur over several day's growth in high light, although this was not examined. However, it should be noted that calcein marked biominerals of fishes, invertebrates, and foraminifera have been tracked for extended periods, with calcein fluorescence detected after several weeks and even months (see **Table 1** and references therein).

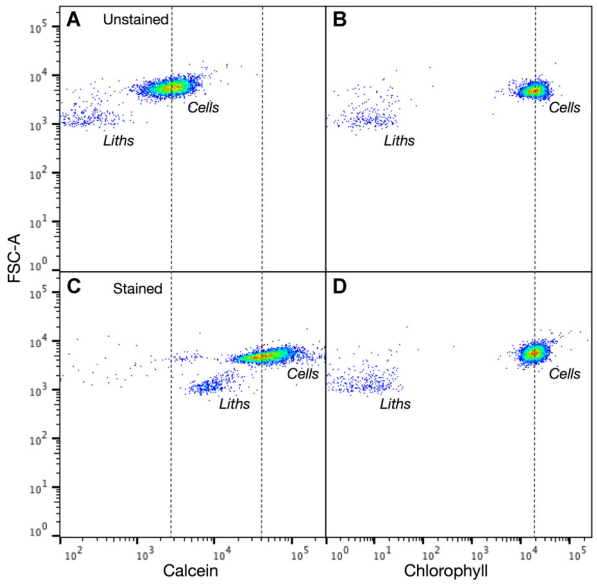

FIGURE 8 | Calcein labeled and unlabeled *Emiliania huxleyi* cells are readily detected using flow cytometry. Intensity dot plots of **(A)** calcein and **(B)** chlorophyll signals vs. forward scatter (FSC-A) for unstained *E. huxleyi* cells. **(C,D)** Intensity dot plots of calcein and chlorophyll channels for cells after 2 h staining with calcein. Both cells and detached coccoliths are readily identified in each channel. For chlorophyll there is no change in the distribution of unstained and stained cells or coccoliths (dotted line for reference). The stained and unstained populations of cells and coccoliths are clearly distinguished in the calcein channel (dotted lines for reference). 5,000 events counted.

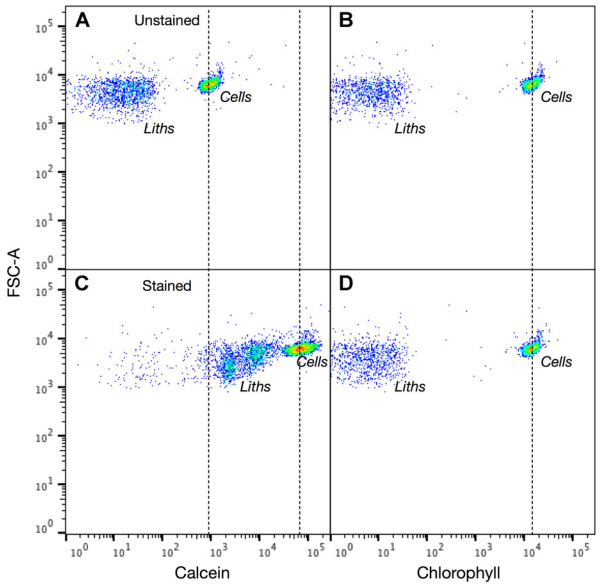

FIGURE 9 | Calcein labeled and unlabeled *Coccolithus braarudii* cells are readily detected using flow cytometry. Intensity dot plots of **(A)** calcein and **(B)** chlorophyll signals vs. forward scatter (FSC-A) for unstained *C. braarudii* cells. **(C,D)** Intensity dot plots of calcein and chlorophyll channels for cells after 2 h staining with calcein. Both cells and detached coccoliths are readily identified in each channel. For chlorophyll there is no change in the distribution of unstained and stained cells or coccoliths (dotted line for reference). The stained and unstained populations of cells and coccoliths are clearly distinguished in the calcein channel (dotted lines for reference). 5,000 events counted.

The pattern of calcein staining of coccoliths was heterogeneous with bright fluorescence associated with specific structures or crystal surfaces. Unlike live coral microcolonies (Tambutte et al., 2012) or foraminifera (Bernhard et al., 2004), calcein is not incorporated into the coccolith calcite structure during intracellular precipitation. Rather, calcein interacts with the surface of pre-existing secreted coccoliths. The specific crystal face, presence of coccolith associated organic material, and boundary layer pH will all affect binding and fluorescence of calcein.

We considered the possibility of labeling internal coccoliths with Calcein-AM which is an uncharged acetoxymethyl ester of calcein that is cell permeable and becomes internalized and Ca^{2+} sensitive when acted upon by cellular esterases. However, Sviben et al. (2016) used calcein-AM to identify an intracellular Ca and P rich vacuole-like compartment in *E. huxleyi* that was distinct from the coccolith vesicle. In a preliminary study, we also found internalization and staining of non-coccolith compartments using the calcein-AM probe (data not shown) and deemed it unsuitable for further analysis.

Tracking Calcification, Polar Secretion, and Patterns of Cell Growth

By monitoring newly synthesized (and unstained) coccoliths, we were able to confirm the polar secretion of coccoliths which appear clustered at the apical pole of the coccolithophore cell, which was especially apparent in *C. braarudii* (**Figure 6**). This approach will be valuable in monitoring calcification at the single cell level over a wide range of species and in response to environmental variables and treatments that may influence the calcification machinery. Additionally, calcein labeling of holococcoliths should provide critical insights into the biomineralization of these organic scales decorated with clusters of minute (∼100 nm) calcite rhombohedra. In contrast to heterococcoliths, little is known about mechanisms and dynamics of holococcolith production, although it has been proposed to occur in an extracellular compartment (Rowson et al., 1986).

A further valuable discovery arising from our assessment was that calcein labeling of the whole coccosphere allows for detection of viable but non-dividing cells versus actively calcifying and growing cells among a coccolithophore population. For example, a subpopulation of cells in stationary phase cultures of *E. huxleyi* produced new coccoliths and underwent cell division over 12 h after calcein staining and sub-culturing into fresh media. The remaining cells were not actively calcifying over this period, as evidenced by coccospheres in which all coccoliths were fluorescing. After 40 h, all cells had resumed calcification, and presumably growth, at least to some degree (**Figure 7**). Growth resumption from stationary phase cultures has been studied extensively in microbes where a resource 'bet-hedging' strategy has been proposed to function in which sub populations of

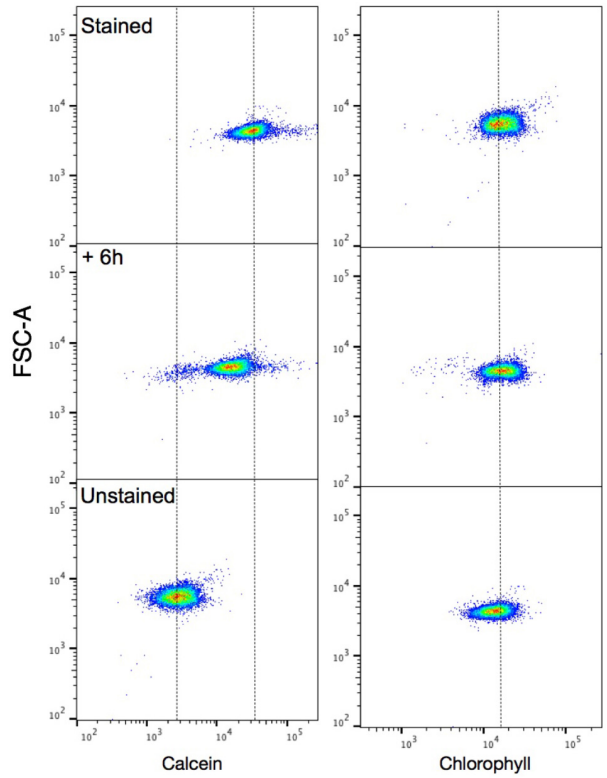

FIGURE 10 | Tracking of calcification in *Emiliania huxleyi* using flow cytometry. Intensity dot plots of calcein **(Left)** and chlorophyll **(Right)** signals vs. forward scatter (FSC-A) for stained *E. huxleyi* cells. From top; stained, +6 h, and unstained cells showing a shift in the +6 h population toward an unstained signature. 10,000 events were collected and a threshold on the chlorophyll channel was used to exclude collection of detached coccoliths. Dotted lines are used for reference on each channel.

cells rapidly resume growth in response to newly available carbon, while others remain quiescent (Grimbergen et al., 2015; Martins and Locke, 2015; Bergkessel et al., 2016). The heterogeneous resumption of growth insures whole population viability when resources for growth may only be transiently available over temporal or spatial scales (Lidstrom and Konopka, 2010). Given the dynamic and unpredictable environment that phytoplankton experience, it is likely that heterogenous growth phenotypes exist among their isogenic populations, as has been determined in *Chlamydomonas* (Damodaran et al., 2015). The identification of cells in different metabolic (using calcein) and cell-cycle states (e.g., combining with DNA staining) has the potential to advance our understanding of the role that growth arrest and metabolic heterogeneity plays in coccolithophore population dynamics. Moreover this can be implemented with high-throughput approaches (below), and could be amenable to single-cell omics (Martinez Martinez et al., 2011) and single cell metabolic profiling (Taylor G.T. et al., 2017).

Flow Cytometry

High throughput methods of determining coccolithophore abundance include well established SSC, FSC, and pigment analysis of mixed populations (Tarran et al., 2001; Zubkov and Burkill, 2006) with specificity improved by analysing the forward scattering depolarization of the incident laser which allows for the degree of calcification to be estimated (von Dassow et al., 2012). In this study, an unstained mixed coccolithophore population was readily separated into two populations based on SSC and FSC signal. This confirmed that even relatively large complex coccolithophores such as *S. apsteinii* are amenable to flow cytometer analysis, although rapid sedimentation of these larger heavy cells needs to be taken into consideration. Calcein stained and unstained *E. huxleyi* and *C. braarudii* were easily distinguished in either separate or combined populations. We also demonstrated the ability to optically label coccoliths and monitor calcification using high throughput flow cytometry. Calcein labeling could therefore be applied to environmental or field samples using flow cytometry to distinguish calcified cells and discarded coccoliths from other similarly sized particles. Calcein could also be used to detect calcified structures using high throughput 3D fluorescence imaging that was recently developed for rapid morphological profiling and taxonomic classification of marine microbial eukaryotes (Colin et al., 2017).

CONCLUDING REMARKS

Calcein labeling has been used extensively as a non-toxic fluorescent marker in order to investigate biomineralization of calcified structures in a wide range of marine organisms. Remarkably, its application to coccolithophore calcification has not been previously reported. Here, we successfully addressed our main objectives to validate the use of calcein to label the extracellular coccosphere and follow new production of coccoliths over multiple days in cells of several coccolithophore species using fluorescence and confocal fluorescence microscopy. We also demonstrated the usefulness of calcein labeling for high throughput analysis of coccolithophore populations using flow cytometry. The ability to simultaneously mark batches of cells could also be a valuable tool with which to examine metabolic heterogeneity.

AUTHOR CONTRIBUTIONS

AT conceived the study, collected the data, supervised the experiments, analyzed the data, and wrote the paper. EF conducted confocal imaging, growth and physiology experiments, analyzed the data, and edited the paper. EM conducted SEM, growth and physiology experiments, and edited the paper. NP conducted preliminary proof of concept experiments and analyzed the literature.

FUNDING

AT acknowledges financial support from the NSF (NSFGEO-NERC 1638838) and a UNCW Summer Undergraduate Research and Creativity Award. NP acknowledges support through a NOAA Hollings Undergraduate Scholarship.

ACKNOWLEDGMENTS

We thank Katie Valentine and Kelsey Billet for preliminary technical assistance. We acknowledge the Richard M. Dillaman Biological Imaging Facility at UNCW.

SUPPLEMENTARY MATERIAL

The Supplementary Material for this article can be found online at: https://www.frontiersin.org/articles/10.3389/fmars.2018.00326/full#supplementary-material

FIGURE S1 | Heterogeneous calcein staining among cells. The graph illustrates that in each species a proportion of cells exhibit a saturating signal in the calcein channel, suggesting more calcein is bound to calcite in these coccospheres, or the local boundary layer chemistry may be sufficiently different in these cells to cause higher fluorescence emission.

FIGURE S2 | Flow cytometry of coccoliths. Forward scatter (FSC, proxy for cell size) versus side scatter (granularity), chlorophyll, and calcein for a mixed population of unstained *E. huxleyi* (94%) cells and *S. apsteinii* (~6%) cells. The side scatter signal is characteristic of coccolithophores due to their calcite coccosphere. The two very different sized coccolithophore species were readily distinguished. The signal in the calcein channel for each species is likely due to autofluorescence of photopigments that are not excluded by the FITC filterset.

FIGURE S3 | Flow cytometry of a mixed population of *E. huxleyi*. Forward scatter (FSC, proxy for cell size) versus side scatter (granularity), chlorophyll, and calcein for a mixed population of unstained (46.6% of events) and unstained (38.1% of events) *E. huxleyi* cells. The mixed sample is described by a single population in the SSC and chlorophyll plots, whereas discrete populations of stained and unstained cells are detected in the calcein plot.

REFERENCES

Balch, W., Drapeau, D., Bowler, B., and Booth, E. (2007). Prediction of pelagic calcification rates using satellite measurements. *Deep Sea Res. Part II Top. Stud. Oceanogr.* 54, 478–495. doi: 10.1016/j.dsr2.2006.12.006

Balch, W. M. (2018). The ecology, biogeochemistry, and optical properties of coccolithophores. *Annu. Rev. Mar. Sci.* 10, 71–98. doi: 10.1146/annurev

Beaufort, L. (2005). Weight estimates of coccoliths using the optical properties (birefringence) of calcite. *Micropalentology* 51, 289–297. doi: 10.2113/gsmicropal.51.4.289

Bentov, S., Brownlee, C., and Erez, J. (2009). The role of seawater endocytosis in the biomineralization process in calcareous foraminifera. *Proc. Natl. Acad. Sci. U.S.A.* 106, 21500–21504. doi: 10.1073/pnas.0906636106

Bergkessel, M., Basta, D. W., and Newman, D. K. (2016). The physiology of growth arrest: uniting molecular and environmental microbiology. *Nat. Rev. Microbiol.* 14, 549–562. doi: 10.1038/nrmicro.2016.107

Bernhard, J. M., Blanks, J. K., Hintz, C. J., and Chandler, G. T. (2004). Use of the fluorescent calcite marker calcein to label foraminiferal tests. *J. Foraminifer. Res.* 34, 96–101. doi: 10.2113/0340096

Bernhard, J. M., Phalen, W. G., McIntyre-Wressnig, A., Mezzo, F., Wit, J. C., Jeglinski, M., et al. (2015). Technical note: towards resolving in situ, centimeter-scale location and timing of biomineralization in calcareous meiobenthos - the calcein-osmotic pump method. *Biogeosciences* 12, 5515–5522. doi: 10.5194/bg-12-5515-2015

Brussaard, C. P. D., Marie, D., Thyrhaug, R., and Bratbak, G. (2001). Flow cytometric analysis of phytoplankton viability following viral infection. *Aquat. Microb. Ecol.* 26, 157–166. doi: 10.3354/ame026157

Castillo, G., Morinaka, J., Fujimura, R., DuBois, J., Baskerville-Bridges, B., Lindberg, J., et al. (2014). Evaluation of calcein and photonic marking for cultured delta smelt. *N. Am. J. Fish. Manag.* 34, 30–38. doi: 10.1080/02755947.2013.839970

Chen, Y., Zhou, J. L., Cheng, L., Zheng, Y. Y., and Xu, J. (2017). Sediment and salinity effects on the bioaccumulation of sulfamethoxazole in zebrafish (*Danio rerio*). *Chemosphere* 180, 467–475. doi: 10.1016/j.chemosphere.2017.04.055

Colin, S., Coelho, L. P., Sunagawa, S., Bowler, C., Karsenti, E., Bork, P., et al. (2017). Quantitative 3D-imaging for cell biology and ecology of environmental microbial eukaryotes. *eLife* 6:e26066. doi: 10.7554/eLife.26066

Damodaran, S. P., Eberhard, S., Boitard, L., Rodriguez, J. G., Wang, Y., Bremond, N., et al. (2015). A millifluidic study of cell-to-cell heterogeneity in growth-rate and cell-division capability in populations of isogenic cells of *Chlamydomonas reinhardtii*. *PLOS One* 10:e0118987. doi: 10.1371/journal.pone.0118987

De Vargas, C., Aubry, M.-P., Probert, I., and Young, J. R. (2007). "Origin and evolution of coccolithophores: from coastal hunters to oceanic farmers," in *The Evolution of Aquatic Photoautotrophs*, eds P. G. Falkowski and A. H. Knoll (New York, NY: Academic Press).

Dissard, D., Nehrke, G., Reichart, G. J., Nouet, J., and Bijma, J. (2009). Effect of the fluorescent indicator calcein on Mg and Sr incorporation into foraminiferal calcite. *Geochem. Geophys. Geosyst.* 10:Q11001. doi: 10.1029/2009gc002417

Diz, P., Barras, C., Geslin, E., Reichart, G.-J., Metzger, E., Jorissen, F., et al. (2012). Incorporation of Mg and Sr and oxygen and carbon stable isotope fractionation in cultured *Ammonia tepida*. *Mar. Micropaleontol.* 9, 16–28. doi: 10.1016/j.marmicro.2012.04.006

Fitzpatrick, M. P., Jeffs, A. G., and Dunphy, B. J. (2013). Efficacy of calcein as a chemical marker of green-lipped mussel (*Perna canaliculus*) larvae and its potential use for tracking larval dispersal. *Aquac. Res.* 44, 345–353. doi: 10.1111/j.1365-2109.2011.03034.x

Frenkel, V., Kindschi, G., and Zohar, Y. (2002). Noninvasive, mass marking of fish by immersion in calcein: evaluation of fish size and ultrasound exposure on mark endurance. *Aquaculture* 214, 169–183. doi: 10.1016/S0044-8486(02)00135-7

Fuertes, M. -Á, Flores, J.-A., and Sierro, F. J. (2014). The use of circularly polarized light for biometry, identification and estimation of mass of coccoliths. *Mar. Micropaleontol.* 113, 44–55. doi: 10.1016/j.marmicro.2014.08.007

Gómez, C. E., Paul, V. J., Ritson-Williams, R., Muehllehner, N., Langdon, C., and Sánchez, J. A. (2014). Responses of the tropical gorgonian coral Eunicea fusca to ocean acidification conditions. *Coral Reefs* 34, 451–460. doi: 10.1007/s00338-014-1241-3

Green, J. C., Course, P. A., and Tarran, G. A. (1996). The life-cycle of *Emiliania huxleyi*: a brief review and a study of relative ploidy levels analysed by flow cytometry. *J. Mar. Syst.* 9, 33–44. doi: 10.1016/0924-7963(96)00014-0

Grimbergen, A. J., Siebring, J., Solopova, A., and Kuipers, O. P. (2015). Microbial bet-hedging: the power of being different. *Curr. Opin. Microbiol.* 25, 67–72. doi: 10.1016/j.mib.2015.04.008

Holcomb, M., Cohen, A. L., and McCorkle, D. C. (2013). An evaluation of staining techniques for marking daily growth in scleractinian corals. *J. Exp. Mar. Biol. Ecol.* 440, 126–131. doi: 10.1016/j.jembe.2012.12.003

Honeyfield, D. C., Kindschi, G. A., Bell, T. A., and Mohler, J. W. (2011). Dietary calcein marking of shovelnose sturgeon and the effect of sunlight on mark retention. *N. Am. J. Aquac.* 73, 129–134. doi: 10.1080/15222055.2011.559869

Jacinto, D., Penteado, N., Pereira, D., Sousa, A., and Cruz, T. (2015). Growth rate variation of the stalked barnacle *Pollicipes pollicipes* (Crustacea: Cirripedia) using calcein as a chemical marker. *Sci. Mar.* 79, 117–123. doi: 10.3989/scimar.04135.08B

Jacquet, S., Heldal, M., Iglesias-Rodriguez, D., Larsen, A., Wilson, W., and Bratbak, G. (2002). Flow cytometric analysis of an *Emiliania huxleyi* bloom terminated by viral infection. *Aquat. Microb. Ecol.* 27, 111–124. doi: 10.3354/ame027111

Kaehler, S., and McQuaid, C. D. (1999). Use of the fluorochrome calcein as an in situ growth marker in the brown mussel *Perna perna*. *Mar. Biol.* 133, 455–460. doi: 10.1007/s002270050485

Kurtarkar, S. R., Saraswat, R., Nigam, R., Banerjee, B., Mallick, R., Naik, D. K., et al. (2015). Assessing the effect of calcein incorporation on physiological processes of benthic foraminifera. *Mar. Micropaleontol.* 114, 36–45. doi: 10.1016/j.marmicro.2014.10.001

Lambert, G., and Lambert, C. (1996). Spicule formation in the New Zealand Ascidian *Pyura pachydermatina* (Chordata, Ascidiacea). *Connect. Tissue Res.* 34, 263–269. doi: 10.3109/03008209609005270

Lidstrom, M. E., and Konopka, M. C. (2010). The role of physiological heterogeneity in microbial population behavior. *Nat. Chem. Biol.* 6, 705–712. doi: 10.1038/nchembio.436

Logsdon, D. E., and Pittman, B. J. (2012). Evaluation of osmotic induction of calcein treatments for marking Juvenile Walleyes. *N. Am. J. Fish. Manag.* 32, 796–805. doi: 10.1080/02755947.2012.690821

Lü, H., Chapelsky, A., Zhang, Z., Li, R., Rao, W., and Fu, M. (2017). Can calcein and alizarin complexone be used for double immersion marking of juvenile qingbo *Spinibarbus sinensis*? *Fish. Sci.* 83, 767–776. doi: 10.1007/s12562-017-1105-1

Markuszewski, R. (1976). *Structure, Fluorescence, and Chelating Properties of Calcein.* Ph.D. thesis, University of Iowa, Iowa City.

Marschal, C., Garrabou, J., Harmelin, J. G., and Pichon, M. (2004). A new method for measuring growth and age in the precious red coral *Corallium rubrum* (L.). *Coral Reefs* 23, 423–432. doi: 10.1007/s00338-004-0398-6

Martinez Martinez, J., Poulton, N. J., Stepanauskas, R., Sieracki, M. E., and Wilson, W. H. (2011). Targeted sorting of single virus-infected cells of the coccolithophore *Emiliania huxleyi*. *PLOS One* 6:e22520. doi: 10.1371/journal.pone.0022520

Martins, B. M., and Locke, J. C. (2015). Microbial individuality: how single-cell heterogeneity enables population level strategies. *Curr. Opin. Microbiol.* 24, 104–112. doi: 10.1016/j.mib.2015.01.003

Medeiros-Bergen, D. E., and Ebert, T. A. (1995). Growth, fecundity and mortality rates of two intertidal brittlestars (Echinodermata: Ophiuroidea) with contrasting modes of development. *J. Exp. Mar. Biol. Ecol.* 189, 47–64. doi: 10.1016/0022-0981(95)00010-O

Mohler, J. W. (1997). Management briefs: immersion of larval Atlantic Salmon in calcein solutions to induce a non-lethally detectable mark. *N. Am. J. Fish. Manag.* 17, 751–756. doi: 10.1577/1548-8675(1997)017<0751:MBIOLA>2.3.CO;2

Moran, A. L. (2000). Calcein as a marker in experimental studies newly-hatched gastropods. *Mar. Biol.* 137, 893–898. doi: 10.1007/s002270000390

Rogers-Bennett, L., Rogers, D. W., Bennett, W. A., and Ebert, T. A. (2003). Modeling red sea urchin (*Strongylocentrotus franciscanus*) growth using six growth functions. *Fish Bull.* 101, 614–626.

Rowley, A. F., and MacKinnon, D. I. (1995). Use of the fluorescent marker calcein in biomineralisation studies of brachiopods and other marine organisms. *Bull. Inst. Oceanogr. Monaco Spec.* 14, 111–120.

Rowson, J. D., Leadbeater, B. S. C., and Green, J. C. (1986). Calcium carbonate deposition in the motile (Crystallolithus) phase of *Coccolithus pelagicus* (Prymnesiophyceae). *Br. Phycol. J.* 21, 359–370. doi: 10.1080/00071618600650431

Sotje, I., Dishon, T., Hoffmann, F., and Holst, S. (2017). New methods of morphometric analyses on scyphozoan jellyfish statoliths including the first direct evidence for statolith growth using calcein as a fluorescent marker. *Microsc. Microanal.* 23, 553–568. doi: 10.1017/S1431927617000344

Sviben, S., Gal, A., Hood, M. A., Bertinetti, L., Politi, Y., Bennet, M., et al. (2016). A vacuole-like compartment concentrates a disordered calcium phase in a key Coccolithophorid alga. *Nat. Commun.* 7:11228. doi: 10.1038/ncomms11228

Tambutte, E., Tambutte, S., Segonds, N., Zoccola, D., Venn, A., Erez, J., et al. (2012). Calcein labelling and electrophysiology: insights on coral tissue permeability and calcification. *Proc. R. Soc. B Biol. Sci.* 279, 19–27. doi: 10.1098/rspb.2011.0733

Tarran, G. A., Zubkov, M. V., Sleigh, M. A., Burkill, P. H., and Yallop, M. (2001). Microbial community structure and standing stocks in the NE Atlantic in June and July of 1996. *Deep Sea Res. Part II Top. Stud. Oceanogr.* 48, 963–985. doi: 10.1016/s0967-0645(00)00104-1

Taylor, A. R., Brownlee, C., and Wheeler, G. (2017). Coccolithophore cell biology: chalking up progress. *Annu. Rev. Mar. Sci.* 9, 283–310. doi: 10.1146/annurev-marine-122414-034032

Taylor, A. R., Chrachri, A., Wheeler, G., Goddard, H., and Brownlee, C. (2011). A voltage-gated H^+ channel underlying pH homeostasis in calcifying coccolithophores. *PLoS Biol.* 9:e1001085. doi: 10.1371/journal.pbio.1001085

Taylor, G. T., Suter, E. A., Li, Z. Q., Chow, S., Stinton, D., Zaliznyak, T., et al. (2017). Single-cell growth rates in photoautotrophic populations measured by stable isotope probing and resonance raman microspectrometry. *Front. Microbiol.* 8:1449. doi: 10.3389/fmicb.2017.01449

Vidavsky, N., Addadi, S., Schertel, A., Ben-Ezra, D., Shpigel, M., Addadi, L., et al. (2016). Calcium transport into the cells of the sea urchin larva in relation to spicule formation. *Proc. Natl. Acad. Sci. U.S.A.* 113, 12637–12642. doi: 10.1073/pnas.1612017113

von Dassow, P., van den Engh, G., Iglesias-Rodriguez, D., and Gittins, J. R. (2012). Calcification state of coccolithophores can be assessed by light scatter depolarization measurements with flow cytometry. *J. Plankton Res.* 34, 1011–1027. doi: 10.1093/plankt/fbs061

Wilson, W. H., Tarran, G., and Zubkov, M. V. (2002). Virus dynamics in a coccolithophore-dominated bloom in the North Sea. *Deep Sea Res. Part II Top. Stud. Oceanogr.* 49, 2951–2963. doi: 10.1016/s0967-0645(02)00065-6

Zhou, S., Zhang, X., Li, W., Li, L., and Cai, X. (2016). Experimental evaluation of fluorescent (alizarin red S and calcein) and clip-tag markers for stock assessment of ark shell. *Chin. J. Oceanol. Limnol.* 35, 265–274. doi: 10.1007/s00343-016-5137-7

Zubkov, M. V., and Burkill, P. H. (2006). Syringe pumped high speed flow cytometry of oceanic phytoplankton. *Cytometry A* 69, 1010–1019. doi: 10.1002/cyto.a.20332

Conflict of Interest Statement: The authors declare that the research was conducted in the absence of any commercial or financial relationships that could be construed as a potential conflict of interest.

frontiers in Marine Science

REVIEW
published: 26 September 2018
doi: 10.3389/fmars.2018.00353

Physical and Biological Determinants of the Fabrication of Molluscan Shell Microstructures

Antonio G. Checa[1,2]*

[1] Department of Stratigraphy and Paleontology, University of Granada, Granada, Spain, [2] Instituto Andaluz de Ciencias de la Tierra, Consejo Superior de Investigaciones Científicas-University of Granada, Granada, Spain

Molluscs are grand masters in the fabrication of shells, because these are composed of the largest variety of microstructures found among invertebrates. Molluscan microstructures are highly ordered aggregates of either calcite or aragonite crystals with varied morphologies and three-dimensional arrangements. Classically, every aspect of the fabrication of microstructural aggregates is attributed to the action of proteins. There was, however, only direct evidence that the mineral phase, and indirect evidence that nucleation and the crystal shape, are determined by the types of soluble proteins. Some authors imply that crystal competition may also play a role. In addition, the fabrication of intergranular organic matrices typical of some microstructures (nacre, columnar prismatic) cannot have a protein-based explanation. Over the last decade I and collaborators have been applying a holistic view, based on analyzing and interpreting the features of both the organic (mantle, extrapallial space, periostracum, organic matrices) and inorganic (crystallite morphology, arrangement, and crystallography) components of the biomineralization system. By interpreting them on biophysical principles, we have accumulated evidence that, in addition to the activity of proteins, other mechanisms contribute in an essential way to the organization of molluscan microstructures. In particular, we have identified processes such as: (1) crystal nucleation on preformed membranes, (2) nucleation and growth of crystals between and within self-organized membranes, (3) active subcellular processes of contact recognition and deposition. In summary, besides the activity of organic macromolecules, physical (crystal competition, self-organization) and/or biological (direct cellular activity) processes may operate in the fabrication of microstructures. The balance between the physical and biological determinants varies among microstructures, with some being based exclusively on either physical or biological processes, and others having a mixed nature. Other calcifying invertebrates (e.g., corals, cirripeds, serpulids) secrete microstructures that are very similar to inorganic crystal aggregates, and only some brachiopods and, to a lesser extent, bryozoans may have secretory abilities comparable to those of molluscs. Here I provide a new perspective, which may allow microstructures to be understood in terms of evolutionary constraints, to compare the secretional abilities among taxa, and even to evaluate the probability of mimicking microstructures for the production of functional synthetic materials.

Keywords: molluscs, shells, microstructures, biomineralization, calcium carbonate, self-organization, mantle cells, crystallography

OPEN ACCESS

Edited by:
Pei-Yuan Qian,
Hong Kong University of Science and Technology, Hong Kong

Reviewed by:
Gary H. Dickinson,
The College of New Jersey, United States
Adam Michael Reitzel,
University of North Carolina at Charlotte, United States

***Correspondence:**
Antonio G. Checa
acheca@ugr.es

Specialty section:
This article was submitted to Marine Molecular Biology and Ecology, a section of the journal Frontiers in Marine Science

Received: *29 January 2018*
Accepted: *12 September 2018*
Published: *26 September 2018*

Citation:
Checa AG (2018) Physical and Biological Determinants of the Fabrication of Molluscan Shell Microstructures. Front. Mar. Sci. 5:353. doi: 10.3389/fmars.2018.00353

INTRODUCTION

Molluscs are, after the Arthropoda, the most diverse marine phylum of invertebrates, with an imprecise known diversity between 41,000 and 53,000 species (Appeltans et al., 2012). An essential element of their basic body plan is a calcareous shell, which can be unique (gastropods, monoplacophorans and scaphopods), twofold (bivalves) or eightfold (polyplacophorans). Aplacophorans only secrete aragonitic spicules embedded in a peripheral cuticle. During the course of evolution within the different classes, some groups have reduced, internalized or even suppressed the shell (e.g., coleoidean cephalopods - cuttlefishes, squids, octopuses-, opisthobranch and pulmonate gastropods).

Mollusc shells are organo-mineral biocomposites, in which the mineral part constitutes 95–99% of the shell weight while the organic fraction makes up 0.1–5% (Hare and Abelson, 1965). Exceptional values of up to 16% organic matter have been recorded in the calcitic columnar prismatic layers of the pteriomorph bivalve *Pinna nobilis* (Checa et al., 2016a). Despite its small volumetric representation, the organic fraction is extremely complex, with hundreds of proteins, polysaccharides and lipids, which can differ according to molluscan group. The mineral part of the molluscan shell is typically made entirely of calcium carbonate, in particular, calcite and/or aragonite. Vaterite, a third anhydrous polymorph of calcium carbonate, is only found exceptionally (Ma and Lee, 2006; Wehrmeister et al., 2007; Spann et al., 2010; Nehrke et al., 2012). Amorphous calcium carbonate (ACC) has been encountered within the shells of some bivalves and gastropods (Nudelman et al., 2007; Baronnet et al., 2008; Macías-Sánchez et al., 2017), but it is regarded as a transient precursor phase. Today it is known that a small fraction of the initial ACC can be permanently stabilized within the biominerals (Macías-Sánchez et al., 2017, and references therein).

The shell of molluscs comprises an outer, entirely organic or sparsely mineralized layer (the periostracum) and a series of superposed shell layers. Some groups exceptionally produce deposits over the shell exterior, such as the external crusts on the shells of the venerid bivalves *Granicorium* and *Samarangia*, composed of cemented sediment grains (Taylor et al., 1999), or the inductural deposits, present in some cardiid bivalves and common in cypraeid gastropods (Checa and Salas, 2017). Shell layers are monomineralic, but molluscs are able to superpose layers with the two mineralogies. When calcite is present, it is typically restricted to the outer shell layer, or it may comprise all subperiostracal shell layers except for myostracal prisms and ligament fibers, which are invariably aragonitic. Shell layers are made of crystals with varied and recurrent morphologies and 3-D configurations and arrangements, which define the different microstructures. In general, it is recognized that shell biomineralization in the Mollusca is largely biologically controlled (i.e., the organism directs the nucleation, growth, morphology, orientation and location of the biominerals), rather than merely biologically mediated (i.e., biominerals precipitate as a result of metabolic activities on cell surfaces, with little or no control on the morphology and organization of biominerals) (Lowenstam, 1981; Mann, 1983). According to the range of microstructures and their degree of sophistication, molluscs are unrivaled among invertebrates.

The number of molluscan microstructures is limited (Carter et al., 2012). Microstructural patterns, in general, depend on the mineralogy (**Figure 1**). The most typical calcitic microstructures are columnar prismatic, granular prismatic, fibrous, foliated, chalk and crossed-foliated. The most characteristic aragonitic microstructures are columnar prismatic, fibrous prismatic, lamellar, nacre and crossed lamellar. While every microstructure has a certain morphological range, no transitions exist between microstructures. This suggests some kind of crystallographic/fabricational constraints. At the same time, homeomorphic microstructures (e.g., nacre, crossed-lamellar or foliated) have developed independently in and within the different classes. The most dramatic examples of convergence are nacre, which appeared independently in Bivalvia, Gastropoda, Cephalopoda, and Monoplacophora (Vendrasco et al., 2011), and the crossed lamellar microstructure, which developed separately in all extant molluscan classes with the exception of the Cephalopoda and Aplacophora. Certain extinct Monoplacophora (i.e., the Bellerophontida), and the extinct molluscan classes Hyolitha (but see Moysiuk et al., 2017, for a lophophorate affinity of hyoliths) and Rostroconchia also developed crossed-lamellar microstructures independently.

One of the most distinctive features of microstructures is their high degree of morphological and crystallographic ordering. This is best appreciated in the construction of pole figures derived from diffraction methods (X-ray diffraction, XRD, or electron back-scatter diffraction, EBSD). Pole figures plot the distribution (usually as density curves) of the poles of particular faces or crystallographic directions in stereographic projection. Concentrations of values within one or several maxima indicate that the different crystals making up the aggregate are co-oriented along a given crystallographic direction. The degree of alignment is inversely related to the spread of the maxima. All microstructures hitherto analyzed display a defined maximum for the *c*-axis of either calcite or aragonite, which indicates that the *c*-axes of crystals are relatively co-oriented. In some cases, the maxima for the rest of the axes are ring-like. This pattern is the so-called fiber texture, with the *c*-axis as the fiber axis. This texture is displayed by aragonitic and calcitic prismatic, aragonitic granular prismatic microstructures, and gastropod nacre (Checa and Salas, 2017). Other microstructures display a higher degree of ordering, with all axes co-oriented. This is called a sheet texture and is found in bivalve and *Nautilus* nacre (Hedegaard and Wenk, 1998; Chateigner et al., 2000), the crossed lamellar layers of all extant molluscan classes (Hedegaard and Wenk, 1998; Chateigner et al., 2000; Almagro et al., 2016), the foliated aragonite of monoplacophorans (Checa et al., 2009b,c), the foliated calcite of bivalves (Checa et al., 2007), and the fibrous calcite of Mytilidae (Checa et al., 2014a). A rare case is that in which there are two maxima for the *c*-axis, as in many instances of crossed-lamellar microstructures (Almagro et al., 2016).

Prior to or at the initiation of the postlarval stage, shell secretion is carried out by the mantle, which has a thin external epithelium composed of a single layer of cells. The outer surface of the mantle epithelium is in contact with the internal (growth)

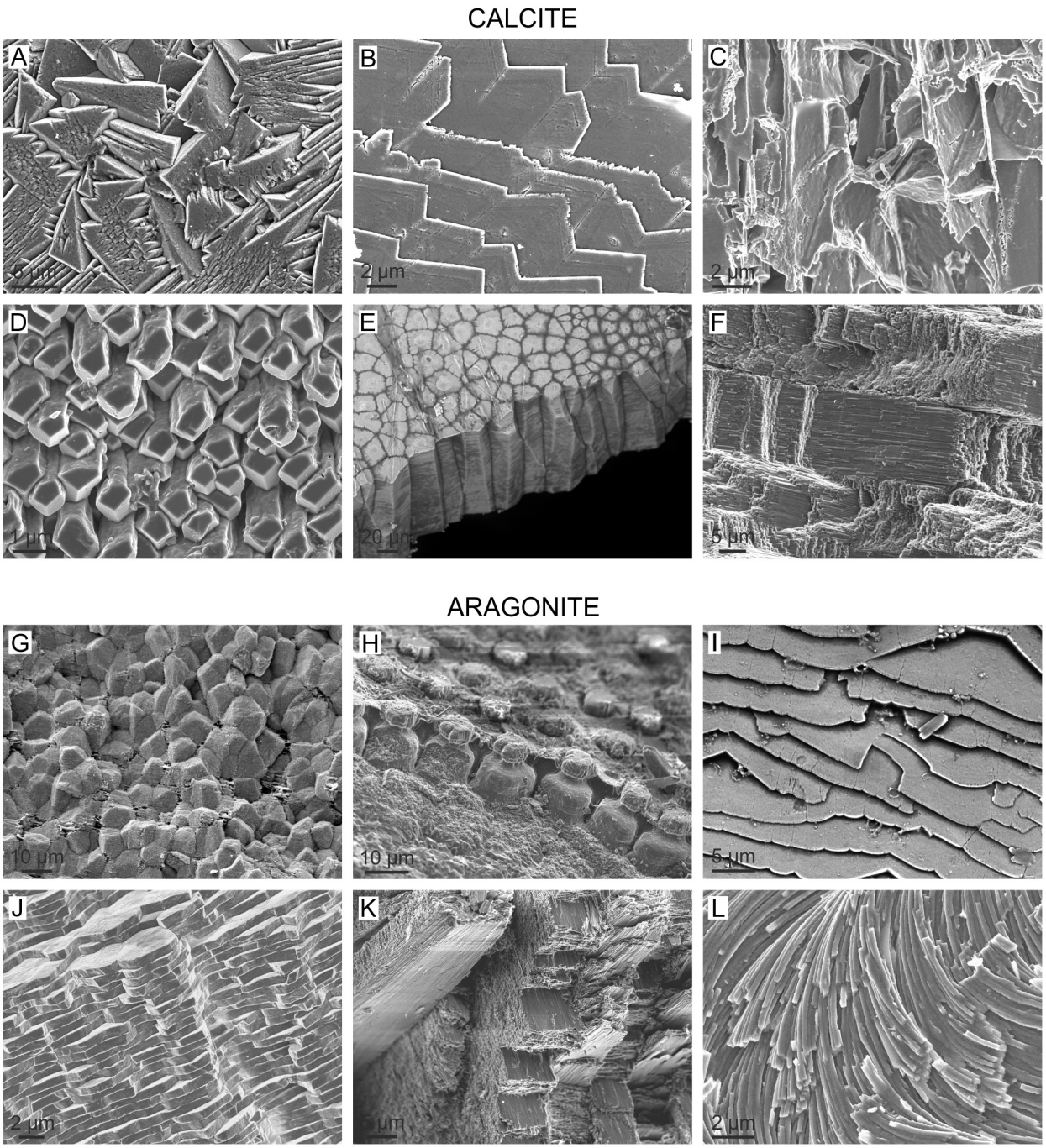

FIGURE 1 | The high diversity of molluscan microstructures, illustrated with selected representative calcitic and aragonitic cases. **(A)** Granular (rhombohedral) calcite. Outer layer of the patellogastropod *Cellana toreuma*. **(B)** Foliated calcite. Bivalve *Anomia ephippium*. **(C)** Chalk. Bivalve *Crassostrea angulata*. **(D)** Anvil-type fibrous calcite. Outer layer of the bivalve *Mytilus chilensis*. **(E)** Columnar prismatic calcite. Outer layer of the bivalve *Pinctada margaritifera*. **(F)** Crossed-foliated. Middle layer of the patellogastropod *Scutellastra tabularis*. **(G)** Granular prismatic aragonite. Outer layer of the bivalve *Entodesma navicula*. **(H)** Columnar prismatic aragonite. Outer layer of the bivalve *Neotrigonia lamarckii*. **(I)** Foliated aragonite. Inner layer of the monoplacophoran *Rokopella euglypta*. **(J)** Nacre. Internal layer of the bivalve *Neotrigonia bednalli*. **(K)** Crossed lamellar. Internal layer of the caenogastropod *Semicassis granulata*. **(L)** Helical fibrous aragonite. Opisthobranch gastropod *Cuvierina columnella*.

surface of the shell. The mantle edge is divided into several folds (usually three, but up to five). Shell secretion begins with the formation of the periostracum, at the base of a groove between the outer and the middle mantle folds, called the periostracal groove. The calcified part of the shell begins to be secreted more or less at the edge of outer mantle fold. At this position, the periostracum

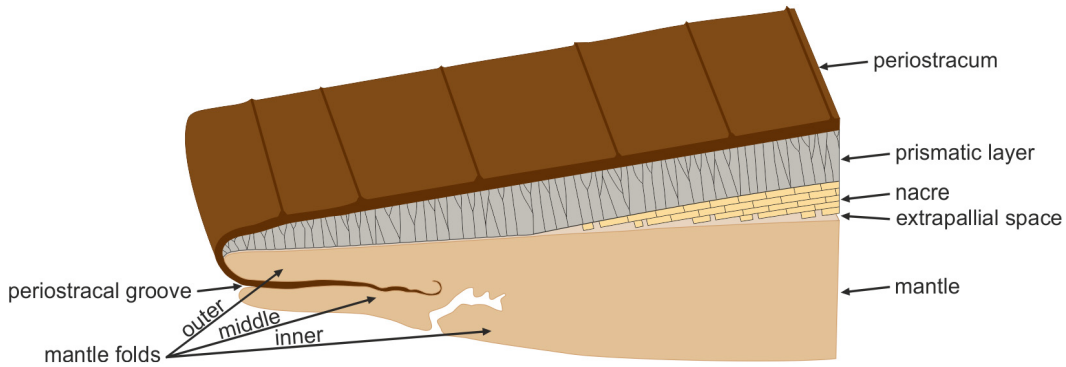

FIGURE 2 | The bivalve mollusc biomineralization system. The mantle is separated from the shell by the extrapallial space. The first component to be secreted is the periostracum, at the groove between the outer and middle mantle folds. The mineral shell layers are secreted by the outer surface of the outer mantle fold. The archetypical prismato-nacreous shell is used for the illustration.

is reflected backward toward the dorsum and the first crystals begin to be secreted below the periostracum, or, occasionally, within a not-yet-tanned internal periostracum (Checa and Salas, 2017). In either case, the periostracum seals the biomineralization compartment between mantle and shell. This process is depicted in **Figure 2**.

The space between the growing shell and the adjacent mantle epithelium is a thin fluid film called the extrapallial space, across which the transference of mineral and organic components from the mantle to the shell takes place (**Figure 2**). The fluid filling in the extrapallial space is the extrapallial fluid. The extrapallial space also contains inorganic (Wilbur and Saleuddin, 1983), as well as organic compounds, including amino acids (Wada and Fujinuki, 1976; Misogianes and Chasteen, 1979), proteins (Kobayashi, 1964a,b; Pietrzak et al., 1973; Misogianes and Chasteen, 1979), mucopolysaccharides (Kobayashi, 1964b; Crenshaw, 1972; Misogianes and Chasteen, 1979) and organic acids (Wilbur and Simkiss, 1968). This organic fraction is presumably incorporated into the shell as extra- and intracrystalline organic fractions.

There is very little evidence available about the dimensions of the extrapallial space. The exceptional transmission electron microscopy (TEM) micrographs on sections of the shell-mantle complex of the pterioid bivalve *Pinctada radiata* provided by Bevelander and Nakahara (1969), Nakahara and Bevelander (1971), and Nakahara (1991) show that in nacre the approximate thickness of the extrapallial space is ∼100 nm (**Figure 3A**), whereas in prismatic layers, the thickness can be less precisely estimated, but is submicrometric. It is assumed that the mantle-shell relationship was not altered during sample preparation. The thickness of the extrapallial space could be precisely estimated by Checa et al. (2014b) in the intraperiostracal mineralized bosses of the aragonitic prisms of the bivalve *Neotrigonia*. Since these bosses were formed within a deep spiral-shaped periostracal groove (**Figure 3B**), it is highly unlikely that the relative positions and dimensions of crystals and the mantle were affected during ultramicrotome sectioning for TEM. The observed thickness of the extrapallial space below the forming bosses is *ca.* 100 nm (**Figures 3C,D**), which is in agreement with the figures derived from Bevelander and Nakahara's illustrations of nacre. The fact that the boundaries between shell layers with different microstructures (and, sometimes, also different mineralogies) are so well defined, argues for a submicron thick extrapallial space, which imposes strict limits on the lateral diffusion of organic and inorganic components.

The organic fraction of the major shell layers is mainly composed of proteins, acidic polysaccharides and chitin (presumably the β polymorph) (Lowenstam and Weiner, 1989; Levi-Kalisman et al., 2001; Pereira-Mouriès et al., 2002; Weiner and Dove, 2003). In nacre and in calcitic and aragonitic columnar prismatic layers, part of the organic fraction assembles into an extracrystalline 3-D organic matrix framework. Some other macromolecules are absorbed by crystals during growth, forming an intracrystalline organic phase (Berman et al., 1993; Weiner and Addadi, 1997). In 1996, two independent research groups demonstrated that polymorph secretion is controlled by macromolecules associated with either calcitic or aragonitic shell layers. In particular, Belcher et al. (1996) precipitated calcium carbonate in the presence of soluble proteins extracted from either calcitic or aragonitic shells from a variety of taxa, preabsorbed on a substrate of squid chitin and silkworm fibroin. They consistently found coincidence of the precipitated polymorph with that of the original shell. Falini et al. (1996) obtained similar results, although they concluded that crystal nucleation and orientation do not require pre-organized organic matrices.

There is presently a significant amount of studies aiming at isolating and characterizing the soluble molluscan shell proteins, despite their low representation (0.03–0.5% weight). Good reviews have been provided by Cusack and Freer (2008) and Marin et al. (2008). Highly acidic proteins are preferentially associated with calcitic shells and, due to the preponderance of negatively charged Asp-rich residues, are Ca-binding proteins. They are particularly suited for control over crystal growth and interaction with crystal faces. Nacreins and pearlins are intermediate proteins extracted from nacre and display a diversity of functions, such as Ca-binding, carbonic anhydrase activity and inhibition of calcium carbonate precipitation. Basic proteins have

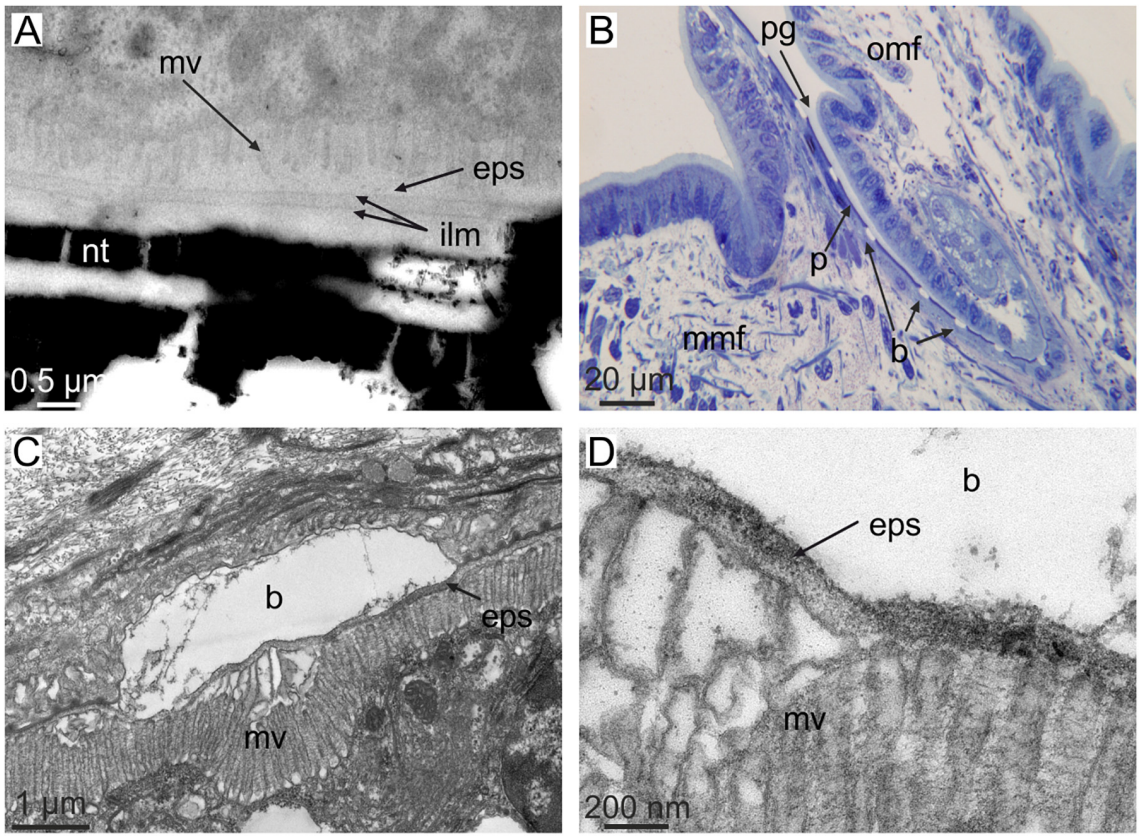

FIGURE 3 | The dimensions of the extrapallial space in bivalves. **(A)** Section through the shell and mantle of *Pinctada fucata*. Note the short distance between microvilli and the forming interlamellar membranes (i.e., the extrapallial space). Original material from H. Nakahara. **(B–D)** Sections through the mantle edge **(B)** and periostracal groove **(C,D)** of *Neotrigonia margaritacea* (decalcified sample). The view in **(B)** shows the periostracum, together with mineral bosses of the prisms being formed within the periostracal groove. **(C,D)** Show the relative positions of the crystalline bosses and the cell microvilli. The close-up view in **(D)** permits estimating an approximate thickness of the extrapallial space of *ca*. 100 nm. b, boss; mv, cell microvilli; eps, extrapallial space; ilm, interlamellar membrane; mmf, middle mantle fold; nt, nacre tablet; omf, outer mantle fold; p, periostracum; pg, periostracal groove. **(C,D)** Modified from Checa et al. (2014b).

been extracted both from calcitic and aragonitic layers. Some of them display interesting *in vitro* activities, like the nucleation of calcium carbonate (perlucin) or its inhibition (perlwappin). In summary, there is presently reliable, direct evidence that proteins control the polymorph. *In vitro* assays also suggest that proteins promote crystal nucleation and, by attaching to particular crystal faces, they are likely to control the shapes of crystals. However, the molecular aspects of the shell building process are still far from fully understood, because soluble and insoluble organic molecules synergistically control the nucleation, growth, polymorphism, and orientation of biomineral deposition. For this reason, it is difficult to mimic the biomineralization process and to distinguish the precise roles played by these soluble and insoluble organic phases.

Based on the above discussion, it is presently clear that proteins determine the mineral polymorph and, possibly, also the nucleation and shape of crystals, but it is not at all clear how they determine other aspects, such as crystal orientation and growth rate. Particularly intriguing is the production of conspicuous intercrystalline organic membranes. Here I will review the existing knowledge on the mechanisms of microstructure fabrication, i.e., those which help us to understand how microstructures acquire their incredible degree of sophistication. These properties are essential with regards to the biomechanical properties. The unveiling of the fabricational strategies is also essential for future biomimetic studies, since, in theory, these strategies could be used as inspiration for the production of highly functional synthetic materials.

MECHANISMS OF MICROSTRUCTURE ORGANIZATION

Crystal Competition

This process happens in aggregates of elongated crystals growing with a well-defined growth front. The crystals within the aggregate with their fastest growth (crystal) axes subperpendicular or perpendicular to the growth front will intercept those growing obliquely and will outcompete them (crystal selection). In this way, the fastest growth axes of the survivors will be progressively co-oriented in the growth direction of the aggregate. Crystal selection may account for

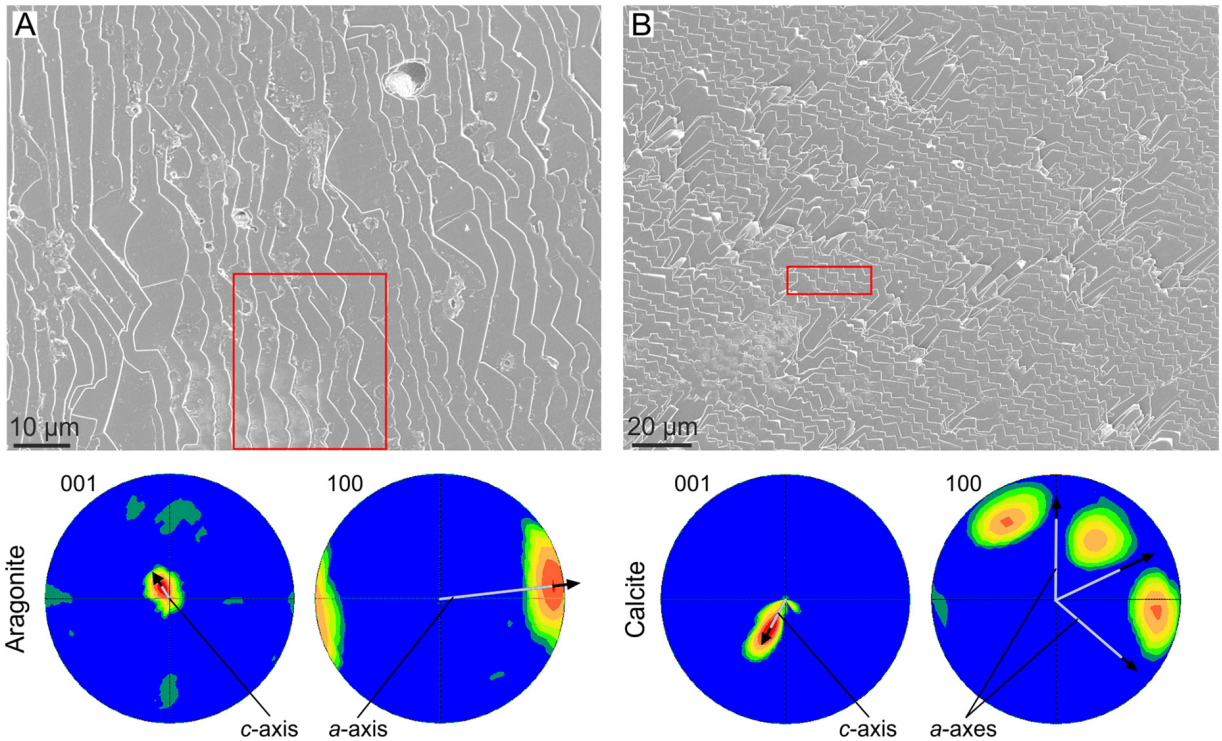

FIGURE 4 | Crystal coorientation in foliated materials. **(A)** Foliated aragonite of the monoplacophoran *Rokopella euglypta*. **(B)** Foliated calcite of the bivalve *Anomia ephippium*. In both cases, the EBSD pole figures of the areas framed in red [the position of the area in **(B)** is approximate] are shown below. For both materials, the small scatter of the pole figure maxima indicate a good co-orientation of both the *c*- (001 pole figures) and *a*-axes (100 pole figures). The average orientations of the crystallographic axes is indicated. Their inclinations with respect to the plane of the image are inversely proportional to their lengths, e.g., for aragonite, the *c*-axis is at a high angle to the image plane, whereas the *a*-axis is at a low angle (close to the horizontal).

cases in which crystals are elongated (fibers, prisms) and grow with their long axis perpendicular or at a high angle to the common growth front. As a result, only the axis of elongation (usually, though not always, the *c*-axes in biocalcite and the *a*- or *c*-axes in bioaragonite) becomes co-oriented and a fiber texture finally results.

Crystal selection by competition has been postulated in the columnar prismatic calcite of pinnoideans and pterioideans (Ubukata, 1994), the columnar prismatic aragonite of unionids (Ubukata, 1994; Checa and Rodríguez-Navarro, 2001), the calcitic prismatic layers of the *Argonauta* shell (Stevens et al., 2017), the foliated calcite of bivalves (Checa et al., 2007), the foliated aragonite of monoplacophorans (Checa et al., 2009a, b) and the nacre of bivalves (Checa et al., 2006). From the above-mentioned cases of prismatic materials referred to in the literature to orient by competition, the columnar prismatic layers of pinnoideans, pterioideans and unionoids can be excluded because the columnar prismatic units are surrounded by thick organic membranes, which determine the growth dynamics of the aggregate (see below). Additionally, no evidence that crystal co-orientation progresses with time has been provided. Presently, the only well-documented case is that of the calcitic prismatic layer of the shell secreted by the female *Argonauta* (which is not homologous to the shells of other molluscs). Stevens et al. (2017) showed how crystal co-orientation increases during growth of the layer, which is fully consistent with selection by competition. The non-columnar calcitic prismatic layers of euheterodont bivalves also display fiber textures (Harper and Checa, 2017). Since they do not bear intermediate organic membranes and crystals elongate in the growth direction, this crystallographic pattern is quite possibly acquired also by crystal competition.

Crystal co-orientation will also be attained when lath-like crystals are arranged into 2D lamellae. Provided that individual crystals have consistent crystallographies, competition will give rise to a sheet texture. This is the case of the foliated aragonite of the monoplacophorans (Checa et al., 2009b) and of the foliated calcite of the Ostreoidea and Pectinida (Checa et al., 2007), where foliae are composed of evenly oriented crystals, with all axes co-oriented (**Figure 4**). The case of progressive co-orientation of bivalve nacre implied by Checa et al. (2006) is doubtful, because it only applies when nacre tablets elongate along the *b*-axis, which is not always the case.

Crystal interaction in molluscan microstructures is particularly intense because they are compact materials, with a negligible amount of porosity. The only exception known is that of chalk (**Figure 1C**), a particularly soft and porous material (up to 80%; Korringa, 1951) fabricated by oysters. It is composed of an apparently disorganized array of laths. In coincidence, it seemingly displays a high degree of crystallographic disorder (Checa et al., 2018). Although more information is needed on the

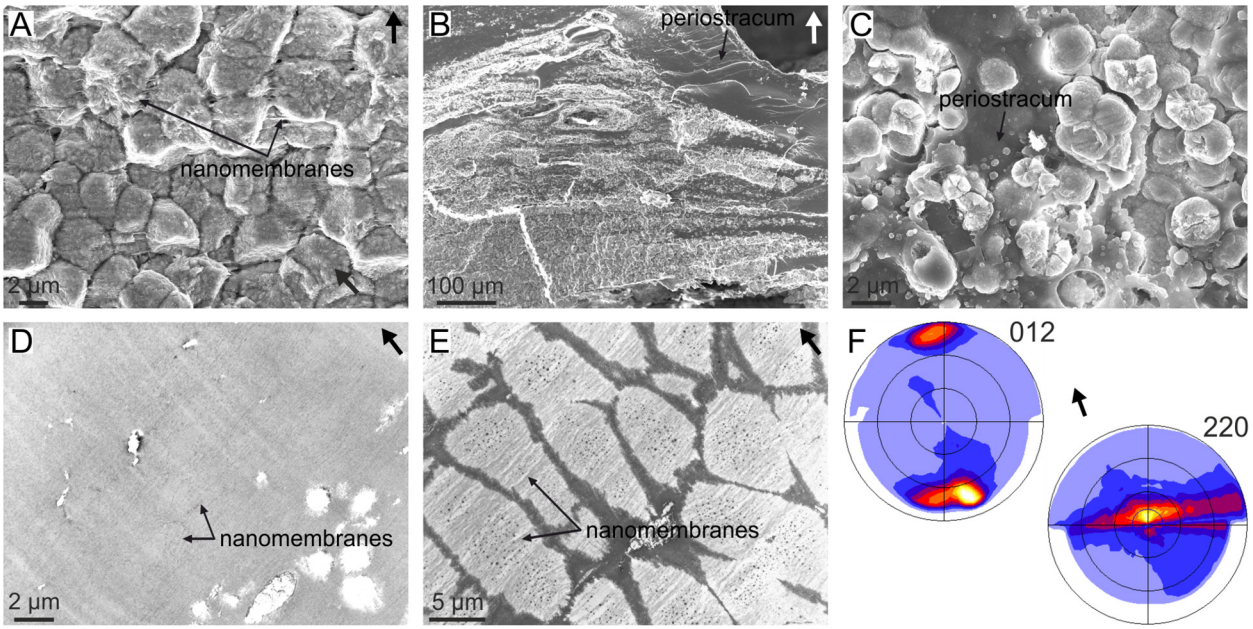

FIGURE 5 | Organization of the granular prismatic microstructure of the outer shell layer of the bivalve *Entodesma navicula*. **(A)** Vertical fracture of the granular layer, showing the aspect of the granular crystals. The horizontal organic nanomembranes of the translucent periostracal layer are also visible. **(B)** General view of the outer granular prismatic layer. The granules are distributed into bands interbedded within the periostracum (dark organic material). **(C)** Prismatic granules growing within the periostracum (dark organic material). **(D)** TEM view of the non-calcified periostracum, showing its nanolaminated structure. **(E)** Decalcified granular prisms. The periostracal nanomembranes incorporated by the crystals are evident. **(F)** XRD pole figures obtained on a fracture similar to that in **(A)**. The 012 pole figure indicates that the *c*-axis is perpendicular to the outer shell surface (or the nanomembranes) and the 220 pole figure implies that the *a*- and *b*-axes are rotated around *c*. This is called a fiber texture, with the *c*-axis as fiber axis. Arrows point to the outer shell surface. **(E,F)** Modified from Harper et al. (2009).

chalk, it provides an example of how important space restriction is for an effective organization based on crystal competition.

Orientation by Interaction With Organic Matrices

The presence of organic sheets may provide sites for oriented nucleation. In particular, the interaction of charged ions on the surface of the organic sheets (i.e., aspartic acid-rich proteins) favors the oriented nucleation of aragonite or calcite with the positively charged calcium layers (i.e., the {001} basal planes, which are perpendicular to the crystallographic *c*-axis) parallel to the sheets (Addadi et al., 1987). This effect is undoubtedly due to the activity of proteins, but it should be differentiated from other instances because it happens at extracrystalline level and affects crystal aggregates instead of single crystals, and the protein fraction is organized onto a chitin or chitin + protein scaffold instead of proteins being dispersed within the extrapallial fluid.

Cases in which short crystals develop a fiber texture cannot be due to crystal competition, because a *sine qua non*-condition is that crystals elongate in the fastest growth direction with time. This is the case of the granular (i.e., very short) prismatic units of the outer shell layer of the anomalodesmata bivalve *Entodesma* (Harper et al., 2009) (**Figure 5A**). These granules grow within the so-called translucent layer of the periostracum, which is a non-tanned periostracal layer composed of parallel nanolaminae (**Figures 5A–D**). During growth, the granules absorb the nanolaminae, which is revealed upon the decalcification of the granular units (**Figure 5E**). Despite their morphology, the granular units are oriented with their *c*-axes perpendicular to the periostracum (i.e., the outer shell surface) (**Figure 5F**). This orientation is most probably determined during the nucleation stage by the interaction of the negatively charged protein sheets making up the nanolaminae with the positively charged calcium planes of the aragonite structure (which are perpendicular to the crystallographic *c*-axis). The same applies to mineralized spikes and plaques that form intraperiostracally in many other anomalodesmatans, and which always grow with their *c*-axes perpendicular to the periostracum surface (Checa and Harper, 2010).

The anvil-type calcitic fibrous outer shell layer of *Mytilus* (**Figures 1D**, **6A**) has a sharp sheet texture (**Figure 6B**), which is unexpected since competition would only lead to a fiber texture, with the *c*-axis of calcite fibers as fiber axis. The mineralization compartment of this microstructure is covered by a proteinaceous layer called the surface membrane (**Figures 6C–E**). This membrane has a fibrous aspect under the scanning electron microscope (SEM) (**Figure 6C**), and appears nanolaminated internally under TEM (Checa et al., 2014a) (**Figure 6D**). How fibers inevitably have one of their $\{10\bar{1}4\}$ rhombohedral surfaces strictly parallel to and in contact with the surface membrane can also be observed (**Figure 6E**). Experiments of precipitation of synthetic calcite both on the unaltered membranes and after decalcification demonstrate that:

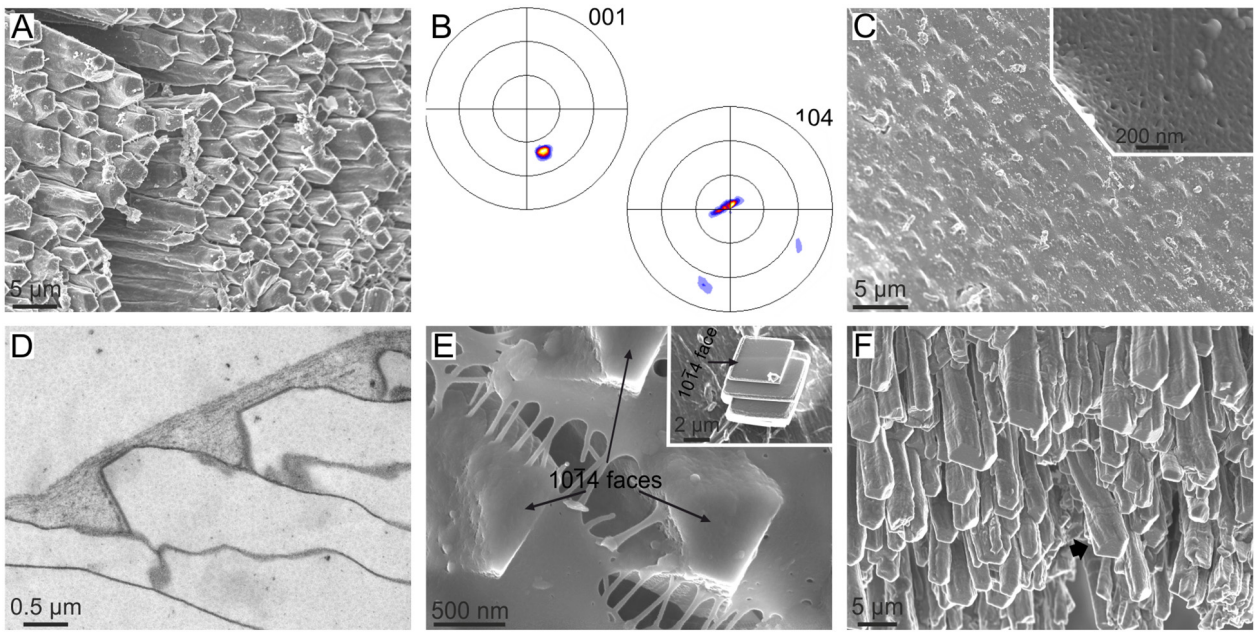

FIGURE 6 | The calcitic fibrous layer of mytilid bivalves and its relationship with the surface membrane. **(A–E)** *Mytilus galloprovincialis*. **(A)** Aspect of the growth surface of the fibrous layer. Note the even orientation of the $10\bar{1}4$ faces (slightly darker in the image). **(B)** XRD pole figures of the fibrous layer seen from the growth surface. The orientation is similar to that in **(A)**, but the pole figures are rotated clockwise by *ca.* 70°. The pole figures reveal a sheet texture. **(C)** Outer aspect of the membrane, with the calcitic fibers slightly protruding from below the membrane. Inset, fibrous texture of the surface membrane. **(D)** TEM section along the axis of fibers and the surface membrane. The nanolaminated aspect of the latter is evident. **(E)** Detail of the tips of fibers. Their $10\bar{1}4$ faces are perfectly cooriented, and one of them (the one looking toward the observer) is strictly parallel to the surface membrane. Inset, synthetic calcite crystal grown on the underside of an isolated surface membrane. It grows on a $10\bar{1}4$ face. **(F)** Growth ends of the fibers of *Bathymodiolus azoricus*. Note the bending and twisting (arrow) fibers. **(A–D,F)** Modified from Checa et al. (2014a).

(1) the surface membrane is transparent to ions or $CaCO_3$ nanoaggregates, and (2) synthetic calcite crystals nucleate on the underside of the membrane on their $\{10\bar{1}4\}$ faces (**Figure 6E**, inset), i.e., this membrane has an affinity for such crystallographic faces. Additionally, the calcite fibers of *Mytilus* have been shown to be able to twist and bend (**Figure 6F**). Checa et al. (2014a) hypothesized that during growth, every fiber twists and/or bends until one of its rhombohedral faces becomes parallel to the surface membrane. From here on, this face becomes "locked" to the surface membrane. In this way, the aggregate of fibers finally acquires a sheet texture by interaction with the surface membrane.

Self-Organization Processes

The Interlamellar Membranes of Nacre

Nacre is the most iconic molluscan microstructure and is characterized by having a brickwall stacking mode in which the bricks are aragonitic tablets (**Figure 1J**) and the mortar is horizontal, interlamellar membranes (**Figures 7A–D**) and vertical, intertabular membranes. While the intertabular membranes have no defined structure and seemingly consist only of organic material trapped between platelets, the interlamellar membranes have a felt-like structure (**Figures 7C,E**), consisting of fibrils of a chitin (most probably β-chitin) + protein complex, surrounded by proteins (Levi-Kalisman et al., 2001; Osuna-Mascaró et al., 2015). In excellent TEM sections across the shell and mantle of the bivalve *P. radiata*, Bevelander and Nakahara (1969) and Nakahara (1991) showed how tablets in a given lamella are ineluctably covered by an interlamellar membrane, which is at a very short distance to the mantle cell microvilli. At its distal end, every new interlamellar membrane is at a distance of *ca.* 90 nm from the preceding interlamellar membrane (Cartwright and Checa, 2007; **Figure 7D**). Moving back from the growth rim, this distance increases progressively to the usual platelet thickness of mature nacre (300–500 nm). Around this distance (estimated at ∼20 µm in Cartwright and Checa, 2007), nacre crystals begin to grow within the interlamellar spaces (**Figure 7D**). This process is sketched in **Figure 7F**. The cells of the mantle surface are never in contact with the forming nacre platelets because there is always an interlamellar membrane in-between. The same applies to gastropods in which the whole nacre biomineralization compartment is isolated by a relatively thick (∼100 nm) surface membrane (**Figures 7A,B**), from which the successive interlamellar membranes detach. Nacre platelets later begin to grow within the newly created interlamellar spaces (see sketch in **Figure 7G**). In any case, it is necessary for the interlamellar membranes to be transparent to the aggregation units, whether ions or nanoparticles.

How the animal is able to precisely control the distribution and distances between interlamellar membranes at such a nanometric scale is difficult to explain, unless by a physical process operating at a molecular or nanoparticle level. If we make

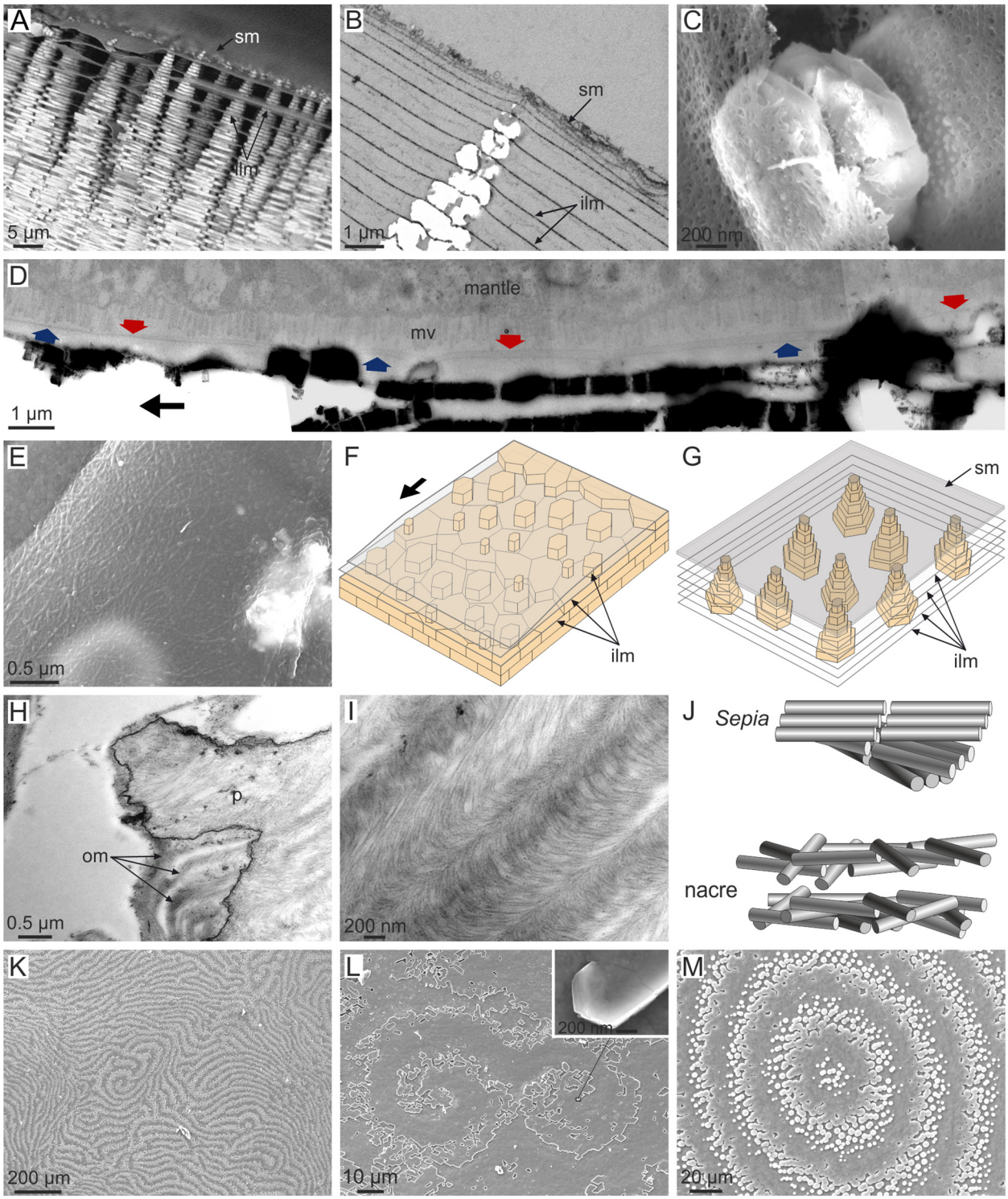

FIGURE 7 | Distribution and structure of interlamellar membranes in gastropod **(A–C,G)** and bivalve **(D–F,K–M)** nacre, and comparison to the organic membranes in *Sepia* **(H–J)**. **(A)** *Jujubinus pseudogravinae*. Typical tower-like arrangement of gastropod nacre, with interlamellar membranes subtending between tablets. The tips of the towers are embedded within the surface membrane. **(B)** *Monodonta labio*. TEM section through a tower of tablets and intervening interlamellar membranes. The latter predates the former. **(C)** *Steromphala pennanti*. Growing nacre tablets between interlamellar membranes. Note the fibrous nature of the membranes. **(D)** *Pinctada fucata*. Section through the mantle and nacre (composite TEM micrograph). The tracings of two interlamellar membranes covering the two most recent lamellae are indicated with arrows in different colors. The membranes become progressively closer in the growth direction (indicated by the black arrow).

(Continued)

FIGURE 7 | Continued
(E) *Anodonta cygnea*. Interlamellar membrane displaying a fibrous aspect. **(F)** Model for the growth of nacre in bivalves. A fresh membrane is progressively secreted in the growth direction (arrow) at a very short distance from the previous membrane, and later separates to the usual tablet thickness. Tablets later initiate and grow within the newly created interlamellar spaces. **(G)** Model for the growth of nacre in gastropods. The interlamellar membranes detach from the surface membrane and tablets grow within the created interlamellar spaces. **(H)** Cephalopod *Sepia officinalis*. TEM view of the interior of a decalcified chamber showing the arrangement of horizontal organic membranes. These are continuous from the interior of the pillar to the empty space of the chamber. **(I)** *Sepia officinalis*. Detail of such membranes showing the arcuate arrangement of chitin fibrils. **(J)** Models for the 3D arrangement of fibrils in the organic membranes of *Sepia* and in the interlamellar membranes of nacre. **(K)** *Pteria avicula*. Digitiform arrangement of the growth fronts of nacre lamellae. **(L)** *Pteria hirundo*. Nacre growth fronts forming a double spiral. The inset shows a spirally growing nacre tablet at the very origin of the right spiral. **(M)** *Pteria avicula*. Target pattern formed by the growth fronts of nacre. ilm, interlamellar membrane; mv, microvilli; om, organic membrane; p, pillar; sm, surface membrane. **(B,E)** Modified from Cartwright et al. (2009); **(D,K,M)** modified from Cartwright and Checa (2007); **(H,I)** modified from Checa et al. (2015).

an abstraction of nacre platelets (which come later, Nakahara, 1991; **Figures 7F,G**), we are left with a series of parallel layers (the interlamellar membranes), each having a fibrous nature. In particular, such a situation is obtained during the formation of liquid crystals. Liquid crystals are a state of matter which have properties of both liquids (e.g., fluidity) and crystals (e.g., optical or magnetic properties) (e.g., Andrienko, 2018). Liquid crystals are made of polar fibers or molecules, which align due to electrostatic interactions. There are many different types of liquid-crystal phases. Of the several possibilities, a common final configuration is the so-called cholesteric or chiral-nematic phase, in which fibers or molecules are arranged in planes, with the fibers in each plane being parallel to each other and slightly rotated with respect to those of the preceding plane. After a certain distance ("pitch") the orientation of the fibers is exactly the same. When a series of planes with a cholesteric configuration are sectioned, it provides a typical arcuate pattern with a regular repetition.

Liquid-crystal self-organization has been applied to explain the plywood structures of many fibrous biocomposites ranging from plant cell walls to bone, including invertebrate skeletons (Neville, 1993). Possibly the best-known example is that of the arthropod exoskeleton, which is made of α-chitin fibers (Bouligand, 1972). In molluscs, patterns typical of cholesteric phases have been recognized in the periostracum of some gastropods (Neville, 1993), the squid pen (Levi-Kalisman et al., 2001), and the chambers of *Sepia* (Checa et al., 2015; **Figures 7H,I**). The material composing the chamber of *Sepia* is, interestingly, homologous to the cephalopod nacre.

Compared to a typical cholesteric phase, in which fibers in a layer are oriented in parallel, the interlamellar membranes appear disorganized (**Figure 7J**). This may happen because either they have not had sufficient time to assemble in parallel or the observed length of the fibers (tens of microns; **Figures 7C,E**) hinders a parallel arrangement.

Another important difference is that in liquid crystals formed *in vitro* all layers develop at once from a suspension. Regarding nacre, we need to consider the case of a layer-by-layer liquid crystal, in which every new layer is added during growth at the same time as the preexisting layers extend at their edges.

The liquid-crystal hypothesis for the formation of the interlamellar membranes of nacre is an easy way to understand how such a complex structure is secreted via a simple physical mechanism. This is particularly relevant in the case of gastropod nacre in which the nacre compartment is protected by the surface organic membrane (**Figures 7A,B,G**), such that the mantle is never in direct contact with the forming interlamellar membranes (Checa et al., 2009a). In these circumstances, an explanation based on self-organization by liquid crystallization seems the only available resource.

Similar to crystals, defects are also common in liquid crystals. Screw and edge dislocations are typically developed in cholesteric liquid crystals, with layers of crystallites or molecules being analogous to atomic or molecular terraces in crystals. Comparable features are also found in the interlamellar membranes of bivalve nacre (**Figure 7K**). Screw dislocations manifest themselves as the spiral patterns typically observed in the nacre of bivalves (**Figure 7L**) and gastropods, which are resolved at their very axis in a single tablet with screw growth (**Figure 7L**, inset). Spiral and target patterns have been modeled theoretically by assuming that the nacre formation system is an excitable medium, which conforms to a layer-by-layer liquid crystal (Cartwright et al., 2009). Bivalve nacre forms target patterns (**Figure 7M**), which are comparable to growth hillocks produced during the formation of new atom planes in a growing crystal. That these patterns belonged to the interlamellar membranes and were later mineralized during tablet formation is manifested by the fact that it affected not just one (which would be the case if they were defects arising in single tablets) but hundreds of tablets, i.e., the whole growth front of the interlamellar membrane.

Bevelander and Nakahara (1969) and Nakahara (1991) demonstrated that nacre tablets begin to grow within the spaces between the preformed interlamellar membranes (**Figures 7A–D,F,G**). It is now clear that tablets do not nucleate onto the interlamellar membranes, but rather find their way through them through tiny holes (>100 nm), which result during initial (as in gastropods) or advanced (as in bivalves) growth of tablets (Checa et al., 2011). In this way, parental and filial tablets connect across the so-called mineral bridges (initially defined by Schäffer et al., 1997).

Although there is no hitherto evidence, it is likely that nanolayered organic membranes of the kind described in the preceding section (the periostracum of anomalodesmatan bivalves and the surface membrane carpeting the calcitic fibrous layer of mytilids internally) are also self-organized.

Organic Envelopes Around Columnar Prismatic Units

Bayerlein et al. (2014) presented a physical explanation for the external calcitic prismatic layers of the pen shell *P. nobilis*, based on synchrotron X-ray tomography. These prismatic layers

belong to a family of materials found in many bivalves of the order Pteriomorphia (including pen-shells, pearl oysters, oysters, saddle oysters, and some scallops). They are strictly termed calcitic columnar prismatic microstructures and consist of prismatic units of calcite with regular polygonal cross-sectional outlines surrounded by relatively thick (0.5–3 μm) organic membranes, which elongate and grow perpendicular to the shell surfaces (**Figures 1E**, **8A**). Bayerlein et al. (2014) presented reliable evidence that the columnar prismatic units evolve in such a way that those units with larger cross-sectional area and/or a number of sides greater than six grow at the expense of the units with smaller area and/or a number of sides lower than six (**Figure 8A**). The latter will shrink with time, eventually disappearing. They interpreted this pattern on the basis of the normal grain growth theory (von Neumann, 1952; Mullins, 1956) which predicts exactly the same evolution in an aggregate of crystals (mainly metals) subjected to high temperatures. They also remarked on how the sides of the polygons form triple junctions at 120° (**Figures 8A–D**), which is the condition for surface tension to remain constant throughout the aggregate (Plateau's law). Alternatively, Checa et al. (2016a) objected to such an explanation because in biogenic prismatic calcite regular polygonal outlines are only found in the presence of organic membranes, whereas in their absence, boundaries are complex pseudodendritic. In addition, in many instances, the prismatic units are polycrystalline (**Figures 8B,C**), cavities can exist in the absence of mineral infilling and the outlines of the prismatic units change with the growth or disappearance of organic walls (**Figures 8D,E**). This and additional evidence led these authors to propose that the evolutionary dynamics observed by Bayerlein et al. (2014), instead of being due to the crystals, can be attributed to the organic envelopes of the prisms. Normal grain growth is only one of a series of phenomena to which the von Neumann–Mullins topological law can be applied, including foams (on which the von Neumann–Mullins law was originally developed) and emulsions. It is hard to conceive which kind of physical process a system composed of the polymerized membranes and the mineral grains may correspond to, but the picture becomes much clearer if we think about the precursors of the two materials: (1) the fluid, gel-like precursor of the membranes, and (2) the liquid precursor of the mineral phase. The latter is the so called polymer-induced liquid precursor (PILP), and there is evidence that it is generated by acidic biopolymers in synthetic systems (Gower, 2008; Schenk et al., 2012). This PILP phase is hypothesized to be present during biomineral formation as well. This two-liquid system would constitute an emulsion (i.e., a dispersion of minute droplets of one liquid into another in which it is not soluble or miscible); the fluid precursor of the organic web would constitute the continuous phase and the PILP, the discontinuous phase (Checa et al., 2005, 2016a) (**Figure 8F**). Accordingly, the growth of the calcitic columnar prismatic layers is a self-organized process, in which the membranes control the pattern and the mineral enclosed within the organic membranes passively adjusts to the dynamics dictated by the latter.

Exactly the same growth dynamics of organic membranes has been observed in the aragonitic columnar prismatic layers of the freshwater bivalves of the order Unionida (**Figure 8D**). This material is made of organic cavities, which are, in turn, filled with fibrous aragonite, and to which the emulsion hypothesis of self-organization can also be applied confidently.

Similar prisms are produced by the only extant representative of the bivalve order Trigoniida (closely allied to Unionida), *Neotrigonia*. Unlike in the Unionida, the prisms of *Neotrigonia* are all the same size and retain a hexagonal outline (Checa et al., 2014b) (**Figures 1H**, **8G**). As a consequence, they do not compete during growth and the same number of units which initiated at the outer side of the layer reach the internal side. This is achieved by the animal precisely placing the initial prism nuclei equidistant from each other (see below).

Direct Cellular Activity

As discussed above, the thickness of the extrapallial space in molluscs is negligible or, in other words, the microvilli of the mantle cells are virtually in contact with the forming shell (**Figure 3**). According to Bevelander and Nakahara (1969), Nakahara and Bevelander (1971) and Nakahara (1991), this is also the case of the pearl oyster *Pinctada*. Directly in contact with the growth surface of the columnar prismatic layers, independent of whether they are calcitic or aragonitic, there are mantle cells with diameters of 5–10 μm, which secrete a network of membranes 0.5–3 μm wide, and mineral domains of up to 120 μm. We are faced with two possibilities: (1) the cells secrete mineral and organic components in an undifferentiated manner and these diffuse across the extrapallial space to the corresponding positions in either the membranes or the mineral domains or (2) the cells selectively add new organic components to the organic membranes and mineral components to the mineral units to extend the pattern. In case (1) the molecules or ions have to travel laterally for distances of microns to tens of μm to their corresponding positions, without any particular driving mechanism (e.g., electrochemical) being known. In the much more likely case (2), every mantle cell (whose diameters are far greater than the thicknesses of the membranes) must be secreting both organic and inorganic materials, depending on exactly which components it is in contact with. Since shell secretion is a periodical process, and the mantle is able to move relative to the shell surface, the mantle-shell contact is not permanent (**Figure 8F**, left panel). This implies that, every time a secretion period is about to start, the mantle cells must first be able to recognize the exact configuration of the organic-mineral pattern which they are in contact with (**Figure 8F**, right panel). In summary, contact recognition followed by secretion must take place. It should also be emphasized that these processes must occur at *subcellular* level (Checa et al., 2016a), which is so far unknown in biomineralization. This implies that cells are actively controlling the deposition process, although they do not influence the pattern of the organic network, which is only guided by physical laws (see above).

As commented on above, the regular distribution of the prisms of the bivalve *Neotrigonia* causes them to have even dimensions and regular pseudohexagonal crossed sectional outlines. In this way, competition is totally inhibited (**Figure 8G**). Their deposition already begins within the periostracal groove (**Figures 3B,C**) with mineral bosses (∼5 μm in diameter)

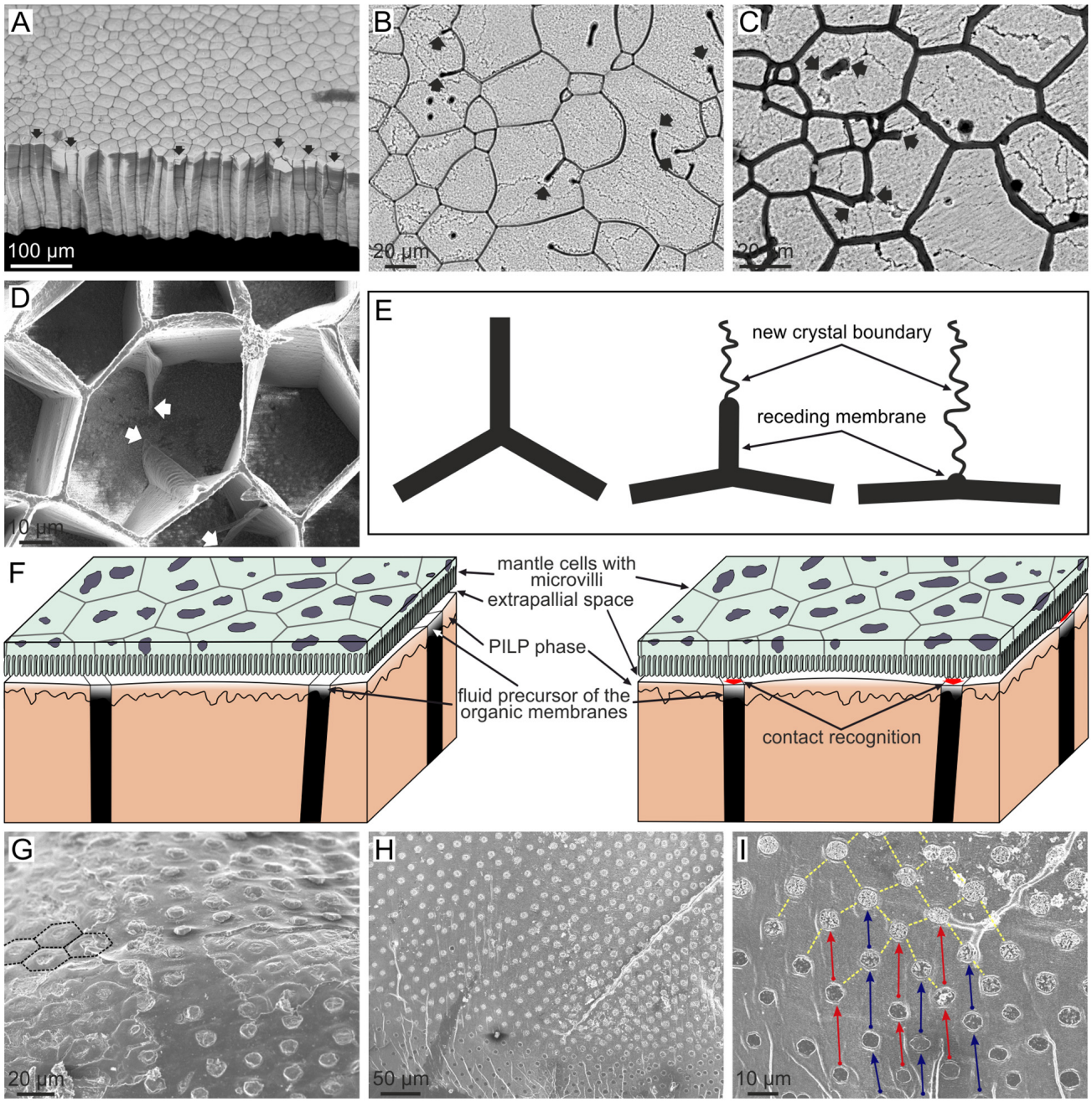

FIGURE 8 | Evolution of columnar prismatic layers in bivalves. **(A)** Fracture of the calcitic layer of *Pinctada margaritifera*. Those prisms with less than six sides (arrowed) wedge out and disappear during growth (bottom of the image). The contrary is true for prisms with six or more than six sides. **(B,C)** Growth surface of the prismatic layers of *Pinctada margaritifera*. The mineral columnar units are polycrystalline; the boundaries between crystals are visible under slight etching. Receding membranes are indicated with arrows. Note that they leave crystal boundaries behind. **(D)** Semi decalcified aragonitic layer of *Anodonta cygnea* seen from the growth surface. The arrows point to receding membrane. Note how the triple points formed by membranes at the depressed mineral surface progressively revert to flat membranes. **(E)** Mechanism of recession of a membrane and resulting change in the morphology of the triple meeting point. The receding membrane, which originally separated two crystals, leaves a crystal boundary behind. **(F)** Model for the formation of columnar prismatic materials. The left sketch corresponds to the non-secretion period. When secretion is about to resume (right sketch), the cells recognize the positions of the organic membranes in order to secrete both the organic and mineral phases separately. The emulsion is formed between the fluid precursors of the organic and mineral phases. **(G)** Outer shell surface of *Neotrigonia lamarckii*. The prismatic units have a regular distribution and pseudo-hexagonal contours (some of them have been outlined with broken lines). **(H,I)** Free periostracum of *Neotrigonia gemma*. The bosses, which constitute the nuclei of the aragonitic prisms, have a regular grid-like distribution. In the close up view **(I)** corresponding bosses are joined by arrows, which also indicate the growth direction. **(B,E)** Modified from Checa et al. (2016a).

distributed into radial rows spaced 20–30 μm apart. The bosses in every row are spaced at approximately the same distance, and offset with respect to bosses in adjacent rows (**Figures 8H,I**). In this way, they form a regular grid on the outer periostracal and shell surface. This arrangement implies that there must be specific positions of the outer mantle epithelium where cells or, more strictly, subcellular areas, are specialized in the production of new bosses and which are evenly spaced along a comarginal direction (Checa et al., 2014b). Once a new boss has been produced, the subcellular site enters a refractory period until it becomes activated again for the production of a new boss (**Figure 8I**). In this way, the bosses also become regularly spaced in the longitudinal direction. For the grid-like pattern to arise, production sites should become activated alternatively in adjacent radial rows.

Possibly, the most 'exotic' microstructure (in the sense that it looks anything but a crystalline aggregate) is the so-called aragonitic helical fibrous microstructure (Bé et al., 1972), which is fabricated by a small group of planktonic gastropods, the Cavolinioidea. It consists of very thin (∼300 nm thick) aragonite fibers which coil helically in several turns (up to 3.5 in some instances, e.g., *Cuvierina*; **Figure 9A**) along an axis perpendicular to the shell's surface. All helices within the material have their coiling axes parallel, having exactly the same leading angle and amplitude, and are in phase, so that, at a given depth within the shell, all fibers are co-oriented. Only their coiling axes are mutually displaced. Accordingly, the fibers permanently intersect each other, which causes permanent changes in their cross-sectional outlines, although all of them manage to survive the constant process of interlocking (**Figures 9B,C**). Each fiber consists of a myriad of {110} twinned aragonite crystals, with their common *c*-axis parallel to the coiling axis (Willinger et al., 2016). Accordingly, it is clear that the helical trajectories are not guided by crystal growth. On the internal (growth) surface of the shell, the outlines of the fibers appear very elongated in the growth direction, and, invariably, there is a minute bulge positioned at the anteriormost end of every fiber (**Figures 9D,E**), which elevates between 30 and 90 nm above the internal shell surface, depending on the species (Checa et al., 2016b) (**Figure 9F**). This feature has never been observed in the growth surface of any other molluscan microstructure. The elevated bulge is the means by which a given fiber avoids extinction, since, in being elevated above the growth surface, it cannot be overgrown by neighboring fibers. However, at the same time, the bulges provide a clue as to the fabrication of helical fibers. Despite their minute sizes and elevations, they can be perceived (recognized) by the mantle cells, which would acquire the necessary positional information to continue the secretion of the corresponding fiber (**Figure 9G**).

In order for the tips to move with time along helical trajectories, the mantle cells must be able to propagate their secretion onto the 2D mantle surface along circular trajectories (by e.g., reaction-diffusion processes of morphogens) (**Figure 9H**). The increase in shell thickness with time provides the necessary translation along the coiling axis (perpendicular to the shell surface) to generate the helical movement. In summary, each fiber would be produced 'à la carte' by the mantle cells. In more detail, taking into account that bulges are much smaller than mantle cells, their detection, secretion and translation has to take place within areas much smaller than those typical of single cells.

PHYSICAL VS. BIOLOGICAL INFLUENCES ON INDIVIDUAL MICROSTRUCTURES

According to the above discussion, some microstructures are strongly influenced by physical processes (crystal competition and self-organization), whereas others are mainly influenced by biological processes, including the simple activity of proteins on the crystal shape. Others result from a combination of both types of influences. It is then possible to plot the known positions of those microstructures in the fabrication process on a bivariate diagram, with one axis corresponding to physical determinants and the other to the biological determinants, such as that of **Figure 10**.

Some microstructures (e.g., foliated) acquire their degree of organization according to simple crystal growth (i.e., physical) processes (crystal selection by competition). This is the case of the non-columnar prismatic microstructures, which are the closest analogs to non-biogenic calcite (e.g., the cephalopod *Argonauta* and the bivalve *Chama*). Foliated materials, also organize basically by similar processes, although the shapes of crystals are largely influenced by soluble proteins. Microstructures which organize by interaction with organic matrices (e.g., fibrous calcitic of mytilids) must be considered as a separate strategy. By assuming that these organic matrices are formed by self-organization, they can be placed in the top half of the diagram. A particular category is constituted by those having conspicuous separate organic phases, which organize into frameworks according to self-organization processes. This is the case of nacre (self-organized by liquid crystallization) and of the prismatic columnar microstructures (organic-PILP emulsion). There is nevertheless a distinction between them, because the fabrication of the prismatic columnar microstructures also demands direct cellular activity in the form of subcellular recognition and secretion, therefore being of a mixed physical/biological nature. The columnar prismatic layers of *Neotrigonia* are particularly appealing, since the mantle cells also actively determine the regular disposition of the prismatic units, which hinders their further evolution. The extreme case of biological control described so far is that of the aragonitic helical fibrous microstructure, in which the whole pattern is determined by cellular (subcellular, in strict terms) activity.

This kind of classification allows us to make some adaptive and evolutionary inferences. From this suite of microstructures, the two based on self-organization are particularly suited for biomechanical purposes. Nacre is known for being the strongest of all molluscan microstructures, whereas the columnar prismatic materials are exceptional in flexibility, due to the high elasticity of the constituent organic membranes. From an evolutionary perspective, microstructures based on physical laws (either crystal growth or self-organization) seem particularly prone to appear repeatedly during evolution. Foliated

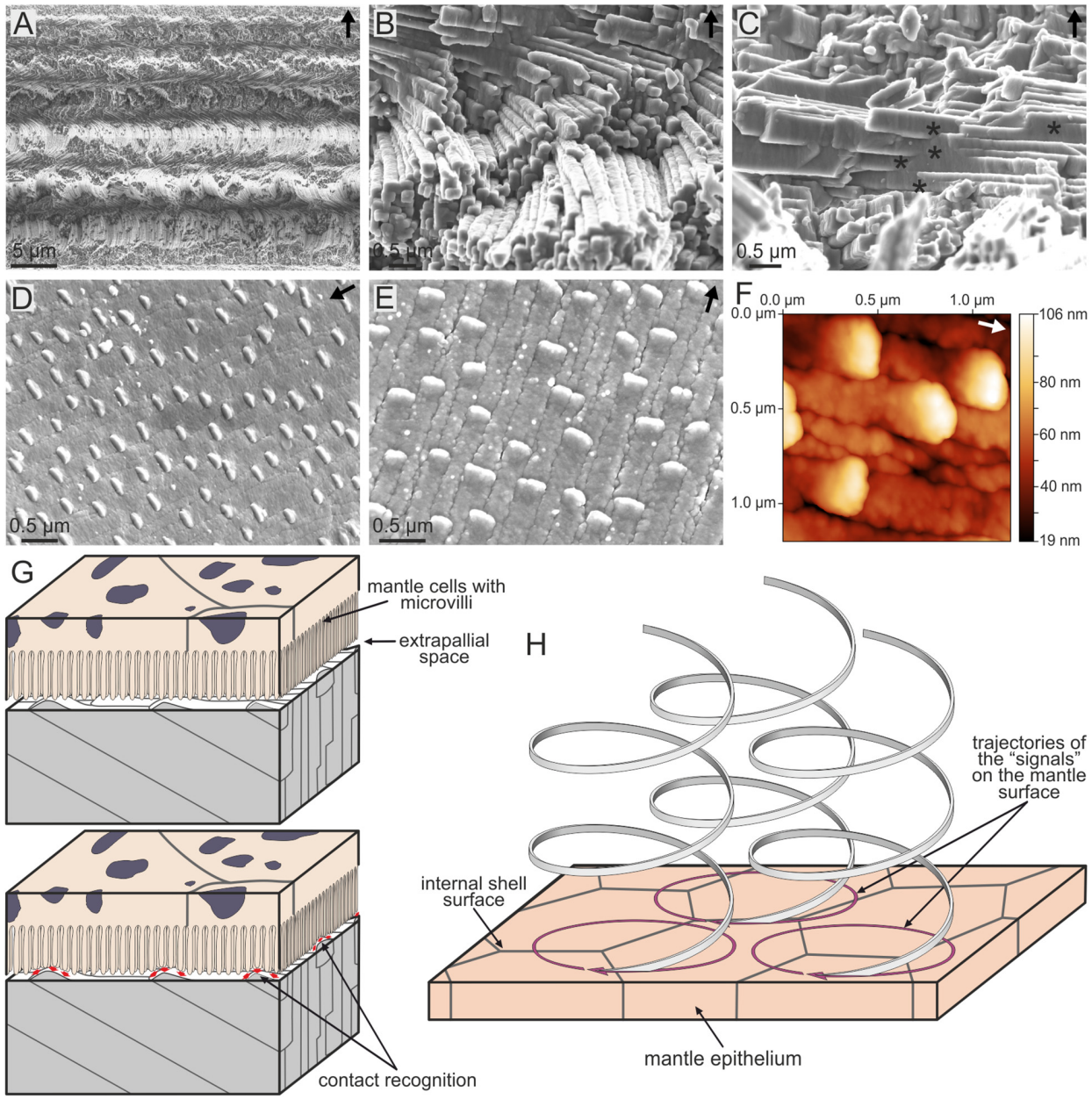

FIGURE 9 | The aragonitic helical fibrous microstructure of cavolinioidean gastropods. **(A)** Fracture through the shell of *Cuvierina columnella*. The helices coil for more than three complete turns. **(B)** Detail of the microstructure of *Clio pyramidata*. Note the close packing and the high degree of interpenetration of fibers. **(C)** Interpenetration of fibers (asterisks) in *Creseis acicula*. **(D)** Oblique view of the internal shell surface of *Cuvierina columnella*, showing the elevated anteriormost tips of fibers. **(E)** Plan view of the internal shell surface of *Creseis clava*. As in **(D)**, each fiber has an elevated growth tip. **(F)** Atomic force microscopy view (topography image) of the internal shell surface of *Cuvierina columnella*. The tips of fibers rise by *ca.* 85 nm above the surface. **(G,H)** Model for the secretion of spiral fibers. The upper panel in **(G)** corresponds to the non-secretional stage. When shell secretion resumes, the mantle cells recognize the positions of the tips of fibers in order to continue their secretion [lower panel in **(G)**]. **(H)** In order for the spiral path to be achieved, the cells have to displace the tips of the fibers along circular trajectories. The displacement along the coiling axis is caused by the thickening of the shell. Arrows point to the external shell surface in **(A–C)**, whereas they indicate the growth direction of fibers in **(D–F)**. **(E–H)** Modified from Checa et al. (2016b).

calcite, despite its weakness, has developed independently in bivalves and gastropods. Even brachiopods and bryozoans have developed analogous calcitic foliated microstructures (see section "OTHER INVERTEBRATES"). The nacre 'solution' was reached independently by bivalves, gastropods, cephalopods, and monoplacophorans (Vendrasco et al., 2011). The probability that a given microstructure emerges seems to decrease when the organic influence increases. For example, the columnar prismatic layers are only found in two separate groups of bivalves, the subclasses Pteriomorphia (oysters, pearl oysters, pens shells,

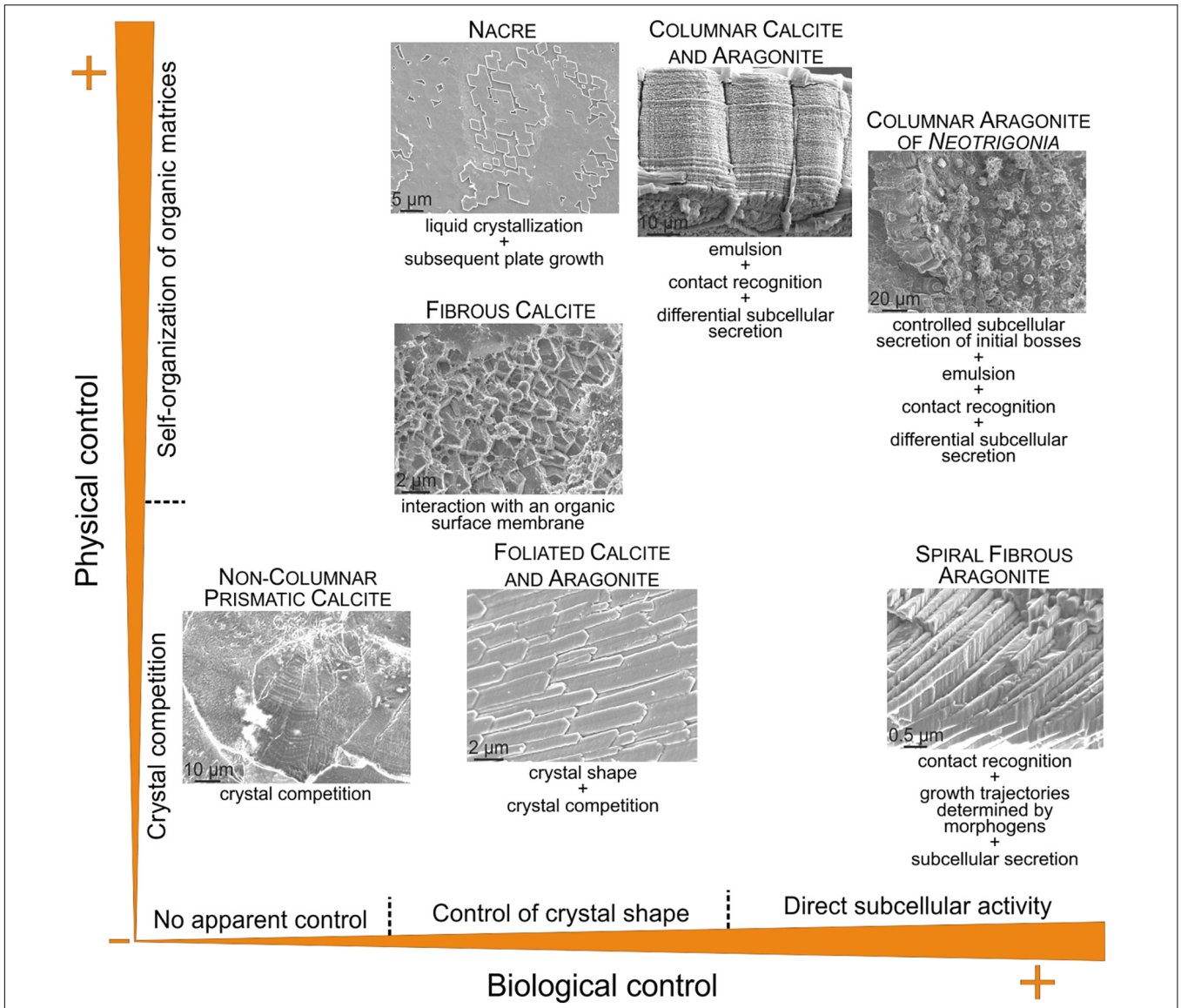

FIGURE 10 | Approximate position of selected microstructures discussed in the text according to the physical and biological influences on their fabrication. In the columnar calcitic and aragonitic microstructures (including the columnar aragonitic microstructure of *Neotrigonia*), the aspects of calcite (with irregular outlines) and aragonite prisms (fibrous aggregates) suggest little to no control of the crystal shape. The microstructures represented correspond to the bivalves *Pteria hirundo* (nacre), *Isognomon legumen* (columnar prismatic calcite), *Neotrigonia lamarckii* (columnar prismatic aragonite), *Mytilus galloprovincialis* (fibrous calcite), *Chama pellucida* (prismatic, non-columnar, calcite) and *Propeamussium dalli* (foliated calcite), and to the gastropod *Cuvierina columnella* (helical fibrous aragonite).

some scallops) and Paleoheterodonta (naiads, *Neotrigonia*). The most extreme case of biological influence, the aragonitic helical fibrous microstructure, is only found in the Cavolinioidea, a small (52 species) and relatively recent (appeared ∼50 Ma ago) group of planktonic gastropods. This evolutionary restriction might have to do with the high amount of genetic information necessary for its fabrication process, which is not the case of nacre, for example.

Unfortunately, there is currently no clear explanation for the fabrication of the crossed-lamellar microstructure, which is by far the most repeated microstructure during the evolution of molluscs and presently the most frequently occurring across the group. This characteristic suggests that, within the above evolutionary framework, the construction of the crossed-lamellar microstructure should be based rather on simple physical rules. Further knowledge on the fabrication of this microstructure will constitute a good test for our conclusions.

As commented on in the Introduction the dominant view some 10 years ago established that every aspect of the organization of the microstructures depended on the action of proteins and organic matrices. For example, the discussion of crystal orientation has traditionally focused on nacre, which is the classical example of a biomineral composed of oriented crystal tablets. Weiner and Traub (1980, 1984) proposed an epitaxial relationship between crystals and a preformed protein-chitin

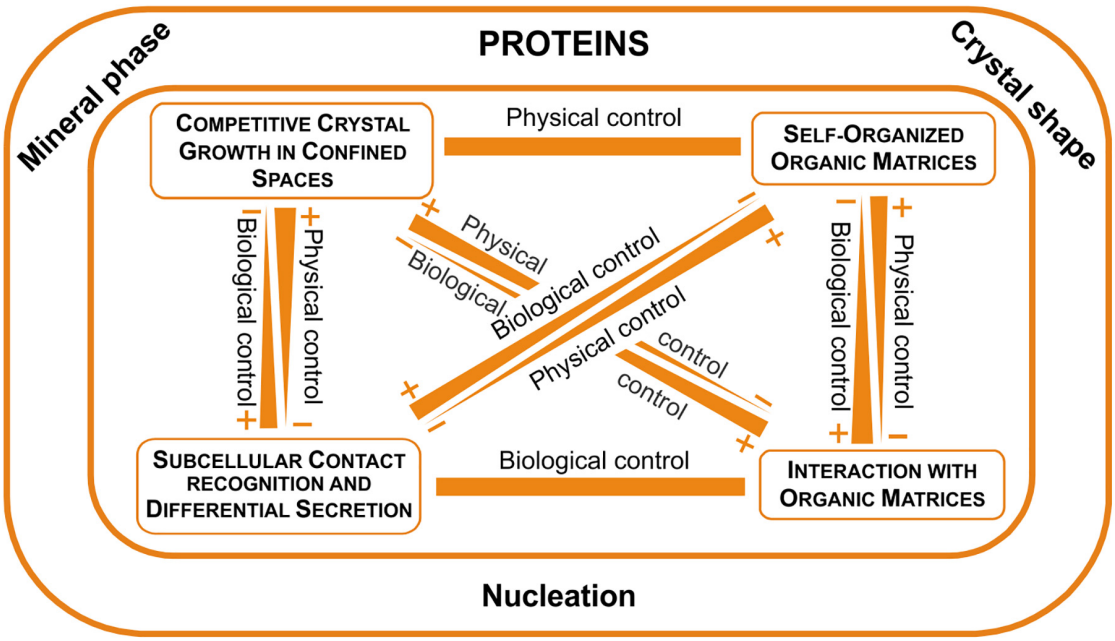

FIGURE 11 | The fabricational space of molluscan microstructures. Proteins clearly determine the mineral phase, crystal shape (with few exceptions) and nucleation, while other aspects of the fabrication process are determined by physical (crystal competition and self-organization), as well as biological determinants (interaction with organic matrices and direct cellular activity).

organic scaffold. This explanation stood until Nassif et al. (2005) revealed that nacre platelets are surrounded by a thin (3–5 nm) cortex of amorphous calcium carbonate which would make the epitaxial explanation impossible. Today, we know that nucleation is not even necessary for the initiation of nacre tablets, because tablets communicate across the lamellae through mineral bridges (Checa et al., 2011).

Our new view of the microstructures leads to a new fabricational framework according to which the soluble proteins determine the mineral phase and are responsible for crystal shape and nucleation. Other important aspects of the organization of microstructures are due to the interaction of crystals with organic matrices, the operation of self-organization mechanisms and the direct action of the mantle cells. Every microstructure would be organized according to a particular combination of these operators. All this is outlined in **Figure 11**.

OTHER INVERTEBRATES

Molluscs are exceptional among other biocalcifying taxa in two respects. First, they employ the two basic mineralogies: calcite and aragonite, and even combine them within a single shell. Second, they employ an unprecedented variety of calcitic and aragonitic microstructures as construction materials. Only bryozoans and serpulid polychaetes presently employ both mineralogies, but only the former make bimineralic shells.

Regarding the ability to control the fabrication of shell microstructures, groups such as scleractinian corals, serpulids and barnacles (**Figures 12A–C**) seem relatively unable to do that, since they secrete microstructures that are reminiscent of inorganic aggregates. Coral skeletons are made basically with aragonitic fibers radiating from calcification centers (Wendt, 1990; Nothdurft and Webb, 2007; Cuif et al., 2011; **Figure 12A**), thus being reminiscent of, for example, fibrous aragonitic cements. The microstructures of barnacles are virtually unknown, but our observations on the balanid *Perforatus* reveal that the plates are composed of calcite granules, sometimes with a neat rhombohedral morphology (**Figure 12B**), similar to any synthetic precipitate. Serpulids most commonly fabricate bimineralic tubes with fibrous (**Figure 12C**), prismatic or granular (sometimes rhombohedral) microstructures (Vinn et al., 2008; Vinn and Mutvei, 2009; Vinn, 2013). Some species secrete lamello-fibrillar microstructures, which consist of horizontal lamellae of co-oriented fibers. In adjacent lamellae, fibers have different orientations, but similar to those of alternating lamellae. This arrangement is reminiscent of that of chiral nematic liquid crystals, i.e., it could be a case of a self-organized material. The absence of further evidence on the organization and the crystallographic structure of this material hinders any definite interpretation.

Lophophorates, bryozoans, and brachiopods secrete a large suite of calcitic microstructures (Williams, 1990, 1997; Taylor and Weedon, 2000; Taylor et al., 2015). Some cases display low degrees of organization, such as the granular microstructure of bryozoans or the fibrous primary layer of calcareous brachiopods, and they appear to be under little, if any, biological control. Other microstructures, such as the foliated microstructure (**Figure 12D**) and the semi-nacre (**Figure 12E**) are much more elaborate. The foliated microstructure is indistinguishable from that of molluscs

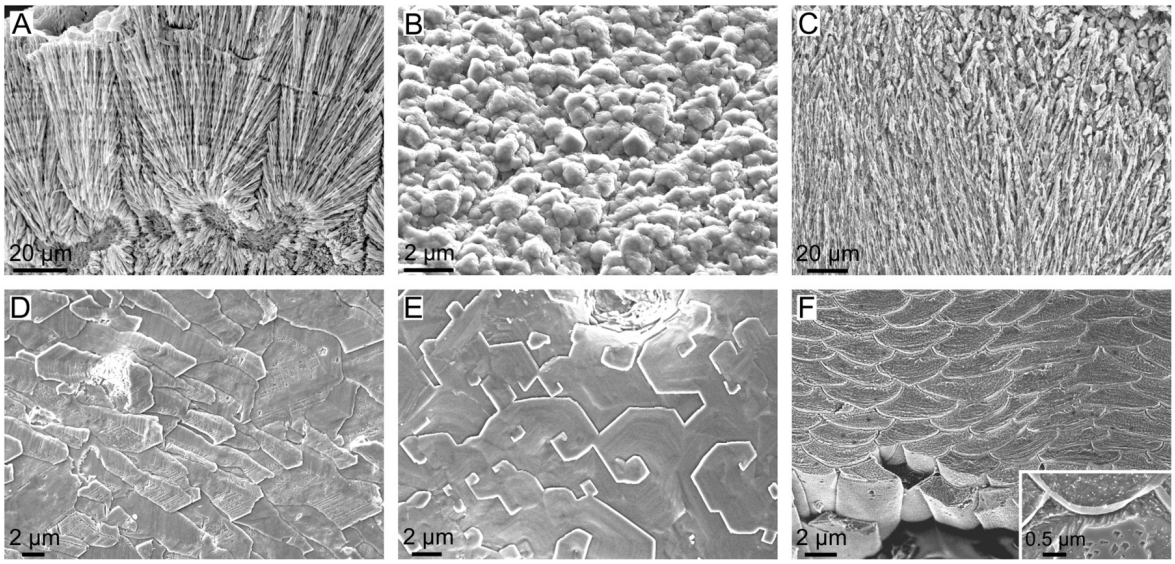

FIGURE 12 | Microstructures of calcifying invertebrates other than mollucs. **(A)** Fibrous aragonite of the scleractinian coral *Goniastrea stelligera* (etched fracture). **(B)** Calcitic granular microstructure of the balanomorph crustacean *Perforatus perforatus* (growth surface), Salobreña, Granada, Spain. **(C)** Aragonitic spherulitic prismatic structure of the serpulid polychaete *Spiraserpula caribensis* (polished and etched section), Netherlands Antilles, Curaçao. **(D)** Foliated calcite of the stenolaemata bryozoan *Fasciculipora ramosa* (growth surface), Australia. **(E)** Semi nacre of the cranioidea brachiopod *Novocrania anomala* (growth surface), Scotland. **(F)** Calcitic fibers of the secondary layer of the terebratulid brachiopod *Laqueus rubellus* (polished and etched section). Inset, close-up view of a similar fiber of the brachiopod *Terebratalia transversa*, showing the organic membranes between fibers.

and could be placed in the same position in the diagram of physical/biological determinants of **Figure 10**. The spiral growth of semi-nacre tablets is remarkable. It is similar to the spiral growth of nacre tablets of bivalves and, to a lesser extent, gastropods, which takes place when nacre tablets replicate the spiral defects previously formed in the interlamellar membranes (see subsection "The Interlamellar Membranes of Nacre"). In fact, Williams (1970) showed the existence of organic sheets, which he assumed to be proteins, between the tablets of the semi-nacre of *Novocrania anomala*. The semi-nacre sheets are thinner (∼10 nm) than the interlamellar membranes of nacre (∼30 nm), and nothing is known about their ultrastructure. In addition, spiral growth in semi-nacre affects only individual tablets (**Figure 12E**) and not big sets, as in nacre. Further ultrastructural evidence is needed in order to ascertain how the semi-nacre is organized. The only microstructure that might theoretically involve the direct action of the mantle cells is the calcitic fibrous microstructure, which constitutes the secondary layer of terebratulid brachiopods (e.g., Williams, 1997). It is made up of evenly sized and shaped, highly co-oriented calcitic fibers, each sheathed by a submicrometric organic membrane (**Figure 12F**). It also has a sharp crystallographic fiber texture (Schmahl et al., 2004). The uniform shapes of fibers and the persistent thicknesses of membranes around individual fibers imply that it is not simply a passive organic coating. The TEM sections of MacKinnon and Williams (1974) show that the mantle cells are in contact with the fibers through an extremely reduced extrapallial space, so that it is clear that they are actively producing such membranes. In view of the present evidence, the biological (cellular) control on the fabrication of this microstructure might be one of the highest among invertebrates.

FINAL REMARKS

The fabrication of microstructures is a complex process. With the increasing knowledge, it is becoming evident that molluscs can employ different strategies to fabricate different microstructures. Some of them are aimed at producing highly functional microstructures, as is the case of nacre. Why, despite its exceptional mechanical performance, nacre seems to have been losing ground in the benefit of other, less resistant microstructures, particularly the crossed lamellar, is unclear, but it has been related to the trade-off between mechanical performance and the metabolic cost of production (crossed lamellar is much cheaper to produce because of its relatively low organic content) (Palmer, 1983, 1992). But it is also possible that there is a phylogenetic aspect implied, i.e., the groups which have increased their diversity most dramatically during mollusc evolution (e.g., caenogastropods, heteroconch bivalves) are those traditionally secreting crossed lamellar layers. The demise of ammonoids at the end of the Cretaceous also dramatically reduced the diversity of nacreous cephalopods.

A particularly hot topic is the potential for marine organisms to adapt to increasing CO_2 levels and the broad implications for ocean ecosystems; both are high priorities for future research. One well-known effect is the lowering of calcium carbonate saturation states, which impacts shell-forming marine organisms

from plankton to benthic molluscs, echinoderms, and corals (e.g., Doney et al., 2009). Gazeau et al. (2013) provided a good summary of the results of studies dealing with the impacts of acidification on marine molluscs, including embryos and larvae. Many species of oysters, mussels, scallops, other bivalves, and some gastropods (including pteropods) become affected in several ways, which results in increased shell dissolution, reduced shell growth and several other physiological alterations. Particularly relevant to the topic covered in this review is a series of experimental studies (Hahn et al., 2012, 2014; Fitzer et al., 2014a,b, 2016), which have focused on microstructural changes under high pCO_2, dealing with the outer fibrous layer of two species of *Mytilus*, *M. galloprovincialis* and *M. edulis*. All of them found that the otherwise highly oriented fibers (**Figure 6A**) became locally disorganized. Subsequent EBSD analyses demonstrated that the 001 pole figures showed a bimodal or multi-modal distribution, instead of a single, low-spread maximum, typical of shells grown in normal conditions (**Figure 6B**). Accordingly, the animals exerted less crystallographic control under high-CO_2 conditions. McCoy et al. (2017) also applied EBSD to the outer calcitic fibrous layers of shells of *M. californianus* dating from the present to 2440 BP. They found evidence for consistent mineral structure in *M. californianus* over the preceding 2500 years, except for the most recent samples (from 2010 to 2015), which showed greater disorder among crystals and smaller crystal sizes. Thus, they provided historical evidence that crystallographic control diminished in coincidence with increasing ocean acidification. Regrettably, these studies do not reveal which element or elements of the fabricational system (e.g., periostracum, surface membrane, organic sheaths around fibers; see subsection "Orientation by Interaction With Organic Matrices") became altered due to increasing acidification. This knowledge is essential in studies about the impact of global climatic change on biomineralization. An additional point of interest is to estimate the correlation between the degree of physical/biological control on particular microstructures and their susceptibility to increasing acidification levels.

The knowledge of the fabricational strategies of molluscan microstructures is essential, for instance, for future biomimetic studies, which aim at using the biofabrication strategies as inspiration. As with the probability of a particular microstructure to evolve convergently, those microstructures based on physical principles (which can eventually be reproduced in the laboratory) will have a better chance to be biomimetized in the future than those in which a complex subcellular activity is an essential part of the fabrication process.

AUTHOR CONTRIBUTIONS

The author confirms being the sole contributor of this work and approved it for publication.

FUNDING

AC received funding from Project CGL2013-48247-P and CGL2017-85118-P of the Spanish Ministerio de Economía y Competitividad (MINECO) and the Fondo Europeo de Desarrollo Regional (FEDER), from the Research Group RNM363 (Consejería de Economía, Innovación, Ciencia y Empleo of the Junta de Andalucía) and from the Unidad Científica de Excelencia UCE-PP2016-05 of the University of Granada.

ACKNOWLEDGMENTS

Particular thanks are given to my friends and collaborators Julyan H. E. Cartwright (Instituto Andaluz de Ciencias de la Tierra, CSIC-Universidad de Granada, Armilla, Spain) and Elizabeth M. Harper (Department of Earth Sciences, University of Cambridge, United Kingdom) for sharing their knowledge on physical self-organization and on the diversity of molluscan microstructures. The following colleagues kindly provided images: Elizabeth M. Harper, University of Cambridge, United Kingdom (**Figure 1G**), Jalosław Stolarski, University of Warsaw, Poland (**Figure 12A**), Olev Vinn, University of Tartu, Estonia (**Figure 12C**), Erika Griesshaber, Ludwig Maximilian University, Munich, Germany (**Figure 12F**, including the inset).

REFERENCES

Addadi, L., Moradian, J., Shay, E., Maroudas, N. G., and Weiner, S. (1987). A chemical model for the cooperation of sulfates and carboxylates in calcite crystal nucleation: Relevance to biomineralization. *Proc. Natl. Acad. Sci. U.S.A.* 84, 2732–2736. doi: 10.1073/pnas.84.9.2732

Almagro, I., Drzymała, P., Berent, K., Sainz-Díaz, C. I., Willinger, M. G., Bonarski, J., et al. (2016). New crystallographic relationships in biogenic aragonite: the crossed-lamellar microstructures of mollusks. *Cryst. Growth Des.* 16, 2083–2093. doi: 10.1021/acs.cgd.5b01775

Andrienko, D. (2018). Introduction to liquid crystals. *J. Mol. Liquids* (in press). doi: 10.1016/j.molliq.2018.01.175

Appeltans, W., Ahyong, S. Y., Anderson, G., Angel, M. V., Artois, T., Bailly, N., et al. (2012). The magnitude of global marine species diversity. *Curr. Biol.* 22, 2189–2202. doi: 10.1016/j.cub.2012.09.036

Baronnet, A., Cuif, J. P., Dauphin, Y., Farre, B., and Nouet, J. (2008). Crystallization of biogenic Ca-carbonate within organo-mineral micro-domains. Structure of the calcite prisms of the Pelecypod *Pinctada margaritifera* (Mollusca) at the submicron to nanometre ranges. *Mineral. Mag.* 72, 617–626. doi: 10.1180/minmag.2008.072.2.617

Bayerlein, B., Zaslansky, P., Dauphin, Y., Rack, A., Fratzl, P., and Zlotnikov, I. (2014). Self-similar mesostructure evolution of the growing mollusc shell reminiscent of thermodynamically driven grain growth. *Nat. Mater.* 13, 1102–1107. doi: 10.1038/nmat4110

Bé, A. W. H., MacClintock, C., and Currie, D. C. (1972). Helical shell structure and growth of the pteropod *Cuvierina columnella* (Rang) (Mollusca, Gastropoda). Biomineralization. *Res. Rep.* 4, 47–79.

Belcher, A. M., Wu, X. H., Christensen, R. J., Hansma, P. K., Stucky, G. D., and Morse, D. E. (1996). Control of crystal phase switching and orientation by soluble mollusc-shell proteins. *Nature* 381, 56–58. doi: 10.1038/381056a0

Berman, A., Hanson, J., Leiserowitz, L., Koetzle, T. F., Weiner, S., and Addadi, L. (1993). Biological control of crystal texture: a widespread strategy for adapting crystal properties to function. *Science* 259, 776–779. doi: 10.1126/science.259.5096.776

Bevelander, G., and Nakahara, H. (1969). An electron microscope study of the formation of the nacreous layer in the shell of certain bivalve molluscs. *Calcif. Tissue Res.* 3, 84–92. doi: 10.1007/BF02058648

Bouligand, Y. (1972). Twisted fibrous arrangements in biological materials and cholesteric mesophases. *Tissue Cell* 4, 189–217. doi: 10.1016/S0040-8166(72)80042-9

Carter, J. G., Harries, P. J., Malchus, N., Sartori, A. F., Anderson, L. C., Bieler, R., et al. (2012). *Illustrated Glossary of the Bivalvia: Treatise Online, part N, Revised*, Vol. 1, Chap. 31. Lawrence, KS: Kansas University Paleontological Institute, 1–209.

Cartwright, J. H. E., and Checa, A. G. (2007). The dynamics of nacre self-assembly. *J. R. Soc. Interface* 4, 491–504. doi: 10.1098/rsif.2006.0188

Cartwright, J. H. E., Checa, A. G., Escribano, B., and Sainz-Díaz, C. I. (2009). Spiral and target patterns in bivalve nacre manifest a natural excitable medium from layer growth of a biological liquid crystal. *Proc. Natl. Acad. Sci. U.S.A.* 106, 10499–10504. doi: 10.1073/pnas.0900867106

Chateigner, D., Hedegaard, C., and Wenk, H. R. (2000). Mollusc shell microstructures and crystallographic textures. *J. Struct. Geol.* 22, 1723–1735. doi: 10.1016/S0191-8141(00)00088-2

Checa, A. G., Cartwright, J. H. E., Sánchez-Almazo, I., Andrade, J. P., and Ruiz-Raya, F. (2015). The cuttlefish *Sepia officinalis* (Sepiidae, Cephalopoda) constructs cuttlebone from a liquid-crystal precursor. *Sci. Rep.* 5:11513. doi: 10.1038/srep11513

Checa, A. G., Cartwright, J. H. E., and Willinger, M. G. (2009a). The key role of the surface membrane in why gastropod nacre grows in towers. *Proc. Natl. Acad. Sci. U.S.A.* 106, 38–43. doi: 10.1073/pnas.0808796106

Checa, A. G., Cartwright, J. H. E., and Willinger, M. G. (2011). Mineral bridges in nacre. *J. Struct. Biol.* 176, 330–339. doi: 10.1016/j.jsb.2011.09.011

Checa, A. G., Esteban-Delgado, F. J., and Rodríguez-Navarro, A. B. (2007). Crystallographic structure of the foliated calcite of bivalves. *J. Struct. Biol.* 157, 393–402. doi: 10.1016/j.jsb.2006.09.005

Checa, A. G., and Harper, E. M. (2010). Spikey bivalves: intra-periostracal crystal growth in anomalodesmatans. *Biol. Bull.* 219, 231–248. doi: 10.1086/BBLv219n3p231

Checa, A. G., Harper, E. M., and González-Segura, A. (2018). Structure and crystallography of foliated and chalk shell microstructures of the oyster *Magallana*: the same materials grown under different conditions. *Sci. Rep.* 8:7507. doi: 10.1038/s41598-018-25923-6

Checa, A. G., Macías-Sánchez, E., Harper, E. M., and Cartwright, J. H. E. (2016a). Organic membranes determine the pattern of the columnar prismatic layer of mollusc shells. *Proc. R. Soc. B* 283:20160032. doi: 10.1098/rspb.2016.0032

Checa, A. G., Macías-Sánchez, E., and Ramírez-Rico, J. (2016b). Biological strategy for the fabrication of highly ordered aragonite helices: the microstructure of the cavolinioidean gastropods. *Sci. Rep.* 6:25989. doi: 10.1038/srep25989

Checa, A. G., Okamoto, T., and Ramírez, J. (2006). Organisation pattern of nacre in Pteriidae (Bivalvia: Mollusca) explained by crystal competition. *Proc. R. Soc. B* 273, 1329–1337. doi: 10.1098/rspb.2005.3460

Checa, A. G., Pina, C. M., Osuna-Mascaró, A. J., Rodríguez-Navarro, A. B., and Harper, E. M. (2014a). Crystalline organization of the fibrous prismatic calcitic layer of the Mediterranean mussel *Mytilus galloprovincialis*. *Eur. J. Mineral.* 26, 495–505. doi: 10.1127/0935-1221/2014/0026-2374

Checa, A. G., Ramírez-Rico, J., González-Segura, A., and Sánchez-Navas, A. (2009b). Nacre and false nacre (foliated aragonite) in extant monoplacophorans (= Tryblidiida: Mollusca). *Naturwissenschaften* 96, 111–122. doi: 10.1007/s00114-008-0461-1

Checa, A. G., and Rodríguez-Navarro, A. (2001). Geometrical and crystallographic constraints determine the self-organization of shell microstructures in Unionidae (Bivalvia: Mollusca). *Proc. R. Soc. B* 268, 771–778. doi: 10.1098/rspb.2000.1415

Checa, A. G., Rodríguez-Navarro, A. B., and Esteban-Delgado, F. J. (2005). The nature and formation of calcitic columnar prismatic shell layers in pteriomorphian bivalves. *Biomaterials* 26, 6404–6414. doi: 10.1016/j.biomaterials.2005.04.016

Checa, A. G., and Salas, C. (2017). *Periostracum and shell formation in the Bivalvia: Treatise Online, part N, Revised*, Vol. 1, Chap. 3. Lawrence, K: Kansas University Paleontological Institute, 1–51.

Checa, A. G., Salas, C., Harper, E. M., and Bueno-Pérez, J. D. (2014b). Early stage biomineralization in the periostracum of the 'living fossil' bivalve *Neotrigonia*. *PLoS One* 9:e90033. doi: 10.1371/journal.pone.0090033

Checa, A. G., Sánchez-Navas, A., and Rodríguez-Navarro, A. B. (2009c). Crystal growth in the foliated aragonite of monoplacophorans (Mollusca). *Cryst. Growth Des.* 9, 4574–4580. doi: 10.1021/cg9005949

Crenshaw, M. A. (1972). The inorganic composition of molluscan extrapallial fluid. *Biol. Bull.* 143, 506–512. doi: 10.2307/1540180

Cuif, J. P., Dauphin, Y., and Sorauf, J. E. (2011). *Biominerals and Fossils through Time*. Cambridge: Cambridge University Press.

Cusack, M., and Freer, A. (2008). Biomineralization: elemental and organic influence in carbonate systems. *Chem. Rev.* 108, 4433–4454. doi: 10.1021/cr078270o

Doney, S. C., Fabry, V. J., Feely, R. A., and Kleypas, J. A. (2009). Ocean acidification: the other CO_2 problem. *Annu. Rev. Mar. Sci.* 1, 169–192. doi: 10.1146/annurev.marine.010908.163834

Falini, G., Albeck, S., Weiner, S., and Addadi, L. (1996). Control of aragonite or calcite polymorphism by mollusk shell macromolecules. *Science* 271, 67–69. doi: 10.1126/science.271.5245.67

Fitzer, S. C., Chung, P., Maccherozzi, F., Dhesi, S. S., Kamenos, N. A., Phoenix, V. R., et al. (2016). Biomineral shell formation under ocean acidification: a shift from order to chaos. *Sci. Rep.* 6:21076. doi: 10.1038/srep21076

Fitzer, S. C., Cusack, M., Phoenix, V. R., and Kamenos, N. A. (2014a). Ocean acidification reduces the crystallographic control in juvenile mussel shells. *J. Struct. Biol.* 188, 39–45. doi: 10.1016/j.jsb.2014.08.007

Fitzer, S. C., Phoenix, V. R., Cusack, M., and Kamenos, N. A. (2014b). Ocean acidification impacts mussel control on biomineralisation. *Sci. Rep.* 4:6218. doi: 10.1038/srep06218

Gazeau, F., Parker, L. M., Comeau, S., Gattuso, J.-P., O'Connor, W. A., Martin, S., et al. (2013). Impacts of ocean acidification on marine shelled molluscs. *Mar. Biol.* 160, 2207–2245. doi: 10.1007/s00227-013-2219-3

Gower, L. B. (2008). Biomimetic model systems for investigating the amorphous precursor pathway and its role in biomineralization. *Chem. Rev.* 108, 4551–4627. doi: 10.1021/cr800443h

Hahn, S., Griesshaber, E., Schmahl, W. W., Neuser, R. D., Ritter, A.-C., Hoffmann, R., et al. (2014). Exploring aberrant bivalve shell ultrastructure and geochemistry as proxies for past sea water acidification. *Sedimentology* 61, 1625–1658. doi: 10.1111/sed.12107

Hahn, S., Rodolfo-Metalpa, R., Griesshaber, E., Schmahl, W. W., Buhl, D., Hall-Spencer, J. M., et al. (2012). Marine bivalve shell geochemistry and ultrastructure from modern low pH environments: environmental effect versus experimental bias. *Biogeoscience* 9, 1897–1914. doi: 10.5194/bg-9-1897-2012

Hare, P. E., and Abelson, P. H. (1965). Amino acid composition of some calcified proteins. *Carnegie Inst. Washington Year Book* 64, 223–232.

Harper, E. M., and Checa, A. G. (2017). Physical versus biological control in bivalve calcite prisms: comparison of euheterodonts and pteriomorphs. *Biol. Bull.* 232, 19–29. doi: 10.1086/691382

Harper, E. M., Checa, A. G., and Rodríguez-Navarro, A. B. (2009). Organization and mode of secretion of the granular prismatic microstructure of *Entodesma navicula* (Bivalvia: Mollusca). *Acta Zool.* 90, 132–141. doi: 10.1111/j.1463-6395.2008.00338.x

Hedegaard, C., and Wenk, H.-R. (1998). Microstructure and texture patterns of mollusc shells. *J. Molluscan Stud.* 64, 133–136. doi: 10.1093/mollus/64.1.133

Kobayashi, S. (1964b). Studies in shell formation. X. A study of the proteins of the extrapallial fluid in some molluscan species. *Biol. Bull.* 126, 414–422. doi: 10.2307/1539310

Kobayashi, S. (1964a). Calcification in fish and shellfish. II. A paper electrophoretic study on the acid mucopolysaccharides and PAS-positive materials of the extrapallial fluid in some molluscan species. *Bull. Jpn. Soc. Sci. Fish.* 30, 893–907. doi: 10.2331/suisan.30.893

Korringa, P. (1951). On the nature and function of "chalky" deposits in the shell of *Ostrea edulis* Linnaeus. *Proc. Calif. Acad. Sci.* 27, 133–158.

Levi-Kalisman, Y., Falini, G., Addadi, L., and Weiner, S. (2001). Structure of the nacreous organic matrix of a bivalve mollusk shell examined in the hydrated state using cryo-TEM. *J. Struct. Biol.* 135, 8–17. doi: 10.1006/jsbi.2001.4372

Lowenstam, H. A. (1981). Minerals formed by organisms. *Science* 211, 1126–1131. doi: 10.1126/science.7008198

Lowenstam, H. A., and Weiner, S. (1989). *On Biomineralization*. New York, NY: Oxford University Press.

Ma, H. Y., and Lee, I. S. (2006). Characterization of vaterite in low quality freshwater-cultured pearls. *Mater. Sci. Eng. C* 26, 721–723. doi: 10.1016/j.msec.2005.09.109

Macías-Sánchez, E., Willinger, M. G., Pina, C. M., and Checa, A. G. (2017). Transformation of ACC into aragonite and the origin of the nanogranular structure of nacre. *Sci. Rep.* 7:12728. doi: 10.1038/s41598-017-12673-0

MacKinnon, D. I., and Williams, A. (1974). Shell structure of terebratulid brachiopods. *Palaeontology* 17, 179–202.

Mann, S. (1983). Mineralization in biological systems. *Struct. Bonding* 54, 125–174. doi: 10.1007/BFb0111316

Marin, F., Luquet, G., Marie, B., and Medakovic, D. (2008). Molluscan shell proteins: primary structure, origin, and evolution. *Curr. Top. Dev. Biol.* 80, 209–276. doi: 10.1016/S0070-2153(07)80006-8

McCoy, S. J., Kamenos, N. A., Chung, P., Wootton, T. J., and Pfister, C. A. (2017). A mineralogical record of ocean change: decadal and centennial patterns in the California mussel. *Global Change Biol.* 24, 2554–2562. doi: 10.1111/gcb.14013

Misogianes, M. J., and Chasteen, N. D. (1979). A chemical and spectral characterization of the extrapallial fluid of *Mytilus edulis*. *Anal. Biochem.* 100, 324–334. doi: 10.1016/0003-2697(79)90236-7

Moysiuk, J., Smith, M. R., and Caron, J. B. (2017). Hyoliths are Palaeozoic lophophorates. *Nature* 541, 394–397. doi: 10.1038/nature20804

Mullins, W. W. (1956). Two-dimensional motion of idealized grain boundaries. *J. Appl. Phys.* 27, 900–904. doi: 10.1063/1.1722511

Nakahara, H. (1991). "Nacre formation in bivalve and gastropod mollusks," in *Mechanisms and Phylogeny of Mineralization in Biological Systems*, eds S. Suga and H. Nakahara (Berlin: Springer), 343–350. doi: 10.1007/978-4-431-68132-8_55

Nakahara, H., and Bevelander, G. (1971). The formation and growth of the prismatic layer of *Pinctada radiata*. *Calcif. Tissue Res.* 7, 31–45. doi: 10.1007/BF02062591

Nassif, N., Pinna, N., Gehrke, N., Antonietti, M., Jäger, C., and Cölfen, H. (2005). Amorphous layer around aragonite platelets in nacre. *Proc. Natl. Acad. Sci. U.S.A.* 102, 12653–12655. doi: 10.1073/pnas.0502577102

Nehrke, G., Poigner, H., Wilhelms-Dick, D., Brey, T., and Abele, D. (2012). Coexistence of three calcium carbonate polymorphs in the shell of the Antarctic clam *Laternula elliptica*. *Geochem. Geophys. Geosyst.* 13:Q05014. doi: 10.1029/2011GC003996

Neville, A. C. (1993). *Biology of Fibrous Composites*. Cambridge: Cambridge University Press. doi: 10.1017/CBO9780511601101

Nothdurft, L. D., and Webb, G. E. (2007). Microstructure of common reef-building coral genera *Acropora*, *Pocillopora*, *Goniastrea* and *Porites*: constraints on spatial resolution in geochemical sampling. *Facies* 53, 1–26. doi: 10.1007/s10347-006-0090-0

Nudelman, F., Chen, H. H., Goldberg, H. A., Weiner, S., and Addadi, L. (2007). Lessons from biomineralization: comparing the growth strategies of mollusc shell prismatic and nacreous layers in *Atrina rigida*. *Faraday Discuss.* 136, 9–25. doi: 10.1039/B704418F

Osuna-Mascaró, A. J., Cruz-Bustos, T., Marin, F., and Checa, A. G. (2015). Ultrastructure of the interlamellar membranes of the nacre of the bivalve *Pteria hirundo*, determined by immunolabelling. *PLoS One* 10:e0122934. doi: 10.1371/journal.pone.0122934

Palmer, A. R. (1983). Relative cost of producing skeletal organic matrix versus calcification: evidence from marine mollusks. *Mar. Biol.* 75, 287–292. doi: 10.1007/BF00406014

Palmer, A. R. (1992). Calcification in marine molluscs: how costly is it? *Proc. Natl. Acad. Sci. U.S.A.* 89, 1379–1382. doi: 10.1073/pnas.89.4.1379

Pereira-Mouriès, L., Almeida, M. J., Ribeiro, C., Peduzzi, J., Barthélemy, M., Milet, C., et al. (2002). Soluble silk-like organic matrix in the nacreous layer of the bivalve *Pinctada maxima*. A new insight in the biomineralization field. *Eur. J. Biochem.* 269, 4994–5003. doi: 10.1046/j.1432-1033.2002.03203.x

Pietrzak, J. E., Bates, J. M., and Scott, R. M. (1973). Constituents of unionid extrapallial fluid. I. Electrophoretic and immunological studies of protein components. *Biol. Bull.* 144, 391–399. doi: 10.2307/1540016

Schäffer, T. E., Ionescu-Zanetti, C., Proksch, R., Fritz, M., Walters, D. A., Almquist, N., et al. (1997). Does abalone nacre form by heteroepitaxial nucleation or by growth through mineral bridges? *Chem. Mater.* 9, 1731–1740. doi: 10.1021/cm960429i

Schenk, A. S., Zope, H., Kim, Y. Y., Kros, A., Sommerdijk, N. A. J. M., and Meldrum, F. C. (2012). Polymer-induced liquid precursor (PILP) phases of calcium carbonate formed in the presence of synthetic acidic polypeptides—relevance to biomineralization. *Faraday Discuss.* 159, 327–344. doi: 10.1039/c2fd20063e

Schmahl, W. W., Griesshaber, E., Neuser, R., Lenze, A., Job, R., and Brand, U. (2004). The microstructure of the fibrous layer of terebratulide brachiopod shell calcite. *Eur. J. Mineral.* 16, 693–697. doi: 10.1127/0935-1221/2004/0016-0693

Spann, N., Harper, E. M., and Aldridge, D. C. (2010). The unusual mineral vaterite in shells of the freshwater bivalve *Corbicula fluminea* from the UK. *Naturwissenschaften* 97, 743–751. doi: 10.1007/s00114-010-0692-9

Stevens, K., Griesshaber, E., Schmahl, W., Casella, L. A., Iba, Y., and Mutterlose, J. (2017). Belemnite biomineralization, development, and geochemistry: the complex rostrum of *Neohibolites minimus*. *Palaeogeogr. Palaeoclimatol. Palaeoecol.* 468, 388–402. doi: 10.1016/j.palaeo.2016.12.022

Taylor, J. D., Glover, E. A., and Braithwaite, C. J. R. (1999). Bivalves with 'concrete overcoats': *Granicorium* and *Samarangia*. *Acta Zool.* 80, 285–300. doi: 10.1046/j.1463-6395.1999.00019.x

Taylor, P. D., Lombardi, C., and Cocito, S. (2015). Biomineralization in bryozoans: present, past and future. *Biol. Rev.* 90, 1118–1150. doi: 10.1111/brv.12148

Taylor, P. D., and Weedon, M. J. (2000). Skeletal ultrastructure and phylogeny of cyclostome bryozoans. *Zool. J. Linn. Soc.* 128, 337–399. doi: 10.1006/zjls.1999.0195

Ubukata, T. (1994). Architectural constraints of the morphogenesis of prismatic structures in Bivalvia. *Palaeontology* 37, 241–261.

Vendrasco, M. J., Checa, A. G., and Kouchinsky, A. V. (2011). Shell microstructure of the early bivalve *Pojetaia* and the independent origin of nacre within the mollusca. *Palaeontology* 54, 825–850. doi: 10.1111/j.1475-4983.2011.01056.x

Vinn, O. (2013). Occurrence, formation and function of organic sheets in the mineral tube structures of Serpulidae (Polychaeta, Annelida). *PLoS One* 8:e75330. doi: 10.1371/journal.pone.0075330.g001

Vinn, O., and Mutvei, H. (2009). Calcareous tubeworms of the Phanerozoic. *Estonian J. Earth Sci.* 58, 286–296. doi: 10.3176/earth.2009.4.07

Vinn, O., Ten Hobe, H. A., Mutvei, H., and Kirsimäe, K. (2008). Ultrastructure and mineral composition of serpulid tubes (Polychaeta, Annelida). *Zool. J. Linn. Soc.* 154, 633–650. doi: 10.1111/j.1096-3642.2008.00421.x

von Neumann, J. (1952). "Written discussion on a paper of C. S. Smith," in *Metal Interfaces*, ed. C. Herring (Cleveland, OH: American Society of Metals), 108–110.

Wada, K., and Fujinuki, T. (1976). "Biomineralization in bivalve molluscs with emphasis on the chemical composition of the extrapallial fluid," in *Mechanisms of Mineralization in the Invertebrates and Plants*, eds N. Watabe and K. M. Wilbur (Columbia, SC: University of South Carolina Press), 175–190.

Wehrmeister, U., Jacob, D. E., Soldati, A. L., Häger, T., and Hofmeister, W. (2007). Vaterite in freshwater cultured pearls from China and Japan. *J. Gemmol.* 31, 269–276. doi: 10.15506/JoG.2007.30.7.399

Weiner, S., and Addadi, L. (1997). Design strategies in mineralized biological materials. *J. Mater. Chem.* 7, 689–702. doi: 10.1039/A604512J

Weiner, S., and Dove, P. M. (2003). An overview of biomineralization processes and the problem of the vital effect. *Rev. Mineral. Geochem.* 54, 1–29. doi: 10.2113/0540001

Weiner, S., and Traub, W. (1980). X-ray diffraction study of the insoluble organic matrix of mollusk shells. *FEBS Lett.* 111, 311–316. doi: 10.1016/0014-5793(80)80817-9

Weiner, S., and Traub, W. (1984). Macromolecules in mollusk shells and their functions in biomineralization. *Phil. Trans. R. Soc. B* 304, 425–434. doi: 10.1098/rstb.1984.0036

Wendt, J. (1990). "Corals and coralline sponges," in *Skeletal Biomineralization: Patterns, Processes and Evolutionary Trends*, Vol. 1, ed. J. G. Carter (New York, NY: Van Nostrand Reinhold), 45–66.

Wilbur, K. M., and Saleuddin, A. S. M. (1983). "Shell formation," in *The Mollusca*, Vol. 4, Part 1, eds A. S. M. Saleuddin and K. M. Wilbur (New York, NY: Academic Press), 235–287.

Wilbur, K. M., and Simkiss, K. (1968). "Calcified shells," in *Comprehensive Biochemistry*, Vol. 26A, eds M. Florkin and E. H. Stotz (New York, NY: Elsevier), 229–295.

Williams, A. (1970). Spiral growth of the laminar shell of the brachiopod *Crania*. *Calcif. Tissue Res.* 6, 11–19. doi: 10.1007/BF02196180

Williams, A. (1990). "Biomineralization in the lophophorates," in *Skeletal Biomineralization: Patterns, Processes and Evolutionary Trends*, Vol. 1, ed. J. G. Carter (New York, NY: Van Nostrand Reinhold), 67–82.

Williams, A. (1997). "Shell structures," in *Treatise on Invertebrate Paleontology, Part H, Brachiopoda Revised*, eds A. Williams, C. H. C. Brunton, and S. J. Carlson (Lawrence, K: University Press of Kansas), 267–320.

Willinger, M. G., Checa, A. G., Bonarski, J. T., Faryna, M., and Berent, K. (2016). Biogenic crystallographically continuous aragonite helices: the microstructure of the planktonic gastropod *Cuvierina*. *Adv. Funct. Mater.* 26, 553–561. doi: 10.1002/adfm.201504034

Conflict of Interest Statement: The author declares that the research was conducted in the absence of any commercial or financial relationships that could be construed as a potential conflict of interest.

frontiers in Marine Science

ORIGINAL RESEARCH
published: 03 October 2018
doi: 10.3389/fmars.2018.00347

Chitin Facilitated Mineralization in the Eastern Oyster

Vera Bin San Chan, Mary Beth Johnstone, A. P. Wheeler and Andrew S. Mount**

Department of Biological Sciences, Clemson University, Clemson, SC, United States

Chitin is often reported in molluscan shells, where it likely contributes to the mechanical strength of the biomineral. However, the role of this polysaccharide in relation to the process of shell formation is not well understood. We investigated the deposition of chitin during shell repair in the Eastern oyster, *Crassostrea virginica*, by inserting stainless steel and glass implants in a region of shell damage. This work documents the time course of deposition of both chitin fibrils and calcium carbonate layers. Chitin was detected by confocal laser scanning microscopy (CLSM) using a chitin-specific fluorescent probe that was produced from clones of a chitin-binding domain. The presence of fibrils was confirmed using electron microscopy of implants. The fibrils' dimensions were reduced after treatment with both acid and bleach, suggesting that chitin interacts with inorganic minerals and other organic components such as proteins and lipids as early as 5 h after shell damage. With CLSM, it was shown that chitin co-localized with the cell membrane, suggesting the importance of cells located on the implants in the process of fibril formation. Using observations from this study as well as those from the literature on chitin synthase production, we propose two cellular models for chitin deposition related to shell formation.

Keywords: biomineralization, chitin, oyster, chitin-binding domain, hemocytes, *Crassostrea*, shell formation, shell repair

OPEN ACCESS

Edited by:
Pei-Yuan Qian,
The Hong Kong University of Science and Technology, Hong Kong

Reviewed by:
Gary H. Dickinson,
The College of New Jersey, United States
Ting Xu,
Hong Kong Baptist University, Hong Kong

****Correspondence:***
Vera Bin San Chan
vbschan@g.clemson.edu
Andrew S. Mount
mount@clemson.edu

Specialty section:
This article was submitted to Marine Molecular Biology and Ecology, a section of the journal Frontiers in Marine Science

Received: *17 April 2018*
Accepted: *07 September 2018*
Published: *03 October 2018*

Citation:
Chan VBS, Johnstone MB, Wheeler AP and Mount AS (2018) Chitin Facilitated Mineralization in the Eastern Oyster. Front. Mar. Sci. 5:347. doi: 10.3389/fmars.2018.00347

INTRODUCTION

Chitin is the second most abundant naturally occurring polysaccharide after cellulose (Kumar, 2000; Cohen, 2010), and this biopolymer is also a subject of major interest in material science (Merzendorfer and Zimoch, 2003). It has a crystalline structure made up of straight chain polysaccharides and is typically used by organisms for structural support (Stern and Jedrzejas, 2008). There are three allomorphic forms of chitin described in the literature, designated α-, ß-, and γ- chitin (Carlström, 1957; Kaya et al., 2017). The more commonly known allomorphs are α- and ß-chitin, which are differentiated based on the relative position of the constituent microfibril units. α-chitin is the more stable structure because it contains alternating chains, a configuration that enhances the number of intermolecular hydrogen bonds between the polysaccharide chains. The α- polymorph is found in crustacean and insect cuticles and the cell walls of yeast and other fungi. On the other hand, ß-chitin, with a parallel arrangement of chains, has fewer inter-chain hydrogen bonds. The ß-form is commonly hydrated and associated with proteins, such as in the cell walls of diatoms, and the internal skeleton of cephalopods (Carlström, 1957; Brunner et al., 2009). Kaya et al. (2017) characterized γ-chitin extracted from the cocoon of a moth and the stomach of a squid and concluded that this rarer form of chitin is structurally more similar to α- than ß-chitin.

Chitin is broadly distributed in the shells of mollusks where it constitutes 3.5 wt% of the insoluble organic components of calcified shell layers and their outermost organic covering layer, the periostracum (Galtsoff, 1964; Peters, 1972; Goffinet and Jeuniaux, 1979; Heinemann, 2008). Peters (1972) observed the presence of microfibrils in the shell, which he interpreted as chitin because of the fibers' resistance to treatments with alkaline hydroxides and dilute acids (Goffinet and Jeuniaux, 1979). Using X-ray diffraction, Weiner and Traub (1980) concluded that the insoluble extracellular matrix of nacre from some species contained ß-chitin. However, the prominence of chitin was not uniform among the species and mineral microstructures they examined, and its presence was especially ambiguous in the foliated layers of *Crassostrea irridescens* and *Crassostrea gigas* (alternatively known as *Magallana gigas*). A chitin-rich membrane between the myostracum and foliated shell layer appears to define the boundary of the two crystal polymorphs at the adductor muscle scar of *C. gigas* (Lee and Choi, 2007).

While chitin plays a role in increasing the strength and resilience of many structures, including perhaps mineralized shell layers (Heredia et al., 2007), the toughness of the molluscan shell has most typically been associated with the extracellular matrix proteins which are interspersed between layers of micro- to nano-sized crystals thus forming a bio ceramic (Currey, 1999). Some of these proteins have also been repeatedly associated with the formation of different crystal morphologies (Gotliv et al., 2003). The presence of chitin-binding domains in matrix proteins suggests that chitin is a protein-anchoring material and may thereby play a role through matrix proteins both in the mechanical properties of the shell as well as in mineral formation. For example, Pif 177, a shell matrix protein from the inner aragonitic nacreous layer of the pearl oyster, *Pinctada fucata*, is cleaved post-translationally into Pif 80 and Pif 97. While Pif 80 binds aragonitic crystals and mediates their growth orientation, Pif 97 binds chitin (Suzuki et al., 2009, 2016). Chitin-binding domains have been identified in both the organic periostracal covering and outer prismatic layer of the shell of *P. fucata* as well (Suzuki et al., 2007; Nakayama et al., 2013). A homolog of Pif 177, which contained the chitin-binding cleavage product Pif 97 only, was cloned from the mantle of the oyster, *C. gigas*, and was found to be selectively expressed in the mantle (Wang et al., 2013). These findings suggest that the gene plays an important role in calcitic foliated shell similar to that of the homologs in the nacre of *Pinctada*. In fact, when these workers injected siRNA of Pif 97 into the adductor muscle of the animal, the structure of the foliar laths became thinner and narrower. In earlier studies, Falini et al. (1996) demonstrated that soluble proteins isolated from the molluscan shell were able to control the mineralogy of calcium carbonate *in vitro* when absorbed to chitin and silk protein. Using cryo-transmission electron microscopy (TEM), Levi-Kalisman et al. (2001) demonstrated the presence of chitin in the extracellular matrix between layers of nacre (interlamellar sheets) of *Atrina rigida* and proposed a model, based also on *in vitro* assemblages of protein and chitin, in which chitin was the principal organizing element of these sheets. This model was reinforced by Nudelman et al. (2008) using environmental and cryo-scanning electron microscopy (SEM) of chitinase and protease treated samples of nacre from two species.

The presence of chitin synthase in mineralizing tissue also indicates the potential significance of chitin in shell formation. For example, Suzuki et al. (2007) cloned a cDNA from mantle and demonstrated its expression in this tissue. Zhang et al. (2012) demonstrated that the enzyme transcript was highly expressed during early stages of *C. gigas* development when larval shell formation occurs, and, among all tissues, it was almost exclusively expressed in the mantle of adult oysters. Furthermore, *in vivo* partial inhibition of chitin synthase of developing *Mytilus galloprovincialis* larvae resulted in structurally and likely functionally abnormal larval shells (Schönitzer and Weiss, 2007). Molluscan chitin synthase has a unique myosin domain structure (Weiss, 2012), suggesting that the mechanism of chitin synthesis is very different from the better-studied taxonomic groups, such as yeast and fungi (Cohen, 2010).

In other systems, the biological role of chitin has been expanded beyond that of a structural molecule to include its involvement in various biological cascades (Hasegawa et al., 2001; Ichinohe et al., 2007; Di Rosa et al., 2016). When combined with various chitin-binding properties of proteins, chitin has the potential to be a spatial framework for biological functions, which may include cell-to-cell recognition and oxidative stress protection (Wang et al., 2012), actin bundling and organization (Öztürk-Çolak et al., 2016), and various innate immune responses (Lee et al., 2011), including apoptosis and necrosis (Jeon et al., 2012). Molluscan shell repair is known to begin with cell-driven inflammation and wound-healing responses at the shell margin mediated by the nervous system and hemocytes (Liu et al., 2017). Considering these examples of biological processes that are influenced by chitin, it is plausible that chitin may interact with cells and tissues as part of the cellular responses during mineral formation.

An important step in determining the role of chitin in shell formation is to understand its cellular origins and delivery to the mineralization front. Processes involved in shell formation of the Eastern oyster, *Crassostrea virginica*, have been successfully observed by the authors using a patented method for inducing shell repair (Mount et al., 2013, 2016; Johnstone et al., 2015). By inserting sterile metal implants between the mantle margin and the shell near the adductor muscle, adherence of granulocytic hemocytes containing 100 nm-sized crystals and deposition of prismatic and foliated layers was effectively observed within hours (Johnstone et al., 2015). In these studies, the outer mantle epithelium (OME), which is the closest to the shell inner surface, serves as a source of extracellular matrices and appears to introduce the junctional boundaries for the prismatic and foliated minerals (Johnstone et al., 2015). Because of their involvement in the production of other components of regenerating shell, hemocytes and OME are likely sources of chitin in this process as well.

Using the same method in this study, we followed the temporal changes of chitin deposition during shell regeneration in the Eastern oyster, employing a correlative microscopy approach. To specifically identify chitin at the mineralization front, we applied confocal laser scanning microscopy (CLSM) to detect

a fluorescent conjugated chitin-binding domain produced in *Escherichia coli* using a circular plasmid vector. Counter staining of nuclei and membrane structures was used to uncover the relationship of adhering hemocytes to chitin-rich areas. To observe structural changes in chitin during the regeneration process, SEM was used to observe the ultrastructure of materials deposited on the implants. At high resolution, the interaction of putative chitin structures with other components was determined by treatment with acid to remove calcium carbonate and treatment with bleach to remove proteins and lipids. By using the Eastern oyster *C. virginica* as a model, the overall aim of this study was to examine the presence of chitin in the early stages of shell repair and its interaction with minerals and other molecules as well as with hemocytes.

MATERIALS AND METHODS

Animal Collection and Maintenance

Wild Eastern oysters, *C. virginica*, were obtained from their natural habitats and were immediately transferred via overnight shipping to the Okeanos Research Laboratory at Clemson University. The animals used for stainless steel implant experiments were obtained from Louisiana[1] in October 2015, while animals used for coverslip glass implant experiments were obtained from the Baruch Marine Field Lab, South Carolina in March 2018.

Upon arrival of each collection, 60–100 oysters were brushed to remove any adhering macrofauna and were submerged in an aerated holding tank which contained 680 L of artificial seawater (Red Sea salt mix, United States) maintained at 24 ppt salinity and 18°C. The water of the tank was recirculated through two cartridge containing cotton string-wound filters to remove particulates and one cartridge containing biological media to remove ammonia and nitrate waste. For the 2018 collection, a more advanced water treatment system was installed, including a 50 L sump, a sock filter, a protein skimmer, and a moving-bed Bio-reactor (Bashsea, United States). Ammonia and nitrate levels in the tanks for both experiments were monitored every other day using commercially available aquarium test solutions (Aquarium Pharmaceuticals, API). If these levels exceeded 0.25 ppm, the water was changed. The filtration system was bypassed during feeding hours which lasted 4–6 h per day, 5 days a week. The animals were fed *ad libitum* with a mix of six marine microalgae–*Isochrysis* sp., *Pavlova* sp., *Tetraselmis* sp., *Chaetoceros calcitrans*, *Thalassiosira weissflogii*, and *Thalassiosira pseudonana* (Shellfish Diet 1800, Reed Mariculture). Oysters were used within a month of collection.

Preparation of Materials for Implantation

Two types of implantation materials were prepared for microscopic observation of shell regeneration processes. In experiment 1, 1 cm × 1 cm × 1 mm polished stainless steel foil was applied for an improved conductivity during SEM. In experiment 2, circular glass cover slips (#1.5) were applied for CLSM. Before the experiments, all implant materials were cleaned to remove organic deposits (sequentially, methanol, 5 min; acetone, 5 min; isopropyl alcohol, 5 min; and ethanol, 5 min) prior to autoclave sterilization and air-drying.

[1]bonsecourfisheries.com

Shell Regeneration Protocol

Shell repairing events were observed using an implantation procedure described in previous studies (Johnstone et al., 2015), and in United States Patents 8,541,031 and 9,371,451 (Mount et al., 2013, 2016). Briefly, the posterior margin adjacent to the adductor muscles of the oysters (length, 7.5–8.5 cm) were carefully cut with a cement saw to allow an approximately 1 cm opening to the extrapallial cavity where the implants were introduced. Then, rubber bands were wrapped around the oysters, covering the opening. The tightness of the rubber bands was adjusted by wrapping around the oysters 1–2 times, in order to prevent the implants from being rejected and yet allow normal opening of the valve and mantle activity during shell repair. Stainless steel implants (experiment 1) were collected at 5, 15, and 27 h and 6 days of incubation and glass coverslip implants (experiment 2) were collected at 5, 18, and 27 h of incubation. These time points were selected to optimize the capture of cellular activities (5, 15, and 27 h) on CLSM and mineral ultrastructures (27 h and 6 days) on the SEM. Oysters were kept in the same tank but not fed during the implantation experiment to avoid accumulation of dead algal cells on the implants which would compromise these observation. Foliated mineral is commonly deposited at the 6 days time point. After incubation, the implants were retrieved from the opening using a tweezer when possible. When necessary, the shell valves were separated by cutting through the adductor muscles with a shucking knife on the anterior side of the shell to minimize the introduction of shell fragments to the implant surfaces.

Preparation of Chitin-Binding Domain From Engineered Bacteria

To localize the presence of chitin during shell repair, a SNAP-conjugated chitin-binding domain (SNAP-CBD) fusion protein was produced by incubation and inoculation. A stab culture of *E. coli* transfected with the plasmid vector pYZ205 hosted by NEB T7 Express cells was obtained from Yinghua Zhang (New England Biolabs). The expression of plasmid pYZ205 produces a conserved chitin binding domain originating from the bacteria *Bacillus circulans* (superfamily cluster cl00046; NCBI). The domain has the following amino acid sequence: AWQVNTAYTAGQLVTYNGKTYKCLQP HTSLAGWEPSNVPALWQLQ. In addition to the chitin-binding domain, the construct has a polyhistidine site for protein purification, and a conjugation site with a SNAP fluorescent probe (Tang et al., 2015). The workflow of preparing a probe for fluorescent chitin detection includes (1) isolating a single colony of transfected *E. coli* and inducing expression of SNAP-CBD, (2) extraction and purification of SNAP-CBD, and (3) conjugating SNAP-CBD with a SNAP reactive fluorescent probe. A SNAP site on the CBD allows the use of a great variety of fluorescent

probes. Here, we have made CBD-546 from SNAP-Surface Alexa Fluor 546 (New England Biolabs).

Determination of Specificity for Chitin Probes

Treatment of hemocytes with chitinase was used to test the specificity of the CBD signals (Heath-Heckman and McFall-Ngai, 2011). Hemocytes were drawn at 24 h after shell damage using the same oysters which were incubated with implants for the 5 and 18 h time points. The hemolymph from four oysters was spread on different glass coverslips and the hemocytes were allowed to aggregate for 20 min before fixation. Fixation of hemocytes was performed with 4% paraformaldehyde buffered in PBS for 20 min. Fixed hemocytes were washed twice with 0.4% Triton X-100 for 15 min and then permeabilized with phosphate buffered saline at pH 6.0 (PBS) with 0.4% Triton X-100 for 1 h. The permeabilized samples were washed three times with PBS at room temperature, with the duration of each wash being 15 min. Permeabilized hemocytes were exposed to three different conditions for 0.5 h at 37°C: (1) PBS; (2) PBS containing 0.25 mg/mL each of two chitinases one from *Streptomyces griseus* (Sigma-Aldrich) and one from *Trichoderma viride* (Sigma-Aldrich) (T); and (3) PBS containing heat-inactivated chitinases (inactivated at 75°C for 20 min) (HT).

The treatment time of 0.5 h at 37°C was chosen according to a trial study in which 1 and 2 h of chitinase treatment resulted in the disaggregation of the hemocytes and a major loss of cells for sampling. At the end of incubation, hemocytes were washed three times for 10 min with PBS and were labeled with SNAP-546 and 4',6-diamidino-2-phenylindole (DAPI) as described for the glass implants. Each hemocyte sample was observed using a z-stack image from three random regions. The mean values of intensity (range from 0 to 255) from 10 areas around a cell nuclei were measured with point measurement tools from the maximum projection image using ImageJ Fiji (Schindelin et al., 2012).

CLSM Observation of Implants

One circular glass implant from each of three oysters at each time point was either unstained, stained only with the chitin probe, or triple-stained for chitin, nuclei and membranes. After fixation in 4% paraformaldehyde buffered with 0.1 M cacodylate trihydrate at pH 8.0 for 1 h, the implants were washed in a solution of 0.1 M cacodylate trihydrate buffer at pH 8.0 and 0.4% Triton X-100 detergent three times for 10 min, and then for 2 h to increase the permeability of the adherent cells. The implants were then washed with 0.1 M cacodylate trihydrate buffer, pH 8.0, three times for 10 min, and subsequently with freshly made 1 mg/mL sodium borohydride in cacodylate trihydrate buffer at pH 8.0, three times for 5 min to quench autofluorescence from fixation. They were then washed with 0.1 M cacodylate trihydrate buffer, pH 8.0, three times for 5 min prior to washing and incubating with blocking buffer (PBS with 1% BSA) for 1 h at room temperature. The implants were labeled with CBD-546, at a 1:10 dilution of CBD-546 in 1% BSA PBS overnight at 4°C. In addition, implants were counterstained for nuclei with 1 μg/mL DAPI for 30 min and for cell membranes with 5 μg/mL CellMask Deep Red plasma membrane stain (Thermo Fisher Scientific) for 30 min. Prior to CLSM, all implants were washed three times with PBS, for 15 min between and after staining procedures. Following the final wash they were mounted on microscope slides with liquid mountant (ProLong Gold,

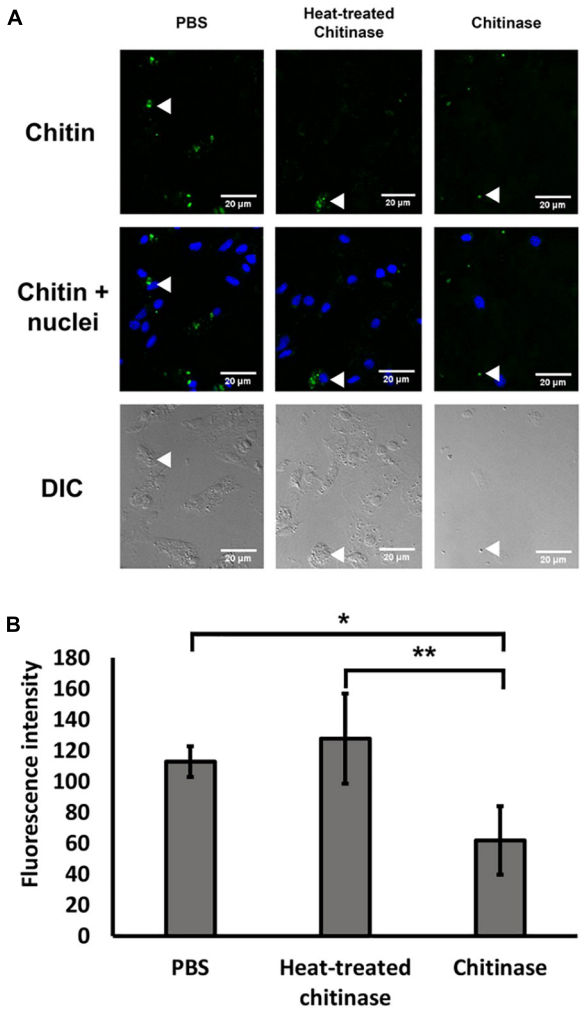

FIGURE 1 | Specific detection of chitin by Alexa 546-labeled chitin-binding domain (CBD-546) in oyster hemocytes as demonstrated by chitinase digestion. **(A)** CLSM micrographs reveal that enzymatic digestion of chitin results in a reduction of fluorescence after treatment with chitinase, representative areas of the hemocytes by are quantified for comparison (white arrows). In this panel, fixed oyster hemocytes were treated with phosphate buffered saline (PBS) as a control (left column), or treated with heat inactivated chitinase in PBS (Heat-treated chitinase; middle column), or treated with active chitinase in PBS (Chitinase; right column) for 0.5 h. Chitin (in green, stained by CBD-546), cell nuclei (in blue, stained by DAPI). Differential interference contrast (DIC) microscopy (bottom row) shows the loss of cells after chitinase treatment. **(B)** Quantitation of fluorescence intensity (mean ± SD) from the CLSM images from the three experimental groups (PBS, Heat-treated Chitinase, and Chitinase; four replicates), demonstrates a reduction in pixel intensity with chitinase treatment. Statistical significance was determined by one-way ANOVA and Tukey's *post hoc* test. $p < 0.05$ and $p < 0.01$ were denoted by * and **, respectively.

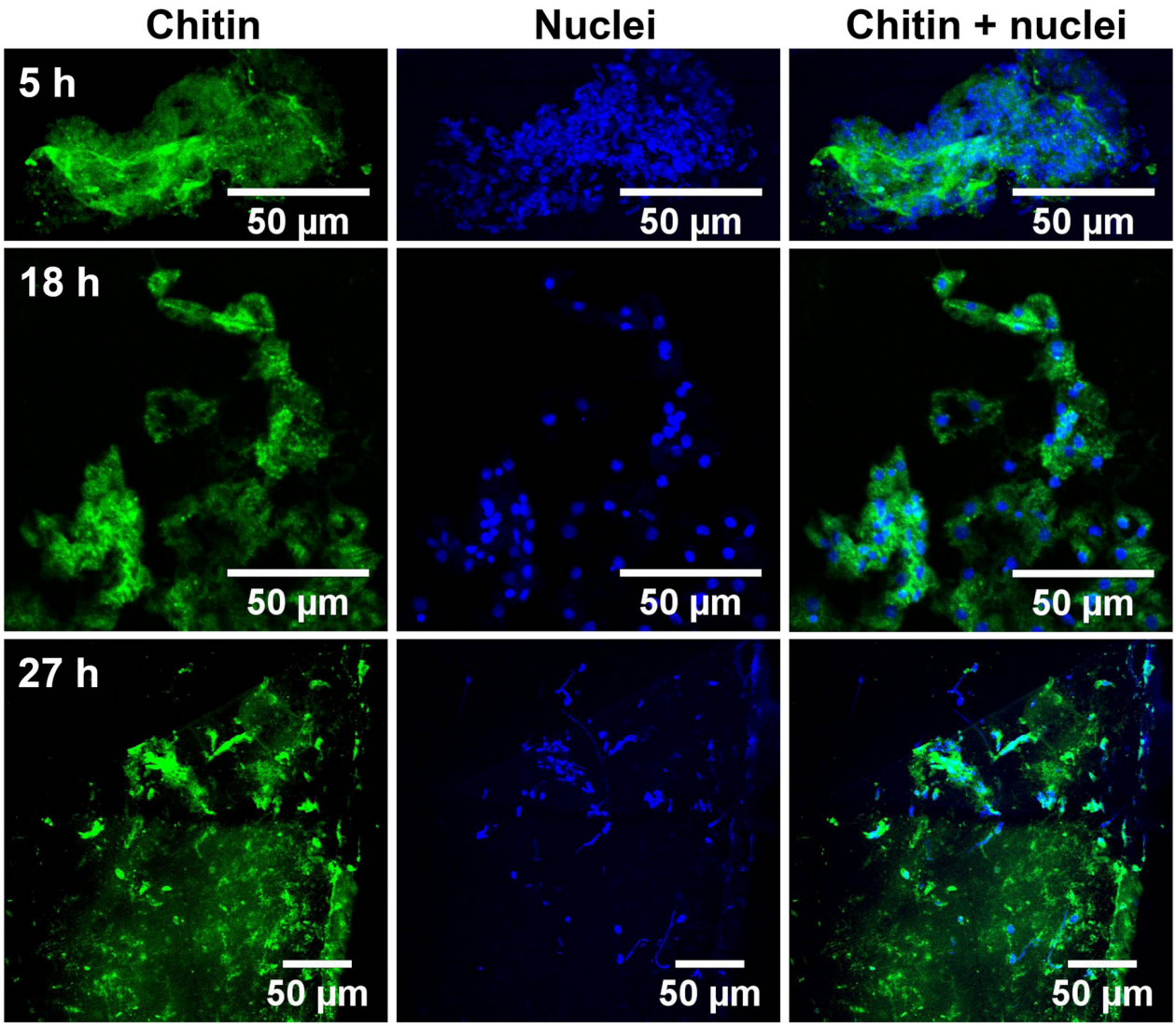

FIGURE 2 | Succession of shell repair on glass implants, visualized at 5, 18, and 27 h after implantation. Maximum intensity projection of CLSM image at 5 (top row), 18 (middle row), and 27 h (bottom row). Chitin (in green, stained by CBD-Alexa 546 probe) and cell nuclei (in blue, stained by DAPI), merged image shows the distribution of nuclei and their relationship to chitin.

Thermo Fisher Scientific), and dried overnight before imaging on a CLSM.

An untreated 18 h implant was visualized on CLSM for 2 h in order to examine any changes of fluorescence intensity of the chitin probe due to photobleaching. Additionally, an 18 h implant was visualized to examine any changes in fluorescence intensity of due to chitinase treatment.

SEM Observation of Implants

The stainless steel foil implants were fixed in 4% paraformaldehyde buffered with 0.1 M cacodylate trihydrate buffer at pH 8.0 for 1 h. Following fixation, they were washed three times and stored in 0.1 M cacodylate trihydrate buffer at pH 8.0 prior to SEM imaging. To determine the chemical composition of the fibrils and any associated materials, the implants were treated with either 0.1% acetic acid for 1 min, 0.5% commercial bleach for 30 min or PBS as a control. After the chemical treatments, the implants were washed for 5 min with distilled water to remove salts in the buffer, then fixed in 1% osmium tetroxide for 30 min and finally washed with distilled water for 5 min to stop the fixation process. To enhance conductivity of the cells on the implants, the specimens were serially dehydrated with ethanol (50% for 10 min, 70% for 10 min, 85% for 10 min, 95% for 10 min, and 100% three times for 10 min), and then washed with 50% hexamethyldisilazane (HMDS) in ethanol, followed by 100% HMDS. The implants were then placed in a fume hood to dry overnight, after which they were mounted onto an aluminum stub with carbon tape. The cells and fibrous deposits on the implant were observed using a Hitachi 4800 SEM. The diameter of the fibril structures

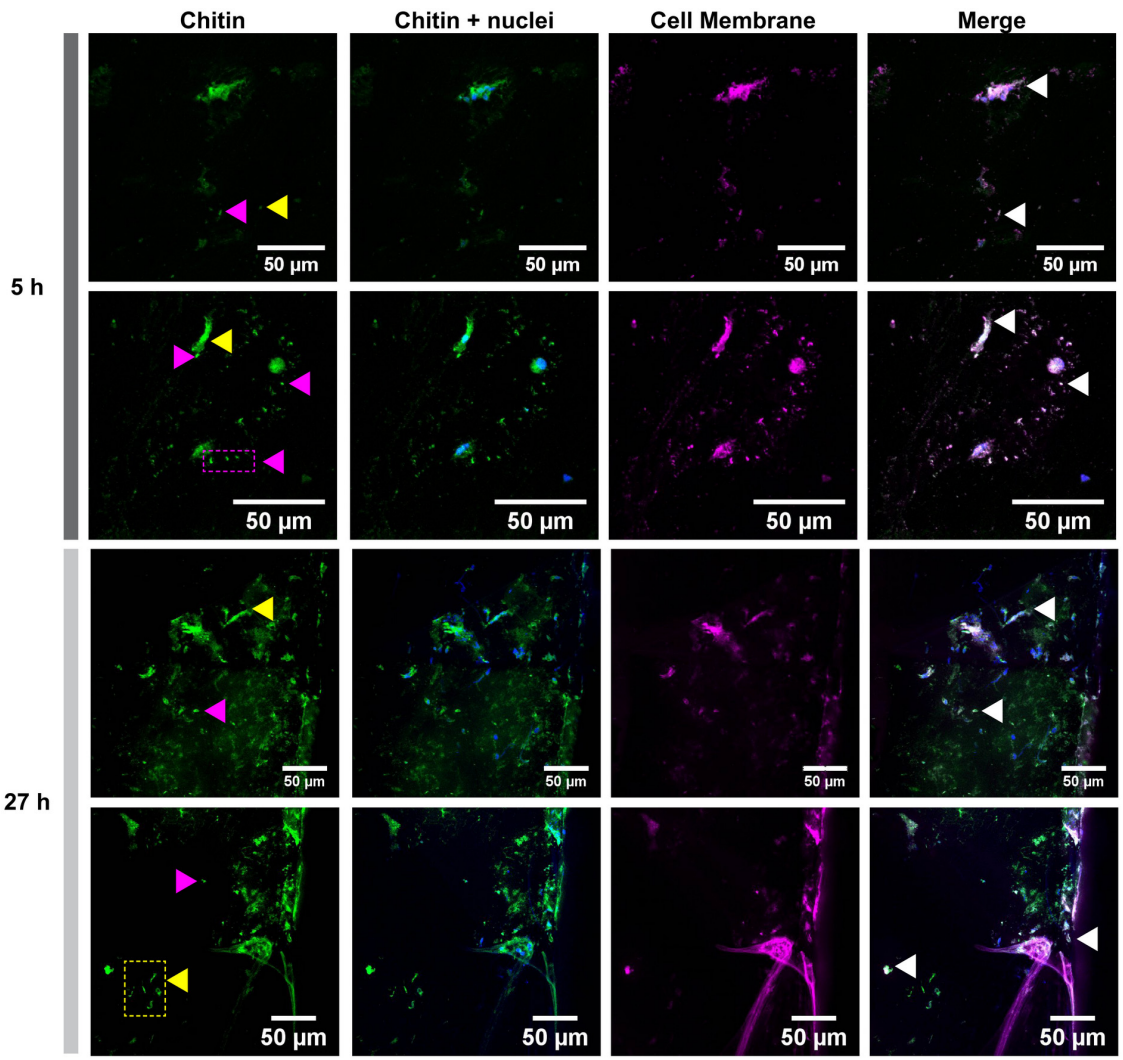

FIGURE 3 | Cell membrane and chitin on glass implants visualized at 5 and 27 h after implantation. Maximum intensity projection of CLSM image shows the distribution of chitin (in green, stained by CBD-Alexa 546 probe), its location with respect to cell nuclei (in blue, stained by DAPI), and cell membrane (in magenta, stained by CellMask). A merge of all three channels shows a large overlapping of lipid membrane and chitin signals (white arrows). Fibrous chitin (yellow arrows) and micron sized particles (magenta arrows) are present. Two representative regions from 5 and 27 h implants are provided.

was quantified at high magnification of 10,000–90,000 times. Mean fibril diameters (FD) were measured from 7 to 10 fibrils chosen randomly, from implants for each time points point (5, 15, and 27 h and 6 days) and each experimental treatment level (control, acid, and bleach). Fibril that were partially covered were avoided for FD measurement. The typical morphology of fibrils which FD was measured are labeled in **Figures 4–6**.

Statistical Analysis

The effect of chitinase on the mean fluorescence intensity of CBD-546 was assessed using one-factor analysis of variance (ANOVA) and the *post hoc* Tukey's HSD tests. The effects of experimental treatments (control, acid, and bleach) on the mean FD at 5, 15, and 27 h and 6 days after shell repair were assessed using two-factor ANOVA and the *post hoc* Tukey's HSD tests. Before the analysis, data were checked to ensure a good fit for ANOVA assumptions such as data normality and variance heterogeneity using the Shapiro–Wilk test and the O'Brien test, respectively.

RESULTS

Chitinase Digestion Reduces Fluorescence Intensity

Following the protocol by Heath-Heckman and McFall-Ngai (2011), we tested the specificity of the CBD Alexa-546 fluorescence to enzymatic digestion of chitin. In the cases of 1 and 2 h digestion, total removal of chitin signals were found; therefore, no pixel values were quantifiable. As

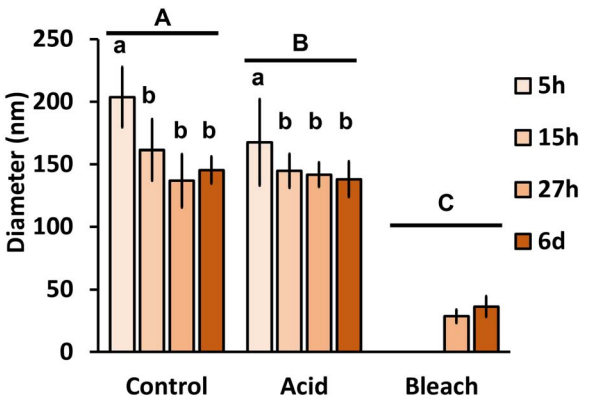

FIGURE 4 | The effect of acid and bleach treatments on fibril diameter. PBS control fibril diameter (mean ± SD) from 5, 15, and 27 h and 6 days after implantation were compared to either acid (1 min incubation with 0.1% acetic acid) or bleach (30 min incubation with 0.5% bleach) treatment. Control fibril structures were the thickest at 5 h, and became thinner over time (two-way ANOVA: $p < 0.0001$, 5 h > 15 h = 27 h = 6 days). Acid treatment reduced fibril diameter (two-way ANOVA: $p < 0.0001$, Control > Acid etched > Bleached), suggesting the presence of mineral in these fibrils. Only fibrils from 27 h and 6 days remained after bleach treatment, indicating all of the fibrils are rich in organic components. Same letter denotes groups that are not significantly different. Lower case letters compare the different sampling time points; upper case letters compare the treatments.

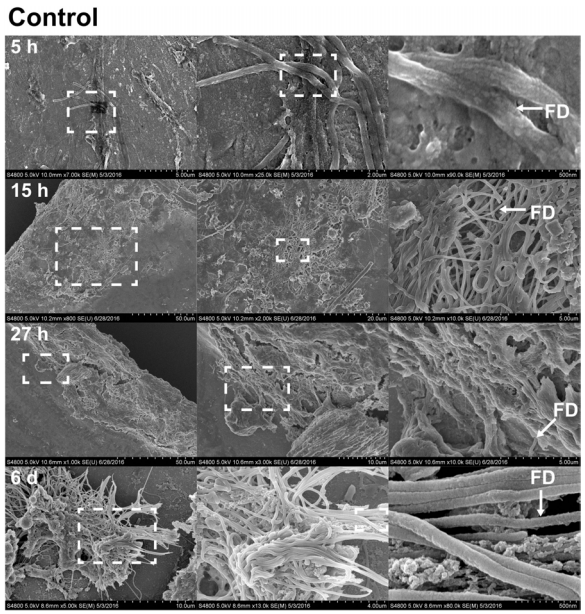

FIGURE 5 | Fibril structures on stainless steel implants, 5, 15, and 27 h and 6 days after implantation on SEM. At 5 h (first row), chitin-like fibers are apparent over the entire surface of the implant. Enlarged view of the boxed region from A shows the interwoven chitin fibers. Scale bars from left to right = 5 μm, 2 μm, and 500 nm. At 15 h (second row), cell clusters are shown interacting with fibril structures. Scale bars from left to right = 50, 20, and 5 μm. At 27 h (third row), thick clusters of cells interacting with fibrils are found. Scale bars from left to right = 50, 10, and 5 μm. On sixth day (forth row), fibrils are organized to form a more complex structure. Scale bars from left to right = 10 μm, 4 μm, and 500 nm. Representative regions for the measurement of fibril diameter (FD) are shown on the right column (white arrows).

shown in **Figure 1**, 0.5 h of chitinase treatment significantly reduced CBD Alexa-546 fluorescence associated with hemocytes when compared with PBS control and heat treated chitinase preparations, thus confirming the presence of chitin in the hemocytes and suggesting a high specificity of the probe for chitin (one-way ANOVA $p < 0.05$, Tukey's test: PBS = HT > T; $p < 0.01$; O'Brien test demonstrated variance was homogeneous: $p > 0.05$). Our result demonstrated the probe is sensitive to not only the presence of chitin, but also the abundance of chitin.

To control for the possibility of photobleaching effects, the same CLSM setting that was used for a chitin treated implant was used to visualize an 18 h implant treated with PBS. The fluorescence intensity after 120 min in the control showed no reduction (intensity before: 222.7 ± 18.6; intensity after: 230.3 ± 18.0; mean ± SD), while the intensity for the chitinase-treated implant showed a 56% reduction in fluorescence intensity from 222.0 ± 44.8 to 96.4 ± 18.6.

CLSM Observation of Cells on the Glass Implants

Glass coverslips imaged by CLSM at 5, 18, and 27 h after implantation are shown in **Figures 2**, **3**. Chitin structures, represented in green, appeared to be associated with cell nuclei at the early times of shell regeneration (5 and 18 h; **Figure 2**). These structures take the form of fibers (yellow arrows, **Figure 3**) and micron sized vesicles (magenta arrows, **Figure 3**). By a later stage of shell repair (27 h), the number of cells associated with the chitin materials was reduced while the coverage of chitin expanded on the implant surface. The 5, 18, and 27 h implants had no significant autofluorescence. Cell nuclei labeled with DAPI were represented in blue, and the membrane structures labeled with plasma membrane stain were represented in magenta (**Figure 3** and **Supplementary Figure S1**). Since the complementary colors of green and magenta overlay to produce white pixels, structures where both chitin and membrane are present appear white. In addition to membrane associated with the expected fibrous structures, the presence of chitin-rich micron-sized spheres also looked white and appeared to be membrane-bound extracellular vesicles (white arrows, **Figure 3** and **Supplementary Figure S1**).

SEM Observation of Fibril Dimension on Metal Implants

With the benefit of the greater structural resolution provided by SEM, the fibrous features of the deposited chitin at 5, 15, and 27 h and 6 days after implantation were compared (**Figure 4**) and revealed (**Figures 5**–**7**). The deposition of fibril structures began as early as the time point of 5 h after shell repair, possibly as a result of cellular activities at the mineralization front. The thickness of these fibrous materials was reduced after this time point (**Figure 4**, two-way ANOVA: $p < 0.0001$,

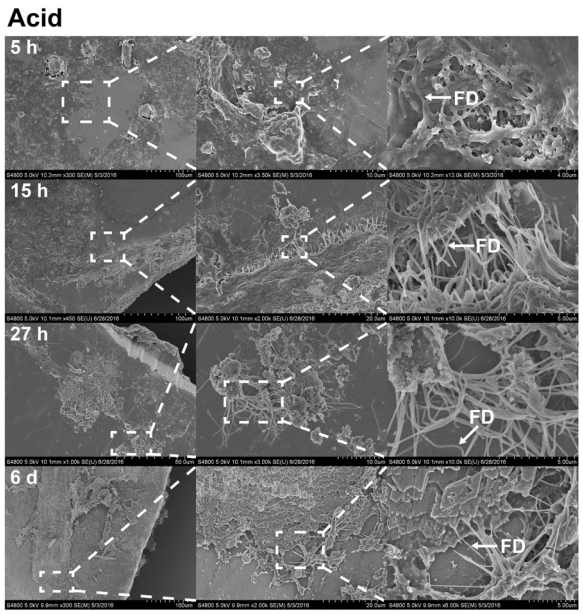

FIGURE 6 | The effects of acetic acid on stainless steel implants, 5, 15, and 27 h and 6 days after implantation. 1 min incubation with 0.1% acetic acid treatment resulted in extracellular matrix becoming more open. The surface has become partially digested, revealing interacting fibrils. On sixth day (forth row), foliated shell structures and fibrils are organized as sheets across the surface of the implant. Scale bars from left to right, at 5 h (first row): 100, 10, and 4 μm; at 15 h (second row): 100, 20, and 5 μm; at 27 h (third row): 50, 10, and 5 μm; at sixth day (forth row): 100, 20, and 5 μm. Representative regions for the measurement of fibril diameter (FD) are shown on the right column (white arrows).

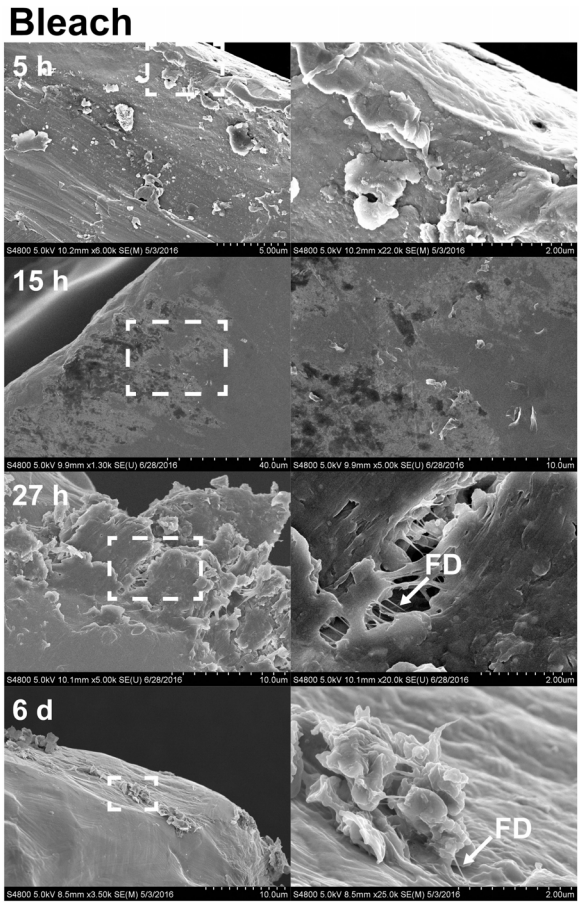

FIGURE 7 | The effects of bleach on stainless steel implants, 5, 15, and 27 h and 6 days after implantation. Implant after 30 min incubation with 0.5% bleach treatment shows a total removal of fibril structures at 5 and 15 h (first and second rows). (right column) Enlarged view of boxed region from E indicates that fibril structures appeared to become thinner (arrow). Partial degradation of the implant surface and thinner fibril (arrow) were visible. Scale bars from left to right, at 5 h (first row): 5 and 2 μm; at 15 h (second row): 40 and 10 μm; at 27 h (third row): 10 and 2 μm; at sixth day (forth row): 10 and 2 μm. Representative regions for the measurement of fibril diameter (FD) are shown on the right column (white arrows).

5 h > 15 h = 27 h = 6 days). Overall thickness of the fibrous materials was reduced by treatment with acid and bleach (**Figure 4**, two-way ANOVA: $p < 0.0001$, Control > Acid etched > Bleached). These observations suggested that the fibril structures were likely conjugated to microcrystals in the first 5 h of shell repair (**Figures 4**, **5**) and that these crystals were dissolved after treatment with dilute acid (**Figures 4**–**6**). Bleach reactivity agreed with the CLSM observation that some chitin structures are associated with membrane and possibly also with protein. We observed that the later stages (27 h and 6 days, **Figures 6**, **7**) had more fibrils that were resistant to acid and bleach treatments, suggesting that these implants contained more chitin than in the earlier stages of shell repair (such as the 5 and 15 h time points, **Figures 4**, **5**). In fact, the 5 h implants were devoid of fibers and the 15 h implants had nearly unobservable fibers (**Figure 7**). In general, we observed an increased level of structural complexity of fibers over the time course of shell repair (**Figures 5**–**7**). The deposition of fibril structures began as quickly as 5 h after the damage, with fibrils appearing tightly packed and in a random orientation. The fibrous structures later appeared to elaborate into a three-dimensional network by 27 h and 6 days (**Figures 4**, **7**). In addition, a horizontally arranged foliated shell appeared by day 6, with the fibrous materials and the folia having an interconnected ultrastructure (**Figure 6**). Upon treatment with chitinase, the fibril structures remain, but appeared more membranous (**Supplementary Figure S2**).

DISCUSSION

One of the goals of biomineralization research is to use approaches that capture the involvement of cells and molecules in this process as close to their native biological state as possible. Previously established work on chitin in mineral and biological samples were often treated using harsh chemicals such as NaOH or bleach (Peters, 1972; Ehrlich et al., 2010, 2013). Although these approaches were effective in revealing the chemical-resistant chitin fibers, cells and other molecules were degraded. The alternative approach of using advanced microscopy methods has greatly improved the biological

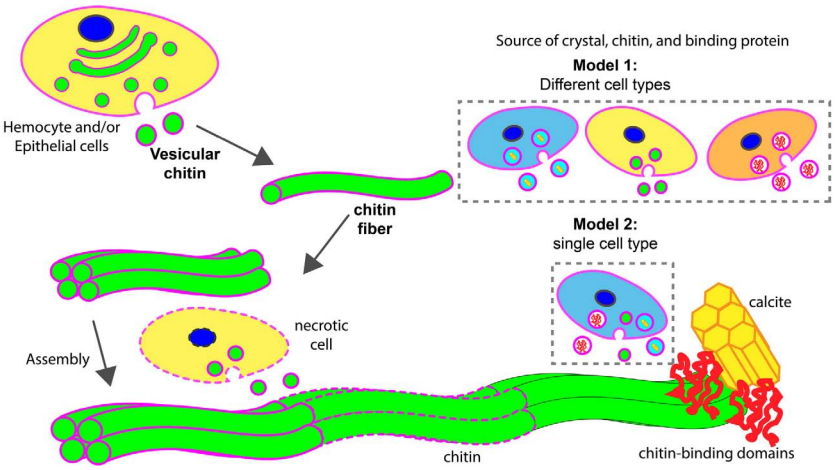

FIGURE 8 | Models of chitin assisted mineralization. Cell secretes vesicular chitin, leading to chitin fibril maturation. These fibrils are assembled into a larger chitin fiber, often followed by multiple fiber assembly into a compact structural framework. This fiber assemblage interacts with chitin-binding domains of extracellular matrix proteins which in turn are associated with calcite. Upon maturation, lipid membrane (in magenta) disintegrates (dotted outlines). During the assembly process, necrotic cells (in dotted line) may serve as a supply of vesicular chitin. Two hypothetical models described the potential sources of chitin, mineral, and chitin-binding proteins for the assembly of minerals. In model 1, different cell types are involved. In model 2, a specialized cell type is responsible to supply all components for mineralization.

relevance of observations on biominerals, including those related to chitin. Such methods would include cryo-preservation of the initial mineralization states in vitrified conditions (Levi-Kalisman et al., 2001; Addadi and Weiner, 2014). Previous studies demonstrated that shell repair can be observed on implants positioned between the shell and the mantle in *C. virginica* (Johnstone et al., 2015). In this study, when CLSM and SEM techniques were combined with the use of the implant system, we were able to reveal molecular and cellular aspects of chitin synthesis associated with shell deposition in real-time and under conditions which approximate *in situ* observations.

The use of recombinant green fluorescent protein-tagged chitin-binding protein has been used in earlier studies to perform fluorescent labeling of acid-etched shell structures (Nudelman et al., 2007), demineralized larvae (Schönitzer and Weiss, 2007), and squid hemocytes (Heath-Heckman and McFall-Ngai, 2011). The specificity of the chitin probe used in this study and the association of chitin with hemocytes was confirmed by subjecting fixed hemocytes to chitinase digestion and then observing the change in fluorescence by CLSM. Furthermore, chitin appeared to be involved in anchoring the hemocytes to the surface of the coverslips, as extended incubation with chitinase resulted in the loss of adhesive cells from the surface. This observation implied a role of chitin in cell adhesion and possibly in the molecular cascade of wound healing (Lee et al., 2011).

To address how cellular components are involved in the process of forming new biological minerals, glass implant surfaces were evaluated using various fluorescent stains under CLSM. In addition to the chitin probe, we counterstained cell nuclei and plasma membrane at the active sites of mineralization. In the early stages of regeneration, chitin fibers were found near where nuclei and thus cells were located. In addition, micron-sized structures that appeared to be membrane-bound stained for chitin, suggesting that exosomal-like structures are involved in chitin deposition.

Exosomes, called chitosomes, are well known for the production of chitin in yeast and fungi (Mills and Cantino, 1981; Gozalbo et al., 1993; Bartnicki-Garcia, 2006). In gastropod molluscs, chitin secretion appears to derive from Golgi-derived secretory granules in the columnar cells of mantle epithelia (Bevelander and Nakahara, 1970; Paillard and Le Pennec, 1993). In the process of periostracum formation, fine materials with a periodicity of 300 Å were abundant in these enlarged granules, and the materials are dispersed in the extracellular environment (Bevelander and Nakahara, 1970). Alternatively, the production of chitin may begin in the hemocytes where chitin synthase is abundantly expressed (Zhang et al., 2012; Ivanina et al., 2017). Furthermore, endogenous chitin production has been reported in a lysosomal compartment of hemocytes in squid (Heath-Heckman and McFall-Ngai, 2011). A recent study on molluscan shell formation examined the cooperative roles of mantle epithelial tissue and hemocytes (Ivanina et al., 2017), a relationship which may apply to chitin synthesis. The origin of the exosomes observed in this study, whether it is mantle or adherent hemocytes, or both tissues, remains unresolved.

In addition to the possibility that shell-matrix chitin may be made in vesicles, calcification sites are also often found within membrane-bound subcellular compartments. Examples of such sites include the microvesicles in magnetotactic bacteria (Hershey et al., 2016), the tubeworm (Neff, 1971), the Golgi in the coccolithophorids (Young and Henriksen, 2003), and the pinocytotic proton-transporting vesicles in the foraminifera

(Bentov et al., 2009; de Nooijer et al., 2009; Toyofuku et al., 2017). Perhaps the most germane to this study, Mount et al. (2004) demonstrated the intracellular presence of calcite crystals in hemocytes of oysters during shell repair. In general, studies that target the cellular parameters required for biomineralization, such as intracellular or intraorganellar pH and calcium supply, are only emerging in the cases of multicellular organisms (Venn et al., 2009; Chan et al., 2015).

SEM observations of stainless steel implants revealed the presence of fibers. If these fibers contain chitin, a portion of them would be expected to be resistant to both bleach and acid treatments, as demonstrated in this study. Changes in the fiber dimensions after chemical treatments further suggest that the chitin does not exist as an isolated component, but is associated with other organics, such as proteins and lipids, as well as a calcium carbonate mineral phase. The presence of thicker fibrils found at 5 h of implantation compared to later stages could be a consequence of the inclusion of cellular products such as mineral, lipid membrane and proteins. In fact, after a 3 h chitinase treatment on an 18 h stainless steel implant, only morphological changes in fibers occurred without noticeable reduction in their diameter (**Supplementary Figure S2**). The complexity of the chitin structures increased over time, starting with a tightly packed random orientation and developing into a three dimensional structure. By the sixth day, the chitin became interconnected with mineral, which had an ultrastructure that appeared identical to the native foliated microstructure of the inner shell layer. The early appearance of chitin and its ultimate relationship to shell crystals suggests that chitin may play a significant role in shell regeneration, which resembles normal shell formation.

Based on previous studies and the work reported herein, we propose two hypothetical models of chitin involvement at the mineralization front in oysters (**Figure 8**). In both cases, chitin is produced in an intracellular compartment like the Golgi apparatus. The deposition of chitin at the site of mineral formation relies on an exosome-like microvesicle secretion process. These chitin-producing compartments could be generated from cell types different from those that produce mineral phase precursors and other organic matrix materials (model 1) or all these products could be produced by the same cell type (model 2). The latter products may be released in exosomes, or by more traditional secretion processes. The precise cellular origin of chitin exosomes putatively observed in this study and their cellular relationship of other shell components await additional study. Furthermore, the fact that hemocytes are present at the site of shell formation in conjunction with chitin, their role in secreting chitin or their use of it as a scaffold to advance mineralization events bears special scrutiny.

AUTHOR CONTRIBUTIONS

VC carried out the experiments. VC and AW wrote the manuscript. MJ assisted VC with the protocol of expression and purification of the chitin-binding domain, and the design of the implant study. AM conceived and supervised the project and edited the manuscript.

FUNDING

This work was partially supported by ONR award # N00014-14-1-0488 and by the Clemson University Experimental Research Station.

ACKNOWLEDGMENTS

The authors thank New England Biolabs for their supply of transfected *E. coli*. They thank Charles Rice, Amy Anderson, and Matthew Turnbull for their helpful discussion at the early stage of this work. They also thank Hermann Ehrlich, David Kisailus, Michiko Nemoto, and Michio Suzuki whose discussion with VC during the Biomin14 meeting greatly improved this project. They would also like to acknowledge Dr. S. Ramaswami for proof-reading of this manuscript, and Ms. Jan Lay for improving the quality of the figures.

SUPPLEMENTARY MATERIAL

The Supplementary Material for this article can be found online at: https://www.frontiersin.org/articles/10.3389/fmars.2018.00347/full#supplementary-material

FIGURE S1 | Cell membrane and chitin on glass implants visualized at 18 h after implantation. Maximum intensity projection of CLSM image shows the distribution of chitin (in green, stained by CBD-Alexa 546 probe), its location with respect to cell nuclei (in blue, stained by DAPI), and cell membrane (in magenta, stained by CellMask). A merge of all three channels shows a large overlapping of lipid membrane and chitin signals (white arrows). Fibrous chitin (yellow arrows) and micron sized particles (magenta arrows) are present.

FIGURE S2 | The effects of chitinase treatment on stainless steel implants 18 h after implantation. Implant after 3 h of incubation treatment with chitinase shows a change in fibril morphology. **(A–C)** Untreated control fibril, **(B)** is the enlarged box region of **(A)**, and **(C)** is the enlarged boxed region of **(B)**. A representative fibril is indicated by a white arrow. **(D–I)** Chitinase treated fibril. **(E)** is the enlarged box region of D, and F is the enlarged boxed region of panel **(E)**. Degradation by chitinase caused the implant surface to be more membranous. Panel **(G)** represents a mineralized region of the implant which appears to be free of fibrils after chitinase treatment. Panel **(H)** is a vesicle rich region and **(I)** is the enlarged box region of panel **(H)**. Remaining fibril-like structures are indicated by white arrows in **(F)** and **(I)**. Scale bars for **(A–D)**: 10, 5, 3, and 20 μm; **(E, F, G, I)**: 5 μm; **(H)**: 1 μm.

REFERENCES

Addadi, L., and Weiner, S. (2014). Biomineralization: mineral formation by organisms. *Phys. Scr.* 89:098003. doi: 10.1088/0031-8949/89/9/098003

Bartnicki-Garcia, S. (2006). Chitosomes: past, present and future. *FEMS Yeast Res.* 6, 957–965. doi: 10.1111/j.1567-1364.2006.00158.x

Bentov, S., Brownlee, C., and Erez, J. (2009). The role of seawater endocytosis in the biomineralization process in calcareous foraminifera. *Proc. Natl. Acad. Sci. U.S.A.* 106, 21500–21504. doi: 10.1073/pnas.0906636106

Bevelander, G., and Nakahara, H. (1970). An electron microscope study of the formation and structure of the periostracum of a gastropod,

Littorina littorea. *Calcif. Tissue Int.* 5, 1–12. doi: 10.1007/bf02017528

Brunner, E., Richthammer, P., Ehrlich, H., Paasch, S., Simon, P., Ueberlein, S., et al. (2009). Chitin-based organic networks: an integral part of cell wall biosilica in the diatom *Thalassiosira pseudonana*. *Angew. Chem. Int. Ed.* 48, 9724–9727. doi: 10.1002/anie.200905028

Carlström, D. (1957). The crystal structure of α-chitin (poly-N-acetyl-D-glucosamine). *J. Cell Biol.* 3, 669–683. doi: 10.1083/jcb.3.5.669

Chan, V. B. S., Toyofuku, T., Wetzel, G., Saraf, L., Thiyagarajan, V., and Mount, A. S. (2015). Direct deposition of crystalline aragonite in the controlled biomineralization of the calcareous tubeworm. *Front. Mar. Sci.* 2:97. doi: 10.3389/fmars.2015.00097

Cohen, E. (2010). Chitin biochemistry: synthesis, hydrolysis and inhibition. *Adv. Insect Physiol.* 38, 5–74. doi: 10.1016/S0065-2806(10)38005-2

Currey, J. (1999). The design of mineralised hard tissues for their mechanical functions. *J. Exp. Biol.* 202, 3285–3294.

de Nooijer, L. J., Toyofuku, T., and Kitazato, H. (2009). Foraminifera promote calcification by elevating their intracellular pH. *Proc. Natl. Acad. Sci. U.S.A.* 106, 15374–15378. doi: 10.1073/pnas.0904306106

Di Rosa, M., Distefano, G., Zorena, K., and Malaguarnera, L. (2016). Chitinases and immunity: ancestral molecules with new functions. *Immunobiology* 221, 399–411. doi: 10.1016/j.imbio.2015.11.014

Ehrlich, H., Ilan, M., Maldonado, M., Muricy, G., Bavestrello, G., Kljajic, Z., et al. (2010). Three-dimensional chitin-based scaffolds from Verongida sponges (Demospongiae: Porifera). Part I. Isolation and identification of chitin. *Int. J. Biol. Macromol.* 47, 132–140. doi: 10.1016/j.ijbiomac.2010.05.007

Ehrlich, H., Kaluzhnaya, O. V., Brunner, E., Tsurkan, M. V., Ereskovsky, A., Ilan, M., et al. (2013). Identification and first insights into the structure and biosynthesis of chitin from the freshwater sponge *Spongilla lacustris*. *J. Struct. Biol.* 183, 474–483. doi: 10.1016/j.jsb.2013.06.015

Falini, G., Albeck, S., Weiner, S., and Addadi, L. (1996). Control of aragonite or calcite polymorphism by mollusk shell macromolecules. *Science* 271, 67–69. doi: 10.1126/science.271.5245.67

Galtsoff, P. S. (1964). The American oyster *Crassostrea virginica* Gmelin. *Fish. Bull.* 64, 421–425.

Goffinet, G., and Jeuniaux, C. (1979). Distribution et importance quantitative de la chitine dans les coquilles de mollusques. *Cah. Biol. Mar.* 20, 341–349.

Gotliv, B., Addadi, L., and Weiner, S. (2003). Mollusk shell acidic proteins: in search of individual functions. *ChemBioChem* 4, 522–529. doi: 10.1002/cbic.200200548

Gozalbo, D., Dubón, F., and Sentandreu, R. (1993). Effect of digitonin on membrane-bound and chitosomal chitin synthetase activity in protoplasts from yeast cells of *Candida albicans*. *Antonie Van Leeuwenhoek* 64, 67–74. doi: 10.1007/BF00870923

Hasegawa, M., Yagi, K., Iwakawa, S., and Hirai, M. (2001). Chitosan induces apoptosis via caspase-3 activation in bladder tumor cells. *Jpn. J. Cancer Res.* 92, 459–466. doi: 10.1111/j.1349-7006.2001.tb01116.x

Heath-Heckman, E. A., and McFall-Ngai, M. J. (2011). The occurrence of chitin in the hemocytes of invertebrates. *Zoology* 114, 191–198. doi: 10.1016/j.zool.2011.02.002

Heinemann, F. (2008). *Investigation of Biopolymer- Mineral Interactions in the Natural Composite Material Nacre*. Ph.D. thesis, University of Bremen, Bremen.

Heredia, A., Aguilar-Franco, M., Magaña, C., Flores, C., Piña, C., Velázquez, R., et al. (2007). Structure and interactions of calcite spherulites with α-chitin in the brown shrimp (*Penaeus aztecus*) shell. *Mater. Sci. Eng. C* 27, 8–13. doi: 10.1016/j.msec.2005.11.003

Hershey, D. M., Ren, X., Melnyk, R. A., Browne, P. J., Ozyamak, E., Jones, S. R., et al. (2016). MamO is a repurposed serine protease that promotes magnetite biomineralization through direct transition metal binding in Magnetotactic bacteria. *PLoS Biol.* 14:e1002402. doi: 10.1371/journal.pbio.1002402

Ichinohe, T., Nagata, N., Strong, P., Tamura, S. I., Takahashi, H., Ninomiya, A., et al. (2007). Prophylactic effects of chitin microparticles on highly pathogenic H5N1 influenza virus. *J. Med. Virol.* 79, 811–819. doi: 10.1002/jmv.20837

Ivanina, A. V., Falfushynska, H. I., Beniash, E., Piontkivska, H., and Sokolova, I. M. (2017). Biomineralization-related specialization of hemocytes and mantle tissues of the Pacific oysters *Crassostrea gigas*. *J. Exp. Biol.* 220, 3209–3221. doi: 10.1242/jeb.160861

Jeon, D.-W., Ahn, W. S., You, S. J., Chae, G. T., Shim, Y. B., and Chun, H. J. (2012). Induction of classical activation of macrophage in vitro by water soluble chitin. *Appl. Surf. Sci.* 262, 134–139. doi: 10.1016/j.apsusc.2012.03.078

Johnstone, M. B., Gohad, N. V., Falwell, E. P., Hansen, D. C., Hansen, K. M., and Mount, A. S. (2015). Cellular orchestrated biomineralization of crystalline composites on implant surfaces by the eastern oyster, *Crassostrea virginica* (Gmelin, 1791). *J. Exp. Mar. Biol. Ecol.* 463, 8–16. doi: 10.1016/j.jembe.2014.10.014

Kaya, M., Mujtaba, M., Ehrlich, H., Salaberria, A. M., Baran, T., Amemiya, C. T., et al. (2017). On chemistry of gamma-chitin. *Carbohydr. Polym.* 176, 177–186. doi: 10.1016/j.carbpol.2017.08.076

Kumar, M. N. R. (2000). A review of chitin and chitosan applications. *React. Funct. Polym.* 46, 1–27. doi: 10.1016/S1381-5148(00)00038-9

Lee, C. G., Da Silva, C. A., Dela Cruz, C. S., Ahangari, F., Ma, B., Kang, M. J., et al. (2011). Role of chitin and chitinase/chitinase-like proteins in inflammation, tissue remodeling, and injury. *Annu. Rev. Physiol.* 73, 479–501. doi: 10.1146/annurev-physiol-012110-142250

Lee, S., and Choi, C. (2007). The correlation between organic matrices and biominerals (myostracal prism and folia) of the adult oyster shell, *Crassostrea gigas*. *Micron* 38, 58–64. doi: 10.1016/j.micron.2006.03.018

Levi-Kalisman, Y., Falini, G., Addadi, L., and Weiner, S. (2001). Structure of the nacreous organic matrix of a bivalve mollusk shell examined in the hydrated state using cryo-TEM. *J. Struct. Biol.* 135, 8–17. doi: 10.1006/jsbi.2001.4372

Liu, Z., Zhou, Z., Jiang, Q., Wang, L., Yi, Q., Qiu, L., et al. (2017). The neuroendocrine immunomodulatory axis-like pathway mediated by circulating haemocytes in pacific oyster *Crassostrea gigas*. *Open Biol.* 7:160289. doi: 10.1098/rsob.160289

Merzendorfer, H., and Zimoch, L. (2003). Chitin metabolism in insects: structure, function and regulation of chitin synthases and chitinases. *J. Exp. Biol.* 206, 4393–4412. doi: 10.1242/jeb.00709

Mills, G. L., and Cantino, E. C. (1981). Chitosome-like vesicles from gamma particles of *Blastocladiella emersonii* synthesize chitin. *Arch. Microbiol.* 130, 72–77. doi: 10.1007/BF00527075

Mount, A., Wheeler, A., Paradkar, R., and Snider, D. (2004). Hemocyte-mediated shell mineralization in the eastern oyster. *Science* 304, 297–300. doi: 10.1126/science.1090506

Mount, A. S., Gohad, N. V., Hansen, D. C., Hansen, K. M., and Johnstone, M. B. (2013). *Deposition of Nanocrystalline Calcite on Surfaces by a Tissue and Cellular Biomineralization*. Available at: https://www.google.com/patents/US9371451

Mount, A. S., Gohad, N. V., Hansen, D. C., Hansen, K. M., and Johnstone, M. B. (2016). *Deposition of Nanocrystalline Calcite on Surfaces by a Tissue and Cellular Biomineralization*. Available at: https://www.google.com/patents/US9371451

Nakayama, S., Suzuki, M., Endo, H., Iimura, K., Kinoshita, S., Watabe, S., et al. (2013). Identification and characterization of a matrix protein (PPP-10) in the periostracum of the pearl oyster, *Pinctada fucata*. *FEBS Open Bio* 3, 421–427. doi: 10.1016/j.fob.2013.10.001

Neff, J. M. (1971). Ultrastructural studies of the secretion of calcium carbonate by the serpulid polychaete worm, *Pomatoceros caeruleus*. *Cell Tissue Res.* 120, 160–186. doi: 10.1007/BF00335534

Nudelman, F., Chen, H., Goldberg, H., Weiner, S., and Addadi, L. (2007). Spiers Memorial Lecture. Lessons from biomineralization: comparing the growth strategies of mollusc shell prismatic and nacreous layers in *Atrina rigida*. *Faraday Discuss.* 136, 9–25. doi: 10.1039/b704418f

Nudelman, F., Shimoni, E., Klein, E., Rousseau, M., Bourrat, X., Lopez, E., et al. (2008). Forming nacreous layer of the shells of the bivalves *Atrina rigida* and *Pinctada margaritifera*: an environmental- and cryo-scanning electron microscopy study. *J. Struct. Biol.* 162, 290–300. doi: 10.1016/j.jsb.2008.01.008

Öztürk-Çolak, A., Moussian, B., Araujo, S. J., and Casanova, J. (2016). A feedback mechanism converts individual cell features into a supracellular ECM structure in *Drosophila* trachea. *eLife* 5:e09373. doi: 10.7554/eLife.09373

Paillard, C., and Le Pennec, M. (1993). Ultrastructural studies of the mantle and the periostracal lamina in the manila clam, *Ruditapes philippinarum*. *Tissue Cell* 25, 183–194. doi: 10.1016/0040-8166(93)90018-G

Peters, W. (1972). Occurence of chitin in mollusca. *Comp. Biochem. Physiol. B* 41, 541–550. doi: 10.1016/0305-0491(72)90117-4

Schindelin, J., Arganda-Carreras, I., Frise, E., Kaynig, V., Longair, M., Pietzsch, T., et al. (2012). Fiji: an open-source platform for biological-image analysis. *Nat. Methods* 9, 676–682. doi: 10.1038/nmeth.2019

Schönitzer, V., and Weiss, I. M. (2007). The structure of mollusc larval shells formed in the presence of the chitin synthase inhibitor Nikkomycin Z. *BMC Struct. Biol.* 7:71. doi: 10.1186/1472-6807-7-71

Stern, R., and Jedrzejas, M. J. (2008). Carbohydrate polymers at the center of life's origins: the importance of molecular processivity. *Chem. Rev.* 108, 5061–5085. doi: 10.1021/cr078240l

Suzuki, M., Mukai, H., Aoki, H., Yoshimura, E., Sakuda, S., Nagasawa, H., et al. (2016). Microstructure of iridescence-lacking pearl formed in *Pinctada fucata*. *J. Cryst. Growth* 433, 148–152. doi: 10.1016/j.jcrysgro.2015.10.014

Suzuki, M., Sakuda, S., and Nagasawa, H. (2007). Identification of chitin in the prismatic layer of the shell and a chitin synthase gene from the Japanese pearl oyster, *Pinctada fucata*. *Biosci. Biotechnol. Biochem.* 71, 1735–1744. doi: 10.1271/bbb.70140

Suzuki, M., Saruwatari, K., Kogure, T., Yamamoto, Y., Nishimura, T., Kato, T., et al. (2009). An acidic matrix protein, Pif, is a key macromolecule for nacre formation. *Science* 325, 1388–1390. doi: 10.1126/science.1173793

Tang, W. J., Fernandez, J. G., Sohn, J. J., and Amemiya, C. T. (2015). Chitin is endogenously produced in vertebrates. *Curr. Biol.* 25, 897–900. doi: 10.1016/j.cub.2015.01.058

Toyofuku, T., Matsuo, M. Y., De Nooijer, L. J., Nagai, Y., Kawada, S., Fujita, K., et al. (2017). Proton pumping accompanies calcification in foraminifera. *Nat. Commun.* 8:14145. doi: 10.1038/ncomms14145

Venn, A., Tambutté, E., Lotto, S., Zoccola, D., Allemand, D., and Tambutté, S. (2009). Imaging intracellular pH in a reef coral and symbiotic anemone. *Proc. Natl. Acad. Sci. U.S.A.* 106, 16574–16579. doi: 10.1073/pnas.0902894106

Wang, L., Li, F., Wang, B., and Xiang, J. (2012). Structure and partial protein profiles of the peritrophic membrane (PM) from the gut of the shrimp *Litopenaeus vannamei*. *Fish Shellfish Immunol.* 33, 1285–1291. doi: 10.1016/j.fsi.2012.09.014

Wang, X., Song, X., Wang, T., Zhu, Q., Miao, G., Chen, Y., et al. (2013). Evolution and functional analysis of the Pif97 gene of the Pacific oyster *Crassostrea gigas*. *Curr. Zool.* 59, 109–115. doi: 10.1093/czoolo/59.1.109

Weiner, S., and Traub, W. (1980). X-ray diffraction study of the insoluble organic matrix of mollusk shells. *FEBS Lett.* 111, 311–316. doi: 10.1016/0014-5793(80)80817-9

Weiss, I. (2012). Species-specific shells: chitin synthases and cell mechanics in molluscs. *Z. Kristallogr. Cryst. Mater.* 227, 723–738. doi: 10.1524/zkri.2012.1530

Young, J. R., and Henriksen, K. (2003). Biomineralization within vesicles: the calcite of coccoliths. *Rev. Mineral. Geochem.* 54, 189–215. doi: 10.2113/0540189

Zhang, G., Fang, X., Guo, X., Li, L., Luo, R., Xu, F., et al. (2012). The oyster genome reveals stress adaptation and complexity of shell formation. *Nature* 490, 49–54. doi: 10.1038/nature11413

Conflict of Interest Statement: The authors declare that the research was conducted in the absence of any commercial or financial relationships that could be construed as a potential conflict of interest.

frontiers in Marine Science

ORIGINAL RESEARCH
published: 16 October 2018
doi: 10.3389/fmars.2018.00373

Functional Analyses of MMPs for Aragonite Crystal Formation in the Ligament of *Pinctada fucata*

*Kazuki Kubota[1], Hiroyuki Kintsu[1], Akihiro Matsuura[1], Yasushi Tsuchihashi[2], Takeshi Takeuchi[3], Noriyuki Satoh[3] and Michio Suzuki[1]**

[1] Department of Applied Biological Chemistry, Graduate School of Agricultural and Life Sciences, The University of Tokyo, Tokyo, Japan, [2] Mie Prefecture Fisheries Research Institute, Shima, Japan, [3] Marine Genomics Unit, Okinawa Institute of Science and Technology Graduate University, Onna, Japan

The mollusk class, Bivalvia, plays an important role in the formation of calcium carbonate in the ocean. The bivalve hinge ligament is a hard but pliant tissue that resists the stress placed on the hinge during opening and closing. The ligament comprises a fine microstructure of fibrous aragonite crystals surrounded by a dense organic matrix. The matrix consists of organic fibers that are aligned with the fibrous aragonite crystals. Previous studies identified a tissue inhibitor of metalloproteinase (Pf-TIMP: *Pinctada fucata*-Tissue Inhibitor of Metalloproteinase) in the organic fibers of *P. fucata* ligaments. This enzyme exhibited strong inhibition of matrix metalloproteinase (MMP) activity *in vitro*, suggesting that MMPs also play a role in formation of the organic fibers of the ligament. Using transcriptome data, we identified MMP genes from the mantle isthmus, which is a soft tissue attached to the ligament. To investigate the function of MMP genes *in vivo*, we performed RNA interference experiments. The expression of MMP14973 and MMP07860 genes was inhibited after injection of each dsRNA. Cumulative injection of MMP07860 dsRNA induced aggregated aragonite fiber orientation, whereas the injection of MMP14973 showed minor effects. When the decalcified ligament was incubated in a solution saturated with calcium carbonate, aragonite fibers aligned along the surface. When the decalcified ligament was treated with recombinant human (hr) MMP-13, the precipitation of calcium carbonate was inhibited. To investigate general MMP functions in calcium carbonate crystallization in detail, we precipitated aragonite crystals in collagen gels treated with or without recombinant human (hr) MMP-1. Treatment with hrMMP-1 increased the interaction between collagen gels and calcium carbonate. These results imply that *Pinctada fucata* (Pf)-MMPs degrade extracellular matrices in the ligament to produce the fine organic fibers that regulate the orientation of fibrous aragonite crystals.

Keywords: aragonite, biomineralization, ligament, matrix metalloproteinase (MMP), *Pinctada fucata*

OPEN ACCESS

Edited by:
Vera Bin San Chan, Clemson University, United States

Reviewed by:
Takashi Toyofuku, Japan Agency for Marine-Earth Science and Technology, Japan
Vengatesen Thiyagarajan, University of Hong Kong, Hong Kong
Gary H. Dickinson, The College of New Jersey, United States

****Correspondence:***
Michio Suzuki
amichiwo@mail.ecc.u-tokyo.ac.jp

Specialty section:
This article was submitted to Marine Molecular Biology and Ecology, a section of the journal Frontiers in Marine Science

Received: *16 April 2018*
Accepted: *26 September 2018*
Published: *16 October 2018*

Citation:
Kubota K, Kintsu H, Matsuura A, Tsuchihashi Y, Takeuchi T, Satoh N and Suzuki M (2018) Functional Analyses of MMPs for Aragonite Crystal Formation in the Ligament of Pinctada fucata. Front. Mar. Sci. 5:373. doi: 10.3389/fmars.2018.00373

INTRODUCTION

The precipitation of calcium carbonate in the ocean is a source of significant carbon translocation. Mollusk shells consist of calcium carbonate and small amounts of organic matrices. The crystallization of calcium carbonate is regulated by these organic matrices to produce the fine microstructures of the shell. Bivalve shells are made of two valves that protect the two sides of

the animal. These two shells are connected by the hinge ligament, which functions as a joint allowing the shells to open and close. The hinge exists in the bottom of the bivalve shells and consists of a fibrous microstructure to resist the mechanical pressure. A previous study identified a positive correlation between nacre deposition capability and shell closing strength in the Japanese pearl oyster *Pinctada fucata* (Aoki et al., 2012). It has also been reported that the photonic structure of the ligament was determined by the humidity, because the water absorption changed the structural color of the ligament (Zhang and Zhang, 2015). This report suggested that the ligament is an interesting biomaterial for development of biomimetic material. Therefore, an investigation of the mechanism of ligament formation would be of interest for understanding bivalve biomineralization processes, and may provide useful insight into the efficient development of high-quality pearl production methods or functional materials.

The components of the ligament are secreted by the mantle isthmus, which is part of the soft mantle tissue attached to the shell hinge. Small, fibrous aragonite crystals, and organic frameworks are secreted from mantle isthmus cells and then align. The small crystals connect to form long aragonite crystals within the organic fibrous matrices (Bevelander and Nakahara, 1969). Short aragonite rods extend vertically toward the growing surface of the ligament. Transmission electron microscopy (TEM) observations revealed a pseudohexagonal aragonite crystal in the cross-section of a ligament (Kahler et al., 1976; Marsh and Sass, 1980) that reflects the euhedral shape of the aragonite crystal. The diameters of the aragonite crystals are ca. 50–100 nm, and the *c* axis is parallel to the morphological long axis. In contrast, the *a* and *b* axes are oriented randomly between crystals. The contrast due to the {110} twinning defects were observed in the center of the aragonite crystals (Kahler et al., 1976; Marsh and Sass, 1980).

The crystals and the fibers of the matrix are aligned in in the growth direction and the ligament in this direction is strengthened by the embedded crystals (Ono et al., 1990). Millon and xanthoprotein staining methods were used to demonstrate that the *Anodonta* ligament contains proteins tanned by quinone (Trueman, 1950). Amino acid composition analysis showed that the unmineralized outer layer of the ligament contains a high concentration of glycine, whereas the crystalized inner layer of the ligament is dominated by methionine and proline (Hare, 1963). A comparison of the amino acid compositions of the crystalized inner layer of the ligament and those of other calcified microstructures in bivalve shells showed that the ratio of acidic residues in the ligament was lower than those in other microstructures of the shell. One previous study suggested that the ligament of *Pecten* consists of a rubber-like protein, abductin (Kelly and Rice, 1967). Although the physical characteristics of abductin are similar to those of elastin and resilin, the protein sequence of abductin has not yet been determined. Kikuchi et al. (1987) discovered that the *Pseudocardiurn sachalinensis* ligament contains components that form a connection between the proteins desmosine and isodesmosine, which are related to elastin formation. Another study reported that aragonite crystals in the ligament of *P. fucata* contain a ligament intra-crystalline peptide (Suzuki et al., 2015), which inhibited the growth of the first deposited crystals along the *c* axis, keeping the aragonite crystals small. These small aragonite crystals were aligned in the same direction and stacked to form long aragonite fibers within the organic framework. However, the mechanism by which these small crystals are assembled in the organic matrix of the ligament is still unknown.

Recently, a tissue inhibitor of metalloproteinase (Pf-TIMP) was identified from organic fibers in the *P. fucata* ligament (Kubota et al., 2017). As the previous research revealed that TIMP inhibited the activity of matrix metalloproteinases (MMPs) *in vitro*, the authors investigated if the purified Pf-TIMP from the ligament has the true function of inhibitory activity using human MMPs. However, the functions of MMPs and TIMP in *P. fucata* are unknown, because no other publications about TIMP in the hinge ligament of bivalves have not been reported yet. The results of knockdown experiments using a double-stranded RNA (dsRNA) targeting MMP54089, which was identified from the *P. fucata* genome database, showed that the disordered aragonite fibers in the ligament were observed indicating that MMP54089 protein plays an important role in the formation of organic fibers between aragonite crystals.

The periodontal ligament in the tooth of mammals has similar structure of the hinge ligament of bivalves. Similar function of human MMPs has been reported in human bones and teeth (Sasano et al., 2012). MMPs degrade extracellular matrices which inhibit the growth of hydroxyapatite to make some space and hydroxyapatite crystals can then be formed in this space. Our first discovery of Pf-MMPs and Pf-TIMP functions in the hinge ligament means the convergent evolution of two similar structures in mammals and mollusks. Then, we assumed that the combination of human MMPs and collagen is a useful model system to study molluscan biomineralization in the hinge ligament. Because many other *Pinctada fucata* (Pf)-MMP genes are encoded by the *P. fucata* genome, the functions of Pf-MMPs and organic fibers in the ligament needs detailed clarification.

The objectives of this study are described below.

(1) Identification of MMP genes from transcriptome data.
(2) Functional analyses of MMP genes for the formation of the ligament using RNAi technique.
(3) Functional analyses of MMP proteins using *in vitro* calcium carbonate crystallization.

We analyzed transcriptome data from the *P. fucata* mantle isthmus and identified the expressed Pf-MMP genes. Knockdown and *in vitro* calcium carbonate crystallization experiments demonstrated the function of organic fibers in ligament formation. To gain further insight into possible ways that the matrix can influence aragonite formation, we also carried out experiments on Pf-MMP treated collagen matrices in which aragonite was induced to form. Knockdown and *in vitro* experiments revealed the formation process of organic fibers by Pf-MMP functions. Lastly, calcium carbonate crystallization experiment showed that human MMP treatments increased the interaction between aragonite crystals and organic fibers

suggesting that Pf-MMP have some functions for calcification in the ligament.

MATERIALS AND METHODS

Collection of Shells and Living Tissues

The Japanese pearl oyster *P. fucata* was cultured in Ago Bay (Mie Prefecture, Japan) by the Fisheries Research Division, Mie Prefectural Science and Technology Promotion Center, Japan (latitude, 34.3 degree and longitude, 136.8 degree), and sent to The University of Tokyo, where *P. fucata* was cultured for 1–2 weeks before collecting the shells by removing the soft bodies. Live *P. fucata* were cultured in 10 L aquarium filled with natural seawater (natural seawater from outside of Tokyo bay was kept in 10 ton tank) at 20°C. We changed the natural seawater every 2 days. Other shells were washed, dried, and separated by MIKIMOTO COSMETICS (Mie, Japan) and sent to the University of Tokyo. Living mantle isthmus tissue was collected and stored in a freezer at −80°C.

Transcriptome Analysis by Next-Generation Sequencing

Total RNA was extracted from the mantle isthmus of three individuals at the age of 2 years using Sepasol-RNA I Super G (Nacalai), following the manufacturer's instructions. We chose the *P. fucata* which kept tightly closed of bivalve shells. Transcriptome libraries were prepared using the TruSeq RNA Library Preparation Kit v2 (Illumina). RNA was sequenced using an Illumina Miseq (Illumina), following the manufacturer's instructions. Only high-quality sequences (quality value $\geq$ 20) were assembled using Trinity ver. 2.2.1[1] (Grabherr et al., 2011). Read preprocessing, assembly, and mapping were performed in the read annotation pipeline of the DNA Databank of Japan (DDBJ) using the default parameters[2].

Identification of Pf-MMP Genes From Transcriptome Data

To identify the Pf-MMP genes, we performed a homology search in transcriptome data from the mantle isthmus using the basic local alignment search tool (BLAST). Identified Pf-MMP sequences were combined with those of Pf-MMP genes from the *P. fucata* genome database (Takeuchi et al., 2012) to determine the entire sequences. The sequences of Pf-MMP genes were registered to the DDBJ and assigned accession numbers (MMP21914: LC388937, MMP07860: LC388938, MMP60936: LC388939, MMP32404: LC388940, MMP23659: LC388941, MMP54089: LC388942, MMP14973: LC388943).

RNA Interference (RNAi)

To reveal the function of other Pf-MMPs other than MMP54089 (Kubota et al., 2017), we chose MMP07860, which showed a similar expression pattern to MMP54089, and MMP14973, which showed lower expression level than MMP54089. A dsRNA targeting MMP07860 or MMP14973 was generated to observe the growing end of the ligament in the absence of MMP07860 or MMP14973 using a scanning electron microscope (SEM). To prepare the template to construct dsRNAs targeting MMP07860 and MMP149739, we conducted polymerase chain reaction (PCR) using cDNA prepared from oyster mantle isthmus RNA. PCR was performed using the following cycling conditions: 30 cycles of 30 s at 94°C (3 min 30 s for the first cycle), 30 s at 55°C, and 30 s at 72°C. The PCR product was diluted with distilled water to 100× the volume and used as a template for the following nested PCR. The primers used in the nested PCR contained a T7 polymerase recognition sequence, enabling T7 polymerase to recognize the sequence and start transcription. For MMP14973, the 5′ primer sequence was GGGTAATACGACTCACTATAGGGTCAAAGAATATCAAAAGAGG and that of the 3′ primer GGGTAATACGACTCACTATAGGGTCACCATTTCCAGATGTCAT (Under bars mean the sequence of T7 promoter). For MMP07860, the 5′ primer sequence was GGGTAATACGACTCACTATAGGGAGTACTGGTCTGACGTCACT and that of the 3′ primer GGGTAATACGACTCACTATAGGGAGTTGGTGACACTGGGGTTA. The nested PCR was performed under the same conditions, and the resulting product was used as a template to produce dsRNA. The *in vitro* Transcription T7 Kit for siRNA synthesis (TaKaRa) was used to produce dsRNA according to the manufacturer's instructions. A dsRNA targeting enhanced green fluorescence protein (EGFP) was also prepared as a control. We dissolved 30 μg each of dsRNA in 50 μL phosphate-buffered saline and injected the dsRNA into the adductor muscle of *P. fucata*. We used more than three individuals of young oysters (shell size: 7 cm) in this experiment, because it was necessary to observe the growth process of the ligament, which can be difficult to observe in mature oysters. We extracted total RNA from the mantle isthmus of each sample 4 days post-injection using the method described above; reverse transcription was performed using the PrimeScript Perfect Real Time Reagent Kit (TaKaRa) according to the manufacturer's instructions.

SEM Observations of the Ligament

Fresh ligaments were collected from living pearl oysters following dsRNA injection. The ligament was washed with distilled water and dried on an aluminum stage. The growing end of the ligament in each sample (more than three individuals in each condition) was observed using an SEM (Hitachi S-4800, Tokyo, Japan). The surface of the ligament was observed via secondary electron images at an acceleration voltage of 2 kV. The samples were coated with Pt–Pd for high-resolution secondary electron image recording.

Real-Time PCR

Real-time quantitative PCR (qPCR) was performed to quantity gene expression levels of MMP14973 and MMP07860. qPCR primers were designed using the Primer3Plus software. For MMP14973, the 5′ primer sequence was AGGTCGGTGCAATGATAGCA and that of the 3′ primer

[1]https://github.com/trinityrnaseq/trinityrnaseq/wiki

[2]https://p.ddbj.nig.ac.jp/pipeline/Login.do

CGTTTTCGTCTTTCCTCTTCTGT. For MMP07860, the 5′ primer sequence was CGACACACATTTCGATGACG and that of the 3′ primer TTTGGGCTCACTTGAGTGTC. Actin was used as an internal control gene for qPCR (5′ primer: CAGAAGGAAATCACCGCACT; 3′ primer: AGAGGGAAGCAAGGATGGAG). We performed qPCR using the Applied Biosystems 7300 Fast Real-Time PCR System with SYBR Premix Ex Taq II (Takara). To compare gene expression levels, we used the ΔΔCT method. The qPCR reaction mixture (10 μl) was adjusted according to the manufacturer's instructions. The cycling parameters were: 1 cycle of 0.5 min at 95°C, 40 cycles of 5 s at 95°C, and 34 s at 60°C. Dissociation curves were analyzed at the end of each run to determine the purity of the product and the amplification specificity.

Calcium Carbonate Crystallization in the Decalcified Ligament

The ligaments were decalcified individually in 15 ml tubes with 5 ml of 1 M acetic acid solution for 24 h. We collected the decalcified ligament after centrifugation to remove the acetic acid. The decalcified ligament was washed with distilled water using centrifugation. The ligaments were collected from more than three individuals for each condition. The experimental treatments were described below.

(1) 20 μl of human recombinant MMP-13 (hrMMP-13) (340 mU; MMP inhibitor profiling kit, fluorometric red; ENZO) was mixed with the ligament from one individual in the 1.5 ml tube.
(2) The solution of (1) was mixed with 20 μl of assay buffer from MMP inhibitor profiling kit and 60 μl of 10 mM Tris-HCl (pH 8.0) for 3 h at 37°C.
(3) The ligament treated with or without human MMP13 in 20 mM $CaCl_2$/5 mM $MgCl_2$/25 mM Tris-HCl (pH 7.4) solution was then placed in a desiccator with 5 g ammonium carbonate powder in 50 ml beaker.
(4) After 24 h, the recalcified ligament was placed on the sample stage for SEM observation (Hitachi, S-4800) and coated with Pt–Pd at 20 mA for 60 s (Hitachi, E-1030).

In vitro Calcium Carbonate Crystallization in a Collagen Gel

To synthesize collagen gels, we followed the method of Nudelman et al. (2010) with modifications. Collagen type I from bovine skin (Nippi, Inc., Tokyo, Japan) was dissolved in 1 M acetic acid at 4°C. The collagen solution was then dialyzed in 67 mM phosphate buffer (pH 6.0) using a dialysis membrane for 3 h at 4°C; the buffer was replaced three times (every 3 h) at 4°C. The solution was then placed in a dish to produce gels. These collagen gels were treated with 734.4 U of the hrMMP-1 described above for 14 h at 37°C. The collagen gels treated with or without human MMP13 in the 20 mM $CaCl_2$/5 mM $MgCl_2$/25 mM Tris-HCl (pH 7.4) solution were then placed in the desiccator. The calcification experiment was performed as described above. After calcification, the collagen gel was degraded with 18% sodium hypochlorite solution to purify the calcium carbonate precipitates, which were then observed by SEM. The Hitachi FB-2100 focused ion beam (FIB) was used to cut electron-transparent cross-sections from synthetic precipitate aggregates. The cross-sections were transferred to a JEOL JEM-2010 TEM operating at 200 kV for imaging and electron diffraction.

The collagen gels and calcium carbonate crystals were mounted on an aluminum platelet with a cavity of 200 μm depth and filled with 1-hexadecene (Sigma -Aldrich, St. Louis, MO, United States) for cryo-SEM. The samples were then cryo-immobilized in the HPM10 high-pressure freezing device (Bal-Tec AG, Balzers, Liechtenstein). The frozen samples were mounted on a holder and transferred to the BAF 60 FF device (Bal-Tec) using the VCT 100 vacuum cryo-transfer device (Bal-Tec). Frozen samples were fractured at 120°C and etched for 5 min at 105°C. Samples were then transferred to the Ultra 55 SEM using the VCT 100 cryo-transfer device and observed using secondary electron and backscattered electron in-lens detectors at 120°C. The backscattered electron in-lens detector was operated at 2 kV using an energy selective backscattered detector (ESB) grid voltage of 300 V. Stronger signals in the backscattered images were obtained from elements with higher atomic masses, i.e., calcium atoms within the mineral phase, which provided information on the distribution of the mineral relative to the organic material.

RESULTS AND DISCUSSION

Identification of Pf-MMPs in *P. fucata*

In a previous study (Kubota et al., 2017), we identified seven Pf-MMP genes in the *P. fucata* genome database (Takeuchi et al., 2012). However, the assembled genome sequence in the genome database was insufficient to reveal the entire sequence of each Pf-MMP gene. To determine the whole sequence of Pf-MMP genes expressed in the mantle isthmus, we performed a homology search of the amino acid sequence of the MMP activity domain using transcriptome data from mantle isthmus tissue. We identified seven Pf-MMP genes (MMP21914, 07860, 60936, 32404, 23659, 54089, and 14973) from the transcriptome data (**Figure 1** and **Supplementary Figure S1**). All Pf-MMPs in the transcriptome database except for MMP32404 contained a signal peptide, an MMP superfamily domain, a putative peptidoglycan-binding domain, and hemopexin-like repeats. As signal peptide sequences in Pf-MMP genes were not identified in our previous study, we extended the sequences used for analysis using the transcriptome data. Signal peptides and hemopexin-like repeats were not found in MMP32404, suggesting that MMP32404 expression was too low to obtain many fragments from the mantle isthmus. We also checked that the whole sequence of Pf-TIMP was included in the transcriptome data.

Peptidoglycan-binding domain and hemopexin-like repeats have also been identified in human MMPs (Sekhon, 2010). Previous studies have shown that these regions are related to the interaction between human MMPs and their substrates (Gillian and Vera, 1997). A cysteine switch (PRCGVP) occurs after the peptidoglycan-binding domain binds to zinc in the human MMP activity domain, thereby inhibiting the activity

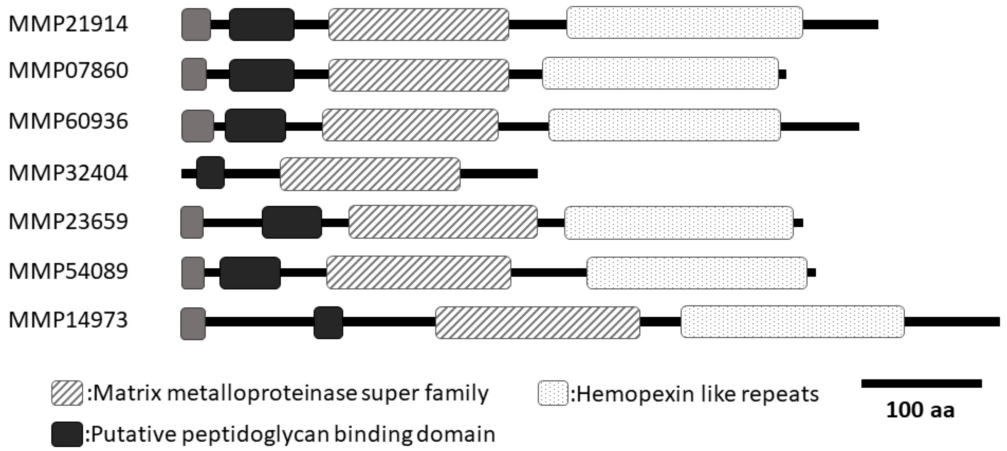

FIGURE 1 | A schematic of the domain structures of seven MMPs from *Pinctada fucata*. All MMPs, except for MMP32404, had similar lengths and domain structures. Only MMP32404 did not contain hemopexin like repeats in the C-terminal region. Black boxes indicate the putative peptidoglycan-binding domain. Dotted boxes indicate hemopexin-like repeats. Hashed boxes indicate the MMP superfamily domain. Gray boxes indicate the signal peptide. DDBJ accession numbers (MMP21914: LC388937, MMP07860: LC388938, MMP60936: LC388939, MMP32404: LC388940, MMP23659: LC388941, MMP54089: LC388942, MMP14973: LC388943).

(Springman et al., 1990; Van Wart and Hansen, 1990). Processing of the propeptide in human MMPs is necessary to activate human MMPs. All pf-MMPs in *P. fucata* exhibit conservation of this cysteine switch, suggesting that Pf-MMP activity in *P. fucata* may require this processing step.

RNAi of Pf-MMPs

In the previous study, a knockdown experiment using a dsRNA targeting MMP54089 affected the growth direction of aragonite fibers in the ligament. To investigate the functions of MMP07860 and MMP14973 in the ligament, we performed RNAi experiments in the current study. The growing edge of the ligament after RNAi experiments was observed by SEM 4 days after injection (**Figure 2**). In the control treatment, the tips of aragonite crystals were observed as white dots along the surface of the growing edge. Similar microstructures were observed after injection of EGFP-specific dsRNA that is a negative control of RNAi experiment. Some aggregation of the aragonite fibers was observed after MMP07860-specific dsRNA injection. The knockdown of MMP14973 increases the diameter of each aragonite tips in the ligament. However, the effect of MMP14973 is small, because the expression level of MMP14973 is too low in the ligament to cause a marked impact by knockdown. MMP07860 expression after injection was measured using qPCR (**Figure 3**). Expression was lower 12 h after injection, suggesting that MMP07860 production was inhibited by MMP07860-specific dsRNA injection. However, it was difficult to detect MMP14973 PCR products using qPCR (data not shown), preventing us from assessing the efficacy of the RNAi procedure.

The RNAi knockdown experiment conducted in our previous study showed that MMP54089 regulates the organic framework to align aragonite fiber orientation in the ligament (Kubota et al., 2017). MMP07860 knockdown led to minor aggregation of aragonite fibers, whereas knockdown of MMP14973 had small effect, because the expression level of MMP14973 was very low. Although the expression level and pattern of MMP07860 were similar to those of MMP54089, the results of RNAi experiments were different. The knockdown of MMP54089 disordered the orientation of aragonite fibers and disrupted the organic matrices (Kubota et al., 2017), while the knockdown of MMP07860 resulted in small aggregations of aragonite fibers.

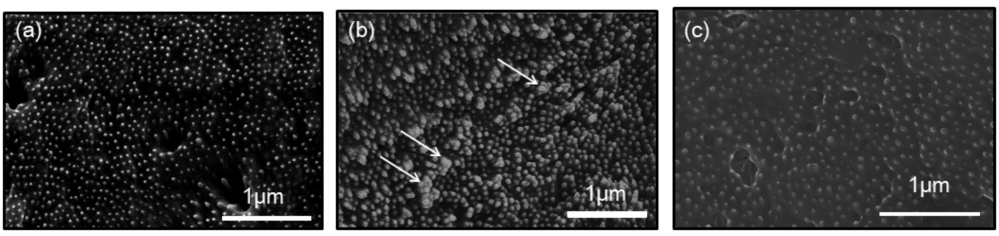

FIGURE 2 | Scanning electron microscopy (SEM) observations of the surface of the growing edge of the ligament in the samples injected with dsRNA targeting **(a)** enhanced green fluorescence protein (EGFP), **(b)** MMP07860, and **(c)** MMP14973. The injection of EGFP and MMP14073 showed normal surface, while the injection of MMP07860 showed small aggregation of aragonite crystals. White arrows indicate the aggregation of aragonite crystals.

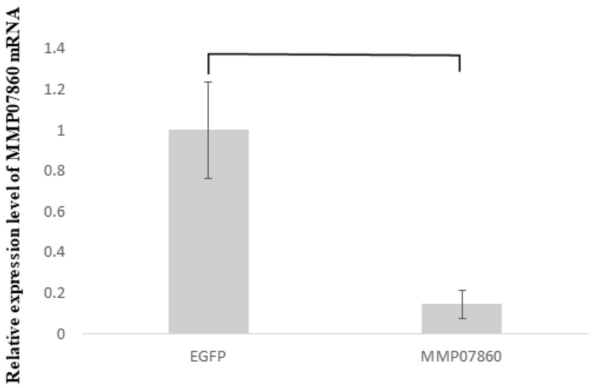

FIGURE 3 | Expression levels of MMP07860 mRNA in the mantle isthmus, determined using real-time quantitative polymerase chain reaction (qPCR) 12 h after injection. The injection of dsRNA (MMP07860) depressed the expression level of MMP07860. The MMP07860 mRNA expression in the EGFP group (EGFP–dsRNA injected) was given a relative value of 1.0. Five oysters (n = 5) were used. Statistically significant differences were determined by t-test ($p < 0.05$).

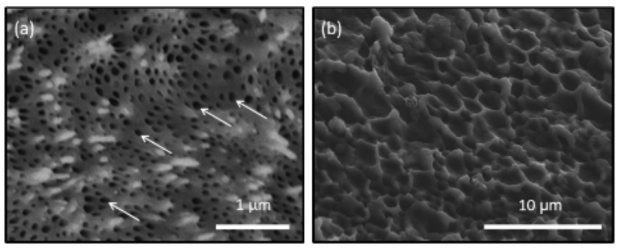

FIGURE 4 | Scanning electron microscopy observations of the surface of the growing edge of the ligament **(a)** after decalcification using 1 M CH_3COOH and **(b)** after treatment with hrMMP-13. The decalcified treatment showed many holes on the surface of the ligament. Treatment of hrMMP-13 degraded the microstructure of the ligament. White arrows indicate the holes.

These results suggest that MMP07860 has few effects for the ligament formation. The knockdown effects of these Pf-MMP genes were dramatically different, suggesting that each Pf-MMP has a specific function in the formation of the ligament.

Previous work has reported on the functions of human MMPs related to biomineralization. In the process of tooth formation, expression of human MMP 20 was detected. Human MMP20 degrades amelogenin to induce calcification of hydroxyapatite in tooth enamel (Uskokovic et al., 2011). Pf-MMP proteins in *P. fucata* probably have similar functions during ligament formation.

Organic Fibers in the Decalcified Ligament Treated With Recombinant MMP-13

To investigate Pf-MMP function in the ligament, we investigated if organic fibers in the ligament were degraded by human MMP activity, or not. The decalcified ligament was washed with distilled water and observed by SEM (**Figure 4**). The dissolution of aragonite fibers created holes in its surface (**Figure 4a**). Some aragonite fibers remained after decalcification. The decalcified ligament was treated with hrMMP-13, because hrMMP-13 activity was most inhibited by Pf-TIMP. Treatment with hrMMP-13 resulted in alteration of the surface structure; the holes disappeared, and the hexagonal shape of the organic framework appeared (**Figure 4b**).

Many small holes (diameter ca. 50–100 nm) were observed following decalcification treatment, which were the sites of the aragonite fibers. These holes disappeared in the decalcified ligament after hrMMP-13 treatment, and a large, hexagonal organic framework (diameter ca. 1–3 μm) appeared, suggesting that large (micrometer order) organic frameworks formed following the formation of a small (nanometer order) space for aragonite fibers. Calcium carbonate crystallization on the decalcified ligament following hrMMP-13 treatment indicated that hrMMP-13 indirectly prevented calcium carbonate formation by destroying the surface which promoted mineral formation; thus, excessive hrMMP-13 degradation depressed calcification in the framework. During the biomineralization process, fibrous organic matrices such as chitin play an important role as a framework for crystals (Kintsu et al., 2017).). As human MMPs are essential for the ordered assembly of collagen, it is conceivable that the hinge ligament protein contains a collagen-like protein. Collagen in various mineralized tissues forms a fibrous framework.

Calcium Carbonate Crystallization on the Decalcified Ligament

The existence of TIMP in the ligament (Kubota et al., 2017) suggested that excess MMP activity may inhibit the formation of the ligament. The effect for calcification of the ligament after hrMMP-13 treatment was investigated. The decalcified ligament was incubated in a calcium carbonate-supersaturated solution containing 50 mM $MgCl_2$ to induce the formation of aragonite crystals on the surface. Many fibrous aragonite crystals were observed on the surface (**Figures 5a,b**). Each fiber was aligned, and large grains were formed. In contrast, no crystals formed on the surface treated with hrMMP-13, indicating that degraded organic frameworks cannot induce the formation of aragonite crystals (**Figures 5c,d**). These results suggested that the excess treatment of hrMMP-13 changed a good balance of MMP and TIMP functions in the ligament to inhibit the calcification.

Calcium Carbonate Crystallization in the Collagen Gels Treated With hrMMP-1

To observe the organic fibers after MMP treatment, we used collagen fiber and hrMMP-1 as *in vitro* model system. The components of the organic framework in the ligament are similar to those of extracellular matrices such as collagen proteins. Aragonite crystals were precipitated in the collagen fibers to mimic ligament formation. We dissolved type 1 bovine collagen in acid and transferred to phosphate buffer at a neutral pH to induce collagen gel formation. Then, the collagen gel was treated with hrMMP-1. TEM observations showed that the

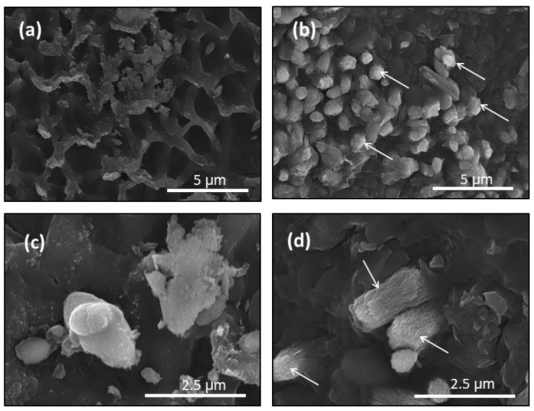

FIGURE 5 | Scanning electron microscopy observations of the surface of the growing edge of the ligament after crystallization. **(a,c)** hrMMP-13 treatment and **(b,d)** no MMP treatment (decalcification only). **(a,b)** Low magnification; **(c,d)** high magnification. The treatment of hrMMP-13 inhibited the calcification of the decalcified ligament. White arrows indicate the aragonite crystals.

untreated collagen gels retained the same thickness and elongated separately (**Figure 6a**). Collagen gels treated with hrMMP-1 became short, thin fibers (**Figure 6b**); the tips of some of these fibers aggregated to form a spherical shape.

The collagen gels with or without treatment of hrMMP-1 with aragonite crystals were observed by SEM. A ball shape covered by needles was observed under both conditions. The needle shape is typical of aragonite crystals. Each needle was clearly observed in the collagen gels that were not treated with hrMMP-1 (**Figures 7a–d**), whereas the surface of the ball in the collagen gels treated with hrMMP-1 was covered with organic substances (**Figures 7e–h**), which were attached to the needles to form a complex shape, suggesting that degraded collagen fibers enhanced the interaction with the calcium carbonate surface.

To observe the interface between crystal and collagen fibers treated with hrMMP-1, a crystal cross-section was prepared by FIB and freeze fracturing. TEM observations showed that the organic layer covered the spiky aragonite surface (**Figure 8**). Cryo-SEM observations also showed that the collagen fibers interacted with the aragonite surface (**Figure 9**). Back-scattered images clearly revealed the boundary between calcium carbonate and the collagen fibers (**Figures 9b,d**).

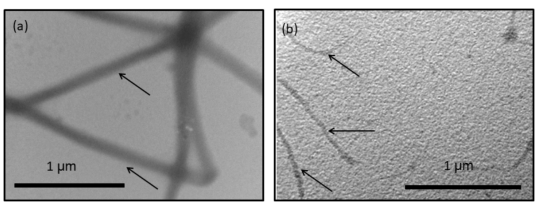

FIGURE 6 | Transmission electron microscopy (TEM) observation of collagen fibers treated with **(a)** no hrMMP-1 and **(b)** hrMMP-1. The treatment of hrMMP-1 degraded the collagen fibers and made the fibers thin. Black arrows indicate the collagen fibers.

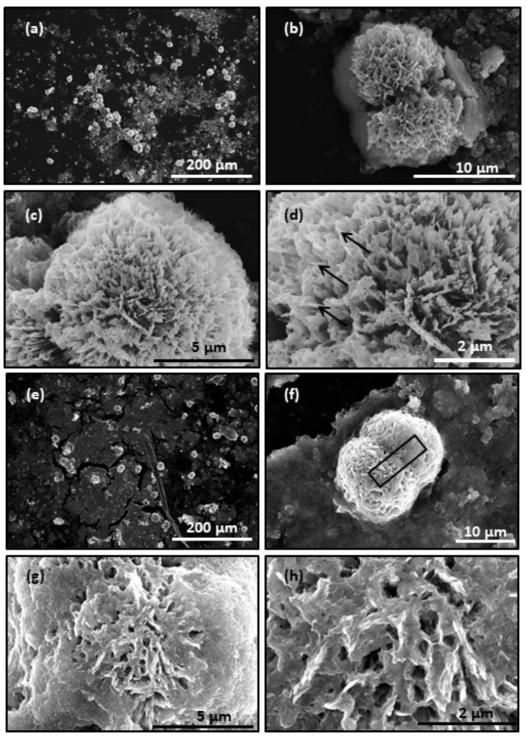

FIGURE 7 | Scanning electron microscopy observation of $CaCO_3$ crystals in the collagen gel. **(a–d)** No hrMMP-1 treatment; same region, different magnification. **(e–h)** hrMMP-1 treatment; same region, different magnification. The treatment of hrMMP-1 increased the interaction between collagen fibers and aragonite crystals. Black arrows show the needles covering the ball crystal. Black rectangle in **(f)** indicates the region where the cross-section was made for FIB-TEM analysis.

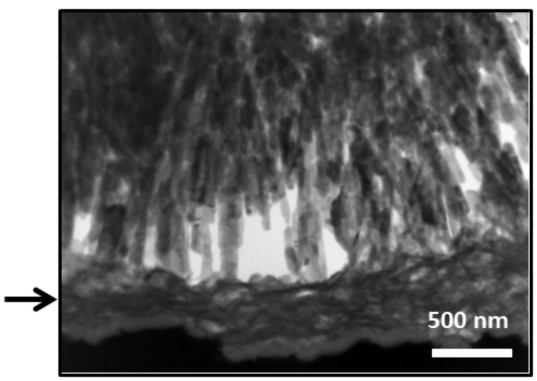

FIGURE 8 | Transmission electron microscopy images of the FIB cross-section. The collagen fibers covered the aragonite needles. Crystal surface with organic fibers covering the calcium carbonate crystal. Arrow indicated the localization of collagen fibers.

Our results showed that the degradation process of organic fibers increased the interaction of calcium carbonate and collagen fibers. The contents of organic compounds will be regulated by this technique. The organic content affects the toughness and stiffness of the organic-inorganic hybrid materials.

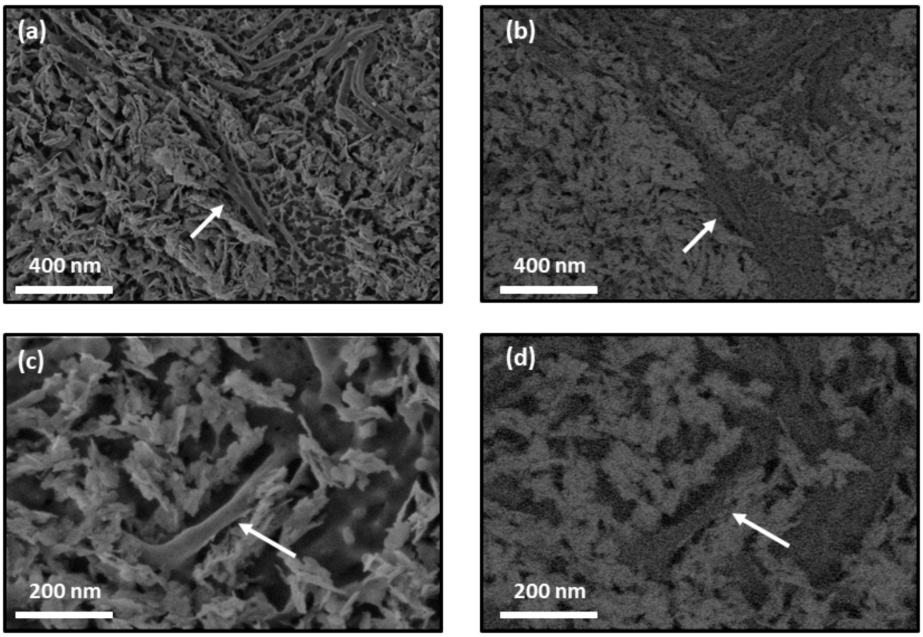

FIGURE 9 | Cryo-SEM images of collagen gel with calcium carbonate crystals. Collagen fibers treated with hrMMP-1 tightly interacted with aragonite crystals. **(a,c)** Secondary electron images of calcium carbonate with collagen fibers. **(b,d)** Back-scattered images of **(a,c)**, respectively. White arrows indicate collagen fibers.

CONCLUSION

We identified seven Pf-MMP genes from the *P. fucata* genome database in a previous study (Kubota et al., 2017). Because MMP is a proteinase for extracellular matrix proteins, MMP is secreted from the cell and must contain an N-terminal signal peptide to do so. However, the length of the nucleotide sequence was insufficient to reveal the entire gene sequence of each Pf-MMP, and the N-terminal signal peptide was not detected in almost all Pf-MMP genes. In the *P. fucata* genome database, the intron–exon prediction may have misidentified the Pf-MMPs open reading frame region, or whole Pf-MMP gene sequences may have been separated into different scaffolds. The mantle isthmus transcriptome data in this study was used to extend the nucleotide sequences of the Pf-MMP genes successfully. All Pf-MMP proteins, except for MMP32404, had similar lengths and domain structures. Only MMP32404 did not contain hemopexin like repeats in the C-terminal region.

Pf-TIMP plays an important role in regulating human MMP activity (Kubota et al., 2017). Calcium carbonate crystallization on the decalcified ligament that was not treated with hrMMP-13 induced the orientation of bundled aragonite crystals. Normal aragonite crystals in the calcium carbonate-supersaturated solution containing magnesium ions were covered by radiating needles. The components of the ligament may have a role in regulating the growth direction of aragonite crystals.

To investigate general MMP functions during calcification in detail, we performed *in vitro* calcium carbonate crystallization experiments with collagen gels. TEM observations showed that fine collagen fibers covered the surface of the aragonite needles. Cryo-SEM showed the boundary between collagen fibers and aragonite needles. These results suggest that hrMMP-1 degraded the collagen fibers and increased the interaction between aragonite surface and collagen fibers. The previous work also showed the collagen fibers regulated the orientation of aragonite crystals (Falini et al., 1997). In this study, we revealed that hrMMP-13 functions in the matrix calcification of the *P. fucata* ligament. This information provides insight into the biomineralization mechanism and will contribute to the development of novel applications in material science.

AUTHOR CONTRIBUTIONS

KK did the experiments and described the images of figures. HK supported the experiments and paper preparation. AM did the experiments of next generation sequencer. YT cultured and sent the living *P. fucata*. TT and NS supported to do the next generation sequencer. MS organized this project and wrote the manuscript.

FUNDING

This work was supported by a Grant-in-Aid for Young Scientists B (JP25850078 and JP16K20995) (to MS) from Japan Society for the Promotion of Science (JSPS). This study was also supported by the JSPS-ISF (Israel Science Foundation) Joint Academic Research Program.

ACKNOWLEDGMENTS

We thank Prof. Toshihiro Kogure in The University of Tokyo, Prof. Stephen Weiner and Prof. Lia Addadi in Weizmann Institute of Science for their invaluable helps.

SUPPLEMENTARY MATERIAL

The Supplementary Material for this article can be found online at: https://www.frontiersin.org/articles/10.3389/fmars.2018.00373/full#supplementary-material

REFERENCES

Aoki, H., Tanaka, S., Atsumi, T., Abe, H., Fujiwara, T., Kamiya, N., et al. (2012). Correlation between Nacre-deposition ability and shell-closing strength in Japanise Pearl Oyster *Pinctada fucata*. *Aquac. Sci.* 60, 451–457.

Bevelander, G., and Nakahara, H. (1969). An electron microscope study of the formation of the ligament of *Mytilus edulis* and *Pinctada radiata*. *Calcif. Tissue Res.* 4, 101–112. doi: 10.1007/BF02279112

Falini, G., Fermani, S., Gazzano, M., and Ripamonti, A. (1997). Biomimetic crystallization of calcium carbonate polymorphs by means of collagenous matrices. *Chem. Eur. J.* 3, 1807–1814. doi: 10.1002/chem.19970031113

Gillian, M., and Vera, K. (1997). Relating matrix metalloproteinase structure to function: why the 'hemopexin' domain? *Matrix Boil.* 15, 511–518.

Grabherr, M. G., Haas, B. J., Yassour, M., Levin, J. Z., Thompson, D. A., Amit, I., et al. (2011). Full-length transcriptome assembly from RNA-Seq data without a reference genome. *Nat. Biotechnol.* 29, 644–652. doi: 10.1038/nbt.1883

Hare, P. (1963). Amino acids in the proteins from aragonite and calcite in the shells of *Mytilus californianus*. *Science* 139, 216–217. doi: 10.1126/science.139.3551.216

Kahler, G., Sass, R., and Fisher, F. (1976). The fine structure and crystallography of the hinge ligament of *Spisula solidissima* (Mollusca: Bivalvia: Mactridae). *J. Comp. Physiol.* 109, 209–220. doi: 10.1007/BF00689419

Kelly, R., and Rice, R. (1967). Abductin: a rubber-like protein from the internal triangular hinge ligament of Pecten. *Science* 155, 208–210. doi: 10.1126/science.155.3759.208

Kikuchi, Y., Tsuchiura, O., Hirama, M., and Tamiya, N. (1987). Desmosine and isodesmosine as cross-links in the hinge-ligament protein of bivalves. 3,3'-Methylenebistyrosine as an artifact. *Eur. J. Biochem.* 164, 397–402. doi: 10.1111/j.1432-1033.1987.tb11071.x

Kintsu, H., Okumura, T., Negishi, L., Ifuku, S., Kogure, T., Sakuda, S., et al. (2017). Crystal defects induced by chitin and chitinolytic enzymes in the prismatic layer of *Pinctada fucata*. *Biochem. Biophys. Res. Commun.* 489, 89–95. doi: 10.1016/j.bbrc.2017.05.088

Kubota, K., Tsuchihashi, Y., Kogure, T., Maeyama, K., Hattori, F., Kinoshit, S., et al. (2017). Structural and functional analyses of a TIMP and MMP in the ligament of *Pinctada fucata*. *J. Struct. Biol.* 199, 216–224. doi: 10.1016/j.jsb.2017.07.010

Marsh, M., and Sass, R. (1980). Aragonite twinning in the molluscan bivalve hinge ligament. *Science* 208, 1262–1263. doi: 10.1126/science.208.4449.1262

Nudelman, F., Pieterse, K., George, A., Bomans, P. H., Friedrich, H., and Brylka, L. J. (2010). The role of collagen in bone apatite formation in the presence of hydroxyapatite nucleation inhibitors. *Nat. Mater.* 9, 1004–1009. doi: 10.1038/nmat2875

Ono, K., Kikuchi, Y., Higashi, K., and Tamiya, N. (1990). Elastic anisotropy of bivalve hinge-ligament. *J. Biomech.* 23, 307–312. doi: 10.1016/0021-9290(90)90058-B

Sasano, Y., Nakamura, M., Okata, H., Henmi, A., and Mikami, Y. (2012). Remodeling of extracellular matrices initiates and advances calcification during development and healing of bones and teeth. *J. Oral Biosci.* 54, 25–29. doi: 10.1016/j.job.2011.06.001

Sekhon, B. S. (2010). Matrix metalloproteinases – an overview. *Res. Rep. Biol.* 1, 1–20.

Springman, E. B., Angleton, E. L., Birkedal-Hansen, H., and Van Wart, H. E. (1990). Multiple modes of activation of latent human fibroblast collagenase: evidence for the role of a Cys73 active-site zinc complex in latency and a "cysteine switch" mechanism for activation. *Proc. Natl. Acad. Sci. U.S.A.* 87, 364–368. doi: 10.1073/pnas.87.1.364

Suzuki, M., Kogure, T., Sakuda, S., and Nagasawa, H. (2015). Identification of Ligament Intra-Crystalline Peptide (LICP) from the Hinge Ligament of the Bivalve, *Pinctada fucata*. *Mar. Biotechnol.* 17, 153–161. doi: 10.1007/s10126-014-9603-y

Takeuchi, T., Kawashima, T., Koyanagi, R., Gyoja, F., Tanaka, M., Ikuta, T., et al. (2012). Draft genome of the pearl oyster *Pinctada fucata*: a platform for understanding bivalve biology. *DNA Res.* 19, 117–130. doi: 10.1093/dnares/dss005

Trueman, E. (1950). Quinone-tanning in the Mollusca. *Nature* 165, 397–398. doi: 10.1038/165397c0

Uskokovic, V., Khan, F., Liu, H. C., Witkowska, H. E., Zhu, L., Li, W., et al. (2011). Hydrolysis of amelogenin by matrix metalloprotease-20 accelerates mineralization in vitro. *Arch. Oral Biol.* 56, 1548–1559. doi: 10.1016/j.archoralbio.2011.06.016

Van Wart, H. E., and Hansen, B. H. (1990). The cysteine switch: a principle of regulation of metalloproteinase activity with potential applicability to the entire matrix matelloproteinase gene family. *Proc. Natl. Acad. Sci. U.S.A.* 87, 5578–5582. doi: 10.1073/pnas.87.14.5578

Zhang, W., and Zhang, G. (2015). A humidity sensitive two-dimensional tunable amorphous photonic structure in the outer layer of bivalve ligament from Sunset Siliqua. *Mater. Sci. Eng. C Mater. Biol. Appl.* 52, 18–21. doi: 10.1016/j.msec.2015.03.029

Conflict of Interest Statement: The authors declare that the research was conducted in the absence of any commercial or financial relationships that could be construed as a potential conflict of interest.

frontiers in Marine Science

ORIGINAL RESEARCH
published: 22 October 2018
doi: 10.3389/fmars.2018.00369

Assessing the Impacts of Ocean Acidification on Adhesion and Shell Formation in the Barnacle *Amphibalanus amphitrite*

*Jessica A. Nardone[1], Shrey Patel[1], Kyle R. Siegel[1], Dana Tedesco[1], Conall G. McNicholl[1], Jessica O'Malley[2], Jack Herrick[2], Rebecca A. Metzler[2], Beatriz Orihuela[3], Daniel Rittschof[3] and Gary H. Dickinson[1]**

[1] Department of Biology, The College of New Jersey, Ewing, NJ, United States, [2] Department of Physics and Astronomy, Colgate University, Hamilton, NY, United States, [3] Marine Science and Conservation, Duke University Marine Laboratory, Beaufort, NC, United States

OPEN ACCESS

Edited by:
Pei-Yuan Qian, Hong Kong University of Science and Technology, Hong Kong

Reviewed by:
Adam Michael Reitzel, University of North Carolina at Charlotte, United States
Ciro Rivera-Casas, Florida International University, United States

***Correspondence:**
Gary H. Dickinson
dickinga@tcnj.edu

Specialty section:
This article was submitted to Marine Molecular Biology and Ecology, a section of the journal Frontiers in Marine Science

Received: *01 March 2018*
Accepted: *25 September 2018*
Published: *22 October 2018*

Citation:
Nardone JA, Patel S, Siegel KR, Tedesco D, McNicholl CG, O'Malley J, Herrick J, Metzler RA, Orihuela B, Rittschof D and Dickinson GH (2018) Assessing the Impacts of Ocean Acidification on Adhesion and Shell Formation in the Barnacle Amphibalanus amphitrite. Front. Mar. Sci. 5:369. doi: 10.3389/fmars.2018.00369

Barnacles are dominant members of marine intertidal communities. Their success depends on firm attachment provided by their proteinaceous adhesive and protection imparted by their calcified shell plates. Little is known about how variations in the environment affect adhesion and shell formation processes in barnacles. Increased levels of atmospheric CO_2 have led to a reduction in the pH of ocean waters (i.e., ocean acidification), a trend that is expected to continue into the future. Here, we assessed if a reduction in seawater pH, at levels predicted within the next 200 years, would alter physiology, adhesion, and shell formation in the cosmopolitan barnacle *Amphibalanus (=Balanus) amphitrite*. Juvenile barnacles, settled on silicone substrates, were exposed to one of three static levels of pH_T, 8.01, 7.78, or 7.50, for 13 weeks. We found that barnacles were robust to reduced pH, with no effect of pH on physiological metrics (mortality, tissue mass, and presence of eggs). Likewise, adhesive properties (adhesion strength and adhesive plaque gross morphology) were not affected by reduced pH. Shell formation, however, was affected by seawater pH. Shell mass and base plate area were higher in barnacles exposed to reduced pH; barnacles grown at pH_T 8.01 exhibited approximately 30% lower shell mass and 20% smaller base plate area as compared to those at pH_T 7.50 or 7.78. Enhanced growth at reduced pH appears to be driven by the increased size of the calcite crystals that comprise the shell. Despite enhanced growth, mechanical properties of the base plate (but not the parietal plates) were compromised at the lowest pH level. Barnacle base plates at pH_T 7.50 broke more easily and crack propagation, measured through microhardness testing, was significantly affected by seawater pH. Other shell metrics (plate thickness, relative crystallinity, and atomic disorder) were not affected by seawater pH. Hence, a reduction in pH resulted in larger barnacles but with base plates

that would crack more readily. It is yet to be determined if such changes would alter the survival of *A. amphitrite* in the field, but changes in the abundance of this ecologically dominant species would undoubtedly affect the composition of biofouling communities.

Keywords: biomineralization, climate change, mechanical properties, biofouling, cement, adhesive tenacity, calcite, *Balanus*

INTRODUCTION

Barnacles are dominant members of marine biofouling communities throughout much of the world's oceans. They settle and tenaciously adhere to nearly any inert surface in the marine environment, including ship hulls and maritime facilities, and once established can serve as a substrate for less tenacious species. This results in a tremendous cost burden for Naval and maritime industries in the form of coating application, cleaning and maintenance, as well as lost operational time (Callow and Callow, 2011; Schultz et al., 2011).

The success of Balanomorph barnacles depends on the firm attachment provided by their secreted adhesive and the protection imparted by their heavily calcified outer shell plates. Adult barnacles adhere using a largely proteinaceous glue which forms adhesive bonds with surfaces and cures (Walker, 1972; Naldrett, 1993; Kamino et al., 2000; Kamino, 2008). The glue is comprised of at least ten major proteins, which are thought to play differing but specific roles in the adhesion process, including displacement of water from the substratum, integrating the cement with the base plate, adsorption to the substratum, assembly, and curing (Kamino, 2016; So et al., 2016). Shell calcification in juvenile barnacles occurs soon after metamorphosis (LeFurgey et al., 1995). In the genus *Amphibalanus*, barnacles are protected by six parietal (i.e., lateral) shell plates that sit atop a calcified basal plate (Pitombo, 2004). Shell plates are composed of calcite, held within a matrix of chitin, acidic proteins, and sulfate-rich polymers (Fernandez et al., 2002; Rodriguez-Navarro et al., 2006; Khalifa et al., 2011). The base plate, and a narrow uncalcified growth region, are glued to the substrate. The calcified base plate is composed of layered structures, with grain size of calcite crystallites increasing with distance from the glue layer (Lewis et al., 2014; De Gregorio et al., 2015).

Although we are beginning to understand the biochemical mechanisms involved in barnacle adhesion and shell formation, relatively little is known about how variations in the environment, for example in seawater pH, affect barnacle adhesion and shell formation. Daily, monthly, and seasonal fluctuations in pH have been well-documented in coastal and intertidal habitats and are typically attributed to cycles of photosynthesis and respiration (Truchot and Duhamel-Jouve, 1980; Morris and Taylor, 1983; Wootton et al., 2008; Moulin et al., 2011; Baumann et al., 2015). Assessing the effects of seawater pH is particularly relevant given current and predicted changes in the pH of ocean waters, a process known as ocean acidification (OA). Resulting from the absorption of CO_2 by the world's oceans, the pH of global surface waters has decreased by 0.1 pH units since the industrial revolution and is projected to drop a further 0.3 – 0.5 pH units by the year 2100 (Caldeira and Wickett, 2003; Doney et al., 2009). Such changes will be more extreme in coastal regions, due to a decreased buffering capacity of coastal waters and biological CO_2 production (Waldbusser et al., 2011; Baumann et al., 2015). Effects of reduced seawater pH or associated changes in carbonate chemistry (i.e., reduced calcium carbonate saturation states) have previously been found to affect adhesion and shell formation in other marine invertebrates. For example, in marine mussels reduced pH led to diminished attachment strength and changes in the expression of proteins that comprise the byssus and adhesive plaques (O'Donnell et al., 2013; Zhao et al., 2017). Alterations in calcification, growth, and shell properties resulting from decreased pH or calcium carbonate saturation states have been documented in a broad range of calcifying organisms (Kroeker et al., 2010; Kroeker et al., 2013).

Given the general sensitivity of protein conformation to pH, and evidence of a reduction in marine mussel attachment with reduced pH, we hypothesized that the barnacle adhesive system is sensitive to seawater pH. Specifically, we predicted that barnacles grown under different levels of pH would vary in: (1) adhesive strength, and (2) gross morphology of the adhesive plaque (i.e., whether the adhesive plaque was thin and transparent, or thick and opaque when grown on silicone: Berglin and Gatenholm, 2003; Wiegemann and Watermann, 2003; Holm et al., 2005). The effect of reduced pH (to pH_{NBS} 7.4) on barnacle adhesion strength was tested previously in the barnacle *Amphibalanus (=Balanus) amphitrite* by McDonald et al. (2009), but in this experiment, barnacles were grown on glass and all barnacles broke upon removal. Therefore, force recordings reflected mechanical properties of the shell rather than adhesive properties *per se*. Here, we assessed if pH affects barnacle adhesion strength when barnacles were grown on silicone coatings and measured following the ASTM "Standard test method for measurement of barnacle adhesion strength in shear" (ASTM International, 2005). In this test, barnacles whose shells break during removal are excluded from analysis, and therefore force measurements are solely dependent on properties of the adhesive bond with the substrate and cohesive properties of the glue itself.

Interestingly, McDonald et al. (2009) observed an overall increase in exoskeleton calcification at pH_{NBS} 7.4 as compared to the ambient level of 8.2, despite weakened mechanical strength of

Abbreviations: EDS, energy dispersive X-ray spectroscopy; FTIR, Fourier-transform infrared [spectroscopy]; OA, ocean acidification; pH_{NBS}, pH calibrated against National Bureau of Standards buffers; pH_T, pH total hydrogen ion concentration scale; SEM, scanning electron microscopy; TA, total alkalinity.

the parietal plates in barnacles exposed to low pH. We predicted that alterations in the shell formation and maintenance processes in barnacles would occur even under more moderately reduced seawater pH. Specifically, we tested the shell size, mass, and plate thickness of barnacles exposed to seawater at pH_T (total H^+ concentration scale) levels of 8.01, 7.78, and 7.50. These values are common targets in OA studies and approximate the current average for oceanic surface waters (8.01) and predicted global averages for oceanic surface waters in the years ∼2100 and ∼2200, respectively (Caldeira and Wickett, 2003; Doney et al., 2009). Although oceanic pH is a dynamic parameter, which can be influenced by a large number of biotic and abiotic factors (Riebesell et al., 2011), pH_T values of 8.01, 7.78 and 7.50 roughly correspond to current atmospheric pCO_2 levels (∼400 μatm), twice the current level (∼800 μatm), and four times the current level (∼1600 μatm), respectively. Shell mechanical properties for barnacles grown at these pH levels were assessed in both the base and parietal plates using microhardness testing. Further, using a combination of SEM and FTIR spectroscopy, we tested if alterations in calcification or mechanical properties are driven by changes in ultrastructure, composition, crystallinity, or atomic disorder of the shell plates.

To address these predictions, we exposed juvenile barnacles, *Amphibalanus (=Balanus) amphitrite*, to one of three static pH_T levels (8.01, 7.78, or 7.50) for a total of 13 weeks. *A. amphitrite* is a cosmopolitan intertidal species, inhabiting tropical and semi-tropical waters, and both larvae and adults of this species have been found to tolerate reduced pH (McDonald et al., 2009). Therefore, in addition to the adhesion and shell formation metrics described, we also assessed if pH affects the general physiology of *A. amphitrite*. This was done by monitoring mortality throughout the exposure period and assessing tissue mass and the presence of eggs at the conclusion of the experiment. Overall, the goal of this work is to provide a comprehensive assessment of the effect of seawater pH on *A. amphitrite*; alterations in the presence or abundance of this common species could alter the composition of intertidal and biofouling communities.

MATERIALS AND METHODS

Animal Collection, Larval Culture, and Experimental Exposure

Barnacle larvae were reared from field-collected adult barnacles following the methods of Rittschof et al. (1984, 1992, 2008). Barnacle cyprid larvae were settled on T2 silicone-coated glass panels (15.2 × 7.6 cm) on July 22, 2015. At 11 days post-settlement, barnacles were shipped overnight mail to The College of New Jersey (TCNJ; Ewing, NJ, United States) and placed individually in 1 L plastic bins filled with Artificial Seawater (Instant Ocean, mixed to a salinity of 35).

Panels with juvenile barnacles were randomly assigned to one of three target pH_T treatments, 8.01, 7.78, or 7.50, with a total of 8 panels per pH treatment. Replicate panels were split evenly between two, replicate 5 gallon glass aquaria per pH treatment. Panels were placed into their assigned pH treatment on August 19, 2015 (26 days post-settlement). To prevent accumulation of organic matter in tanks and to enhance feeding, panels were removed from the aquaria once a day, 6 days a week, for feeding. Panels were placed individually in 1 L plastic bins (12.5 × 10.5 × 10.5 cm) that had been filled with seawater from the specific aquarium from which that panel had been taken. A dense solution of brine shrimp (*Artemia* sp.) was distributed evenly among bins using a serological pipette and barnacles fed for approximately an hour per day. Additional detail on feeding can be found in the **Supplementary Material**. The experimental exposure lasted for 13 weeks (91 days).

Adjustment and Monitoring of Seawater Conditions

Experimental exposures at TCNJ were run in artificial seawater (Instant Ocean), mixed to a salinity of 35. Since Instant Ocean is formulated with total alkalinity (TA) above what is found in natural seawater (SW), TA was reduced to ∼2200 μmol kg^{-1} SW by addition of 12 M HCl (Lunden et al., 2014). The value of ∼2200 μmol kg^{-1} SW was chosen to approximate typical TA values in Beaufort, NC where the barnacle broodstock was collected. The TA of artificial seawater was measured following SOP 3b (Dickson et al., 2007) on an automated titrator (Hanna Instruments, HI902) with 0.1 M HCl (Fluke #35335, certified volumetric) as a titrant, and values were checked against certified reference material from the Dickson Laboratory (Scripps Institution of Oceanography, La Jolla, CA, United States). All TA samples were run at least in duplicate.

Target pH and temperature levels were achieved using an automated aquarium control system (Apex AquaController, Neptune Systems), which functioned as both a pHstat and thermostat. Temperature was held at 25°C for all aquaria. Each aquarium was equipped with a temperature probe (Neptune Systems, Extended Life Temperature Probe) and a 50-watt submersible aquarium heater (Aqueon 06105 Pro). Each tank was also equipped with a pH probe (Neptune Systems, Lab Grade pH Probe). Seawater pH was brought to the set point for each aquarium (8.01, 7.78, or 7.50) by addition of pure CO_2 gas (AirGas, food grade) or CO_2-free air. Water within each aquarium was continuously circulated using an 80 GPH (gallons per hour) submersible aquarium pump (Patuoxun 80 GPH Submersible Pump).

Seawater conditions (salinity, pH_T, and temperature) were measured 6 days per week using a handheld multiparameter meter (YSI, Professional Plus). A summary of seawater conditions is provided in **Table 1** and reflects multiparameter meter readings. TA was measured weekly as described above. To ensure consistency of temperature and pH monitoring among replicate aquaria, the aquarium control system was calibrated against the multiparameter meter readings. Additional detail on the experimental exposure and monitoring seawater conditions can be found in the **Supplementary Material**.

Adhesion and Growth Assessments

Adhesion strength in shear (critical shear stress) was measured in all barnacles after 13 weeks exposure. Adhesion testing followed

TABLE 1 | Seawater chemistry parameters (means ± standard deviation).

	Treatment		
	8.01	**7.78**	**7.50**
pH_T	8.01 ± 0.03	7.78 ± 0.04	7.50 ± 0.04
Temperature (°C)	25.0 ± 0.1	25.0 ± 0.1	25.0 ± 0.1
Salinity	35.8 ± 0.5	35.7 ± 0.5	35.8 ± 0.5
pCO_2 (μatm)	412.8 ± 35.5	810.4 ± 119.5	1747.7 ± 263.4
DIC (μmol kg^{-1} SW)	1889.6 ± 41.3	2015.5 ± 49.7	2330.6 ± 92.5
HCO_3^- (μmol kg^{-1} SW)	1687.5 ± 40.5	1871.7 ± 53.5	2203.9 ± 89.8
CO_3^{2-} (μmol kg^{-1} SW)	190.5 ± 14.3	120.9 ± 17.1	77.4 ± 10.4
Total alkalinity (μmol kg^{-1} SW)	2166.6 ± 47.7	2174.7 ± 49.6	2394.1 ± 86.3
$\Omega_{Calcite}$	4.55 ± 0.33	2.89 ± 0.41	1.85 ± 0.25

pH_T, temperature, and salinity were measured 6 days per week (n = 76), total alkalinity was measured weekly (n = 12). pCO_2, DIC (dissolved inorganic carbon), HCO_3^-, CO_3^{2-}, and $\Omega_{Calcite}$ (saturation state with respect to calcite) were calculated using CO2Calc.

ASTM D 5618-94 (ASTM International, 2005). Barnacles were removed from panels using a hand-held digital force gauge (Shimpo, FGE-5X). Force values were discarded if damage to the barnacle shell or to the silicone panel occurred during removal. To enable determination of base plate area, base plate diameter was measured on each barnacle in two dimensions (along and perpendicular to the operculum) using a digital caliper. Removal force values were normalized to base plate area. The height of each barnacle was also measured with a digital caliper as the perpendicular distance from the bottom of the base plate to the top of the highest parietal plate. Lastly, the presence or absence of gummy, opaque glue (as described in Berglin and Gatenholm, 2003; Wiegemann and Watermann, 2003; Holm et al., 2005) was recorded for each barnacle.

Following assessments, barnacles from each panel were placed in shallow glass finger bowls with seawater taken from the aquarium in which that panel had been held. Within 72 h of removal, barnacles were individually removed from water and dissected to remove the soft body from the shell plates. Opercular plates were removed from the soft tissue and were not included in subsequent analyses. Dissected barnacle bodies were placed individually on pre-weighed pieces of weigh paper, allowed to dry for 48 h at room temperature and then dried in a vacuum oven at 45°C, 25 in. Hg. Dried barnacle bodies were weighed individually on an analytical balance with 0.02 mg precision (Metler-Toledo, XSE105DU) to determine tissue mass. During dissections, the presence or absence of eggs within the mantle cavity was recorded. Eggs, if present, were removed from the mantle cavity but were not included in tissue mass measurements. Remaining barnacle shells (base and all parietal plates) were then cleaned thoroughly with water to ensure all tissue had been removed. Shells were dried overnight at room temperature, then dried in a vacuum oven at 45°C, 25 in. Hg, for 24 h, and then weighed individually on an analytical balance with 0.02 mg precision. Visibly damaged shells were not included in shell mass measurements.

Structural and Mechanical Assessments

All barnacle shells were inspected after shell mass measurements using a stereomicroscope (Leica, S8Apo) and any damage to the base plate that had not been observed by eye (e.g., micro-scale cracks or holes) was recorded. Two undamaged barnacle shells per panel (16 per pH treatment) were then randomly selected for structural and micromechanical assessments. These assessments required embedding and polishing of the shell as shown in **Figure 1** and as described in the **Supplementary Material**.

Thickness of barnacle shell plates was measured on polished shell cross-sections using an upright reflected light microscope (Zeiss AxioScope.A1) equipped with a digital camera (Zeiss Axiocam 105 color). Images were taken of the entire shell cross-section at 2.5 X magnification. Typically, this required 2–4 images per sample, depending on the size of the barnacle. Using the camera's analysis software (Zeiss Zen 2), a 100 × 100 μm grid was placed on each image. Thickness of the base or parietal plate was measured at each point the grid crossed the plate, resulting in about 40 measurements per shell plate. For the base plate, replicate measurements were averaged to determine the mean base plate thickness for each sample. At least two separate parietal plates were visible in each sample, and measurements were taken within all plates. Replicate measurements were combined among parietal plates, and values were averaged to determine the mean parietal plate thickness for each sample.

Micromechanical properties were quantified using a microindentation hardness tester (Mitutoyo HM-200). Indents were made at 20 g load, 5 s dwell time. Testing was conducted in the base and one of the parietal plates, with 10 replicate indents made in each plate. For the base plate, 5 indents were made on each side of the plate, spaced about 200 μm apart, starting at approximately 500 μm from the distal edge of the plate on each of the two sides (**Figure 1A**). Replicate indents were typically made throughout the length of a single parietal plate. Individual indents were measured directly on the hardness tester at 50 X magnification in two dimensions, and Vickers microhardness values were automatically calculated. An image of each indent was taken on the hardness tester using a digital microscope camera (Moticam 2.0MP), which enabled quantification of crack propagation (**Figure 1B**). Crack length was determined as the radius of a circle emanating from the center of the indent and encompassing all visible cracks. Replicate measurements within a shell plate were averaged to determine the mean microhardness and crack propagation for each shell plate.

SEM Imaging, Elemental Analysis, and Calcite Crystal Area Assessment

After micromechanical testing, SEM imaging was conducted on all polished shell cross-sections. Imaging was conducted on uncoated samples, at low vacuum (50 Pa), in back-scattered electron mode on a field emission SEM (Hitachi America, SU5000). An accelerating voltage of 15 kV was used at a working

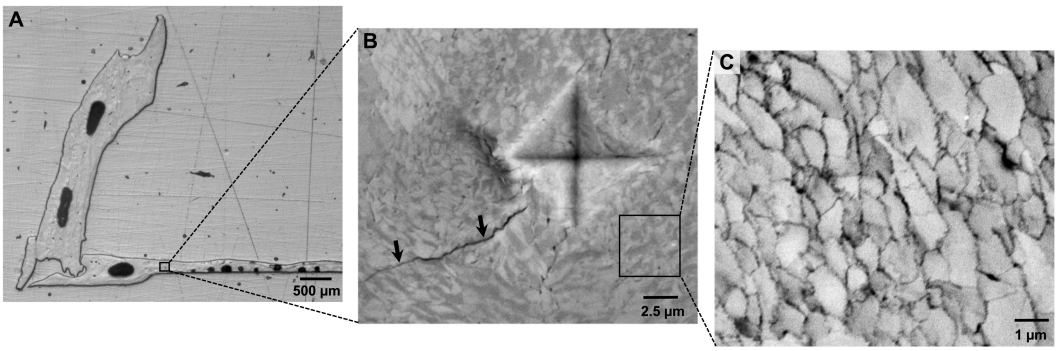

FIGURE 1 | (A) Assessments of barnacle shell properties were conducted on polished cross-sections of individual barnacle shells, which exposed both the base and parietal plates. **(B)** Mechanical testing was conducted using microindentation, which results in a diamond shaped indent and induces crack formation (arrows). Image was taken under polarized light, revealing organization of calcite crystals. **(C)** Shell ultrastructure was assessed using SEM. Shells are comprised of a cobblestone-like network of calcite crystallites, the area of which can be measured using image analysis software.

distance of approximately 8 µm. For each sample, images were taken within two separate regions of the base plate, and two regions of one of the parietal plates. In all cases, images were taken in close proximity (typically within 100 µm) to the indents made during micromechanical testing. Images were taken at 1,000 and 5,000X magnification.

Elemental analysis was conducted on all samples at 1,000X magnification using an EDAX EDS (energy dispersive X-ray spectroscopy) detector (AMTEK Materials Analysis Division, Octane Plus). Imaging conditions resulted in a count rate of 5,000–10,000 counts per second. For each region, a total of five point spectra were taken across the region. Replicate spectra were averaged within and between the two regions per plate, to determine the mean elemental composition for each shell plate.

Individual calcite crystals were readily resolved at 5000X magnification (**Figure 1C**). The area of individual calcite crystals was determined on SEM images using image analysis software (ImageJ, Ver. 1.49). For each image, a total of 15 different calcite crystals were randomly selected for area determination. For selection, a 2 μm^2 grid was first placed on the image. Pairs of random numbers were generated using a random number generator, and each pair was used as coordinates to identify a specific calcite crystal on the image. The perimeter of each identified crystal was traced by hand using the polygon tool in ImageJ and area within the traced region was automatically determined. One SEM image per shell plate was assessed, and replicate area measurements within the image were averaged to provide a mean crystal area for each shell plate.

FTIR Analysis

FTIR spectroscopy was used to assess: (1) the polymorph of calcium carbonate present in barnacle shells; (2) relative crystallinity of shells and; (3) atomic disorder of shells. Spectra were collected for polymorph and relative crystallinity determination using a PerkinElmer Spectrum Two spectrometer and for atomic disorder using a PerkinElmer Spectrum 100 spectrometer. In all cases, individual barnacle shells that had been cleaned of soft tissue were powdered using a mortar and pestle. For these assessments, the base and all parietal plates were included for each sample, but the opercular plates had been removed. Powdered sample was placed directly on the instrument's ATR (attenuated total reflectance) crystal and compressed to a uniform force with a built-in anvil. Spectra were taken at 4 wavenumbers resolution, with 32 scans per sample. Spectra were normalized and baseline corrected within the 600–2000 cm^{-1} region. The ratio of ν_2 to ν_4 peak absorbance was used as a measure of crystallinity of the shells (Beniash et al., 1997). For atomic disorder assessments, each sample was ground into a coarse powder for the first spectrum. Following the first spectrum the sample was then ground with the mortar and pestle to make a slightly finer powder, and a second spectrum was acquired. This process was carried out 5–8 times, depending on how much the spectrum changed after each subsequent grind. Each spectrum was ATR corrected and background removed before peak height measurements were acquired following Regev et al. (2010).

Statistical Analysis

Statistical analyses were conducted using SPSS (V. 23, IBM Analytics). Categorical data (mortality, presence of eggs, expression of gummy glue) were assessed using chi-square tests. All other data were assessed using one-way ANOVA (analysis of variance) followed by Tukey HSD *post hoc* testing. Prior to analyses, outliers were calculated for all metrics as values greater than three times the interquartile range above or below the third or first quartile, respectively, and were removed from the dataset. Following removal of outliers, assumptions of normality and equal variance were assessed using Shapiro–Wilk and Levene tests, respectively, and data were log transformed if necessary to meet these assumptions. If assumptions of normality or equal variance could not be met after log transforming data, a non-parametric Kruskal–Wallis test was used in place of the parametric ANOVA. In all cases, individual barnacles within a pH treatment were pooled among panels and tanks and treated as individual replicates. Testing for both panel and tank effects was conducted for metrics yielding a significant response to pH. No significant panel or tank effects were found.

RESULTS

Seawater Chemistry

A summary of seawater chemistry over the 13 week exposure is provided in **Table 1**. pH targets were met in all treatments throughout the duration of the exposure. As expected, pCO_2 increased with decreasing pH. Seawater remained supersaturated with respect to calcite for all treatments. Total alkalinity tended to be higher in pH 7.50 aquaria as compared to those at pH 7.78 and 8.01.

Physiology

Mortality of barnacles was low and variable throughout the experimental exposure and was not significantly influenced by pH treatment (chi-square: $p > 0.05$). Cumulative mortality was 21.0, 25.3, and 14.7% for the 7.50, 7.78, and 8.01 pH treatments, respectively. The value for the 8.01 treatment excludes a single panel in which 85% of barnacles died during the third week of the exposure. The reason for this die-off is unknown, but given that this level of mortality was not observed in any of the other panels, it is unlikely that this was driven by pH treatment.

Barnacles were dissected at the conclusion of the experiment, enabling quantification of soft body tissue mass and identification of eggs within the mantle cavity. The effect of pH treatment on tissue dry mass was not significant (**Tables 2**, **3**). At the conclusion of the experiment, nearly all barnacles had eggs within the mantle cavity (96.4, 95.2, and 94.6% of barnacles in the 7.50, 7.78, and 8.01 pH treatments, respectively); the proportion of ovigerous barnacles was not affected by pH treatment (chi-square: $p > 0.05$).

Adhesion

Adhesion strength, measured as critical shear force, was assessed after the 13 week exposure. Adhesion strength was not affected by pH treatment (**Tables 2**, **3**). Likewise, the proportion of barnacles expressing opaque, gummy glue was not affected by pH treatment (chi-square: $p > 0.05$). Gummy glue was found on the base of most barnacles, with 72.9, 80.8, and 62.9% of barnacles exhibiting gummy glue in the 7.50, 7.78, and 8.01 pH treatments, respectively.

Shell Formation

Assessments of shell growth and materials properties were conducted following adhesion assays. Exposure pH was found to significantly affect barnacle shell mass and the area of the base plate (**Tables 2**, **3** and **Supplementary Figure S1**). Barnacles grown at pH 8.01 exhibited approximately 30% lower shell mass and 20% smaller base plate area as compared to barnacles grown at pH 7.50 or 7.78. Height of the barnacles, measured from the base plate to the highest parietal plate, was not affected by exposure pH (**Tables 2**, **3**). Shell thickness was measured in both the base and parietal plates on polished shell cross-sections (see **Figure 1A**). Exposure pH did not significantly influence thickness in either the base or parietal plates. SEM imaging of polished cross-sections revealed a cobblestone like composite of calcite crystals (**Figure 1C**). Exposure pH was found to significantly alter calcite crystal area in both the base and parietal plates (**Tables 2**, **3** an **Supplementary Figure S1**). In the base plate, calcite crystals were approximately 95% smaller in barnacles grown at pH 8.01 as compared to barnacles grown at pH 7.50 or 7.78. The difference in calcite crystal area was less pronounced in the parietal plates, but on average calcite crystals were 35 and 23% smaller in barnacles grown at pH 8.01 as compared to barnacles grown at pH 7.50 or 7.78, respectively.

Qualitative assessments of barnacle base plates following adhesion testing and dissection suggested that damage to the base plate (identified by the presence of cracks or holes) occurred more often in barnacles exposed to pH 7.50 as compared to those exposed to pH 7.78 or 8.01. Base plate damage was identified in 38.6% of barnacles grown at pH 7.50 as compared to 21.3 and 18.8% at pH 7.78 and 8.01, respectively. Rigorous assessments of micromechanical properties were conducted on polished shell cross-sections. Mechanical testing revealed that microhardness was not affected by exposure pH in the base or parietal plates (**Tables 2**, **3**). A significant overall effect of pH on crack propagation, however, was observed when tested in the base plate (**Table 2** and **Supplementary Figure S1**). Within the base plate, cracks radiating from indents were, on average, 28% longer in barnacles exposed to pH 7.50 as compared to those at pH 8.01 (**Figure 2**; Tukey HSD: $p = 0.058$). Crack propagation

TABLE 2 | Assessment of the effects of seawater pH on physiology, adhesion, and shell formation in the barnacle *Amphibalanus amphitrite*.

Parameter	df	Test statistic	*p*
Physiology			
Tissue dry mass	134	1.860	0.160
Adhesion			
Adhesive strength	168	1.363	0.259
Shell formation			
Whole shell			
Dry mass	**2**	**8.366**	**0.015**
Height	172	0.938	0.393
Crystallinity	2	1.088	0.581
Atomic disorder	9	1.021	0.408
Base plate			
Area	**171**	**6.016**	**0.003**
Thickness	46	2.019	0.145
Microhardness	47	0.367	0.695
Crack propagation	**46**	**3.244**	**0.049**
Calcite crystal area	**47**	**16.736**	**0.000**
Ca content	47	0.094	0.911
Mg content	47	3.083	0.056
Parietal plate			
Thickness	2	2.642	0.267
Microhardness	47	0.354	0.704
Crack propagation	2	1.108	0.575
Calcite crystal area	**47**	**7.080**	**0.002**
Ca content	47	0.076	0.927
Mg content	47	0.620	0.542

ANOVA results are shown for all metrics except shell dry mass, crystallinity, parietal plate thickness, and parietal plate crack propagation, where Kruskal–Wallis tests were applied. Significant p-values are shown in bold.

TABLE 3 | Summary statistics for physiology, adhesion, and shell formation metrics.

	8.01		7.78		7.50	
Parameter	**Mean ± SE**	***n***	**Mean ± SE**	***n***	**Mean ± SE**	***n***
Physiology						
Tissue dry mass (mg)	0.94 ± 0.06	45	1.06 ± 0.06	40	1.08 ± 0.05	50
Adhesion						
Adhesive strength (MPa)	0.10 ± 0.01	58	0.09 ± 0.01	50	0.10 ± 0.01	61
Shell formation						
Whole shell						
Dry mass (mg)	12.5 ± 0.7^{A}	41	16.4 ± 1.1^{B}	44	16.2 ± 0.9^{B}	49
Height (mm)	2.43 ± 0.06	59	2.53 ± 0.07	52	2.53 ± 0.06	62
Crystallinity (ν_2/ν_4)	4.29 ± 0.05	8	4.45 ± 0.17	8	4.25 ± 0.10	8
Atomic disorder (slope of ν_2/ν_3 vs. ν_4/ν_3)	2.04 ± 0.12	4	2.33 ± 0.56	3	1.53 ± 0.48	3
Base plate						
Area (mm^2)	15.3 ± 0.7^{A}	59	18.4 ± 0.8^{B}	52	18.1 ± 0.7^{B}	61
Thickness (μm)	116 ± 10.4	16	98 ± 6.3	15	122 ± 8.5	16
Microhardness (VHN)	256 ± 9.0	16	245 ± 8.8	16	252 ± 10.3	16
Crack propagation (μm)	12.0 ± 0.6	15	12.6 ± 0.8	16	15.3 ± 1.2	16
Calcite crystal area (μm^2)	0.74 ± 0.05^{A}	16	1.45 ± 0.12^{B}	16	1.46 ± 0.15^{B}	16
Ca content (wt %)	39.6 ± 0.8	16	40.0 ± 0.8	16	39.9 ± 0.8	16
Mg content (wt %)	0.49 ± 0.03	16	0.47 ± 0.03	16	0.41 ± 0.02	16
Parietal plate						
Thickness (μm)	214 ± 8.6	14	239 ± 12.8	16	257 ± 19.3	16
Microhardness (VHN)	251 ± 9.3	16	256 ± 12.3	16	243 ± 11.9	16
Crack propagation (μm)	10.8 ± 0.7	16	11.3 ± 0.6	16	10.6 ± 0.6	16
Calcite crystal area (μm^2)	1.13 ± 0.05^{A}	16	1.39 ± 0.08^{B}	16	1.52 ± 0.10^{B}	16
Ca content (wt %)	41.6 ± 0.8	16	41.7 ± 0.8	16	42.0 ± 0.6	16
Mg content (wt %)	0.39 ± 0.02	16	0.38 ± 0.03	16	0.36 ± 0.01	16

Means ± standard error (SE) and sample sizes are shown. Groups marked with different letters are significantly different as shown by Tukey HSD post hoc analysis.

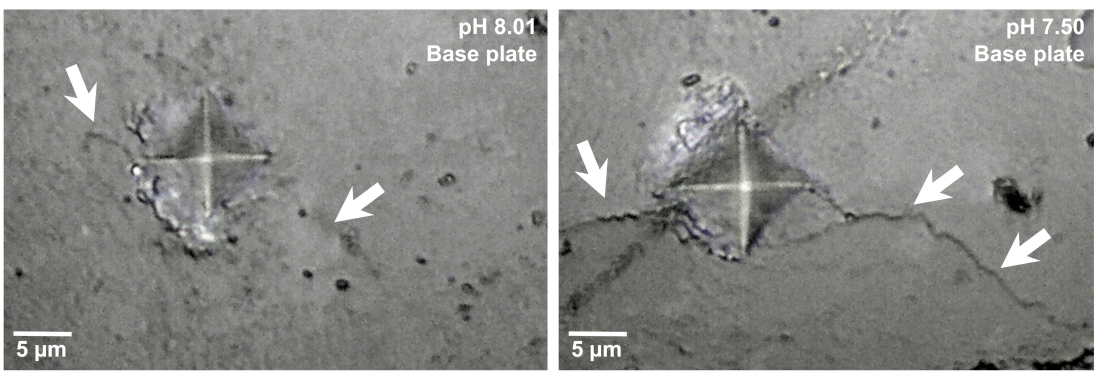

FIGURE 2 | Indents and cracks (arrows) resulting from mechanical testing within the base plate of a barnacle (*A. amphitrite*) held as pH 8.01 (left) and 7.50 (right).

was not affected by exposure pH when tested in the parietal plates.

FTIR spectroscopy was used to assess the polymorph of calcium carbonate present in barnacle shells, as well as their relative crystallinity and atomic disorder. Spectroscopy was conducted on powdered shell samples and both base and all parietal plates were included in each sample. At all pH levels, identified peaks were characteristic of calcite with no other polymorphs of calcium carbonate present (**Figure 3**). Relative crystallinity of the shells (assessed as the ratio of the ν_2 to ν_4 absorbance) was not affected by pH (**Tables 2**, **3**). Atomic disorder, assessed through FTIR grinding curves, varied among samples and was not significantly affected by pH (**Tables 2**, **3**).

Elemental composition was assessed on polished shell cross-sections using EDS. Eight elements were identified in all samples: in order of abundance, Ca, O, C, S, Sr, Mg, Na, and Cl. The vast majority of the shell was comprised of Ca, O and C, with all other elements occurring at less than 1 wt %. Exposure pH did not

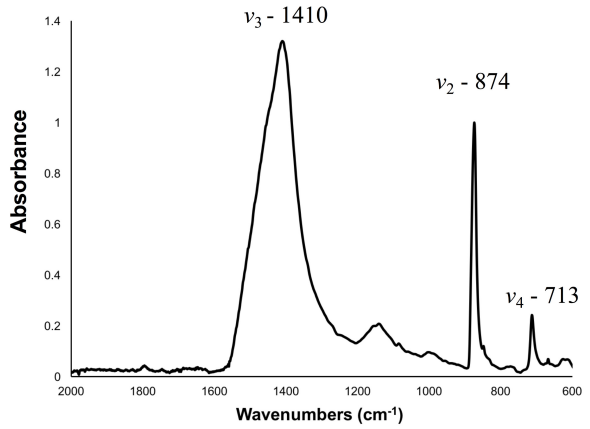

FIGURE 3 | Representative FTIR spectra of a powdered barnacle (*A. amphitrite*) shell with peaks characteristic of calcite. The ν_2, ν_3, and ν_4 peaks, used for crystallinity and atomic order assessments, are labeled.

affect calcium content when assessed in the base or parietal plates (**Tables 2**, **3**). While no elements showed a significant effect of pH, magnesium content tended to be lower (on average by 19%) in barnacles exposed pH 7.50 as compared to those at pH 8.01 (**Table 3**; Tukey HSD: $p = 0.052$; **Supplementary Figure S1**).

DISCUSSION

Barnacles are dominant members of marine intertidal communities and their success depends on both the firm attachment provided by their proteinaceous adhesive and the protection imparted by their calcified shell plates. Here we assessed if a reduction in static seawater pH, at levels predicted within the next 200 years (i.e., to pH_T 7.78 and 7.50, based on oceanic projections), would alter physiology, adhesion, and shell formation in the cosmopolitan barnacle *A. amphitrite*. Changes in the abundance of *A. amphitrite* could affect the composition of biofouling communities. We found that barnacles were generally robust to reduced pH, with no effect of pH on physiological metrics, and, contrary to our prediction, adhesive properties were not affected by reduced pH. Shell mass and base plate area were found to be higher in barnacles exposed to even moderately reduced pH, a trend that appears to be driven by increased size of the calcite crystals that comprise the shell. Although microhardness of the shell plates, a measure of resistance to permanent or plastic deformation, was not affected by pH, the length of cracks propagating from indents in the base plate was, suggesting that the toughness of base plates grown at the lowest pH level was reduced. Hence, a reduction in pH resulted in larger barnacles but with base plates that would crack more readily.

Physiology

Over the course of 13 weeks, we found no effect of seawater pH on cumulative mortality, tissue mass, or egg production in *A. amphitrite*. Assessments of OA responses in juvenile or adult *A. amphitrite* are limited, but consistent with our observations, McDonald et al. (2009) found no effect of pH on *A. amphitrite* egg production after 11 weeks exposure to pH_{NBS} 7.4. Campanati et al. (2016) exposed *A. amphitrite* larvae to reduced pH (pH_{NBS} 7.6) and tracked survival of juveniles settled from these larvae for 11 days. Mortality was actually reduced at low pH as compared to the pH_{NBS} 8.2 control when assessed at 3 and 9 days post-settlement. At their final time point (11 days post settlement), there was no effect of seawater pH on juvenile survival.

Amphibalanus improvisus (Pansch et al., 2014; Eriander et al., 2016) and *Elminius modestus* (Findlay et al., 2010a) have also been found to be robust to OA, as least in terms of survival and reproduction. Eriander et al. (2016) found no effect of reduced seawater pH (to pH_{NBS} 7.7) on mortality in *A. improvisus* over 12 weeks, either when the pH reduction was kept at a stable level or when pH was allowed to fluctuate over the course of the day to mimic diurnal pH cycles. Pansch et al. (2014) similarly found no effect of reduced pH on *A. improvisus* mortality or reproduction (larval release rate) after 20 weeks in juveniles collected from a field site that shows natural variability in seawater pH (Kiel Fjord, Germany). In contrast though, juveniles collected from a field site with limited variability in seawater pH (Tjärnö Archipelago, Sweden) showed increased mortality at the lowest pH tested (pH_{NBS} 7.2). Exposure of *Elminius modestus* to reduced pH (pH_{NBS} 7.7) for 30 days did not affect mortality when tested at 14 or 19°C (Findlay et al., 2010a).

Semibalanus balanoides, a boreoarcitic species, appears considerably more sensitive to OA. Increased mortality has been shown in both short (30 days) and longer term (80 or 104 days) exposures to reduced pH (pH_{NBS} 7.7–7.8)(Findlay et al., 2009, 2010a; Harvey and Moore, 2017). Barnacles in these studies were collected near the southern limit of the range for *S. balanoides*. Similar to what was shown for *A. improvisus*, environmental conditions of the collection site impacted responses to OA (Findlay et al., 2010b). When Findlay et al. (2010b) exposed *S. balanoides* collected near the northern limit of their range to reduced pH (to pH_{NBS} 7.7 or 7.3) for 20 days, survival of juveniles did not differ from the pH_{NBS} 8.1 control. Hence, barnacles show a mixed response to seawater pH. Individual responses vary by species as well as within a species based on local conditions of the breeding population.

In general, crustaceans tend to be more tolerant of the effects of OA as compared to other taxa that build a mineralized shell (e.g., mollusks, corals: Kroeker et al., 2013) and such tolerance has been hypothesized to be due to their capacity for ion and acid-base regulation (Melzner et al., 2009; Whiteley, 2011). Populations that are routinely exposed to varying environmental conditions are likely to exhibit a considerable scope for physiological adjustment to a changing environment, making them well-adapted physiologically to changes in seawater pH (Wong et al., 2011; Pansch et al., 2012, 2013). In *A. amphitrite* larvae for example, expression of energy metabolism related proteins was altered at reduced pH, illustrating the potential for proteomic plasticity in this robust species, and a possible mechanism for mediating the stress of OA (Wong et al., 2011). Variations among species and populations may stem from differences in ion and acid-base regulation ability, as well as

differences in the ability to adjust energy metabolism (Whiteley, 2011).

Adhesion

We hypothesized that the barnacle adhesive system is sensitive to seawater pH, and based on this hypothesis, tested the prediction that barnacles grown under different levels of pH would vary in adhesive strength and gross morphology of the adhesive plaque. Previous work with marine mussels (*Mytilus trossulus*) found a reduction in both strength and extensibility of byssal threads when animals were exposed to reduced pH (tested at a range of pH_T values from 8.1 to 7.5: O'Donnell et al., 2013). Such changes in mechanical properties of the byssal threads were calculated to lead to a 35-41% reduction in attachment tenacity, which could substantially affect a mussel's ability to anchor itself in high energy environments. O'Donnell et al. (2013) suggest that this response is due to sensitivity of DOPA (dihydroxyphenylalanine) to pH. DOPA is a major component of byssal threads that is involved in cross-linking and adhesion. A similar response was found in the mussel *Mytilus coruscus* (Zhao et al., 2017). Decreased pH (tested at a range of pH_{NBS} values from 8.1 to 7.4) led to a decrease in byssal thread breaking force and toughness, as well as a reduction in the number of threads produced. Incorporating mechanical data with thread counts per mussel, Zhao et al. (2017) predicted a 60–65% reduction in attachment tenacity. Reduced seawater pH also led to significant alteration in expression of byssal thread related genes, thereby providing a mechanism that, in combination with direct effects of pH on DOPA chemistry, could explain the response of byssal threads to reduced pH.

Data collected here did not support the hypothesis that the barnacle adhesive system is sensitive to seawater pH; neither adhesive strength (measured in shear following the ASTM standard for measurement of barnacle adhesive strength: ASTM International, 2005) nor the gross morphology of the adhesive plaque (i.e., if the glue layer was thin and hard or thick and gummy) were affected by seawater pH. A number of factors may contribute to the observed difference in sensitivity to pH between marine mussels and the barnacle (*A. amphitrite*) tested here. First, the Balanomorph barnacle adhesive system is fundamentally different from that of marine mussels in that the adhesive interface is relatively protected from the external environment. Glue is delivered directly to the substrate at the periphery of the base and parietal plates (Saroyan et al., 1970; Burden et al., 2014). Although the cured glue layer is partially hydrated (Barlow et al., 2009), there is no component of the adhesive system that is constantly exposed to seawater, as is the case for a mussel's byssal threads. Second, the chemistry of barnacle glue differs from that of marine mussels. Barnacle glue is composed of at least ten major proteins, which play differing but specific roles in the adhesion process (Kamino, 2016; So et al., 2016). DOPA, which is pH sensitive (O'Donnell et al., 2013), has not been identified in barnacle glue (Naldrett, 1993; Kamino et al., 1996; Naldrett and Kaplan, 1997), although evidence of oxidative activity and cross-linking has been found (Dickinson, 2008; Golden et al., 2016; Essock-Burns et al., 2017; So et al., 2017). The sensitivity of isolated barnacle glue proteins to altered pH has yet to be assessed. Last, reduced seawater pH may lead to changes in the suite of glue proteins expressed, either in terms of the specific proteins expressed or the relative abundance of these proteins. Such a mechanism has not been tested in barnacles, but hypothetically could compensate for altered structure and activity of individual glue proteins. Recent advances in sequencing of the barnacle glue proteome (Wang et al., 2015; So et al., 2016) will enable direct assessment of proteomic responses to varied seawater conditions.

In our study, barnacles were settled on silicone substrates, which enabled them to be removed intact. Individuals with broken shells were excluded from analysis, and therefore the response to pH described here reflects only adhesive and cohesive properties of the adhesive plaque. When barnacles were settled on hydrophilic glass beakers, the force required to shear the barnacles from the glass was actually enhanced in barnacles exposed to reduced pH (McDonald et al., 2009). In this case, all barnacles broke upon removal. On hydrophilic substrates, mechanical properties of the shell plates are weaker than the adhesive bond between the glue layer and the substrate, and therefore shear removal measurements reflect integrity of the lower shell plates where the force is applied. McDonald et al. (2009) suggest that thickening of the growing edge of the barnacle was responsible for the observed difference in shear removal force. Clearly surface chemistry, and hence whether failure will occur within the adhesive layer or within the shell plates, will mediate the effect of seawater pH on attachment tenacity. Assessments of barnacle responses to varied pH when grown on substrates that naturally occur in the marine environment may shed light on if OA will affect attachment ability in the field.

Shell Formation

Consistent with what was found previously for *A. amphitrite* (McDonald et al., 2009), reduced seawater pH resulted in elevated shell formation. We found that even a moderate reduction in seawater pH (to pH_T 7.78) resulted in greater shell mass as compared to the pH_T 8.01 control. After 13 weeks growth, barnacle base plates were larger at reduced pH. Thickness of shell plates, measured directly on cross-sectioned shells, was not affected by seawater pH, although thickness of the parietal plates did tend to increase with decreasing pH. Enhanced shell formation at reduced seawater pH has been documented in several other crustaceans (i.e., *Callinectes sapidus*, *Penaeus plebejus*, *Homarus americanus*: Ries et al., 2009). Given that bicarbonate ion concentration increases under OA (increased pCO_2), enhanced growth in crustaceans may stem from their ability to utilize bicarbonate in the mineralization process (Cameron and Wood, 1985; Whiteley, 2011; Roleda et al., 2012). Enhanced growth though, is not universal in crustaceans (e.g., mixed growth responses have been observed in *A. improvisus* and *S. balanoides*: Findlay et al., 2010b; Pansch et al., 2014) and likely depends on an individual's capacity to mitigate the stress of reduced pH (see Section "Physiology").

Scanning electron microscopy imaging of cross-sectioned barnacle shells revealed that the shell plates were composed of crystals, with dimensions on the order of 1 μm. FTIR spectroscopy confirmed that these crystallites were composed of calcite with no other polymorphs of calcium carbonate present, and EDS spectroscopy identified both magnesium and strontium within the calcitic shell plates. Consistent with previous assessments of *A. amphitrite* shells, individual crystallites were irregular in shape, did not take on a uniform orientation, and the boundaries of larger crystals appear rough, suggestive of smaller crystallites on the surface of the larger crystals (Khalifa et al., 2011; Lewis et al., 2014). The organic matrix surrounding calcite crystals is composed of chitin, acidic proteins, and sulfate-rich polymers (Fernandez et al., 2002; Rodriguez-Navarro et al., 2006; Khalifa et al., 2011), and in *A. amphitrite* comprises approximately 2 wt% of the shell (Khalifa et al., 2011). We did not assess the organic matrix specifically in this study, but observations of a double peak at 1145 cm^{-1} in the FTIR spectrum (taken on whole, crushed shells) are suggestive of sulfate-rich polymers within the organic matrix (Khalifa et al., 2011).

Although seawater pH did not alter the overall shape or orientation of calcite crystals, the size of individual crystals increased dramatically in barnacles grown at reduced seawater pH. Calcite crystals comprising the base plate were nearly twice as large in barnacles at reduced pH (pH_T 7.50 or 7.78) as compared to the pH_T 8.01 control. Seawater pH resulted in a graded response in parietal plates, with the largest calcite crystals at the lowest seawater pH, a trend that closely followed parietal plate thickness. Shell formation in barnacles is directed by cells of the mantle epithelium, which participate in deposition of organic matrix and calcium transport (Nousek, 1984; Fernandez et al., 2002; Rodriguez-Navarro et al., 2006; Gohad et al., 2009). Crystal nucleation, structure, and orientation of calcite crystals is proposed to be controlled by the organic matrix (Fernandez et al., 2002; Khalifa et al., 2011).

At present, the mechanisms driving such differences in calcite crystal size are unclear. Increased size of calcite crystals under reduced seawater pH may reflect differences in the process of organic matrix deposition by mantle cells or the rate by which matrix deposition occurs. Similar to what was observed here, an increase in the size of shell microstructures (folia) was observed in eastern oysters (*Crassostrea virginica*) when exposed to pH_{NBS} 7.5 for 20 weeks (Beniash et al., 2010). In this case it was proposed that energy limitations could impede organic matrix deposition or cell division. Here though, we did not observe an effect of seawater pH on *A. amphitrite* soft tissue mass, and therefore it does not appear as though animals at reduced pH were functioning under an energy deficit. An alternative hypothesis is that reduced seawater pH led to differences in intracellular pH, which could alter the ability of cells to participate in the mineralization process. In another crustacean (the Tanner crab, *Chionoecetes bairdi*), a reduction in intracellular pH was observed in animals held at reduced pH, a response that was proposed to have implications on the shell formation process (Meseck et al., 2016). Direct assessments of intracellular pH in barnacles grown at reduced pH as well as further investigation into the role of cells in the shell formation process in barnacles would be helpful in evaluating these mechanisms.

Changes in the shell formation process under reduced pH may have implications in terms of functionality of the shell. The base plates of barnacles grown at the lowest pH tested (pH_T 7.50) tended to break more easily than those of barnacles grown at pH_T 7.78 or 8.01. Rigorous mechanical testing supported this observation. When tested in the base plate, hardness, a material's ability to resist plastic or permanent deformation, was not affected by pH, but the cracks that propagated from mechanical tests were longer at low pH, indicating that reduced seawater pH led to a reduction in toughness. This response may partially be driven by the dramatic increase in calcite crystal size at low pH. Larger crystals would imply a lower ratio of organic to inorganic material within the shell. Organic matrix plays an important toughening role in biological materials, serving to trap and deflect cracks (Fratzl et al., 2007; Beniash et al., 2010; Meyers and Chen, 2014). Therefore, as the ratio of organic matrix to inorganic mineral decreases, crack deflection ability is also diminished. This mechanism, however, cannot fully explain the trends observed, given that animals at pH_T 7.78 showed larger calcite crystal size but did not exhibit a reduction in base plate toughness.

Several additional factors could contribute to the observed reduction in base plate toughness. Assessment of the shell organic matrix was beyond the scope of this study, but given the ability of the organic matrix to trap and deflect cracks (Fratzl et al., 2007; Meyers and Chen, 2014) alterations in the composition or density of the organic matrix could also lead to changes in toughness. Considering the calcite crystals themselves, two factors could have influenced mechanical properties. First, organic constituents (e.g., amino acids) can be occluded within biogenic calcite crystals and can dramatically impact mechanical properties via alterations in the crystal lattice (Cho et al., 2016; Kim et al., 2016). If the identity or quantity of these organic inclusions was altered at low pH, this could influence shell mechanical properties. Second, inclusion of magnesium into the calcite crystal lattice can have a major impact on mechanical properties of shells, with the addition of even small amounts of magnesium leading to enhanced mechanical properties (Kunitake et al., 2012; Long et al., 2014). Correspondingly, in the base plate of pH_T 7.50 barnacles, we observed a trend ($p = 0.056$) toward decreased magnesium content as compared to animals at pH_T 7.78 or 8.01. Such a reduction in magnesium content could contribute to the observed reduction in toughness. At this point it is unclear if the reduced magnesium content at low pH is due to lower uptake and incorporation of magnesium, or increased dissolution of weekly bound magnesium (Findlay et al., 2009).

A reduction in the force needed to break parietal plates was observed previously in *A. amphitrite* (McDonald et al., 2009) and *A. improvisus* (Pansch et al., 2013) after exposure to reduced pH. Force needed to break parietal plates was not assessed in this study, but at the micro-scale, we did not observe an effect of seawater pH on parietal plate hardness or crack propagation. Hence differences in force needed to break parietal plates may stem from structural changes in the plates (e.g., local dissolution of mineral: McDonald et al., 2009), rather than differences in their

material properties. We did not observe damage or erosion of parietal plates for any of the treatments in this study, although alkalinity was consistently elevated at pH_T 7.50, suggesting that some dissolution of shells at this pH may have occurred.

Neither shell crystallinity nor atomic disorder, both measures of the level of structural order within a crystal at the atomic scale, were affected by seawater pH. Changes in formation conditions or the composition of molecules at the time of crystal formation could affect these metrics (Khalifa et al., 2011). Interestingly, although the mean values of these metrics were not significantly affected by seawater pH, variance around the mean was dramatically greater at reduced pH as compared to pH_T 8.01 (e.g., for atomic disorder, standard error at reduced pH was 4–5 times greater than at pH_T 8.01). This suggests that reduced pH may increase variability among individuals in their ability to control the environment in which mineral forms. A similar response in terms of increased variability in crystal properties among individuals at decreased pH was observed previously in the marine mussel, *Mytilus californianus* (McCoy et al., 2018).

CONCLUSION

A reduction in static seawater pH at levels predicted within the next 200 years (i.e., to pH_T 7.78 and 7.50, based on oceanic projections: Caldeira and Wickett, 2003; Doney et al., 2009) had little impact on physiological and adhesive metrics in the barnacle *A. amphitrite*. Shell growth, though, was significantly enhanced at reduced pH, while toughness of the base plate was diminished at pH_T 7.50. If these changes impact the survival of *A. amphitrite* in the field, and how growth in a dynamic, natural environment would affect the magnitude of such changes, are yet to be determined. Alterations in the abundance of this ecologically dominant species, if they were to occur, would undoubtedly affect the composition of biofouling communities. Given the economic impact of marine biofouling (Callow and Callow, 2011; Schultz et al., 2011), additional assessments of *A. amphitrite* under changing environmental conditions are warranted. Multi-stressor and transgenerational assessments, as well as experiments that test natural sources of mortality in barnacles (e.g., predators or hydrodynamic stresses) would be especially helpful in predicting population level responses in *A. amphitrite*.

DATA AVAILABILITY STATEMENT

The raw data supporting the conclusions of this manuscript can be found in the **Supplementary Material**.

ETHICS STATEMENT

This study was carried out in accordance with standard procedures for invertebrates.

AUTHOR CONTRIBUTIONS

JN developed the seawater exposure system, collected and compiled data on seawater chemistry, physiology and adhesive metrics, and oversaw daily operations of the exposure. SP assessed shell thickness, mechanical properties, and crystallinity. KS and DT collected data on mortality, egg presence, adhesive properties, and shell mass and area. CM developed a prototype seawater exposure system and initiated a pilot study. JO'M, JH, and RM prepared shells and collected data on atomic disorder and RM analyzed atomic disorder data. BO and DR provided juvenile barnacles and algae and provided expertise on barnacle growth and assessment throughout the exposure. GD conceived of the experiments, analyzed final datasets, oversaw the experiment, and wrote the manuscript. All authors contributed to editing of the manuscript.

FUNDING

This material is based upon research supported by the Office of Naval Research under Award Number (N00014-14-1-0491) to GD.

ACKNOWLEDGMENTS

The authors would like to thank Julian Sison, Shai Bejerano, Christine Makdisi, Aparna Yarram, and Mihir Soni for assistance in barnacle maintenance.

SUPPLEMENTARY MATERIAL

The Supplementary Material for this article can be found online at: https://www.frontiersin.org/articles/10.3389/fmars.2018.00369/full#supplementary-material

FIGURE S1 | Shell assessments of barnacles, *Amphibalanus amphitrite*, exposed to one of three levels of pH_T for 13 weeks (mean ± s.e.m.). Groups marked with different letters are significantly different as shown by Tukey HSD post-hoc analysis. Sample sizes can be found in **Table 3** of the main text.

DATA SHEET S1 | Raw data for physiology, adhesion, and shell formation metrics.

REFERENCES

ASTM International (2005). *Standard Test Method for Measurement of Barnacle Adhesion Strength in Shear*. West Conshohocken, PA: ASTM International.

Barlow, D. E., Dickinson, G. H., Orihuela, B., Rittschof, D., and Wahl, K. J. (2009). In situ ATR-FTIR characterization of primary cement interfaces of the barnacle *Balanus amphitrite*. *Biofouling* 25, 359–366. doi: 10.1080/08927010902812009

Baumann, H., Wallace, R. B., Tagliaferri, T., and Gobler, C. J. (2015). Large natural pH, CO2 and O2 fluctuations in a temperate tidal salt marsh on diel, seasonal, and interannual time scales. *Estuar. Coast.* 38, 220–231. doi: 10.1007/s12237-014-9800-y

Beniash, E., Aizenberg, D., Addadi, L., and Weiner, S. (1997). Amorphous calcium carbonate transforms into calcite during sea urchin larval spicule growth. *Proc. R. Soc. B* 264, 461–465. doi: 10.1098/rspb.1997.0066

Beniash, E., Ivanina, A., Lieb, N. S., Kurochkin, I., and Sokolova, I. M. (2010). Elevated level of carbon dioxide affects metabolism and shell formation in oysters *Crassostrea virginica*. *Mar. Ecol. Prog. Ser.* 419, 95–108. doi: 10.1016/j.aquatox.2017.06.009

Berglin, M., and Gatenholm, P. (2003). The barnacle adhesive plaque: morphological and chemical differences as a response to substrate properties. *Colloid Surf. B* 28, 107–117. doi: 10.1016/S0927-7765(02)00149-2

Burden, D. K., Spillmann, C. M., Everett, R. K., Barlow, D. E., Orihuela, B., Deschamps, J. R., et al. (2014). Growth and development of the barnacle *Amphibalanus amphitrite*: time and spatially resolved structure and chemistry of the base plate. *Biofouling* 30, 799–812. doi: 10.1080/08927014.2014.930736

Caldeira, K., and Wickett, M. E. (2003). Anthropogenic carbon and ocean pH. *Nature* 425, 365–365. doi: 10.1038/425365a

Callow, J. A., and Callow, M. E. (2011). Trends in the development of environmentally friendly fouling-resistant marine coatings. *Nat. Commun.* 2:244. doi: 10.1038/ncomms1251

Cameron, J. N., and Wood, C. M. (1985). Apparent H^+ excretion and CO_2 dynamics accompanying carapace mineralization in the blue crab (*Callinectes sapidus*) following molting. *J. Exp. Biol.* 114, 181–196.

Campanati, C., Yip, S., Lane, A., and Thiyagarajan, V. (2016). Combined effects of low pH and low oxygen on the early-life stages of the barnacle *Balanus amphitrite*. *ICES J. Mar. Sci.* 73, 791–802. doi: 10.1093/icesjms/fsv221

Cho, K. R., Kim, Y. Y., Yang, P., Cai, W., Pan, H., Kulak, A. N., et al. (2016). Direct observation of mineral–organic composite formation reveals occlusion mechanism. *Nat. Commun.* 7:10187. doi: 10.1038/ncomms10187

De Gregorio, B. T., Stroud, R. M., Burden, D. K., Fears, K. P., Everett, R. K., and Wahl, K. J. (2015). Shell structure and growth in the base plate of the barnacle *Amphibalanus amphitrite*. *ACS Biomat. Sci. Eng.* 1, 1085–1095. doi: 10.1080/08927014.2014.930736

Dickinson, G. H. (2008). *Barnacle Cement: a Polymerization Model Based on Evolutionary Concepts*. Ph.D. Thesis, Duke University, Durham, NC.

Dickson, A. G., Sabine, C. L., and Christian, J. R. (2007). *Guide to Best Practices for Ocean CO_2 Measurements. PICES Special Publication* 3. Sidney: North Pacific Marine Science Organization.

Doney, S. C., Fabry, V. J., Feely, R. A., and Kleypas, J. A. (2009). Ocean acidification: the other CO2 problem. *Annu. Rev. Mar. Sci.* 1, 169–192. doi: 10.1146/annurev.marine.010908.163834

Eriander, L., Wrange, A. L., and Havenhand, J. (2016). Simulated diurnal pH fluctuations radically increase variance in—but not the mean of—growth in the barnacle *Balanus improvisus*. *ICES J. Mar. Sci.* 73, 596–603. doi: 10.1093/icesjms/fsv214

Essock-Burns, T., Gohad, N. V., Orihuela, B., Mount, A. S., Spillmann, C. M., Wahl, K. J., et al. (2017). Barnacle biology before, during and after settlement and metamorphosis: a study of the interface. *J. Exp. Biol.* 220, 194–207. doi: 10.1242/jeb.145094

Fernandez, M. S., Vergara, I., Oyarzun, A., Arias, J. I., Rodriguez, R., Wiff, J. P., et al. (2002). "Extracellular matrix molecules involved in barnacle shell mineralization," in *Proceedings of the MRS Online Library Archive*, Warrendale, PA, 724.

Findlay, H. S., Kendall, M. A., Spicer, J. I., and Widdicombe, S. (2009). Future high CO_2 in the intertidal may compromise adult barnacle *Semibalanus balanoides* survival and embryonic development rate. *Mar. Ecol. Prog. Ser.* 389, 193–202. doi: 10.3354/meps08141

Findlay, H. S., Kendall, M. A., Spicer, J. I., and Widdicombe, S. (2010a). Post-larval development of two intertidal barnacles at elevated CO_2 and temperature. *Mar. Biol.* 157, 725–735. doi: 10.1007/s00227-009-1356-1

Findlay, H. S., Kendall, M. A., Spicer, J. I., and Widdicombe, S. (2010b). Relative influences of ocean acidification and temperature on intertidal barnacle post-larvae at the northern edge of their geographic distribution. *Estuar. Coast. Shelf Sci.* 86, 675–682. doi: 10.1016/j.ecss.2009.11.036

Fratzl, P., Gupta, H. S., Fischer, F. D., and Kolednik, O. (2007). Hindered crack propagation in materials with periodically varying Young's modulus - lessons from biological materials. *Adv. Mater.* 19, 2657–2661. doi: 10.1002/adma.200602394

Gohad, N. V., Dickinson, G. H., Orihuela, B., Rittschof, D., and Mount, A. S. (2009). Visualization of putative ion-transporting epithelia in *Amphibalanus amphitrite* using correlative microscopy: potential function in osmoregulation and biomineralization. *J. Exp. Mar. Biol. Ecol.* 380, 88–98. doi: 10.1016/j.jembe.2009.09.008

Golden, J. P., Burden, D. K., Fears, K. P., Barlow, D. E., So, C. R., Burns, J., et al. (2016). Imaging active surface processes in barnacle adhesive interfaces. *Langmuir* 32, 541–550. doi: 10.1021/acs.langmuir.5b03286

Harvey, B. P., and Moore, P. J. (2017). Ocean warming and acidification prevent compensatory response in a predator to reduced prey quality. *Mar. Ecol. Prog. Ser.* 563, 111–122. doi: 10.3354/meps11956

Holm, E. R., Orihuela, B., Kavanagh, C., and Rittschof, D. (2005). Variation among families for characteristics of the adhesive plaque in the barnacle *Balanus amphitrite*. *Biofouling* 21, 121–126. doi: 10.1080/08927010512331344188

Kamino, K. (2008). Underwater adhesive of marine organisms as the vital link between biological science and material science. *Mar. Biotechnol.* 10, 111–121. doi: 10.1007/s10126-007-9076-3

Kamino, K. (2016). "Barnacle underwater attachment," in *Biological Adhesives*, eds A. M. Smith and J. A. Callow (Cham: Springer), 153–176.

Kamino, K., Inoue, K., Maruyama, T., Takamatsu, N., Harayama, S., and Shizuri, Y. (2000). Barnacle cement proteins. Importance of disulfide bonds in their insolubility. *J. Biol. Chem.* 275, 27360–27365.

Kamino, K., Odo, S., and Maruyama, T. (1996). Cement proteins of the acorn barnacle, *Megabalanus rosa*. *Biol. Bull.* 190, 403–409. doi: 10.2307/1543033

Khalifa, G. M., Weiner, S., and Addadi, L. (2011). Mineral and matrix components of the operculum and shell of the barnacle *Balanus amphitrite*: calcite crystal growth in a hydrogel. *Cryst. Growth Des.* 11, 5122–5130. doi: 10.1021/cg2010216

Kim, Y. Y., Carloni, J. D., Demarchi, B., Sparks, D., Reid, D. G., Kunitake, M. E., et al. (2016). Tuning hardness in calcite by incorporation of amino acids. *Nat. Mater.* 15, 903–910. doi: 10.1038/nmat4631

Kroeker, K. J., Kordas, R. L., Crim, R., Hendriks, I. E., Ramajo, L., Singh, G. S., et al. (2013). Impacts of ocean acidification on marine organisms: quantifying sensitivities and interaction with warming. *Glob. Change Biol.* 19, 1884–1896. doi: 10.1111/gcb.12179

Kroeker, K. J., Kordas, R. L., Crim, R. N., and Singh, G. G. (2010). Meta-analysis reveals negative yet variable effects of ocean acidification on marine organisms. *Ecol. Lett.* 13, 1419–1434. doi: 10.1111/j.1461-0248.2010.01518.x

Kunitake, M. E., Baker, S. P., and Estroff, L. A. (2012). The effect of magnesium substitution on the hardness of synthetic and biogenic calcite. *MRS Commun.* 2, 113–116. doi: 10.1557/mrc.2012.20

LeFurgey, A., Freudenrich, C., Wallace, N., Ingram, P., and Wilbur, K. (1995). The onset of biomineralization during cyprid to juvenile metamorphosis of the barnacle (*Balanus amphitrite* amphitrite). *FASEB J.* 9:A639.

Lewis, A. C., Burden, D. K., Wahl, K. J., and Everett, R. K. (2014). Electron backscatter diffraction (EBSD) study of the structure and crystallography of the barnacle *Balanus amphitrite*. *JOM* 66, 143–148. doi: 10.1007/s11837-013-0793-y

Long, X., Ma, Y., and Qi, L. (2014). Biogenic and synthetic high magnesium calcite–a review. *J. Struct. Biol.* 185, 1–14. doi: 10.1016/j.jsb.2013.11.004

Lunden, J. J., Turner, J. M., Mcnicholl, C. G., Glynn, C. K., and Cordes, E. E. (2014). Design, development, and implementation of recirculating aquaria for maintenance and experimentation of deep-sea corals and associated fauna. *Limnol. Oceanogr. Meth.* 12, 363–372. doi: 10.4319/lom.2014.12.363

McCoy, S. J., Kamenos, N. A., Chung, P., Wootton, T. J., and Pfister, C. A. (2018). A mineralogical record of ocean change: decadal and centennial patterns in the California mussel. *Glob. Change Biol.* 24, 2554–2562. doi: 10.1111/gcb.14013

McDonald, M. R., Mcclintock, J. B., Amsler, C. D., Rittschof, D., Angus, R. A., Orihuela, B., et al. (2009). Effects of ocean acidification over the life history of the barnacle *Amphibalanus amphitrite*. *Mar. Ecol. Prog. Ser.* 385, 179–187. doi: 10.3354/meps08099

Melzner, F., Gutowska, M. A., Langenbuch, M., Dupont, S., Lucassen, M., Thorndyke, M. C., et al. (2009). Physiological basis for high CO_2 tolerance in marine ectothermic animals: pre-adaptation through lifestyle and ontogeny? *Biogeosciences* 6, 2313–2331. doi: 10.5194/bg-6-2313-2009

Meseck, S. L., Alix, J. H., Swiney, K. M., Long, W. C., Wikfors, G. H., and Foy, R. J. (2016). Ocean acidification affects hemocyte physiology in the Tanner crab (*Chionoecetes bairdi*). *PLoS One* 11:e0148477. doi: 10.1371/journal.pone.0148477

Meyers, M. A., and Chen, P. Y. (2014). *Biological Materials Science: Biological Materials, Bioinspired Materials, and Biomaterials*. Cambridge: Cambridge University Press. doi: 10.1017/CBO9780511862397

Morris, S., and Taylor, A. C. (1983). Diurnal and seasonal variation in physico-chemical conditions within intertidal rock pools. *Estuar. Coast. Shelf Sci.* 17, 339–355. doi: 10.1016/0272-7714(83)90026-4

Moulin, L., Catarino, A. I., Claessens, T., and Dubois, P. (2011). Effects of seawater acidification on early development of the intertidal sea urchin *Paracentrotus lividus* (Lamarck 1816). *Mar. Pollut. Bull.* 62, 48–54. doi: 10.1016/j.marpolbul.2010.09.012

Naldrett, M. J. (1993). The importance of sulfur cross-links and hydrophobic interactions in the polymerization of barnacle cement. *J. Mar. Biol. Assoc. UK* 73, 689–702. doi: 10.1017/S0025315400033221

Naldrett, M. J., and Kaplan, D. L. (1997). Characterization of barnacle (*Balanus eburneus* and *B. crenatus*) adhesive proteins. *Mar. Biol.* 127, 629–635. doi: 10.1007/s002270050053

Nousek, N. A. (1984). Shell formation and calcium transport in the barnacle *Chthamalus fragilis*. *Tissue Cell* 16, 433–442. doi: 10.1016/0040-8166(84)90061-2

O'Donnell, M. J., George, M. N., and Carrington, E. (2013). Mussel byssus attachment weakened by ocean acidification. *Nat. Clim. Change* 3, 587–590. doi: 10.1038/nclimate1846

Pansch, C., Nasrolahi, A., Appelhans, Y. S., and Wahl, M. (2012). Impacts of ocean warming and acidification on the larval development of the barnacle *Amphibalanus improvisus*. *J. Exp. Mar. Biol. Ecol.* 420, 48–55. doi: 10.1016/j.jembe.2012.03.023

Pansch, C., Nasrolahi, A., Appelhans, Y. S., and Wahl, M. (2013). Tolerance of juvenile barnacles (*Amphibalanus improvisus*) to warming and elevated pCO_2. *Mar. Biol.* 160, 2023–2035. doi: 10.1007/s00227-012-2069-4

Pansch, C., Schaub, I., Havenhand, J., and Wahl, M. (2014). Habitat traits and food availability determine the response of marine invertebrates to ocean acidification. *Glob. Change Biol.* 20, 765–777. doi: 10.1111/gcb.12478

Pitombo, F. B. (2004). Phylogenetic analysis of the Balanidae (Cirripedia, Balanomorpha). *Zool. Scr.* 33, 261–276. doi: 10.1111/j.0300-3256.2004.00145.x

Regev, L., Poduska, K. M., Addadi, L., Weiner, S., and Boaretto, E. (2010). Distinguishing between calcites formed by different mechanisms using infrared spectrometry: archaeological applications. *J. Archaeol. Sci.* 37, 3022–3029. doi: 10.1016/j.jas.2010.06.027

Riebesell, U., Fabry, V. J., Hansson, L., and Gattuso, J. P. (2011). *Guide to Best Practices for Ocean Acidification Research and Data Reporting*. Luxembourg: Office for Official Publications of the European Communities.

Ries, J. B., Cohen, A. L., and Mccorkle, D. C. (2009). Marine calcifiers exhibit mixed responses to CO_2-induced ocean acidification. *Geology* 37, 1131–1134. doi: 10.1130/G30210A.1

Rittschof, D., Branscomb, E., and Costlow, J. (1984). Settlement and behavior in relation to flow and surface in larval barnacles, *Balanus amphitrite* Darwin. *J. Exp. Mar. Biol. Ecol.* 82, 131–146. doi: 10.1016/0022-0981(84)90099-6

Rittschof, D., Clare, A., Gerhart, D., Mary, S. A., and Bonaventura, J. (1992). Barnacle *in vitro* assays for biologically active substances: toxicity and settlement inhibition assays using mass cultured *Balanus amphitrite amphitrite* Darwin. *Biofouling* 6, 115–122. doi: 10.1080/08927019209386217

Rittschof, D., Orihuela, B., Stafslien, S., Daniels, J., Christianson, D., Chisholm, B., et al. (2008). Barnacle reattachment: a tool for studying barnacle adhesion. *Biofouling* 24, 1–9. doi: 10.1080/08927010701784920

Rodriguez-Navarro, A. B., Cabraldemelo, C., Batista, N., Morimoto, N., Alvarez-Lloret, P., Ortega-Huertas, M., et al. (2006). Microstructure and crystallographic-texture of giant barnacle (*Austromegabalanus psittacus*) shell. *J. Struct. Biol.* 156, 355–362. doi: 10.1016/j.jsb.2006.04.009

Roleda, M. Y., Boyd, P. W., and Hurd, C. L. (2012). Before ocean acidification: calcifier chemistry lessons. *J. Phycol.* 48, 840–843. doi: 10.1111/j.1529-8817.2012.01195.x

Saroyan, J. R., Lindner, E., and Dooley, C. A. (1970). Repair and reattachment in the Balanidae as related to their cementing mechanism. *Biol. Bull.* 139, 333–350. doi: 10.2307/1540088

Schultz, M. P., Bendick, J. A., Holm, E. R., and Hertel, W. M. (2011). Economic impact of biofouling on a naval surface ship. *Biofouling* 27, 87–98. doi: 10.1080/08927014.2010.542809

So, C. R., Fears, K. P., Leary, D. H., Scancella, J. M., Wang, Z., Liu, J. L., et al. (2016). Sequence basis of barnacle cement nanostructure is defined by proteins with silk homology. *Sci. Rep.* 6:36219. doi: 10.1038/srep36219

So, C. R., Scancella, J. M., Fears, K. P., Essock-Burns, T., Haynes, S. E., Leary, D. H., et al. (2017). Oxidase activity of the barnacle adhesive interface involves peroxide-dependent catechol oxidase and lysyl oxidase enzymes. *ACS Appl. Mater. Inter.* 9, 11493–11505. doi: 10.1021/acsami.7b01185

Truchot, J. P., and Duhamel-Jouve, A. (1980). Oxygen and carbon dioxide in the marine intertidal environment: diurnal and tidal changes in rockpools. *Respir Physiol.* 39, 241–254. doi: 10.1016/0034-5687(80)90056-0

Waldbusser, G. G., Voigt, E. P., Bergschneider, H., Green, M. A., and Newell, R. I. (2011). Biocalcification in the eastern oyster (*Crassostrea virginica*) in relation to long-term trends in Chesapeake Bay pH. *Estuar. Coast.* 34, 221–231. doi: 10.1007/s12237-010-9307-0

Walker, G. (1972). The biochemical composition of the cement of the two barnacle species, *Balanus hameri* and *Balanus crenatus*. *J. Mar. Biol. Assoc. UK* 52, 429–435. doi: 10.1017/S0025315400018786

Wang, Z., Leary, D. H., Liu, J., Settlage, R. E., Fears, K. P., North, S. H., et al. (2015). Molt-dependent transcriptomic analysis of cement proteins in the barnacle *Amphibalanus amphitrite*. *BMC Genomics* 16:859. doi: 10.1186/s12864-015-2076-1

Whiteley, N. M. (2011). Physiological and ecological responses of crustaceans to ocean acidification. *Mar. Ecol. Prog. Ser.* 430, 257–271. doi: 10.3354/meps09185

Wiegemann, M., and Watermann, B. (2003). Peculiarities of barnacle adhesive cured on non-stick surfaces. *J. Adhes. Sci. Technol.* 17, 1957–1977. doi: 10.1163/156856103770572070

Wong, K. K. W., Lane, A. C., Leung, P. T. Y., and Thiyagarajan, V. (2011). Response of larval barnacle proteome to CO_2-driven seawater acidification. *Comp. Biochem. Physiol. Part D Genomics Proteomics* 6, 310–321. doi: 10.1016/j.cbd.2011.07.001

Wootton, J. T., Pfister, C. A., and Forester, J. D. (2008). Dynamic patterns and ecological impacts of declining ocean pH in a high-resolution multi-year dataset. *Proc. Natl. Acad. Sci. U.S.A.* 105, 18848–18853. doi: 10.1073/pnas.0810079105

Zhao, X., Guo, C., Han, Y., Che, Z., Wang, Y., Wang, X., et al. (2017). Ocean acidification decreases mussel byssal attachment strength and induces molecular byssal responses. *Mar. Ecol. Prog. Ser.* 565, 67–77. doi: 10.3354/meps11992

Conflict of Interest Statement: The authors declare that the research was conducted in the absence of any commercial or financial relationships that could be construed as a potential conflict of interest.

frontiers in Marine Science

REVIEW
published: 19 February 2019
doi: 10.3389/fmars.2019.00041

Recent Advances of Shell Matrix Proteins and Cellular Orchestration in Marine Molluscan Shell Biomineralization

*Xiaorui Song[1], Zhaoqun Liu[1], Lingling Wang[1] and Linsheng Song[1,2,3]**

[1] Liaoning Key Laboratory of Marine Animal Immunology, Dalian Ocean University, Dalian, China, [2] Laboratory for Marine Fisheries Science and Food Production Processes, Qingdao National Laboratory for Marine Science and Technology, Qingdao, China, [3] Liaoning Key Laboratory of Marine Animal Immunology and Disease Control, Dalian Ocean University, Dalian, China

Biomineralization refers to the dynamic physiological processes whereby living organisms elaborate mineralized tissues. The existence of extremely abundant molluscan species shows the diversity of mineralized tissues, since the majority of them (Conchifera) produce shells that vary in size and shape. Over the past decades, great progress has been made on the study of the cellular biology of shell biomineralization. The construction of the molluscan shell is the archetype of biologically controlled mineralization which requires specialized cellular machinery. It has been so far demonstrated that the cells involved in shell formation come from two different sources: outer mantle epithelial cells (OME) and circulating hemocytes. OMEs secrete the organic matrix, among which shell matrix proteins (SMPs) determine mineralogical and crystallographic properties of shell. Circulating hemocytes take part in the deposition of intracellular biominerals and deliver them to the mineralization sites. Many novel SMPs have been identified by using molecular biology techniques (i.e., gene cloning, *in situ* hybridization, immunohistochemistry) coupled with high-throughput sequencing data (genome, proteome, secretome and transcriptome), and their corresponding functions during the shell formation have also been confirmed. The cellular activity of OME and hemocytes during shell formation are significantly increased during shell regeneration process. A potential cellular basis model for molluscan shell formation is proposed. The shell matrix proteins, mostly secreted from OME, and a few secreted from hemocytes or other organs, are either directly delivered to the mineralization site *via* exosome or classical secretory pathway, or first transported to the hemolymph, and then engulfed by hemocytes (mainly granulocytes), which will disintegrate and release shell proteins and $CaCO_3$ crystals at the mineralization front. OME and hemocytes may also be involved in the nucleation and remodeling process of $CaCO_3$ mineral. These cells and cell products work co-operatively to produce an organo-mineral shell, which is composed of various biomineral ultra-structures and macromolecular organic components.

Keywords: biomineralization, outer mantle epithelial cells, shell matrix proteins, hemocytes, marine molluscs

OPEN ACCESS

Edited by:
Vera Bin San Chan,
Clemson University, United States

Reviewed by:
Vengatesen Thiyagarajan,
The University of Hong Kong, Hong Kong
Gary H. Dickinson,
The College of New Jersey, United States

***Correspondence:**
Linsheng Song
lshsong@dlou.edu.cn

Specialty section:
This article was submitted to Marine Molecular Biology and Ecology, a section of the journal Frontiers in Marine Science

Received: *16 February 2018*
Accepted: *28 January 2019*
Published: *19 February 2019*

Citation:
Song X, Liu Z, Wang L and Song L (2019) Recent Advances of Shell Matrix Proteins and Cellular Orchestration in Marine Molluscan Shell Biomineralization. Front. Mar. Sci. 6:41. doi: 10.3389/fmars.2019.00041

INTRODUCTION

Biomineralization refers to an extraordinary dynamic biological process whereby a living organism produces biomineral structures (a rigid skeleton or a non-skeletal mineral) at ambient temperature in environments ranging from polar to tropical (Simkiss and Wilbur, 1989; Cusack and Freer, 2008; Shi et al., 2013; Tang et al., 2018). Biomineral structures are of wide existence in nature with polymorphism and multiple functions. So far, at least 60 different biominerals have been identified to play versatile functions, including tissues support, embryonic and UV protection, shelter against predation, nutrition, reproduction, gravity, light or magnetic field perceptions, storage of mineral ions (Cusack and Freer, 2008; Marin et al., 2008; Islam and Peng, 2018). In the metazoan world, $CaCO_3$ skeletons are the most abundant and most commonly encountered biominerals (Lowenstam and Weiner, 1989; Simkiss and Wilbur, 1989; Marin et al., 2007; Cusack and Freer, 2008; Marin et al., 2008). The phylum Mollusca is the second largest invertebrate phylum, which benefits from the protection from their external biomineralized structure, the shell, a kind of the mastery of cellular-engineered microstructures (Kocot et al., 2016).

Molluscan separate the biomineral formation from the ambient environment (Rahman and Shinjo, 2012) and exhibit a huge diversity of biomineral morphologies, such as shells from most molluscs, epithelial spicules of the basal mollusk *Wirenia argentea* (Solenogastres) (Todt and Wanninger, 2010), scales and plates in bivalves, operculum in gastropod *Rapana venosa* (Hashimoto et al., 2012), intracellular detoxifying granules in the common garden snail *Helix aspersa* (Howard et al., 1981), egg capsules of the Patagonian neogastropod *Odontocymbiola magellanica* (Bigatti et al., 2010), love dart of land snails (Lodi and Koene, 2016), pearls from pearl oyster, statoconia in *Aplysia californica* (Kondrachuk and Wiederhold, 2004), and statoliths in *Nassarius reticulatus* (Caenogastropoda) (Galante-Oliveira et al., 2014). The shell is the most well-known $CaCO_3$ biominerals in molluscan animals, which contributes to support and protect them from predators, pathogens and to some extent from other environmental conditions, such as desiccation, wave action and iceberg damage (Kouchinsky, 2000; Cusack and Freer, 2008). Molluscs utilize a highly cross-linked protein layer (periostracum) and the outer mantle epithelial cells (OME), between where they elaborate a matrix comprising various macromolecules serving as the framework (Wilbur and Saleuddin, 1983; Lowenstam and Weiner, 1989; Addadi et al., 2006). Generally, the molluscan shell is made of approximately 95% $CaCO_3$ and 1–5% organic matrix. $CaCO_3$ exists as different crystal polymorphs (i.e., calcite, aragonite, vaterite) under natural conditions, and is arranged in layers with a distinctive pattern to form complex biomineral microstructures in molluscan shells. So far, more than 30 different biomineral microstructures of mollusc $CaCO_3$, such as nacre, foliate, prismatic, cross lamellar, and homogeneous microstructure, have been documented based on the scanning electron microscopy (SEM) observations (Chateigner et al., 2000; Kouchinsky, 2000; Furuhashi et al., 2009).

A typical molluscan shell (i.e., the shells of the mussel, the oyster, the abalone and the nautilus) exhibits a trilayered structure: the outermost layer periostracum (a thin organic leathery layer), and two calcified layers (the outer prismatic layer and the inner nacreous layer) (Saruwatari et al., 2009). The prismatic layer is composed of elongated calcitic crystals in the form of prisms perpendicular to the periostracum. The nacreous layer, namely the inner lustrous shell layer, is composed of laminar structure made up of aragonite crystals, organized in a brick wall-like structure (Marie et al., 2012). Because of its extremely high fracture-resistance properties, nacre is considered as the most fascinating mollusk shell microstructures (Marin et al., 2012). As mentioned above, molluscan shell is a composite of inorganic mineral (mainly $CaCO_3$) and organic matrix, which is secreted from the mantle epithelium, and comprised of proteins, peptides, lipids, and carbohydrates (Lowenstam and Weiner, 1989; Addadi et al., 2006). The cooperation mechanism of these disparate components in producing a highly structured biomineralized shell has not been fully understood despite decades of investigations. Scientists have traditionally recognized the matrix-mediated hypothesis, which states that the organic matrix exclusively control the molluscan shell formation by providing the framework, inducing crystal nucleation, and regulating crystal growth extracellularly, thereby forming the crystal morphologies that are unique to the various layers of molluscan shell (Addadi et al., 1987, 2006; Lowenstam and Weiner, 1989). However, these results were mostly revealed from *in vitro* experiments through mimicking internal microenvironment, thus the effect of matrix proteins on shell mineralization is questionable (Sikes et al., 2000; Mount et al., 2004). One alternative to the matrix-mediated hypothesis is the cell-mediated hypothesis, which proposes that crystal nucleation occurs in hemocytes or OME, and that crystal-bearing cells transport nascent crystals intracellularly to the mineralization front (Mount et al., 2004; Gong et al., 2008a; Xiang et al., 2014). Although the cellular basis has been reported in many other biomineralization, such as osteoclasts and primary mesenchyme cells involved in bone and spicule formation in vertebrates and echinoderms, respectively (Wilt, 2002; Kylmaoja et al., 2016), this hypothesis still largely scraps the dominant paradigm in molluscan biomineralization, and has been supported by increasing evidence, which will be introduced in the following text (Mount et al., 2004; Fleury et al., 2008; Johnstone et al., 2008, 2015; Cho and Jeong, 2011; Kong et al., 2015; Li et al., 2016). To date, cells coming from two different sources have been observed involved in shell formation: (1) OMEs mediate shell formation by either directly involving in the nucleation and remodeling process of $CaCO_3$ mineral (Kong et al., 2015) or secreting the organic matrix, among which shell matrix proteins (SMPs) regulate the diversity of shell shapes by orchestrating the $CaCO_3$ crystals in a specific manner (Lowenstam and Weiner, 1989; Zhang and Zhang, 2006; Marin et al., 2008; Ivanina et al., 2017); and (2) hemocytes participate in the deposition of intracellular $CaCO_3$ crystals and deliver them to the mineralization site (Mount et al., 2004; Fleury et al., 2008; Kádár, 2008; Mount and Pickering, 2009; Cho and Jeong, 2011; Johnstone et al., 2015; Li et al., 2016; Ivanina et al., 2017). In this

review, we give a brief description of the OME- and hemocyte-mediated cellular biomineralization of marine molluscs.

OME-MEDIATED SHELL MINERALIZATION IN MOLLUSCS

The mantle tissue can be divided into several specialized regions (inner epithelium, internal tissues, and outer epithelium) from inside to outside (**Figure 1**). The outer epithelium is known to be related to the shell formation process, owing to its proximity to the mineralization front (Nudelman et al., 2006). The OMEs on the surface of outer epithelium further comprise a subtle cell zonation (mantle edge and mantle pallial), and appears to be strictly associated with the different microstructures of shell formation (Marin et al., 2008). Generally, SMPs secreted from the mantle edge cells are involved in the prismatic layer formation, while SMPs produced from mantle pallial cells participate in nacreous layer formation (Miyamoto et al., 1996). This zonation has been evidenced in molluscs by *in situ* hybridization or immunohistology techniques. For example, the localization of Pif 80 was checked by means of immunohistochemical SEM image analysis, and positive immunosignals could be observed throughout the nacreous layer after incubation with the antibody to Pif 80 (Suzuki et al., 2009). Shell organic constitutes synthesized by OME can be generally classified into two categories: insoluble (mostly chitin and silk) and soluble proteins. The insoluble proteins often act as a framework for shell formation and involves in the strengthening of shell mechanical properties, while the soluble ones are essential factors determining mineralogical and crystallographic properties (Addadi et al., 2006; Morse et al., 2007; Cusack and Freer, 2008; Marin et al., 2008; Marie et al., 2012). For example, some molecules function as Ca^{2+} chelators, mineral nucleators or inhibitors (Nudelman et al., 2006; Yan et al., 2007), some regulate crystal shape (Albeck et al., 1993), and some determine which $CaCO_3$ polymorph will form (Falini et al., 1996; Fu et al., 2005; Marie et al., 2012). This section summarizes the SMPs identified so far from the shells of molluscs, and emphasizes the physiological function of several critical SMPs through biochemical and micromorphological studies during shell biosynthesis.

The Molecular Characteristic of SMPs

Shell matrix proteins are crucial factors for biomineralization processes, and the evolution of SMPs can reflect the diversification characters of molluscan shell (Marin et al., 2008; Marie et al., 2012). Traditionally, SMPs were retrieved from the soluble or insoluble organic fractions after dissolving the shell powder into calcium-chelating agents (i.e., EDTA or weak acid) (Marin et al., 2008). The soluble organic fractions were usually enriched in acidic hydrophilic residues (i.e., Asp), while the insoluble fraction contained a high ratio of Gly and Ala (Lowenstam and Weiner, 1989). With the widespread use of molecular biology techniques, more transcripts encoding SMPs were identified (Miyashita et al., 2000; Zhang et al., 2003). In recent years, the mollusc genome project has made great progress (Zhang et al., 2012; Du et al., 2017). Increases the sequence data of SMPs combined with transcriptome and proteome of molluscan mantle and shell have enabled a more thorough investigation into the biomineralization process (Zhang and Zhang, 2006; Politi et al., 2007; Cusack and Freer, 2008; Marin et al., 2008; Furuhashi et al., 2009; Kadar et al., 2009; Marie et al., 2010). For example, the mantle edge of *Mytilus galloprovincialis* was divided into three regions, and large amounts of differentially abundant transcripts across the three mantle regions were revealed (Bjärnmark et al., 2016). The highly polymorphic genome of the pearl oyster *Pinctada fucata martensii*, together with transcriptomic and proteomic analyses, allowed the identification of many SMPs (Du et al., 2017). So far, more than 60 different SMPs have been reported (**Table 1**). In this section, we will discuss the identification and evolution of functional SMPs from the prismatic and nacreous layers of molluscan shells as well as from extrapallial fluid (EPF), and the function of some critical SMPs is highlighted.

SMPs in the Nacreous Layer

The nacreous layer has attracted most attention for its unique material properties and hierarchical order as well as contribution to the pearl agriculture industry (Jackson et al., 1988; Chateigner et al., 2000; Kono et al., 2000). According to transmission electron microscope (TEM)/SEM observations and X-Ray diffraction (XRD) measurements, the nacreous layer is mainly constituted of aragonite tablets (Marie et al., 2015, 2017). A large number of SMPs involved in the nacreous layer formation have been identified, such as Pif (Suzuki et al., 2009), MSI60 (Sudo et al., 1997), lustrin A (Shen et al., 1997), N16/pearlin (Samata et al., 1999; Miyashita et al., 2000), perlucin, perlustrin (Weiss et al., 2000), N14, N66 (Kono et al., 2000), mucoperlin (Marin et al., 2000), AP7, AP24 (Michenfelder et al., 2003), P10 (Zhang et al., 2006a), perlwapin (Treccani et al., 2006), perlinhibin (Mann et al., 2007), N19 (Yano et al., 2007), N40 (Yan et al., 2007) and blue mussel shell protein (BMSP) (Suzuki et al., 2011). The following paragraphs will introduce pif, a well-studied SMP from the nacreous layer.

Pif, a key macromolecule for nacre formation, is translated into a large precursor and then cleaved into Pif 97 and Pif 80 *via* posttranslational proteolytic processing (Suzuki et al., 2009). Pif 97, containing a von Willebrand factor type A (VWA) domain, is located at the N-terminal region of the Pif protein, along with the C-terminal Pif 80, which lacks of conserved domains (Burgess and Kelly, 1987; Suzuki et al., 2013). Pif homologs have a wide distribution among various molluscs. The VWA and chitin-binding domains in Pif 97 are highly conserved even among distant species, whereas the sequences of Pif 80 are markedly different (Suzuki et al., 2013; Wang et al., 2013b). Surprisingly, Pif 80's homolog was not detected in Pacific oyster *C. gigas* (Wang et al., 2013b). The laminin G domain, a Ca^{2+}-mediated receptor, usually interacts with extracellular matrix proteins (Marin et al., 2008). The N-terminus of the laminin G domain is present between the chitin-binding domain and the C-terminus of Pif 97, while the C-terminus of the laminin G is located at the center of Pif 80, which may contribute to the $CaCO_3$-binding activity of Pif (Suzuki et al., 2013). In *C. gigas*, the morphology of the

TABLE 1 | The main shell matrix proteins identified from Molluscs.

Species	Name	Structure (polymorph)	Accession Number	Reference	Domains	Function
Pinctada maxima	N66	Nacre (aragonite)	JC7210	Kono et al., 2000	α-CA domain G-X-N repeat domain	HCO_3^- synthesis
	N45 protein	—	ACT55367.1	Wang et al., 2011	α-CA domain G-X-N repeat domain	HCO_3^- synthesis
	N36	–	ACS50182.1	Wang et al., 2011	α-CA domain G-X-N repeat domain	HCO_3^- synthesis
	Aspein	Prisms (calcite)	AB685319	Isowa et al., 2012	Ser-Glu-Pro repetitive sequence Asp-Ala repetitive sequence	–
	N14	Nacre (aragonite)	JC7211	Kono et al., 2000	Short acidic domains GN domain	Ca-binding?
	Nacrein like protein	Nacre	BAF42330.1/A0ZSF3.1	Norizuki and Samata, 2008	α-CA domain G-X-N repeat domain	HCO_3^- synthesis
	pif	Nacre (aragonite)	BAJ08001.1	Suzuki et al., 2013	VWA domain chitin-binding domain	Binding chitin; crystal morphology
	Shematrin -2β	Prisms (calcite)	KC494066	Mcdougall et al., 2013	Glycine-rich domain	Provide a framework for calcification
	Shematrin-4	Prisms (calcite)	KC494067	Mcdougall et al., 2013	Glycine-rich domain	Provide a framework for calcification
	Shematrin-5	Prisms (calcite)	KC494068	Mcdougall et al., 2013	Glycine-rich domain	Provide a framework for calcification
	Shematrin-6	Prisms (calcite)	KC494069	Mcdougall et al., 2013	Glycine-rich domain	Provide a framework for calcification
	Shematrin-7	Prisms (calcite)	KC494070	Mcdougall et al., 2013	Glycine-rich domain	Provide a framework for calcification
	Shematrin-1a	Prisms (calcite)	KC505164	Mcdougall et al., 2013	Glycine-rich domain	Provide a framework for calcification
	Shematrin-1b	Prisms (calcite)	KC505165	Mcdougall et al., 2013	Glycine-rich domain	Provide a framework for calcification
	Shematrin -2α	Prisms (calcite)	KC505166	Mcdougall et al., 2013	Glycine-rich domain	Provide a framework for calcification
	Shematrin-3	Prisms (calcite)	KC505167	Mcdougall et al., 2013	Glycine-rich domain	Provide a framework for calcification
Pinctada fucata	Nacrein	Nacre (aragonite)	Q27908	Miyamoto et al., 1996	α-CA domain G-X-N repeat domain	HCO_3^- synthesis Ca-binding?
	Nacrein like protein F	Nacre (aragonite)	A0ZSF2.1	Yu et al., 2006	α-CA domain G-X-N repeat domain	HCO_3^- synthesis
	N16 or pearlin	Nacre (aragonite)	O97048	Samata et al., 1999	Short acidic domains GN repeats	Ca-binding?
	MSI 60	Nacre (aragonite)	O02402	Sudo et al., 1997	poly-A/G blocks A-rich domains short acidic domains	Ca-binding?
	MSI 31	Prisms (calcite)	O02401	Sudo et al., 1997	10 poly-G blocks 6 ESEEDX	(ß-sheet) structural Ca-binding?
	MSI 7	Prisms (calcite)	Q7YWA5	Zhang et al., 2003	G-rich domain	Structural (ß-sheet)
	Aspein	Prisms (calcite)	BAD00044	Tsukamoto et al., 2004	D-rich domain	Ca-binding
	Prismalin-14	Prisms	BAD27406	Suzuki et al., 2004	PIYR-repeat domain Gly/Tyr-rich region	Framework protein
	Pif	Nacre (aragonite)	BAH97338.1	Suzuki et al., 2009	VWA domain chitin-binding domain	Binding chitin; crystal morphology
	KRMP-1	Prisms (calcite)	DQ114788	Zhang et al., 2006b	Lysine-rich basic domain Gly/Tyr domain	The formation of prismatic layer
	KRMP-2	Prisms (calcite)	DQ114789	Zhang et al., 2006b	Lysine-rich basic domain Gly/Tyr domain	The formation of prismatic layer
	KRMP-3	Prisms (calcite)	DQ114790	Zhang et al., 2006b	Lysine-rich basic domain Gly/Tyr domain	The formation of prismatic layer
	KRMP-4	Prisms (calcite)		Masaoka and Kobayashi, 2009	Lysine-rich basic domain Gly/Tyr domain	The formation of prismatic layer
	PfN44	Nacre (aragonite)	KC238310	Pan et al., 2014	Tandem repeat domain	Inhibition aragonite formation
	PFMG1		DQ104255.1	Liu et al., 2007	EF-hand calcium-binding domains	Nacre biomineralization
	EFCBP		DQ494416	Huang et al., 2007	EF-hand motifs	
	P10	Nacre (aragonite)		Zhang et al., 2006a		Regulate the mineral phase
	Shematrin-1	Prisms (calcite)	AB244419	Yano et al., 2006	Glycine repeat domain [G_n(L/Y), (I/Y)G_n(I/L/V)]	
	Shematrin-2	Prisms (calcite)	AB244420	Yano et al., 2006	Glycine repeat domain [G_n(L/Y), IG_nI]	
	Shematrin-3	Prisms (calcite)	AB244421	Yano et al., 2006	Glycine repeat domain [G_n(A/V/Y), IGGGGV]	

(Continued)

TABLE 1 | Continued

Species	Name	Structure (polymorph)	Accession Number	Reference	Domains	Function
	Shematrin-4	Prisms (calcite)	AB244422	Yano et al., 2006	Glycine repeat domain [GG(L/Y)]	
	Shematrin-5	Prisms (calcite)	AB244423	Yano et al., 2006	Glycine repeat domain [GG(L/Y)]	
	Shematrin-6	Prisms (calcite)	AB244424	Yano et al., 2006	Glycine repeat domain Gn(A/I/L/V)]	
	Shematrin-7	Prisms (calcite)	AB244425	Yano et al., 2006	Glycine repeat domain [GG(A/L/M)]	
	PfY2		KY436033	Yi et al., 2017		
	ACCBP		DQ473430	Ma et al., 2007	α7 nAChR inhibit the growth of calcite	
	SPARC		KU310669	Xie, 2016	Acidic region, follistatin-like region, and extracellular Ca^{2+}-binding domain	Control the transition among ACC, vaterite, calcite and aragonite.
Pinctada margaritifera	Nacrein A1	Nacre (aragonite)	AEC03970.1	Joubert et al., 2010	α-CA domain G-X-N repeat domain	HCO_3^- synthesis
	Nacrein B4	Nacre (aragonite)	AEC03972.1	Joubert et al., 2010	α-CA domain G-X-N repeat domain	HCO_3^- synthesis
	Nacrein B3	Nacre (aragonite)	AEC03971.1	Joubert et al., 2010	α-CA domain G-X-N repeat domain	HCO_3^- synthesis
	Nacrein B2	Nacre (aragonite)	ADY69618.1	Joubert et al., 2010	α-CA domain G-X-N repeat domain	HCO_3^- synthesis
	Nacrein C5	Nacre (aragonite)	AEC03973.1	Joubert et al., 2010	α-CA domain G-X-N repeat domain	HCO_3^- synthesis
	Pif	Nacre (aragonite)	BAM66823.1	Suzuki et al., 2013	VWA domain chitin-binding domain	Binding chitin; crystal morphology
Crassostrea nippona	Nacrein-like protein C1	—	A0ZSF6.1	Norizuki and Samata, 2008	α-CA domain G-X-N repeat domain	HCO_3^- synthesis
	Nacrein-like protein C2	—	A0ZSF7.1	Norizuki and Samata, 2008	α-CA domain G-X-N repeat domain	HCO_3^- synthesis
Crassostrea gigas	Pif97	Calcite	JQ619625	Wang et al., 2013b	VWFA domain and one CHIT_BIND_II domain	Bind the chitin framework
	Nacrein-like proteins F1		KC563208	Song et al., 2014	α-CA domain	
	Nacrein-like proteins F2		KC563207	Song et al., 2014	α-CA domain	
	Nacrein-like proteins F3		KC563209	Song et al., 2015		
Pinna nobilis	Mucoperlin	Nacre (aragonite)	AF145215	Marin et al., 2000	SP-rich modules short acidic motifs	$CaCO_3$ inhibition? Ca-binding ?
Mizuhopecten yessoensis	MSP-1	Foliated (calcite)	Q95yf6	Sarashina and Endo, 1998	4 GS domains 4 D-rich domains 1 basic domain 3 G-rich domains	Loop Ca-binding ? Anchorage?
	Nacrein-like protein P1	—	A0ZSF4.1	Norizuki and Samata, 2008	α-CA domain G-X-N repeat domain	HCO_3^- synthesis
	Nacrein-like protein P2	—	A0ZSF5.1	Norizuki and Samata, 2008	α-CA domain G-X-N repeat domain	HCO_3^- synthesis
Haliotis rufescens	Lustrin A	Nacre (aragonite)	AF023459	Shen et al., 1997	C/P-rich modules GS domain basic protease inhib.	Loop anchorage? Protease inhib.?
	AP7	Nacre (aragonite)	AF225916	Michenfelder et al., 2003	Altern. hydrophob/hydrophil. motifs	Calcite-binding
	AP8	Nacre (aragonite)		Fu et al., 2005		Crystal morphology
	AP24	Nacre (aragonite)	AF225915	Michenfelder et al., 2003	Short acidic motifs 2 *N*-glycosylations	Calcite-binding
Haliotis laevigata	Perlustrin	Nacre (aragonite)	P82595	Weiss et al., 2001	IGF-BP domain	IGF-binding cell interaction
	Perlucin	Nacre (aragonite)	P82596	Mann et al., 2000	C-type lectin domain adhesin-like repeats	Sugar-binding
Biomphalaria glabrata	Dermato-pontin	Cr-lamellar (aragonite)	P83553	Marxen et al., 2003	Dermatopontin *N*-glycosylation	ECM-binding cell interaction
Turbo marmoratus	Nacrein	Nacre (aragonite)	AB073680	Miyamoto et al., 2003	α-CA domain G-X-N repeat domain	HCO_3^- synthesis
Mytilus galloprovincialis	BMSP	(aragonite and calcite)	BAK86420.1	Fang et al., 2011	VWA domain chitin-binding domain	Binding chitin; crystal morphology
	MSP22.8	Prisms (calcite)	–	Calvoiglesias et al., 2016		
Patella vulgata	BSMP protein	–	CCJ09597	Werner et al., 2013	VWA domain chitin-binding domain	Binding chitin; crystal morphology

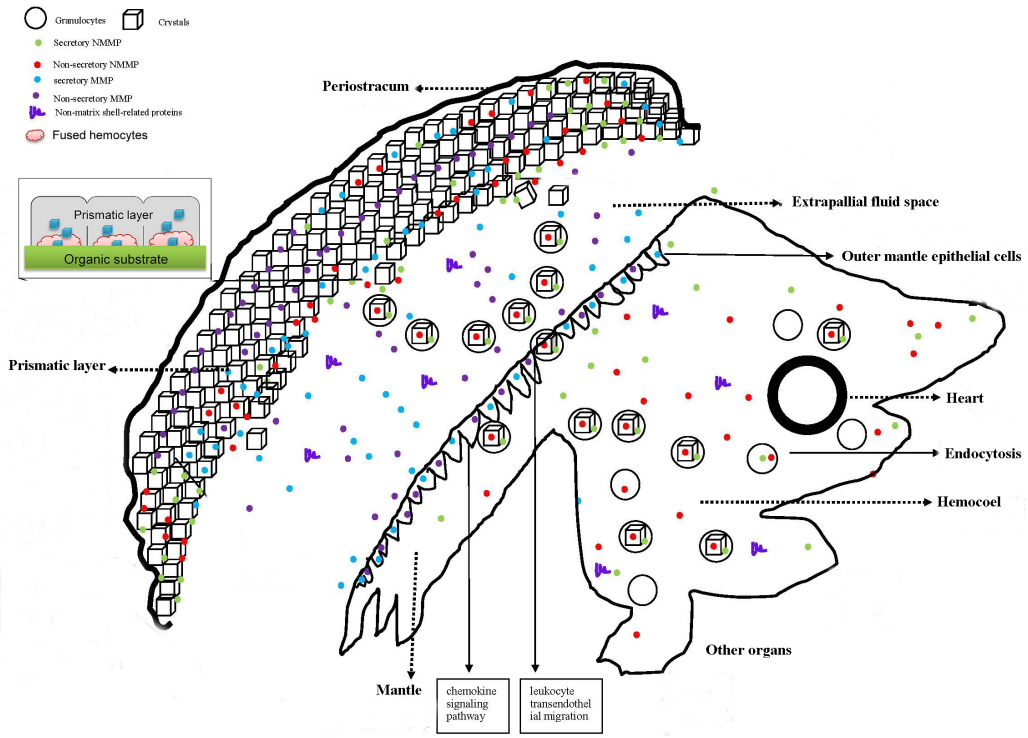

FIGURE 1 | Schematic presentation of shell biomineralization in the oyster (Wang et al., 2013a; Kong et al., 2015; Li et al., 2016). The notes for some of the shapes included in this figure are shown on the upper left. In general, the figure is divided into two parts: soft body and shell. Crystal-bearing hemocytes in the circulating system of oyster are released into the EPF by secretory cavities on the mantle surface and then transported to the biomineralization front. These hemocytes fuse into the prismatic layer columns. They release $CaCO_3$ crystals to form the calcite of the prismatic layers. The fragmented hemocytes assist organic matrices secreted from OMEs to produce the substrate of the prismatic layer. Some shell proteins produced by organs other than the mantle (i.e., the shell proteins not produced by the mantle) may arrive into the hemocoel first and then be engulfed by the granulocytes. The hemocytes and OMEs might be directly involved in the shell regeneration by affixing on the shell regeneration area.

inner shell surface exhibited significant changes after injection of dsRNA of *Cg*-Pif 97. The calcite laths of the shell became thinner and narrower along with increasing dose of *Cg*-Pif 97 dsRNA, indicating that the *Cg*-Pif 97 is indispensable during calcite shell formation in oysters (Wang et al., 2013b). Similarly, the injection of *Pf*-Pif dsRNA resulted in disordered growth of the nacreous layer in the pearl oyster *P. fucata*, suggesting that *Pf*-Pif might be essential for normal growth of the nacreous layer (Suzuki et al., 2009). Although lacking conserved domains, Pif 80 has some typical structural features, i.e., high proportion of charged and repetitive amino acid residues [17 repeats of Asp-Asp-Arg (Lys)-Lys (Arg) motif], which contributes to its specific binding ability to the aragonite crystals. In addition, Pif 80 is proposed to be critical in the transformation from inorganic phase to organic mineral during nacre formation. Through strong Ca^{2+} binding property, recombinant Pif 80 plays crucial roles in transformation from inorganic phase to organic minerals as well as regulation of aragonite crystallization during nacre formation (Bahn et al., 2017). The fraction containing Pif 80, Pif 97, and the N16 complex can induce the formation of aragonite and vaterite crystals in *in vitro* $CaCO_3$ crystallization experiments, further confirming the essential roles of Pif 80 and Pif 97 during shell formation (Suzuki et al., 2009). Based on above results, the potential function of Pif during aragonite crystal formation is proposed. After first binding to chitin framework, Pif 80 and Pif 97 complex accumulates $CaCO_3$ crystals precipitation inside the chitin membrane, and then regulates them vertical alignment.

Shell matrix proteins are generally classified according to the theoretical isoelectric point (pI). Presently, SMPs associated with nacreous layer formation are classified into two categories: moderately acidic SMPs (pI = 4.5–7, such as pif, MSI60, N16/Pearlin, N14, AP7, AP24 et al.) and basic SMPs (pI = 7–10.5, such as lustrin A, perlucin, perlustrin, perlwapin, perlinhibin, N19, N66 et al.) (Marin et al., 2008). Some SMPs of this category contain a short acidic domain, mainly participating in Ca^{2+} binding. Besides, other typical domains, such as VWA domain, IGF-BP domain, and C-type lectin domain, usually possess binding function. Thus it is supposed that these SMPs may be related to the extracellular microenvironment, which is critical for shell formation.

SMPs in the Prismatic Layer

The prismatic layer of mulluscan shell is mainly composed of columnar calcite crystals, which are enclosed in compact organic matrices (Carter, 1985; Chateigner et al., 2000). Lys (K)-rich mantle proteins (KRMPs) (Zhang et al., 2006b), MSI31

(Sudo et al., 1997), prismalin-14 (Suzuki et al., 2004), aspein (Tsukamoto et al., 2004), prisilkin-39 (Kong et al., 2009), P43 (Gong et al., 2008b), Alv (Kong et al., 2018), and asprich proteins (Gotliv et al., 2005; Politi et al., 2007) have been retrieved from calcitic prism textures and demonstrated to be critical in prismatic layer formation.

KRMPs represent a group of small proteins with a molecular weight of 10 kDa, and are unique to pearl oysters (*P. fucata*, *P. maxima* and *P. margaritifera*) (Zhang et al., 2006b; Jackson et al., 2010; Berland et al., 2011; Kinoshita et al., 2011; Mcdougall et al., 2013). KRMPs are typical basic SMPs (pI = 9.5–9.8) and rich in Lys, Gly and Tyr amino acids (Zhang et al., 2006b). Four KRMP proteins (KRMP-1 to KRMP-4), with 98-101 residues, differ only by few amino acids (Zhang et al., 2006b; Masaoka and Kobayashi, 2009). KRMPs contain two functional domains: a Lys-rich basic (BR) domain and a Gly/Tyr-rich (GYR) domain. The BR domain also exists in some other SMPs, i.e., Lustrin A (Shen et al., 1997) and MSP-1 (Sarashina and Endo, 1998), interacting with negatively charged ions or acidic SMPs. The GYR domain exhibits some homology with quinone-tanned proteins, which suggests that the Tyr residues may be oxidized in DOPA in the mature protein. KRMPs are specifically located at the mantle edge, which is recognized as the secretion zone of prismatic layer. The prismatic tablets exhibit irregular morphology after the treatment with dsRNA of KRMP. The surface of prismatic layer become lacunose and the borders between the prisms and the framework are broken along with the increased dosage (Fang et al., 2011). Furthermore, KRMP-3, retrieved from the EDTA-insoluble matrix of the prismatic layer, is located at the organic sheet and the prismatic sheath. Recombinant KRMP-3 binds tightly to chitin *via* the GYR domain, while the BR domain of KRMP-3 is crucial for inhibition of $CaCO_3$ precipitation and growth of aragonite, as well as regulation of calcite morphology (Liang et al., 2015). Taken together, KRMPs are restricted to pearl oysters as well as their closest relative species, and participate in the framework formation of the prismatic layer.

Prismalin-14, is the first prismatic matrix protein identified at both protein and nucleotide levels (Suzuki et al., 2004). Prismalin-14 contains only 11 types of amino acids with a total length of 105 amino acids. Hydrophobic residues are mostly located at the interzonal region, while hydrophilic residues are distributed at both termini. The structural composition of prismalin-14 is diverse, containing a pyroglutamate, four tandem Pro-Ile-Tyr-Arg (PIYR) repeats, a Gly/Tyr-rich (GY) domain, and two Asp-rich regions at the N- and the C-termini (Takeuchi et al., 2016). The structure-function relationships of prismalin-14 have been studied through construction of recombinant proteins with different functional domains. Recombinant Prismalin-14 inhibits $CaCO_3$ precipitation in a dose-response (Suzuki and Nagasawa, 2007; Mann et al., 2012). While ΔN (including the PIYR repeats, GY-rich, C-terminal regions) shows lower activity and ΔNΔC (including the PIYR repeats and GY-rich domain) shows hardly any inhibitory activity at the equal concentration, showing that Asp-rich domains at both termini are inhibitors of $CaCO_3$ precipitation. In addition, the GY-rich domain is indispensable for chitin-binding activity (Suzuki and Nagasawa, 2007). Recently, transcription factor POU3F4 has been shown to directly bind the promoter of prismalin-14, and is essential for its activation function (Jing et al., 2016). Northern blot and *in situ* hybridization analysis show that Prismalin-14 is selectively and highly expressed at the mantle edge (Suzuki et al., 2004). Taken together, prismalin-14 acts as a scaffold which combines with chitin and $CaCO_3$ crystals in the prismatic layer.

Aspein, the most acidic of all known SMPs (pI = 1.45), has a high ratio of Asp and is located at the mantle edge (Joubert et al., 2010). It was first identified from the mantle of *P. fucata* (Tsukamoto et al., 2004), and its homologs have been characterized from several other pterioid species (Isowa et al., 2012). Aspein has a signal peptide sequence (19 amino acids), which is similar to that of Asprich (63% identity), the acidic shell matrix protein identified from *Atrina rigida* (Gotliv et al., 2005). The expression levels of Aspein during larval and juvenile stages increase at the onset of calcite formation, while it is also weakly expressed when the shell is only composed of amorphous calcium carbonate (Miyazaki et al., 2010). Aspein especially promotes calcite precipitation *via* the Asp-rich domain *in vitro*, indicating its specific function during calcite formation (Takeuchi et al., 2008).

Except for KRMPs, other SMPs involved in prismatic layer formation share a common characteristic, namely, they are enriched in acidic amino acid residues. Thus they usually possess a relatively low pI (i.e., Aspein, pI = 1.67; MSI31, pI = 3.81; Prismalin-14, pI = 4.16; PfN44, pI = 4.25) and are categorized as extremely acidic SMPs (Marin et al., 2008). The striking finding that acidic proteins are preferentially associated with calcite in molluscan shell, was first reported in *M. californianus* in 1960s (Hare, 1963), which has been further confirmed with the increasing number of SMPs identified and sequenced (Marin et al., 2008; Liao et al., 2015; Kocot et al., 2016). However, the reason for this intriguing selection remains unknown. Generally, proteins with a high amount of acidic amino acid residues are negatively charged. Thus acidic SMPs should be more liable to bind Ca^{2+} during shell formation process. Traditionally, acquisition of acidic SMPs is not easy since they are difficult to purify. Nowadays, an increasing number of novel acidic SMPs have been identified and their corresponding primary structures also have been analyzed by virtue of genomic, proteomic and transcriptomic approaches, which will help immensely to reveal the aforementioned phenomenon, such as the preferential choice of acidic proteins associated with calcite in molluscan shell.

SMPs Involved in the Formation of Both Nacreous and Prismatic Layers

Although outer prisms and inner nacre layers in molluscan shells are assembled from very different protein repertoires, several SMPs, such as Nacrein (Miyamoto et al., 1996), MSI7 (Zhang et al., 2003; Feng et al., 2009), PfY2 (Yi et al., 2017), and shematrins (Yano et al., 2006), have reported to exert dual-function in both layers.

Nacrein, the first reported molluscan organic SMP, has a carbonic anhydrase (CA)-like domain with an insertion of Gly-X-Asn (G-X-N, X = Asp, Asn, or Glu) or Gly-Asn (G-N) repeats, and functions in both nacreous and prismatic layers (Miyamoto et al., 1996, 2005; Miyashita et al., 2002).

Nacrein homologs have been identified from turban shell *Turbo marmoratus* (Miyamoto et al., 2003), the edible Iwagaki oyster *Crassostrea nippona* (Norizuki and Samata, 2008), Yesso scallop *Patinopecten yessoensis* (Norizuki and Samata, 2008), giant clam *Tridacna gigas* (Baillie and Yellowlees, 1998; Leggat et al., 2005), Pacific oyster *C. gigas* (Song et al., 2014), and pearl oyster *P. maxima* (Kono et al., 2000; Norizuki and Samata, 2008; Wang et al., 2011). The CA-like domains of the nacrein homologues share high similarity with nacrein, while the repeat sequences exhibit variability in length and composition. For example, the composition and length of repeat sequence from *T. marmoratus* nacrein is markedly different from that of nacrein in *P. fucata* and *P. maxima*. The former is composed of G-N two amino-acid repeat with 132 amino acids in length, while the latter is composed of G-X-N three amino-acid repeat with length of 80 amino acids (Miyamoto et al., 2003). The nacre microstructure of gastropods is in column form, whereas in sheet form in bivalves. It is speculated that the structural variance of nacrein may reflect functional difference, which may consequently lead to the production of divergent microstructures (Miyamoto et al., 2003). The structure of nacrein exhibits N-shape *via* small-angle X-ray scattering, which is consistent with its sequence structural features (Norizuki and Samata, 2008). Nacrein from the pearl oyster *P. fucata* exhibits tissue-specific expression pattern and specifically distributes at the OME (Miyamoto et al., 2005; Gong et al., 2008b). The function of nacrein during shell formation has been further demonstrated. During the *in vitro* experiments, the addition of recombinant nacrein protein to a saturated solution of Ca^{2+} and HCO_3^-, significantly inhibit the precipitation of $CaCO_3$. The deletion of G-X-N repeats of nacrein significantly affects the inhibitory ability to the precipitation of $CaCO_3$ (Miyamoto et al., 2005). Aragonite crystals exhibited aberrant growth, and aragonitic tablets became thickened when nacrein is suppressed by the antibodies (Gong et al., 2008b). It is speculated that nacrein is a negative regulator in aragonitic tablet growth, and the G-X-N or G-N repeat sequence may show inhibitory activity during $CaCO_3$ precipitation (Miyamoto et al., 2005; Norizuki and Samata, 2008).

The novel SMP *Pf*Y2 is found in both prisms and nacre layers, suggesting its dual roles in the shell formation of *P. fucata* (Fang et al., 2011). The expression level of *Pf*Y2 peaks at 36 h after shell-notching, indicating its involvement of shell repairing and regenerating process. The recombinant *Pf*Y2 can significantly suppress $CaCO_3$ precipitation rate, participate in the crystal nucleation process, and mediate the transition of amorphous $CaCO_3$ to steady calcite or aragonite (Yi et al., 2017). The results clearly demonstrate that *Pf*Y2 is a critical macromolecule and performs a variety of biological functions during shell formation.

Shematrins, a family of Gly-rich structural proteins, is comprised of at least nine members with molecular weights of 25∼33 kDa (Yano et al., 2006; Mcdougall et al., 2013). With one exception (shematrin-5, pH = 7.7), all shematrins have a pI between 9 and 10.3, and are considered as the second family of basic SMPs. They all share characteristic primary structures and exhibit Gly-rich domains, comprised of short motifs of the type XG_nX (with $2 \leq n \leq 6$ and X = L/Y/A/V/I/M). All shematrins have a RKKKY, RRKKY or RRRKY motif at the C-terminal region (Yano et al., 2006). The Gly-rich domain of shematrin-2 is exactly identical to another acidic SMP MSI31 (98% homology in a 227 residue overlap), but their C-termini are completely different. Shematrin is strongly basic and is supposed to work as a framework for calcification, while MSI31 is extremely acidic and may be involved in nucleating crystals (Sudo et al., 1997). The C-terminal parts of shematrins exhibit a high homology (above 60% on 26 residues) with the C-terminal Gly-rich region of KRMPs (Zhang et al., 2006a). Shematrin-5 is the single protein of the family which contains an acidic domain and is similar to aspein (Tsukamoto et al., 2004). Shematrins exhibit tissue-specific expression and are located at the mantle edge. In addition, shematrin-1, -2, -3, -4, and -6 are also expressed in mantle pallial layer (Yano et al., 2006), indicating that shematrins possess dual roles in the formation of the nacreous and prismatic layers. Surprisingly, the shematrins are non-detectable in the abalone *H. asinina*, but exhibit active expansion and diversification within the pearl oysters, suggesting the hypothesis that the shell basic toolkit genes evolved rapidly among molluscs (Jackson et al., 2010).

Similar to the SMPs from nacreous layer, SMPs from both layers are either moderately acidic (i.e., nacrein, MSI7,) or basic (i.e., Shematrins). The functions of these SMPs show no difference between the two layers, indicating their important roles during the shell formation process.

SMPs From the Extrapallial Fluid (EPF)

Extrapallial fluid is an aqueous microenvironment located between the OME and the inner face of shell, and serves as the final medium of nacre calcification (Saha et al., 1988; Lowenstam and Weiner, 1989). EPF contains a variety of ions (Na^+, K^+, Ca^{2+}, Mg^{2+}, HCO_3^-), whereas the composition of ion content is different from that of the hemolymph and seawater (Saha et al., 1988; Wilt, 2002). EPF also contains various macromolecules secreted by the OME or transported from elsewhere to the EPF, such as proteins, polysaccharides, and lipids, among which the proteins are speculated to perform certain key function during shell biomineralization (Kylmaoja et al., 2016). However, largely due to the difficulty of obtaining EPF, there are few studies on the protein components. Previous studies showed that crude extraction mixtures of EPF proteins have significant influence on the morphology of crystal formation (Yin et al., 2009). Recently, amounts of novel EPF proteins have been identified by liquid chromatography-tandem mass spectrometry (LC-MS/MS) analysis of EPF proteins binding to the $CaCO_3$ crystals (Xie et al., 2016). So far, several SMPs have been extracted from the EPF, such as EP fluid protein from *M. edulis* (Hattan et al., 2001; Yin et al., 2005), Amorphous calcium carbonate-binding protein (ACCBP) (Ma et al., 2007), Secreted Protein Acidic and Rich in Cysteine (SPARC) from *P. fucata* (Xie, 2016).

Amorphous calcium carbonate-binding protein (ACCBP) containing an acetylcholine-binding site was the first purified EPF protein from *P. fucata* (Ma et al., 2007). Size-exclusion Chromatography, chemical cross-linking experiments coupled with negative staining electron microscopy revealed that ACCBP is a decamer composed of two adjacent pentamers, containing two Ca0562-binding sites, which are arranged in a 5-fold

symmetry. The unique structure is essential for ACC formation and affects the ACC induction efficiency (Su et al., 2013). ACCBP shows inhibitory activity on the growth of calcite and $CaCO_3$ precipitation both *in vitro* and *in vivo* (Ma et al., 2007). Besides, ACCBP can identify diverse phases and faces of $CaCO_3$ crystal *via* acetylcholine-binding site. With this capacity, ACCBP is demonstrated to alter the morphology of nacre lamellae by inhibiting the growth of certain aragonite faces, and simultaneously keep the $CaCO_3$-supersaturated solution in steady-state by terminating the nucleation and growth of calcite (Ma et al., 2007). ACCBP mainly functions as a negative regulator during the shell formation.

Secreted Protein Acidic and Rich in Cysteine (SPARC) contain three typical functional domains (acidic region, follistatin-like region, and extracellular Ca^{2+}-binding domain) and exist in the extracellular matrix of *P. fucata* (Xie, 2016). The expression levels of SPARC in EPF increase after shell-notching in *P. fucata*, indicating its involvement in shell repair process. SPARC is also found in both nacre and prismatic soluble extracts, and the blocking of SPARC with a polyclonal antibody was shown to inhibit the formation of nacre platelets (Xie, 2016). Furthermore, SPARC regulates the morphology of $CaCO_3$ crystals and induces the formation of vaterite in the calcite crystallization system. However, Mg^{2+} counteracts this effect and induces the formation of aragonite. Further intrinsic fluorescence and circular dichroism spectrum studies indicate that SPARC may exert function by changing the conformation of its secondary structure. In conclusion, SPARC participates in nacre formation by stabilizing vaterite to inhibit calcite formation *via* its EC domain and secondary structure variation, as well as by assisting aragonite formation in the presence of Mg^{2+} or other proteins (Xie, 2016).

Compared with SMPs identified from shell, most EPF proteins perform dual roles during the transition between prism and nacre, which is closely connected with their secondary structures and specific binding capacity to calcite or aragonite. Previous results also suggest that EPF proteins play a critical role in the biomineralization balance process (i.e., shell formation and ablation) (Xie et al., 2016). Remarkably, the amino acid constituents in the EPF proteins inducing aragonite or calcite formation had different preference, which was similar with the SMPs from shell (Hare, 1963; Evans, 2008; Marie et al., 2012; Xie et al., 2016).

The Regulatory Mechanism of SMPs in Molluscs

In molluscs, their functions of more than 40 SMPs have been elucidated, while the transcriptional regulation mechanisms are poorly studied. So far, only four transcription factors, *Pf*-MSX (Zhao et al., 2014), *Pf*-AP-1 (Zheng et al., 2015), *Pf*-Rel (Sun et al., 2015), and *Pf*-POU3F4 (Jing et al., 2016), have been reported to participate in shell formation through regulating expression of SMPs in molluscs.

Pf-AP-1, *Pf*-MSX, and *Pf*-Rel, are homologous genes of MSX, AP-1, and NF-κB, which are all involved in bone/tooth formation in vertebrates (Bakiri et al., 2007; Kim et al., 2010; Saadi et al., 2013). In pearl oyster *P. fucata*, *Pf*-AP-1, *Pf*-MSX, and *Pf*-Rel could directly bind to the promoters of SMPs KRMP, Pearlin, Prisilkin-39, Pif, and nacrein, respectively, and enhances their promoter activities in a dose-dependent manner (Zhao et al., 2014; Sun et al., 2015; Zheng et al., 2015). The mRNA transcripts of KRMP, Pearlin, Prisilkin-39, Pif, and nacrein all exhibited significant depression under the treatment either with inhibitors of AP-1 and NF-κB or dsRNA of *Pf*-MSX and *Pf*-Rel (Zhao et al., 2014; Sun et al., 2015; Zheng et al., 2015). Moreover, after injection of *Pf*-MSX dsRNA, the lamellar sheet from nacreous layer exhibited disorder orientation (Zhao et al., 2014). Similarly, knockdown of *Pf*-Rel led to crystal particles on the surface of inner nacreous layer to be scattered and irregular (Sun et al., 2015), which was similar to the morphological changes when Nacrein was blocked by its antibody (Gong et al., 2008b). A putative AP-1 binding site was predicted at the 5′-flanking region of the nacrein gene, and human AP-1(c-jun) has been reported with regulatory function in nacrein transcription *in vitro* (Miyashita et al., 2012). However in *P. fucata*, the expression pattern of nacrein showed almost no correlation with *Pf*-AP-1, and the inhibitor of AP-1 (SR11302) had no effect on the expression of nacrein (Zheng et al., 2015). In vertebrates, transcription factor POU mainly functions in the neuroendocrine system (Andersen and Rosenfeld, 2001). In molluscs, homolog of POU3F4 (*Pf*-POU3F4) has been identified and demonstrated to participate in shell formation through binding to the promoters of SMPs Aspein and Prismalin-14, and enhancing their transcriptional activities (Jing et al., 2016).

It is evident that some conservative transcription factors such as AP-1, MSX, and Rel, share similar function among diverse animals, playing important roles in bone/teeth formation in vertebrates and shell formation in molluscs. The distinct functions of POU between mammals and molluscs also suggest that there exist unique features in the regulation mechanism of shell formation in molluscs. So far, most results were obtained from transfection experiments *in vitro*; more direct evidence within primary culture of molluscan cells will be further highlighted in the future.

The Rapid Evolution of SMPs in Molluscs

Molluscs began to mineralize at the dawn of the Cambrian times, in a very short time interval, about 544 million years ago (Conway Morris, 2001). Like several other metazoan phyla, molluscs acquired the capacity to form a mineralization exoskeleton far after their emergence as a phylum, implicating that the 'molecular tool box' required for mineralizing is produced and employed. However, the mechanisms underlying production of calcified shell, whether originated from an ancestral biomineralization repertoire, or the production of lateral genetic transfer, are still unclear (Marin et al., 2008). The recent sequencing of several mollusc genomes coupled with the analysis of multi-omics demonstrates that many SMPs evolved independently and the shell proteome may have a much higher plasticity than expected.

The highly complex, robust and patterned shells are diverse among molluscs. Conventionally, the diverse of shell types can best be expressed by the diversity secretory repertoires from outer fold of mantle organ. One might expect that the representative

characteristics of shell are reflected by evolutionary changes of SMPs. Recent multi-omics studies have revealed the existence of tremendous diversity in the mantle secretomes. For example, a comparative scan between the obtained EST sequences of the abalone *H. asinina* and the genome of the patellogastropod *Lottia scutum*, shows that only 19% of the secreted proteins of *H. asinina* have their homologues in *L. scutum* (Jackson et al., 2006). Less than 15% of the secreted proteins are shared between a bivalve (*P. maxima*) and a gastropod (*H. asinina*), by comparing their nacre-secreting mantle transcriptomes (Jackson et al., 2010). In addition, a large proportion of novel secreted proteins are identified in the shell proteomes of *L. gigantea* when searched in the public databases. Few homologous proteins (1.1 to 7.7%) are found between any two molluscan species (Marie et al., 2013). Interestingly, the number of homologous SMPs shared between different classes is more than that between the same class, based on the comparison of the mantle transcriptomic of *L. gigantea*, *P maxima,* and *H. asinina* (Jackson et al., 2010). In addition, SMP genes are reported to be frequently duplicated in the *Pinctada* and *Lottia* genome (Marie et al., 2013; Takeuchi et al., 2016). For example, five genes of the shematrins tandemly cluster in two scaffolds. Three and two transcripts of N19 and N16 locate at same scaffold, respectively. Amazingly, homologous to shematrin, N19 and N16 are not detected in the *C. gigas* genome (Miyamoto et al., 2013; Takeuchi et al., 2016). Thus it could be concluded that these SMP genes are unique to the *P. fucata* lineage, and duplication occurred after speciation.

The acid-insoluble matrices (AIMs) associated with prismatic and nacreous layers are extremely different. Prism AIM is rich in Tyr, Pro, and Val, while nacre AIM contains more Ala and Asx (Asn and Asp). Eighty different SMPs have been identified between prismatic and nacreous layer, among which 64 are entirely unique (Marie et al., 2012). In *Pinctada* spp., 47/50 prism-related proteins are restricted to prisms, while 30/33 nacre-related proteins, are unique to nacre. A high ratio of the analyzed 61 transcripts were selectively overexpressed at the edge or pallium cells of the mantle organ, which is in line with the protein distribution either in prism or in nacre (Marie et al., 2012). Homologs of aragonite-and calcite-associated SMPs were searched through the oyster genome. Surprisingly, homologs of calcite-associated SMPs were non-detectable (0/29), while nine homologs of aragonite-associated SMPs are identified in the oyster genome (9/28). Since the oyster shell mainly is composed of calcite crystal, only the zone of the adductor muscle scar is composed of aragonite (Lee et al., 2011). Thus, aragonite-associated SMPs may be more conserved than the calcite-associated SMPs in the Molluscs.

Repetitive, low-complexity domains (RLCDs), in particular Gly-rich structural proteins, usually existed in tough, extracellular structures, and also have been identified in molluscan shell, such as KRMP (Masaoka and Kobayashi, 2009) and shematrin (Yano et al., 2006). Previous studies suggest that KRMPs and shematrins have large paralogous genes (at least 11 KRMPs, and 9 shematrins) in *Pinctada* spp., but show significant sequence divergence among orthologous genes, supporting the hypothesis that many SMPs are rapidly evolving (Yano et al., 2006; Masaoka and Kobayashi, 2009). RLCDs usually function in structure construction, and appear to evolve rapidly under selective pressures through Metazoans (Smith-Keune and Jerry, 2009). Therefore, it is proposed that the rapid evolution of KRMPs and shematrins probably arise from the RLCDs, which usually endow new mechanical properties with the structure they comprise (Jackson et al., 2010; Mcdougall et al., 2013).

The recent availability of complete genome data for several molluscs (Zhang et al., 2012; Takeuchi et al., 2016; Du et al., 2017; Nam et al., 2017; Wang et al., 2017), and the vastly increasing transcriptome, proteome, and secretome data, enable identification of more novel SMPs, and to comparatively study the origin and evolution of biomineralization in molluscs. Existing results reveal that SMPs are divergent in different molluscs, consistent with the heterogeneity of shell microstructures, which is constructed from a rapidly evolving secretome and has evolved convergent. However, since lack of steady cell line, the functions and transcription regulation of most SMPs have been investigated using *in vivo* experiments, which cannot truly reflect the interaction among SMPs under physiological conditions. More insight into the true functions of SMPs should be obtained either *via in vitro* cell culture system from molluscs or *in vivo* reverse genetics, such as RNAi or CRISPR/Cas9 genome editing technique.

Hemocyte-Mediated Shell Mineralization in Molluscs

Hemocytes are essential during the innate immune response, which has been shown to be related to biomineralization in molluscs. For example, amounts of hemocytes accumulate in the pearl sac after transplantation in pearl oyster (Kishore and Southgate, 2015). Immune-associated genes also exhibit significant expression during the shell regeneration period in *Laternula elliptica* (Sleight et al., 2015). Recently, more evidence directly demonstrated that hemocytes (mainly granulocytes) participate in the synthesis and delivery of $CaCO_3$ crystals as well as SMPs during the shell regeneration process (Mount et al., 2004; Mount and Pickering, 2009; Cho and Jeong, 2011; Johnstone et al., 2015; Li et al., 2016).

Shell damage-repair is a routine method to study shell formation. During shell regeneration, granulocytes have been shown to participate in the synthesis and transportation of $CaCO_3$ (Mount et al., 2004; Johnstone et al., 2015). The granular inclusions of hemocytes are Ca^{2+}-positive in the green ormer *H. tuberculata* (Fleury et al., 2008), Pacific oyster *C. gigas* (Ivanina et al., 2017), deep-sea mussel *Bathymodiolus azoricus* (Kadar et al., 2009), and pearl oyster *P. fucata* (Li et al., 2016), suggesting that the granulocytes may be a calcium pool and act as a calcium conveyor during shell formation (Kadar et al., 2009; Cho and Jeong, 2011). Intracellular $CaCO_3$ crystals are observed in hemocytes of various shelled molluscs. For example, x-ray microanalysis (SEM-EDS) reveals that crystal-shaped inclusions with rhombohedral appearance are enclosed in the refractive granulocytes (REF granulocytes), a subclass of granulocytes in Eastern oyster *C. virginica*. Some REF granulocytes have only one or two crystals, while others have numerous (Mount et al., 2004). Crystal-like structures with various shapes are also observed in

granulocytes of *P. fucata*, but one crystal could be only found in one cell. The chemical components of crystal-like structures were analyzed *via* SEM-EDS, which mainly contain Ca, C, O_2, P, and Si, similar to natural $CaCO_3$ crystals (Li et al., 2016). There are varied shapes of the crystals in *P. fucata*, but only hexahedron crystals are observed in *C. virginica*. Furthermore, REF cells are present on the prismatic shell surface in lines with fibrous materials and crystals (Mount et al., 2004). Similarly, the granulocytes are embedded into the column and fragmentation of matured shell, which was observed in oyster *C. gigas* (Cho and Jeong, 2011) and *P. fucata* (Li et al., 2016), directly showing that living hemocytes are present at the mineralization front. In addition, a highly refractive structure is detected in the hemocytes of *B. azoricus* induced by shell damage (Kádár, 2008), and insoluble $CaCO_3$ is synthesized in the hemocytes of *Venerupis philippinarum* during the initial period of shell regeneration (Trinkler et al., 2011). The crystal bearing hemocytes present in the EPF of the oyster *C. virginica* and the mussel *B. azoricus*, are able to start $CaCO_3$ crystal nucleation *in vivo* (Kadar et al., 2009; Cho et al., 2011). Remarkably, after incubation with EPF mixture, the hemocytes in Pacific oyster *C. gigas* produce numerous spherical calcium granules, which are almost identical in morphology and chemistry to those on the regenerated shell, suggesting the involvement of hemocytes during the regeneration of prismatic layer (Cho and Jeong, 2011). Given that the prismatic layer locates outside the calcified shell and is first produced during biomineralization, the granulocytes may participate in the initiating process of shell biomineralization. The involvement of hemocytes in the nacreous layer formation remains concern.

Besides to crystal synthesis and transport, the hemocytes are reported to function in the organic framework formation. Multi-omics data reveal that various SMPs are highly expressed in the hemocytes of various shelled molluscs. For example, SMPs (e.g., Shematrin 2 and ACCBP) and Ca^{2+} binding proteins α-subunit are abundant in the hemocytes of *P. fucata* (Liao et al., 2015; Li et al., 2016). In the Pacific oyster *C. gigas*, several shell formation related genes, i.e., chitin synthases, nacrein-like protein, casein kinases, VEGF and VEGF-R, are highly expressed in H2 and H3 hemocytes (kinds of larger, irregularly shaped cells, similar to granulocytes), which are potential players in biomineralization processes (Ivanina et al., 2017). SMPs were visualized in molluscan hemocytes during the shell repair process, suggesting the contribution of hemocytes to the formation of the shell framework (Shitalbahen, 2004; Johnstone et al., 2008). For example, SMP coated with collagen fibers were secreted from hemocytes of the Eastern oyster, *C. virginica* during the shell repair process (Shitalbahen, 2004). A 48 kDa SMP has been localized in hemocytes, but is unobservable after induction of shell repair (Johnstone et al., 2008). It is reported that circulating hemocytes can internalize the antigen when exposed to a hemocyte-free EPF liquid (Calvoiglesias et al., 2016). Due to limited knowledge, the specific function of hemocytes during the secretion and transportation of SMPs needs further investigation.

In conclusion, there is a suitable microenvironment in hemocytes of molluscs for depositing $CaCO_3$ crystal. Hemocytes might play crucial roles during shell formation by regulating the *in vivo* formation of $CaCO_3$ crystals, transferring the crystals *via* the EPF to the regenerated prismatic layer, assisting SMPs to form crystal template. The hemocyte might function in immune response with the similar role during soft tissue repair. More focus of the hemocytes function during the larvae ontogenesis, the demineralization, abnormal biomineralization as well as nacreous layer formation, would be helpful to investigate the hemocyte-mediated shell mineralization in molluscs.

THE POTENTIAL CELLULAR MODEL AND MECHANISM OF SHELL BIOMINERALIZATION

The mechanisms of shell formation have been investigated over the past several decades. Calcite and aragonite are two common polymorphs in molluscan shell structure, which mainly differ in the organization and orientation of the carbonate molecules (Stenzel, 1963). Hare (1963) indicated the composition difference of organic matrices in aragonite and calcite, and thus proposed that the organic matrix proteins might be responsible for the formation of various shell structures and mineral phases. It was reported that the addition of excessive Mg^{2+} (400 mg/500 ml) promotes the accumulation of aragonite in $CaCO_3$ solutions during *in vitro* experiments (Tokuyama, 1969), suggesting that the concentration of ions (in particular Mg^{2+}) in the precipitating solution could regulate the polymorphism between aragonite-calcite in molluscan shell (Blackwelder et al., 1976; Wilbur and Bernhardt, 1984). In order to determine the significance of organic matrices, especially the proteins that function in shell formation, Falini et al. (1996) reassembled a substrate *in vitro* composed of β-chitin and silk fibroin for crystal nucleation. They found that proteins extracted from the aragonitic- and calcitic- shell layers could mainly induce aragonite and calcite formation *in vitro*, respectively (Falini et al., 1996). A large number of subsequent studies support the matrix-mediated shell formation hypothesis, and it has been widely believed that shell calcification occurs in mantle-secreted compartments of chitin, silk fibroin and matrix proteins, and the matrix proteins are associated with the mineral phase and influence on crystal growth (Watabe, 1965; Addadi et al., 2006; Furuhashi et al., 2009). The first observation of hemocytes at the mineralization front using vital fluorescent staining and SEM raised the cellular basis for shell formation (Mount et al., 2004). Secretome and transcriptome data reveal that some SMPs are non-secretory, and some others were abundant in other tissues (Marie et al., 2010, 2012; Kinoshita et al., 2011; Mann et al., 2012; Wang et al., 2013a). Furthermore, biominerals and SMPs are observed in the hemocytes (Johnstone et al., 2008; Calvoiglesias et al., 2016), and hemocytes as well as OME assembling on the surface of regenerated prismatic layer (Cho and Jeong, 2011; Johnstone et al., 2015; Kong et al., 2015), prompt us to investigate the mechanism of shell formation from cellular aspects. The hypothesis that co-operative interaction of hemocytes and OME during shell formation have been developed (**Figure 1**).

Most SMPs are produced and secreted by the OME, while a few SMPs are produced from hemocytes or other organs

(Miyamoto et al., 2013; Wang et al., 2013a). The SMPs produced by the OME will be directly delivered to the crystallization surface *via* exosome (Zhang et al., 2012) or classical secretory pathway, while those produced from other organs are first transported to the hemolymph *via* classical or non-classical secretory pathways (Gardella et al., 2002), then engulfed by hemocytes (mainly granulocytes). The $CaCO_3$ crystal either produced in the mantle or synthesized in hemocytes (granulocytes) will be delivered to the biomineralization front *via* the EPF (Mount et al., 2004; Weiner and Addadi, 2011; Li et al., 2016). The organic matrix or mucus secreted from OME can load with Ca^{2+} and deliver them to the biomineralization front *via* the EPF (Fleury et al., 2008; Kadar et al., 2009). During the shell regeneration process, the granulocytes are embedded into the columns of the prismatic layer, and interact with SMPs, or with polysaccharide or chitin, to construct the shell framework. $CaCO_3$ crystals discharged from hemocytes (granulocytes), organic matrix or mucus, are subsequently deposited on the calcite of the prismatic layer (Wang et al., 2013a; Li et al., 2016).

CONCLUDING REMARKS

Biomineralization occurs widely in nature, and the shell formation of molluscs is considered as a good model of this process. The molluscan shells are produced under a series of sophisticated regulation steps involving cells (OME and hemocytes) and cell products (macromolecules mainly including SMPs, chitin and silk fibroin). The coordination between them reveals the cellular and molecular mechanism of biologically controlled mineralization. Multi-omics analyses together with molecular biology techniques has unveiled novel findings, i.e., the diversity of SMPs and significant variation between different SMP repertoires, the multiple-organ origin of SMPs, and the involvement of hemocytes in the formation of prismatic layer. These findings illustrate the complicated processes during shell formation, which will prompt a more detailed investigation on biomineralization in molluscan shell. Recent research have found that shell extracts from *M. edulis* and *C. gigas* promote the catabolic pathway of primarily cultured human dermal fibroblasts, which might be helpful in the context of anti-fibrotic strategies, particularly against scleroderma. Future studies in shell formation of molluscs are likely to uncover potential links to immunity as well as human disease, thus revealing a better understanding of the evolution of biomineralization.

AUTHOR CONTRIBUTIONS

XS and ZL collected the literature and prepared the manuscript. LW and LS revised the manuscript. LS designed the manuscript.

FUNDING

The work is supported by a grant (No. U1706204) from National Science Foundation of China, and earmarked fund (CARS-49) from Modern Agro-industry Technology Research System, AoShan Talents Cultivation Program Supported by Qingdao National Laboratory for Marine Science and Technology (No. 2017ASTCP-OS13), Key R&D Program of Liaoning Province (201703165), and the Fund for Outstanding Talents and Innovative Team of Agricultural Scientific Research.

REFERENCES

Addadi, L., Joester, D., Nudelman, F., and Weiner, S. (2006). Mollusk shell formation: a source of new concepts for understanding biomineralization processes. *Chemistry* 12, 980–987. doi: 10.1002/chem.200500980

Addadi, L., Moradian, J., Shay, E., Maroudas, N. G., and Weiner, S. (1987). A chemical model for the cooperation of sulfates and carboxylates in calcite crystal nucleation: relevance to biomineralization. *Proc. Natl. Acad. Sci. U.S.A.* 84, 2732–2736. doi: 10.1073/pnas.84.9.2732

Albeck, S., Aizenberg, J., Addadi, L., and Weiner, S. (1993). Interactions of various skeletal intracrystalline components with calcite crystals. *J. Am. Chem. Soc.* 115, 11691–11697. doi: 10.1021/ja00078a005

Andersen, B., and Rosenfeld, M. G. (2001). POU domain factors in the neuroendocrine system: lessons from developmental biology provide insights into human disease. *Endocr. Rev.* 22, 2–35. doi: 10.1210/er.22.1.2

Bahn, S. Y., Jo, B. H., Choi, Y. S., and Cha, H. J. (2017). Control of nacre biomineralization by Pif80 in pearl oyster. *Sci. Adv.* 3:e1700765. doi: 10.1126/sciadv.1700765

Baillie, B. K., and Yellowlees, D. (1998). Characterization and function of carbonic anhydrases in the zooxanthellae-giant clam symbiosis. *Proc. Biol. Sci.* 265, 465–473. doi: 10.1098/rspb.1998.0318

Bakiri, L., Takada, Y., Radolf, M., Eferl, R., Yaniv, M., Wagner, E. F., et al. (2007). Role of heterodimerization of c-Fos and Fra1 proteins in osteoclast differentiation. *Bone* 40, 867–875. doi: 10.1016/j.bone.2006.11.005

Berland, S., Marie, A., Duplat, D., Milet, C., Sire, J. Y., and Bédouet, L. (2011). Coupling proteomics and transcriptomics for the identification of novel and variant forms of mollusk shell proteins: a study with *P. margaritifera*. *Chembiochem* 12, 950–961. doi: 10.1002/cbic.201000667

Bigatti, G., Giraudbilloud, M., Vega, I. A., Penchaszadeh, P. E., and Castrovazquez, A. (2010). The calcareous egg capsule of the Patagonian neogastropod *Odontocymbiola magellanica*: morphology, secretion and mineralogy. *J. Molluscan Stud.* 76, 279–288. doi: 10.1093/mollus/eyq006

Bjärnmark, N. A., Yarra, T., Churcher, A. M., Felix, R. C., Clark, M. S., and Power, D. M. (2016). Transcriptomics provides insight into *Mytilus galloprovincialis* (Mollusca: Bivalvia) mantle function and its role in biomineralisation. *Mar. Genomics* 27, 37–45. doi: 10.1016/j.margen.2016.03.004

Blackwelder, P. L., Weiss, R. E., and Wilbur, K. M. (1976). Effects of calcium, strontium, and magnesium on the coccolithophorid *Cricosphaera (Hymenomonas) carterae*. I. Calcification. *Mar. Biol.* 34, 11–16. doi: 10.1007/BF00390781

Burgess, T. L., and Kelly, R. B. (1987). Constitutive and regulated secretion of proteins. *Annu. Rev. Cell Biol.* 3, 243–293. doi: 10.1146/annurev.cb.03.110187.001331

Calvoiglesias, J., Pérezestévez, D., Lorenzoabalde, S., Sánchezcorrea, B., Quiroga, M. I., and Fuentes, J. M. (2016). Characterization of a monoclonal antibody directed against *Mytilus spp* larvae reveals an antigen involved in shell biomineralization. *PLoS One* 11:e0152210. doi: 10.1371/journal.pone.0152210

Carter, J. (1985). Classification and phylogenetic significance of molluscan shell microstructure. *Mollusks* 13, 50–71.

Chateigner, D., Hedegaard, C., and Wenk, H.-R. (2000). Mollusc shell microstructures and crystallographic textures. *J. Struct. Geol.* 22, 1723–1735. doi: 10.1016/S0191-8141(00)00088-2

Cho, S. M., and Jeong, W. G. (2011). Prismatic shell repairs by hemoctyes in the extrapallial fluid of the Pacific Oyster, *Crassostrea gigas*. *Korean J. Malacol.* 27, 223–228. doi: 10.9710/kjm.2011.27.3.223

Cho, S. M., Lee, Y. M., and Jeong, W. G. (2011). Effect of polycyclic aromatic hydrocarbon (PAH) on shell repair in the pacific oyster, *Crassostrea gigas*. *Korean J. Malacol.* 27, 35–42. doi: 10.9710/kjm.2011.27.1.035

Conway Morris, S. (2001). "Significance of early shells," in *Palaeobiology II*, eds P. R. Crowther and D. Briggs (Oxford: Blackwell Science), 31–40. doi: 10.1002/9780470999295.ch6

Cusack, M., and Freer, A. (2008). Biomineralization: elemental and organic influence in carbonate systems. *Chem. Rev.* 108, 4433–4454. doi: 10.1021/cr078270o

Du, X., Fan, G., Jiao, Y., Zhang, H., Guo, X., Huang, R., et al. (2017). The pearl oyster *Pinctada fucata martensii* genome and multi-omic analyses provide insights into biomineralization. *Gigascience* 6, 1–12. doi: 10.1093/gigascience/gix059

Evans, J. S. (2008). "Tuning in" to mollusk shell nacre- and prismatic-associated protein terminal sequences. Implications for biomineralization and the construction of high performance inorganic-organic composites. *Chem. Rev.* 108, 4455–4462. doi: 10.1021/cr078251e

Falini, G., Albeck, S., Weiner, S., and Addadi, L. (1996). Control of aragonite or calcite polymorphism by mollusk shell macromolecules. *Science* 271, 67–69. doi: 10.1126/science.271.5245.67

Fang, D., Xu, G., Hu, Y., Pan, C., Xie, L., and Zhang, R. (2011). Identification of genes directly involved in shell formation and their functions in pearl oyster, *Pinctada fucata*. *PLoS One* 6:e21860. doi: 10.1371/journal.pone.0021860

Feng, Q., Fang, Z., Yan, Z., Xing, R., Xie, L., and Zhang, R. (2009). The structure–function relationship of MSI7, a matrix protein from pearl oyster *Pinctada fucata*. *Acta Biochim. Biophys. Sin.* 41, 955–962. doi: 10.1093/abbs/gmp086

Fleury, C., Marin, F., Marie, B., Luquet, G., Thomas, J., Josse, C., et al. (2008). Shell repair process in the green ormer *Haliotis tuberculata*: a histological and microstructural study. *Tissue Cell* 40, 207–218. doi: 10.1016/j.tice.2007.12.002

Fu, G., Valiyaveettil, S., Wopenka, B., and Morse, D. E. (2005). CaCO3 biomineralization: acidic 8-kDa proteins isolated from aragonitic abalone shell nacre can specifically modify calcite crystal morphology. *Biomacromolecules* 6, 1289–1298. doi: 10.1021/bm049314v

Furuhashi, T., Schwarzinger, C., Miksik, I., Smrz, M., and Beran, A. (2009). Molluscan shell evolution with review of shell calcification hypothesis. *Comp. Biochem. Physiol. B Biochem. Mol. Biol.* 154, 351–371. doi: 10.1016/j.cbpb.2009.07.011

Galante-Oliveira, S., Marcal, R., Guimaraes, F., Soares, J., Lopes, J. C., Machado, J., et al. (2014). Crystallinity and microchemistry of *Nassarius reticulatus* (Caenogastropoda) statoliths: towards their structure stability and homogeneity. *J. Struct. Biol.* 186, 292–301. doi: 10.1016/j.jsb.2014.03.023

Gardella, S., Andrei, C., Ferrera, D., Lotti, L. V., Torrisi, M. R., Bianchi, M. E., et al. (2002). The nuclear protein HMGB1 is secreted by monocytes via a non-classical, vesicle-mediated secretory pathway. *EMBO Rep.* 3, 995–1001. doi: 10.1093/embo-reports/kvf198

Gong, N., Ma, Z., Li, Q., Li, Q., Yan, Z., Xie, L., et al. (2008a). Characterization of calcium deposition and shell matrix protein secretion in primary mantle tissue culture from the marine pearl oyster *Pinctada fucata*. *Mar. Biotechnol.* 10, 457–465. doi: 10.1007/s10126-008-9081-1

Gong, N., Shangguan, J., Liu, X., Yan, Z., Ma, Z., Xie, L., et al. (2008b). Immunolocalization of matrix proteins in nacre lamellae and their in vivo effects on aragonitic tablet growth. *J. Struct. Biol.* 164, 33–40. doi: 10.1016/j.jsb.2008.05.009

Gotliv, B. A., Kessler, N., Sumerel, J. L., Morse, D. E., Tuross, N., Addadi, L., et al. (2005). Asprich: a novel aspartic acid-rich protein family from the prismatic shell matrix of the bivalve *Atrina rigida*. *Chembiochem* 6, 304–314. doi: 10.1002/cbic.200400221

Hare, P. E. (1963). Amino acids in the proteins from aragonite and calcite in the shells of *Mytilus californianus*. *Science* 139, 216–217. doi: 10.1126/science.139.3551.216

Hashimoto, N., Kurita, Y., and Wada, H. (2012). Developmental role of dpp in the gastropod shell plate and co-option of the dpp signaling pathway in the evolution of the operculum. *Dev. Biol.* 366, 367–373. doi: 10.1016/j.ydbio.2012.04.010

Hattan, S. J., Laue, T. M., and Chasteen, N. D. (2001). Purification and characterization of a novel calcium-binding protein from the extrapallial fluid of the mollusc, *Mytilus edulis*. *J. Biol. Chem.* 276, 4461–4468. doi: 10.1074/jbc.M006803200

Howard, B., Mitchell, P. C., Ritchie, A., Simkiss, K., and Taylor, M. (1981). The composition of intracellular granules from the metal-accumulating cells of the common garden snail (*Helix aspersa*). *Biochem. J.* 194, 507–511. doi: 10.1042/bj1940507

Huang, J., Zhang, C., Ma, Z., Xie, L., and Zhang, R. (2007). A novel extracellular EF-hand protein involved in the shell formation of pearl oyster. *Biochim. Biophys. Acta* 1770, 1037–1044. doi: 10.1016/j.bbagen.2007.03.006

Islam, T., and Peng, C. (2018). Morphological and cellular diversity of magnetotactic bacteria: a review. *J. Basic Microbiol.* 58, 378–389. doi: 10.1002/jobm.201700383

Isowa, Y., Sarashina, I., Setiamarga, D. H., and Endo, K. (2012). A comparative study of the shell matrix protein aspein in pterioid bivalves. *J. Mol. Evol.* 75, 11–18. doi: 10.1007/s00239-012-9514-3

Ivanina, A. V., Falfushynska, H. I., Beniash, E., Piontkivska, H., and Sokolova, I. M. (2017). Biomineralization-related specialization of hemocytes and mantle tissues of the Pacific oysters *Crassostrea gigas*. *J. Exp. Biol.* 220(Pt 18), 3209–3221. doi: 10.1242/jeb.160861

Jackson, A., Vincent, J., and Turner, R. (1988). The mechanical design of nacre. *Proc. R. Soc. Lond. Ser. B Biol. Sci.* 234, 415–440.

Jackson, D. J., McDougall, C., Green, K., Simpson, F., Wörheide, G., and Degnan, B. M. (2006). A rapidly evolving secretome builds and patterns a sea shell. *BMC Biol.* 4:40. doi: 10.1186/1741-7007-4-40

Jackson, D. J., Mcdougall, C., Woodcroft, B., Moase, P., Rose, R. A., Kube, M., et al. (2010). Parallel evolution of nacre building gene sets in molluscs. *Mol. Biol. Evol.* 27, 591–608. doi: 10.1093/molbev/msp278

Jing, G., Yan, C., Yi, Y., Jian, L., Xie, J., Liu, J., et al. (2016). The transcription factor Pf-POU3F4 regulates expression of the matrix protein genes Aspein and Prismalin-14 in pearl oyster (*Pinctada fucata*). *FEBS J.* 283, 1962–1978. doi: 10.1111/febs.13716

Johnstone, M. B., Ellis, S., and Mount, A. S. (2008). Visualization of shell matrix proteins in hemocytes and tissues of the Eastern oyster, *Crassostrea virginica*. *J. Exp. Zool. B Mol. Dev. Evol.* 310, 227–239. doi: 10.1002/jez.b.21206

Johnstone, M. B., Gohad, N. V., Falwell, E. P., Hansen, D. C., Hansen, K. M., and Mount, A. S. (2015). Cellular orchestrated biomineralization of crystalline composites on implant surfaces by the eastern oyster, *Crassostrea virginica* (Gmelin, 1791). *J. Exp. Mar. Biol. Ecol.* 463, 8–16. doi: 10.1016/j.jembe.2014.10.014

Joubert, C., Piquemal, D., Marie, B., Manchon, L., Pierrat, F., Zanella-Cléon, I., et al. (2010). Transcriptome and proteome analysis of *Pinctada margaritifera* calcifying mantle and shell: focus on biomineralization. *BMC Genomics* 11:613. doi: 10.1186/1471-2164-11-613

Kádár, E. (2008). Haemocyte response associated with induction of shell regeneration in the deep-sea vent mussel *Bathymodiolus azoricus* (Bivalvia: Mytilidae). *J. Exp. Mar. Biol. Ecol.* 362, 71–78. doi: 10.1016/j.jembe.2008.05.014

Kadar, E., Lobo-Da-Cunha, A., and Azevedo, C. (2009). Mantle-to-shell CaCO3 transfer during shell repair at different hydrostatic pressures in the deep-sea vent mussel *Bathymodiolus azoricus* (Bivalvia: Mytilidae). *Mar. Biol.* 156, 959–967. doi: 10.1007/s00227-009-1140-2

Kim, K., Kim, J. H., Youn, B. U., Jin, H. M., and Kim, N. (2010). Pim-1 regulates RANKL-induced osteoclastogenesis via NF-kappaB activation and NFATc1 induction. *J. Immunol.* 185, 7460–7466. doi: 10.4049/jimmunol.1000885

Kinoshita, S., Wang, N., Inoue, H., Maeyama, K., Okamoto, K., Nagai, K., et al. (2011). Deep sequencing of ESTs from nacreous and prismatic layer producing tissues and a screen for novel shell formation-related genes in the pearl oyster. *PLoS One* 6:e21238. doi: 10.1371/journal.pone.0021238

Kishore, P., and Southgate, P. C. (2015). Haemocyte persistence after grafting for pearl production in *Pinctada margaritifera* (Linnaeus, 1758). *Fish Shellfish Immunol.* 42, 530–532. doi: 10.1016/j.fsi.2014.11.035

Kocot, K. M., Aguilera, F., Mcdougall, C., Jackson, D. J., and Degnan, B. M. (2016). Sea shell diversity and rapidly evolving secretomes: insights into the evolution of biomineralization. *Front. Zool.* 13:23. doi: 10.1186/s12983-016-0155-z

Kondrachuk, A. V., and Wiederhold, M. L. (2004). On generation of statoconia in gravireceptors of mollusks. *Hear. Res.* 197, 24–34. doi: 10.1016/j.heares.2004.06.001

Kong, J., Liu, C., Yang, D., Yan, Y., Chen, Y., Huang, J., et al. (2018). Alv protein plays opposite roles in the transition of amorphous calcium carbonate to calcite and aragonite during shell formation. *Cryst. Growth Des.* 7, 3794–3804. doi: 10.1021/acs.cgd.8b00025

Kong, W., Li, S., Xiang, L., Xie, L., and Zhang, R. (2015). Calcium carbonate mineralization mediated by in vitro cultured mantle cells from *Pinctada fucata*. *Biochem. Biophys. Res. Commun.* 7, 1053–1058. doi: 10.1016/j.bbrc.2015.06.057

Kong, Y., Jing, G., Yan, Z., Li, C., Gong, N., Zhu, F., et al. (2009). Cloning and characterization of Prisilkin-39, a novel matrix protein serving a dual role in the prismatic layer formation from the oyster *Pinctada fucata*. *J. Biol. Chem.* 284, 10841–10854. doi: 10.1074/jbc.M808357200

Kono, M., Hayashi, N., and Samata, T. (2000). Molecular mechanism of the nacreous layer formation in *Pinctada maxima*. *Biochem. Biophys. Res. Commun.* 269, 213–218. doi: 10.1006/bbrc.2000.2274

Kouchinsky, A. (2000). Shell microstructures in Early Cambrian molluscs. *Acta Palaeontol. Pol.* 45, 119–150.

Kylmaoja, E., Nakamura, M., and Tuukkanen, J. (2016). Osteoclasts and remodeling based bone formation. *Curr. Stem Cell Res. Ther.* 11, 626–633. doi: 10.2174/1574888X10666151019115724

Lee, S. W., Jang, Y. N., and Kim, J. C. (2011). Characteristics of the aragonitic layer in adult oyster shells, *Crassostrea gigas*: structural study of myostracum including the adductor muscle scar. *Evid. Based Complement. Alternat. Med.* 2011:742963. doi: 10.1155/2011/742963

Leggat, W., Dixon, R., Saleh, S., and Yellowlees, D. (2005). A novel carbonic anhydrase from the giant clam *Tridacna gigas* contains two carbonic anhydrase domains. *FEBS J.* 272, 3297–3305. doi: 10.1111/j.1742-4658.2005.04742.x

Li, S., Liu, Y., Liu, C., Huang, J., Zheng, G., Xie, L., et al. (2016). Hemocytes participate in calcium carbonate crystal formation, transportation and shell regeneration in the pearl oyster *Pinctada fucata*. *Fish Shellfish Immunol.* 51, 263–270. doi: 10.1016/j.fsi.2016.02.027

Liang, J., Xu, G., Xie, J., Lee, I., Liang, X., Wang, H., et al. (2015). Dual roles of the lysine-rich matrix protein (KRMP)-3 in shell formation of pearl oyster, *Pinctada fucata*. *PLoS One* 10:e0131868. doi: 10.1371/journal.pone.0131868

Liao, Z., Bao, L., Fan, M., Gao, P., Wang, X., Qin, C., et al. (2015). In-depth proteomic analysis of nacre, prism, and myostracum of Mytilus shell. *J. Proteomics* 122, 26–40. doi: 10.1016/j.jprot.2015.03.027

Liu, H., Liu, S., Ge, Y., Liu, J., Wang, X., Xie, L., et al. (2007). Identification and characterization of a biomineralization related gene PFMG1 highly expressed in the mantle of *Pinctada fucata*. *Biochemistry* 46, 844–851. doi: 10.1021/bi061881a

Lodi, M., and Koene, J. M. (2016). The love-darts of land snails: integrating physiology, morphology and behaviour. *J. Molluscan Stud.* 82:eyv046.

Lowenstam, H. A., and Weiner, S. (1989). *On Biomineralization*. New York, NY: Oxford University Press.

Ma, Z., Huang, J., Sun, J., Wang, G., Li, C., Xie, L., et al. (2007). A novel extrapallial fluid protein controls the morphology of nacre lamellae in the pearl oyster, *Pinctada fucata*. *J. Biol. Chem.* 282, 23253–23263. doi: 10.1074/jbc.M700001200

Mann, K., Siedler, F., Treccani, L., Heinemann, F., and Fritz, M. (2007). Perlinhibin, a cysteine-, histidine-, and arginine-rich miniprotein from abalone (*Haliotis laevigata*) nacre, inhibits in vitro calcium carbonate crystallization. *Biophys. J.* 93, 1246–1254. doi: 10.1529/biophysj.106.100636

Mann, K., Weiss, I. M., André, S., Gabius, H. J., and Fritz, M. (2000). The amino-acid sequence of the abalone (*Haliotis laevigata*) nacre protein perlucin. Detection of a functional C-type lectin domain with galactose/mannose specificity. *Eur. J. Biochem.* 267, 5257–5264. doi: 10.1046/j.1432-1327.2000.01602.x

Mann, K., Edsinger-Gonzales, E., and Mann, M. (2012). In-depth proteomic analysis of a mollusc shell: acid-soluble and acid-insoluble matrix of the limpet *Lottia gigantea*. *Proteome Sci.* 10:28. doi: 10.1186/1477-5956-10-28

Marie, B., Arivalagan, J., Dubost, L., Berland, S., Marie, A., and Marin, F. D. R. (2015). Unveiling the evolution of bivalve nacre proteins by shell proteomics of unionoidae. *Key Eng. Mater.* 672, 158–167. doi: 10.4028/www.scientific.net/KEM.672.158

Marie, B., Arivalagan, J., Mathéron, L., Bolbach, G., Berland, S., Marie, A., et al. (2017). Deep conservation of bivalve nacre proteins highlighted by shell matrix proteomics of the Unionoida *Elliptio complanata* and *Villosa lienosa*. *J. R. Soc. Interface* 14:20160846. doi: 10.1098/rsif.2016.0846

Marie, B., Jackson, D. J., Ramossilva, P., Zanellacléon, I., Guichard, N., and Marin, F. (2013). The shell-forming proteome of *Lottia gigantea* reveals both deep conservations and lineage-specific novelties. *FEBS J.* 280, 214–232. doi: 10.1111/febs.12062

Marie, B., Joubert, C., Tayalé, A., Zanella-Cléon, I., Belliard, C., Piquemal, D., et al. (2012). Different secretory repertoires control the biomineralization processes of prism and nacre deposition of the pearl oyster shell. *Proc. Natl. Acad. Sci. U.S.A.* 109, 20986–20991. doi: 10.1073/pnas.1210552109

Marie, B., Marie, A., Jackson, D. J., Dubost, L., Degnan, B. M., Milet, C., et al. (2010). Proteomic analysis of the organic matrix of the abalone *Haliotis asinina* calcified shell. *Proteome Sci.* 8:54. doi: 10.1186/1477-5956-8-54

Marin, F., Corstjens, P., De Gaulejac, B., de Vrind-De Jong, E., and Westbroek, P. (2000). Mucins and molluscan calcification Molecular characterization of mucoperlin, a novel mucin-like protein from the nacreous shell layer of the fan mussel *Pinna nobilis* (Bivalvia, Pteriomorphia). *J. Biol. Chem.* 275, 20667–20675. doi: 10.1074/jbc.M003006200

Marin, F., Le Roy, N., and Marie, B. (2012). The formation and mineralization of mollusk shell. *Front. Biosci.* 4, 1099–1125. doi: 10.2741/s321

Marin, F., Luquet, G., Marie, B., and Medakovic, D. (2008). Molluscan shell proteins: primary structure, origin, and evolution. *Curr. Top. Dev. Biol.* 80, 209–276. doi: 10.1016/S0070-2153(07)80006-8

Marin, F., Pokroy, B., Luquet, G., Layrolle, P., and Groot, K. D. (2007). Protein mapping of calcium carbonate biominerals by immunogold. *Biomaterials* 28, 2368–2377. doi: 10.1016/j.biomaterials.2007.01.029

Marxen, J. C., Nimtz, M., Becker, W., and Mann, K. (2003). The major soluble 19.6 kDa protein of the organic shell matrix of the freshwater snail *Biomphalaria glabrata* is an N-glycosylated dermatopontin. *Biochim. Biophys. Acta* 1650, 92–98. doi: 10.1016/S1570-9639(03)00203-6

Masaoka, T., and Kobayashi, T. (2009). Analysis of nucleotide variation and inheritance of lysine-rich matrix protein (KRMP) genes participating in shell formation of pearl oyster. *DNA Polymorphism* 17, 126–135.

Mcdougall, C., Aguilera, F., and Degnan, B. M. (2013). Rapid evolution of pearl oyster shell matrix proteins with repetitive, low-complexity domains. *J. R. Soc. Interface* 10:20130041. doi: 10.1098/rsif.2013.0041

Michenfelder, M., Fu, G., Lawrence, C., Weaver, J. C., Wustman, B. A., Taranto, L., et al. (2003). Characterization of two molluscan crystal-modulating biomineralization proteins and identification of putative mineral binding domains. *Biopolymers* 70, 522–533. doi: 10.1002/bip.10536

Miyamoto, H., Endo, H., Hashimoto, N., Limura, K., Isowa, Y., Kinoshita, S., et al. (2013). The diversity of shell matrix proteins: genome-wide investigation of the pearl oyster, *Pinctada fucata*. *Zoolog. Sci.* 30, 801–816. doi: 10.2108/zsj.30.801

Miyamoto, H., Miyashita, T., Okushima, M., Nakano, S., Morita, T., and Matsushiro, A. (1996). A carbonic anhydrase from the nacreous layer in oyster pearls. *Proc. Natl. Acad. Sci. U.S.A.* 93, 9657–9660. doi: 10.1073/pnas.93.18.9657

Miyamoto, H., Miyoshi, F., and Kohno, J. (2005). The carbonic anhydrase domain protein nacrein is expressed in the epithelial cells of the mantle and acts as a negative regulator in calcification in the mollusc *Pinctada fucata*. *Zoolog. Sci.* 22, 311–315. doi: 10.2108/zsj.22.311

Miyamoto, H., Yano, M., and Miyashita, T. (2003). Similarities in the structure of nacrein, the shell-matrix protein, in a bivalve and a gastropod. *J. Molluscan Stud.* 69, 87–89. doi: 10.1093/mollus/69.1.87

Miyashita, T., Takagi, R., Miyamoto, H., and Matsushiro, A. (2002). Identical carbonic anhydrase contributes to nacreous or prismatic layer formation in *Pinctada fucata* (Mollusca: Bivalvia). *Veliger* 45, 250–255.

Miyashita, T., Takagi, R., Okushima, M., Nakano, S., Miyamoto, H., Nishikawa, E., et al. (2000). Complementary DNA cloning and characterization of pearlin, a new class of matrix protein in the nacreous layer of oyster pearls. *Mar. Biotechnol.* 2, 409–418.

Miyashita, T., Takami, A., and Takagi, R. (2012). Molecular cloning and characterization of the 5′-flanking regulatory region of the carbonic anhydrase nacrein gene of the pearl oyster *Pinctada fucata* and its expression. *Biochem. Genet.* 50, 673–683. doi: 10.1007/s10528-012-9510-8

Miyazaki, Y., Nishida, T., Aoki, H., and Samata, T. (2010). Expression of genes responsible for biomineralization of *Pinctada fucata* during development. *Comp. Biochem. Physiol. B Biochem. Mol. Biol.* 155, 241–248. doi: 10.1016/j.cbpb.2009.11.009

Morse, J. W., Arvidson, R. S., and Lüttge, A. (2007). Calcium carbonate formation and dissolution. *Chem. Rev.* 107, 342–381. doi: 10.1021/cr050358j

Mount, A., and Pickering, C. M. (2009). Testing the capacity of clothing to act as a vector for non-native seed in protected areas. *J. Environ. Manage.* 91, 168–179. doi: 10.1016/j.jenvman.2009.08.002

Mount, A. S., Wheeler, A., Paradkar, R. P., and Snider, D. (2004). Hemocyte-mediated shell mineralization in the eastern oyster. *Science* 304, 297–300. doi: 10.1126/science.1090506

Nam, B. H., Kwak, W., Kim, Y. O., Kim, D. G., Kong, H. J., Kim, W. J., et al. (2017). Genome sequence of pacific abalone (*Haliotis discus hannai*): the first draft genome in family Haliotidae. *Gigascience* 6, 1–8. doi: 10.1093/gigascience/gix014

Norizuki, M., and Samata, T. (2008). Distribution and function of the nacrein-related proteins inferred from structural analysis. *Mar. Biotechnol.* 10, 234–241. doi: 10.1007/s10126-007-9061-x

Nudelman, F., Gotliv, B. A., Addadi, L., and Weiner, S. (2006). Mollusk shell formation: mapping the distribution of organic matrix components underlying a single aragonitic tablet in nacre. *J. Struct. Biol.* 153, 176–187. doi: 10.1016/j.jsb.2005.09.009

Pan, C., Fang, D., Xu, G., Liang, J., Zhang, G., Wang, H., et al. (2014). A novel acidic matrix protein, PfN44, stabilizes magnesium calcite to inhibit the crystallization of aragonite. *J. Biol. Chem.* 289, 2776–2787. doi: 10.1074/jbc.M113.504027

Politi, Y., Mahamid, J., Goldberg, H., Weiner, S., and Addadi, L. (2007). Asprich mollusk shell protein: in vitro experiments aimed at elucidating function in CaCO3 crystallization. *Crystengcomm* 9, 1171–1177. doi: 10.1039/b709749b

Rahman, M. A., and Shinjo, R. (2012). "Control of CaCO3 crystal growth by the acidic proteinaceous fraction of calcifying marine organisms: an in vitro study of biomineralization," in *Advanced Topics in Biomineralization*, ed. J. Seto (London: InTech).

Saadi, I., Das, P., Zhao, M., Raj, L., Ruspita, I., Xia, Y., et al. (2013). Msx1 and Tbx2 antagonistically regulate Bmp4 expression during the bud-to-cap stage transition in tooth development. *Development* 140, 2697–2702. doi: 10.1242/dev.088393

Saha, A., Jana, T., and Choudhury, A. (1988). The extrapallial fluid of *Macoma birmanica*: an environment for calcium carbonate deposition. *Philipp. J. Crop Sci.* 117, 395–399.

Samata, T., Hayashi, N., Kono, M., Hasegawa, K., Horita, C., and Akera, S. (1999). A new matrix protein family related to the nacreous layer formation of *Pinctada fucata*. *FEBS Lett.* 462, 225–229. doi: 10.1016/S0014-5793(99)01387-3

Sarashina, I., and Endo, K. (1998). Primary structure of a soluble matrix protein of scallop shell: implications for calcium carbonate biomineralization. *Am. Mineral.* 83, 1510–1515. doi: 10.2138/am-1998-11-1239

Saruwatari, K., Matsui, T., Mukai, H., Nagasawa, H., and Kogure, T. (2009). Nucleation and growth of aragonite crystals at the growth front of nacres in pearl oyster, *Pinctada fucata*. *Biomaterials* 30, 3028–3034. doi: 10.1016/j.biomaterials.2009.03.011

Shen, X., Belcher, A. M., Hansma, P. K., Stucky, G. D., and Morse, D. E. (1997). Molecular cloning and characterization of lustrin A, a matrix protein from shell and pearl nacre of *Haliotis rufescens*. *J. Biol. Chem.* 272, 32472–32481. doi: 10.1074/jbc.272.51.32472

Shi, M., Lin, Y., Xu, G., Xie, L., Hu, X., Bao, Z., et al. (2013). Characterization of the zhikong scallop (*Chlamys farreri*) mantle transcriptome and identification of biomineralization-related genes. *Mar. Biotechnol.* 15, 706–715. doi: 10.1007/s10126-013-9517-0

Shitalbahen, V. P. (2004). *A Novel Function of Invertebrate Collagen in the Biomineralization Process During the Shell Repair of Eastern Oyster, Crassostrea virginica*. Clemson, SC: Clemson University.

Sikes, C. S., Wheeler, A. P., Wierzbicki, A., Mount, A. S., and Dillaman, R. M. (2000). Nucleation and growth of calcite on native versus pyrolyzed oyster shell folia. *Biol. Bull.* 198, 50–66. doi: 10.2307/1542803

Simkiss, K., and Wilbur, K. M. (1989). *Biomineralization: Cell Biology and Mineral Deposition*. San Diego, CA: Academic Press.

Sleight, V. A., Thorne, M. A., Peck, L. S., and Clark, M. S. (2015). Transcriptomic response to shell damage in the Antarctic clam, *Laternula elliptica*: time scales and spatial localisation. *Mar. Genomics* 20, 45–55. doi: 10.1016/j.margen.2015.01.009

Smith-Keune, C., and Jerry, D. R. (2009). High levels of intra-specific variation in the NG repeat region of the *Pinctada maxima* N66 organic matrix protein. *Aquac. Res.* 40, 1054–1063. doi: 10.1111/j.1365-2109.2009.02199.x

Song, X., Wang, X., Li, L., and Zhang, G. (2014). Identification two novel nacrein-like proteins involved in the shell formation of the Pacific oyster *Crassostrea gigas*. *Mol. Biol. Rep.* 41, 4273–4278. doi: 10.1007/s11033-014-3298-z

Song, X., Wang, X., Li, L., and Zhang, G. (2015). Molecular cloning and characterization of nacrein gene in Pacific oyster (*Crassostrea gigas*). *Mar. Sci.* 39:9.

Stenzel, H. (1963). Aragonite and calcite as constituents of adult oyster shells. *Science* 142, 232–233. doi: 10.1126/science.142.3589.232

Su, J., Liang, X., Zhou, Q., Zhang, G., Wang, H., Xie, L., et al. (2013). Structural characterization of amorphous calcium carbonate-binding protein: an insight into the mechanism of amorphous calcium carbonate formation. *Biochem. J.* 453, 179–186. doi: 10.1042/BJ20130285

Sudo, S., Fujikawa, T., Nagakura, T., Ohkubo, T., Sakaguchi, K., Tanaka, M., et al. (1997). Structures of mollusc shell framework proteins. *Nature* 387, 563–564. doi: 10.1038/42391

Sun, J., Xu, G., Wang, Z., Li, Q., Cui, Y., Xie, L., et al. (2015). The effect of NF-kappaB signalling pathway on expression and regulation of nacrein in pearl oyster, *Pinctada fucata*. *PLoS One* 10:e0131711. doi: 10.1371/journal.pone.0131711

Suzuki, M., Iwashima, A., Kimura, M., Kogure, T., and Nagasawa, H. (2013). The molecular evolution of the Pif family proteins in various species of mollusks. *Mar. Biotechnol.* 15, 145–158. doi: 10.1007/s10126-012-9471-2

Suzuki, M., Iwashima, A., Tsutsui, N., Ohira, T., Kogure, T., and Nagasawa, H. (2011). Identification and characterisation of a calcium carbonate-binding protein, blue mussel shell protein (BMSP), from the nacreous layer. *Chembiochem* 12, 2478–2487. doi: 10.1002/cbic.201100317

Suzuki, M., Murayama, E., Inoue, H., Ozaki, N., Tohse, H., Kogure, T., et al. (2004). Characterization of Prismalin-14, a novel matrix protein from the prismatic layer of the Japanese pearl oyster (*Pinctada fucata*). *Biochem. J.* 382(Pt 1), 205–213. doi: 10.1042/BJ20040319

Suzuki, M., and Nagasawa, H. (2007). The structure-function relationship analysis of Prismalin-14 from the prismatic layer of the Japanese pearl oyster, *Pinctada fucata*. *FEBS J.* 274, 5158–5166. doi: 10.1111/j.1742-4658.2007.06036.x

Suzuki, M., Saruwatari, K., Kogure, T., Yamamoto, Y., Nishimura, T., Kato, T., et al. (2009). An acidic matrix protein, Pif, is a key macromolecule for nacre formation. *Science* 325, 1388–1390. doi: 10.1126/science.1173793

Takeuchi, T., Koyanagi, R., Gyoja, F., Kanda, M., Hisata, K., Fujie, M., et al. (2016). Bivalve-specific gene expansion in the pearl oyster genome: implications of adaptation to a sessile lifestyle. *Zoological Lett.* 2:3. doi: 10.1186/s40851-016-0039-2

Takeuchi, T., Sarashina, I., Iijima, M., and Endo, K. (2008). In vitro regulation of CaCO3 crystal polymorphism by the highly acidic molluscan shell protein Aspein. *FEBS Lett.* 582, 591–596. doi: 10.1016/j.febslet.2008.01.026

Tang, R., Wang, X., Liu, X., Xiao, Y., Hao, H., and Zhang, Y. (2018). Biomineralization state of viruses and their biological potentials. *Chemistry* 24, 11518–11529. doi: 10.1002/chem.201705936

Todt, C., and Wanninger, A. (2010). Of tests, trochs, shells, and spicules: development of the basal mollusk *Wirenia argentea* (Solenogastres) and its bearing on the evolution of trochozoan larval key features. *Front. Zool.* 7:6. doi: 10.1186/1742-9994-7-6

Tokuyama, A. (1969). Effects of organic matter on solubilities and crystal form of carbonates. *Am. Zool.* 9, 681–688. doi: 10.1093/icb/9.3.681

Treccani, L., Mann, K., Heinemann, F., and Fritz, M. (2006). Perlwapin, an abalone nacre protein with three four-disulfide core (Whey Acidic Protein) domains, inhibits the growth of calcium carbonate crystals. *Biophys. J.* 91, 2601–2608. doi: 10.1529/biophysj.106.086108

Trinkler, N., Bardeau, J. F., Marin, F., Labonne, M., Jolivet, A., Crassous, P., et al. (2011). Mineral phase in shell repair of Manila clam *Venerupis philippinarum* affected by brown ring disease. *Dis. Aquat. Organ.* 93, 149–162. doi: 10.3354/dao02288

Tsukamoto, D., Sarashina, I., and Endo, K. (2004). Structure and expression of an unusually acidic matrix protein of pearl oyster shells. *Biochem. Biophys. Res. Commun.* 320, 1175–1180. doi: 10.1016/j.bbrc.2004.06.072

Wang, S., Zhang, J., Jiao, W., Li, J., Xun, X., Sun, Y., et al. (2017). Scallop genome provides insights into evolution of bilaterian karyotype and development. *Nat. Ecol. Evol.* 1:0120.

Wang, X., Li, L., Zhu, Y., Du, Y., Song, X., Chen, Y., et al. (2013a). Oyster shell proteins originate from multiple organs and their probable transport pathway to the shell formation front. *PLoS One* 8:e66522. doi: 10.1371/journal.pone.0066522

Wang, X., Song, X., Wang, T., Zhu, Q., Miao, G., Chen, Y., et al. (2013b). Evolution and functional analysis of the Pif97 gene of the Pacific oyster *Crassostrea gigas*. *Curr. Zool.* 59, 109–115. doi: 10.1093/czoolo/59.1.109

Wang, Y., Xia, J., Tang, R., et al. (2011). Cloning and characterization of nacre-related genes in silver-lip pearl oyster *Pinctada maxima*. *J. Shanghai Ocean Univ*. 1:003.

Watabe, N. (1965). Studies on shell formation. XI. Crystal-matrix relationships in the mollusk shells. *J. Ultrastruct. Res.* 12, 351–370. doi: 10.1016/S0022-5320(65)80104-6

Weiner, S., and Addadi, L. (2011). Crystallization pathways in biomineralization. *Cells Tissues Organs* 41, 21–40.

Weiss, I. M., Göhring, W., Fritz, M., and Mann, K. (2001). Perlustrin, a *Haliotis laevigata* (Abalone) nacre protein, is homologous to the insulin-like growth factor binding protein N-terminal module of vertebrates. *Biochem. Biophys. Res. Commun.* 285, 244–249. doi: 10.1006/bbrc.2001.5170

Weiss, I. M., Kaufmann, S., Mann, K., and Fritz, M. (2000). Purification and characterization of perlucin and perlustrin, two new proteins from the shell of the mollusc *Haliotis laevigata*. *Biochem. Biophys. Res. Commun.* 267, 17–21. doi: 10.1006/bbrc.1999.1907

Werner, G. D., Gemmell, P., Grosser, S., Hamer, R., and Shimeld, S. M. (2013). Analysis of a deep transcriptome from the mantle tissue of *Patella vulgata* Linnaeus (Mollusca: Gastropoda: Patellidae) reveals candidate biomineralising genes. *Mar. Biotechnol.* 15, 230–243. doi: 10.1007/s10126-012-9481-0

Wilbur, K., and Saleuddin, A. (1983). Shell formation. *Mollusca* 4, 235–287. doi: 10.1016/B978-0-12-751404-8.50014-1

Wilbur, K. M., and Bernhardt, A. M. (1984). Effects of amino acids, magnesium, and molluscan extrapallial fluid on crystallization of calcium carbonate: in vitro experiments. *Biol. Bull.* 166, 251–259. doi: 10.2307/1541446

Wilt, F. H. (2002). Biomineralization of the spicules of sea urchin embryos. *Zoolog. Sci.* 19, 253–261. doi: 10.2108/zsj.19.253

Xiang, L., Kong, W., Su, J. T., Liang, J., Zhang, G. Y., Xie, L. P., et al. (2014). Amorphous calcium carbonate precipitation by cellular biomineralization in mantle cell cultures of *Pinctada fucata*. *PLoS One* 9:e113150. doi: 10.1371/journal.pone.0113150

Xie, J. (2016). *The Mechanism Study of Extrapallial Fluid Protein in the Shell Formation of Pinctada fucata*. Beijing Shi: Tsinghua University.

Xie, J., Liang, J., Sun, J., Gao, J., Zhang, S., Liu, Y., et al. (2016). Influence of the extrapallial fluid of *Pinctada fucata* on the crystallization of calcium carbonate and shell biomineralization. *Cryst. Growth Des.* 16, 672–680. doi: 10.1021/acs.cgd.5b01203

Yan, Z., Jing, G., Gong, N., Li, C., Zhou, Y., Xie, L., et al. (2007). N40, a novel nonacidic matrix protein from pearl oyster nacre, facilitates nucleation of aragonite in vitro. *Biomacromolecules* 8, 3597–3601. doi: 10.1021/bm0701494

Yano, M., Nagai, K., Morimoto, K., and Miyamoto, H. (2006). Shematrin: a family of glycine-rich structural proteins in the shell of the pearl oyster *Pinctada fucata*. *Comp. Biochem. Physiol. B Biochem. Mol. Biol.* 144, 254–262. doi: 10.1016/j.cbpb.2006.03.004

Yano, M., Nagai, K., Morimoto, K., and Miyamoto, H. (2007). A novel nacre protein N19 in the pearl oyster *Pinctada fucata*. *Biochem. Biophys. Res. Commun.* 362, 158–163. doi: 10.1016/j.bbrc.2007.07.172

Yi, Y., Dong, Y., Xue, Y., Liu, C., Xie, J., Zheng, G., et al. (2017). A novel matrix protein, PfY2, functions as a crucial macromolecule during shell formation. *Sci. Rep.* 7:6021. doi: 10.1038/s41598-017-06375-w

Yin, H., Ji, B., Dobson, P. S., Mosbahi, K., Glidle, A., Gadegaard, N., et al. (2009). Screening of biomineralization using microfluidics. *Anal. Chem.* 81, 473–478. doi: 10.1021/ac801980b

Yin, Y., Huang, J., Paine, M. L., Reinhold, V. N., and Chasteen, N. D. (2005). Structural characterization of the major extrapallial fluid protein of the mollusc *Mytilus edulis*: implications for function. *Biochemistry* 44, 10720–10731. doi: 10.1021/bi0505565

Yu, Z., Xie, L., Lee, S., and Zhang, R. (2006). A novel carbonic anhydrase from the mantle of the pearl oyster (*Pinctada fucata*). *Comp. Biochem. Physiol. B Biochem. Mol. Biol.* 143, 190–194. doi: 10.1016/j.cbpb.2005.11.006

Zhang, C., Li, S., Ma, Z., Xie, L., and Zhang, R. (2006a). A novel matrix protein p10 from the nacre of pearl oyster (*Pinctada fucata*) and its effects on both CaCO3 crystal formation and mineralogenic cells. *Mar. Biotechnol.* 8, 624–633. doi: 10.1007/s10126-006-6037-1

Zhang, C., Xie, L., Huang, J., Liu, X., and Zhang, R. (2006b). A novel matrix protein family participating in the prismatic layer framework formation of pearl oyster, *Pinctada fucata*. *Biochem. Biophys. Res. Commun.* 344, 735–740. doi: 10.1016/j.bbrc.2006.03.179

Zhang, C., and Zhang, R. (2006). Matrix proteins in the outer shells of molluscs. *Mar. Biotechnol.* 8, 572–586. doi: 10.1007/s10126-005-6029-6

Zhang, G., Fang, X., Guo, X., Li, L., Luo, R., Xu, F., et al. (2012). The oyster genome reveals stress adaptation and complexity of shell formation. *Nature* 490, 49–54. doi: 10.1038/nature11413

Zhang, Y., Xie, L., Meng, Q., Jiang, T., Pu, R., Chen, L., et al. (2003). A novel matrix protein participating in the nacre framework formation of pearl oyster, *Pinctada fucata*. *Comp. Biochem. Physiol. B Biochem. Mol. Biol.* 135, 565–573. doi: 10.1016/S1096-4959(03)00138-6

Zhao, M., He, M., Huang, X., and Wang, Q. (2014). A homeodomain transcription factor gene, PfMSX, activates expression of Pif gene in the pearl oyster *Pinctada fucata*. *PLoS One* 9:e103830. doi: 10.1371/journal.pone.0103830

Zheng, X., Cheng, M., Xiang, L., Liang, J., Xie, L., and Zhang, R. (2015). The AP-1 transcription factor homolog Pf-AP-1 activates transcription of multiple biomineral proteins and potentially participates in *Pinctada fucata* biomineralization. *Sci. Rep.* 5:14408. doi: 10.1038/srep14408

Conflict of Interest Statement: The authors declare that the research was conducted in the absence of any commercial or financial relationships that could be construed as a potential conflict of interest.

frontiers in Marine Science

ORIGINAL RESEARCH
published: 02 July 2019
doi: 10.3389/fmars.2019.00366

Folian-cv1 Is a Member of a Highly Acidic Phosphoprotein Class Derived From the Foliated Layer of the Eastern Oyster (*Crassostrea virginica*) Shell and Identified in Hemocytes and Mantle

Mary Beth Johnstone[1]†, A. P. Wheeler[1], Elizabeth P. Falwell[1†], Meg E. Staton[2], Christopher A. Saski[3] and Andrew S. Mount[1]**

[1] Department of Biological Sciences, Clemson University, Clemson, SC, United States, [2] Department of Entomology and Plant Pathology, The University of Tennessee, Knoxville, Knoxville, TN, United States, [3] Department of Plant and Environmental Sciences, Clemson University, Clemson, SC, United States

The proteins derived from the foliated shell layer of the oyster, *Crassostrea virginica*, are unusually acidic and highly phosphorylated. Here we report the identification of a gene encoding a member of this class of phosphoproteins that we collectively refer to as folian. Using an *in silico* approach, a virtual probe was constructed from an N-terminal sequence (DEADAGD) determined for a 48 kDa folian phosphoprotein and used to screen an oyster EST databank. A sequence that matched the N-terminus of the 48 kDa protein was found and used to identify the full-length gene from a *C. virginica* BAC library. The molecular weight of the deduced gene product is 32 kDa and was named folian-cv1. Genomic Southern analysis revealed two variants of the gene. The mature protein is composed of 43.3% Asp, 32.6% Ser, and 9.1% Glu with 37.5% of the amino acids of the protein potentially phosphorylated. The primary sequence of folian-cv1 is organized in blocks, with a short relatively hydrophobic block at the N-terminus and with the remainder containing low complexity regions largely dominated by aspartic acid and serine. Overall, the protein is predicted to be highly disordered. PCR and sequence analyses identified folian-cv1 expression in the mantle and hemocytes. Immuno-histochemical staining of mantle tissue reveals that cells of the shell-facing epithelium and in the periostracal groove secrete a continuous layer of folian-positive material and that folian-positive hemocytes move through the mantle epithelium. The function in shell formation of folian proteins including folian-cv1 is not known. However, based on the complexity of this class of proteins and the two methods of their delivery to the region of shell formation, it is possible they are involved in diverse ways in this process.

Keywords: oyster, *Crassostrea*, shell formation, matrix phosphoproteins, hemocytes, mantle, shell protein evolution

OPEN ACCESS

Edited by:
Pei-Yuan Qian,
The Hong Kong University of Science and Technology, Hong Kong

Reviewed by:
Yang Zhang,
South China Sea Institute of Oceanology (CAS), China
Vengatesen Thiyagarajan (Rajan),
The University of Hong Kong, Hong Kong

****Correspondence:***
Mary Beth Johnstone
mbj@clemson.edu
Andrew S. Mount
mount@clemson.edu

†Present address:
Mary Beth Johnstone, Department of Genetics and Biochemistry, Clemson University, Clemson, SC, United States
Elizabeth P. Falwell, Academic Analytics, LLC, Charlotte, NC, United States

Specialty section:
This article was submitted to Marine Molecular Biology and Ecology, a section of the journal Frontiers in Marine Science

Received: *11 February 2019*
Accepted: *13 June 2019*
Published: *02 July 2019*

Citation:
Johnstone MB, Wheeler AP, Falwell EP, Staton ME, Saski CA and Mount AS (2019) Folian-cv1 Is a Member of a Highly Acidic Phosphoprotein Class Derived From the Foliated Layer of the Eastern Oyster (Crassostrea virginica) Shell and Identified in Hemocytes and Mantle. Front. Mar. Sci. 6:366. doi: 10.3389/fmars.2019.00366

INTRODUCTION

Molluscan shell is composed of layers of nano- to micro-scaled calcium carbonate crystals embedded in an organic extracellular matrix. This composite structure is responsible for the exceptional toughness of the shell to fracture (Currey, 1999). Broadly speaking the matrix is composed of a variety of macromolecules, including predominately protein, as well as carbohydrates, such as chitin. Among the former are a class of uniquely acidic (anionic at physiological pH) proteins (Weiner and Dove, 2003; Marin et al., 2008). Beyond their role in enhancing the mechanical properties of shell, it has been proposed often that these proteins play a role in controlling the nucleation as well as the microstructure and mineralogy of the mineral phase (Lowenstam, 1981; Addadi and Weiner, 1985, 1989, 2014; Mann, 1988; Wheeler and Sikes, 1989). As evidence of crystal growth control, the microstructures of shell layers are diverse and differ from inorganically grown crystals but generally are conserved within closely related taxonomic groups (Carter, 1980; Carter and Clark, 1985; Lowenstam and Weiner, 1989). For example, the principal shell layer of the Eastern oyster, *Crassostrea virginica*, is foliated calcite, which is generally prominent among true oysters (Ostreidae) as well as related groups normally included in the order Ostreoida, such as scallops (Checa et al., 2007; Esteban-Delgado et al., 2008).

Most of the studies directed at understanding matrix function have been performed on isolated preparations *in vitro* or through traditional microscopial techniques. However, more recent studies of matrix gene expression in mineral forming tissues (Zhang et al., 2012; Hüning et al., 2016; Ivanina et al., 2017; Jackson et al., 2017), as well as those using cryo-microscopic techniques (Nudelman et al., 2008) and knockdown studies (Suzuki et al., 2009), among others, show promise in refining our understanding of matrix function. Despite this recent progress, clarity as to the function of individual matrix proteins is still in the formative stages of development.

For some time, several of the authors have analyzed the function, biochemistry and cytology of the extracellular matrix from the inner foliated shell layer of *C. virginica* (e.g., Wheeler et al., 1987, 1988, 1991; Rusenko et al., 1991; Wheeler, 1992b; Sikes et al., 1998; Mount, 1999; Myers et al., 2007; Johnstone et al., 2008, 2015). These studies showed that the oyster foliated matrix is dominated by highly phosphorylated proteins which are also enriched in aspartic acid, a composition that makes them highly acidic. The oyster phosphoproteins are enigmatic in that extracts from dissolved shell yield soluble forms with a wide range of molecular weight as well as gel-forming insoluble forms, all having similar amino acid compositions. We refer to this family of proteins collectively as folian. Some of these earlier studies also revealed the capacity of the folian proteins to bind to crystals and thereby inhibit and regulate crystal growth *in vitro* and provided evidence for crystal-matrix interactions *in situ*. Based on oyster protein structure and activity, synthetic proteins have been produced for use as anti-scalants, dispersants, superabsorbents and many other possible applications (e.g., Wheeler and Koskan, 1993; Sikes and Wierzbicki, 1995). Outside of *C. virginica*, there appears to be a correlation between the foliated microstructure and the presence of highly phosphorylated matrix proteins (Borbas et al., 1991; Sarashina and Endo, 2001; Samata et al., 2008). However, no causal relationship between this highly phosphorylated matrix and the formation of the foliated microstructure has been established. One of the limitations to understanding oyster matrix function is that previous studies were performed using preparations of varying degrees of heterogeneity. In fact, to date no individual folian protein from *C. virginica* has been fully characterized for functional assessment. Accordingly, in this study, using an *in silico* approach, we report the complete sequence of one gene from this class which we have named folian-cv1.

Traditionally, it has been assumed that most or all components necessary for mineralization are secreted by the mantle into the extrapallial space (Lowenstam and Weiner, 1989; Simkiss and Wilbur, 1989; Wheeler, 1992a). In fact, immuno-cytochemical studies have demonstrated secretion of matrix proteins by the mantle of *C. virginica* (Kawaguchi and Watabe, 1993; Myers et al., 2007; Johnstone et al., 2008) and their inclusion in mineralized layers during shell formation (Kawaguchi and Watabe, 1993). A special class of cells in the outer mantle epithelium has been identified as the likely candidate for secretion of folian proteins (Myers et al., 2007). More recently, hemocytes have also been implicated in shell formation or regeneration (Mount et al., 2004; Kádár, 2008; Li et al., 2016; Ivanina et al., 2017; Huang et al., 2018). In addition, they have been shown to form mineral *ex vivo* on surfaces, a process which has potential anti-fouling, protective coating and cellular adhesive applications (Mount et al., 2016). In the oyster, hemocytes are immuno-positive for folian proteins (Johnstone et al., 2008) and a class of these cells which contain calcium carbonate crystals has been demonstrated in association with regenerating shell (Mount et al., 2004) or shell formed on implants (Johnstone et al., 2015). In this study, immuno-histochemical staining of mantle tissue confirms the secretion of folian from mantle cells and the movement of folian-positive hemocytes through the mantle epithelium toward the sites of mineralization. The expression of folian-cv1 by mantle and hemocytes was confirmed by PCR. It therefore can be deduced that folian-cv1 is directly active in shell formation. However, because folian proteins are diverse and produced not only by both mantle and hemocytes but other tissues in the oyster as well (Johnstone et al., 2008), it is possible that folian, and by extension folian-cv1, may have multiple and, in some cases, indirect roles in mineralization, such serving as a part of the scaffolding for cell attachment (Chan et al., 2018), and possibly function in other processes as well.

MATERIALS AND METHODS

Shell Protein Extraction and Purification

Shells from live specimens of the Eastern oyster, *Crassostrea virginica*, were collected from Sixty Bass Creek of North Inlet estuary, Georgetown, SC, United States. The shell proteins were extracted following protocols described in Wheeler et al. (1988) and Johnstone et al. (2008). Specifically, the shells were scrubbed under tap water and the outer shell layers, including the periostracum and the underlying prismatic layer, were removed with a sanding tool. Shell pieces composed of foliated mineral,

free of myostracum and conchiolin patches, were selected and ground into powder. Protein was extracted from the $CaCO_3$ phase by dissolving 25 g of the ground foliated shell in 750 ml of 17% ethylenediamine tetraacetic acid (EDTA), pH 8 at 4°C until the mineral was fully dissolved (about 48 h). The resulting shell extracellular matrix suspension was centrifuged at 27,000 × g for 30 min to pellet the insoluble matrix. The supernatant containing the soluble matrix was decanted, concentrated to approximately 50 ml, then dialyzed against 1 L of 10 mM NaCl using a Millipore Minitan tangential flow filtration apparatus with a molecular weight exclusion limit of 10 kDa. The resultant dialysate was further dialyzed against distilled water and lyophilized. Soluble matrix stock solutions were made by reconstituting the protein in distilled water to a concentration of 5 mg ml^{-1} based on total weight of the dried material. The pellet containing the insoluble matrix portion of the shell extract was reconstituted with 2 ml of 8 M urea and agitated end-over-end overnight at 4°C. The urea solubilized matrix suspension was centrifuged at 27,000 × *g* for 30 min to pellet the residual insoluble matrix. The supernatant containing the urea soluble matrix extract was dialyzed against distilled water and the dialysate concentrated using Microcon concentrators (Millipore).

Soluble matrix proteins were purified electrophoretically using protocols outlined in Johnstone (2008) by applying 2 mg of dry weight extract to 12% Tris-glycine sodium dodecyl sulfate polyacrylamide (SDS-PAGE) preparative gels. Protein bands were visualized by staining with 0.3 M $CuCl_2$, and bands of interest were excised from the gel, de-stained for approximately 30 min in three washes of 50 mM EDTA, pH 8 and eluted using an electro-elution module (Bio-Rad) according to manufacturer's protocols. Following electro-elution, protein was dialyzed against distilled water using Microcon concentrators or dialysis cassettes (Pierce), both having a MW cut-off of 10–12 kDa. Purified protein was lyophilized and stored at −20°C. Wherever protein quantities are reported they were determined using the BCA (Pierce) assay according to the manufacturer's protocol.

Antibody Production

Antibody probes were prepared using two strategies. For Western analyses comparing the reactivity of soluble matrix proteins to antibodies made to 48 and 55 kDa proteins, 100 μg each of preparative SDS-PAGE-purified 48 and 55 kDa protein was eluted from gels, reconstituted in 200 μl of Tris buffered saline, pH 7.5 (TBS) and emulsified with an equal volume of complete Freud's adjuvant. The emulsion for each eluted band was injected subcutaneously into two New Zealand White rabbits. After 3 weeks, the rabbits were boosted with an additional 100 μg of protein in the same manner. Sera containing anti-48 kDa or anti-55 kDa antibodies were harvested 6 weeks after the boosts and were stored in 1 ml aliquots at −20°C.

For immuno-histochemical analyses, an affinity purified antibody preparation made against the 48 kDa protein was produced by applying anti-sera generated against whole soluble matrix to a column packed with resin linked to gel purified 48 kDa protein (Johnstone et al., 2008). This method produced similar banding patterns on Western blots to that for the antibody produced as described above, but it was a more efficient way to produce sufficient antibody for these analyses.

SDS-PAGE and Western Analyses

Thirty-five μg of water soluble and urea-solubilized matrix were resolved in duplicate on gradient (4-20%) Tris-Glycine ready gels (Novex) in the presence of sodium dodecyl sulfate (SDS). One gel was stained with Stains-all (Sigma) to reveal the positions of acidic and phosphorylated proteins according to methods described by Campbell et al. (1983) as modified by Myers et al. (1996). The duplicate gel was transferred onto nitrocellulose for 1 h at 100 v in buffer containing 25 mM Tris, 192 mM glycine, 20% v/v methanol at pH 8.3 using a mini-transfer unit (Invitrogen). Following transfer, the membrane was rinsed once with TBS, then placed into 50 ml of TBS containing 3% bovine serum albumin (BSA) and 1% goat serum (blocking buffer) and allowed to incubate overnight at 4°C. After blocking, membranes were incubated in 25 ml of solution containing either the anti-55 kDa or anti-48 kDa sera diluted 1:800 in BS containing 3% BSA (Western buffer) for 2 h at room temperature. Membranes were washed 3X in 50 ml of TBS containing 1% BSA and 0.05% Tween-20 (wash buffer) for 5 min each. The membrane was incubated in 50 ml of alkaline phosphatase conjugated goat anti-rabbit IgG (Sigma) diluted to 1:30,000 in Western buffer for 1.5 h, and then washed 3X for 5 min each in wash buffer. A final rinse was carried out in TBS and color was developed with BCIP/NBT (Sigma). Development was stopped by repeated washing in distilled water over 10 min. All incubations and washes were carried out with continuous gentle shaking at room temperature. Molecular weight estimates of bands were determined from plots of the log MW of the SeeBlue standards (Novex) as a function of their relative migration distances.

Amino Acid Analyses

Amino acid analyses were conducted following the method of Waite and Benedict (1984) to optimize recovery of dihydroxyphenylalanine (dopa). Briefly, 10 μg of dry weight protein was re-suspended in 6 N HCL containing 5% v/v phenol. Hydrolysis was carried out *in vacuo* at 110°C for 24 h. Following hydrolysis, samples were dried in a Speed Vac apparatus, re-suspended in 150 μl of sample buffer and analyzed on a Beckman 6300 Autoanalyzer with post-column ninhydrin detection. All reagents used for the analyses were obtained from the manufacturer.

Phosphate and Carbohydrate Analyses

Protein-bound phosphate was determined by the spectrophotometric method of Eisenreich et al. (1975). Absorbance was determined at 880 nm against a standard range of 0.07–5.0 μg ml^{-1} total phosphate. Carbohydrate content was analyzed by two methods. A weight estimation was obtained using the spectrophotometric Glycoprotein Carbohydrate Estimation Kit (PIERCE) according to manufacturer's protocol. Absorbance was read at 550 nm and is proportional to the percentage of carbohydrate component in the protein. A standard curve was generated using proteins of known total carbohydrate content. Additionally, the DIG Glycan/Protein Double labeling

kit (Boehringer-Mannheim) was used to qualitatively label both glycosylated and non-glycosylated protein from blots following separation on SDS-PAGE gels following manufacture's protocols. Once blots identifying glycoproteins were photographed, the blots were re-stained to identify all proteins.

Edman Sequencing

Prior to sequencing, approximately 200 μg of whole soluble matrix protein and protein solubilized with urea from insoluble matrix protein were resolved on a 4–20% Tris-glycine SDS gel, blotted onto Immobilon CD membrane (Milipore) and stained with a stain developed specifically for Immobilon CD according to the manufacturer's directions. Protein bands of interest stained white against a purple background. Two bands with estimated molecular weights of 48 and 55 kDa were excised from the blot, rinsed three times in distilled H_20 for 10 min each, air-dried and submitted to the Proteomics Center at the Medical University of South Carolina for sequencing.

Probing of BAC Library

Using amino acid sequence data deduced from the N-terminal sequence of the 48 kDa protein corresponding to DEADAGD, a perl script was developed to convert the amino acid sequence into a regular expression encompassing all possible codon combinations, which were used to scan all molluscan nucleotide sequences in the National Center for Biotechnology Information database (NCBI)[1]. All candidate genes with the potential to create the target amino acid sequence were examined further by performing a 6-frame translation and inspecting start codons, stop codons, and acidic characters. A single candidate transcript sequence was identified and Primer3 (Rozen and Skaletsky, 2000) was used to develop primers for this transcript.

The folian-cv1 probe was developed by PCR amplification with the candidate primers and surplus genomic DNA (template) from a BAC library previously constructed using a South Atlantic population of *C. virginica* collected from Wadmalaw Sound, South Carolina (Cunningham et al., 2006). The Advantage2 polymerase from Clonetech was used and cycled 25 times as follows: 95 C for 5 min; 60°C for 30 s; 68°C for 1 min. A final extension was carried out at 72°C for 10 min and the products were held at 4°C. The raw PCR products were removed of primer-dimers and unincorporated dNTPs by ethanol precipitation and their size validated by agarose gel electrophoresis on a 1.2% Tris-acetate-EDTA (TAE) mini-gel. Verified amplification products were eluted from the gel and ligated into the EcoRV site of the pGEM-Teasy vector (Promega) for Sanger sequence verification. Confirmed PCR products were purified and 100 ng was used to construct probes that were radiolabeled with dATP*, using the DECAprime^{TM}II random-primer labeling kit (Ambion) according to the manufacturer's protocols. Three BAC macroarrays from the BAC library (CVBa) were pre-hybridized overnight in 50 ml hybridization buffer (0.25 M Na_2HPO_4, 7% SDS, 1 mM EDTA and 1% w/v BSA, pH 7.2) at 65°C in a hybridization oven. Radio-labeled probe was then added and hybridization was performed overnight at 65°C. Filters were exposed to phosphor storage screens (GE Healthcare) overnight. Positively identified BAC clones were PCR verified and the complete gene sequence recovered by custom oligo design and direct BAC sequencing with standard Sanger sequencing procedures. Individual sequences across each BAC were assembled by Phrap (Gordon et al., 1998).

Sequence Annotation and Proteomic Analysis

The genomic sequences encompassing the folian-cv1 gene and upstream regulatory elements were annotated by a series of software applications and final manual examination. BLASTn (Altschul et al., 1990) was used to align the candidate transcript to the genomic sequence. GeneMark (Lomsadze et al., 2005) and FGENEsH (Burge and Karlin, 1997) were used to determine start/stop codons and open reading frames, and to discover nearby flanking genes. Splice sites (exon/intron boundaries) were determined by the Drosophila Neural Network Splice Site Prediction tool, running NNSPLICE 0.9 (Reese et al., 1997). A final amino acid sequence for folian-cv1 was assembled from all of this information and was input to InterProScan to identify any previously reported protein signatures (Zdobnov and Apweiler, 2001). Additional proteomic analyses were conducted using the tools and servers available on the ExPASy Proteomics Server[2]. Folian-cv1 BAC isolates were confirmed by searching the NCBI database using the Genome Browser interface and tBLASTn query tool[3]. Multiple protein sequence alignment was performed with Clustal Omega sequence alignment tool; pairwise protein alignment was performed with the Needleman–Wunsch alignment tool. Both tools are provided online by the European Bioinformatics Institute (EMBL-EBI)[4].

Southern Hybridization

Gene copy number for folian-cv1 in the *C. virginica* genome was determined by fully digesting approximately 10 μg of genomic DNA with 2 complimentary 6-base cutters (BamHI and HindIII) and resolving the fragments by pulsed-field gel electrophoresis. Digested genomic DNA was denatured and transferred to positively charged nylon membrane (GE Healthcare Life Sciences) using downward capillary methods following published procedures (Brown, 1999). Hybridization was conducted as previously described (see BAC probing methodology) using amplification products derived from the folian-cv1 gene.

PCR Analyses

PCR primers for folian-cv1 were designed using the NCBI primer blast tool[5]. A forward primer (5′-GACACCGATGGATATGGCCC-3′) corresponding to the 127–146 bp region of folian-cv1 and a reverse primer (5′-TCATCGGCACTTGAGTCGTC-3′) corresponding to the

[1]https://www.ncbi.nlm.nih.gov/nucest

[2]http://www.expasy.ch/tools/

[3]https://www.ncbi.nlm.nih.gov/genome/gdv/

[4]www.ebi.ac.uk/services

[5]http://www.ncbi.nlm.nih.gov/tools/primer-blast/

263-244 bp region were purchased from Integrated DNA Technologies (IDT). These primers had a predicted melting temperature (Tm) of 58 and 57°C respectively. The expected length of the target folian-cv1 product was 135 bp. Two ml of hemolymph was obtained from the adductor muscle of 5 oysters using a 21-gauge needle and syringe and spun at 6000 × *g* for 5 min to pellet hemocytes. The resulting pellets were combined into one tube in RNAlater (Life Technologies). RNA was extracted from hemocyte pellets and pieces of mantle excised from the edge, using the RNeasy mini kit (Qiagen) according to the manufacturer's protocol. Extracted RNA was quantified using an Eppendorf Biophotometer. Following normalization, RNA was incubated at 65°C for 5 min and reverse transcribed for 1 h at 37°C using an RT mastermix comprised of RNA free water, 5x MMLV Buffer (Promega), 10 mM dNTP mix (Qiagen), 50 ng/μL random primers (Promega) and Moloney murine leukemia virus (MMLV) RT enzyme (Promega). Finally, tubes were incubated at 95°C for 10 min. For PCR amplification 100 ng of cDNA was combined with 47.5 μL PCR mastermix (Qiagen) comprised of sterile filtered water, 10x PCR buffer, 10mM dNTP mix (Qiagen), 10 μM forward primers, 10 μM reverse primers and Taq Polymerase. A cDNA-free control was also run. PCR was performed on an Applied Biosystems Veriti Thermal Cycler with an initial denaturation at 94°C for 3 min followed by 25–35 cycles at 94°C for 30 s, 60°C for 30 s, and 72 C for 1 min. A final extension was carried out at 72°C for 10 min and the products were held at 4°C. Products were run on a 2% agarose gel with Tris-acetate-EDTA buffer (TAE) at pH 8 in sample buffer (Promega) including 10 μl of 10 mg ml^{-1} ethidium bromide. The target sequence was validated using ExoSAP-IT® reagent (Affymetrix) followed by Sanger sequencing contracted through the Clemson University Genomics Institute.

For qPCR, the collection of hemocytes and extraction of RNA were as described above. Three separate collections were analyzed. Comparison of the expression of folian-cv1 was made to cv-actin and cv1-MMP (matrix metalloproteinase) using cv-18S rRNA as a reference gene. Cv-actin served as an example of a housekeeping gene and cv1-MMP is a gene belonging to a class that has been linked to both immunity (Bonnans et al., 2014) and biomineralization (Luke and William, 2001; Ortega et al., 2003) and has been identified in oyster hemocytes (Falwell, 2015). The folian-cv1 primer set was described above. Primers for the other genes were as follows with Tm in parentheses: cv-actin forward, 5′-TTGGACTTCGAGCAGGAGATGGC-3′ (61 C) and cv-actin reverse, 5′-ACATGGCCTCTGGGCACCTGA-3′ (63 C); cv1-MMP forward, 5′-ATGGTTCATTGTATGCGACCCGGA-3′ (61 C) and cv1-MMP reverse, 5′-TTGGGCGCTCTC TTGTACACCTTT-3′ (61C); cv-18S rRNA forward, 5′-CTGGTT AATTCCGATAACGAACGAGACTCTA-3′ (59 C) and cv-18S rRNA reverse, 5′-TGCTCAATCTCGTGTGGCTAAACGCC ACTTG-3′ (65 C). The sequences for cv-actin and cv1-MMP were obtained from the Gomez-Chiarri lab and those for cv-18S rRNA from those provided by Jing et al. (2011). Primers were validated as described above for folian-cv1 and their concentrations optimized for 1-step qPCR.

For all primer sets, a mastermix containing SYBR®Green 1 dye and buffers, a RT enzyme mix, and optimized dilutions of primers were prepared according to the instrument manufacturer's recommendations. The reactions were carried out in a total volume of 25 μL with 1 μL of target RNA on a BioRad iCycler iQ5 with the following program: holding at 48°C for 30 min, holding at 95°C for 10 min followed by 40 cycles of denaturation at 95°C for 15 s and extension at 60°C for 1 min. Seventy cycles of the melt curve were run as follows: denaturation at 95°C for 15 s, annealing at 60 C for 15 s and extension at 95 C for 15 s. Melt curve predictions were performed with uMelt software[6].

Expression for genes of interest was normalized to that of the reference gene cv-18S rRNA for each hemocyte sample collection. The formula used for calculating normalized gene expression (NE), based on Muller et al. (2002) as modified by Roling et al. (2004) is:

$$NE = E^{Ct}ref/E^{Ct}goi.$$

E is the efficiency of amplification for a particular gene, Ct is the threshold cycle, "ref" is cv-18s rRNA and "goi" is one of the genes of interest, folian-cv1, cv1-MMP or cv-actin. The null hypothesis that the qPCR expression means of the three genes of interest were equal was evaluated with an Analysis of Variance Test (ANOVA). The three follow-up null hypotheses that the qPCR expression means of pairs of the genes of interest were equal was evaluated using Fisher's Protected Least Significant Difference Test.

Histochemistry and Immuno-Histochemistry

Prior to histochemical analysis, oysters were perfused and fixed intact with 4% paraformaldehyde in phosphate buffered saline (PBS), pH 7.4. PBS was adjusted using 1M NaCl, to match osmolality of the holding tank at the time of tissue harvest. Tissue was embedded in Immunobed™ (Poly Sciences) and sectioned at 1–1.5 μm. To assess general tissue morphology and integrity, sections were stained using a solution that contained equal parts 1% Azure II in double distilled water and 1% Methylene Blue in 1% sodium borate. The working solution was filtered through a 0.22 μm syringe filter and applied directly to dried mounted sections for 10–30 s. The slides were rinsed with doubly- distilled water and dried with a jet of air.

Immuno-histochemical staining was carried out using the affinity purified anti-48 kDa antibody as previously described (Johnstone et al., 2008). Antibodies were diluted in PBS containing 1% BSA and 0.1% Triton X100. This buffer was also used as the wash buffer. The anti-48kDa antibody was diluted to 1:700. Prior to staining, slides were rehydrated through a graded series of alcohol solutions in distilled water, starting with 100% EtOH and ending with PBS for 2 min each. Slides were blocked in PBS buffer containing 5% BSA, 10% normal goat serum (Sigma) and 0.1% Triton X 100, for 6 h at room temperature. After a brief rinse in PBS, slides were incubated in primary antibody solutions overnight at 4°C. Washes following the primary and secondary incubations were carried out 3X for 10 min each. Immuno-reactivity was detected using Alexafluor

[6]https://www.dna.utah.edu/umelt/um.php

488 goat anti-rabbit fluorescent antibody at a concentration of 6 μg ml-1. All incubations were carried out in a covered humid chamber with gentle agitation. Sections were mounted in a 1:1 solution of glycerol and PBS and then examined with a Zeiss Axiovert 135 inverted fluorescent microscope equipped with a Diagnostic Instruments SPOT-RT Cooled Color CCD camera.

Confocal Laser Scanning Microscopy (CLSM) of Live Mantle and Hemocytes

To observe potential channels in the mantle, an approximately 1 cm^2 piece of live tissue was excised from the mantle edge, mounted in a depression slide in filtered seawater and covered by a 1.5 cover glass. Autofluorescence was observed directly with a Zeiss 510 CLSM at 488 nm excitation using a ZeissPlan Neofluar 40X/1.3 oil DIC objective.

In an alternative experiment, 600 μl of hemolymph was collected from the adductor muscle using a sterile 21-gauge needle affixed to a sterile 3 ml plastic syringe. The adductor muscle was accessed by notching the oyster shell with a diamond blade saw and the oyster was immediately placed into a holding vessel containing 2 L of fresh aerated seawater. The hemolymph was transferred into a sterile 1.5 ml plastic microfuge tube and the hemocytes were labeled in suspension by adding 50 μl of 2 μM Calcein AM ester. The preparation was mixed gently and incubated at room temperature for 30 min. Following incubation, the preparation containing the labeled hemocytes was re-injected into the adductor muscle using a sterile syringe. After 2 min, the oyster was returned to the holding vessel for 60 min to allow time for the hemocytes to circulate throughout the hemocoel. Following incubation, a piece of mantle was collected and observed at excitation wavelengths of 488 and 594 nm. A 60-slice image stack was then post-processed using the Quorum Technologies Volocity visualization software to show rotation of the outer shell facing mantle epithelium about two axes.

RESULTS

Identification and Characterization of the Folian Protein Family

Proteins extracted from the foliated shell layer were visualized by Stains-all following SDS-PAGE. This cationic stain has been successful in identifying highly anionic proteins and phosphoproteins derived from shell, tooth and bone (Campbell et al., 1983; Myers et al., 1996). Proteins enriched in negatively charged groups stain a deep purple color while proteins with less of, or lacking, these groups stain pink, and the color fades quickly upon exposure to light. **Figures 1A,B**, show the electrophoretic patterns of the EDTA soluble matrix proteins (SM) and proteins rendered soluble after extraction of the EDTA insoluble matrix protein (IM) by urea (uSM). The SM extract pictured in **Figure 1A** resulted in two prominent bands at 48 and 55 kDa and two adjacent minor bands at 43 and 63 kDa. In addition, staining spanned nearly the entire length of the gel, with a relatively discrete set of bands from 5 to 50 kDa. In a separate shell extract (**Figure 1B**), only the 48 kDa band was prominent. However, a 55 kDa band is clearly visible in the uSM fraction of this extract, suggesting that the protein(s) in this band may be more tightly bound to the insoluble structures than those of the 48 kDa protein.

Western analyses indicated that antibodies made against either the 48 or 55 kDa bands reacted with a wide range of molecular weight classes from the SM (**Figure 1C**). Each antibody recognized four discrete bands corresponding to the Stains-all positive bands following gradient SDS-PAGE, including highly reactive proteins at 48 and 55 kDa and more moderately reactive bands at 43 and 63 kDa. The anti-48 kDa antibody identified a broad low molecular weight continuum of proteins, much like Stains-all, while the anti-55 kDa antibody did not react broadly with proteins in this region. In addition to the Stains-all bands, a high molecular weight band was also immuno-reactive. The significant cross-reactivity observed among this class of proteins demonstrates that they share common epitopes and suggests that they are related.

The electrophoretically separated and blotted proteins of SM reveal a range of molecular weight bands that are glycosylated, including the 48 kDa band (**Figure 2A**). Some of these bands, such as one that is about 34 kDa, are not evident with Stains-all staining. The highly variable level of glycosylation becomes evident when the blots are re-stained for protein (**Figure 2B**). The prominent 48 kDa band would be classified as moderately glycosylated given the color shift from blue to more of a brown color in the band after re-staining. This color shift is not evident for the 34 kDa band or some of the higher molecular weight bands, suggesting they are more highly glycosylated than the 48 kDa band. However, the color shift is more pronounced in some of the lower molecular weight bands, suggesting they have lower levels of glycosylation than the 48 kDa band.

Amino acid analysis confirmed the close relation among the matrix protein fractions (**Table 1**). A comparison of the 48 and 55 kDa proteins shows that they have a markedly similar overall amino acid composition, with the common distinguishing characteristic of being approximately 80% asp, ser and gly, and having a nearly identical overall hydrophobicity. The overall similarity of their amino acid composition was supported using the Cornish-Bowden index (Cornish-Bowden, 1983) from which it could be concluded that these fractions have a 95% certainty of being related (**Supplementary Table 1**). Using the same comparisons, there is also a relatively close correspondence of the composition of both the 48 and 55 kDa proteins with that of the whole SM extract. IM is also similar enough in its composition to the soluble fractions as to be weakly related to them. Further, like SM, IM is highly phosphorylated and moderately glycosylated. Despite their otherwise high degree of similarity, the folian proteins from the 48 and 55 kDa bands are clearly distinct in their amino terminal regions (**Table 2**). Amino terminal regions obtained from the 55 kDa band are nearly identical regardless of their origin from SM or urea solubilized from IM (uSM) (**Table 2**), suggesting they may contain identical proteins.

Identification of the Folian-cv1 Gene

Probing the *C. virginica* BAC library with a nucleotide sequence based on an EST that encoded the N-terminal sequence of the 48 kDa band resulted in 36 positive BAC clones. Genomic Southern analysis revealed that the folian-cv1 gene occurred at

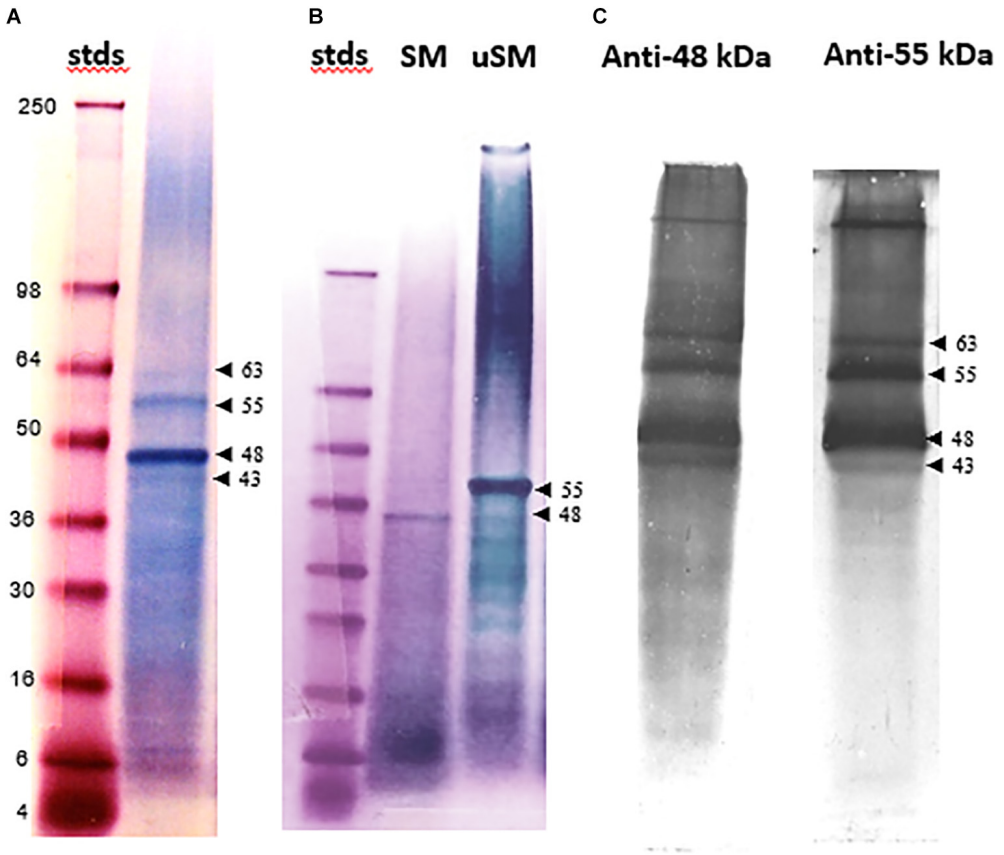

FIGURE 1 | SDS-PAGE and Western analyses of soluble shell matrix proteins. **(A)** Thirty-five μg of EDTA soluble matrix (SM) was resolved on a 4–20% gradient Tris-glycine gel and stained with Stains-all. Standards (stds) were SeeBlue protein molecular weight markers labeled in kDa. Two prominent bands appear at 55 and 48 kDa while two adjacent minor bands occur at 63 and 43 kDa (arrow heads). **(B)** Thirty-five μg SM and urea-solubilized matrix (uSM) were electrophoresed and stained as in **(A).** The position of the 55 and 48 kDa bands are indicated with arrow heads. While the 55 kDa band is not prominent in this preparation of SM, it is clearly the dominant band upon urea extraction of the insoluble matrix from this preparation. **(C)** Western analyses of SM extract immuno-stained separately with anti-48 kDa and anti-55 kDa antibodies. Both lanes contained 50 μg of SM and were resolved on 12% Tris-glycine SDS gels. All four of the Stains-all positive bands identified in **(A)** are immuno-reactive with the anti-48 and anti-55 kDa antibodies (arrow heads). An additional high molecular protein that exceeded 98 kDa was also immune-reactive. All matrix loads are in quantities of protein as determined by BCA analysis. For these analyses, only lanes showing data pertinent to this study are presented.

two independent loci (**Supplementary Figure 1**). PCR analysis of the 36 BAC clones identified representative BACs harboring the two variants, which were used for direct BAC sequencing to determine the full length of the coding and regulatory sequences. The first region contained 1716 bp and the second, 2604 bp. The 1716 bp region aligned within the 2604 bp region with greater than 97% identity. Each region encompassed an entire gene, with a transcriptional start site, a start codon, two exons defined by splice boundaries, a stop codon, and a putative poly-A site (**Supplementary Figure 2**). The deduced transcribed products resulted in two nearly identical gene variants differing by 4 point mutations (**Figure 3**); three of these mutations result in amino acid substitutions which are discussed further below. The gene and deduced gene product were named folian-cv1 for the shell layer and species from which they were derived.

The two variants of the folian-cv1 gene identified from BAC cloning were verified by searching the recently released *C. virginica* genome constructed from a Delaware population of oyster (Gomez-Chiarri and McDonnell, 2017). Using BlastX tools and the folian-cv1 deduced protein sequence as a virtual probe, two variations of folian-cv1 were identified on chromosome 1 at two distinct loci (NCBI accession number NC_035780; gene ID: 111101504 and NCBI accession number NC_035780; gene ID: 111119246). The two Delaware genome isolates (1504 and 9246) demonstrate a slightly higher level of heterogeneity compared with the two South Carolina BAC isolates reported in **Figure 3**, differing not only by substitutions but by gap regions or insertions as well (**Supplementary Figure 3**). Alignment of copy 1 of the folian-cv1 BAC isolate derived from the South Carolina population with the two variants identified from the Delaware genome revealed strong sequence agreement between the two populations, differing slightly in length and composition due to gap regions or insertions, and substitutions (**Supplementary Figure 3**). Some of the sequence variations

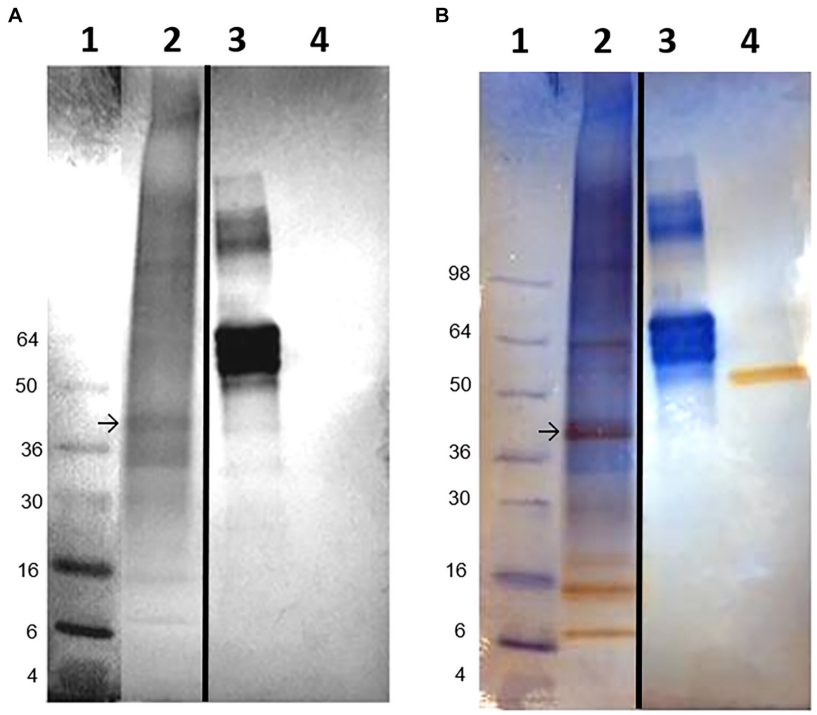

FIGURE 2 | Glycoprotein detection in soluble shell matrix proteins. **(A)** Twenty-five μg (dry weight) of each protein was resolved using a 10% Tris-glycine gel and transferred onto nitrocellulose. The blot was stained to identify glycosylated protein. Lane 1- SeeBlue protein molecular weight standards labeled in kDa. Lane 2- SM. Lane 3- Fetuin (glycosylated protein control). Lane 4- Creatinase (non-glycosylated protein control). The intensity of staining is proportional to the amount of carbohydrate present on each protein. SM appears to contain a broad range of lightly glycosylated proteins. The 48 kDa band is indicated with an arrow and shifted to a lower apparent molecular weight following blotting when compared to **Figure 1A**. This shift was observed commonly following blotting. A band identified at approximately 34 kDa was not identifiable in **Figure 1A** following Stains-all staining. Stained gels were photographed in black and white to enhance detectability of faint blue bands. **(B)** The same blot as in **(A)** was re-stained for protein to distinguish non-glycosylated proteins from glycosylated proteins. In lane 3, fetuin remains blue and is indicative of its heavy glycosylation. Creatinase is now apparent in lane 4. In lane 1, the 48 kDa band shifts toward brown staining indicating less glycosylation than the 34 kDa band which remains blue. For this analysis, only lanes showing data pertinent to this study are presented. Lanes 1 and 2 were cropped from the original blot and digitally placed next to lanes 3 and 4 (controls) which were also cropped from the original image; the splice sites are demarcated by a black line. In **(A)**, the contrast in Lane 1 was digitally adjusted to visually discern the protein standards.

between the populations likely reflects their geographic isolation. Because only two variants of folian-cv1 were found in either population and were localized on chromosome 1 in the Delaware population, it is likely these copies result from gene duplication.

Structure of the Folian-cv1 Deduced Protein

The complete gene and deduced folian-cv1 protein of 325 amino acids is shown in **Figure 3**. The only domain recognized by InterProScan software was a putative signal peptide (italicized) and signal cleavage site (black arrow), which indicates the protein is secreted (Zdobnov and Apweiler, 2001). After the first three amino acids following the signal sequence, the subsequent sequence (underlined) matches that obtained by Edman chemistry for the 48 kDa protein as reported in **Table 2**. The four point mutations that distinguish the two copies of folian-cv1 occur toward the N-terminus. Two mutations at nucleotide positions 96 and 240 result in substitutions for aspartic acid to glutamic acid, thus resulting in no change in charge. A mutation at position 243 results in a substitution for serine to arginine, and potentially a change to a positively charged group from a negatively charged group if the serine were phosphorylated. The fourth point mutation at 326 does not produce an amino acid substitution.

Removal of the 18 amino acid signal sequence results in a 307 amino acid protein with a calculated molecular weight of 32 kDa. The secreted form of folian-cv1 is highly acidic, as approximately 52% of its amino acid composition is comprised of aspartic acid (132 residues) and glutamic acid (28 residues) (**Table 1**). While its high proportion of aspartic acid and serine and its low hydrophobicity are comparable to other folian fractions, it is distinctive in having a considerably lower glycine content than these fractions. This difference, in large measure, explains its low relatedness to the other fractions when compared by the Cornish-Bowden index (**Supplementary Table 1**). The theoretical pI for folian-cv1 is 2.19; however, the possibility for additional anionic charge is present in the 115 potential phosphorylation sites (100 for Ser, 12 for Tyr, and 3 for Thr) predicted by NetPhos 3.1[7]. Bearing in mind that

[7]www.cbs.dtu.dk/services/NetPhos

TABLE 1 | Amino acid compositions of shell matrix fractions compared with the deduced amino acid composition for folian-cv1.

Amino acid[1]	IM	SM	48 kDa band	55 kDa band	folian-cv1
Asp	22.7	29.7	31.9	31.7	43.3
Asn	ND[2]	ND	ND	ND	0.7
Thr	1.3	1.7	0.8	0.9	1.0
Ser	25.6	23.2	19.4	23.6	32.6
Glu	7	6.9	7.0	6.4	9.1
Pro	1.3	1.6	1.0	1.9	1.0
Gly	30.0	25.5	32.8	29.5	4.2
Ala	3.4	3.1	1.6	1.5	2.3
Cys	X[3]	X	X	X	0.0
Val	1.5	1.4	1.2	0.4	1.3
Met	0.2	0.2	0.0	0.0	0.0
Ile	0.5	0.4	0.2	0.2	0.0
Leu	1.3	1.0	0.6	0.6	0.0
Dopa	X	X	X	X	NA[4]
Tyr	2.0	3.0	2.6	2.5	4.2
Phe	0.3	0.4	X	X	0.0
His	0.5	0.6	X	X	0.0
Lys	1.6	1.1	0.4	0.8	0.0
Arg	0.9	0.5	0.5	0.0	0.3
Phosphate[5]	10.9	15.1 ± 0.39	ND	ND	NA
Carbohydrate[5]	3.5	3.9 ± 1.4	ND	ND	NA
Hydrophobicity[6]	−15.4	−19.2	−24.0	−23.9	−33.8

[1]Compositions are reported in mole percent. The amino acid composition of folian-cv1 protein was calculated from the folian-cv1 gene. [2]ND, not determined. [3]X, not detectable. [4]NA, not available for deduced gene product. [5]Phosphate and carbohydrate values are reported as percent of total dry weight of IM and SM fractions (SM: mean ± standard deviation, N = 3). [6]Hydrophobicity was calculated as the sum of the products of the hydrophobicity constant for the R groups of each amino acid from Fauchére and Pliška (1983) times the mole percent for each amino acid. Amino acids more hydrophobic than glycine have positive constants and those less hydrophobic than glycine have negative constants.

TABLE 2 | Amino-terminal sequences for the 48 and 55 kDa bands[1].

Protein band/shell matrix fraction[2]	
48 kDa/SM	D-E-A-D-A-G-D-A-Y-D-V-A-D-T-()-()-V-Y-D-()-D
55 kDa/SM	()-S-K-G-X-E-P-D-()-()-Y-()-()-()-()-Q-K
55 kDa/uSM	()-Q-K-G-X-E-P-D-X-()-Y-()-D-()-()

[1]Sequences were determined by Edman chemistry analyses. "()" indicates positions where definitive assignment was ambiguous. "X" denotes amino acids that were modified. [2]Proteins were analyzed from blots or following electro-elution. SM is soluble matrix protein following demineralization of shell in EDTA; uSM is protein extracted from insoluble matrix using 8M urea.

the protein-bound phosphate would have a second ionizable group with a reported pKa near neutrality (Lee et al., 1977), then more than half of these groups would be doubly ionized at physiological or seawater pH. Accordingly, assuming full theoretical phosphorylation and 1.5 charges per phosphate group, the net charge of folian-cv1 under these conditions would be −332.5 per molecule, or just over a −1 charge per amino acid residue. If all these sites were phosphorylated, the protein would have an isoelectric point of 0.36[8]. A high level of phosphorylation would be consistent with the phosphate content of the whole matrix fractions. If the actual level of phosphorylation of folian-cv1 were, at a minimum, the same by weight as for the whole soluble extract, then approximately 50% of the theoretical sites would be phosphorylated. Under these circumstances, the pI would still be less than 0.7. Twenty-eight potential mucin type, *O*-glycosylation sites were predicted, with 25 of these sites in the region including residues 153–188 and three additional sites in the region including residues 234-238 (NetOGlyc 3.1 Server[9]). Some level of glycosylation would be consistent with the presence of carbohydrate in the whole matrix fractions (**Table 1**) and the apparent glycosylation of the 48 kDa band (**Figure 2**). Four of the 13 tyrosine residues are potentially sulfated including residue positions 40, 291, 295, and 325[10].

Notable features of the folian-cv1 primary structure are shown in **Figure 4**, which illustrates its repetitive and modular structure. As expected from its composition, much of the primary structure is dominated by aspartic acid and serine residues, which are concentrated from position 71 on. These two amino acids appear together in various configurations. Conspicuous arrangements are 7 tandem repeats of DDS and 8 tandem repeats of DS. An additional DS-rich region is made up of 3 tandem repeats of DSDSGSDSDS. There are multiple poly-D blocks, six of which have runs of 4–10 residues. These are bracketed by S residues and are located from the middle of the protein to near the C-terminus. A ser-rich region has poly-S blocks totaling 19 residues near the middle of the protein. There are two tyrosine-rich blocks containing YS or SYSD repeats, one following the ser-rich region and another located near the C-terminus. With only a few exceptions, the hydrophobic residues (other than those associated with the signal sequence) are near the N-terminus giving the region from position 19–51 a hydrophobicity index of +14.7 compared to −33.1 for that of the whole post-signal sequence protein (see **Table 1**). This region is punctuated with regularly spaced asp residues in D-X-X-D and D-X-D arrangements. A glu-rich region, containing a 5-residue poly-E block, occurs between the hydrophobic N-terminus and the asp-ser-rich region.

Folian-cv1 Gene Expression in Hemocytes and Mantle

PCR analyses of mantle and hemocyte tissue demonstrated that these tissues expressed folian-cv1 (**Figure 5A**), which was validated by sequence analysis (**Figure 5B**). The results of qPCR analysis of gene expression in hemocytes for the housekeeping gene cv-actin and cv1-MMP, a gene implicated in immunity as well as biomineralization, are compared to that of folian-cv1 in **Figure 5C**. ANOVA suggested that their expression relative to that of cv-18s rRNA was different (p = 0.0217). Subsequent pairwise comparisons suggested that the relative expression of both folian-cv1 and cv1-MMP was different from that of actin (p = 0.0125 for both comparisons), but that the expression

[8]https://scansite4.mit.edu/webservice/

[9]http://www.cbs.dtu.dk/services/NetOGlyc-3.1/

[10]https://web.expasy.org/sulfinator/

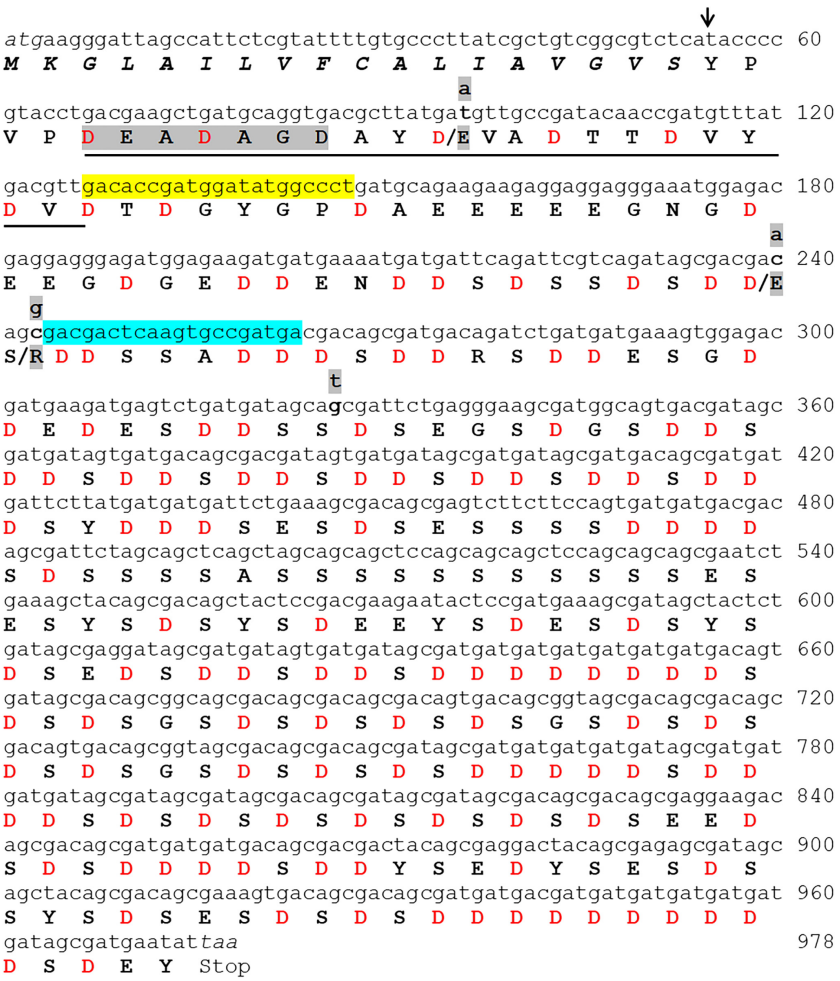

FIGURE 3 | The complete folian-cv1 gene and deduced amino acid sequence. Two copies of folian-cv1, identical with the exception of four point mutations, were identified. The full sequence is shown for copy 1. The point mutations shown in copy 2 occur in the N-terminal region of the protein and are indicated in lower case highlighted letters above the DNA sequence. Three of the four mutations resulted in an amino acid change indicated by the highlighted amino acids following the "/". Mutations at positions 96 and 240 result in a substitution for Asp to Glu. The mutation located at position 243 resulted in a change from serine to arginine. The putative signal sequence starting with the *ATG* start codon appears in italics. The putative cleavage site of the signal sequence is indicated with an arrow (↓) and cleaves between the "S" and "Y" residues. The deduced amino acid sequence minus the signal sequence encodes a 307 amino acid product enriched in aspartic acid and serine. The underlined sequence matches well with the N-terminal sequence identified by Edman sequencing (**Table 2**) and the gray highlighted sequence "DEADAGD" was used to design the *in silico* probe which identified the transcript used to screen the BAC library. The yellow highlighted region from 127 to 146 bp and the blue highlighted region from 263 to 244 bp indicate the regions that were used to construct forward and reverse primers respectively for subsequent PCR analyses.

of folian-cv1 and cv1-MMP were not statistically different (p = 0.992). Based on the averages, the expression of cv-actin is 2–3 orders of magnitude higher than either cv1-MMP and folian-cv1, and the expression of the latter pair are nearly identical.

Immuno-Histochemical Localization of Folian Proteins in the Mantle and Evidence for Hemocyte Movement Through the Mantle Using Confocal Imagining

The mantle organ lies in close approximation to the entire inner shell surface, separated by a nominal extrapallial space (Simkiss and Wilbur, 1989). In *C. virginica*, as is the typical case for bivalves, the organ elaborates into three lobes at its margin (Ebel and Scro, 1996; Figure 6A from Johnstone et al., 2008). The outer lobe and the general shell-facing outer epithelium of the mantle are generally considered responsible for the formation of shell layers in the extrapallial space. The outer and middle lobes form the periostracal groove (PG) which at its base secretes periostracum. During shell formation this material nominally completes the isolation of the extrapallial space at the shell edge and has been reported as the primary surface on which the mineral layers form in this oyster and other molluscs (Galstoff, 1964; Saleuddin and Petit, 1983; Checa, 2000).

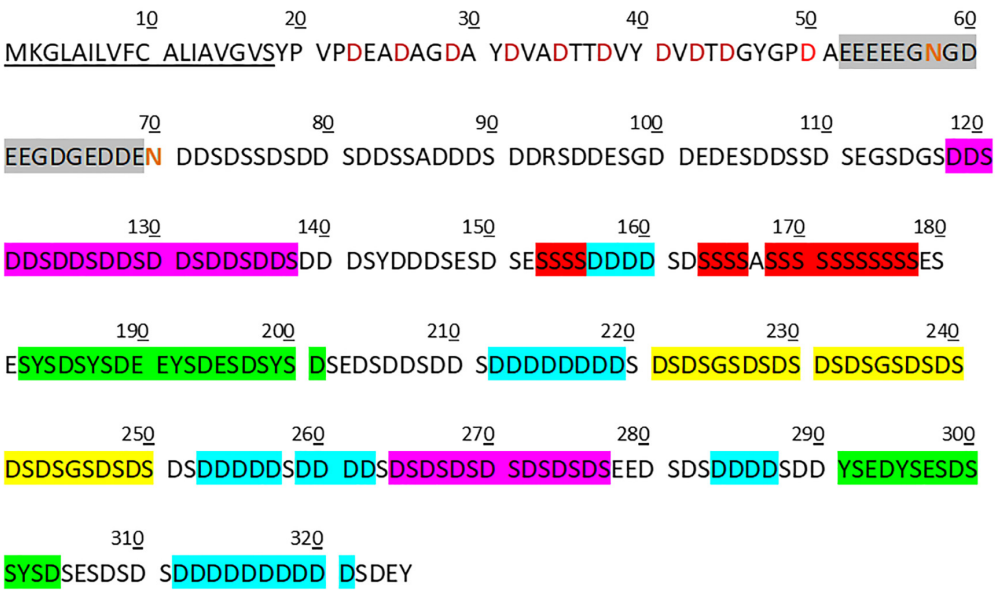

FIGURE 4 | Features of copy 1 of the folian-cv1 primary structure. The secreted protein can be divided approximately into three distinct regions following the signal peptide (underlined). The first is a relatively hydrophobic N-terminal region (33 residues in length) with regularly spaced asp residues (red symbols). This is in turn followed by a short glu-rich region (18 residues in length; gray box) which contains a 5-residue glu run and has the two asparagine residues in the protein (red symbols) in or immediately following the run. The remainder of the protein (255 residues) is generally asp-ser-rich. Notable sub-regions in the asp-ser-rich region include one that is exclusively DDS (7 tandem repeats in residues 118–138) and one that is exclusively DS (8 tandem repeats in residues 262–277) (pink boxes). In addition, there are three 10-residue tandem repeats for which each repeat has a single GS bracketed by two DS pairs (yellow box). Other repeat regions include poly-D runs (those runs greater than three shown in blue boxes), which are bracketed by S, poly-S runs (red boxes) and those that are Y-rich containing YS or SYSD sequences (green boxes). Nearly all of the ser, tyr, and thr were predicted to be possible phosphorylation sites using NetPhos 3.1 (www.cbs.dtu.dk/services/NetPhos).

Previously, immuno-histochemical staining showed that folian protein-positive cells were by far most concentrated along the outer lobe of the mantle epithelium (**Figure 6A**). In this study, we expand the analysis of this section by showing that the folian proteins are an integral part of what appears to be a structurally cohesive sheet, which is evidenced by regions where the structure is broken and lifted off the surface (**Figure 6B**). This sheet extends across the outer lobe surface in the direction of the adductor muscle further than previously reported (**Supplementary Figure 4**). Further analysis of **Figure 6A** also reveals folian-positive hemocytes in numerous locations, some of which appear to be moving through the outer lobe into the extrapallial space (**Figure 6C**). A confocal stack of a living outer lobe outer epithelium shows channels approximately 10 μm in diameter that span the entire thickness of the epithelial layer (**Supplementary Figures 5A–E**). These channels could act as conduits for cell movement into the extrapallial space evident in **Figure 6A**. A 3-D rendering of a confocal stack of a living shell-facing mantle epithelium shows a Calcein-stained hemocyte moving through the mantle, presumably within a channel (**Supplementary Figures 6A–L**). The confocal stack of **Supplementary Figure 6** can be dynamically viewed in 3D in the **Supplementary Video 1**.

At higher magnification, immuno-staining shows folian localizes heavily inside cells lining the outer lobe epithelium and at the outer lobe epithelial surface in the PG (**Figure 7A**). A different material, presumed to be nascent periostracum), is not appreciably immuno-reactive and in general is spatially distinct from the folian-positive material. Folian is secreted nearly but not completely to the base of the PG. Some faint staining at the base of the PG may be due to displacement of material by the mantle, which is highly mobile (Galstoff, 1964). A section analyzed at less saturation shows distinct folian-positive granules inside secretory cells (**Figure 7B**). Non-reactive cells appear black and are concentrated near the base of the PG.

The diversity of secretory cells and their products are evident in an Azure II-stained companion section from the same region (**Supplementary Figure 7A**), which also demonstrates that the integrity of the tissue was retained during fixation and sectioning. While it is impossible to specifically correlate the cells in the Azure II-stained sections with the folian-positive cells, some of the lighter staining cells in the Azure-II sections are distributed more or less like the folian-positive cells and appear to have a morphology and vesicle size described by Myers et al. (2007) for phosphoprotein secreting cells, Other, darker staining secretory and cuboidal cells are concentrated near the base of the periostracal groove and appear to be the non-folian staining cells from **Figure 7B**. It could be hypothesized that these secretory cells are involved in the production of periostracum.

Figure 7C shows two folian-positive cells of interest: one that appears to be a secretory cell releasing folian material (perhaps still in vesicles) into the PG, and a second

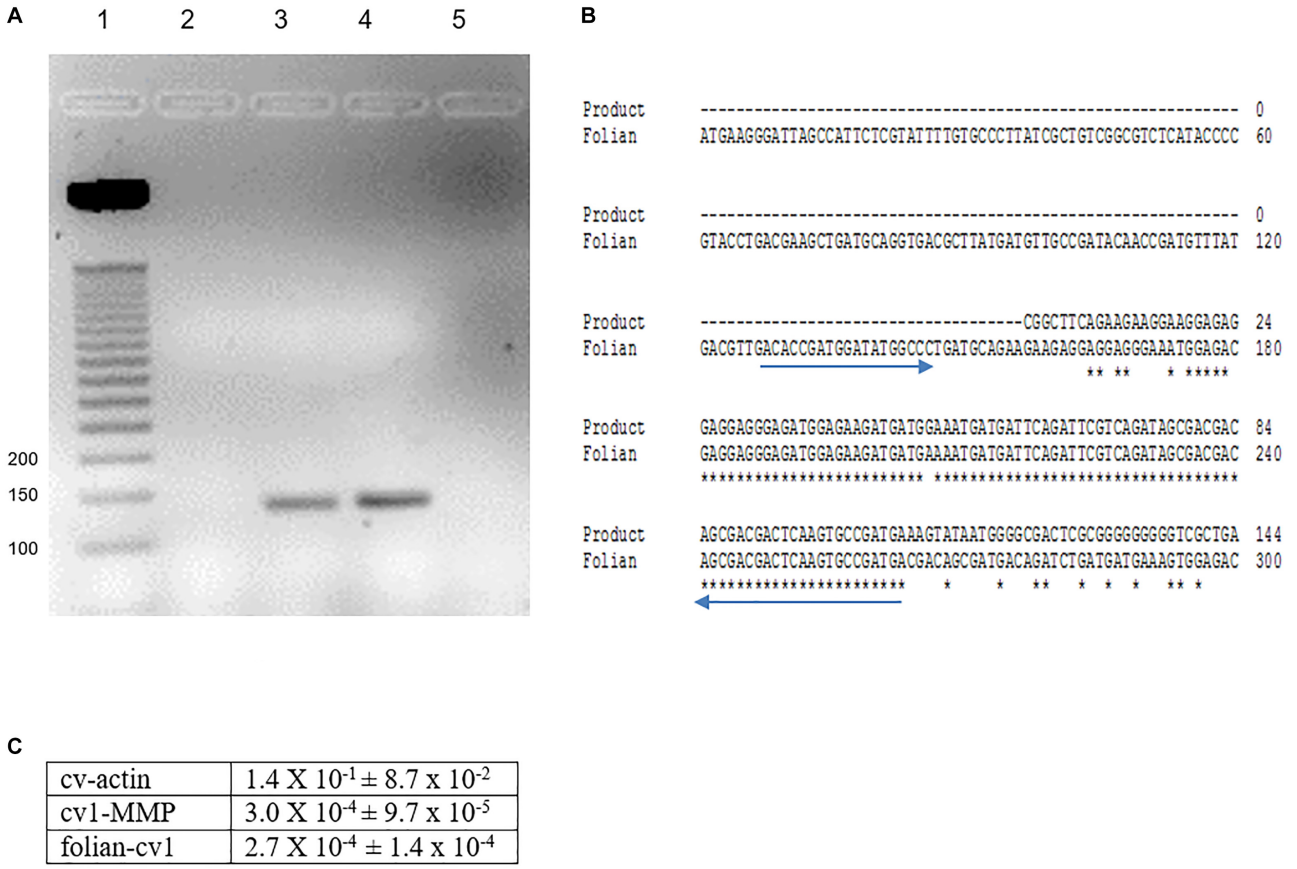

cv-actin	$1.4 \times 10^{-1} \pm 8.7 \times 10^{-2}$
cv1-MMP	$3.0 \times 10^{-4} \pm 9.7 \times 10^{-5}$
folian-cv1	$2.7 \times 10^{-4} \pm 1.4 \times 10^{-4}$

FIGURE 5 | Identification of folian-cv1 gene expression in mantle tissue and hemocytes. **(A)** PCR products amplified from mantle and hemocytes using folian-cv1 forward and reverse primers resolved on a 2% agarose gel and stained with EtBr. Lane 1- standards labeled in base pairs; Lane 2- negative control, no template; Lane 3- hemocytes; Lane 4- mantle tissue; Lane 5-blank. The products are similar in size to the length of the region delimited by the primers (135 bp). **(B)** Sequence validation of PCR target. The PCR product from hemocytes was sequenced and aligned with the folian-cv1 gene sequence. Primers indicated with blue arrows. High fidelity matching occurred between nucleotides 159 and 266 on the folian-cv1 sequence. **(C)** Comparison of qPCR expression for cv-actin, cv1-MMP and folian-cv1 in hemocytes. Values are relative to cv-18S rRNA expression (Mean ± standard deviation; *N* = 3 hemocyte extracts).

appears to be a hemocyte en route to the PG. Hemocytes are abundant in the tissue of this region (**Supplementary Figure 7B**) and can be seen associated with periostracal material (**Supplementary Figure 7C**).

DISCUSSION

In this study, we report the identification of a gene encoding a highly acidic protein that is part of a diverse family of similar extracellular matrix proteins from the foliated shell layer of the Eastern oyster, *Crassostrea virginica*. Because of its microstructural origin, we refer to the family as folian and have named this gene folian-cv1. The gene was elucidated starting with the N-terminus sequenced from an electrophoretic band of approximately 48 kDa. The deduced protein has an amino acid composition that is 76% asp and ser and has a molecular weight of 32 kDa, excluding the signal peptide and any post-translational modifications. If fully predicted phosphorylation were included, the molecular weight would be approximately 41 kDa, more closely matching the apparent molecular weight of the electrophoretic band. If the predicted *O*-glycosylation sites indeed contain carbohydrate, the match between theoretical and observed molecular weight would be even closer. The 48 kDa band and a second prominent 55 kDa band were initially identified by Myers et al. (1996) as containing prominent acidic phosphoproteins based on their Stains-all staining characteristics. Here, the 48 and 55 kDa proteins are shown to be very similar in amino acid composition, with asp, ser, and gly constituting in excess of 80% of the molar content. Moreover, their compositions are very similar to the highly phosphorylated whole EDTA-soluble shell extracellular matrix extract.

Although there are clear defining similarities among the various folian proteins, it is equally clear that there is an underlying diversity and complexity as well. For example, the 48 and 55 kDa bands have proteins that are distinct in their N-terminal regions and their solubility following shell dissolution in EDTA. Further, the composition of the folian-cv1, with its comparably lower gly and concomitantly higher ser and

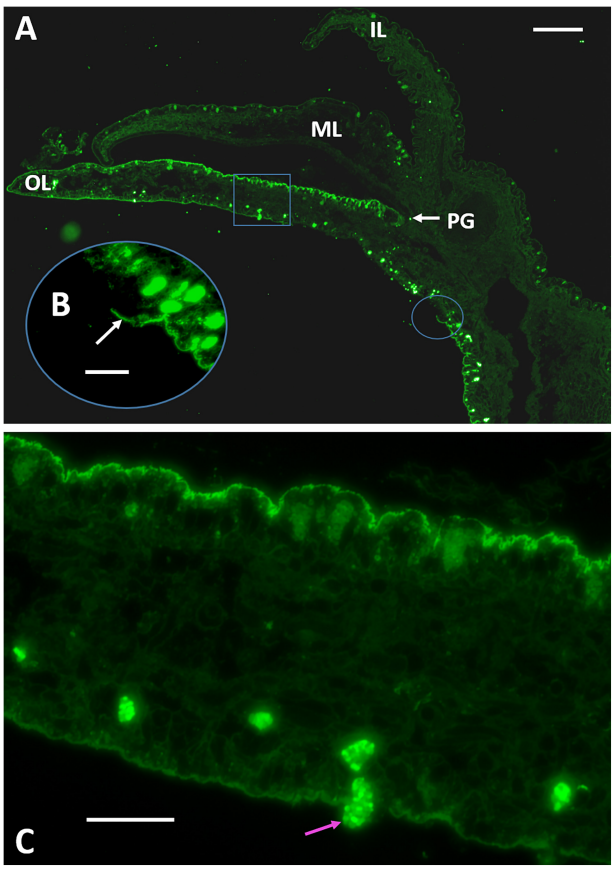

FIGURE 6 | Immuno-fluorescence microscopy of transverse sections of the mantle organ using an anti-48 kDa affinity purified antibody. **(A)** The mantle edge elaborates into three lobes; the inner lobe (IL) faces the body of the animal and the outer lobe **(**OL**)** faces the shell and joins to the middle lobe **(**ML**)** at its base. The space between the OL and ML is termed the periostracal groove. Folian-positive material localizes along the outer lobe epithelium. Scale bar 125 μm. **(B)** Oval inset indicated in **(A)** showing the sheet-like character of the folian material where it is broken and lifted from the epithelium surface (white arrow). Scale bar 40 μm. **(C)** Square inset indicated in **(A)** showing folian positive hemocytes regularly spaced along the length and near the surface of the outer lobe on the shell-facing side. A folian-positive hemocyte is shown moving through the epithelium into the extrapallial cavity (pink arrow). Scale bar 40 μm. Micrograph in **(A)** without insets from Johnstone et al. (2008).

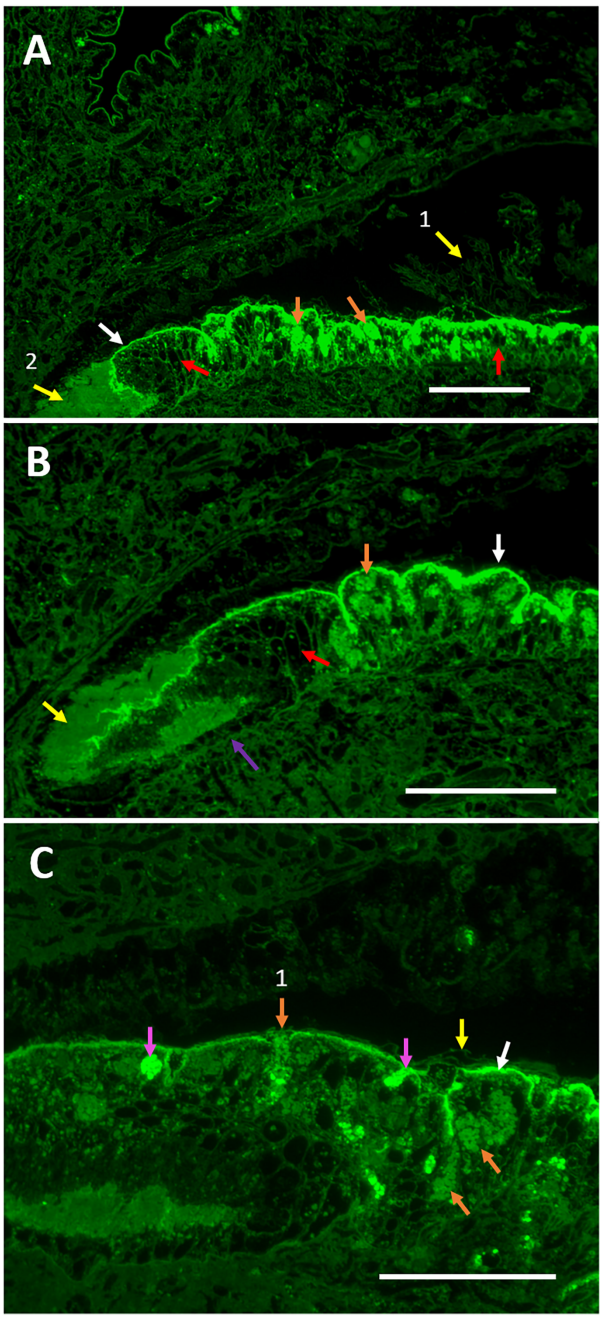

FIGURE 7 | Folian immuno-reactivity in the periostracal groove region between the outer and middle mantle lobes. **(A)** Intensely staining folian-positive material localizes along the surface of the outer lobe epithelium (white arrow) along with but separate from a different material presumed to be periostracal material (yellow arrow 1). It is presumed that the material at the very base of the groove is periostracal material that collected there and is moved distally to the shell edge during shell formation (yellow arrow 2). Numerous folian-positive secretory cells (orange arrows) are visible and interspersed with non-staining cells which appear black (red arrows). Scale bar 140 μm. **(B)** Increased magnification shows the groove appears to be lined with simple cuboidal cells (purple arrow) adjacent to the non-staining secretory cells evident on the distal end of the groove (red arrow). At this lower saturation, folian-positive granules are visible (orange arrow) within cells.

(Continued)

asp content, is distinct from the composition of the 48-kDa band. This observation suggests that there are other proteins in this band, especially those that are high in glycine. Further evidence for other proteins co-migrating with folian-cv1 come from mass spectroscopy results in Johnstone et al. (2008), who revealed specific sequences from the 48 kDa band that are not present in folian-cv1. Additional diversity of folian proteins was evident in this study, as other electrophoretic bands were identified by Western analysis or staining for phosphoprotein and carbohydrate. In the latter case, it was evident that the level of glycosylation varied from band to band.

The complexity of the phosphoprotein components of *C. virginica* foliated shell has been documented extensively

FIGURE 7 | Continued
Periostracal material (yellow arrow) and folian-positive material (white arrow) are evident. Scale bar 120 μm. **(C)** Additional magnification shows intensely folian-positive cells (pink arrows), possibly hemocytes, which appear to be moving through the epithelium. Secretory cells containing folian-positive granules are visible (orange arrows), one of which appears to be actively secreting product (orange arrow 1). Periostracal material (yellow arrow) is distinct from folian-positive material and appears to float above the folian sheet (white arrow). Scale bar 70 μm.

in earlier studies. For example, the principal component of the EDTA-insoluble extracellular foliated shell matrix is a hydrogel-forming aspartate-, glycine-, and phosphoserine-rich complex (Rusenko, 1988; Wheeler, 1992b; Wheeler and Koskan, 1993; see also **Table 1**) whose water absorption capacity is similar to that of commercial superabsorbents (Mount, 1999). Based on gel permeation studies, the whole EDTA-soluble extract has components that range from approximately 15–20,000 kDa (Rusenko et al., 1991). The various broad molecular weight classes have amino acid compositions nearly identical to each other (Wheeler et al., 1988) and to that reported herein for the whole soluble matrix fraction. Sub-fractionation of the lower molecular class (∼15–600 kDa) by reverse phase HPLC yields two classes of protein, with the principal one being very hydrophilic (RP-1) and having a composition and level of phosphorylation nearly identical to the extracted matrix fractions described in this study (Rusenko et al., 1991). Using chemical degradation analyses, Rusenko et al. (1991) and Donachy et al. (1992) demonstrated that RP-1 and other matrix fractions have runs of aspartic acid much like folian-cv1.

While the origin of the complexity of the folian family of phosphoproteins is not known, prior to acquiring their final form in the shell, matrix proteins may sustain significant post-translational processing. For example, crosslinking of lower molecular weight proteins into the higher molecular weight and insoluble fractions seems likely. The chemical origin of any cross-links of this matrix remains subject to speculation (Wheeler et al., 1988). Comparable to *C. virginica*, Samata et al. (2008) also reported a gel-like insoluble matrix from the shell of the Iwagaki oyster, *Crassostrea nippona*. This complex was rendered largely soluble by reducing disulfide linkages, yielding what appears to be a single electrophoretic band of 52 kDa. These observations led the authors to deduce that the matrix could be largely a polymer of this solubilized protein. In contrast, Mount (1999) was able to render soluble only a small percentage of *C. viginica* insoluble matrix with reduction of these linkages. This is consistent with analyses which show that matrix protein fractions of *C. virginica* either have considerably lower or, in some studies including the current one, undetectable levels of cys (Wheeler et al., 1988; Rusenko et al., 1991; Kawaguchi and Watabe, 1993). Further, the deduced sequence of folian-cv1 contains no cys.

Non-covalent bonds are another potential source of stabilization of matrix complexes. From the results of the urea extraction of insoluble matrix in this study, it appears that some of the soluble matrix proteins, and in particular those of the 55 kDa band, can be associated with the insoluble matrix in this way. However, these types of interactions do not account for the majority of the insoluble complex, as Mount (1999) showed that only a few percent of the *C. virginica* insoluble matrix was rendered soluble when treated with chaotropic agents such as urea and SDS. Interestingly, Kawaguchi and Watabe (1993) were able to solubilize much of this matrix with acetone, suggesting the involvement of lipids or perhaps highly hydrophobic regions of the protein in stabilizing the gel.

In addition to cross-linking, post-translation heterogeneity of folian proteins could result from proteolytic cleavage or processing steps at the gene level, such as exon shuffling and gene duplication, recruitment and replication, and slippage (Kocot et al., 2016; Jackson et al., 2017). Some of these genetic processes may explain what appears to be the insertion of significant gly-rich regions into many of the folian proteins and the variants of folian-cv1 from the two populations of oysters as identified in this study.

An overarching question about shell proteins is to what extent their properties are consistent for species that from the same microstructure. In this regard, a comparative analysis of the composition and structure of proteins from foliated structures can be found in the **Supplementary Discussion** and **Supplementary Tables 2, 3**. What is perhaps among the most noteworthy of the similarities among these foliated proteins is their high theoretical or actual levels of phosphorylation (Borbas et al., 1991; Sarashina and Endo, 1998, 2001; Johnstone, 2008; Samata et al., 2008; **Table 1** and **Supplementary Table 3**). As the highly phosphorylated matrix proteins described in these various studies come from species that fall within the same order (Ostreoida), it is tempting to speculate that phosphorylation could represent the preservation of an ancestral property necessary for production of the foliated microstructure in this taxon.

It is not known with any certainty what specific role these phosphoproteins have in directing the formation of folia, but there efficacy in controlling mineral growth *in vitro* has been established. Most models of crystal regulation have some direct interaction between matrix proteins and forming mineral. In this context, it has been demonstrated repeatedly that soluble matrix proteins, like most polyanions, can bind to crystals and their nuclei thereby inhibiting their growth (e.g., Wheeler et al., 1991). Using *in vitro* crystal growth assays, Borbas et al. (1991) have shown that highly phosphorylated foliated matrices are better inhibitors of calcite growth than less phosphorylated matrices from other microstructures or dephosphorylated *C. virginica* matrix. Further, the addition of even a single phosphoserine to a polyaspartate molecule greatly increases its capacity to inhibit calcite nucleation (Sikes et al., 1991). Recently, Du et al. (2018) demonstrated that an anti-phosphoserine/threonine/tyrosine antibody injected into the extrapallial cavity of *Pinctada fucata* effected abnormal prismatic and nacreous layer formation. Further, the authors showed that enzymatic dephoshorylation of matrix proteins reduced their *in vitro* efficacy for inhibiting calcite growth, modifying calcite crystal morphology and occlusion in growing calcite crystals. It should be noted that the proteins from the shell layers of *P. fucata* are moderately phosphorylated compared

to those from foliated shell, suggesting that phosphorylation of *C. virginica* shell proteins would be equally, if not more critical for regulating shell formation in this latter species.

In addition to phosphorylation, the primary sequences of oyster folian proteins, in particular their polyaspartate regions, would clearly have an impact on crystal growth regulation. This was demonstrated in a study of direct crystal binding as correlated with inhibition of calcite crystal growth by the oyster folian reverse phase fraction RP-1 and synthetic peptides (Wheeler et al., 1991). Of all the synthetic peptides tested, polyaspartate could bind to the most sites on crystals and resulted in complete inhibition of crystal growth, whereas peptides with combinations of ser and gly inserted between aspartic acids reduced their binding capacity on the crystals with the same fractional loss of inhibitory activity. Like polyaspartate, RP-1 could render complete inhibition of calcite growth when bound at the capacity of the crystals for the protein. However, it had a higher affinity and lower capacity than the polyaspartate, indicating multiple binding sites and, because of its molecular size, coverage of multiple growth sites. It is not immediately obvious what, if any, role the relatively hydrophobic N-terminus of folian-cv1 might be in the control of crystal growth. However, Sikes et al. (1991) demonstrated that the addition of hydrophobic tails to polyaspartate enhanced its ability to inhibit nucleation, presumably by creating a diffusion barrier for the lattice ions to the surface of the forming crystal.

An often-cited role for matrix-biomineral interaction is the control of crystal morphology (Addadi and Weiner, 1989). One reason this function has been promoted results from the presence of crystal faces in shell mineral atypical of inorganically grown calcite, including those of foliar laths (e.g., Checa et al., 2007). In fact, matrix soluble proteins from other microstructures operating from solution can specifically affect crystal morphology and mineralogy (Berman et al., 1988; Belcher et al., 1996). However, Berman et al. (1988) and Addadi and Weiner (1989) pointed out that highly anionic molluscan soluble proteins similar to folian-cv1 are typically adsorbed non-specifically to crystal surfaces. Such non-specific binding could lead to the steps on calcite crystals observed by Wheeler and Sikes (1984) when they were grown in the presence of soluble matrix from *C. virginica.* Nevertheless, Sikes and Wierzbicki (1995) provided evidence that oyster folian RP-1 proteins selectively adsorbed to these steps, forming crystallographic faces arguably like those found on the surface of folia. Samata et al. (2008) has also shown changes in morphology of crystals grown *in vitro* with the *C. nippona* protein solubilized from insoluble matrix. Under select media conditions, structures that resemble foliar laths were observed in their assays.

In addition to operating from solution, earlier models suggest that insoluble proteins form a framework to which crystal growth-controlling anionic proteins attach (e.g., Weiner et al., 1983). In fact, soluble proteins when immobilized *in vitro* are capable of producing crystal morphologies representative of those that grow *in vivo* (Belcher et al., 1996; Falini et al., 1996). The association of soluble proteins with insoluble matrix in oyster is suggested by the release of the 55 kDa protein from the insoluble phase with urea and the 48 kDa antibody-reactive sheet discussed below.

Calcium binding by matrix proteins has often been invoked as playing a role in the formation of biomineral. The sequence of folian-cv1 contains no high affinity binding sites for calcium such as might be found in some intracellular calcium-binding proteins. However, its polyanionic structure, especially due to runs of aspartic acid, is likely conducive to low affinity high capacity calcium binding typical of weak carboxylic acids (Williams, 1980), including some asp-rich proteins, such as the sarcoplasmic reticulum calcium-reservoir protein calsequestrin (Milner et al., 1992; Shin et al., 2000; Beard et al., 2004). Citing domains similar to calsequestrin, Gotliv et al. (2005) postulate calcium binding for asprich, a matrix protein from the calcitic prismatic layer of *Atrina rigida.* Such binding by matrix proteins has been invoked specifically in the process of inducing nucleation and oriented crystal growth in molluscs (e.g., Crenshaw, 1972b; Greenfield et al., 1984; Addadi and Weiner, 1985, 1989). The role of calcium binding in these processes was called into question by Wheeler et al. (1987), who demonstrated that much of the calcium binding in EDTA-extracted matrices was due to residual chelating agent. This finding is supported by chemical and histological observations of matrix preparations (Wada, 1980; Samata and Matsuda, 1986; Pereira-Mouriès et al., 2002; Nudelman et al., 2006). In addition, even the high capacity, low affinity binding of EDTA-free oyster soluble matrix protein was nearly eliminated at the ionic strength equivalent of that of seawater or the extrapallial fluid (Wheeler et al., 1987). EDTA-free oyster insoluble matrix also showed little calcium binding in high ionic strength solutions (Mount, 1999). It should be noted that binding studies conducted *in vitro* may not represent conditions in mineralizing compartments, including those created by matrix, the mantle epithelium or in vesicles. In this context, Crenshaw (1972a) identified some non-dialyzable calcium when extrapallial fluid was dialyzed against seawater, suggesting that proteins in this mineralization compartment retained some calcium binding activity.

Higher order structures of matrix proteins may have functional significance as well. For example, Addadi and Weiner (1989) provide models, based on crystal growth assays, that support the idea that polyanionic β-pleated sheets would present the optimal stereochemical configuration of protein carboxylate groups to stabilize growth axes and crystal surfaces that are typical of molluscan biominerals. The β configuration for both insoluble matrix (immobilized with and without fixation of the soluble components) and soluble matrix proteins upon binding calcium is supported by X-ray and FTIR analyses, including in some cases matrix from the genus Crassostrea (Weiner and Traub, 1980; Wourms and Weiner, 1986). Lee and Choi (2007) further demonstrated significant β structure in *C. gigas* soluble matrix using circular dichroism analyses.

Predictions of secondary structure for folian-cv1 using the algorithms PSIPRED, http://bioinf.cs.ucl.ac.uk/psipred (Buchan et al., 2013; Jones, 1999), MESSA, http://prodata.swmed.edu/MESSA/ (Cong and Grishin, 2012), APSSP2, http://crdd.osdd.net (Raghava, 2000), CFSSP, http://www.biogem.org/tool

(Chou and Fasman, 1974, 1978; Ashok Kumar, 2013), revealed that there was a high probability that either all or the majority of this protein was a random coil, especially in the asp-ser-rich region. Any exceptions to the random coil structure revealed by these programs occurred in the hydrophobic or glu-rich regions near the N-terminus. Not unexpected by the low complexity, random coil characteristics of folian-cv1, PSIPRED predicts that the vast majority of the structure has a very high probability of intrinsic disorder. Some of the work cited above suggests that the flexibility that comes with disorder might result in induced structures depending on such factors as whether or not the protein is immobilized to insoluble components, is calcium loaded or is interacting with crystals. As an example of an induced secondary structure, the longer runs of aspartic acid may take on β-sheet-like configurations when binding to crystals, as suggested in models and AFM observations for polyaspartate by Sikes and Wierzbicki (1995).

Specialized sequences have been identified in matrix proteins, which may be significant for their higher order structure and function. For example, using various modeling programs, Evans (2012) has revealed cross-β aggregation regions for numerous nacre matrix proteins that could function in the aggregation of matrix proteins. However, using TANGO algorithms, http://tango.crg.es/about.jsp (Linding et al., 2004), no such aggregation regions were identified for folian-cv1. In addition, loop structures have been predicted for much of MPP1 (Samata et al., 2008). These correspond to the phosphorylated SG domains with DE domain inserts. These sequences together would give a regular pattern of the phosphate and carboxylate anions, which the authors suggest could participate in crystal nucleation. This arrangement would appear not applicable to folian-cv1, as the serine in folian-cv1 is not in domains of SG. Glycine loops have also been predicted for Lustrin (Jackson et al., 2017) in which GS rich domains are interspersed with aromatic domains. The authors suggest such loops contribute to the elastic properties of matrix. Again, neither of these regions exist for folian-cv1. Despite lacking the loop forming characteristics described for MPP1 and Lustrin, CFSSP evaluation predicts that the sequence of folian-cv1 is in fact punctuated at irregular intervals with turns. However, any significance for such structures would be hard to predict.

Although from the earlier sections in this discussion it can be concluded that the biochemical relationship and higher structural order of the folian components of *C. virginica* remain unresolved, the immuno-histological studies presented herein suggest that at least some of the soluble matrix components are included in a cohesive sheet-like structure upon secretion. This extracellular structure is present throughout the region of the mantle that would interface with forming mineral. An association of soluble components with more insoluble ones is consistent with the immuno-histochemical studies of Kawaguchi and Watabe (1993) who showed binding of soluble components to an insoluble matrix in *C. virginica* shell.

In TEM studies of nacre, the formation of interlamellar sheets is quite evident (Bevelander and Nakahara, 1969; Nakahara et al., 1980) and these authors consider them as significant in defining the limits or compartments of crystal growth. Hydrophobic (silk, fibroin-like) insoluble matrix of nacre appears to be gel-like and is hypothesized to be displaced from the compartments into the intercrystalline matrix by growing crystals (Nudelman et al., 2008). These authors envision the gel as containing acidic proteins which inhibit nucleation events in the general matrix compartment, confining crystal nucleation to specific sites that have been identified on the interlamellar matrix (Crenshaw and Ristedt, 1976; Nudelman et al., 2006).

In earlier TEM studies, Watabe (1965) also described interlamellar sheets for nacre, but he did not identify such sheets in the lamellae of the foliated layer of *C. virginica*. It is possible that any sheets in the foliated lamellae of the oyster do not remain identifiable as such once they are included into mineral layers. Accordingly, what may represent an alternate final arrangement of the secreted matrix was suggested by Sikes et al. (1998) from AFM studies on what would be interlamellar surfaces of isolated pieces of folia. The authors revealed extensive globular structures on this surface that contained both mineral, and, based on their sensitivity to proteolysis and reactivity to an anti-folian (48 kDa) antibody, they contained matrix protein as well (Sikes et al., 1998).

Watabe (1965) did identify a thinner intercrystalline matrix that surrounds the individual folia and Kawaguchi and Watabe (1993) argued that soluble proteins are attached to this matrix in a way that brings them in contact with crystals. In contrast to nacre, there is no evidence of silk-like proteins in the *C. gigas* transcriptome (Zhang et al., 2012). However, as mentioned above, the insoluble folian matrix of *C. virginica* is in fact a gel-forming material. The gel-forming properties of oyster insoluble matrix combined with the proposed association of soluble proteins with the insoluble matrix may be analogous to and have a similar inhibitory function as described above for nacre. Consistent with this inhibitory hypothesis, isolated insoluble matrix gel from *C. virginica* does not lower the supersaturation required for nucleation *in vitro* (Mount, 1999). Also, crystal growth does not occur readily on the surface of foliated shell pieces with matrix intact compared to the facile nucleation that occurs on these surfaces from which the matrix was removed (Sikes et al., 2000).

Using the results of cryo-transmission electron microsocopy, Levi-Kalisman et al. (2001) postulate that the interlamellar sheets of nacre are made up largely of chitin, which is perhaps associated with acidic proteins. In contrast to this hypothesis, using multiple analytical techniques, Agbaje et al. (2018) were unable to demonstrate significant chitin in nacre or other microstructures, but they did not include shells with foliated microstructures in their study. Indirect evidence exists that chitin is present in this microstructure. For example, Chan et al. (2018), using chitin-specific probes, has demonstrated chitin associated with shell regeneration in *C. virginica*, and in particular with hemocytes involved in this process. Further, among all *C. gigas* tissues, chitin synthase is almost exclusively expressed in mantle, and chitin-binding domains are enriched in shell proteins (Zhang et al., 2012). As yet, no chitin-binding domains have been identified in the folian proteins and are not present in folian-cv1.

From this study, it is evident that the cells involved in the production of the antibody-positive sheet material by the outer mantle epithelium are a fraction of the pseudostratified

secretory cells of this mantle region. In TEM studies, Myers et al. (2007) have shown that a class of folian-producing cells are in fact morphologically distinct from the many other secretory cells in this region and have confirmed that they produce folian using the traditional membrane-associated pathway for a secretory protein. As discussed earlier, it is evident that the mineralizing matrix is a complex of proteins, making it possible that they are likely assembled in a variety of cellular and extracellular sites. To this point, Kawaguchi and Watabe (1993) have shown that various oyster matrix proteins are synthesized separately and then assembled either in secretory vesicles or at the mineralization front.

Consistent with earlier studies (Johnstone et al., 2008), the immuno-cytochemistry along with the quantitative PCR results of this study confirm that folian proteins, and specifically folian-cv1, are synthesized within hemocytes, a class of cells that function in non-specific immunity. The granulocytic sub-set of these cells have been shown to function in *C. virginica* shell formation during experimental induced regeneration of shell by delivering crystals to the mineralization front (Mount et al., 2004). Further, hemocytes participate in mineral formation on implants placed between the outer mantle epithelium and the shell of this oyster (Johnstone et al., 2015). Hemocytes have been shown to be active in shell regeneration of other molluscs as well (e.g., Kádár, 2008; Cho et al., 2011; Li et al., 2016). Further, Huang et al. (2018) have demonstrated the presence of hemocytes with calcium-rich vesicles and crystals in the extrapallial cavity during normal shell formation of *Pinctada fucata*. Although, in this latter study most shell matrix proteins were not shown to be expressed in hemocytes, Ivanina et al. (2017) have isolated classes of hemocytes from *C. gigas* that are distinct from the immune response cells and which express genes for both lattice ion transport and shell extracellular matrix production. Of interest in this regard, Patel (2004) has demonstrated that hemocytes from *C. virginica* release collagen along with folian *in vitro*. In fact, collagen fibers have been identified on newly regenerated oyster shell (unpublished observations) and a proteomic analysis of *C. gigas* shell matrix, Zhang et al. (2012) showed that collagen was identified in shell along with other extracellular matrix proteins. As mentioned above, Chan et al. (2018) has demonstrated that hemocytes from *C. virginica* produce chitin that appears to be involved in shell mineralization.

From the current study, immune-reactive hemocytes appear to move directly from the blood across mantle epithelium into the area of shell layer formation. This movement across the epithelium was described for *C. virginica* by Galstoff (1964), who used the term diapedesis, implying an analogy to the process of extravasation of leukocytes across blood vessels in vertebrates as part of their immune response. Whether hemocyte movement involves the complex steps found in this immune response is not clear at this time. The results of this study demonstrate channels through which the hemocytes appear to move, suggesting that the process of their passage might be relatively passive. Johnstone et al. (2015) present SEM images of the surface of the outer mantle facing the edge of the shell that appears to be punctuated regularly with pores. The number of these putative pores is greatest at the edge, where the rate of shell formation is the highest, and decreases markedly away from the edge in areas where the rate of shell formation is less. Alternatively, Li et al. (2016) described the hemocyte movement during shell regeneration in the pearl oyster, *P. fucata*, as a release from secretory cavities. Earlier, Neff (1972a) showed hemocytes with calcium-rich granules positioned under the outer mantle epithelium of the quahog, *Mercenaria mercenaria,* and speculated that the cells delivered these granules to the mantle via the intercellular space. He further speculated that the granules were matrix protein-calcium complexes. Hemocyte mobilization toward the mineralization front may account for the decrease in folian levels observed in these cells collected from the adductor muscle during experimentally induced shell regeneration (Johnstone et al., 2008). That is, the folian-loaded cells may be selectively recruited to the mineralization front by factors yet unknown, thereby depleting this class of cells in other tissues. Once there, they can aggregate on the substrate in a process that resembles wound healing (Johnstone et al., 2008). In fact, hemocytes were shown to be aligned with matrix fibers during shell regeneration (Mount et al., 2004) suggesting these structures provide recognition or binding sites for the cells.

Beyond the outer mantle epithelium and hemocytes, folian proteins are expressed on the inner mantle epithelium of oyster (Myers et al., 2007) and in a number of other tissues as well (Johnstone et al., 2015), suggesting the possibility that other tissues are involved in the production of shell proteins. Wang et al. (2013) suggests that such proteins could be delivered from tissues to the mineralization front by hemocytes, which, as mentioned above, are present at the sites of shell mineralization. Alternatively, these proteins might have functions that are not directly related to interactions with shell mineral. As an example, bone morphogenic proteins, regulators of orthotopic bone formation, are also present at the sites of vascular calcification (Hruska et al., 2005). Alternatively, rather than promoting mineralization, perhaps folian proteins in these non-shell forming tissues simply prevent ectopic calcification.

CONCLUSION AND PROSPECTUS

Folian-cv1 is a deduced highly acidic phosphoprotein protein from the foliated shell microstructure of the oyster *Crassostrea virginica.* Its relationship to the apparent myriad of other foliated shell phosphoproteins found in this species (folian family) is unknown and will require detailed biochemical and molecular biological analysis. Of especial interest in this regard is the relatively high glycine content of the general folian class compared to folian-cv1, a situation that poises a genetic dilemma at this time. Nonetheless, the cross reactivity of folian antibodies suggest that the members of the folian family have epitopes in common and thus are related on some level. Folian-cv1 has minimal, if any, identifiable higher order structure, has no known functional domains and is intrinsically disordered. Disorder may be of value if the protein needs to conform to crystal or macromolecular surfaces. Although its specific functions are unknown, because it was deduced from a shell protein and is expressed in mantle, it seems likely that it plays a direct role in

shell formation. Given its primary structure and composition, it is likely to have the capacity for crystal growth regulation. Further implicating this class in shell formation, folian proteins are clearly secreted by the shell-forming epithelia, forming a sheet-like structure on their surface. Folian-cv1 is also expressed in hemocytes, expanding the idea that these cells are directly involved in shell formation. It appears that they carry folian proteins through mantle epithelial pores from the hemolymph to the site of mineral formation. More indirect involvement of folian proteins in shell formation or their involvement in non-shell forming process cannot be ruled out at this time. An understanding of folian-cv1 function may be advanced through the use of antibodies made to a recombinant protein in order to localize this protein in shell, cells and secretory products. Also, the change of expression during larval development, especially during the transition from aragonite to calcite shell, and following induced shell repair may provide functional insights, especially if studied in combination with knock-down studies. While folian-cv1 is unique, other bivalves that secrete the foliated microstructure have genes for phosphoproteins which appear to be homologous to varying degrees. A more thorough study of folian-type proteins from a range of species in the order Ostreoida may provide insight into their functions, the origins and expansion of the foliated microstructure and the reasons why this class of proteins is not more rigidly conserved.

DATA AVAILABILITY

The datasets generated for this study can be found in GenBank, with the following accession numbers: Folian cv-1, variant 1: MN108493, Folian cv-1 variant 2: MN108494.

AUTHOR CONTRIBUTIONS

MJ contributed to the data acquisition and analysis, drafting the manuscript, major editing, and critical review. AW contributed to the data analysis, drafting the manuscript, major editing, and critical review. EF, CS, and AM contributed to the data acquisition and analysis, narrative contribution, and critical review. MS contributed to the data acquisition and analysis, narrative contribution, and review. All authors read and approved the final manuscript.

FUNDING

This study was supported by the South Carolina Sea Grant Consortium and the United States Airforce Office of Scientific Research project # AFOSR-AF29550-06-1-0133.

ACKNOWLEDGMENTS

We extend our gratitude to Marta Gomez-Chirarri for her contribution of MMP data and her expertise in the *Crassostrea virginica* genome and to Jan Lay from the Clemson Computing and Information Technologies and Vera Chan for their help with image layout and quality.

SUPPLEMENTARY MATERIAL

The Supplementary Material for this article can be found online at: https://www.frontiersin.org/articles/10.3389/fmars.2019.00366/full#supplementary-material

REFERENCES

Addadi, L., and Weiner, S. (1985). Interactions between acidic proteins and crystals: Stereochemical requirements in biomineralization. *Proc. Nat. Acad. Sci. U.S.A.* 82, 4110–4114. doi: 10.1073/pnas.82.12.4110

Addadi, L., and Weiner, S. (1989). "Stereochemical and structural relations between macromolecules and crystals in biomineralization," in *Biomineralization: Chemical and Biochemical Perspectives*, eds S. Mann, J. Webb, and R. J. P. Williams (Weinheim, FRG: VCH Publishers), 133–156.

Addadi, L., and Weiner, S. (2014). Biomineralization: mineral formation by organisms. *Phys. Scr.* 89:098003. doi: 10.1088/0031-8949/89/9/098003

Agbaje, O. B. A., Ben Shir, I., Zax, D. B., Schmidt, A., and Jacob, D. E. (2018). Biomacromolecules within bivalve shells: is chitin abundant? *Acta Biomater.* 80, 176–187. doi: 10.1016/j.actbio.2018.09.009

Aguilera, F., McDougall, C., and Degnan, B. (2017). Co-option and de novo gene evolution underlie molluscan shell diversity. *Mol. Biol. Evol.* 34, 799–792. doi: 10.1093/molbev/msw294

Altschul, S. F., Gish, W., Miller, W., Myers, E. W., and Lipman, D. J. (1990). Basic local alignment search tool. *J. Mol. Biol.* 215, 403–410. doi: 10.1016/S0022-2836(05)80360-2

Ashok Kumar, T. (2013). CFSSP: chou and fasman secondary structure prediction server. *Wide Spectr.* 1, 15–19. doi: 10.5281/zenodo.50733

Beard, N. A., Laver, D. R., and Dulhunty, A. F. (2004). Calsequestrin and the calcium release channel of skeletal and cardiac muscle. *Prog. Biophys. Mol. Biol.* 85, 33–69. doi: 10.1016/j.piomolbio.2003.07.001

Belcher, A. M., Wu, X. H., Christensen, R. J., Hansma, P. K., Stucky, G. D., and Morse, D. E. (1996). Control of crystal phase switching and orientation by soluble mollusk-shell proteins. *Nature* 381, 56–58. doi: 10.1038/381056a0

Berman, A., Addadi, L., and Weiner, S. (1988). Interactions of sea-urchin skeleton macromolecules with growing calcite crystals-a study of intracrystalline proteins. *Nature* 331, 546–548. doi: 10.1038/331546a0

Bevelander, G., and Nakahara, H. (1969). An electron microscope study of the formation of the nacreous layer in the shell of certain bivalve molluscs. *Calc. Tiss. Res. Int.* 3, 84–92. doi: 10.1007/BF02058648

Bonnans, C., Chou, J., and Werb, Z. (2014). Remodeling the extracellular matrix in development and disease. *Nat. Rev. Mol. Cell. Biol.* 15, 786–801. doi: 10.1038/nrm3904

Borbas, J. E., Wheeler, A. P., and Sikes, C. S. (1991). Molluscan shell matrix phosphoproteins: correlation of degree of phosphorylation to shell mineral microstructure and to in vitro regulation of mineralization. *J. Exp. Zool.* 258, 1–13. doi: 10.1002/jez.1402580102

Brown, T. (1999). Analysis of DNA sequences by blotting and hybridization. *Curr. Protoc. Mol. Biol.* 9, 1–20.

Buchan, D. W. A., Minneci, F., Nugent, T. C. O., Bryson, K., and Jones, D. T. (2013). Scalable web services for the PSIPRED protein analysis workbench. *Nucl. Acids Res.* 41, 340–348. doi: 10.1093/nar/gkt381

Burge, C., and Karlin, S. (1997). Prediction of complete gene structures in human genomic DNA. *J. Mol. Biol.* 268, 78–94. doi: 10.1006/jmbi.1997.0951

Campbell, K. P., MacLennan, D. H., and Jorgensen, A. O. (1983). Staining for the Ca2+-binding proteins, calsequestrin, calmodulin, troponin C, and S-100, with the carbocyanine dye "Stains-all". *J. Biol. Chem.* 258, 11267–11273.

Carter, J. G. (1980). "Selected mineralogical data for the bivalvia," in *Skeletal Growth of Aquatic Organisms: Biological Records of Environmental Change*, eds D. C. Rhoads and R. A. Lutz (New York, NY: Plenum Press), 627–643.

Carter, J. G., and Clark, G. R. (1985). "Classification and phylogenetic significance of molluscan shell microstructure," in *Mollusks: Notes for a Short Course*, ed. T. W. Broadhead (Knoxville TN: Univ. of Tennessee, Dept. of Geological Studies, Studies in Geology).

Chan, V. B. S., Johnstone, M. B., Wheeler, A. P., and Mount, A. S. (2018). Chitin facilitated mineralization in the Eastern oyster. *Front. Mar. Sci.* 5:347. doi: 10.33891/fmars.2018.00347

Checa, A. (2000). A new model for periostracum and shell formation in Unionidae (Bivalvia, Mollusca). *Tissue Cell* 32, 405–416. doi: 10.1054/tice.2000.0129

Checa, A. G., Esteban-Delgado, F. J., and Rodríquez-Navarro, A. B. (2007). Crystallographic structure of the foliated calcite of bivalves. *J. Struct. Biol.* 157, 393–402. doi: 10.1016/j.jsb.2006.09.005

Cho, S. M., Lee, Y. M., and Jeong, W. G. (2011). Effect of polycyclic aromatic hydrocarbon (PAH) on shell repair in the Pacific Oyster, *Crassostrea gigas*. *Korean J. Malacol.* 27, 35–42. doi: 10.9710/kjm.2011.27.1.035

Chou, P. Y., and Fasman, G. D. (1974). Prediction of protein conformation. *Biochemistry* 13, 222–245. doi: 10.1021/bi00699a002

Chou, P. Y., and Fasman, G. D. (1978). Prediction of the secondary structure of proteins from their amino acid sequence. *Adv. Enzymol.* 47, 145–148.

Cong, Q., and Grishin, N. V. (2012). MESSA: Meta-server for protein sequence analysis. *BMC Biol.* 10:82. doi: 10.1186/1741-7007-10-82

Cornish-Bowden, A. (1983). Relating proteins by amino acid composition. *Meth. Enzymol.* 91, 60–75. doi: 10.1016/S0076-6879(83)91011-x

Crenshaw, M. A. (1972a). The inorganic composition of molluscan extrapallial fluid. *Biol. Bull.* 143, 506–512. doi: 10.2307/1540180

Crenshaw, M. A. (1972b). The soluble matrix from *Mercenaria mercenaria* shell. *Biomineralization* 6, 6–11.

Crenshaw, M. A., and Ristedt, H. (1976). "The histochemical localization of reactive groups in septal nacre from *Nautilus pompilius* L," in *The Mechanisms of Mineralization in the Invertebrates and Plants*, eds N. Watabe and K. M. Wilbur (Columbia, SC: University of South Carolina Press), 355–367.

Cunningham, C., Hikima, J., Jenny, M. J., Chapman, R. W., Fang, G. C., Saski, C., et al. (2006). New resources for marine genomics: bacterial artificial chromosome libraries for the Eastern and Pacific oysters (*Crassostrea virginica* and *C. gigas*). *Mar. Biotechnol.* 8, 521–533. doi: 10.1007/S10126-006-6013-9

Currey, J. D. (1999). The design of mineralized hard tissues for their mechanical functions. *J. Exp. Biol.* 202, 3285–3294.

Donachy, J. E., Drake, B., and Sikes, C. S. (1992). Sequence and atomic-force microscopy analysis of a matrix protein from the shell of the oyster *Crassostrea virginica*. *Mar. Biol.* 114, 423–428. doi: 10.1007/BF00350033

Du, J., Xu, G., Liu, C., and Zhang, R. (2018). The role of phosphorylation and dephosphorylation of shell matrix proteins in shell formation: an *in vivo* and *in vitro* study. *Crystal Eng. Comm.* 20, 3905–3916. doi: 10.1039/c8ce00755a

Ebel, A. E., and Scro, R. (1996). "General anatomy," in *The Eastern Oyster: Crassostrea virginica*, eds V. S. Kennedy, R. I. E. Newell, and A. F. Eble (College Park, MD: Maryland Sea Grant), 19–73.

Eisenreich, S. J., Bannerman, R. T., and Armstrong, D. E. (1975). A simplified phosphorus analysis technique. *Environ. Lett.* 9, 43–53. doi: 10.1080/00139307509437455

Esteban-Delgado, F. J., Harper, E. M., Checa, A. G., and Rodríguez-Navarro, A. B. (2008). Origin and expansion of foliated microstructure in pteriomorph bivalves. *Biol. Bull.* 214, 153–165. doi: 10.2307/25066672

Evans, J. S. (2012). Aragonite-associated biomineralization proteins are disordered and contain interactive motifs. *Bioinformatics* 28, 3182–3185. doi: 10.1093/bioinformatics/bts604

Falini, G., Albeck, S., Weiner, S., and Addadi, L. (1996). Control of aragonite or calcite polymorphism by mollusk shell macromolecules. *Science* 271, 67–69. doi: 10.1126/science.271.5245.67

Falwell, E. P. (2015). *The Role of Folian and Collagenases on Shell Repair in the Eastern oyster, Crassostrea virginica. Ph.D. dissertation*. Clemson: Virginia Polytechnic and State University.

Fauchére, J.-L., and Pliška, V. (1983). Hydrophobic parameters of amino-acid side chains from the partitioning of N-acetyl-amino-acid amines. *Eur. J. Med. Chem. Chim. Ther.* 18, 369–375.

Galstoff, P. S. (1964). *The American Oyster, Crassostrea virginica* (Gmelin). *Fishery Bulletin 64*. Washington, D.C: U. S. Fish and Wildlife Services.

Gomez-Chiarri, M., and McDonnell, W. W. (2017). *Crassostrea virginica sequence assembly Version 3.0*.

Gordon, D., Abajian, C., and Green, P. (1998). Consed: a graphical tool for sequence finishing. *Genome Res.* 8, 195–202. doi: 10.1101/gr.8.3.195

Gotliv, B. A., Kessler, N., Sumerel, J. L., Morse, D. E., Tuross, N., Addadi, L., et al. (2005). Asprich: a novel aspartic acid-rich protein family from the prismatic shell matrix of the bivalve *Atrina rigida*. *Chembiochem* 6, 304–318. doi: 10.1002/cbic.200400221

Greenfield, E. M., Wilson, D. C., and Crenshaw, M. (1984). Ionotropic nucleation of calcium carbonate by molluscan matrix. *Am. Zool.* 24, 925–932. doi: 10.1093/icb/24.4.925

Hruska, K. A., Suresh, M., and Saab, G. (2005). Bone morphogenetic proteins in vascular calcification. *Circ. Res.* 97, 105–114. doi: 10.1161/01.RES.0000017551.53833.6c

Huang, J., Li, S., Liu, Y., Liu, C., Xie, L., and Zhang, R. (2018). Hemocytes in the extrapallial space of *Pinctada fucata* are involved in immunity and biomineralization. *Sci. Rep.* 8:4657. doi: 10.1038/s41598-018-22961-y

Hüning, A. K., Lange, S. M., Ramesh, K., Jacob, D. E., Jackson, D. J., Panknin, U., et al. (2016). A shell regeneration assay to identify biomineralization candidate genes in mytilid mussels. *Mar. Genomics* 27, 57–67. doi: 10.1016/j.margen.2016.03.011

Ivanina, A. V., Falfushynska, H. I., Beniash, E., Piontkivska, H., and Sokolova, I. M. (2017). Biomineralization-related specialization of hemocytes and mantle tissues of the Pacific oysters *Crassostrea gigas*. *J. Exp. Biol.* 220, 3209–3221. doi: 10.1242/jeb.160861

Jackson, D. J., Reim, L., Randow, C., Cerveau, N., Degnan, B., and Fleck, C. (2017). Variation in orthologous shell-forming proteins contribute to molluscan shell diversity. *Mol. Biol. Evol.* 34, 2959–2969. doi: 10.1093/molbev/msx232

Jing, X., Espinosa, E. P., Perrigault, M., and Adam, B. (2011). Identification, molecular characterization and expression analysis of a mucosal C-type lectin in the eastern oyster, *Crassostrea virginica*. *Fish. Shellfish Immunol.* 30, 851–858. doi: 10.1016/j.fsi.2011.01.007

Johnstone, M. B. (2008). *A Comparative Study of Molluscan Shell Proteins With an Emphasis on the Structure of Two Phosphoproteins Derived From the Eastern Oyster, Crassostrea virginica*. Ph.D. dissertation, Clemson University, Clemson, SC.

Johnstone, M. B., Ellis, S., and Mount, A. S. (2008). Visualization of shell matrix proteins in hemocytes and tissues of the Eastern oyster. Crassostrea virginica. *J. Exper. Zool.* 310B, 227–239. doi: 10.1002/jez.b.21206

Johnstone, M. B., Gohad, N. V., Falwell, E. P., Hansen, D. C., Hansen, K. M., and Mount, A. S. (2015). Cellular orchestrated biomineralization of crystalline composites on implant surfaces by the eastern oyster, *Crassostrea virginica* (Gmelin, 1791). *J. Exp. Biol. Ecol.* 463, 8–16. doi: 10.1016/j.jembe.2014.10.014

Jones, D. T. (1999). Protein secondary structure prediction based on position-specific scoring matrices. *J. Mol. Biol.* 292, 195–202. doi: 10.1006/jmbi.1999.3091

Kádár, E. (2008). Hemocyte response associated with induction of shell regeneration in the deep-sea vent mussel *Bathymodiolus azoricus* (Bivalvia: Mytilidae). *J. Exp. Mar. Biol. Ecol.* 362, 71–78. doi: 10.1016/jembe.2008.05.014

Kawaguchi, T., and Watabe, N. (1993). The organic matrices of the shell of the American oyster *Crassostrea virginica* Gmelin. *J. Mar. Biol. Ecol.* 170, 11–28. doi: 10.1016/0022-0981(93)90126-9

Kocot, K. M., Aguilera, F., McDougall, C., Jackson, D. J., and Degnan, B. M. (2016). Seashell diversity and rapidly evolving secretomes: insights into the evolution of biomineralization. *Front. Zool.* 13:23. doi: 10.1186/s12983-016-0155-z

Lee, S. L., Veis, A., and Glonek, T. (1977). Dentin phosphoprotein: an extracellular calcium-binding protein. *Biochemistry* 16, 2971–2979. doi: 10.1021/bi00632a026

Lee, S. W., and Choi, S. C. (2007). The correlation between organic matrices and biominerals (myostracal prism and folia) of the adult oyster shell. *Crassostrea gigas*. *Micron* 38, 58–64. doi: 10.1016/j.micron.2006.03.018

Levi-Kalisman, Y., Falini, G., Addadi, L., and Weiner, S. (2001). Structure of the nacreous organic matrix of a bivalve mollusk shell examined in the hydrated state using cryo-TEM. *J. Struct. Biol.* 135, 8–17. doi: 10.1006/jsbi.2001.4372

Li, S., Liu, Y., Liu, C., Huang, J., Zheng, G., and Xie, L. (2016). Hemocytes participate in calcium carbonate crystal formation, transportation and shell

regeneration in the pearl oyster *Pinctada fucata*. *Fish Shellfish Immunol.* 51, 263–270. doi: 10.1016/j.fsi.2016.02.027

Linding, R., Schymkowitz, J., Rousseau, F., Diella, F., and Serrano, L. (2004). A comparative study of the relationship between protein structure and β-aggregation in globular and intrinsically disordered proteins. *J. Mol. Biol.* 342, 345–353. doi: 10.1016/j.jmb.2004.06.088

Lomsadze, A., Ter-Hovhannisyan, V., Chernoff, Y. O., and Borodovsky, M. (2005). Gene identification in novel eukaryotic genomes by self-training algorithm. *Nucleic Acids Res.* 33, 6494–6506. doi: 10.1093/nar/gki937

Lowenstam, H. A. (1981). Minerals formed by organisms. *Science* 211, 1125–1131. doi: 10.1126/science.7008198

Lowenstam, H. A., and Weiner, S. (1989). *On Biomineralization*. New York, NY: Oxford University Press.

Luke, G. H., and William, J. L. (2001). Inhibitors of procollagen C-terminal proteinase block gastrulation and spicule elongation in the sea urchin embryo. *Dev. Growth Diff.* 43, 415–424. doi: 10.1046/j.1440-169x2001.00589.x

Mann, S. (1988). Molecular recognition in biomineralization. *Nature* 332, 119–124. doi: 10.1038/332119a0

Marin, F., Luquet, G., Marie, B., and Medakovic, D. (2008). Molluscan shell proteins: primary structure, origin, and evolution. *Curr. Top. Dev. Biol.* 80, 209–276. doi: 10.1016/S0070-2153(07)80006-8

Milner, R. E., Famulski, K. S., and Michalak, M. (1992). Calcium binding proteins in the sarcoplasmic/endoplasmic reticulum of muscle and nonmuscle cells. *Mol. Cell. Biochem.* 112, 1–13. doi: 10.1007/BF00229637

Mount, A. S. (1999). *Nucleation of Calcite in the Eastern oyster, Crassostrea virginica: Biochemical and Functional Studies of the Organic Matrix From Foliated Shell*. Ph.D. dissertation, Clemson University, Clemson, SC.

Mount, A. S., Gohad, N. V., Hansen, D. C., Hansen, K. M., and Johnstone, M. B. (2016). *Deposition of Nanocrystalline Calcite on Surfaces by a Tissue and Cellular Biomineralization*. Available at: https://www.google.com/patents/US9371451 (accessed June 21, 2016).

Mount, A. S., Wheeler, A. P., Paradkar, R. P., and Snider, D. (2004). Hemocyte-mediated shell mineralization in the Eastern oyster. *Science* 304, 297–300. doi: 10.1126/science.1090506

Muller, P. Y., Janovjak, H., Miserez, A. R., and Dobbie, Z. (2002). Processing of gene expression data generated by quantitative real-time RT-PCR. *Biotechniques* 32, 1372–1374.

Myers, J. M. (1999). *Studies on the Secretory Epithelium of the Mantle From the Eastern oyster, Crassostrea virginica, in Relation to Shell Growth*. Ph.D. dissertation, Clemson University, Clemson, SC.

Myers, J. M., Johnstone, M. B., Mount, A. S., Silverman, H., and Wheeler, A. P. (2007). TEM immunocytochemistry of a 48 kDa MW organic matrix phosphoprotein produced in the mantle epithelial cells of the Eastern oyster (*Crassostrea virginica*). *Tissue Cell* 39, 247–256. doi: 10.1016/j/tice.2007.03.006

Myers, J. M., Veis, A., Sabsay, B., and Wheeler, A. P. (1996). A method for enhancing the sensitivity and stability of Stains-All for phosphoproteins separated in sodium dodecyl sulfate-polyacrylamide gels. *Anal. Biochem.* 240, 200–302. doi: 10.1006/abio.1996.0361

Nakahara, H., Kakei, M., and Bevelander, G. (1980). Fine structure and amino acid composition of the organic "envelope" in the prismatic layer of some bivalve shells. *Venus* 39, 167–177.

Neff, J. M. (1972a). Ultrastructure of the outer epithelium of the mantle in the clam *Mercenaria mercenaria*in relation to calcification of the shell. *Tissue Cell* 4, 591–600. doi: 10.1016/S0040-8166(72)80032-6

Neff, J. M. (1972b). Ultrastructure studies of periostracum formation in the hard shelled clam *Mercenaria mercenaria* (L). *Tissue Cell* 4, 311–326. doi: 10.1016/S0040-8166(72)80050-8

Nudelman, F., Gotliv, B. A., Addadi, L., and Weiner, S. (2006). Mollusk shell formation: Mapping the distribution of organic matrix components underlying a single aragonitic table in nacre. *J. Struct. Biol.* 153, 176–187. doi: 10.1016/j.jsb.2005.09.009

Nudelman, F., Shimoni, E., Klein, E., Rousseau, M., Bourrat, X., Lopez, E., et al. (2008). Forming nacreous layer of the shells of the bivalves *Atrina rigida* and *Pinctada margaritifera*: an environmental- and cryo-scanning electron microscopy study. *J. Struct. Biol.* 162, 290–300. doi: 10.1016/j.jsb.2008.01.008

Ortega, N., Behonick, D., Stickens, D., and Werb, Z. (2003). How proteases regulate bone morphogenesis. *Ann. N.Y. Acad. Sci.* 995, 109–116. doi: 10.1111/j.1749-6632.2003.tb03214.x

Patel, S. V. (2004). *A Novel Function of Invertebrate Collagen in the Biomineralization Process During the Shell Repair of Eastern oyster, Crassostrea virginica*. M.S. thesis, Clemson University, Clemson, SC.

Pereira-Mouriès, L., Almeida, M.-J., Ribeiro, C., Peduzzi, J., Barthélemy, M., Milet, C., et al. (2002). Soluble silk-like organic matrix in the nacreous layer of the bivalve *Pinctada maxima*. *Eur. J. Biochem.* 269, 4994–5003. doi: 10.1046/j.1432-1033.2002.03203.x

Raghava, G. P. S. (2000). Protein secondary structure prediction using nearest neighbor and neural network approach. *CASP* 4, 75–76.

Reese, M. G., Eeckman, F. H., Kulp, D., and Haussler, D. (1997). Improved splice site detection in Genie. *J. Comput. Biol.* 4, 311–323. doi: 10.1089/cmb.1997.4.311

Roling, J. A., Bain, L. J., and Baldwin, W. S. (2004). Differential gene expression in mummichogs (*Funulus heteroclitus)* following treatment with pyrene: comparison to a creosote contaminated site. *Mar. Environ. Res.* 57, 377–395. doi: 10.1016/j.marenvires.2003.11.001

Rozen, S., and Skaletsky, H. (2000). Primer3 on the WWW for general users and for biologist programmers. *Meth. Mol. Biol.* 132, 365–386. doi: 10.1385/1-59259-192-2:365

Rusenko, K. (1988). *Studies on the Structure and Function of the Shell Matrix Proteins from the American oyster, Crassostrea virginica*. Ph.D. dissertation, Clemson University, Clemson, SC.

Rusenko, K. W., Donachy, J. E., and Wheeler, A. P. (1991). "Purification and characterization of a shell matrix phosphoprotein from the American oyster," in *Surface Reactive Peptides and Polymers ACS Symposium Series 444*, eds C. S. Sikes and A. P. Wheeler (Washington, DC: ACS), 107–124. doi: 10.1021/bk-1991-0444.ch008

Saleuddin, A. S. M., and Petit, H. P. (1983). "The mode of formation and the structure of periostracum," in *The Mollusca*, Vol. 4, eds K. M. Wilbur and A. S. M. Saleuddin (New York: Academic Press), 199–234. doi: 10.1016/b978-0-12-751404-8.50013-x

Samata, T., Ikeda, D., Kajikawa, A., Sato, H., Nogawa, C., Yamada, D., et al. (2008). A novel phosphorylated glycoprotein in the shell matrix of the oyster *Crassostrea nippona*. *FEBS J.* 275, 2977–2989. doi: 10.1111/j.1742-4658.2008.06453.x

Samata, T., and Matsuda, M. (1986). Contaminating peptides widely present in ion-exchanged water, reagents, experimental implements and natural sample. *Comp. Biochem. Physiol.* 84B, 531–535. doi: 10.1016/0305-0491(86)90118-5

Sarashina, I., and Endo, K. (1998). Primary structure of a soluble matrix protein of the scallop shell: implications for calcium carbonate biomineralization. *Am. Mineral.* 83, 1510–1515. doi: 10.2138/am-1997-11-1239

Sarashina, I., and Endo, K. (2001). The complete primary structure of molluscan shell protein 1 (MSP-1), an acidic glycoprotein in the shell matrix of the scallop *Patinopecten yessoensis*. *Mar. Biotechnol.* 3, 362–369. doi: 10.1007/s10126-001-0013-6

Shin, D. W., Ma, J., and Kim, D. H. (2000). The *asp*-rich region of the carboxyl-terminus of calsequestrin binds to Ca2+ and interacts with triadin. *FEBS Lett.* 486, 178–182. doi: 10.1016/S0014-57193(00)02246-8

Sikes, C. S., Wheeler, A. P., Wierzbicki, A., Dillaman, R. M., and DeLuca, L. (1998). Oyster shell protein and atomic force microscopy of oyster shell folia. *Biol. Bull.* 194, 304–316. doi: 10.2307/1543100

Sikes, C. S., Wheeler, A. P., Wierzbicki, A., Mount, A. S., and Dillaman, R. M. (2000). Nucleation and growth of calcite on native *versus* pyrolyzed oyster shell folia. *Biol. Bull.* 198, 50–66. doi: 10.2307/1542803

Sikes, C. S., and Wierzbicki, A. (1995). "Mechanisms of regulation of crystal growth in selected biological systems," in *Mineral Scale Formation and Inhibition*, ed. Z. Amjad (New York, NY: Plenum Press), 183–206. doi: 10.1007/978-1-4899-1400-2_16

Sikes, C. S., Yeung, M. L., and Wheeler, A. P. (1991). "Inhibition of calcium carbonate and phosphate crystallization by peptides enriched in aspartic acid and phosphoserine," in *Surface Reactive Peptides and Polymers*, eds C. S. Sikes and A. P. Wheeler (Washington, DC: American Chemical Society), 72–84.

Simkiss, K., and Wilbur, K. M. (1989). *Biomineralization: Cell Biology and Mineral Deposition*. San Diego, CA: Academic Press.

Suzuki, M., Saruwatari, K., Kogure, T., Yamamoto, Y., Nishimura, T., Kato, T., et al. (2009). An acidic matrix protein, Pif, is a key macromolecule for nacre formation. *Science* 325, 1388–1390. doi: 10.1126/science.1173793

Wada, K. (1980). "Initiation of mineralization in bivalve molluscs," in *The Mechanisms of Biomineralization in Animals and Plants*, eds M. Omori and N. Watabe (Tokyo: Tokai University Press), 79–92.

Waite, J. H., and Benedict, C. V. (1984). Assay of dihydroxyphenylalanine (dopa) in invertebrate structural proteins. *Meth. Enzymol.* 107, 297–413. doi: 10.1016/0076-6879(84)07028-2

Wang, X., Li, L., Zhu, Y., Du, Y., Song, X., and Chen, Y. (2013). Oyster shell proteins originate from multiple organs and their probable transport pathway to the shell formation front. *PLoS One* 8:e66522. doi: 10.1371/journal.pone.0066522

Watabe, N. (1965). Studies on shell formation XI. Crystal-matrix interactions in the inner layer of mollusk shells. *J. Ultrastruct. Res.* 12, 351–370. doi: 10.1016/S0022-5320(65)80104-6

Weiner, S., and Dove, P. M. (2003). An overview of biomineralization processes and the problem of the vital effect. *Rev. Mineral. Geochem.* 54, 1–29. doi: 10.2113/0540001

Weiner, S., and Traub, W. (1980). X-ray diffraction study of the insoluble organic matrix of mollusk shells. *FEBS Lett.* 111, 311–316. doi: 10.1016/0014-5793(80)80817-9

Weiner, S., Traub, W., and Lowenstam, H. A. (1983). "Organic matrix in calcified exoskeleton," in *Biomineralization and Biological Metal Accumulation*, eds P. Westbroek and E. W. de Jong (Dordrecht Holland: D. Reidel Publishing Co.), 205–224. doi: 10.1007/978-94-009-7944-4_18

Wheeler, A. P. (1992a). "Mechanisms of molluscan shell formation," in *Calcification in Biological Systems*, ed. E. Bonucci (Boca Raton, FL: CRC Press), 179–216.

Wheeler, A. P. (1992b). "Phosphoproteins of oyster (*Crassostrea virginica)* shell organic matrix," in *Hard Tissue Mineralization and Demineralization*, eds S. Suga and N. Watabe (Tokyo: Springer-Verlag), 171–187. doi: 10.1007/978-4-431-68183-0_11

Wheeler, A. P., and Koskan, L. (1993). "Large scale thermally synthesized polyaspartate as a biodegradable substitute in polymer applications," in *Proceedings of the Biomolecular Materials MRS Symposium*, Vol. 292, eds C. Viney, S. K. Case, and J. H. Waite (Pittsburg), 277–283.

Wheeler, A. P., Low, K. C., and Sikes, C. S. (1991). "CaCO3 crystal-binding properties of peptides and their influence on crystal growth," in *Surface Reactive Peptides and Polymers*, eds C. S. Sikes and A. P. Wheeler (Washington, DC: American Chemical Society), 72–84. doi: 10.1021/bk-1991-0444.ch006

Wheeler, A. P., Rusenko, K. W., George, J. W., and Sikes, C. S. (1987). Evaluation of calcium binding by molluscan shell organic matrix and its relevance to biomineralization. *Comp. Biochem. Physiol.* 87B, 953–960. doi: 10.1016/0305-0491(87)90418-4

Wheeler, A. P., Rusenko, K. W., Swift, D. M., and Sikes, C. S. (1988). Regulation of *in vitro* and *in vivo* CaCO3 crystallization by fractions of oyster shell organic matrix. *Mar. Biol.* 98, 71–80. doi: 10.1007/BF00392660

Wheeler, A. P., and Sikes, C. S. (1984). Regulation of carbonate calcification by organic matrix. *Am. Zool.* 24, 933–944. doi: 10.1093/icb/24.4.933

Wheeler, A. P., and Sikes, C. S. (1989). "Matrix-crystal interactions in CaCO3 biomineralization," in *Biomineralization: Chemical and Biochemical Perspectives*, eds S. Mann, J. Webb, and R. J. P. Williams (Weinheim, FRG: VCH Publishers), 95–131.

Williams, R. J. P. (1980). "A general introduction to the special properties of the calcium ion and their deployment in biology," in *Calcium-Binding Proteins: Structure and Function*, eds F. L. Siegel, E. Carafoli, R. H. Kretsinger, D. H. MacLennan, and D. H. Wasserman (New York: Elsevier), 3–10.

Wourms, D., and Weiner, S. (1986). Mollusk shell organic matrix: Fourier transform infrared study of the acidic macromolecules. *J. Exp. Zool.* 237, 11–20. doi: 10.1002/jez.1402370104

Zdobnov, E. M., and Apweiler, R. (2001). InterProScan-an integration platform for the signature-recognition methods in InterPro. *Bioinformatics* 17, 847–848. doi: 10.1093/bioinformatics/17.9.847

Zhang, G., Fang, X., Guo, X., Li, L., Luo, R., Xu, F., et al. (2012). The oyster genome reveals stress adaptation and complexity of shell formation. *Nature* 490, 49–54. doi: 10.1038/nature11413

Conflict of Interest Statement: EF is currently employed by a company, Academic Analytics. However, her contribution to the manuscript was carried out while employed at Clemson University.

The remaining authors declare that the research was conducted in the absence of any commercial or financial relationships that could be construed as a potential conflict of interest.

Advantages of publishing in Frontiers

OPEN ACCESS
Articles are free to read for greatest visibility and readership

FAST PUBLICATION
Around 90 days from submission to decision

HIGH QUALITY PEER-REVIEW
Rigorous, collaborative, and constructive peer-review

TRANSPARENT PEER-REVIEW
Editors and reviewers acknowledged by name on published articles

Frontiers
Avenue du Tribunal-Fédéral 34
1005 Lausanne | Switzerland

Visit us: www.frontiersin.org
Contact us: frontiersin.org/about/contact

REPRODUCIBILITY OF RESEARCH
Support open data and methods to enhance research reproducibility

DIGITAL PUBLISHING
Articles designed for optimal readership across devices

FOLLOW US
@frontiersin

IMPACT METRICS
Advanced article metrics track visibility across digital media

EXTENSIVE PROMOTION
Marketing and promotion of impactful research

LOOP RESEARCH NETWORK
Our network increases your article's readership